

IMPACT FACTOR
10.057

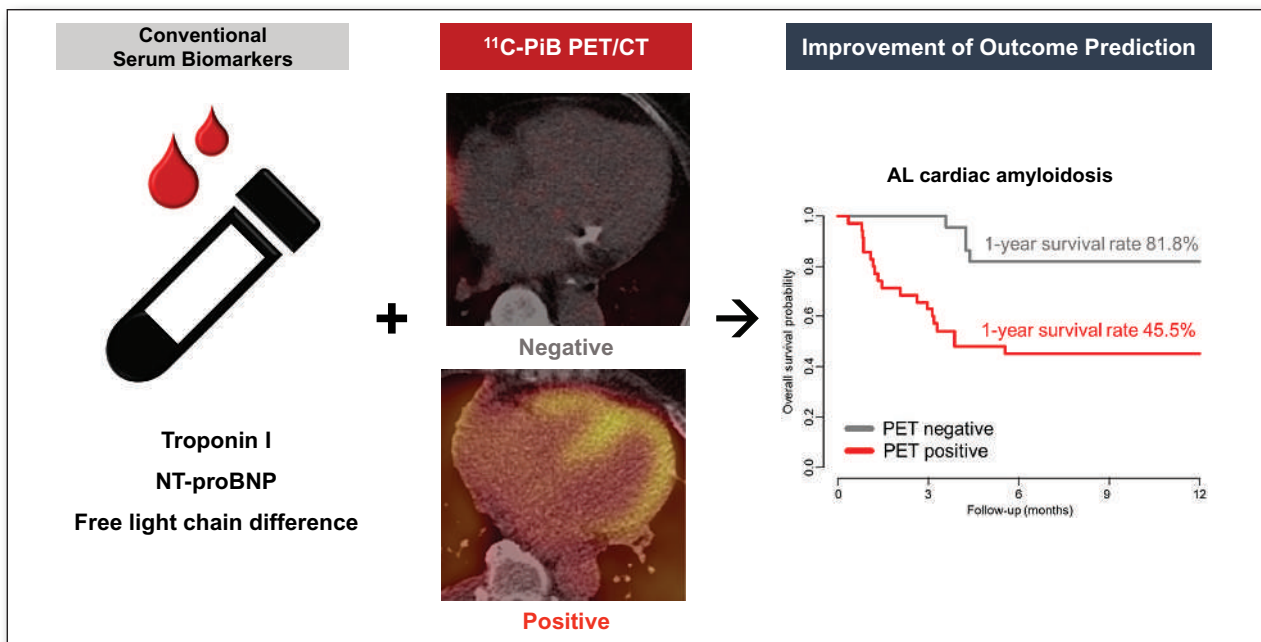
#1 NUCLEAR MEDICINE,
MOLECULAR IMAGING AND
MOLECULAR RADIOTHERAPY
JOURNAL

JNM

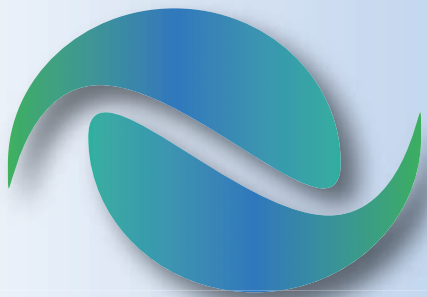
The Journal of Nuclear Medicine

FEATURED ARTICLE

Independent Prognostic Utility of ^{11}C -Pittsburgh Compound B PET in Patients with Light-Chain Cardiac Amyloidosis. You-Jung Choi et al. See page 1064.



Pretargeting + mAb: exploring PNA-mediated pretargeted radionuclides plus trastuzumab in HER2-expressing tumors. Maryam Oroujeni et al. See page 1046.



RADQUAL

Global Sources

Accuracy counts!

Avoid patient administration errors!

THE FIRST EVER simulated I-131 source using NIST traceable Ba-133.

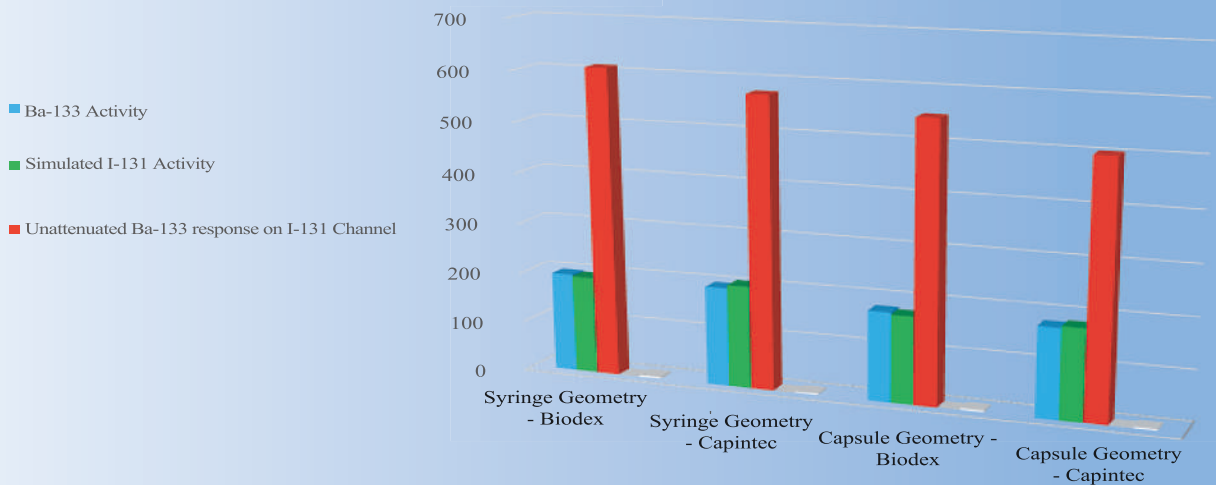
◆ Ensure that your I-131 measurements are accurate to within + or -5% utilizing RadQual's new Simulated I-131 Sources. Available in two different geometries.

◆ RadQual's Patent Pending source designs are intended to mimic a 5 cc syringe or a capsule contained in a 15ml vial.

◆ New Patent Pending Simulated I-131 Capsule design allows calibration of individual doses.



Simulated I-131 Source vs Ba-133 Source Measured Activity (uCi)



	Syringe Geometry - Biodex	Syringe Geometry - Capintec	Capsule Geometry - Biodex	Capsule Geometry - Capintec
Simulated I-131 Error	-1.57%	3.62%	-2.35%	2.02%
Ba-133 Overestimate on I-131 Channel	310%	293%	309%	282%

The design of RadQual's patent pending Simulated I-131 Source geometries better aligns the photon energy spectrum and yield, giving results within 5% of the NIST traceable Ba-133 activity, when measured on the I-131 dial setting of the dose calibrator.

Lantheus Xenon Xe-133 Gas

PROVEN | RELIABLE | TRUSTED



- Optimized vial size and delivery system¹
- Calidose[®] Dispenser System is specifically designed and FDA approved for use with Lantheus Medical Imaging Xenon-133¹
- Lantheus Medical Imaging is a leading U.S. manufacturer of Xenon-133²
- We are the longest continuous supplier of Xenon-133 since its launch in 1971³



Calidose[®] Dispenser

Specify **Lantheus Xenon Xe-133**
when ordering from your local Radiopharmacy

To order from Lantheus, contact your
Lantheus Sales Representative
or call Customer Service: 1-800-299-3431
www.lantheus.com



FIND > FIGHT > FOLLOW™

Lantheus Medical Imaging and the corporate logo are registered trademarks of Lantheus Medical Imaging, Inc. ©2022 Lantheus Medical Imaging, Inc. All rights reserved. PM-US-XE-0006 March 2022

Please see full Prescribing Information on following page.

INDICATIONS AND USAGE:

Inhalation of Xenon Xe 133 Gas has proved valuable for the evaluation of pulmonary function and for imaging the lungs. It may also be applied to assessment of cerebral flow.

CONTRAINDICATIONS:

None known.

Important Safety Information:

Adverse reactions related to the use of this agent have not been reported to date.

WARNINGS:

Xenon Xe 133 Gas delivery systems, i.e., respirators or spirometers, and

associated tubing assemblies must be leakproof to avoid loss of radioactivity into environs not specifically protected by exhaust systems.

Xenon Xe 133 adheres to some plastics and rubber and should not be allowed in tubing or respirator containers.

The unrecognized loss of radioactivity from the dose for administration may render the study non-diagnostic.

The vial stopper contains dry natural rubber latex and may cause allergic reactions in providers or patients who are sensitive to latex.

PRECAUTIONS:

General:

Xenon Xe 133, as well as other radioactive drugs, must be handled with care and appropriate safety measures should be used to minimize radiation exposure to patients and to clinical personnel.

Radiopharmaceuticals should be used only by physicians who are qualified by training and experience in the safe use and handling of radionuclides and whose experience and training have been approved by the appropriate government agency authorized to license the use of radionuclides.

XENON Xe 133 GAS

FOR DIAGNOSTIC USE

DESCRIPTION: Xenon Xe 133 Gas is supplied in a mixture of xenon gas (5%) in carbon dioxide (95%). It is contained within septum sealed glass vials and is suitable for inhalation in the diagnostic evaluation of pulmonary function and imaging, as well as assessment of cerebral blood flow. Xenon Xe 133 Gas is reactor-produced as a by-product of Uranium U235 fission. Each vial contains the labeled amount of Xenon Xe 133 radioactivity at the time of calibration. The contents of the vial are in gaseous form, contain no preservatives, and are ready for use.

Xenon Xe 133 is chemically and physiologically related to elemental Xenon, a non-radioactive monoatomic gas which is physiologically inert except for anesthetic properties at high doses.

PHYSICAL CHARACTERISTICS

Xenon Xe 133 decays by beta and gamma emissions with a half-life of 5.245 days.¹ Significant radiations which are emitted by the nuclide are listed in Table 1.

Table 1. Principal Radiation Emission Data from Xenon-133

Radiation	Mean Energy (KeV)	Mean % per Disintegration
Beta-2	100.6	99.3
Ce-K-2	45.0	53.3
Ce-L-2	75.3	8.1
Ce-M-2	79.8	1.7
Gamma-2	81.0	36.5
K _α X-ray	30.6	13.6
K _{β1} X-ray	31.0	25.3
K _{β2} X-ray	35.0	9.1

¹Kocher, David C., "Radioactive Decay Data Tables," DOE/TIC-11026, p. 138,1981.

EXTERNAL RADIATION

The specific gamma ray constant for Xenon Xe 133 is 3.6 microcoulombs/Kg-MBq-hr (0.51R/hr-mCi) at 1 cm. The first half value thickness of lead is 0.0035 cm. A range of values for the relative attenuation of the radiation emitted by this radionuclide that results from the interposition of various thicknesses of Pb is shown in Table 2. For example, the use of 0.20 cm of Pb will decrease the external radiation exposure by a factor of 1,000.

Table 2. Radiation Attenuation by Lead Shielding

cm of Pb	Radiation Attenuation Factor
0.0035	0.5
0.037	10 ⁻¹
0.12	10 ⁻²
0.20	10 ⁻³
0.29	10 ⁻⁴

To correct for physical decay of this radionuclide, the fractions that remain at selected time intervals after the time of calibration are shown in Table 3.

Table 3. Xenon Xe 133 Physical Decay Chart (Half Life 5.245 days)

Day	Fraction Remaining	Day	Fraction Remaining
0*	1.000	8	.349
1	.877	9	.302
2	.768	10	.268
3	.674	11	.235
4	.591	12	.206
5	.518	13	.181
6	.452	14	.157
7	.398		

* Calibration day

CLINICAL PHARMACOLOGY: Xenon Xe 133 is a readily diffusible gas which is neither utilized nor produced by the body. It passes through cell membranes and freely exchanges between blood and tissue. It tends to concentrate more in body fat than in blood, plasma, water or protein solutions. In the concentrations used for diagnostic purposes it is physiologically inactive. Inhaled Xenon Xe 133 Gas will enter the alveolar wall and enter the pulmonary venous circulation via the capillaries. Most of the Xenon Xe 133 that enters the circulation from a single breath is returned to the lungs and exhaled after a single pass through the peripheral circulation.

INDICATIONS AND USAGE: Inhalation of Xenon Xe 133 Gas has proved valuable for the evaluation of pulmonary function and for imaging the lungs. It may also be applied to assessment of cerebral flow.

CONTRAINDICATIONS: None known.

WARNINGS:

Xenon Xe 133 Gas delivery systems, i.e., respirators or spirometers, and associated tubing assemblies must be leakproof to avoid loss of radioactivity into the environs not specifically protected by exhaust systems.

Xenon Xe 133 adheres to some plastics and rubber and should not be allowed to stand in tubing or respirator containers. The unrecognized loss of radioactivity from the dose for administration may render the study non-diagnostic.

The vial stopper contains dry natural rubber latex and may cause allergic reactions in providers or patients who are sensitive to latex.

PRECAUTIONS:

General

Xenon Xe 133, as well as other radioactive drugs, must be handled with care and appropriate safety measures should be used to minimize radiation exposure to clinical personnel. Also, care should be taken to minimize radiation exposure to patients consistent with proper patient management.

Exhaled Xenon Xe 133 Gas should be controlled in a manner that is in compliance with the appropriate regulations of the government agency authorized to license the use of radionuclides.

Radiopharmaceuticals should be used only by physicians who are qualified by training and experience in the safe use and handling of radionuclides and whose experience and training have been approved by the appropriate government agency authorized to license the use of radionuclides.

Carcinogenesis, Mutagenesis, Impairment of Fertility

No long term animal studies have been performed to evaluate carcinogenic potential or whether Xenon Xe 133 affects fertility in males or females.

Pregnancy

Animal reproductive studies have not been conducted with Xenon Xe 133 Gas. It is also not known whether Xenon Xe 133 Gas can cause fetal harm when administered to a pregnant woman or can affect reproduction capacity. Xenon Xe 133 Gas should be given to a pregnant woman only if clearly needed.

Ideally, examination using radiopharmaceuticals, especially those elective in nature in a woman of childbearing capability, should be performed during the first few (approximately 10) days following the onset of menses.

Nursing Mothers

It is not known whether Xenon Xe 133 is excreted in human milk. Many drugs are excreted in human milk, therefore formula feedings should be substituted for breast feeding, because of the potential for adverse reactions in nursing infants.

Pediatric Use

Safety and effectiveness in the pediatric population has not been established.

Geriatric Use

Clinical studies of Xenon Xe 133 Gas did not include sufficient numbers of subjects aged 65 and over to determine whether they respond differently from younger subjects. Other reported clinical experience has not identified differences in responses between the elderly and younger patients. In general, dose selection for an elderly patient should be cautious, usually starting at the low end of the dosage range, reflecting the greater frequency of decreased hepatic, renal, or cardiac function, and of concomitant disease or other drug therapy.

ADVERSE REACTIONS: Adverse reactions related to the use of this agent have not been reported to date.

DOSAGE AND ADMINISTRATION: Xenon Xe 133 Gas is administered by inhalation from closed respirator systems or spirometers.

The suggested activity range employed for inhalation by the average adult patient (70 kg) is:

Pulmonary function including imaging: 74-1110 MBq (2-30 mCi) in 3 liters of air.

Cerebral blood flow: 370-1110 MBq (10-30 mCi) in 3 liters of air.

The patient dose should be measured by a suitable radioactivity calibration system immediately prior to administration.

RADIATION DOSIMETRY

The estimated absorbed radiation doses² to an average patient (70 kg) for pulmonary perfusion and cerebral blood flow studies from a maximum dose of 1110 MBq (30 mCi) of Xenon Xe 133 in 3 liters of air are shown in Table 4.

Table 4. Radiation Doses

	Effective Half-Time	Lungs*	Brain	Whole Body
				mGy/1110 MBq (rads/30 mCi)
Pulmonary Perfusion	2 min.	2.5 (0.25)	0.014 (0.0014)	0.027 (0.0027)
Cerebral Blood Flow	5 min.	6.3 (0.63)	0.035 (0.0035)	0.068 (0.0068)

* 99% of activity is in lungs.

²Method of Calculation: A Schema for Absorbed-Dose Calculation for Biologically Distributed Radionuclides, Supplement No. 1, MIRD pamphlet No. 1, *J. Nucl. Med.*, p.7 (1968).

HOW SUPPLIED: The Xenon Xe 133 Gas is supplied as part of the Calidose™ system, consisting of 3 mL unit dose vials and the Calidose™ dispenser for shielded dispensing.

Normally vials containing either 370 or 740 MBq (10 or 20 mCi)/vial, packed 1 vial or 5 vials per shield tube, are supplied.

The NDC number for: 10 mCi vial is 11994-127; 20 mCi vial is 11994-128.

Store at room temperature.

This radiopharmaceutical is approved for distribution to persons licensed pursuant to the Code of Massachusetts Regulations 105 CMR 120.100 for the uses listed in 105 CMR 120.547 or 120.552 or under equivalent regulations of the U.S. Nuclear Regulatory Commission, an Agreement State, or a Licensing State.

The contents of the vial are radioactive. Adequate shielding and handling precautions must be maintained.

Lantheus Medical Imaging, Inc.

331 Treble Cove Rd., N. Billerica, MA 01862 USA
For Ordering Tel. Toll Free 800-299-3431
(For Massachusetts & International, Call 978-667-9531)
All Other Business 800-362-2668

Patent: <http://www.lantheus.com/patents/index.html>

Printed in U.S.A.
515083-0719

SNMMI NEWSLINE

- 15N** Iagaru Receives First Sam Gambhir Trailblazer Award
- 15N** SNMMI Honors New Fellows for 2022
- 16N** SNMMI Image of the Year 2022: PET/CT Biomarker Predicts Post-MI Cardiac Remodeling
- 17N** New Officers for SNMMI and SNMMI-TS
- 19N** Recognition of the ABNM by the NRC
George Segall
- 20N** SNMMI Leadership Update: Opportunities for Growth in Nuclear Medicine and Molecular Imaging
Munir Ghesani
- 21N** Newsbriefs
- 23N** From the Literature

EDITOR'S PAGE

- 969** More Unacceptable Denials: Now It's PSMA-Targeted PET/CT Imaging
Johannes Czernin, Thaiza Adams, and Jeremie Calais

THE STATE OF THE ART

- 971** Molecular Imaging Findings on Acute and Long-Term Effects of COVID-19 on the Brain: A Systematic Review
Philipp T. Meyer, Sabine Hellwig, Ganna Blazhenets, and Jonas A. Hosp

STANDARD OF CARE

- 981** Alzheimer Disease: Standard of Diagnosis, Treatment, Care, and Prevention
Stefan Teipel, Deborah Gustafson, Rik Ossenkoppele, Oskar Hansson, Claudio Babiloni, Michael Wagner, Steffi G. Riedel-Heller, Ingo Kilimann, and Yi Tang

CONTINUING EDUCATION

- 986** Radiotracers to Address Unmet Clinical Needs in Cardiovascular Imaging, Part 2: Inflammation, Fibrosis, Thrombosis, Calcification, and Amyloidosis Imaging
John C. Stendahl, Jennifer M. Kwan, Darko Pucar, and Mehran M. Sadeghi

SPECIAL CONTRIBUTION

- 995** Female Authors in Nuclear Medicine Journals: A Survey from 2014 to 2020
Charline Lasnon, Gilles Girault, Rachida Lebtahi, Catherine Ansquer, Justine Lequesne, and Elske Quak

ONCOLOGY

Clinical

- 1001** ¹⁸F-FDG PET Improves Baseline Clinical Predictors of Response in Diffuse Large B-Cell Lymphoma: The HOVON-84 Study
Coreline N. Burggraaff, Jakoba J. Eertink, Pieternella J. Lugtenburg, Otto S. Hoekstra, Anne I.J. Arens, Bart de Keizer, Martijn W. Heymans, Bronno van der Holt, Sanne E. Wiegers, Simone Pieplbosch, et al.
- 1008** Molecular Signature of ¹⁸F-FDG PET Biomarkers in Newly Diagnosed Multiple Myeloma Patients: A Genome-Wide Transcriptome Analysis from the CASSIOPET Study
Jean-Baptiste Alberge, Françoise Kraeber-Bodéré, Bastien Jamet, Cyrille Touzeau, Hélène Caillon, Soraya Wuilleme, Marie-Christine Béné, Tobias Kampfenkel, Pieter Sonneveld, Mark van Duin, et al.

THERANOSTICS

Clinical

- 1014** Prognostic Value of Whole-Body PET Volumetric Parameters Extracted from ⁶⁸Ga-DOTATOC PET/CT in Well-Differentiated Neuroendocrine Tumors
Philippe Thuillier, Virginia Liberini, Serena Grimaldi, Osvaldo Rampado, Elena Gallio, Bruno De Santi, Emanuela Arvat, Alessandro Piovesan, Roberto Filippi, Ronan Abgral, et al.
- 1021** Correlation of ⁶⁸Ga-FAPI-46 PET Biodistribution with FAP Expression by Immunohistochemistry in Patients with Solid Cancers: Interim Analysis of a Prospective Translational Exploratory Study
Christine E. Mona, Matthias R. Benz, Firas Hikmat, Tristan R. Grogan, Katharina Lueckerath, Aria Razmaria, Rana Riahi, Roger Slavik, Mark D. Girgis, Giuseppe Carlucci, et al.
- 1027** The Quest for an Accurate Functional Tumor Volume with ⁶⁸Ga-DOTATATE PET/CT
Ryan P. Reddy, C. Ross Schmidlein, Romina G. Giancipoli, Audrey Mauguen, Daniel LaFontaine, Heiko Schoder, and Lisa Bodei

RADIONUCLIDE THERAPY

Basic

- 1033** Glypican-3-Targeted ²²⁷Th α -Therapy Reduces Tumor Burden in an Orthotopic Xenograft Murine Model of Hepatocellular Carcinoma
Kevin P. Labadie, Donald K. Hamlin, Aimee Kenoyer, Sara K. Daniel, Alan F. Utria, Andrew D. Ludwig, Heidi L. Kenerson, Lily Li, Jonathan G. Sham, Delphine L. Chen, et al.
- 1039** Enhancing ²²³Ra Treatment Efficacy by Anti- β 1 Integrin Targeting
Claudia Paindelli, Stefano Casarin, Feng Wang, Luis Diaz-Gomez, Jianhua Zhang, Antonios G. Mikos, Christopher J. Logothetis, Peter Friedl, and Eleonora Dondossola

1046 ■ FEATURED BASIC SCIENCE ARTICLE. Affibody-Mediated PNA-Based Pretargeted Cotreatment Improves Survival of Trastuzumab-Treated Mice Bearing HER2-Expressing Xenografts

Maryam Oroujeni, Hanna Tano, Anzhelika Vorobyeva, Yongsheng Liu, Olga Vorontsova, Tianqi Xu, Kristina Westerlund, Anna Orlova, Vladimir Tolmachev, and Amelie Eriksson Karlström

NEUROLOGY

Clinical

1052 In Vivo ¹⁸F-Flortaucipir PET Does Not Accurately Support the Staging of Progressive Supranuclear Palsy

Maura Malpetti, Sanne S. Kaalund, Kamen A. Tsvetanov, Timothy Rittman, Mayen Briggs, Kieren S.J. Allinson, Luca Passamonti, Negin Holland, P. Simon Jones, Tim D. Fryer, et al.

1058 Neuropsychologic Profiles and Cerebral Glucose Metabolism in Neurocognitive Long COVID Syndrome

Andrea Dressing, Tobias Bormann, Ganna Blazhenets, Nils Schroeter, Lea I. Walter, Johannes Thurow, Dietrich August, Hanna Hilger, Katarina Stete, Kathrin Gerstaecker, et al.

CARDIOVASCULAR

Clinical

1064 ■ FEATURED ARTICLE OF THE MONTH. Independent Prognostic Utility of ¹¹C-Pittsburgh Compound B PET in Patients with Light-Chain Cardiac Amyloidosis

You-Jung Choi, Youngil Koh, Hyun-Jung Lee, In-Chang Hwang, Jun-Bean Park, Yeonyee E. Yoon, Hack-Lyoung Kim, Hyung-Kwan Kim, Yong-Jin Kim, Goo-Yeong Cho, et al.

PULMONARY/COVID

Clinical

1070 Lung Scintigraphy for Pulmonary Embolism Diagnosis in COVID-19 Patients: A Multicenter Study

Pierre-Yves Le Roux, Pierre-Benoit Bonnefoy, Achraf Bahloul, Benoit Denizot, Bertrand Barres, Caroline Moreau-Triby, Astrid Girma, Amandine Pallardy, Quentin Ceyrat, Laure Sarda-Mantel, et al.

1075 Lung Dose Measured on Postradioembolization ⁹⁰Y PET/CT and Incidence of Radiation Pneumonitis

Martina Stella, Rob van Rooij, Marnix G.E.H. Lam, Hugo W.A.M. de Jong, and Arthur J.A.T. Braat

ENDOCRINOLOGY

Clinical

1081 Diagnostic Performance of Cervical Ultrasound, ^{99m}Tc-Sestamibi Scintigraphy, and Contrast-Enhanced ¹⁸F-Fluorocholine PET in Primary Hyperparathyroidism

Vincent Boudousq, Nicolas Guignard, Olivier Gilly, Benjamin Chambert, Adel Mamou, Olivier Moranne, Mathilde Zemmour, Haitham Sharara, and Benjamin Lallemand

AI/ADVANCED IMAGE ANALYSIS

Clinical

1087 Improved Prognosis of Treatment Failure in Cervical Cancer with Nontumor PET/CT Radiomics

Tahir I. Yusufaly, Jingjing Zou, Tyler J. Nelson, Casey W. Williamson, Aaron Simon, Meenakshi Singhal, Hannah Liu, Hank Wong, Cheryl C. Saenz, Jyoti Mayadev, et al.

RADIOBIOLOGY/DOSIMETRY

Clinical

1094 Biodistribution and Radiation Dosimetry of Intraperitoneally Administered ¹²⁴I-Omburtamab in Patients with Desmoplastic Small Round Cell Tumors

Milan Grkovski, Shakeel Modak, Pat B. Zanzonico, Jorge A. Carrasquillo, Steven M. Larson, John L. Humm, and Neeta Pandit-Taskar

Translational

1101 Radioembolization Dosimetry with Total-Body ⁹⁰Y PET

Gustavo Costa, Benjamin Spencer, Negar Omidvari, Cameron Foster, Michael Rusnak, Heather Hunt, Denise T. Caudle, Rex T. Pillai, Catherine Tram Vu, and Emilie Roncali

Basic

1108 Toward a Patient-Specific Traceable Quantification of SPECT/CT-Based Radiopharmaceutical Distributions

Anna-Lena Theisen, Michael Lassmann, and Johannes Tran-Gia

SPECIAL CONTRIBUTION

1117 Proceedings: PET Drugs—A Workshop on Inspections Management and Regulatory Considerations

Sue Bunning, Christopher Ignace, Steve Mattmuller, Sally W. Schwarz, Peter J.H. Scott, Henry F. VanBrocklin, and Steven S. Zigler on behalf of the Coalition of Drug Manufacturers

LETTERS TO THE EDITOR

1124 Tumor Sink Effect: Myth or Reality?

Andrei Gafita, Jeremie Calais, Wolfgang P. Fendler, and Matthias Eiber

1124 Thoughts on “Tumor Sink Effect in ⁶⁸Ga-PSMA-11 PET: Myth or Reality?”

Bastiaan M. Privé, Steffie M.B. Peters, Maike J.M. Uijen, Marcel J.R. Janssen, Willemijn A.M. van Gemert, Michael C. Kreissl, Samer Ezzidin, Mark W. Konijnenberg, and James Nagarajah

DEPARTMENTS

10A This Month in JNM

13A Recruitment

1000 Errata

The Official Publication of **SNMMI**

Publications Committee

TODD E. PETERSON, PhD, FSNMMI
Chair

CAROLYN ANDERSON, PhD, FSNMMI
PAIGE B. BENNETT, MD
JOYITA DUTTA, PhD
MICHAEL M. GRAHAM, PhD, MD, FSNMMI
HOSSEIN JADVAR, MD, PhD, FACNM,
FSNMMI
STEVEN M. LARSON, MD, FACNM
HEINRICH R. SCHELBERT, MD, PhD, FSNMMI
HEIKO SCHÖDER, MD, MBA
DAVID M. SCHUSTER, MD
JESSICA WILLIAMS, CNMT, RT(N),
FSNMMI-TS
HARVEY A. ZIESSMAN, MD, FSNMMI

Ex officio

JOHANNES CZERNIN, MD
KATHY S. THOMAS, MHA, CNMT,
PET, FSNMMI-TS
HENRY F. VANBROCKLIN, PhD, FSNMMI
RICHARD L. WAHL, MD, FACNM

Associate Director of Communications

SUSAN ALEXANDER

Senior Copyeditor

SUSAN NATH

Senior Publications & Marketing Service Manager

STEVEN KLEIN

Editorial Production Manager

PAULETTE MCGEE

Editorial Project Manager

MARK SUMIMOTO

Director of Communications

REBECCA MAXEY

CEO

VIRGINIA PAPPAS

MISSION STATEMENT: *The Journal of Nuclear Medicine* advances the knowledge and practice of molecular imaging and therapy and nuclear medicine to improve patient care through publication of original basic science and clinical research.

JNM (ISSN 0161-5505 [print]; ISSN 2159-662X [online]) is published monthly by SNMMI, 1850 Samuel Morse Drive, Reston, VA 20190-5316. Periodicals postage is paid at Herndon, VA, and additional mailing offices. Postmaster, send address changes to *The Journal of Nuclear Medicine*, 1850 Samuel Morse Drive, Reston, VA 20190-5316. The costs of publication of all nonsolicited articles in *JNM* were defrayed in part by the payment of page charges. Therefore, and solely to indicate this fact, these articles are hereby designated "advertisements" in accordance with 18 USC section 1734.

DISCLOSURE OF COMMERCIAL INTEREST: Johannes Czernin, MD, editor-in-chief of *The Journal of Nuclear Medicine*, has indicated that he is a founder of Sofie Biosciences and holds equity in the company and in intellectual property invented by him, patented by the University of California, and licensed to Sofie Biosciences. He is also a founder and board member of Trethera Therapeutics and holds equity in the company and in intellectual property invented by him, patented by the University of California, and licensed to Triangle. He also serves on the medical advisory board of Actinium Pharmaceuticals and on the scientific advisory boards of POINT Biopharma, RayzeBio, and Jubilant Pharma and is a consultant for Amgen. No other potential conflicts of interest were reported. Manuscripts submitted to *JNM* with potential conflicts are handled by a guest editor.

EDITORIAL COMMUNICATIONS should be sent to: Editor-in-Chief, Johannes Czernin, MD, *JNM* Office, SNMMI, 1850 Samuel Morse Drive, Reston, VA 20190-5316. Phone: (703) 326-1185; Fax: (703) 708-9018. To submit a manuscript, go to <https://submit-jnm.snmjournals.org>.

BUSINESS COMMUNICATIONS concerning permission requests should be sent to the publisher, SNMMI, 1850 Samuel Morse Drive, Reston, VA 20190-5316; (703) 708-9000; home page address: jnm.snmjournals.org. Subscription requests and address changes should be sent to Membership Department, SNMMI at the address above. Notify the Society of change of address and telephone number at least 30 days before date of issue by sending both the old and new addresses. Claims for copies lost in the mail are allowed within 90 days of the date of issue. Claims are not allowed for issues lost as a result of insufficient notice of change of address. For information on advertising, contact Team SNMMI (Kevin Dunn, Rich Devanna, and Charlie Meitner; (201) 767-4170; fax: (201) 767-8065; TeamSNMMI@cunnasso.com). Advertisements are subject to editorial approval and are restricted to products or services pertinent to nuclear medicine. Closing date is the first of the month preceding the date of issue.

INDIVIDUAL SUBSCRIPTION RATES for the 2022 calendar year are \$603 within the United States and Canada; \$648 elsewhere. Make checks payable to the SNMMI. CPC IPM Sales Agreement No. 1415158. Sales of individual back copies from 1999 through the current issue are available for \$60 at <http://www.snmgi.org/subscribe> (subscriptions@snmgi.org; fax: (703) 667-5134). Individual articles are available for sale online at <http://jnm.snmjournals.org>.

COPYRIGHT © 2022 by the Society of Nuclear Medicine and Molecular Imaging. All rights reserved. No part of this work may be reproduced or translated without permission from the copyright owner. Individuals with inquiries regarding permission requests, please visit <http://jnm.snmjournals.org/site/misc/permission.xhtml>. Because the copyright on articles published in *The Journal of Nuclear Medicine* is held by the Society, each author of accepted manuscripts must sign a statement transferring copyright (available for downloading at <http://jnm.snmjournals.org/site/misc/ifora.xhtml>). See Information for Authors for further explanation (available for downloading at <http://www.snmjournals.org/site/misc/ifora.xhtml>).

The ideas and opinions expressed in *JNM* do not necessarily reflect those of the SNMMI or the Editors of *JNM* unless so stated. Publication of an advertisement or other product mentioned in *JNM* should not be construed as an endorsement of the product or the manufacturer's claims. Readers are encouraged to contact the manufacturer with any questions about the features or limitations of the products mentioned. The SNMMI does not assume any responsibility for any injury or damage to persons or property arising from or related to any use of the material contained in this journal. The reader is advised to check the appropriate medical literature and the product information currently provided by the manufacturer of each drug to be administered to verify the dosage, the method and duration of administration, and contraindications.

EDITOR-IN-CHIEF

Johannes Czernin, MD
University of California at Los Angeles
Los Angeles, California

IMMEDIATE PAST EDITOR

Dominique Delbeke, MD, PhD
Vanderbilt University Medical Center
Nashville, Tennessee

NEWSLINE EDITOR

Harvey A. Ziessman, MD
Takoma Park, Maryland

ASSOCIATE EDITORS, CONTINUING EDUCATION

Heiko Schöder, MD
Memorial Sloan Kettering Cancer Center
New York, New York

H. William Strauss, MD
Memorial Sloan Kettering Cancer Center
New York, New York

ASSOCIATE EDITORS

Ramsey Derek Badawi, PhD

UC Davis Medical Center

Sacramento, California

Henryk Barthel, MD, PhD

Leipzig University

Leipzig, Germany

Frank M. Bengel, MD

Hannover Medical School

Hannover, Germany

Lisa Bodei, MD, PhD

Memorial Sloan Kettering Cancer Center

New York, New York

Irene Buvat, PhD

Université Paris Sud

Orsay, France

Jérémie Calais, MD

University of California at Los Angeles

Los Angeles, California

Marcelo F. Di Carli, MD

Brigham and Women's Hospital

Boston, Massachusetts

Alexander E. Drzezga

University Hospital of Cologne

Cologne, Germany

Jan Grimm, MD, PhD

Memorial Sloan Kettering Cancer Center

New York, New York

Ken Herrmann, MD, MBA

Universitätsklinikum Essen

Essen, Germany

Thomas A. Hope, MD

University of California, San Francisco

San Francisco, California

Lale Kostakoglu, MD, MPH

University of Virginia Health System

Charlottesville, Virginia

Jason S. Lewis, PhD

Memorial Sloan Kettering Cancer Center

New York, New York

David A. Mankoff, MD, PhD

University of Pennsylvania

Philadelphia, Pennsylvania

Wolfgang Weber, MD

Technical University of Munich

München, Germany

SERIES EDITOR, FOCUS ON MI

Carolyn J. Anderson, PhD

University of Missouri

Columbia, Missouri

SERIES EDITOR, HOT TOPICS

Heinrich R. Schelbert, MD, PhD

University of California at Los Angeles

Los Angeles, California

CONSULTING EDITORS

Nancy Knight, PhD

University of Maryland School of Medicine

Baltimore, Maryland

Barry A. Siegel, MD

Mallinckrodt Institute of Radiology

St. Louis, Missouri

Arnold M. Strashun, MD

SUNY Downstate Medical Center

Scarsdale, New York

ASSOCIATE EDITORS (INTERNATIONAL)

Gerald Antoch, MD

Dusseldorf, Germany

Richard P. Baum, MD, PhD

Bad Berka, Germany

Ambros J. Beer, MD

Ulm, Germany

Francois Benard, MD

Vancouver, Canada

Thomas Beyer, PhD

Vienna, Austria

Andreas K. Buck, MD

Würzburg, Germany

Ignasi Carrió, MD

Barcelona, Spain

June-Key Chung, MD

Seoul, Korea

Stefano Fanti, MD

Bologna, Italy

Markus Hacker, MD

Wien, Austria

Rodney J. Hicks, MD

Melbourne, Australia

Michael S. Hofman, MBBS

Melbourne, Australia

Ora Israel, MD

Haifa, Israel

Andreas Kjaer, MD, PhD, DMSc

Copenhagen, Denmark

Adriaan A. Lammertsma, PhD

Amsterdam, The Netherlands

Michael Lassman, PhD

Würzburg, Germany

Helmut R. Mäcke, PhD

Freiburg, Germany

Wim J.G. Oyen, MD, PhD

Milan, Italy

John O. Prior, MD, PhD

Lausanne, Switzerland

Osman Ratib, MD, PhD

Geneva, Switzerland

Mike Sathekge, MBChB, MMed, PhD

Pretoria, South Africa

Markus Schwaiger, MD

München, Germany

Andrew M. Scott, MD

Heidelberg, Australia

Nagara Tamaki, MD, PhD

Kyoto, Japan

Jia-He Tian, PhD

Beijing, China

Mei Tian, MD, PhD

Hangzhou, China

EDITORIAL CONSULTANTS

Martin S. Allen-Auerbach, MD

Los Angeles, California

Magnus Dahlbom, PhD

Los Angeles, California

Andrew Quon, MD

Los Angeles, California

Christiaan Schiepers, MD, PhD

Los Angeles, California

Daniel H. Silverman, MD, PhD

Los Angeles, California

Roger Slavik, PhD

Winterthur, Switzerland

EDITORIAL BOARD

Diane S. Abou, PhD

St. Louis, Missouri

Valentina Ambrosini, MD, PhD

Bologna, Italy

Norbert Avril, MD

Cleveland, Ohio

Shadfar Bahri

Los Angeles, California

Jacques Barbet, PhD

Saint-Herbalin, France

Bradley Jay Beattie, PhD

New York, New York

Matthias Richard Benz, MD

Los Angeles, California

Pradeep Bhambhvani, MD

Birmingham, Alabama

Angelika Bischof-Delaloye, MD

Lausanne, Switzerland

Christina Bluemel, MD

Würzburg, Germany

Ronald Boellaard, PhD

Groningen, The Netherlands

Nicolaas Bohnen, MD

Ann Arbor, Michigan

Wesley E. Bolch, PhD

Gainesville, Florida

Elias H. Botvinick, MD

San Francisco, California

Winfried Brenner, MD, PhD

Berlin, Germany

Richard C. Brunken, MD

Cleveland, Ohio

Ralph Buchert, PhD

Hamburg, Germany

Alfred Buck, MD

Menzingen, Switzerland

Denis B. Buxton, PhD

Bethesda, Maryland

Weibo Cai, PhD

Madison, Wisconsin

Federico Caobelli, MD

Basel, Switzerland

Giuseppe Carlucci, PhD

Los Angeles, California

Richard E. Carson, PhD

New Haven, Connecticut

Paolo Castellucci, MD

Bologna, Italy

Francesco Ceci, MD, PhD

Turin, Italy

Juliano J. Cerci

Curitiba, Brazil

Delphine Chen, MD

Seattle, Washington

Xiaoyuan Chen, PhD

Singapore

Simon R. Cherry

Davis, California

Arturo Chiti, MD

Rozzano, Italy

Peter M. Clark, PhD

Los Angeles, California

Christian Cohade, MD

Montreal, Canada

Ekaterina (Kate) Dadachova, PhD

Saskatoon, Canada

Issa J. Dahabreh, MD

Boston, Massachusetts

Heike Elisabeth Daldrop-Link, MD, PhD

Stanford, California

Farrokh Dehdashti, MD

St. Louis, Missouri

Robert C. Delgado-Bolton, MD, PhD

Logroño, Spain

Thorsten Derlin, MD

Hannover, Germany

Elisabeth G.E. de Vries, PhD

Groningen, The Netherlands

David W. Dick, PhD

Iowa City, Iowa

Vasken Dilsizian, MD

Baltimore, Maryland

Sharmila Dorbala, MBBS

Lexington, Massachusetts

Jacob Dubroff, MD, PhD

Philadelphia, Pennsylvania

Janet F. Eary, MD

Bethesda, Maryland

W. Barry Edwards, PhD

Columbia, Missouri

Matthias Eiber, MD

Munich, Germany

David Eidelberg, MD

Manhasset, New York

Georges El Fakhri, PhD

Boston, Massachusetts

Peter J. Ell, MD

London, United Kingdom

Keigo Endo, MD

Nantan, Japan

MI-5660.TA.JV | © 06.2022 Siemens Healthcare GmbH
Clinical image courtesy of Queen Elizabeth Hospital, Birmingham, United Kingdom.

Introducing Symbia Pro.specta SPECT/CT with myExam Companion

Modernize to MAXIMIZE



Take your nuclear medicine department into the future with intelligent SPECT/CT imaging. Symbia Pro.specta™ with myExam Companion gives you the power of more.

Redefine performance with new standards for SPECT/CT

Automatic SPECT motion correction and up to 64-slice CT enable faster scanning at the highest image quality.¹

Reach your full potential with a smart workflow

An intuitive interface fully integrates SPECT and CT to help you consistently achieve high-quality, reproducible results.

Achieve optimized imaging from dedicated clinical tools

Transform your general SPECT/CT into a specialized camera that optimizes imaging for cardiology, neurology, oncology, and more.

¹ Based on competitive literature at time of publication. Data on file.

Symbia Pro.specta SPECT/CT is not commercially available in all countries.

Due to regulatory reasons, its future availability cannot be guaranteed.

Please contact your local Siemens Healthineers organization for further details.

Learn more at [siemens-healthineers.com/symbiaprospecta](https://www.siemens-healthineers.com/symbiaprospecta)

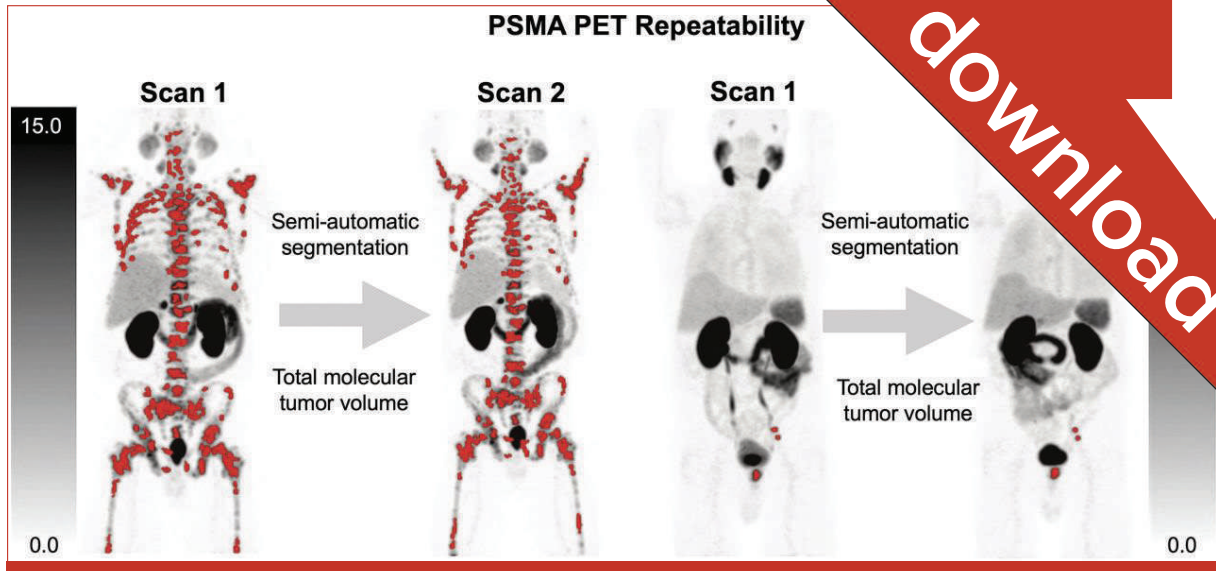
SIEMENS
Healthineers

EDITORIAL BOARD, continued

Einat Even-Sapir, MD, PhD
Tel Aviv, Israel
Frederic H. Fahey, DSc
Boston, Massachusetts
Melpomeni Fani, PhD, MSc
Basel, Switzerland
Wolfgang Peter Fendler, MD
Essen, Germany
James W. Fletcher, MD
Indianapolis, Indiana
Amy M. Fowler, MD, PhD
Madison, Wisconsin
Kirk A. Frey, MD, PhD
Ann Arbor, Michigan
Andrei Gafita
Los Angeles, California
Victor H. Gerbaudo, PhD, MSHCA
Boston, Massachusetts
Frederik L. Giesel, MD, PhD, MBA
Düsseldorf, Germany
Serge Goldman, MD, PhD
Brussels, Belgium
Stanley J. Goldsmith, MD
New York, New York
Martin Gotthardt, MD, PhD
Nijmegen, The Netherlands
Michael Graham, MD, PhD
Iowa City, Iowa
David Groheux, MD, PhD
Paris, France
Uwe A. Haberkorn, MD
Heidelberg, Germany
Mathieu Hatt, PhD, HDR
Brest, France
Wolf-Dieter Heiss, MD
Cologne, Germany
Karl Herholz, MD
Manchester, United Kingdom
Thomas F. Heston, MD
Las Vegas, Nevada
John M. Hoffman, MD
Salt Lake City, Utah
Carl K. Hoh, MD
San Diego, California
Jason P. Holland, DPhil
Zurich, Switzerland
Roland Hustinx, MD, PhD
Liege, Belgium
Andrei H. Iagaru, MD
Stanford, California
Masanori Ichise, MD
Chiba, Japan
Heather A. Jacene, MD
Boston, Massachusetts
Hossein Jadvar, MD, PhD, MPH, MBA
Los Angeles, California
Francois Jamar, MD, PhD
Brussels, Belgium
Jaе Min Jeong, PhD
Seoul, Korea
John A. Katzenellenbogen, PhD
Urbana, Illinois
Kimberly A. Kelly, PhD
Charlottesville, Virginia
Laura M. Kenny, MD, PhD
London, United Kingdom
Fabian Kiessling, MD
Aachen, Germany
E. Edmund Kim, MD, MS
Orange, California
Francoise Kraeber-Bodéré, MD, PhD
Nantes, France
Clemens Kratochwil, MD
Heidelberg, Germany
Kenneth A. Krohn, PhD
Portland, Oregon
Brenda F. Kurland, PhD
Pittsburgh, Pennsylvania
Constantin Lapa, MD
Augsburg, Germany
Suzanne E. Lapi, PhD
Birmingham, Alabama
Steven M. Larson, MD
New York, New York
Dong Soo Lee, MD, PhD
Seoul, Korea
Jeffrey Leyton, PhD
Sherbrooke, Canada
Hannah M. Linden, MD
Seattle, Washington

Martin A. Lodge, PhD
Baltimore, Maryland
Katharina Lückcrath, PhD
Los Angeles, California
Susanne Lütje, MD, PhD
Bonn, Germany
Umar Mahmood, MD, PhD
Boston, Massachusetts
H. Charles Manning, PhD
Nashville, Tennessee
Giuliano Mariani, MD
Pisa, Italy
Chester A. Mathis, PhD
Pittsburgh, Pennsylvania
Alan H. Maurer, MD
Philadelphia, Pennsylvania
Jonathan McConathy, MD, PhD
Birmingham, Alabama
Alexander J.B. McEwan, MD
Edmonton, Canada
Yusuf Menda, MD
Iowa City, Iowa
Philipp T. Meyer, MD, PhD
Freiburg, Germany
Matthias Miederer, MD
Mainz, Germany
Erik Mittra, MD, PhD
Portland, Oregon
Christine E. Mona, PhD
Los Angeles, California
Dae Hyuk Moon, MD
Seoul, Korea
Jennifer Murphy, PhD
Los Angeles, California
Helen Nadel, MD, FRCPC
Stanford, California
Matthias Nahrendorf, MD, PhD
Boston, Massachusetts
Yuji Nakamoto, MD, PhD
Kyoto, Japan
David A. Nathanson, PhD
Los Angeles, California
Sridhar Nimmagadda, PhD
Baltimore, Maryland
Egbert U. Nitzsche, MD
Aarau, Switzerland
Medhat M. Osman, MD, PhD
Saint Louis, Missouri
Christopher J. Palestro, MD
New Hyde Park, New York
Miguel Hernandez Pampaloni, MD, PhD
San Francisco, California
Neeta Pandit-Taskar, MD
New York, New York
Michael E. Phelps, PhD
Los Angeles, California
Gerold Porenta, MD, PhD
Vienna, Austria
Sophie Poty, PhD
Montpellier, France
Edwin (Chuck) Pratt, PhD, MS Eng
New York, New York
Daniel A. Pryma, MD
Philadelphia, Pennsylvania
Valery Radchenko, PhD
Vancouver, Canada
Caius G. Radu, MD
Los Angeles, California
Isabel Rauscher, MD
Munich, Germany
Nick S. Reed, MBBS
Glasgow, United Kingdom
Mark Rijpkema, PhD
Nijmegen, The Netherlands
Steven P. Rowe, MD, PhD
Baltimore, Maryland
Mehran Sadeghi, MD
West Haven, Connecticut
Orazio Schillaci, MD
Rome, Italy
Charles Ross Schmidlein, PhD
New York, New York
David M. Schuster, MD
Atlanta, Georgia
Travis Shaffer, PhD
Stanford, California
Sai Kiran Sharma, PhD
New York, New York
Anthony F. Shields, MD, PhD
Detroit, Michigan

Barry L. Shulkin, MD, MBA
Memphis, Tennessee
Yu Shyr, PhD
Nashville, Tennessee
Albert J. Sinusas, MD
New Haven, Connecticut
Riemer H.J.A. Slart, MD, PhD
Groningen, The Netherlands
Piotr Slomka, PhD, FACC
Los Angeles, California
Ida Sonni, MD
Los Angeles, California
Michael G. Stabin, PhD
Richland, Washington
Lisa J. States, MD
Philadelphia, Pennsylvania
Sven-Erik Strand, PhD
Lund, Sweden
Rathan M. Subramaniam, MD, PhD, MPH
Dunedin, New Zealand
John Sunderland, PhD
Iowa City, Iowa
Suleman Surti, PhD
Philadelphia, Pennsylvania
Julie Sutcliffe, PhD
Sacramento, California
Laura H. Tang, MD, PhD
New York, New York
Ukihide Tateishi, MD, PhD
Tokyo, Japan
James T. Thackeray, PhD
Hannover, Germany
Mathew L. Thakur, PhD
Philadelphia, Pennsylvania
Alexander Thiel, MD
Montreal, Canada
Daniel L.J. Thorek, PhD
St. Louis, Missouri
David W. Townsend, PhD
Singapore
Timothy Turkington, PhD
Durham, North Carolina
Gary A. Ulaner, MD, PhD
Irvine, California
David Ulmert, MD, PhD
Los Angeles, California
Christopher H. van Dyck, MD
New Haven, Connecticut
Douglas Van Nostrand, MD
Washington, District of Columbia
Patrick Veit-Haibach, MD
Toronto, Canada
Nerissa Viola-Villegas, PhD
Detroit, Michigan
John R. Votaw, PhD
Atlanta, Georgia
Richard L. Wahl, MD
St. Louis, Missouri
Anne Marie Wallace, MD
La Jolla, California
Martin A. Walter, MD
Geneva, Switzerland
Rudolf A. Werner, MD
Wuerzburg, Germany
Andreas G. Wibmer, MD
New York, New York
Anna M. Wu, PhD
Duarte, California
Randy Yeh, MD
New York, New York
Hyewon (Helen) Youn, PhD
Seoul, Korea
Pat B. Zanzonico, PhD
New York, New York
Brian M. Zeglis, PhD
New York, New York
Robert Zeiser, MD
Freiburg, Germany
Hong Zhang, MD, PhD
Hangzhou, China
Hongming Zhuang, MD, PhD
Philadelphia, Pennsylvania
Sibylle I. Ziegler, PhD
Munich, Germany
ASSISTANT TO THE EDITOR
Joshua N. Wachtel
Los Angeles, California



Reflection, Renewal and Resolve

SATOSHI MINOSHIMA, MD, PhD; VALUE INITIATIVE BOARD CHAIR

This has been an exciting quarter for the community of Nuclear Medicine and Molecular Imaging. New PSMA-targeting therapy and diagnostic agents have been approved for clinical use for the treatment and management of patients suffering from prostate cancer. The SNMMI has been a forefront of advancing theranostics, and we, as the community of physicians, scientists, healthcare workers, industry, staff, and all stakeholders, are truly excited about our new value of patient care. Thank you so much for your support of the SNMMI Value Initiative.

To further enhance our efforts, the SNMMI is conducting a strategic planning effort for the next 3-5 years, one that ties directly to the work of the Value Initiative's five domains. Through 21 interviews with key leaders and stakeholders, physicians, scientists, technologists, and industry; 18 qualitative responses to an environmental scan; and a full membership survey, a team of SNMMI leaders consolidated the findings to flesh out the needs, trends, and priorities of the field moving forward.

Some key findings and observations reinforced the core work of the Value Initiative. Throughout the strategic planning process, themes emerged around our continued need to improve quality of practice, research

and discovery, the workforce pipeline, advocacy, and outreach. The field is thriving, and we have an abundance of opportunity.

The VI and staff have worked hard to increase the visibility of Nuclear Medicine with the public and have had some excellent mainstream media coverage, and work remains to be done. We also received a great deal of feedback that we need to continue to find ways to communicate to many audiences about the work we are doing, showcasing our progress.

The SWOT analysis identified the ongoing need for not only technical reimbursement, but also physician reimbursement, and agility as the field grows, and more Nuclear Medicine physicians engage in the practice. Expansion of therapies and theranostics is a clear trend. SNMMI has a wealth of resources in theranostics and will continue to consolidate and make them easily accessible on the [Radiopharmaceutical Therapy Central](#) website. Training, education, development and expansion of the workforce, and patient-centered care and practice for clinicians are top needs as nuclear medicine advances. Collaboration throughout the field with other societies, industry, and beyond was another big theme. Our work with other societies and outreach to referring physicians

Continued on page 12. See Reflection, Renewal, Resolve.

COVID-19 and the brain: Meyer and colleagues provide a systematic review of current literature on the applications and findings of molecular imaging techniques in elucidating the effects of COVID-19 on the human brain. *Page 971*

Alzheimer disease standards of care: Teipel and colleagues summarize standards of diagnosis (including advances in molecular imaging), treatment, care, and prevention of Alzheimer disease. *Page 981*

Radiotracers in cardiovascular imaging: Stendahl and colleagues highlight current and promising radiotracers for imaging cardiovascular inflammation, thrombosis, fibrosis, calcification, and amyloidosis, with a focus on addressing unmet clinical needs. *Page 986*

Women authors in nuclear medicine journals: Lasnon and colleagues evaluate recent trends in the gender distribution of first and last authorship of articles published in nuclear medicine journals. *Page 995*

PET and DLBCL response prediction: Burggraaff and colleagues explore the value added by baseline metabolic tumor volume and interim PET to conventional prognostic indices for 2-y progression-free survival in diffuse large B-cell lymphoma and investigate optimal interim PET response criteria. *Page 1001*

¹⁸F-FDG PET molecular signatures in MM: Alberge and colleagues identify gene expression patterns associated with prognostic ¹⁸F-FDG PET biomarkers in newly diagnosed multiple myeloma patients included in the prospective multicenter CASSIOPET study. *Page 1008*

PET tumor burden and NET prognosis: Thuillier and colleagues investigate the prognostic value of somatostatin receptor tumor burden on ⁶⁸Ga-DOTATOC PET/CT in patients with well-differentiated neuroendocrine tumors. *Page 1014*

FAPi PET versus FAP IHC: Mona and colleagues report on the spectrum of fibroblast-activation protein expression across various cancers by immunohistochemistry and explore whether ⁶⁸Ga-FAP inhibitor-46 PET biodistribution accurately reflects FAP expression from resected cancer and noncancer specimens. *Page 1021*

⁶⁸Ga-DOTATATE PET FTV in NETS: Reddy and colleagues compare multiple PET functional tumor volume computational approaches and morphologic volume measurements to identify a candidate for incorporation into ⁶⁸Ga-DOTATATE PET FTV studies to more accurately assess neuroendocrine tumor burden. *Page 1027*

GPC3-targeted ²²⁷Th therapy for HCC: Labadie and colleagues describe the development and in vivo efficacy of a ²²⁷Th-labeled glypican-3-targeting antibody conjugate for treatment of hepatocellular carcinoma in an orthotopic murine model. *Page 1033*

Enhancing ²²³Ra efficacy: Paindelli and colleagues test the effect of a cotargeting strategy combining ²²³Ra and anti-β1 integrin antibody treatment in PC3 and C4-2B prostate cancer cell models expressing high and low β1 integrin levels. *Page 1039*

Pretargeting and trastuzumab combination: Oroujeni and colleagues test in mice a combination of Affibody-based peptide nucleic acid-mediated pretargeted radionuclide therapy and trastuzumab treatment of HER2-expressing xenografts to extend survival. *Page 1046*

¹⁸F-flortaucipir PET in PSP: Malpetti and colleagues use a data-driven approach to determine whether postmortem pathologic staging in progressive supranuclear palsy can be reproduced in vivo with ¹⁸F-flortaucipir PET. *Page 1052*

Cognition and ¹⁸F-FDG PET in long COVID: Dressing and colleagues assess cognitive profiles and the potential of regional cerebral glucose metabolism as a biomarker of neuronal function in outpatients with long-term neurocognitive symptoms after COVID-19. *Page 1058*

¹¹C-PiB PET in AL cardiac amyloidosis: Choi and colleagues determine the independent prognostic value of ¹¹C-Pittsburgh compound B PET/CT in staging and risk assessment in patients with amyloid light-chain cardiac amyloidosis. *Page 1064*

V/P scintigraphy in COVID-19: Le Roux and colleagues evaluate the role of ventilation imaging when lung scintigraphy is performed because of suspected pulmonary embolism in COVID-19

patients and describe associated practices and imaging findings in this population. *Page 1070*

⁹⁰Y radioembolization lung dose and toxicity: Stella and colleagues characterize the relationship between lung dose and eventual occurrence of radiation pneumonitis in patients after ⁹⁰Y-microsphere liver radioembolization. *Page 1075*

¹⁸F-FCH PET/CT in PHPT: Boudousq and colleagues compare contrast-enhanced ¹⁸F-fluorocholine PET/CT, cervical ultrasonography, and conventional scintigraphic imaging, combined and individually, for preoperative localization of hyperfunctional parathyroids in patients with primary hyperparathyroidism. *Page 1081*

PET/CT cervical cancer radiomics: Yusufaly and colleagues develop and validate a model incorporating nontumor PET/CT radiomics, including whole-body features, to predict treatment outcomes in patients with previously untreated locoregionally advanced cervical cancer. *Page 1087*

¹²⁴I-Omburtamab in DSRCT: Grkovski and colleagues use serial PET/CT to assess the pharmacokinetics, biodistribution, and radiation dosimetry of ¹²⁴I-omburtamab administered intraperitoneally in patients with desmoplastic small round cell tumors. *Page 1094*

⁹⁰Y total-body PET TARE dosimetry: Costa and colleagues assess the suitability of the total-body PET/CT uEXPLORER for imaging ⁹⁰Y-microsphere transarterial radioembolization and investigate possible improvements in associated PET-based dosimetry. *Page 1101*

Toward patient-specific kidney phantoms: Theisen and colleagues present a methodology for designing single-compartment kidney phantoms for SPECT/CT that mimic inhomogeneous spatial activity distributions, with potential for reducing uncertainties in planning and monitoring individualized radionuclide therapies. *Page 1108*

PET drug workshop: Bunning and participants detail the proceedings of a workshop on inspections management and regulatory considerations for radiopharmaceuticals held in 2020 at the U.S. Food and Drug Administration. *Page 1117*

Be Recognized as an **SNMMI** **Designated Radiopharmaceutical Therapy Center of Excellence**

SNMMI designated Centers of Excellence in Radiopharmaceutical Therapy are:

- Well-integrated into a patient's care pathway
- Led by physicians appropriately trained in nuclear medicine
- Staffed by highly qualified therapy teams
- Designed to meet strict regulatory, training, qualification, experience, and performance criteria

Learn more about how your site can become an **SNMMI**
Designated Radiopharmaceutical Therapy Center of Excellence.

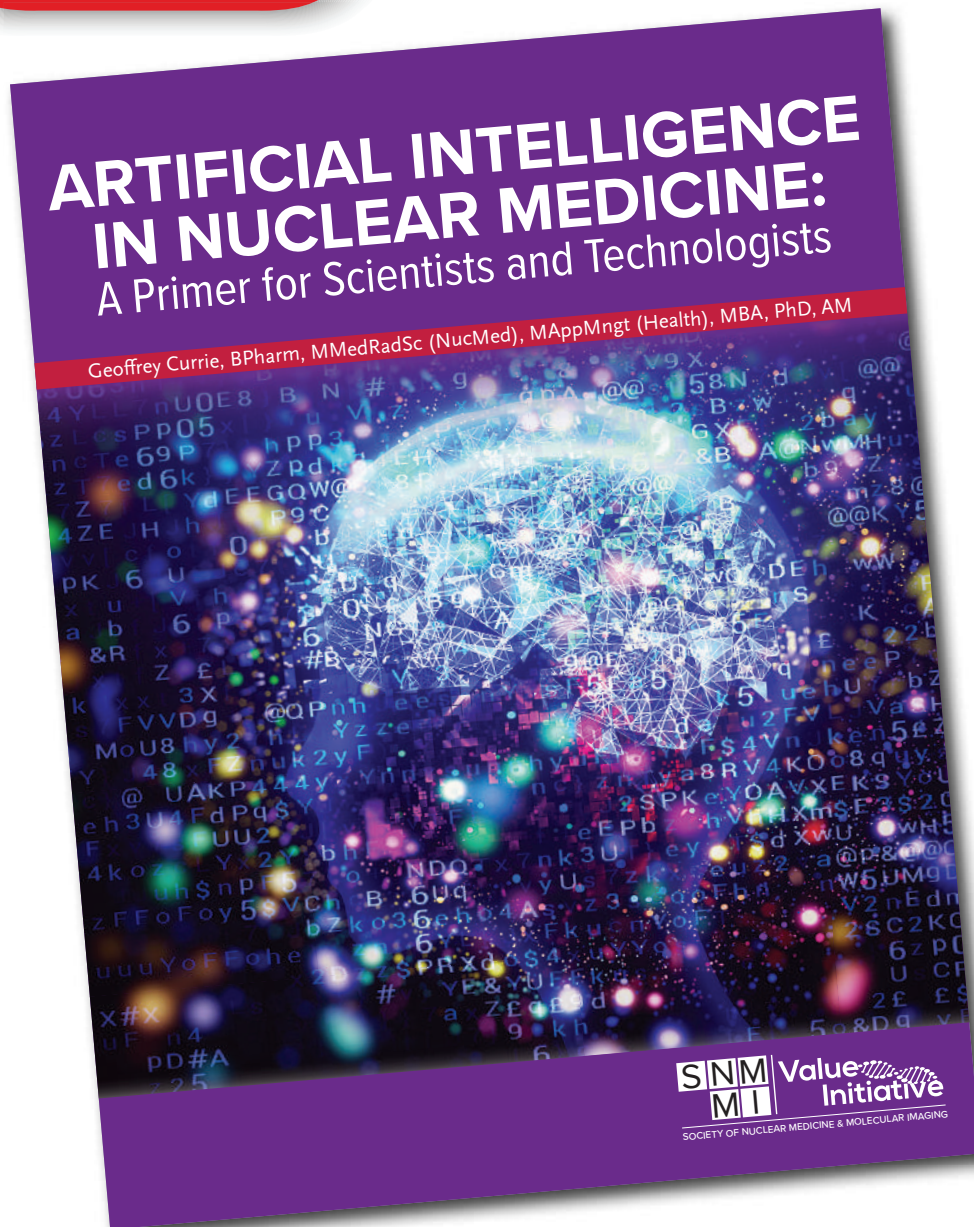
www.snmmi.org/RPTCoE



**NOW
AVAILABLE**

ARTIFICIAL INTELLIGENCE IN NUCLEAR MEDICINE: A Primer for Scientists and Technologists

Geoffrey Currie, BPharm, MMedRadSc (NucMed), MAppMngt (Health), MBA, PhD, AM



Artificial Intelligence in Nuclear Medicine: A Primer for Scientists and Technologists provides a grounding in how artificial intelligence, artificial neural networks, machine learning, and deep learning work; how their capabilities improve outcomes; how and where they should be integrated into your clinical and research practice; and the challenges and considerations involved in their implementation.



Grab your copy today!

www.snmmi.org/Albook

The Indianapolis Richard L. Roudebush VA Medical Center is seeking a full-time board certified/eligible Radiologist, either Nuclear Medicine fellowship or other fellowship training with significant experience and interest in Nuclear Medicine and PET-CT.

Responsibilities: The Radiologist operates independently in the Radiology Service under the supervision of the Chief of Radiology, and primarily within the Diagnostic Radiology section. The Radiology Service is a busy department which performs a wide range of diagnostic and procedural examinations. The selected Radiologist scope of practice includes but is not limited to:
Interpretation of general radiology examinations (plain film, CT, US, MRI) as required. There is limited sub-specialization within the department for advanced imaging, but radiologists are expected to utilize the full breadth of their skill set.
Interpretation of general nuclear medicine studies, PET-CT, and administration of radionuclide therapies if qualified, as part of rotation in Nuclear Medicine (up to 0.3 FTE).
Performance of basic fluoroscopic examinations (such as upper GIs).
Protocolling advanced imaging studies as well as aiding medical providers in selecting the appropriate study.
Participation in Quality Management activities such as image quality, peer review, and other activities as needed.
A tele-service provides radiology coverage after hours, on weekends, and holidays. Radiologists alternate taking pager call (average 1 week in 10-12). Call-ins are rare but include coverage of computer network downtimes and diagnostic fluoroscopy procedures (ex. lumbar puncture and joint aspirations).

Work Schedule: 8:00 am to 4:30 pm, Monday-Friday, or a compressed option is available with four 10 - hour shifts, Monday-Friday. Position eligible for telework 1-2 days per week.

Recruitment Incentive (Sign-on Bonus): Recruitment and/or relocation has been authorized for highly qualified candidate.

Education Debt Reduction Program (Student Loan Repayment): This position is eligible for the **Education Debt Reduction Program (EDRP)**, a student loan payment reimbursement program.

Competitive salary, annual performance bonus, regular salary increases

Paid Time Off: 50-55 days of annual paid time offer per year (26 days of annual leave, 13 days of sick leave, 11 paid Federal holidays per year and possible 5 day paid absence for CME)

Retirement: Traditional federal pension (5 years vesting) and federal 401K with up to 5% in contributions by VA

Insurance: Federal health/vision/dental/term life/long-term care (many federal insurance programs can be carried into retirement)

Licensure: 1 full and unrestricted license from any US State or territory

CME: Possible \$1,000 per year reimbursement

Malpractice: Free liability protection with tail coverage provided

Contract: No Physician Employment Contract and no significant restriction on moonlighting

Please contact Doug Verplank 217-474-3816 email douglkas.verplank@va.gov



SOCIETY OF NUCLEAR MEDICINE & MOLECULAR IMAGING

Learn more
about becoming
a Value Initiative
Industry Alliance
Member Company:



valueinitiative.snmmi.org

Nuclear Medicine Physician Roswell Park Comprehensive Cancer Center

The Nuclear Medicine Section of the Department of Diagnostic and Interventional Radiology of the Roswell Park Comprehensive Cancer Center is seeking a Director. Candidates must be experienced Board-Certified, Fellowship-trained Nuclear Medicine Physicians. Candidates should have extensive clinical and research experience, interest in nuclear oncology, and thorough grounding in multi-probe PET/CT and image-guided radionuclide therapy. Prior practice experience at a tertiary oncology center preferred. Innovative approaches to the treatment of malignancy are emphasized. Additional background and Board Certification in Radiology, Medicine, Surgery or Pathology is a plus. Prior leadership experience is preferred. Beyond oversight of performance of medical and technical staff and ensuring safe and efficient service delivery, responsibilities include the teaching of residents, fellows, and graduate students at the Jacobs School of Medicine and Biomedical Sciences and Graduate Division of the Roswell Park Comprehensive Cancer Center, The State University of New York at Buffalo.

Roswell Park is an NCI-Designated Comprehensive Cancer Center (one of only two in New York State) and a State University of New York at Buffalo affiliate, with academic appointments for staff.

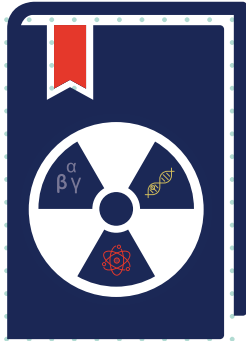
Salary and rank are commensurate with experience and qualifications, and excellent fringe benefits are offered. Interested candidates should forward CV and names of three references to:

Ermelinda Bonaccio, MD, FACR
Chair of Diagnostics and Interventional Radiology
c/o Nicole Robinson
Faculty Recruitment Associate
Roswell Park Comprehensive Cancer Center
Elm and Carlton Streets, Buffalo, NY 14263
Nicole.robinson@roswellpark.org



RPCC and the University of Buffalo are M/F/D/V, M/F/H/V,
Equal Opportunity/Affirmative Action Employer

NOW AVAILABLE



80 Hour Radionuclide Authorized User TRAINING COURSE

The Society of Nuclear Medicine and Molecular Imaging (SNMMI) and American Society of Nuclear Cardiology (ASNC) are excited to announce the launch of a new online course designed to provide nuclear medicine physicians with the knowledge needed to establish a culture of safety and quality in their practice.

The **ASNC/SNMMI 80 Hour Radionuclide Authorized User Training Course** features lectures on radiation protection and safe radioisotope handling, physics and instrumentation, radiochemistry and radiopharmaceuticals, radiation biology, and nuclear medicine mathematics and statistics, and will fulfill the 80 hours of classroom training that the U.S. Nuclear Regulatory Commission (NRC) and Agreement States require for physicians to become authorized users of radioisotopes for imaging and localization studies.

LEARN MORE: www.snmmi.org/80HourCourse



Iagaru Receives First Sam Gambhir Trailblazer Award

Andrei Iagaru, MD, a professor of radiology and chief of the Division of Nuclear Medicine and Molecular Imaging at Stanford University (CA), was presented with the inaugural Sam Gambhir Trailblazer Award on June 14 at the SNMMI Annual Meeting in Vancouver, Canada. Intended for midcareer professionals, the award recognizes outstanding achievement and excellence in transformative research (basic, translational, or clinical science) and exceptional mentorship. The prestigious annual award, announced in 2021 and sponsored by the Education and Research Foundation, honors the memory of Sanjiv Sam Gambhir, MD, PhD, who died at 57 in 2020. Gambhir was an internationally recognized pioneer in molecular imaging and the Virginia and D.K. Ludwig Professor for Clinical Investigations in Cancer Research and chair of the Department of Radiology at Stanford University, where he was also director of the Canary Center at Stanford for Cancer Early Detection, the Precision Health and Integrated Diagnostics Center, and the Molecular Imaging Program. He dedicated his career to developing methods of early disease detection, ushering in a new era of molecular imaging to identify signs of disease in its earliest stages. Within radiology, he was known for development of PET reporter genes and other paradigm-changing discoveries and applications. He was a vocal and highly effective advocate for clinical integration and approval of new molecular imaging techniques and was among the pioneers of the concept of precision medicine.

Iagaru, a colleague of Gambhir at Stanford, completed medical school at Carol Davila University of Medicine and Pharmacy (Bucharest, Romania) and an internship in medicine at Drexel University College of Medicine (Philadelphia, PA). He completed his residency in radiology and a PET/CT fellowship at Stanford. His research interests include PET/MRI and PET/CT for early cancer detection, clinical translation of novel PET radiopharmaceuticals, and targeted radionuclide therapy. He has published more than 200 peer-reviewed articles and been recognized with numerous other honors, including the SNM 2009 Image of the Year Award; the 2009, 2014, and 2015 Western Regional Society of Nuclear Medicine Scientist Award and 2021 Sanjiv Sam Gambhir Distinguished Scientist Award; a 2015 Department of Defense Impact Award; and numerous distinctions at Stanford.



Andrei Iagaru, MD

Iagaru coauthored *The Journal of Nuclear Medicine* in memoriam for Gambhir, writing “We lost a beloved colleague, a mentor and friend, a wonderful human being, and an incredible scientist. Humanity lost a giant who had so much more to contribute toward a better world. For so many of us, Sam was the reason we chose this field.”

SNMMI Honors New Fellows for 2022

Fourteen new SNMMI fellows were recognized on June 13 as part of a special plenary session during the society’s 2022 Annual Meeting in Vancouver, Canada. SNMMI fellowship was established in 2016 to recognize distinguished service to the society as well as exceptional achievement in the field of nuclear medicine and molecular imaging. It is among the most prestigious formal recognitions available to longtime SNMMI members. Recognized as new fellows were: Abass Alavi, MD (Hospital of the University of Pennsylvania/University of Pennsylvania; Philadelphia); Johannes Czernin, MD (David Geffen School of Medicine/University of California at Los Angeles); Farrokh Dehdashti, MD (Mallinckrodt Institute of Radiology/Washington University School of Medicine in St. Louis; MO); Yuni Dewaraja, PhD (University of Michigan Medical School; Ann Arbor); Cameron Foster, MD (University of California Davis Health; Sacramento); Warren Janowitz, MD, JD (Radiology Associates of South Florida/Baptist Health; Miami, FL); Neeta Pandit-Taskar, MD (Memorial Sloan

Kettering Cancer Center/Weill Cornell Medical College; New York, NY); Daniel Pryma, MD (Hospital of the University of Pennsylvania/University of Pennsylvania; Philadelphia); Lalitha Shankar, MD, PhD (National Cancer Institute; Bethesda, MD); John Sunderland, PhD (University of Iowa/University of Iowa Carver College of Medicine; Iowa City); Jerold Wallis, MD (Mallinckrodt Institute of Radiology/Washington University School of Medicine in St. Louis; MO); Dean Wong, MD, PhD (Mallinckrodt Institute of Radiology/Washington University School of Medicine in St. Louis; MO); Anna Wu, PhD (Beckman Research Institute of the City of Hope, Duarte, California); and Katherine Zukotynski, MD, PhD, PEng (McMaster University; Hamilton, Canada).

Selection of SNMMI Fellows is based on documented excellence in both volunteer service to the society and at least 1 of 3 areas: scientific discovery and innovation, educational efforts in nuclear medicine and molecular imaging, or clinical practice of nuclear medicine and molecular imaging. Fellows are entitled to use the FSNMMI designation.

SNMMI Image of the Year 2022: PET/CT Biomarker Predicts Post-MI Cardiac Remodeling

SNMMI announced on June 13 at its Annual Meeting in Vancouver, Canada, the 2022 Henry N. Wagner, Jr., Image of the Year, chosen from more than 1,280 submitted scientific abstracts and voted on by reviewers and society leadership. As part of the presentation “Predicting remodeling and outcome from molecular imaging of fibroblast activation in patients after acute myocardial infarction,” the image from Diekmann et al. from the Hannover Medical School (Germany) contrasted ⁶⁸Ga-fibroblast-activation protein-46 (⁶⁸Ga-FAP-46) PET/CT, ^{99m}Tc-tetrofosmin perfusion SPECT, and cardiac MR images acquired in patients within 11 days after acute myocardial infarction.

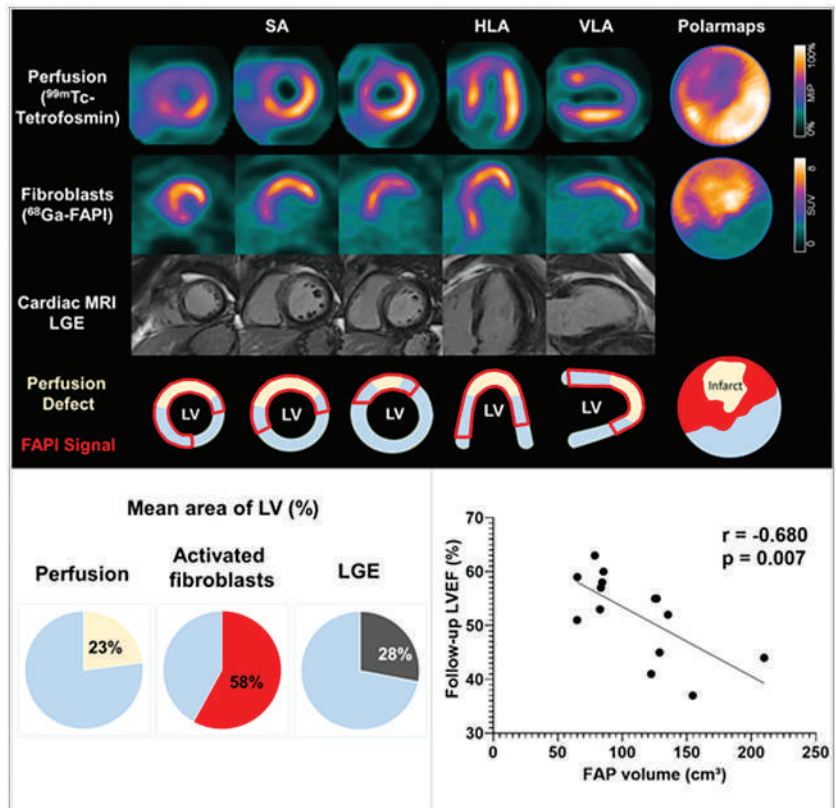
“Molecular PET imaging of the fibroblast activation protein has recently been evaluated in patients after acute myocardial infarction,” stated Johanna Diekmann, MD, lead author of the presentation. “In our study, we sought to obtain further insights by correlating FAP-targeted PET imaging with tissue characteristics from cardiac MRI, as well as functional outcome.”

The study included 35 patients, in whom infarct size was determined from SPECT, cardiac FAP volume was calculated from ⁶⁸Ga-FAP-46 PET/CT uptake values and polar mapping analyses, and MRI provided information on functional parameters, area of injury, and tissue characteristics. Cardiac function in a subgroup of 14 patients was followed up by echocardiography or cardiac MRI at a median of 139.5 days.

In all patients the area of FAP upregulation was significantly larger than that in either SPECT perfusion defect size or infarct area as defined by late gadolinium-enhanced MRI. FAP volume on PET/CT was significantly correlated at baseline with multiple cardiac parameters, including infarct area, left ventricular (LV) mass, and end-systolic and -diastolic volumes. PET/CT segmental analysis showed FAP upregulation in 308 of 496 (62%) myocardial segments. MRI late gadolinium enhancement was found in only 56% of FAP-positive segments, elevated T1 in 74%, and elevated T2 in 68%. Fourteen percent (44/308) of FAP-positive segments showed neither prolonged T1 or T2 nor significant late gadolinium enhancement, with a weak correlation between myocardial FAP volume and LV ejection fraction (LVEF) at baseline. Early myocardial PET values showed a stronger correlation with LVEF at follow-up, suggesting a relationship between

the extent of fibroblast activation and more severe adverse ventricular remodeling. The authors concluded that because a higher extent of myocardial FAP upregulation was predictive of subsequent LV dysfunction and exceeded infarct area as defined by other modalities, fibroblast activation in noninfarcted myocardial areas may contribute to adverse outcomes. FAP imaging with PET/CT may be a complementary biomarker with applications in establishing treatment strategies to mitigate profibrotic activity outside of the primary infarct region to prevent adverse remodeling.

“Myocardial infarction is an important contributor to the development of heart failure, but the early molecular processes involved in the transition from initial injury to heart failure are undertreated,” said Diekmann. “New antifibrotic therapies (such as CAR-T cell therapies) could significantly change future therapy of heart failure. Using FAP PET to select patients suitable for therapy would open a new major application for PET in fibrosis and cardiac diseases.”



SNMMI 2022 Image of the Year. Top: Representative case with acute anterior wall myocardial infarction. ^{99m}Tc-tetrofosmin perfusion SPECT, ⁶⁸Ga-fibroblast-activation protein-46 (⁶⁸Ga-FAP-46) PET/CT, and late gadolinium-enhanced (LGE) cardiac MR images were compared in patients within 11 days after acute myocardial infarction. Bottom: Areas of myocardial FAP upregulation on PET/CT were significantly greater than those with either SPECT or MRI and were predictive of subsequent left ventricular (LV) dysfunction. Global myocardial FAP volume early after acute myocardial infarction inversely correlated with left ventricular ejection fraction (LVEF) at follow-up in the chronic stage. The findings suggest promise for ⁶⁸Ga-FAP-46 PET/CT as a complementary biomarker in predicting adverse cardiac remodeling.

New Officers for SNMMI and SNMMI-TS

During the 2022 SNMMI Annual Meeting, from June 11 to 14, both the SNMMI and SNMMI Technologist Section (SNMMI-TS) welcomed new officers. Elected by the members of the 2 organizations, the new officers will serve in these positions through June 2023.

SNMMI President

Munir Ghesani, MD, associate professor of radiology at Mount Sinai Hospital and chief of nuclear medicine and molecular imaging at Mount Sinai Health System (New York, NY), assumed the office of SNMMI President. He reported that his goals in this position include continuing to increase consumer outreach and medical community awareness of the benefits of nuclear medicine, molecular imaging, and radionuclide therapy; expanding efforts to provide educational offerings to referring and specialty physicians; working closely with U.S. regulators to streamline the approval of promising new diagnostic and therapeutic radiopharmaceuticals; maintaining reliable access to radiopharmaceuticals, particularly new and cutting-edge therapies; and ensuring that SNMMI remains a leading global nuclear medicine organization through its publications, clinical guidelines, quality initiatives, and international representation.



Munir Ghesani, MD

Ghesani earned his medical degree from Gujarat University, NHL Medical College (Ahmedabad, India), in 1984. He completed a diagnostic radiology residency in 1988 at the KM School of Postgraduate Medicine and Research, followed by a diagnostic ultrasound fellowship in 1989 at LG Hospital and KM School of Postgraduate Medicine and Research, also in Ahmedabad. In 1993, he completed an internal medicine residency at Jersey City Medical Center (NJ) and, in 1996, a nuclear medicine residency and fellowship at St. Luke's-Roosevelt Hospital Center (New York, NY), where he also went on to radiology residency. He has held academic appointments at the New York University School of Medicine, the Icahn School of Medicine at Mount Sinai, and Columbia University (all in New York, NY).

Within SNMMI, Ghesani has been an active member of the society's governance, with a strong focus on advocacy. He has served as chair of the Government Relations Committee and the SNMMI/U.S. Food and Drug Administration Task Force, as well as Advocacy Domain chair for the SNMMI Value Initiative. He was a cochair of the SNMMI Membership Task Force and a member of the SNMMI Board of Directors. He has also held multiple leadership positions in the Greater New York Chapter of SNMMI, most recently as president.

In the larger nuclear medicine community, Ghesani has served as chair and director of the American Board of

Nuclear Medicine (ABNM) and as president of the American College of Nuclear Medicine (ACNM). He has published more than 80 peer-reviewed journal articles and a text, *Nuclear Medicine: A Case-Based Approach*. Ghesani is certified by the American Board of Radiology, ABNM, and the American Board of Internal Medicine.

"SNMMI is a unique organization that brings together diverse nuclear medicine and molecular imaging professionals," said Ghesani. "It is my pleasure to work on behalf of each of the SNMMI members to improve our field. I look forward to collaborating with the society's dedicated leadership, volunteers, and staff over the next year in our mission to improve patient care."

SNMMI President-Elect

Helen Nadel, MD, director of pediatric nuclear medicine at Lucile Packard Children's Hospital at Stanford (CA) and clinical professor of radiology at the Stanford School of Medicine, was named as SNMMI president-elect. She has set goals for her tenure that reflect lessons learned from the collective nuclear medicine COVID-19 experience. To accomplish these goals, Nadel proposes



Helen Nadel, MD

creation of an ongoing working group to address preparedness issues, education of members on potential risks, and development of rapid global communication and mobilization plans. She encourages SNMMI's continued cooperation with government and industry to develop and quickly approve diagnostic and theranostic molecular agents, as well as associated technologies. She also supports SNMMI's diversity initiatives to ensure an inclusive working environment and deliver quality health care to all patients regardless of ethnicity or gender.

Nadel earned her medical degree from the University of Manitoba in Winnipeg (Canada) in 1977. She completed a diagnostic radiology residency in 1982 at the University of Toronto (Canada), followed by a fellowship in pediatric radiology at the Hospital for Sick Children at the University of Toronto. She then completed a nuclear medicine residency in 1989 at the University of British Columbia (Vancouver, Canada). She held multiple academic appointments at the University of British Columbia between 1983 and 2018 and was head of the Division of Nuclear Medicine and Department of Radiology at British Columbia Children's Hospital before taking on her current roles at Stanford.

An active SNMMI member for more than 30 years, Nadel has served as a member of the House of Delegates, as president and member of the board of directors of the Pediatric Imaging Council, and as member of the PET Center of Excellence board of directors, Scientific Program Committee,

Membership Committee, and *The Journal of Nuclear Medicine* editorial board, among other posts. She was president of the SNMMI Pacific Northwest Chapter for many years and currently plays an active role in the Northern California chapter. In the greater nuclear medicine community, she has served in multiple positions for the ACNM, the ABNM, and the Children’s Oncology Group. In 2019, Nadel received the Lifetime Achievement Award from the European Society of Pediatric Nuclear Medicine for ongoing contributions to pediatric nuclear medicine. She has published more than 60 peer-reviewed journal articles and 24 text chapters and has been an invited speaker for 180 presentations.

SNMMI Vice President–Elect

Cathy Sue Cutler, PhD, Director of the Medical Isotope Research and Production Program (MIRP) at the Brookhaven National Laboratory (BNL; Upton, NY), was named as the 2022 SNMMI Vice-President Elect. A high-priority goal during her term will be to work with SNMMI on efforts to secure appropriate funding for nuclear medicine services and providers. This goal also includes securing adequate funding for



Cathy Cutler, PhD

researchers developing life-saving radiopharmaceuticals. She will work with SNMMI to encourage the U.S. Congress to pass the FIND Act to guarantee access to high-value radiopharmaceuticals. A third goal is to generate training and education opportunities in theranostics for personalized medicine.

Cutler began her career as a research associate at the Mallinckrodt Institute of Radiology/Washington University at St. Louis (MO), and as a research scientist at the Missouri University Research Reactor (MURR; Columbia) at the University of Missouri. At the University of Missouri she also served as an adjunct faculty member in the Nuclear Engineering Program and a Joint Faculty Member in the Nuclear Sciences and Engineering Institute. She became a Research Professor at MURR in 2010. In 2015 she accepted her current position at BNL, where she was named a Tenured Scientist in 2018. In 2019 she received the BNL 33rd Annual Women’s Recognition Award for Achievements in Science.

For more than 20 years Dr. Cutler has actively participated and served in leadership positions on SNMMI councils, committees, and task forces, including those of the Radiopharmaceutical Council, the Committee on Radiopharmaceuticals (as chair), the Center for Molecular Imaging Innovation and Translation (as president), the Committee on Ethics, the Women in Nuclear Medicine Committee, the Committee on Education, the Committee on Government Relations (chair), the SNMMI Advocacy Domain–Value Initiative (chair), and others. She has published more than 100 peer-reviewed journal articles and participated in national and international radiopharmaceutical leadership activities.

SNMMI-TS President

Krystle W. Glasgow, MIS, CNMT, NMTCB(CT), NMAA, instructor and clinical coordinator at the University of Alabama at Birmingham, became the 2022–2023 SNMMI-TS president. Her focus as president will continue to be on SNMMI-TS membership. Her goals include engaging young nuclear medicine technologists (both students and early career professionals) and strengthening support for all nuclear medicine technologists. Other goals include making SNMMI a 1-stop shop for nuclear medicine needs, enhancing communication between the society and its members, increasing and diversifying educational offerings, and promoting advocacy endeavors.



Krystle W. Glasgow, MIS, CNMT, NMTCB(CT), NMAA

Glasgow received her bachelor of science degree in nuclear medicine technology with a concentration in CT in 2010 from the University of Alabama at Birmingham. She completed a master’s degree in imaging sciences and was certified as a Nuclear Medicine Advanced Associate at the University of Arkansas for Medical Sciences (Little Rock). She is pursuing a doctoral degree in health services administration with a concentration in health informatics at the University of Alabama at Birmingham.

SNMMI-TS President-Elect

Dmitry Beyder, CNMT, MPA, was named as SNMMI-TS President-Elect. His goals for his time in office include guiding technologists and the professional organization as a whole out of the COVID-19 pandemic, strengthening the nuclear medicine technologist workforce and professional pipeline, and growing the nuclear medicine technologist’s role in theranostic practice.



Dmitry Beyder, CNMT, MPA

Beyder received his bachelor of science degree in nuclear medicine technology from the State University of New York at Buffalo and a master of public administration in health policy, management, and international healthcare from the Robert F. Wagner Graduate School of Public Service at New York University (NY). He began his career as a nuclear medicine technology at Memorial Sloan Kettering Cancer Center (New York, NY), followed by 6 years as clinical supervisor of nuclear medicine and PET at Oregon Health and Science University (Portland). He assumed the position of Radiology Program Manager of Nuclear Medicine, PET, CT, and Patient Transport at Barnes–Jewish Hospital/Mallinckrodt Institute of Radiology (St. Louis, MO) in 2014. He has served in numerous SNMMI-TS leadership roles, including as chair of the Scope of Practice Task Force, cochair of the Advocacy Committee, member of the Executive Board, and others.

Recognition of the ABNM by the NRC

George Segall, MD, American Board of Nuclear Medicine Executive Director

Certification by the American Board of Nuclear Medicine (ABNM) is recognized by the U.S. Nuclear Regulatory Commission (NRC) as meeting the training and experience requirements to be an authorized user of byproduct material for medical use. The last time the ABNM's certification process was reviewed by the NRC was in 2005, following publication of the final rule 10 CFR Part 35, "Medical Use of Byproduct Material Recognition of Specialty Boards," defining the criteria such boards must meet before they could be recognized by the NRC or Agreement States (*Fed Reg.* 2005;70:16335). On January 11, 2021, the NRC Office of Nuclear Medicine Safety and Safeguards published Office Procedure 70-03, "Procedures for Recognizing, Monitoring, and Terminating Certification Process of Specialty Boards," Section 3.1, "Monitoring Continued Satisfaction of Recognition Requirements." The purpose was to provide "increased clarity" for the NRC on monitoring for continued satisfaction of the recognition criteria, guidance for determining whether NRC recognition should be terminated, and guidance for maintaining NRC-recognized board certifications on the NRC public website.

The ABNM received a letter on March 15, 2022, asking for confirmation that the ABNM continues to satisfy the recognition criteria for specialty board certification processes. The letter explained that the NRC was contacting all its recognized specialty boards per the procedure published in the preceding year. As part of the review, the NRC staff was evaluating the board's publicly available website for changes that could affect recognition of the board's certification process. The letter also noted that subsequent reviews will be performed on a 5-year basis.

The NRC review of the ABNM website is still underway. The ABNM has responded with proposed changes clarifying the training and work experience required for certification that conform to NRC rules to be an authorized user uses of byproduct material under 10 CFR 35.190 Training for uptake, dilution, and excretion studies; 10 CFR 35.290 Training for imaging and localization studies; and 10 CFR 35.390 Training for use of unsealed byproduct material for which a written directive is required.

Under 10 CFR 35.390, training and experience must include a minimum of 700 hours, all of which are applicable to the medical use of unsealed byproduct material requiring a written directive, including a minimum of 200 hours of classroom and laboratory training in accordance with 10 CFR 35.390(b), and supervised work experience. The 200 hours of classroom and laboratory training must include:

- Radiation physics and instrumentation;
- Radiation protection;
- Mathematics pertaining to the use and measurement of radioactivity;
- Chemistry of byproduct material for medical use; and
- Radiation biology.

Classroom and laboratory training may be obtained using a variety of instructional methods (including online training) as

long as the specific clock hour requirements are met and the subject matter relates to radiation safety and safe handling of byproduct material for the uses for which authorization is being requested. Reviewing case histories or interpreting scans should not be counted toward the minimum 200 hours of required classroom and laboratory training in radiation safety and safe handling of byproduct material.

Supervised work experience must include:

- Ordering, receiving, and unpacking radioactive materials safely and performing the related radiation surveys;
- Performing quality control procedures on instruments used to determine the activity of dosages and performing checks for proper operation of survey meters;
- Calculating, measuring, and safely preparing patient or human research subject dosages;
- Using administrative controls to prevent a medical event involving the use of unsealed byproduct material;
- Using procedures to contain spilled byproduct material safely and proper decontamination procedures; and
- Administering dosages of radioactive drugs to patients or human research subjects involving a minimum of 3 cases in each of the following categories:
 - Oral administration of ≤ 1.22 GBq (33 mCi) of sodium iodide ^{131}I , for which a written directive is required;
 - Oral administration of >1.22 GBq (33 mCi) of sodium iodide ^{131}I ; and
 - Parenteral administration of any radioactive drug that contains a radionuclide that is primarily used for its electron emission, β radiation characteristics, α radiation characteristics, or photon energy <150 keV, for which a written directive is required.

Physicians in training may not dedicate all of their supervised work experience time specifically to these subject areas and will be attending to other clinical matters involving the medical use of the material under the supervision of an authorized user (e.g., reviewing case histories or interpreting scans). This type of supervised work experience may be counted toward the supervised work experience to obtain the required 700 total hours of training.

For 10 CFR 35.290, *additional* work experience is required for eluting generator systems appropriate for preparation of radioactive drugs for imaging and localization studies, measuring and testing the eluate for radionuclidic purity, and processing the eluate with reagent kits to prepare labeled radioactive drugs.

The training and experience described here also meet the requirements of 10 CFR 35.190.

Experience for 10 CFR 35.190, 10 CFR 35.290, and 10 CFR 35.390 must be obtained under the supervision of an authorized user for the same type of procedures.

The ABNM will update its website with this information to ensure that the NRC continues to recognize its certification process.

Opportunities for Growth in Nuclear Medicine and Molecular Imaging

Munir Ghesani, MD, SNMMI President

The discipline of nuclear medicine is stronger than ever, and its future is brighter than ever. Radiopharmaceutical therapies—such as ^{177}Lu -PSMA-617, approved a few months ago, and ^{177}Lu -DOTATATE, approved a few years ago—are propelling theranostics to the forefront of the field. Techniques such as dynamic imaging of an extended field of view now provide an extraordinary photon sensitivity with very low levels of radioactivity. Artificial intelligence and machine learning are reshaping the research and development of nuclear medicine and molecular imaging.

While these advances are driving the science of the field forward, we must also ensure that patients benefit from them. As I begin my term as SNMMI president, I plan to address several issues that will help the field grow while focusing on optimal patient care and quality and the safety of our diagnostic and therapeutic procedures as top priorities. By concentrating on public awareness, patient engagement, and regulatory approvals, we can make great strides to benefit our patients.

Nuclear medicine is not a common household phrase. To educate the public about what nuclear medicine is and what it can accomplish, SNMMI launched an awareness campaign last year. Targeting consumer broadcast media (print and digital news publications, radio, TV), SNMMI has reached a very broad audience, including patients, caregivers, referring physicians, legislators, regulators, and payers. In its first 6 months the campaign reached more than 1 billion consumers. We will continue this important consumer outreach in the coming year. By exposing the public to multiple “stories” about nuclear medicine over an extended period of time, we can enhance their recall and strengthen their understanding.

We must also continue our efforts to ensure that patients and the medical community recognize the value of nuclear medicine, molecular imaging, and radionuclide therapy. SNMMI’s 14-member Patient Advocacy Advisory Board will remain a driving force in advising the society on development of patient education materials and public policy regarding nuclear medicine and molecular imaging. The society will also continue its education of referring physicians during session presentations and symposia at several events, including the Pediatric Endocrine Society, American Society for Radiation Oncology, Large Urology Group Practice Association, American Urological Association, and San Antonio Breast Cancer Symposium.

Access to nuclear medicine and molecular imaging is another key issue for SNMMI. The society will work closely with U.S. regulators to streamline the approval of promising new diagnostic and therapeutic radiopharmaceuticals. Reimbursement of nuclear medicine and molecular imaging procedures also remains a critical issue. SNMMI cosponsors the Facilitating Innovative Nuclear Diagnostics (FIND) Act, which, if passed, would direct the Department of Health and Human Services to pay separately for all outpatient diagnostic radiopharmaceuticals rather than packaging them with other medical supplies. In promoting the FIND Act, SNMMI hopes to help patients achieve greater access to a wide range of diagnostic radiopharmaceuticals.

Radiopharmaceutical access also depends on manufacturers, as we saw in the recent halt in production of Lutathera and Pluvicto. SNMMI members and the patients we serve need a reliable supply chain for innovative radiopharmaceutical therapies to be used regularly and widely. SNMMI is dedicated to contributing to the radiopharmaceutical therapy space to help our field continue to grow.

I feel strongly that SNMMI is the leading global nuclear medicine organization and plan to increase the recognition of the society and its initiatives during my term as president. Our Mid-Winter and Annual Meetings are premier nuclear medicine and molecular imaging events and are attended by thousands of professionals from around the world. *The Journal of Nuclear Medicine* publishes cutting-edge research and enjoys its highest impact factor ever, ranking third among all medical imaging journals worldwide. We lead the way in developing clinical guidelines and promoting quality among the profession. As SNMMI continues its impactful work, we will make sure that the organization and its members are recognized for their contributions to the field.

SNMMI is a unique organization that brings together diverse nuclear medicine and molecular imaging professionals—physicians, scientists, pharmacists, technologists, and lab professionals. It is my pleasure to work on behalf of each of the SNMMI members to improve our field. I look forward to collaborating with the society’s dedicated leadership, volunteers, and staff over the next year in our mission to improve patient care.



Munir Ghesani, MD

Biogen Reassesses Plans for Aduhelm in AD

In a series of press releases and statements in late April and early May, Biogen Inc. (Cambridge, MA), the maker of the Alzheimer disease–targeted treatment Aduhelm (aducanumab), announced new plans following a series of approval setbacks. The drug, a monoclonal antibody directed against β -amyloid, had been given conditional U.S. Food and Drug Administration (FDA) approval on June 7, 2021. Subsequent controversy over the initial proposed cost of the drug (\$56,000/y, later reduced to \$28,000/y) data on effectiveness, and potential side effects was the focus of both public and professional medical commentary. On January 11 the U.S. Centers for Medicare & Medicaid Services (CMS) released a proposed National Coverage Determination (NCD) decision memorandum that would allow only coverage with evidence development (CED), effectively restricting Medicare reimbursement to individuals enrolled in qualifying clinical trials. On April 7, the proposed NCD was finalized.

Biogen informed its investors on April 22 that it had notified the European Medicines Agency (EMA) of a decision to withdraw its Marketing Authorization Application (MAA) for aducanumab for treatment of the early stages of Alzheimer disease. The company withdrew its application following interactions with the EMA Committee for Medicinal Products for Human Use (CHMP) in which the committee indicated that data provided thus far would not be sufficient to support a positive opinion on EMA marketing authorization. Biogen's MAA had been under review by the CHMP in response to the company's request for a reexamination of the negative opinion issued in December 2021.

On April 28, Biogen announced that despite rollbacks of its U.S. and international marketing infrastructure for Aduhelm, all U.S. patients who began treatment on or before April 7, 2022,

would be eligible to receive the drug at no cost for the duration of their treatments or for the duration of the program. In addition, patients who were already enrolled in Biogen's Free Drug Program would automatically continue in the program and continue to receive the medicine at no cost. Biogen's program does not cover diagnostics or other potential fees associated with treatment administration and monitoring. "One of our immediate priorities following the NCD decision is to support patients on therapy who were uncertain whether they could receive their next infusion," said Alisha Alaimo, president of Biogen's U.S. Organization. "This program allows eligible patients continued access to Aduhelm and aims to help them avoid long-term interruptions in their care."

Biogen issued a follow-up to its quarterly statement on May 3 indicating that it would be "substantially eliminating commercial infrastructure" related to Aduhelm and was planning additional associated cost-cutting measures. The statement noted that U.S. Biogen expected to continue funding certain regulatory and research and development activities for Aduhelm, including continuation of the EMBARK redosing study and initiation of the phase 4 postmarketing requirement study, ENVISION. Biogen stated that "additional actions regarding Aduhelm may be informed by upcoming data readouts expected for this class of antibodies, as well as further engagement with the FDA and CMS." The company also announced that its chief executive, Michel Vounatsos, would step down when a replacement could be identified.

Biogen Inc.

Underrepresentation in FDA CAR-T Cell Approval Studies

In an article published on April 20 in *JAMA Network OPEN* (2022;5[4]:e228161), Al Hadidi et al. from the University of Arkansas for Medical

Sciences (Little Rock) reported on a study looking at enrollment of Black participants in clinical trials resulting in subsequent U.S. Food and Drug Administration (FDA) approval of chimeric antigen receptor–T (CAR-T) cell therapies for hematologic malignant neoplasms. Publicly available data from 2017 to 2021 included patients with large B-cell lymphoma, follicular lymphoma, mantle cell lymphoma, acute lymphoblastic leukemia, and multiple myeloma enrolled in 7 clinical trials investigating several CAR-T products. Of the 1,057 patients enrolled in these studies, CAR-T products were administered to 746 (71%), and efficacy was reported for 729 (69%), with 96% of patients enrolled in the United States. Overall, the percentage of Black participants who received CAR-T products and had reported efficacy data varied between 2% and 5% (range, 1–12 participants). Black patients were significantly underrepresented in comparison to actual disease prevalence across all hematologic malignancies. Adjusted prevalence calculations showed the lowest participation-to-prevalence ratio of 0.2 for multiple myeloma and 0.6 for large B-cell lymphoma. The authors concluded that these findings suggest substantial disparities affecting Black patients across all approved CAR-T products used to treat hematologic malignant neoplasms, despite otherwise limited effective treatment options. They added that these findings "might aid policy discussions regarding the immediate need of regulations that enforce certain thresholds of Black patients' enrollment before granting FDA approval."

JAMA Network OPEN

Contrast Media Shortage

The GE Healthcare (Boston, MA) production facility in Shiangai, China, that manufactures almost the entire U.S. supply of the Omnipaque (iohexol) contrast agent product lines was shut down in April as a result of Chinese

government restrictions related to COVID-19. Visipaque (iodixanol) was also in short supply. According to GE Healthcare, the supply impact was not related to quality, raw material supply, or supply chain issues. GE Healthcare announced that they would use a secondary manufacturing facility in Ireland to supplement U.S. Omnipaque supply. The supply interruption had an almost immediate effect on scheduling and performance of contrast-enhanced imaging in the United States, with significant related media coverage. In a May 18 letter to customers, GE referred to the situation as “fluid,” as the company worked to expand production capacity and collaborate with local Shanghai authorities to “enable increasing numbers of operators to return to the site, complying with local COVID-19 protocols.” To enable availability and continuity, GE was “balancing supply of available product globally” and, in some markets, introducing measures “to reduce order quantities but with a higher frequency of delivery, as well as optimizing production to focus on 3 main product variations.” Production output from Shanghai was expected to continue to increase and return to full production capacity “as soon as local authorities allow.” On May 23 GE released an update, indicating that the plant had increased production output from 0% of capacity when first closed to 60% capacity by May 21. Production was expected to be at 75% capacity by mid-June. Deliveries were being accelerated by changing some logistic routes from sea to air.

SNMMI addressed the shortage in mid-May, expressing hope that the supply issue would be resolved quickly but reminding practitioners that radiopharmaceuticals remain available and are an excellent alternative for some diagnostic procedures. For example, V/Q lung scanning can be considered as an alternative to cardiac CT angiography (CTA) of pulmonary arteries, and stress cardiac nuclear studies (PET or SPECT) may serve as alternatives in some patients scheduled for cardiac CTA.

The American College of Radiology Committee on Drugs and Contrast

Media has issued guidance on the contrast agent shortage and suggested strategies to conserve contrast media, including delaying elective procedures. A special report from the Radiological Society of North America suggested short-term strategies, including establishing an incident command center to direct and monitor contrast media usage, converting exams to noncontrast when possible, reducing contrast dose, and substituting other types of exams, such as MRI, ultrasound, or noncontrast PET/CT. As of June 1, the GE contrast media remained on the “backorder” FDA Shortage List.

*GE Healthcare
SNMMI*

Status of Lutathera and Pluvicto Production and Supply

On May 5, Novartis (Basel, Switzerland) announced suspension of production of its agents Lutathera (¹⁷⁷Lu-dotatate; ¹⁷⁷Lu-oxodotretotide) and Pluvicto (¹⁷⁷Lu-PSMA-617; ¹⁷⁷Lu-vipivotide tetraxetan) at radioligand therapy production sites in Ivrea, Italy, and Milburn, NY, affecting both commercial and clinical trial supplies. The company stated that this voluntary shutdown was taken “out of an abundance of caution” as it addresses “potential quality issues identified in its manufacturing processes” and projected that these issues would be resolved within 6 wk, with production gradually resuming thereafter.

Novartis suspended delivery of Lutathera in the United States and Canada and of Pluvicto in the United States (the only approved market for Pluvicto). The statement indicated that some doses of Lutathera would be available in Europe and Asia from a Novartis production site in Zaragoza, Spain, although with potential supply delays. In addition, Novartis put a temporary hold on screening and enrollment for ¹⁷⁷Lu-PSMA-617 clinical trials globally and Lutathera clinical trials in the United States and Canada. Although the company reported “no indication of any risk to patients from doses previously produced,” treatment sites were notified

“to closely monitor” patients who had recently been injected and report any adverse events to Novartis patient safety. “Novartis takes this very seriously and the company is doing everything it can to resolve this issue and resume patient doses as quickly as possible,” said Novartis. “Health authorities have been informed and will receive additional updates as they are available.”

Only 6 wk before, on March 23, FDA announced approval of Pluvicto for treatment of adult patients with prostate-specific membrane antigen-positive metastatic cancer who have been treated with androgen-receptor pathway inhibition and taxane-based chemotherapy. Lutathera, the first radiopharmaceutical marketed for peptide-receptor radionuclide therapy, was approved by the European Medicines Agency in 2017 and the FDA in 2018 for treatment of somatostatin receptor-positive gastroenteropancreatic neuroendocrine tumors. As of June 1, the FDA Drug Shortage list included Lutathera as “Currently unavailable; Estimated remaining duration of Supply Shortage: 3–4 wk” because of issues “related to complying with Good Manufacturing Practices.” Pluvicto did not appear on the list.

*Novartis
U.S. Food and Drug Administration*

FDA Permits Marketing of AD Diagnostic Test

The U.S. Food and Drug Administration (FDA) announced on May 4 marketing permission for the first in vitro diagnostic test for early detection of amyloid plaques associated with Alzheimer disease (AD). The Lumipulse G β-Amyloid Ratio (1-42/1-40) test (Fujirebio Diagnostics, Inc.; Malvern, PA) is intended for use in adult patients ≥55 y presenting with cognitive impairment and being evaluated for AD and other causes of cognitive decline.

The FDA evaluated the safety and effectiveness of the Lumipulse test in a clinical study of 292 cerebrospinal fluid samples from the AD Neuroimaging Initiative sample bank. The samples were tested and compared with amyloid

PET imaging results. In this clinical study, 97% of individuals with Lumipulse G β -amyloid Ratio (1-42/1-40)-positive results had amyloid-positive PET findings, and 84% with negative test results had negative PET findings. The FDA noted that the Lumipulse G β -amyloid Ratio (1-42/1-40) is not a standalone test and that other clinical evaluations or additional tests should be used for determining treatment options.

The Lumipulse G β -amyloid Ratio (1-42/1-40) was granted Breakthrough Device designation, a process designed to expedite the development and review of devices that may provide for more effective treatment or diagnosis of life-threatening or irreversibly debilitating diseases or conditions.

U.S. Food and Drug Administration

Hearing on FIND Act Requested

On April 28, SNMMI and more than 70 organizations sent a letter to U.S. House Energy and Commerce and Ways and Means Committee leadership

requesting a hearing on the Facilitating Innovative Nuclear Diagnostics (FIND) Act. In July 2021, Reps. Scott Peters (CA), Bobby Rush (IL), Greg Murphy (NC), and Neal Dunn (FL) introduced the FIND Act (H.R. 4479), legislation that would significantly expand patient access to advanced nuclear diagnostic imaging technologies. The bill aims for a legislative fix to Centers for Medicare and Medicaid Services bundling of diagnostic radiopharmaceuticals in the hospital outpatient space after a 3-y passthrough period after U.S. Food and Drug Administration (FDA) approval. SNMMI and its coalition partners, the Medical Imaging & Technology Alliance and the Council on Radionuclides and Radiopharmaceuticals—in addition to dozens of patient advocacy organizations—praised the introduction.

The FIND Act addresses structural issues in the packaging methodology used in the Medicare outpatient hospital setting by directing the Department of Health and Human Services to pay

separately for all diagnostic radiopharmaceuticals with a cost threshold per day of \$500. If passed, this bill would give patients greater access to a wide range of diagnostic radiopharmaceuticals. This legislation would also help providers better manage costs while delivering more targeted and cost-efficient care. If passed, patients would not be responsible for the 20% drug copayment. The bill is also budget neutral. “This policy will safeguard Medicare beneficiary access to the most appropriate diagnostic radiopharmaceuticals and help spur continued innovations in nuclear imaging studies,” wrote the letter’s signatories. “To help advance this legislation, we again respectfully ask that your committees hold a hearing to consider the FIND Act and explore the potential of this policy to expand beneficiary access to care, improve health outcomes, create health care savings, and promote innovation and development in this space.”

SNMMI

FROM THE LITERATURE

Each month the editor of Newsline selects articles on diagnostic, therapeutic, research, and practice issues from a range of international publications. Most selections come from outside the standard canon of nuclear medicine and radiology journals. These briefs are offered as a window on the broad arena of medical and scientific endeavor in which nuclear medicine now plays an essential role. The lines between diagnosis and therapy are sometimes blurred, as radiolabels are increasingly used as adjuncts to therapy and/or as active agents in therapeutic regimens, and these shifting lines are reflected in the briefs presented here. We have also added a small section on noteworthy reviews of the literature.

Preoperative PET and Long-Term Survival in Breast Cancer

Perrin et al. from CHU de Martiniq (Fort-de-France), Universitair Ziekenhuis Brussel (Belgium), Howard

University (Washington, DC), and Hackensack University Medical Center (NJ) reported on April 24 in the *World Journal of Clinical Oncology* (2022; 13[4]:287–302) on a study evaluating the predictive value of preoperative ^{18}F -FDG PET for overall long-term survival in patients with breast cancer. In this retrospective study, 104 patients’ preoperative PET images were defined as positive or negative based on anatomic region-of-interest (ROI) findings for breast, axillary, sternal, and distant sites. SUV_{max} results in these ROIs were analyzed in the data from 36 of these patients. The follow-up period for the study was 15 y. PET positivity in axillary, sternal, and combined axillary/sternal nodes was predictive of poor overall survival. PET-positive axillary and combined axillary/sternal status were also predictive of poor disease-free survival. On additional analysis, SUV_{max} results for ipsilateral breast and axilla were significant covariate

predictors of long-term overall survival, with relative increases in risk of death of 25% and 54%, respectively, per SUV_{max} unit. The ratio of the ipsilateral axillary SUV_{max} to that of the contralateral axillary was the most significant predictor of overall survival, suggesting a 2-fold relative increase in mortality risk. The authors concluded that “preoperative PET is valuable for prediction of long-term survival” in patients with breast cancer, adding that “ipsilateral axillary SUV_{max} ratio over the uninvolved side represents a new prognostic finding that warrants further investigation.”

World Journal of Clinical Oncology

Predictive Value of SPECT/CT in Neck Pain Treatment

In an article published on May 7 ahead of print in the *Spine Journal*, Nolan et al. from the University of Vermont Medical Center/Robert Lamer,

MD, College of Medicine (Burlington) reported on a study evaluating the utility of SPECT/CT in patients with axial neck pain for identifying specific facet joints that would benefit from steroid injections and/or medial branch block/radiofrequency ablation treatments. The retrospective study included data from 112 patients with neck pain who had undergone SPECT/CT and had no prior related treatment. All patients were treated with facet intervention by injection with steroid and local anesthetic or medial branch block with local anesthetic at sites determined by physicians based on clinical examination and image interpretation. Positive responses to the interventions were defined at both 50% and 80% thresholds for reduction in pain within 24 h and correlated with the focus of maximal uptake on SPECT/CT. Increased uptake was seen at the level of intervention in 89 patients. In the remaining 23, no uptake was seen at the level of intervention. Analysis of these results showed that intervention at a level concordant with SPECT/CT was significantly correlated with self-reported pain relief thresholds at 24 h. The authors concluded that facet interventions based on uptake on SPECT/CT were more successful in pain reduction than those that were not, suggesting “a role for SPECT/CT in diagnosing therapeutic targets for neck pain.”

Spine Journal

¹²⁵I-BMIPP SPECT/CT vs PET/CT for BAT Imaging

Frankl et al. from the University of Texas Southwestern Medical Center (Dallas), McGovern Medical School/University of Texas Health Science Center at Houston, Central Taiwan University of Science and Technology (Taichung City), and Texas Tech Health Sciences Center (El Paso) reported on April 28 in the *International Journal of Molecular Sciences* (2022; 23[9]:4880) on a preclinical study comparing ¹²⁵I-β-methyl-*p*-iodophenylpentadecanoic acid (¹²⁵I-BMIPP; a fatty acid analog) SPECT/CT and ¹⁸F-FDG PET/CT in noninvasive evaluation of

metabolically active adipose tissue, including brown adipose tissue (BAT). Mice treated with either a BAT-stimulating drug or saline vehicle control were imaged with both ¹²⁵I-BMIPP SPECT/CT and ¹⁸F-FDG PET/CT, and tracer uptake was assessed in interscapular BAT, inguinal white adipose tissue, and gonadal white adipose tissue. Uptake of both tracers increased in BAT and inguinal white adipose tissue after the BAT-stimulating drug, with SUV_{means} correlating closely with the adipose tissue deposits. However, ¹²⁵I-BMIPP uptake in BAT and inguinal white adipose tissue more closely correlated with fold changes in metabolic rate as measured by an extracellular flux analyzer. The authors concluded that “imaging BAT with the radioiodinated fatty acid analogue BMIPP yields more physiologically relevant data than ¹⁸F-FDG-PET/CT” and that its routine use “may be a pivotal tool for evaluating BAT in both mice and humans.”

International Journal of Molecular Sciences

PET/CT and Disease Extent in Kaposi Sarcoma

Pesqué et al. from Saint Louis University Hospital/Assistance-Publique Hôpitaux de Paris, Université de Paris Cité, and Cochin University Hospital (all in Paris, France) reported on April 27 in *Cancers (Basel)* (2022;14[9]: 2189) on a study exploring the diagnostic accuracy of ¹⁸F-FDG PET/CT in defining the extent of disease in patients with Kaposi sarcoma. The study included 75 patients who underwent PET/CT, for which the diagnostic accuracy for cutaneous and extracutaneous Kaposi sarcoma staging was assessed on a per lesion basis. These results were compared with conventional staging from clinical examination, standard imaging, endoscopy, and histologic analyses, as well as follow-up data. The sensitivity and specificity of PET/CT for overall detection of lesions were 71% and 98%, respectively (with corresponding percentages of 100% and 85% for lymph nodes, 87% and 98% for bone, 87% and 100% for lungs, and 100% and 100% for

muscle involvement). Sensitivity was only 17% in detecting digestive involvement. The sensitivity for diagnosing cutaneous involvement was increased from 73% to 88% when whole-body PET/CT was used. The authors concluded that these data suggest that ¹⁸F-FDG could be used for staging patients with active Kaposi sarcoma.

Cancers (Basel)

Postradiation PET in Cervical Cancer Management

In an article published on May 7 ahead of print in *Gynecologic Oncology*, Mckinnish et al. from Washington University School of Medicine in St. Louis (MO), CoxHealth (Springfield, MO), and Dartmouth Hitchcock Medical Center (Lebanon, NH) detailed the effects of postradiation ¹⁸F-FDG PET in management and outcomes in cervical cancer patients. The study included 81 women who showed a partial metabolic response on initial postradiation PET imaging. Thirty of these patients underwent cervical biopsy, of whom 14 (47%) had persistent cancer, with 9 undergoing treatment (surgery, 3; chemotherapy alone, 5; and chemotherapy and radiation; 1). Progression-free and overall survival were similar regardless of treatment type and with or without treatment. A second surveillance PET examination showed a positive-predictive value of 91% and negative-predictive value of 75% for progression and identified the 19% of patients with persistent extracervical disease. The results of cervical biopsy produced a higher positive-predictive value (100%) and lower negative-predictive value (62.5%) for progression. At the end of the study period, 46 (57%) patients had died, including all 8 with paraaortic or supraclavicular involvement. The authors concluded that if partial metabolic response is identified on 3-mo ¹⁸F-FDG PET after completion of radiation for cervical cancer, “repeat FDG PET and/or biopsy are indicated to detect persistence and assist in counseling” and that “partial metabolic response predicts poor outcomes, particularly for those

with positive cervical biopsies and lymphatic involvement.”

Gynecologic Oncology

⁶⁸Ga-PSMA PET and Locally Ablative RT in Prostate Cancer

Hölscher et al. from the University Hospital Carl Gustav Carus/Technische Universität Dresden, National Center for Tumor Diseases (NCT) (Dresden), German Cancer Research Center (DKFZ) (Heidelberg), Klinikum Chemnitz GmbH/Medizin-campus Chemnitz der TU Dresden (Chemnitz), University Hospital Tübingen, RKH-Kliniken Ludwigsburg/Academic Hospital of University Heidelberg (Ludwigsburg), and the Helmholtz-Zentrum Dresden-Rossendorf/Institute of Radiooncology-OncoRay (Dresden, all in Germany) reported on April 21 in *Cancers (Basel)* (2022;14[9]:2073) on the results of a prospective clinical trial to evaluate local control and patterns of tumor progression in patients receiving ⁶⁸Ga-prostate-specific membrane antigen (⁶⁸Ga-PSMA) PET-staged metastasis-directed local ablative radiation treatment (RT) for recurrent oligometastatic prostate cancer. The study included 63 patients who received ablative RT for 89 metastases (68 lymph node, 21 bony) with either 50 Gy in 2-Gy fractions (34 metastases) or 30 Gy in 10-Gy fractions (55 metastases). Mean gross tumor and planning target volumes were 2.2 and 14.9 mL, respectively. Over a median follow-up of 40.7 mo, local progression was identified in 7 metastases, for a 3-y local control rate of 93.5%. Local progression was not associated with treatment schedule, target volumes, or lesion types. Regional progression near lymph node metastases was observed in 19 of 47 patients with at least 1 lymph node metastasis, and distant progression was seen in 33 patients (52%). The overall median time to first tumor-related clinical event was 16.6 mo, with 22.2% of participants experiencing no tumor-related clinical event at 3 y after RT ablation. Fourteen patients (22%) underwent repeat RT ablation. The authors concluded that “local ablative RT in patients with PSMA PET-

staged oligometastatic prostate cancer may achieve local control, but regional or distant progression is common,” adding that additional studies are needed to define optimal target volumes in this setting.

Cancers (Basel)

Experience with Lenvatinib for Advanced Thyroid Cancer

Hamidi et al. from the Centre Hospitalier de l'Université de Montréal (Canada) reported on March 23 ahead of print in the *Journal of the Endocrine Society* on their institution's experience with lenvatinib in treatment of advanced radioiodine-refractory differentiated thyroid carcinomas, with a focus on adverse events of the type reported in clinical trials. The study included 27 patients, whose records were reviewed retrospectively. Twenty-four of the patient records included evaluation of tumor response during treatment. Their overall response rate was 37.0%, and the disease control rate was 85.2%. For all patients, median progression-free survival was 12 mo. Adverse events noted were hypertension (77.8%), fatigue (55.6%), and weight loss (51.9%). Twenty-five patients (92.6%) experienced at least 1 grade ≥ 3 adverse event, with 59.3% experiencing hypertension. Lenvatinib administration was discontinued because of adverse events in 13 patients (48.1%). One patient experienced a grade 4 posterior reversible encephalopathy syndrome, and 1 patient developed a Takotsubo cardiomyopathy. These findings, as well as survival statistics, were similar to those from clinical trials of lenvatinib. The authors concluded that “rigorous blood pressure control is essential to avoid discontinuing therapy” in this setting.

Journal of the Endocrine Society

Reducing Motion-Related Inaccuracies in ^{99m}Tc-MAA SPECT/CT SIRT Planning

In an article published on May 5 in *Physica Medica* (2002;98:98-112) Santoro et al. from the IRCCS Azienda Ospedaliero-Universitaria di Bologna

(Italy) reported on development of a data-driven solution to correct for respiratory motion in ^{99m}Tc-macroaggregated albumin (^{99m}Tc-MAA) SPECT/CT pretreatment planning for ⁹⁰Y selective internal radiation therapy (SIRT) in primary and secondary hepatic lesions. The resulting tool realigns the functional centers of SPECT projection images and shifts them to derive a close registration with attenuation maps. The authors describe validation of the technique using a modified dynamic phantom with varied breathing patterns. The tool was applied and analyzed in 12 patients undergoing SIRT. Significant improvements over conventional techniques were noted. The authors concluded that “the proposed tool allowed the correction of ^{99m}Tc-MAA SPECT/CT images, improving the accuracy of the absorbed dose distribution.”

Physica Medica

Additional Value of SPECT in CCTA

Javaid et al. from the University of Nevada Las Vegas School of Medicine, the Houston Methodist DeBakey Heart and Vascular Center (Texas), and Texas A&M College of Medicine (Bryan) reported on April 15 ahead of print in the *International Journal of Cardiology* on an exploration of the incremental prognostic role of SPECT physiologic assessment to coronary computed tomographic angiography (CCTA) in patients with suspected coronary artery disease. The study included 956 patients (mean age, 61.1 \pm 14.2 y; 54% men, 46% women; 89% with hypertension, 81% with diabetes, and 84% with dyslipidemia) with suspected coronary artery disease who underwent clinically indicated CCTA within 180 d of SPECT imaging. Patients were followed for major adverse cardiovascular events (all-cause death, nonfatal myocardial infarction, and percutaneous coronary intervention or coronary artery bypass grafting within 90 d after imaging). Obstructive stenosis was identified in 14% of patients, scar (fixed perfusion defect) in 17%, ischemia in 14%, and left ventricular ejection fraction <40% in 9%. Additional analyses

showed that perfusion and left ventricular function when added to a model with CCTA obstructive stenosis significantly improved risk prediction and risk reclassification on a continuous scale. The authors concluded that these data indicated that “a combined assessment of perfusion burden and left ventricular function added incremental value over and above a CCTA-based anatomic assessment in patients with suspected coronary artery disease.”

International Journal of Cardiology

Optimal Radioiodine Treatment in Hyperthyroidism

In an article published on April 25 in *Thyroid Research* (2022;15[1]:8) Nilsson et al. from the Karolinska Institutet/Karolinska University Hospital (Stockholm, Sweden) reported on a study addressing appropriate activity dosages and pretherapeutic measurements required for optimal radioiodine treatment of hyperthyroidism. The retrospective study included outcomes and treatment parameters for 904 patients treated for Graves disease (prescribed absorbed dose, 120 Gy), toxic multinodular goiter (200 Gy), or solitary toxic adenoma (300 Gy) from 2016 to 2020 at a single institution. Cure rates for hyperthyroidism after a single radioiodine administration were 79% for Graves disease, 94% for toxic multinodular goiter, and 98% for solitary toxic adenoma. Thyroid mass, uptake, and effective half-life were significantly associated with cure in Graves disease but not in toxic multinodular goiter. Therapy-induced hypothyroidism occurred in 20% and 29% of patients with toxic multinodular goiter and solitary toxic adenoma, respectively. In patients with toxic nodular goiters who received individualized effective half-

life assessments, cure rates and hypothyroidism rates were not improved over patients who did not have such assessments. Poor renal function was found to be associated with what the authors termed “dubious” iodine uptake measurements but did not correlate with worse outcomes. The authors concluded that “multiple measurements of individual iodine uptake for kinetics estimation may be unnecessary” in treatment of hyperthyroidism and that a population-based value may be used instead. Patients with renal impairment were found to have outcomes similar to those of other patients, despite a higher incidence of confounding uptake measurements.

Thyroid Research

Reviews

Review articles provide an important way to stay up to date on the latest topics and approaches through valuable summaries of pertinent literature. The Newsline editor recommends several general reviews accessioned into the PubMed database in April and May. Borgheresi, from the University Politecnica delle Marche (Ancona, Italy), and colleagues from a consortium of research entities in Italy published “Lymph nodes evaluation in rectal cancer: Where do we stand and future perspective” on May 5 in the *Journal of Clinical Medicine* (2022;11[9]:2599). In an article published on April 28 ahead of print in *The Oncologist*, Wirth, from Harvard Medical School/Massachusetts General Hospital (Boston), and researchers from Sapienza University of Rome (Italy), Alfred Health/Monash University (Melbourne, Australia), the University of Western Ontario (London, Canada), Rabin Medical Center/Beilinson Hospital, Tel Aviv University (Israel), Kanagawa Cancer Center (Japan), University Hospital Marburg (Germany), Univer-

sity of Pisa (Italy), Gustave-Roussy Institut (Villejuif, France), the University of Paris-Saclay (Gif-sur-Yvette, France), and the National Cancer Center Hospital East (Kashiwa, Japan) reviewed “Lenvatinib for the treatment of radioiodine-refractory differentiated thyroid cancer: Treatment optimization for maximum clinical benefit.” Huan, from the First Affiliated Hospital of Dalian Medical University (China), and researchers from the Second Affiliated Hospital of Guangzhou University of Chinese Medicine (China), the University of West London (UK), Hainan General Hospital (Haikou, China), and Rutgers University (New Brunswick, NJ) published “Brain imaging changes in patients recovered from COVID-19: A narrative review” on April 22 in *Frontiers in Neuroscience* (2022;16:855868). “New advanced imaging parameters and biomarkers: A step forward in the diagnosis and prognosis of TTR cardiomyopathy” were summarized by Rimbas and colleagues from the University and Emergency Hospital and the University of Medicine and Pharmacy Carol Davila (both in Bucharest, Romania) on April 22 in the *Journal of Clinical Medicine* (2022; 11[9]:2360). Kaliszewski et al. from Wroclaw Medical University (Poland) reported in the April 17 issue of *Cancers (Basel)* (2022;14[8]:2028) on “Advances in the diagnosis and therapeutic management of gastroenteropancreatic neuroendocrine neoplasms.” In an article published on April 22 in *Endocrine-Related Cancer* (2022;29[5]:R57–R66), Karapanou et al. from the General Military Hospital of Athens, Alexandra Hospital/Athens University School of Medicine, and Evangelismos Athens General Hospital (all in Greece) reported on “Advanced RAI-refractory thyroid cancer: An update on treatment perspectives.”

More Unacceptable Denials: Now It's PSMA-Targeted PET/CT Imaging

Johannes Czernin¹, Thaiza Adams¹, and Jeremie Calais²

¹David Geffen School of Medicine at UCLA, Los Angeles, California; and ²Department of Molecular and Medical Pharmacology, UCLA, Los Angeles, California

Following in the footsteps of others (1), we have written about insurance denials. We argued about it in the context of ¹⁸F-FDG PET/CT imaging (2), ⁶⁸Ga-DOTATATE imaging (3), ¹⁷⁷Lu-DOTATATE therapy (Lutathera; Advanced Accelerator Applications) (4), and ¹⁸F-fluciclovine PET/CT imaging (2). Hicks has written about this in the context of Australian and worldwide insurance coverage discussions for ¹⁸F-FDG PET/CT (1).

Now, we must write again about major U.S. insurance companies, including Anthem Blue Cross, United Healthcare, Cigna, Blue Shield, and Aetna, and their repeated and inconsistent non-coverage decisions arbitrarily denying clinically indicated prostate-specific membrane antigen (PSMA) PET/CT imaging studies in around 10% to more than 60% of their patients (Table 1).

Here is one example of the reasoning behind insurance denial in a patient with high-risk prostate cancer (Gleason score of 8, serum prostate-specific antigen level > 10 ng/mL) who needs to know whether pelvic (N1) lymph nodes are involved or distant disease is already present (M1a, M1b, M1c). PSMA PET/CT is the best imaging study to obtain this critically important information for determining the best therapeutic strategy. The insurance denial document states that "there are not enough medical studies showing that this test

is better or safer than other tests that can be done for your problem. Other tests (which are typically considered standard of care) can be covered. These include chest CT and abdomen/pelvis CT."

The U.S. Food and Drug Administration approved University of California San Francisco/UCLA's ⁶⁸Ga-PSMA-11 (December 1, 2020), Lantheus' ¹⁸F-DCFPyL Pylarify (May 27, 2021), and Telix' Illuccix cold kit for ⁶⁸Ga-PSMA-11 (December 20, 2021) for 2 indications: PET of PSMA-positive lesions in men with prostate cancer or with suspected metastasis who are candidates for initial definitive therapy, and men with suspected recurrence based on elevated serum prostate-specific antigen levels. Recently the FDA also approved Novartis' Locametz cold kit for ⁶⁸Ga-PSMA-11 (March 23, 2022) for the same indications and also for selection of patients with metastatic prostate cancer for whom ¹⁷⁷Lu-PSMA-directed therapy is indicated. The Centers for Medicare and Medicaid Services approved reimbursement for ⁶⁸Ga-PSMA-11 on July 1, 2021, and Pylarify and Illuccix late in 2021.

The National Comprehensive Cancer Network (NCCN) has added ⁶⁸Ga- and ¹⁸F-based PSMA PET imaging modalities to its clinical practice guidelines for prostate cancer (5). The NCCN panel has recognized the increased sensitivity and specificity of

TABLE 1
PSMA PET/CT Denials by Insurance from September 2021 to March 2022

Insurance company	Patients (n)	Denials		Authorization (n)
		n	%	
Anthem Blue Cross	133	39	29.3	94
United Healthcare	54	27	50.0	27
Cigna	20	11	55.0	9
Blue Shield	60	15	25.0	45
Aetna	26	13	50.0	13
HealthNet	7	1	14.3	6
SCAN	5	5	100.0	0
Other	32	5	15.6	27
Total	337	116	34.4	221

Data obtained at UCLA, April 2022.

PSMA PET tracers, compared with conventional imaging (CT, MRI), for detecting micrometastatic disease at both initial staging and biochemical recurrence. The updated guidelines state that the NCCN panel does not feel that conventional imaging is a necessary prerequisite to PSMA PET and that PSMA PET/CT or PSMA PET/MRI (performed with either ^{68}Ga -PSMA-11 or ^{18}F -DCFPyL) can serve as equally effective, if not more effective, front-line imaging tools for these patients. The NCCN Panel states that either ^{68}Ga -PSMA-11 or ^{18}F -piflufolastat PSMA imaging can be used to determine eligibility for ^{177}Lu -PSMA therapy. These approvals were based on large-scale clinical trials that unambiguously showed that PSMA-targeted imaging is the most accurate test to determine stage (6,7), site of biochemical recurrence (8), source of rising prostate-specific antigen level at any stage of the disease, and to determine target expression eligibility for PSMA-targeted therapy.

We have repeatedly asked our peers in the denial business to become informed, to read, and to stay up to date. We have asked them to take pride in competence and knowledge and have some compassion for patients who go through very difficult times emotionally and financially (as out-of-pocket costs can be as high as \$6,000 for PET/CT scans).

Yet the denials keep coming, and we are still trapped inside paralyzing phone trees waiting for peer-to-peer discussions that are devoid of common sense and knowledge. Patients deserve better service from the insurance companies who they support with their premium payments.

DISCLOSURE

Johannes Czernin is a founder of Sofie Biosciences and holds equity in the company and in intellectual property invented by

him, patented by the University of California, and licensed to Sofie Biosciences. He is also a founder and board member of Trethera Therapeutics and holds equity in the company and in intellectual property invented by him, patented by the University of California, and licensed to Triangle. He also serves on the medical advisory board of Actinium Pharmaceuticals and on the scientific advisory boards of POINT Biopharma, RayzeBio, and Jubilant Pharma and is a consultant for Amgen. No other potential conflict of interest relevant to this article was reported.

REFERENCES

1. Hicks RJ. The injustice of being judged by the errors of others: the tragic tale of the battle for PET reimbursement. *J Nucl Med.* 2018;59:418–420.
2. Czernin J, Allen-Auerbach M, Calais J. Of sheep and wolves: curtailing coverage for essential imaging tests based on flawed use and cost arguments [editorial]. *J Nucl Med.* 2019;60:1657–1658.
3. Czernin J, Ceci F. Aetna and ^{68}Ga -DOTATATE: a sequel to “the injustice of being judged by the errors of others” [editorial]. *J Nucl Med.* 2018;59:721–722.
4. Czernin J, Allen-Auerbach M. Unacceptable denials [editorial]. *J Nucl Med.* 2020; 61:939.
5. NCCN clinical practice guidelines in oncology (NCCN Guidelines[®]): prostate cancer—version 4.2022. NCCN website. https://www.nccn.org/professionals/physician_gls/pdf/prostate.pdf. January 10, 2022. Accessed May 5, 2022.
6. Hope TA, Eiber E, Armstrong WR, et al. Diagnostic accuracy of ^{68}Ga -PSMA-11 PET for pelvic nodal metastasis detection prior to radical prostatectomy and pelvic lymph node dissection: a multicenter prospective phase 3 imaging trial. *JAMA Oncol.* 2021;7:1635–1642.
7. Pienta KJ, Gorin MA, Rowe SP, et al. A phase 2/3 prospective multicenter study of the diagnostic accuracy of prostate specific membrane antigen PET/CT with ^{18}F -DCFPyL in prostate cancer patients (OSPREY). *J Urol.* 2021;206:52–61.
8. Fendler WP, Calais J, Eiber M, et al. Assessment of ^{68}Ga -PSMA-11 PET accuracy in localizing recurrent prostate cancer: a prospective single-arm clinical trial. *JAMA Oncol.* 2019;5:856–863.

Molecular Imaging Findings on Acute and Long-Term Effects of COVID-19 on the Brain: A Systematic Review

Philipp T. Meyer¹, Sabine Hellwig², Ganna Blazhenets¹, and Jonas A. Hosp³

¹Department of Nuclear Medicine, Medical Center - University of Freiburg and Faculty of Medicine, University of Freiburg, Freiburg, Germany; ²Department of Psychiatry and Psychotherapy, Medical Center - University of Freiburg and Faculty of Medicine, University of Freiburg, Freiburg, Germany; and ³Department of Neurology and Clinical Neuroscience, Medical Center - University of Freiburg and Faculty of Medicine, University of Freiburg, Freiburg, Germany

Molecular imaging techniques such as PET and SPECT have been used to shed light on how coronavirus disease 2019 (COVID-19) affects the human brain. We provide a systematic review that summarizes the current literature according to 5 predominant topics. First, a few case reports have suggested reversible cortical and subcortical metabolic alterations in rare cases with concomitant para- or postinfectious encephalitis. Second, imaging findings in single patients with the first manifestations of parkinsonism in the context of COVID-19 resemble those in neurodegenerative parkinsonism (loss of nigrostriatal integrity), but scarceness of data and a lack of follow-up preclude further etiologic conclusions (e.g., unmasking/hastening of neurodegeneration vs. infectious or parainfectious parkinsonism). Third, several case reports and a few systematic studies have addressed focal symptoms and lesions, most notably hyposmia. The results have been variable, although some studies found regional hypometabolism of regions related to olfaction (e.g., orbitofrontal and mesiotemporal). Fourth, a case series and systematic studies in inpatients with COVID-19-related encephalopathy (acute to subacute stage) consistently found a frontoparietal-dominant neocortical dysfunction (on imaging and clinically) that proved to be grossly reversible in most cases until 6 mo. Fifth, studies on post-COVID-19 syndrome have provided controversial results. In patients with a high level of self-reported complaints (e.g., fatigue, memory impairment, hyposmia, and dyspnea), some authors found extensive areas of limbic and subcortical hypometabolism, whereas others found no metabolic alterations on PET and only minor cognitive impairments (if any) on neuropsychologic assessment. Furthermore, we provide a critical appraisal of studies with regard to frequent methodologic issues and current pathophysiologic concepts. Finally, we devised possible applications of PET and SPECT in the clinical work-up of diagnostic questions related to COVID-19.

Key Words: neurology; PET; SPECT; COVID-19; SARS-CoV-2; SPECT; brain

J Nucl Med 2022; 63:971–980
DOI: 10.2967/jnumed.121.263085

Neurologic complications (1) and neurocognitive aftermaths (2) are frequently described in coronavirus disease 2019 (COVID-19), which is caused by an infection with the severe acute respiratory syndrome coronavirus 2 (SARS-CoV-2). Neurologic symptoms are present in roughly two thirds of hospitalized COVID-19 patients, being associated with a more severe course of disease (3), higher age, and preexisting comorbidities (4). So far, the most widely accepted classification of COVID-19-related symptoms refers to their timing with respect to symptom onset (5): the acute phase covers the first 4 wk, whereas the terminus ongoing symptomatic COVID-19 designates the period between the fifth and twelfth weeks after symptom onset. Symptoms that persist for longer than 12 wk and are not explained by an alternative diagnosis are finally subsumed as a post-COVID-19 syndrome (also referred to as long-COVID-19 syndrome).

During the acute phase of the disease, the following complications have been reported with decreasing frequency: disturbance of smell or taste in approximately 60%–80% of patients (6), myalgia as a sign of viral myositis in approximately 40% of patients (7), encephalopathies with various manifestations in 15%–30% of hospitalized patients (3,8,9), cerebrovascular events (e.g., stroke, hemorrhage, or sinus vein thrombosis) in 1%–5% of hospitalized patients (10), peripheral neuropathies ranging from cranial nerve palsies to Guillain-Barré syndrome in larger case series (11,12), and, only occasionally, encephalitic manifestations (13).

Regarding the phase of ongoing symptomatic COVID-19, various studies report lasting neuropsychiatric symptoms such as fatigue, memory loss, and attentional problems (14,15). Furthermore, cognitive impairment affecting attentional and executive functions, memory, and visuoconstruction are ascertainable by neuropsychologic test batteries (16–18). Especially in patients treated as inpatients or with more severe clinical courses, some of these symptoms may represent residual, though recovering, deficits from an initial COVID-19-related encephalopathy.

Among other symptoms, fatigue, subjective cognitive impairment, and headache extend into the phase of post-COVID-19 syndrome (2,19). Although the term *post-COVID-19 syndrome* in its strict sense (5) is detached from particular symptoms, it is widely used as a label for a syndrome enveloping lasting fatigue, cognitive problems, and shortness of breath, which affect approximately 10% of all patients (2,19). These symptoms, unlike symptoms in cases with COVID-19-related encephalopathy, do not necessarily occur with or shortly after infection but may be noticed weeks to even months later and affect not only initially severely affected patients but also those with an uncomplicated, ambulatory disease course (2,19). During the

Received Nov. 8, 2021; revision accepted Feb. 10, 2022.

For correspondence or reprints, contact Philipp T. Meyer (philipp.meyer@uniklinik-freiburg.de).

Published online Feb. 17, 2022.

Immediate Open Access: Creative Commons Attribution 4.0 International License (CC BY) allows users to share and adapt with attribution, excluding materials credited to previous publications. License: <https://creativecommons.org/licenses/by/4.0/>. Details: <http://jnm.snmjournals.org/site/misc/permission.xhtml>.

COPYRIGHT © 2022 by the Society of Nuclear Medicine and Molecular Imaging.

preparation of this review, the World Health Organization (WHO) published a definition of “post–COVID-19 condition” that demands, in addition to a period of usually 3 mo from symptom onset, the presence of at least one specified symptom (e.g., fatigue or cognitive dysfunction) lasting for at least 2 mo and exerting a relevant impact on everyday functioning (20). Because of the novelty of this publication, all reports reviewed here used institutional or earlier definitions (5).

Furthermore, the incidence of dementia, parkinsonism, and psychiatric disorders (i.e., mood, anxiety, and psychosis) within 6 mo after infection is significantly higher in patients who had COVID-19 than in those affected by influenza or other respiratory tract infections (21). Here, encephalopathy during the acute phase turned out to be the most important risk factor. Thus, COVID-19 may unmask subclinical neurodegenerative disorders or worsen preexisting conditions.

Molecular imaging techniques such as PET and SPECT have been used for the diagnostic work-up of neurologic COVID-19 manifestations. These examinations provided a plethora of sometimes conflicting results in highly variable populations that are often ill defined in terms of symptoms and temporal course. Thus, the objective of the present systematic review is to provide a comprehensive, structured, and critical survey of actual knowledge on molecular imaging in neuropsychiatric COVID-19 manifestations. In addition, we provide a preliminary suggestion on possible future use of PET and SPECT in this particular field of application based on the literature and our personal experience.

MATERIALS AND METHODS

We conducted a MEDLINE (<https://www.ncbi.nlm.nih.gov>) literature search to identify peer-reviewed original studies and case series or case reports using PET or SPECT to investigate central nervous system (CNS) manifestations of COVID-19. The following search criteria were applied: “(corona OR COVID OR SARS-CoV-2) AND (PET OR positron OR SPECT OR single-photon) AND (brain OR cerebral),” limited to 2019–2021. Titles, abstracts, full-text articles, and references were screened to identify appropriate reports. In addition, we conducted a selective search for current literature on general, neurologic, and psychiatric aspects of COVID-19 and related topics to embed the imaging finding into clinical and scientific context.

INSIGHTS FROM MOLECULAR IMAGING WITH PET AND SPECT

The literature search yielded 53 hits (as of November 1, 2021), of which 25 publications included the results of PET and SPECT examinations in patients with various neurologic symptoms and complaints at variable time points after an infection with SARS-CoV-2. These reports comprise 15 case reports or case series (Supplemental Table 1; supplemental materials are available at <http://jnm.snmjournals.org>) and 10 original publications (Tables 1 and 2; Supplemental Table 2). For the sake of clarity, we assigned all reports to 1 of the following 5 topics. According to current knowledge, this assignment does not imply that different mechanisms necessarily underlie each different topic or that these are mutually exclusive.

Encephalitis

There were 3 independent case reports including ^{18}F -FDG PET in patients with autoimmune encephalitis in the acute to subacute phase of COVID-19 (22–24). Given the preliminary nature of case reports, we are summarizing only the most noteworthy findings and refer the interested reader to Supplemental Table 1 for more detail. PET showed diffuse cortical hypometabolism ($n = 1$) and increased metabolism in the basal ganglia ($n = 3$), mesiotemporal

structures ($n = 1$), and cerebellum ($n = 1$), possibly rated to cerebellum- and basal ganglia-specific antineuronal antibodies in 2 of these patients (22,24). Interestingly, immunomodulating treatment led to improvement in all patients, with 6-mo follow-up ^{18}F -FDG PET having normal findings in 1 patient (24). The authors postulated para- or postinfectious encephalitis without evidence of direct virus invasion, which fits into other relative rare cases in the literature (13).

Parkinsonism and Other Neurodegenerative Diseases

Three case reports described molecular imaging findings in 4 patients in whom the first manifestations of parkinsonism occurred only weeks after SARS-CoV-2 infection (in part with other neurologic symptoms such as myoclonus, fluctuating consciousness, ocular abnormalities, and cognitive impairment; Supplemental Table 1). Again, these findings have to be regarded as preliminary although raising the important question of whether and how a COVID-19–related CNS pathology may unmask or worsen neurodegeneration (21): imaging of dopamine transporter availability with ^{123}I -FPCIT SPECT (25,26) and dopamine synthesis and storage with ^{18}F -FDOPA PET (27) in 3 of these patients confirmed a nigrostriatal dopaminergic deficit. In 1 patient, normal cardiac innervation as assessed by ^{123}I -MIBG scintigraphy and subsequent improvement without specific treatment argued against incipient Parkinson disease. The authors speculated that SARS-CoV-2 virus may have gained access to the CNS and affected the midbrain (25). Two patients showed clinical and ^{18}F -FDG PET findings compatible with postinfectious immune-mediated encephalitis that bore similarities to the encephalitis lethargica that was seen after the influenza epidemic in 1918 (26). However, unlike encephalitis cases described in the paragraph above, these patients did not improve (neither spontaneously, nor with immunomodulatory treatment), and it is unclear whether parkinsonism might have been caused by subsequent development or unmasking and hastening of preclinical neurodegeneration (26). Similarly, a patient reported by Cohen et al. (27) was diagnosed with probable Parkinson disease according to current diagnostic criteria, possibly facilitated by genetic susceptibility or virus-induced inflammation. To the best of our knowledge, no imaging follow-up has yet been published, which would help to unravel the underlying mechanism. Finally, the possibility that SARS-CoV-2 infection may precipitate and accelerate neurodegenerative diseases was also raised by Young et al. (28), who presented the case of a previously healthy man who developed rapidly progressive and fatal Creutzfeldt–Jakob disease 2 wk after being diagnosed with COVID-19. In line with Creutzfeldt–Jakob disease, ^{18}F -FDG PET showed left hemispheric hypometabolism. The authors referred to animal and human studies showing that proinflammatory cytokines may promote neuroinflammation and progression of various neurodegenerative forms of dementia and parkinsonism (28).

Focal Symptoms or Lesions

Olfactory dysfunction is the most frequent focal neurologic sign in COVID-19. Several case reports (Supplemental Table 1) and 2 systematic studies (Supplemental Table 2) addressed this symptom. Niesen et al. (29) prospectively examined 12 patients with ^{18}F -FDG PET/MRI about 2 wk after a sudden loss of smell in COVID-19. Single-subject and group analyses of ^{18}F -FDG PET data showed no significant regional findings when using a conservative statistical threshold (i.e., $P < 0.05$, familywise error [FWE]–corrected). When using a liberal threshold ($P < 0.001$), individual analyses showed

TABLE 1
Systematic Studies on Molecular Imaging in Cerebral Manifestations of COVID-19: Encephalopathy

Parameter	Kas et al. (39)	Hosp et al. (18)	Blazhenets et al. (41)
Research question	Longitudinal metabolic pattern in COVID-19 encephalopathy	Neuronal correlates of neurologic and cognitive symptoms (subacute stage)	Recovery of cognitive impairment and regional hypometabolism in subacute COVID-19 during 5- to 6-mo follow-up
Population			
Inclusion (main)	PCR+; new cognitive impairment with focal CNS sign or seizure; other infectious or autoimmune disorders excluded	PCR+; only inpatients; ≥ 1 new neurologic symptom (including cognition [MoCA]); PET, MRI, and neuropsychologic test battery if ≥ 2 new symptoms	Follow-up data of Hosp et al. (18); clinical register, 17 pts with PET during subacute phase; 9 pts without complaints refused follow-up PET
<i>n</i>	7	15 (PET)	8
Age (y)	50–72	65 \pm 14	66 \pm 14
Selected clinical findings	All hospitalized (7); ventilated (3); executive deficit, frontal lobe changes (7); psychiatric manifestation (5); follow-up: improved (6) but residual attention/executive deficit at 4–8 mo; anxiety/depression (4); deterioration (1)	Initial ICU (7/29; 2 only observation; 2 noninvasive and 2 invasive ventilation); impaired gustation (29/29) and smell (25/29); impaired cognition (MoCA < 26; 18/26); prominent deficits in memory (7/14), executive functions (6/13), and attention (6/15); MRI microembolic infarcts (4/13); CSF: PCR– (4/29)	All treated as inpatients during acute phase, ICU (2); self-reported persistent cognitive deficits (4); MoCA: recovery from 19 \pm 5 (1st) to 23 \pm 4 (2nd examination), still impaired (5; especially memory)
¹⁸ F-FDG PET			
Analysis	ROI; SPM: single-subject and group; normalization: scaling to pons; comparison: 32 NCs (identical protocol); <i>P</i> < 0.05 FWE	Single-case: visual inspection; PCA (scaled subprofile model); comparison: 45 control patients (identical protocol); plasma glucose-adjusted SUV; confirmatory analyses with SPM (normalization: white matter, <i>P</i> < 0.01 FDR) and PCA with 35 NC (similar scanner)	PCA: expression of previously established COVID-19-related covariance pattern; SPM: paired (within pts) and unpaired (vs. control patients); (Hosp et al. (18))
Δt	Acute, 4 wk later, or 26 wk after onset	4 \pm 2 wk	23 \pm 7 wk
Major findings	Acute—DEC: frontal, insula, cingulate, CN (group), and posterior cortices (6/7); INC: vermis, dentate nucleus, pons (group; <i>P</i> < 0.05, uncorrected); 4 wk later—DEC: frontal but improved (group); 26 wk after onset—almost normal, residual DEC orbitofrontal, insula, cingulate, CN (group); almost normal (3/7), frontal (3/7), improve/decline (1/7)	Single-case: predominant frontoparietal cortical DEC (10/15), relative INC of striatum (3/15) and vermis (1/15); group PCA: negative voxel weights (DEC) in extensive neocortical regions (especially frontoparietal) and CN; positive voxel weights (interpreted as preserved metabolism) in brain stem, CBL, MTL, and white matter; confirmatory analyses: similar results; significant negative correlation ($r^2 = 0.62$) MoCA vs. pattern expression score	PCA: pattern expression decreased (<i>P</i> = 0.002) but still at trend level higher than in control patients (<i>P</i> = 0.06); negative correlation ($R^2 = 0.39$) between MoCA and pattern expression; SPM (paired): significant recovery of neocortical DEC (<i>P</i> < 0.01 FDR); SPM (unpaired): residual neocortical DEC (trend level, <i>P</i> < 0.005, uncorrected)
Hypothesis	Widespread, frontal-dominant impairment, variably reversible in most patients until 6 mo, due to para- or postinfectious immune mechanism	Cortical dysfunction due to inflammatory process triggered by systemic immune response (e.g., cytokine release), particularly affecting white matter and being possibly reversible	Slow, but evident reversibility of lasting cortical dysfunction due to subcortical perinflammatory processes (triggered by systemic inflammatory response or cytokine release)

MoCA = Montreal Cognitive Assessment; pts = patients; ICU = intensive care unit; CSF = cerebrospinal fluid; PCR = polymerase chain reaction; ROI = region of interest; SPM = statistical parametric mapping; SPM: single-subject or group = SPM-group or single-subject analyses (usually COVID patients vs. NCs); normalization = method/reference region used for count rate normalization of PET scans; NCs = healthy controls; PCA = principal-components analysis; FDR = false-discovery rate correction; Δt = interval between symptom onset or PCR+ for SARS-CoV-2 (as available) and PET; DEC and INC = decreased and increased signal, respectively; CN = caudate nucleus; CBL = cerebellum; MTL = mesial temporal lobe.

Numbers in parentheses refer to number of subjects with specified finding (if subsample assessed is smaller than study group, sample size as indicated). ¹⁸F-FDG target parameter is glucose metabolism.

TABLE 2

Systematic Studies on Molecular Imaging in Cerebral Manifestations of COVID-19: Post-COVID-19 Syndrome

Parameter	Guedj et al. (43)	Sollini et al. (45)	Morand et al. (44)	Dressing et al. (46)
Research question	Metabolic pattern of long COVID	Whole-body PET/CT (including brain) to gain insights into long COVID (for whole body, see report)	Regional metabolic pattern in pediatric patients with suspected long COVID	Regional metabolic pattern in patients with neurocognitive long COVID
Population				
Inclusion (main)	Retrospective; >3 wk after SARS-CoV-2 infection (PCR+ or antibody-positive); persistent fatigue; PET for neurologic complaints; normal CT/MRI	Observational case-control study; ≥1 persistent symptom for >30 d after infection (PCR: NA); NCs: age- and sex-matched, surgically treated melanoma pts with negative PET/CT	Retrospective; children with suspected long COVID (clinical diagnosis); evaluation for various functional complaints ≥ 4 wk after suspected SARS-CoV-2 infection	History of PCR+ SARS-CoV-2 infection; new subjective neurocognitive symptoms > 3 mo since PCR+; no preexisting neurodegenerative disease; PET recommended to all pts (performed in 14/31; clinical findings in PET subgroup not different)
<i>n</i>	35	13	7	31
Age (y)	55 ± 11	54 (46–80)	12 (10–13)	14 (PET), 56 ± 7
Selected clinical findings	Hospitalized in ICU (12/31); ventilated (5/31); memory/cognitive complaints (17), insomnia (16), hyposmia (10)	Hospitalization (7/13); ventilated (2/13); dyspnea (9), fatigue (8), anosmia (4), ageusia (3)	Initial symptoms: fever (6), muscle pain (6), asthenia (5), rhinitis (5), hyposmia (5); long COVID symptoms: fatigue (5), cognitive impairment (5), dyspnea (4), headache (4); PCR+ (1/5) and positive SARS-CoV-2 serology (2/6)	Acute-phase inpatients (10; ICU 4); no current focal sign; subjective difficulties in attention and memory (31), fatigue (24), reduced work quota/unable to work (12); extensive neuropsychology: normal on group level, unimpaired test battery (15), but individual pts with deficits in memory domain (7/31) or impaired MoCA (9/31), fatigue (19/31)
¹⁸ F-FDG PET				
Analysis	SPM: group; normalization: proportional scaling; comparison: 44 NCs (earlier study); <i>P</i> < 0.001, clusterwise <i>P</i> < 0.05 FWE	Brain PET extracted from whole-body scans; SPM: group; normalization: proportional scaling (global); comparison: 26 control patients; <i>P</i> < 0.001/0.005 (uncorrected)	SPM: group; normalization: proportional scaling (global); comparison: 21 pediatric control patients.; findings in adults (Guedj et al. (43)); <i>P</i> < 0.001, clusterwise <i>P</i> < 0.05 FWE	Single case: visual inspection plus single-case statistical analyses (3D-SSP); PCA: expression of COVID-19-related covariance pattern; SPM (confirmatory): group, normalization: brain parenchyma, <i>P</i> < 0.05 FDR; comparison: 45 control patients (Hosp et al., (18))
Δt (wk)	14 ± 4 (4–22)	19 ± 4	20 (4–34)	28 ± 9
Major findings	DEC: rectal/orbital gyrus, R temporal lobe (incl. MTL), R thalamus, pons/medulla, CBL; various weak correlations (<i>r</i> ² < 0.35), e.g., complaints (<i>n</i>), hyposmia, memory/cognitive complaint vs. CBL DEC	DEC (group contrast, <i>P</i> < 0.001)*: R parahippocampal, R thalamus; DEC in persistent anosmia/ageusia (<i>P</i> < 0.005)*: bilateral parahippocampal and orbitofrontal; DEC in persistent fatigue (<i>P</i> < 0.005)*: R parahippocampal, brain stem, bilateral thalamus	Comparison to pediatric control patients: bilateral DEC in MTL, pons, CBL; comparison to adult long COVID pts: no difference	Single case: no distinct pathologic finding; PCA: no elevated expression of COVID-19-related covariance pattern, no correlation with MoCA; SPM (confirmatory): no region of significantly different metabolism, no correlation with clinical scores
Hypothesis	SARS-CoV-2 neurotropism through olfactory bulb, extension of impairment to limbic or paralimbic regions, thalamus, CBL, and brain stem	Neuronal/synaptic dysfunction occurring after inflammatory changes triggered by SARS-CoV-2 infection	Several possible explanations (inflammatory, immune, neurotropism, vascular, gut-brain disturbance, psychologic), but none clearly favored	Factors other than those causing subacute cortical dysfunction in COVID-19 cause or contribute to symptoms in long COVID, in particular fatigue

*Questionable anatomic localization, hard to differentiate from CSF spaces.

3D-SSP = three-dimensional stereotactic surface projection; PCR = polymerase chain reaction; NA = not applicable; NCs = healthy controls; pts = patients; ICU = intensive care unit; DEC = decreased signal; MTL = mesial temporal lobe; CBL = cerebellum; PCA = principal-components analysis; MoCA = Montreal Cognitive Assessment.

Numbers in parentheses refer to number of subjects with specified finding (if subsample assessed is smaller than study group, sample size as indicated). ¹⁸F-FDG target parameter is glucose metabolism.

a heterogeneous pattern of metabolic decreases ($n = 3$), increases ($n = 1$), or both ($n = 8$) in various regions (e.g., olfactory regions, primary and higher-order cortices, and cerebellum), whereas group analyses resulted in clusters of hypometabolism in medial and dorsal frontal areas and hypermetabolism in orbitofrontal and parietal cortex and thalamus. Given the heterogeneity of findings, the authors concluded that the main pathophysiologic hypotheses of COVID-19-related hyposmia (i.e., olfactory cleft obliteration and neuroinvasion of SARS-CoV-2) do not explain dysosmia in all patients and that the PET findings probably reflect deafferentation and functional reorganization (29). In contrast, earlier case reports found orbitofrontal hypometabolism in patients with anosmia (30,31), which was interpreted as a result of direct neuroinvasion of SARS-CoV-2 via the olfactory bulb. As preliminary support for a possible extension of impairment to other brain structures, the latter groups also reported hypometabolism of medial temporal structures in a patient with COVID-19-related parosmia (32) and a patient without olfactory dysfunction (31) (in addition to other regions; Supplemental Table 1). A recent systematic study also found hints of an impairment of mesiotemporal structures in COVID-19-related olfactory dysfunction: Donegani et al. (33) prospectively recruited 14 patients with isolated hyposmia during the recovery phase from COVID-19 (4–12 wk after the first positive PCR result). Compared with control subjects and applying corrections for covariates (age, sex, scanner type) and multiple comparisons (i.e., $P < 0.05$, FWE-corrected), patients with isolated hyposmia were characterized by clusters of hypometabolism bilaterally in the parahippocampal and fusiform gyri and in the left insula, possibly reflecting cortical deafferentation. Beyond its implication in hyposmia, the involvement of limbic regions in COVID-19 may imply a risk of developing long-term neurologic (possibly cognitive) impairment, as discussed by the authors (33).

Other focal signs preliminarily investigated by ^{18}F -FDG PET include a case of facial palsy with putative hypometabolism of the respective facial nerve (34) and a patient with frequent focal seizures possibly due to subacute encephalitis after SARS-CoV-2 infection with a normal ^{18}F -FDG PET result (35) (Supplemental Table 1). Another group reported hypermetabolism of the inferior colliculi as a novel finding in patients with COVID-19 (36,37) that was associated with more frequent seizures and higher blood leukocytes at admission. However, the cause of this finding (e.g., inflammatory reaction (37), hyperactivation (36), and artifact) and its clinical relevance needs to be defined (Supplemental Tables 1 and 2).

Encephalopathy

All patients reported in this “Encephalopathy” section underwent inpatient and possibly intensive care unit treatment because of the overall high severity of COVID-19 symptoms. Furthermore, symptoms compatible with encephalopathy occurred with or briefly after the onset of general COVID-19 symptoms. Thus, the following study populations comprise a fairly homogeneous group. This homogeneity probably constitutes the basis for the observation that available ^{18}F -FDG PET studies in COVID-19-associated encephalopathy yielded very consistent results (Table 1; Supplemental Table 1):

An initial case series by Delorme et al. ((38); $n = 4$) and subsequent systematic prospective studies by Kas et al. ((39); $n = 7$) and Hosp et al. ((18); $n = 15/29$ with PET, exhibiting symptoms compatible with encephalopathy) unanimously showed that the acute to subacute phase (± 1 mo after infection) of COVID-19-associated encephalopathy is characterized by cognitive impairment (e.g., psychomotor agitation or slowing, executive functions, attention, visuoconstruction, and memory) and occasional other neurologic signs

(e.g., hemiparesis, ataxia, apraxia, aphasia, myoclonus, and seizures). This clinical presentation is accompanied by a pronounced hypometabolism of frontoparietal-dominant neocortical areas (visual reads and conventional statistical parametric mapping [SPM] analyses, $P < 0.05$, FWE-corrected, or $P < 0.01$, false-discovery rate-corrected). Similar results were gained from a voxelwise, principal-components analysis-based comparison to age-matched controls, which yielded an extensive pattern of negative voxel weights (i.e., reduced metabolism) in frontoparietal-dominant neocortical areas and the caudate nucleus (18). Although an apparent hypermetabolism of striatum, pons, and cerebellar structures was found on individual visual reads and in statistically liberal ($P < 0.05$, uncorrected) group analyses (18,38,39), more thorough analyses suggest that these regions most likely show a preserved, actually not elevated, metabolism (18,40). Figure 1 shows the results of principal-components analysis and SPM group comparisons of patients with COVID-19-related encephalopathy compared with a group of healthy controls. Moreover, the individual expression score of the COVID-19-related spatial covariance pattern exhibited a highly significant, negative correlation with individual results from cognitive testing using the Montreal Cognitive Assessment ($r^2 = 0.62$, $P < 0.001$ (18)).

Sequential follow-up data 1 mo later (39) and at 5–6 mo after infection (39,41) demonstrated a steady, though not necessarily complete, improvement of the clinical condition and ^{18}F -FDG PET findings in most patients: in the study by Kas et al. (39), all but 1 patient showed a normal neurologic examination and recovered autonomy of daily living on follow-up. Still, all had abnormal cognitive evaluations with at least attentional or executive deficits, and 4 presented with psychiatric impairments. In parallel, cerebral metabolism improved on a group level, with mild residual hypometabolism of the left and right rectal gyri, the right insula, and the caudate nucleus and cerebellum. On a subject level, all but 1 patient, who got worse, showed a moderate to almost complete improvement (39).

Blazhenets et al. (41) provided the follow-up data of 8 patients from the COVID-19 register described by Hosp et al. (Table 1) (18): in parallel to a significant improvement in Montreal Cognitive Assessment performance (from 19 ± 5 to 23 ± 4 , $P = 0.03$; still below normality [$<26/30$] in $n = 5/8$), follow-up ^{18}F -FDG PET examinations showed a significant recovery ($P < 0.01$, false-discovery rate-corrected) of initial neocortical hypometabolism, with small areas of reduced metabolism being still detectable at a liberal statistical threshold ($P < 0.005$) at 6 mo. Likewise, the pattern expression score of the COVID-19-related spatial covariance pattern also significantly decreased over time ($P < 0.005$), albeit being still higher than in controls at a trend level ($P = 0.06$). Again, the pattern expression score correlated inversely with cognitive performance (repeated-measure $r^2 = 0.39$, $P < 0.01$ (41)).

The authors of aforementioned studies agreed that COVID-19-related encephalopathy and the accompanying PET findings are unlikely to be caused by encephalitis due to neuroinvasion of SARS-CoV-2. The findings are more likely explained by a parainfectious systemic immune mechanism (e.g., cytokine release (18,38,39,41)), which according to an autopsy case in the study by Hosp et al. (18) manifests as pronounced microgliosis in the white matter, whereas the gray matter was mostly spared. Furthermore, it was suggested that an underlying neurodegenerative disease may be a predisposing factor (38), particularly in those who do not recover.

Post-COVID-19 Syndrome

Post-COVID-19 syndrome is defined by persisting symptoms at 3 mo after symptom onset. Thus, it may include a highly variable

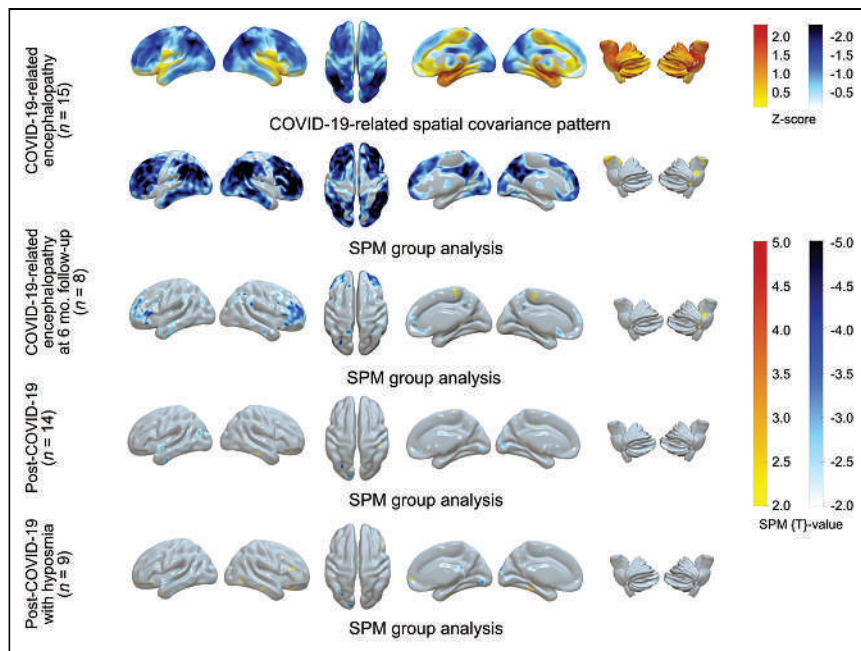


FIGURE 1. ^{18}F -FDG PET in COVID-19-related CNS disorders: principal-components analysis of spatial covariance pattern (first row) and SPM analysis of metabolic group differences (second to fifth rows) in patients with COVID-19-related encephalopathy ($n = 15$; first and second rows, Hosp et al. (18); of them $n = 8$ at 6-mo follow-up examination in third row, Blazhenets et al. (47)), patients with post-COVID-19 syndrome ($n = 14$; fourth row), and patients with post-COVID-19 syndrome and hyposmia ($n = 9$; fifth row, Dressing et al. (46)). Columns from left to right are lateral (left/right), superior, and mesial (right/left) views of cerebrum and lateral (left/right) views of brain stem and cerebellum (overlay created with Surf Ice 2 software; <https://www.nitrc.org/projects/surface/>). Each analysis was performed in comparison to healthy controls ($n = 13$; 7 men and 6 women; mean age, 68 ± 7 y; PET performed under strictly comparable conditions, including age as covariate. SPM analyses entail count rate normalization to white matter (Hosp et al. (18)); virtually identical results were gained with scaling to pons, whereas scaling to total brain parenchyma resulted in apparent [artificial] hypermetabolism in subcortical structures in COVID-19-related encephalopathy (40)). SPM results (t maps) were thresholded liberally for comprehensive display of findings ($t = \pm 2$, corresponding to $P \approx 0.05$, uncorrected). Only extensive neocortical hypometabolism in COVID-19-related encephalopathy survives correction for multiple comparisons (voxel threshold, $P < 0.05$, false discovery rate-corrected).

group of patients in terms of initial disease severity, temporal course, and complaints. Patients still recovering from earlier manifestations (e.g., encephalopathy, usually treated as inpatients) may fall into this category, as will those who experience subjective complaints of brain fog only weeks after infection. Up to now, 1 preliminary case report (Supplemental Table 1) (42) and 4 systematic studies have been published (Table 2).

The team of Guedj et al. reported 2 studies on adults ((43); $n = 35$) and children ((44); $n = 7$) with persistent subjective complaints (mostly memory or cognitive complaints, fatigue, and insomnia) after apparent recovery from COVID-19. The mean or median delay between COVID-19 onset and PET was 3 and 5 mo in the adult and pediatric population, respectively. However, the time spans (26–155 d and 1–8 mo, respectively) indicate that both studies included subjects with ongoing COVID-19 according to the definitions (5) (they would also not fulfill the novel definition of post-COVID-19 condition by the WHO (20)). Both studies provided similar results ($P < 0.05$, FWE-corrected, in adults; $P < 0.001$, uncorrected, in children); compared with healthy adult subjects and control pediatric patients, long-COVID-19 patients showed extensive areas of hypometabolism including the orbitofrontal cortex bilaterally (in children at a liberal statistical threshold only), the medial temporal lobes bilaterally

(hippocampus and amygdala; in adults right side only), the right thalamus (in adults only), and the brain stem and cerebellum. In adults, the number of complaints showed a weak negative association with brain stem and cerebellum uptake ($r^2 = 0.1$ and 0.34 , respectively). In their initial study on adults, the authors proposed neurotropism of SARS-CoV-2 through the olfactory bulb, with extension of impairment to the limbic and other mentioned regions (43), whereas they provided additional alternative explanations in the latter study on children (e.g., inflammatory, dysimmune or vascular changes, disturbance of gut-brain relationship, or psychologic causes (44)). Sollini et al. (45) conducted a case-control study enrolling 13 patients with symptoms (mostly dyspnea and fatigue; Table 2) persisting longer than 30 d after infection recovery (average, 4.4 mo) and extracted brain scans from whole-body ^{18}F -FDG PET/CT examinations. Compared with surgically treated melanoma patients, patients with long-COVID-19 exhibited hypometabolism of the right parahippocampal gyrus and thalamus at a liberal statistical threshold ($P < 0.001$, uncorrected). Exploratory analyses ($P < 0.005$, uncorrected) linked symptoms such as anosmia, ageusia, or fatigue to additional regions such as the orbitofrontal cortex or brain stem (substantia nigra), respectively.

In contrast, Dressing et al. (46) recruited patients with neurocognitive symptoms persisting for more than 3 mo after infection (6.6 mo on average; retrospectively, all meeting the criteria of the post-

COVID-19 condition by the WHO (20)). All patients complained of attention and memory problems, most also complained of fatigue, and 39% could not return to previous levels of independence or employment. However, on extensive neuropsychologic testing, half the patients were completely unimpaired, whereas other patients showed mild to moderate impairment in single domains (most frequently visual memory, 21% of cases). The most consistent finding was fatigue (61%; cognitive fatigue, 67%) when using a self-rating questionnaire. Fourteen patients underwent ^{18}F -FDG PET that yielded no significant regional abnormality in comparison to control patients on either a single-subject or group level (using both SPM [$P < 0.005$, uncorrected] and principal-components analysis; Fig. 1). No correlation between clinical variables and PET measures could be established. Given the striking discrepancy between these findings and findings in COVID-19-related encephalopathy, the authors proposed that mechanisms other than those in encephalopathy probably contribute to post-COVID-19 syndrome, fatigue being foremost (46).

CRITICAL APPRAISAL OF PET AND SPECT LITERATURE

According to the WHO (<https://covid19.who.int/>), there had been almost 250 million confirmed COVID-19 cases and 5 million

deaths by November 1, 2021. In parallel, an unprecedented wealth (or flood) of scientific reports on COVID-19 was published, amounting to 92,940 MEDLINE entries in 2020 and 114,360 in 2021 up to November 1 (search term “COVID-19”; >300 reports per day since January 1, 2020). Although there is no doubt that the COVID-19 pandemic required a fast and collective response of medical research, it is also a frequent perception that in the early phase of the pandemic nearly everything labeled with the term “COVID-19” got published quickly, sometimes too quickly. Still, many questions await definite answers (e.g., mechanism underlying COVID-19–related CNS changes), and it is worthwhile critically gauging existing reports. For instance, a note of caution has recently been published regarding the quality of mental health research in the COVID-19 pandemic, raising concerns about the validity, generalizability, and reproducibility of findings (47).

There are several recurring issues, some of which will be briefly discussed in the following sections. They should be kept in mind when considering the present results. They also represent a request and motivation for further studies.

Study Design and COVID-19 Populations

Given the still high incidence of COVID-19, there is no necessity to rely on retrospective analysis of convenient samples. They pose an inherent risk of bias and, because of the lack or inconsistency of data, do not allow for in-depth analyses of clinicoimaging correlations. Likewise, case reports or series are hardly justified except for very rare conditions, for which they may constitute an interesting starting point. In addition, it is evident that currently available longitudinal studies provided the deepest insight into underlying mechanisms and their course (39,41).

The latter studies demonstrated a strong time dependency of COVID-19–related CNS changes, underlining the need to clearly define the time window of inclusion of patients with respect to the time of SARS-CoV-2 infection. Likewise, it is apparent that a large fraction of inpatients has COVID-19 encephalopathy (~70% (18)), which takes several months to recover from (39,41,48). Despite objective cognitive impairment in these patients, subjective perception of deficits and psychologic strain is frequently lacking in this group (49). In contrast, symptoms such as stress, anxiety, and reduced wellbeing are more prevalent after a mild course of disease (49). Accordingly, long-term symptoms such as subjective cognitive impairment and fatigue typically occur in patients who are younger (<50 y) and have a low rate of hospitalization (<30%; (2,19)). As the definition of “post-COVID-19 syndrome” used so far reflects only temporal aspects (5), there is a tremendous risk of building mixed populations in terms of initial disease severity, treatment, and impairment (subjective/objective). Proper selection of patients will be key in separating protracted COVID-19–related encephalopathy from the post-COVID-19 syndrome in a strict sense (2,19). In this respect, the novel, stricter WHO definition is welcome progress (20). In fact, available PET studies do not support the idea that neurocognitive post-COVID-19 syndrome represents a protracted manifestation of COVID-19–related encephalopathy, because available studies on long-COVID-19 or post-COVID-19 syndrome either yielded no metabolic alteration at all (46) or depicted metabolic changes (43–45) that do not match the highly consistent findings in COVID-19–related encephalopathy (18,39). Concerning the diagnosis of COVID-19, a PCR or at least state-of-the-art antibody proof should be mandatory. From a clinical perspective, typical clinical findings may be sufficient to

ground a diagnosis in a pandemic situation, but this is not sufficient for a scientific study trying to unravel a specific disease.

Up to now, none of the reviewed studies has conducted a proper sample size calculation. Likewise, study registration appears to be an exception (e.g., (18,46)) that needs to be turned into a rule.

Control Populations

The use of convenient samples seems to be an even bigger problem when it comes to PET reference datasets. In fact, the descriptions of methods of most studies do not clearly state whether reference populations were indeed examined under comparable circumstances (e.g., identical scanners, acquisition techniques, reconstruction techniques, or patient preparation). The contribution of technical differences may be negligible if disease effects are large but may be a crucially biasing factor if effects are small (e.g., post-COVID-19 syndrome). Some authors acknowledge inconsistencies and conducted confirmatory analyses (18), whereas most authors ignored this issue. The use of oncologic control patients may be particularly problematic if brain scans are cropped out of whole-body scans, which are usually acquired and reconstructed differently from brain scans. Furthermore, preparation of brain scans requires well-defined resting (or neutral) conditions, whereas adherence to these conditions is lower in patients undergoing whole-body PET/CT (patients may read, talk, or use their smartphones).

Since the publication of the original studies by our group relying on control patients (i.e., patients with unclear neurologic or psychiatric complaints, in whom a somatic CNS disease was carefully excluded (18,41,46)), we had the opportunity to scan a cohort of thoroughly evaluated healthy controls. The local ethics commission and federal office for radiation protection approved this study, and all subjects gave written informed consent. Using these subjects as a reference cohort, we were able to confirm our initial results (Fig. 1). We also conducted an additional analysis on subjects with post-COVID-19 syndrome and hyposmia, but we found no significant hypometabolism of the olfactory regions as described by other groups.

PET Data Analysis

Comparison of datasets by common statistical methods such as SPM requires count rate or intensity normalization. It is well known that extensive, disease-related metabolic alterations in one direction may cause artificial alterations in the other direction on conventional analyses, if diseased brain regions are part of those used for normalization. In cases of neocortical hypometabolism and normalization by whole-brain proportional scaling, apparently “hypermetabolic” areas often include the basal ganglia, thalamus, mesiotemporal regions, brain stem, and cerebellum (40). Several lines of evidence such as ROI analyses (plasma glucose–corrected uptake values), clinicoimaging correlations, and follow-up studies suggest that the areas of hypometabolism in subacute settings most likely reflect true hypometabolism (40). However, in our opinion, and with the possible exception of concomitant autoimmune encephalitis, it is still questionable whether regions of hypermetabolism reported in several studies exhibit true hypermetabolism or inflammation. On one hand, the latter is not convincingly supported by histopathologic data. On the other, an artificial increase seems much more likely, especially if global count rate normalization was applied (40). Still, given the systemic activation of microglia and astrocytes (albeit being most pronounced in the brain stem and cerebellum), one cannot exclude that associated

metabolic changes cause some bias if white matter is used as a reference region (18,41). One way to avoid this problem may be to conduct principal-components analyses as proposed by Hosp et al. (18).

Given the complexity, costs, and radiation exposure, cohorts in PET studies are often rather small, which limits their statistical power. Thus, a pragmatic approach may be to define a liberal statistical threshold and avoid a correction for multiple comparisons. This may lead to type I errors. Several systematic studies (Tables 1 and 2; Supplemental Table 2) used liberal thresholds; consequently, this limitation needs to be kept in mind when considering anatomically (e.g., small clusters near or within CSF spaces (45)) or functionally (e.g., weak correlations with subjective, ill-defined complaints (43)) questionable findings. Such limitations particularly apply to case reports or smaller series, which often suffer from additional flaws (e.g., reliance on observer-dependent visual reads, lack of coregistration to high-resolution structural imaging or MRI; Supplemental Table 1).

Clinicoimaging Correlations

Whereas clinicoimaging correlations cannot prove causality, they may be useful to check for plausibility. For instance, the high correlation of frontoparietal-dominant changes in cerebral metabolism and formally assessed cognitive functions served by frontoparietal regions in COVID-19 encephalopathy (18) supports the notion that these changes depend on each other. The magnitude of metabolic alterations was also in line with imaging studies on patients with comparable cognitive deficits (e.g., dementia).

In turn, some imaging findings need further elucidation: for instance, bilateral hyperactivation of the inferior colliculi (36,37) may be expected to interfere with normal auditory functioning, which, however, was not reported. Given that this finding was reported in rather severely affected patients, one may also consider alternative explanations (e.g., artificial, relative hypermetabolism due to neocortical hypometabolism). Donegani et al. (33) reported a bilateral hypometabolism of the parahippocampal and fusiform gyri in isolated hyposmia. Although they used an 8-item odor test, no correlation analyses were reported. In turn, one may also have expected other deficits such as memory impairment, which unfortunately was not addressed. In cases of post-COVID-19 syndrome, the situation is even more complex: patients commonly complain about multiple symptoms with a high impact on daily functioning, which, however, cannot be verified in such magnitude by formal testing (46,49). Still, extensive patterns of hypometabolism have been reported (43,44), which on first glance may be expected to result in various additional symptoms (e.g., severe objective amnesic problems). Unfortunately, no formal testing was pursued. In contrast, no such metabolic changes were observed in the study by Dressing et al. (46), underscoring the need to verify symptoms and complaints by operationalized formal assessments to gain deeper insights and unravel discrepancies. Such assessments will also benefit from inclusion of additional correlative biomarkers (e.g., PET or CSF biomarkers of neurodegeneration) and, ultimately, imaging-neuropathology correlations, which are still very sparse (18).

Correlations with Knowledge from Related Disciplines

Imaging findings and concepts derived from them have to be aligned with knowledge from related disciplines. It is evident that neurologic or neurocognitive findings in COVID-19 cover a broad spectrum of disciplines. Neuropathologic findings and psychiatric

concepts may be considered as 2 distant ends of such a spectrum. However, we believe that these disciplines are particularly helpful for a better understanding of current findings.

Insights from Neuropathologic Studies. Whereas an early neuropathologic investigation of patients who died from COVID-19 found primarily hypoxic damage (50), more recent reports draw a vivid picture on how COVID-19 may affect the CNS (51,52). Major findings include an activation of microglia (formation of microglia nodules in some patients) and astrocytes, which was pronounced in the brain stem and cerebellum and affected white rather than gray matter. Detection of SARS-CoV-2 (spike protein or RNA) succeeded in approximately 50% of patients, especially in the brain stem and cranial nerves. This detection is remarkable, as the neuroinvasive potential of β -coronaviruses has been broadly discussed (e.g., after nasal inoculation, with axonal and transsynaptic propagation) (53,54). However, because of its sparse detection rate in neuropathologic samples and the absence of lytic figures, infected neurons, or glial cells (51), proofs for direct neuroinvasivity and the occurrence of neuron-to-neuron propagation within the human CNS are lacking. Regarding adaptive immunity, infiltration of CD8 and CD4 T cells especially occurred in the perivascular compartment, being associated with blood-brain barrier dysfunction. Interestingly, the immune activation within the perivascular compartment is specific for COVID-19 and differed from findings in patients with multiple sclerosis or non-COVID-19 respiratory failure (52). Although the SARS-CoV-2 spike protein has been occasionally detected in perivascular cells (52), neuroinflammatory changes are more likely induced by circulating cytokines and inflammatory mediators in the course of a systemic inflammatory response (51,55). These data were derived from unselected patient populations, as the presence of neurologic symptoms was not registered. Thus, additional studies with detailed clinicopathologic correlations are warranted. In addition, PET imaging of activated microglia might represent a promising imaging technique in COVID-19 but to the best of our knowledge has not been explored yet.

Current Concepts of Fatigue. Fatigue might be translated as “extreme and persistent tiredness, weakness or exhaustion that could be mental, physical or both” (56), but there is no further agreement on the definition of this entity (57). Fatigue can cooccur with clinical symptoms such as depression, pain, sleep impairment, and cognitive dysfunction (58) and can be associated with chronic medical conditions (e.g., postviral infection, cancer, inflammatory bowel disease, multiple sclerosis, depression, and fibromyalgia (59)). Thus, a multifactorial etiology with strong impact of somatic as well as psychosocial risk factors has been postulated (60). Fatigue has a significant symptom overlap and comorbidity with psychiatric disorders (61). This is in line with a study investigating predictors of fatigue in individuals recovering from the acute phase of COVID-19: while the female sex and a comorbidity of depression or anxiety were identified as significant predictors for developing fatigue, indicators of COVID-19 severity, markers of peripheral immune activation, and circulating proinflammatory cytokines did not reach statistical significance (62). Still, fatigue seems to be distinct from psychiatric disorders; however, perceptions, attributions, and coping skills of patients with psychiatric comorbidity may perpetuate the fatigue condition (61). This notion is reinforced by a significant therapeutic response of fatigue to cognitive behavior therapy (63). As far as permissible and based on the rather disappointing experience with ^{18}F -FDG PET in psychiatric and somatoform disorders, one may expect that the

contribution of ¹⁸F-FDG PET to understanding and diagnosing a post-COVID-19 syndrome dominated by fatigue is actually limited.

PERSONAL PERSPECTIVE: USE OF MOLECULAR IMAGING IN COVID-19-RELATED CNS DISORDERS

From a scientific point of view, molecular imaging of COVID-19-related CNS disorders represents an exciting field that not only contributes to the understanding of disease mechanisms in COVID-19 but may also provide important implications for other conditions (e.g., neurodegeneration, encephalopathies, and delirium). In this regard, we believe that carefully designed studies on COVID-19 populations are of great interest.

Concerning the clinical application of molecular imaging for diagnosis and management of COVID-19-related CNS disorders, we actually see little impact and, consequently, little need to adjust current clinical practice: ¹⁸F-FDG PET is gaining increasing acceptance for differential diagnosis and follow-up of encephalitis, often showing superior performance over MRI (64,65). Even more so, PET and SPECT are established methods for differential diagnosis of neurodegenerative CNS disorders such as parkinsonism (66,67). Accordingly, in patients with suspected encephalitis or parkinsonism in the context of COVID-19, PET and SPECT may be performed according to established clinical pathways. Follow-up studies would in fact be of particular interest for differentiating between possible reversible COVID-associated nigrostriatal dysfunction and progressive, presumably COVID-independent neurodegenerative parkinsonism. Molecular imaging is also accepted for differential diagnosis in cognitive impairment and dementia (68). However, in the context of COVID-19, it is probably advisable to define the need for additional imaging studies based on the clinical presentation and time course. In cases of possible COVID-19 encephalopathy, a reversible cortical dysfunction can be assumed, while in post-COVID-19 syndrome with predominant fatigue and without decisive pathologic findings on neuropsychologic testing, a pathologic imaging correlate is actually unlikely. In our opinion, patients with “subjective” neuropsychiatric deficits as potential sequelae of COVID-19 should undergo a comprehensive clinical work-up including validated neuropsychologic and neuropsychiatric testing to verify deficits. A diagnostic benefit from ¹⁸F-FDG PET may be expected only if a cognitive impairment is verified and persisting (>3–6 mo) or progressive.

DISCLOSURE

No potential conflict of interest relevant to this article was reported.

REFERENCES

- Paterson RW, Brown RL, Benjamin L, et al. The emerging spectrum of COVID-19 neurology: clinical, radiological and laboratory findings. *Brain*. 2020;143:3104–3120.
- Boesl F, Audebert H, Endres M, Prüss H, Franke C. A neurological outpatient clinic for patients with post-COVID-19 syndrome: a report on the clinical presentations of the first 100 patients. *Front Neurol*. 2021;12:738405.
- Romero-Sánchez CM, Díaz-Maroto I, Fernández-Díaz E, et al. Neurologic manifestations in hospitalized patients with COVID-19: the ALBACOV registry. *Neurology*. 2020;95:e1060–e1070.
- Zádori N, Vánca S, Farkas N, Hegyi P, Eröss B; KETLAK Study Group. The negative impact of comorbidities on the disease course of COVID-19. *Intensive Care Med*. 2020;46:1784–1786.
- NICE Guideline [NG188]: COVID-19 Rapid Guideline—Managing the Long-Term Effects of COVID-19. National Institute for Health and Care Excellence; December 2020.
- Neurological manifestations in COVID-19: update from 02/22/2021 [in German]. Deutsche Gesellschaft für Neurologie website. <https://dgn.org/leitlinien/neurologische-manifestationen-bei-covid-19/>. Accessed March 1, 2022.
- Huang C, Wang Y, Li X, et al. Clinical features of patients infected with 2019 novel coronavirus in Wuhan, China. *Lancet*. 2020;395:497–506.
- Frontera JA, Sabadia S, Lalchan R, et al. A prospective study of neurologic disorders in hospitalized patients with COVID-19 in New York City. *Neurology*. 2021;96:e575–e586.
- Meppiel E, Peiffer-Smadja N, Maury A, et al. Neurologic manifestations associated with COVID-19: a multicentre registry. *Clin Microbiol Infect*. 2021;27:458–466.
- Nannoni S, de Groot R, Bell S, Markus HS. Stroke in COVID-19: a systematic review and meta-analysis. *Int J Stroke*. 2021;16:137–149.
- Andalib S, Biller J, Di Napoli M, et al. Peripheral nervous system manifestations associated with COVID-19. *Curr Neurol Neurosci Rep*. 2021;21:9.
- Palaodimou L, Stefanou M-I, Katsanos AH, et al. Prevalence, clinical characteristics and outcomes of Guillain-Barré syndrome spectrum associated with COVID-19: a systematic review and meta-analysis. *Eur J Neurol*. 2021;28:3517–3529.
- Finsterer J, Scorza FA. Infectious and immune-mediated central nervous system disease in 48 COVID-19 patients. *J Clin Neurosci*. 2021;90:140–143.
- Halpin SJ, McIvor C, Whyatt G, et al. Postdischarge symptoms and rehabilitation needs in survivors of COVID-19 infection: a cross-sectional evaluation. *J Med Virol*. 2021;93:1013–1022.
- Garrigues E, Janvier P, Kherabi Y, et al. Post-discharge persistent symptoms and health-related quality of life after hospitalization for COVID-19. *J Infect*. 2020;81:e4–e6.
- Almeria M, Cejudo JC, Sotoca J, Deus J, Krupinski J. Cognitive profile following COVID-19 infection: clinical predictors leading to neuropsychological impairment. *Brain Behav Immun Health*. 2020;9:100163.
- Woo MS, Malsy J, Pöttgen J, et al. Frequent neurocognitive deficits after recovery from mild COVID-19. *Brain Commun*. 2020;2:fcaa205.
- Hosp JA, Dressing A, Blazhenets G, et al. Cognitive impairment and altered cerebral glucose metabolism in the subacute stage of COVID-19. *Brain*. 2021;144:1263–1276.
- Augustin M, Schommers P, Stecher M, et al. Post-COVID syndrome in non-hospitalized patients with COVID-19: a longitudinal prospective cohort study. *Lancet Reg Health Eur*. 2021;6:100122.
- A Clinical Case Definition of Post COVID-19 Condition by a Delphi Consensus. World Health Organization; October 6, 2021.
- Taquet M, Geddes JR, Husain M, Luciano S, Harrison PJ. 6-month neurological and psychiatric outcomes in 236 379 survivors of COVID-19: a retrospective cohort study using electronic health records. *Lancet Psychiatry*. 2021;8:416–427.
- Grimaldi S, Lagarde S, Harlé J-R, Boucraut J, Guedj E. Autoimmune encephalitis concomitant with SARS-CoV-2 infection: insight from ¹⁸F-FDG PET imaging and neuronal autoantibodies. *J Nucl Med*. 2020;61:1726–1729.
- Pizzanelli C, Milano C, Canovetti S, et al. Autoimmune limbic encephalitis related to SARS-CoV-2 infection: case-report and review of the literature. *Brain Behav Immun Health*. 2021;12:100210.
- Tiraboschi P, Xhani R, Zerbi SM, et al. Postinfectious neurologic complications in COVID-19: a complex case report. *J Nucl Med*. 2021;62:1171–1176.
- Méndez-Guerrero A, Laespada-García MI, Gómez-Grande A, et al. Acute hypokinetic-rigid syndrome following SARS-CoV-2 infection. *Neurology*. 2020;95:e2109–e2118.
- Morassi M, Palmerini F, Nici S, et al. SARS-CoV-2-related encephalitis with prominent parkinsonism: clinical and FDG-PET correlates in two patients. *J Neurol*. 2021;268:3980–3987.
- Cohen ME, Eichel R, Steiner-Birmanns B, et al. A case of probable Parkinson's disease after SARS-CoV-2 infection. *Lancet Neurol*. 2020;19:804–805.
- Young MJ, O'Hare M, Matiello M, Schmahmann JD. Creutzfeldt-Jakob disease in a man with COVID-19: SARS-CoV-2-accelerated neurodegeneration? *Brain Behav Immun*. 2020;89:601–603.
- Niesen M, Trotta N, Noel A, et al. Structural and metabolic brain abnormalities in COVID-19 patients with sudden loss of smell. *Eur J Nucl Med Mol Imaging*. 2021;48:1890–1901.
- Karimi-Galougahi M, Yousefi-Koma A, Bakshayeshkaram M, Raad N, Haseli S. ¹⁸F-FDG PET/CT scan reveals hypoactive orbitofrontal cortex in anosmia of COVID-19. *Acad Radiol*. 2020;27:1042–1043.
- Guedj E, Million M, Dudouet P, et al. ¹⁸F-FDG brain PET hypometabolism in post-SARS-CoV-2 infection: substrate for persistent/delayed disorders? *Eur J Nucl Med Mol Imaging*. 2021;48:592–595.

32. Yousefi-Koma A, Haseli S, Bakhshayeshkaram M, Raad N, Karimi-Galougahi M. Multimodality imaging with PET/CT and MRI reveals hypometabolism in tertiary olfactory cortex in parosmia of COVID-19. *Acad Radiol.* 2021;28:749–751.
33. Donegani MI, Miceli A, Pardini M, et al. Brain metabolic correlates of persistent olfactory dysfunction after SARS-Cov2 infection. *Biomedicines.* 2021;9:287.
34. Karimi-Galougahi M, Yousefi-Koma A, Raygani N, Bakhshayeshkaram M, Haseli S. ¹⁸F-DG-PET/CT assessment of COVID-19-induced Bell's palsy. *Acad Radiol.* 2021;28:144–145.
35. Bozzali M, Grassini A, Morana G, et al. Focal seizures with impaired awareness as long-term neurological complication of COVID-19: a case report. *Neurol Sci.* 2021;42:2619–2623.
36. Chammas A, Bund C, Lersy F, et al. Collicular hyperactivation in patients with COVID-19: a new finding on brain MRI and PET/CT. *AJNR.* 2021;42:1410–1414.
37. Chammas A, Namer JJ, Lersy F, Kremer S, Bund C. Inferior colliculus's hypermetabolism: a new finding on brain FDG PET and perfusion MRI in a patient with COVID-19. *Clin Nucl Med.* 2021;46:413–414.
38. Delorme C, Paccoud O, Kas A, et al. COVID-19-related encephalopathy: a case series with brain FDG-positron-emission tomography/computed tomography findings. *Eur J Neurol.* 2020;27:2651–2657.
39. Kas A, Soret M, Pyatigorskaya N, et al. The cerebral network of COVID-19-related encephalopathy: a longitudinal voxel-based ¹⁸F-FDG-PET study. *Eur J Nucl Med Mol Imaging.* 2021;48:2543–2557.
40. Meyer PT, Blazhenets G, Prinz M, Hosp JA. From early limbic inflammation to long COVID sequelae [reply]. *Brain.* 2021;144:e66.
41. Blazhenets G, Schröter N, Bormann T, et al. Slow but evident recovery from neocortical dysfunction and cognitive impairment in a series of chronic COVID-19 patients. *J Nucl Med.* 2021;62:910–915.
42. Hugon J, Msika E-F, Queneau M, Farid K, Paquet C. Long COVID: cognitive complaints (brain fog) and dysfunction of the cingulate cortex. *J Neurol.* 2022;269:44–46.
43. Guedj E, Campion JY, Dudouet P, et al. ¹⁸F-FDG brain PET hypometabolism in patients with long COVID. *Eur J Nucl Med Mol Imaging.* 2021;48:2823–2833.
44. Morand A, Campion J-Y, Lepine A, et al. Similar patterns of [¹⁸F]-FDG brain PET hypometabolism in paediatric and adult patients with long COVID: a paediatric case series. *Eur J Nucl Med Mol Imaging.* 2022;49:913–920.
45. Sollini M, Morbelli S, Ciccarelli M, et al. Long COVID hallmarks on [¹⁸F]FDG-PET/CT: a case-control study. *Eur J Nucl Med Mol Imaging.* 2021;48:3187–3197.
46. Dressing A, Bormann T, Blazhenets G, et al. Neuropsychological profiles and cerebral glucose metabolism in neurocognitive long COVID-syndrome. *J Nucl Med.* October 14, 2021 [Epub ahead of print].
47. Nieto I, Navas JF, Vázquez C. The quality of research on mental health related to the COVID-19 pandemic: a note of caution after a systematic review. *Brain Behav Immun Health.* 2020;7:100123.
48. Zhao S, Shibata K, Hellyer PJ, et al. Rapid vigilance and episodic memory decrements in COVID-19 survivors. MedRxiv website. <https://www.medrxiv.org/content/10.1101/2021.07.06.21260040v1>. Posted July 8, 2021. Accessed March 1, 2022.
49. Voruz P, Allali G, Benzakour L, et al. Long COVID neuropsychological deficits after severe, moderate or mild infection. MedRxiv website. <https://www.medrxiv.org/content/10.1101/2021.02.24.21252329v1>. Posted February 26, 2021. Accessed March 1, 2022.
50. Solomon IH, Normandin E, Bhattacharyya S, et al. Neuropathological features of Covid-19. *N Engl J Med.* 2020;383:989–992.
51. Matschke J, Lütgehetmann M, Hagel C, et al. Neuropathology of patients with COVID-19 in Germany: a post-mortem case series. *Lancet Neurol.* 2020;19:919–929.
52. Schwabenland M, Salié H, Tanevski J, et al. Deep spatial profiling of human COVID-19 brains reveals neuroinflammation with distinct microanatomical microglia-T-cell interactions. *Immunity.* 2021;54:1594–1610.e11.
53. Desforges M, Le Coupanec A, Dubeau P, et al. Human coronaviruses and other respiratory viruses: underestimated opportunistic pathogens of the central nervous system? *Viruses.* 2019;12:14.
54. Dubé M, Le Coupanec A, Wong AHM, Rini JM, Desforges M, Talbot PJ. Axonal transport enables neuron-to-neuron propagation of human coronavirus OC43. *J Virol.* 2018;92:e00404-18.
55. Mehta P, McAuley DF, Brown M, Sanchez E, Tattersall RS, Manson JJ. COVID-19: consider cytokine storm syndromes and immunosuppression. *Lancet.* 2020;395:1033–1034.
56. Hernandez-Ronquillo L, Moien-Afshari F, Knox K, Britz J, Tellez-Zenteno JF. How to measure fatigue in epilepsy? The validation of three scales for clinical use. *Epilepsy Res.* 2011;95:119–129.
57. Billones R, Liwang JK, Butler K, Graves L, Saligan LN. Dissecting the fatigue experience: a scoping review of fatigue definitions, dimensions, and measures in non-oncologic medical conditions. *Brain Behav Immun Health.* 2021;15:100266.
58. Kinsinger SW, Lattie E, Mohr DC. Relationship between depression, fatigue, subjective cognitive impairment, and objective neuropsychological functioning in patients with multiple sclerosis. *Neuropsychology.* 2010;24:573–580.
59. Saligan LN, Olson K, Filler K, et al. The biology of cancer-related fatigue: a review of the literature. *Support Care Cancer.* 2015;23:2461–2478.
60. Bower JE. The role of neuro-immune interactions in cancer-related fatigue: biobehavioral risk factors and mechanisms. *Cancer.* 2019;125:353–364.
61. Afari N, Buchwald D. Chronic fatigue syndrome: a review. *Am J Psychiatry.* 2003;160:221–236.
62. Townsend L, Dyer AH, Jones K, et al. Persistent fatigue following SARS-CoV-2 infection is common and independent of severity of initial infection. *PLoS ONE.* 2020;15:e0240784.
63. Price JR, Mitchell E, Tidy E, Hunot V. Cognitive behaviour therapy for chronic fatigue syndrome in adults. *Cochrane Database Syst Rev.* 2008;CD001027.
64. Bordonne M, Chawki MB, Doyen M, et al. Brain ¹⁸F-FDG PET for the diagnosis of autoimmune encephalitis: a systematic review and a meta-analysis. *Eur J Nucl Med Mol Imaging.* 2021;48:3847–3858.
65. Baumgartner A, Rauer S, Mader I, Meyer PT. Cerebral FDG-PET and MRI findings in autoimmune limbic encephalitis: correlation with autoantibody types. *J Neurol.* 2013;260:2744–2753.
66. Buchert R, Buhmann C, Apostolova I, Meyer PT, Gallinat J. Nuclear imaging in the diagnosis of clinically uncertain parkinsonian syndromes. *Dtsch Arztebl Int.* 2019;116:747–754.
67. Meyer PT, Frings L, Rücker G, Hellwig S. ¹⁸F-FDG PET in parkinsonism: differential diagnosis and evaluation of cognitive impairment. *J Nucl Med.* 2017;58:1888–1898.
68. Chételat G, Arbizu J, Barthel H, et al. Amyloid-PET and ¹⁸F-FDG-PET in the diagnostic investigation of Alzheimer's disease and other dementias. *Lancet Neurol.* 2020;19:951–962.

Alzheimer Disease: Standard of Diagnosis, Treatment, Care, and Prevention

Stefan Teipel^{1,2}, Deborah Gustafson³, Rik Ossenkoppele^{4,5}, Oskar Hansson⁵, Claudio Babiloni⁶, Michael Wagner^{7,8}, Steffi G. Riedel-Heller⁹, Ingo Kilimann^{1,2}, and Yi Tang¹⁰

¹Department of Psychosomatic Medicine, University Medical Center Rostock, Rostock, Germany; ²Deutsches Zentrum für Neurodegenerative Erkrankungen, Rostock/Greifswald, Rostock, Germany; ³Department of Neurology, Downstate Health Sciences University, State University of New York Brooklyn, New York, New York; ⁴Alzheimer Center Amsterdam, Department of Neurology, Amsterdam Neuroscience, Vrije Universiteit Amsterdam, Amsterdam UMC, Amsterdam, The Netherlands; ⁵Lund University, Clinical Memory Research Unit, Lund, Sweden; ⁶Department of Physiology and Pharmacology "Vittorio Ersparmer," Sapienza University of Rome, Rome, Italy, and San Raffaele Cassino, Cassino, Italy; ⁷Department of Neurodegenerative Diseases and Geriatric Psychiatry, University Hospital Bonn, Bonn, Germany; ⁸Deutsches Zentrum für Neurodegenerative Erkrankungen, Bonn, Germany; ⁹Institute of Social Medicine, Occupational Health and Public Health, Medical Faculty, University of Leipzig, Leipzig, Germany; and ¹⁰Innovation Center for Neurological Disorders, Department of Neurology, Xuanwu Hospital, National Center for Neurological Disorders, Capital Medical University, Beijing, China

Alzheimer disease (AD) is the most frequent cause of dementia in people 60 y old or older. This white paper summarizes the current standards of AD diagnosis, treatment, care, and prevention. Cerebrospinal fluid and PET measures of cerebral amyloidosis and tauopathy allow the diagnosis of AD even before dementia (prodromal stage) and provide endpoints for treatments aimed at slowing the AD course. Licensed pharmacologic symptomatic drugs enhance cholinergic pathways and moderate excess of glutamatergic transmission to stabilize cognition. Disease-modifying experimental drugs moderate or remove brain amyloidosis, but so far with modest clinical effects. Non-pharmacologic interventions and a healthy lifestyle (diet, socioaffective inclusion, cognitive stimulation, physical exercise, and others) provide some beneficial effects. Prevention targets mainly modifiable dementia risk factors such as unhealthy lifestyle, cardiovascular–metabolic and sleep–wake cycle abnormalities, and mental disorders. A major challenge for the future is telemonitoring in the real world of these modifiable risk factors.

Key Words: PET; dementia; amyloid; biomarkers; prevention; treatment

J Nucl Med 2022; 63:981–985

DOI: 10.2967/jnumed.121.262239

Seven of the top 10 causes of death include Alzheimer disease (AD) and related dementias, as well as associated risk factors: ischemic heart disease, stroke, chronic obstructive pulmonary disease, and type 2 diabetes (1). There are about 55 million people with dementia. Dementia is expected to increase 42% (to 78 million people) by 2030 and more than 250% (to 139 million people) by 2050, mostly among women (2). Longitudinal associations exist between AD and overweight and obesity, hypertension, high cholesterol, low respiratory function, high blood levels of homocysteine,

and cooccurring vascular comorbidities. Concomitant associations exist for vascular risk factors and AD-related brain pathologies as well as white matter hyperintensities, neurodegeneration, blood–brain barrier disruption, cerebral infarcts, and various forms of cerebrovascular disease. The evidence base for AD prevention appears strongest for control of vascular risk factors.

Other AD risk factors include environmental risk factors such as high stress, air pollution, and lack of social support; depression; and sociodemographic factors, including low education, low income, and social isolation (3). Susceptibility genes for AD support systems-biology approaches for dyslipidemias, blood pressure dysregulation, body weight dysregulation, type 2 diabetes, systemic inflammation, neuroinflammation, and immune alterations.

These data provide a solid foundation for understanding the pathogenesis of AD as a multifactorial process and for AD prevention strategies.

AD PATHOGENESIS

The most widely accepted view on AD pathogenesis is based on the amyloid cascade hypothesis, published in 1992 (4) and repeatedly revised. This hypothesis is based on the disease-defining presence of amyloid plaques in the brain at autopsy and the observation that rare cases of autosomal-dominant AD are associated with mutations in amyloid-related genes encoding the amyloid precursor protein or one of the two secretases involved in amyloid precursor protein processing, presenilin-1 and presenilin-2. The *APOE* ε4 allele is the most strongly and consistently associated risk gene for sporadic AD. It is associated with many pathogenic pathways, including increased amyloid production.

The widespread failure of amyloid-centered treatments triggered the search for a broader perspective on AD pathogenesis (5). In addition to amyloid, pathologic phosphorylation and subsequent loss of function of the microtubule-associated protein tau, oxidative stress, impaired glucose metabolism, and upregulation of neuroinflammation play key roles in AD pathogenesis and interact with amyloid pathology. Supplemental Table 1 reports AD pathogenic events that are amenable to molecular brain imaging (supplemental materials are available at <http://jnm.snmjournals.org>).

Received Oct. 1, 2021; revision accepted Jan. 24, 2022.

For correspondence or reprints, contact Stefan J. Teipel (stefan.teipel@med.uni-rostock.de).

Published online Feb. 10, 2022.

COPYRIGHT © 2022 by the Society of Nuclear Medicine and Molecular Imaging.

CLINICAL DIAGNOSIS AND DIFFERENTIAL DIAGNOSIS OF AD

Cognitive symptoms such as forgetfulness—or concern by family members—prompts patients to make initial contact with a primary care physician. This physician has a decisive role in the diagnostic journey of the patient. The first diagnostic step, already accessible in primary care, is the medical history of the patient (self or per proxy), complemented by a cognitive screening test and physical examination. These clinical examinations can determine, in most cases, whether cognitive impairment or dementia is present.

One important clinical distinction is a full syndrome of dementia (i.e., cognitive impairment severe enough to impair daily activities) versus mild cognitive impairment (MCI) (i.e., impairment in one or more cognitive domains with maintained global cognitive function and daily activities) versus subjective cognitive decline (i.e., cognitive complaints without impairment on cognitive tests). Both MCI and subjective cognitive decline are recognized as risk states for development of dementia, but most countries do not endorse specific pharmacologic treatments outside clinical trials.

The etiologic diagnosis of MCI or a dementia syndrome will typically be conducted by a specialist. Diagnosis requires in-depth neuropsychologic and neurologic examinations, basic laboratory testing, and structural brain imaging using MRI or CT. Further diagnostic work-up may include biomarkers from PET brain imaging, cerebrospinal fluid (CSF), and (in the future) peripheral blood. Etiologic diagnosis is challenging, since autopsy studies show that comorbidities of two or more neurodegenerative proteinopathies are common.

Clinical and pathologic features of AD and its differential diagnoses are reported in Supplemental Table 2. A thorough account of the AD diagnostic process is provided in the World Alzheimer Report 2021 (6).

Research criteria ushered in the diagnoses of prodromal and preclinical stages of AD. Based on earliest presence of MCI and positive AD biomarkers, the International Working Group 2 criteria allow diagnosis of prodromal AD (7). The criteria of the U.S. National Institute on Aging and Alzheimer Association endorse a diagnosis of preclinical AD with the presence of positive AD biomarkers (CSF or amyloid imaging) and the absence of cognitive impairment (8). These criteria have further been systematized as the A/T/N classification scheme (Table 1) (9).

NEUROPSYCHOLOGY

The diagnostic work-up of patients with suspected AD includes cognitive screening using, for example, the Mini-Mental State Examination or Montreal Cognitive Assessment. Short clinical instruments are well suited to the detection of impairment consistent with dementia and to the quantification of dementia progression over time. However, neuropsychologic tests of specific cognitive domains are more sensitive to early changes and provide useful information for differential dementia diagnoses. Popular short test batteries suited for the detection and characterization of MCI are the Consortium to Establish a Registry for AD Neuropsychological Battery (10), the Uniform Dataset Test Battery of the American AD Research Centers (11), and the Repeatable Battery of Neuropsychological Status (12).

More recent approaches to sensitively detect cognitive decline and account for day-to-day variations in performance include continuous monitoring of cognitive performance using digital devices, such as serious games applications. Descriptions of these approaches are

beyond the scope of this standard-of-care article but have been published (13).

BIOMARKER-BASED DIAGNOSIS

Fluid Biomarkers

Several CSF biomarkers are well established and standard for AD diagnosis. A lower CSF $A\beta_{1-42}$ and higher CSF total tau or phosphorylated tau provide in vivo evidence of AD pathology, as integrated into the A/T/N scheme (Table 1). A lower CSF $A\beta_{1-42}$ concentration is associated with greater amyloid plaque formation (9). Total tau and phosphorylated tau reflect neuronal degeneration and tangle pathology, respectively (9). The combination of CSF markers—CSF $A\beta_{1-42}$ and total tau or phosphorylated tau—performs better than each individually for diagnosing AD (14).

Since CSF collection involves lumbar puncture, this led to the search for minimally invasive blood-based biomarkers. One candidate is plasma neurofilament light chain, which is increased in patients with AD and may be useful to monitor neurodegeneration, disease progression, and treatment response. In addition, plasma $A\beta_{42}$ and $A\beta_{40}$ predict brain amyloid burden status at any stage of AD (15). Plasma $A\beta_{42}$ and $A\beta_{40}$ could be used to screen for individuals likely to develop brain amyloidosis and who are at risk for AD (16). Furthermore, plasma phosphorylated tau 181 levels are increased in AD patients, compared with controls, and are strongly associated with both $A\beta$ and tau PET (17). Moreover, plasma phosphorylated tau 217 has also accurately discriminated AD from other neurodegenerative diseases and was more accurate than other established plasma- and MRI-based biomarkers (18). The sensitivity and specificity of fluid biomarkers for AD are provided in Table 2.

Neuroimaging/PET Biomarkers

Neuroimaging techniques provide the best opportunity to visualize and quantify neurodegenerative and molecular changes in the living human brain over the course of AD (Fig. 1). MRI has been included in dementia-screening protocols for decades. The most widely used MRI techniques to support a diagnosis of clinical AD are measures of regional brain volumes using T1-weighted images. These images are visually assessed by a trained radiologist who uses standardized rating scales to determine the level of atrophy in the medial temporal lobe, posterior brain, or global brain. In addition,

TABLE 1
A/T/N Classification

Classification	Description
A (amyloid)	Decreased CSF $A\beta_{42}$ or $A\beta_{42}/A\beta_{40}$ ratio or positive amyloid PET
T (tau)	Increased CSF phosphorylated tau or positive tau PET
N (neurodegeneration)	Atrophy on structural MRI or decreased uptake on ^{18}F -FDG PET or increased CSF total tau

Amyloid and tau are considered defining biomarkers of AD. Neurodegeneration is used to stage severity of disease (independently from AD pathology).

TABLE 2
Sensitivity and Specificity of CSF- and Blood-Based Biomarkers for AD

Parameter	Biomarker	Sensitivity	Specificity	Reference
CSF	A β_{1-42}	96.4%	89%	(37)
	Phosphorylated tau	81%	91%	(37)
	Mean value of phosphorylated tau			
	Phosphorylated tau 181	79%	96%	(38)
	Phosphorylated tau 217	91%	91%	(38)
	Total tau	81%	91%	(37)
	Combination of A β_{1-42} and total tau or phosphorylated tau	90%–95%	90%	(14)
Plasma	Neurofilament light chain*			(39)
	A β_{42} /A β_{40}	70%	70%	(16)
	Phosphorylated tau 181	92%	87%	(17)
	Phosphorylated tau 217	93%	83%	(18)

*Unspecific marker of neurodegeneration, useful for monitoring progression of disease.

various forms of vascular pathology can be assessed, including white matter hyperintensities (using T2-weighted or fluid-attenuated inversion recovery MRI sequences), infarcts, and microhemorrhages (using susceptibility-weighted T2* MRI sequences). MRI is also used to exclude other causes of cognitive impairment such as stroke, brain tumors, or multiple sclerosis.

Another established neuroimaging marker of neurodegeneration is glucose hypometabolism measured with ¹⁸F-FDG PET. In persons with AD, ¹⁸F-FDG PET shows a hypometabolic pattern that affects primarily the posterior cingulate, precuneus, and lateral temporal and parietal regions.

The neurodegenerative patterns observed on structural MRI and ¹⁸F-FDG PET images show modest differential diagnostic accuracy between AD and non-AD neurodegenerative disorders (~70%–80%). Neurodegenerative disorders are characterized by substantial functional and anatomic heterogeneity; hence, there is substantial overlap between neurodegenerative disorders on MRI and ¹⁸F-FDG PET. The advent of PET tracers that detect the neuropathologic hallmarks of AD in vivo represents a genuine breakthrough in the field. The first PET tracer that could detect the presence of fibrillar amyloid- β pathology was ¹¹C-Pittsburgh compound B. There is a strong association between antemortem ¹¹C-Pittsburgh compound

B PET signal and postmortem amyloid- β load (sensitivity, 92%; specificity, 97%) (19). Findings on ¹¹C-Pittsburgh compound B PET are abnormal early in the disease process, and investigational use of this tracer in the clinic shows positive changes in diagnostic confidence and patient management. Subsequently, several ¹⁸F amyloid- β tracers became available, that is, ¹⁸F-flutemetamol, ¹⁸F-florbetaben, and ¹⁸F-florbetapir, which showed characteristics similar to those of ¹¹C-Pittsburgh compound B and are now approved for clinical use with a visual read metric as the method to determine amyloid- β status by, for example, the U.S. Food and Drug Administration (FDA) and European Medicines Association. The primary strength of amyloid- β tracers for diagnostic purposes is their negative predictive value. A diagnosis of AD can be ruled out with high certainty if the amyloid- β PET scan yields a negative result. A downside of this sensitivity of the amyloid- β tracers is their limited specificity. Amyloid- β -positive PET scans are observed in 10%–40% of the cognitively normal population, and this percentage increases with age (20).

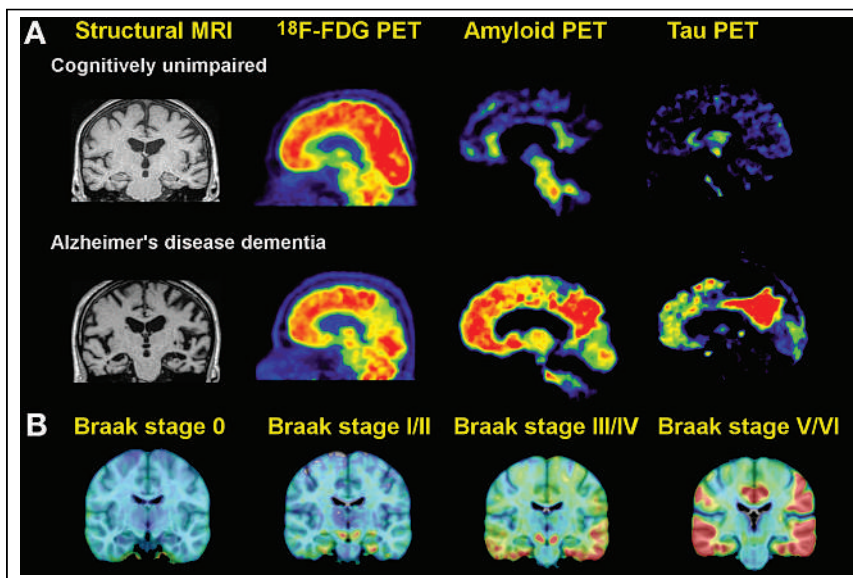


FIGURE 1. Imaging features of AD. (A) Different neuroimaging profiles of cognitively normal individual and patient with AD dementia in terms of brain atrophy on T1-weighted MRI, glucose hypometabolism on ¹⁸F-FDG PET, amyloid burden on ¹¹C-Pittsburgh compound B PET, and tau load on ¹⁸F-flortaucipir PET. (B) Neuropathologic staging system of neurofibrillary tangles proposed by Braak and Braak can be recapitulated using tau PET with ligand ¹⁸F-RO948 and shows increasing tau PET retention from stage 0 to stage V/VI.

Recently, several novel tau PET tracers (e.g., ^{18}F -florbetapir, ^{18}F -MK6240, and ^{18}F -RO948) were introduced that detect the presence of AD-like tau aggregates (i.e., a combination of 3R and 4R tau in paired helical filaments) with high affinity and selectivity. In May 2020, the first tau PET tracer was approved by the FDA to support the diagnosis of suspected AD dementia. Future work regarding tau PET tracers will define optimal methodologies (i.e., visual read metrics or quantitative thresholds) and the most appropriate use.

Section 1 of the supplemental materials expands the perspective on imaging markers to resting-state electroencephalography as a potential screening instrument for AD (21).

MEDICAL TREATMENT OF AD

Pharmacologic treatment of clinically symptomatic AD has 2 major elements. The first element is critical review of the patient's current medications, particularly for potential anticholinergic side effects that impair memory and increase the risk of delirium. Other contraindicated drugs are sedatives, such as benzodiazepines, and (low-potency) antipsychotics. Several indices are available for clinicians and pharmacists to identify potentially inappropriate medication combinations and possible alternatives (22).

The second element is the prescription of an antidementia drug. Supplemental Table 3 lists approved antidementia drugs with their clinical indications, major side effects, and typical dosages. None of these drugs has convincingly shown disease-modifying effects, but all have shown symptomatic benefits, with reduced rates of cognitive decline, reduction of caregiver burden, and, in some studies, delayed institutionalization when compared with placebo (23). Of note, AD is severely underdiagnosed in primary care. Studies show that fewer than 50% of people with AD receive specific dementia drug treatment (24,25). There is much room for improvement.

DISEASE-MODIFYING TREATMENTS

Repeated anti-amyloid failures were a setback for patients and scientists, but they also led to sharpening of inclusion criteria and an early diagnosis of AD. However, until January 2022, and including aducanumab, recently approved by the FDA, no anti-amyloid antibody therapy has successfully reached the clinical endpoint in a completed phase 3 study. Phase 3 trials are ongoing with anti-amyloid antibodies, such as gantenerumab, lecanemab, and donanemab, which, in preclinical studies, selectively bound to aggregated $\text{A}\beta$. These newer-generation anti-amyloid antibodies have consistently shown removal of brain $\text{A}\beta$ through amyloid PET imaging studies (26) and, in phase 2 studies, have shown improvements in primary cognitive outcomes (26,27).

Aducanumab (Aduhelm; Biogen) was approved by the FDA on June 7, 2021, using the FDA's accelerated-approval pathway. On December 16, 2021, the European Medicines Agency recommended refusing the marketing authorization for aducanumab. Of note, treatment with aducanumab was restricted by the FDA in July 2021 to prodromal and mild stages of AD with proven amyloid positivity via CSF or amyloid PET.

Nonpharmacologic treatment options are described in section 2 of the supplemental materials (28,29).

AD PREVENTION AND MULTIMODAL INTERVENTIONS

It is estimated that 40% of all dementias in high-income countries could be prevented or delayed with elimination of low early-life education, midlife obesity, hypertension, alcohol consumption above 21 units a week, diabetes mellitus, depression, physical inactivity,

smoking, traumatic brain injury, late-life hearing loss, social isolation, and exposure to air pollution (3).

In 2019, the World Health Organization issued widely recognized guidelines on risk reduction for cognitive decline and dementia (30). The guidelines provide the knowledge base for health-care providers, governments, policy makers, and other stakeholders to reduce the risks of cognitive decline and dementia.

Knowledge about risk factors is also translated into preventive interventions for individuals at risk (selective prevention) to preserve or improve cognitive function and delay or prevent dementia (31). Although early intervention studies focused on one factor at a time (single-domain intervention studies), multidomain interventions focus on several modifiable risk factors simultaneously among those at risk for cognitive decline and dementia. The prototype Finnish Geriatric Intervention Study to Prevent Cognitive Impairment and Disability (FINGERS) reported a benefit from a multidomain lifestyle intervention on cognitive function over 2 y (32). Similar European trials, such as the French Multidomain Alzheimer Preventive Trial and the Dutch Prevention of Dementia by Intensive Vascular Care Trial have been less conclusive. However, benefits for cognitive function in specific subgroups of adults with higher risk for dementia were suggested (33,34). These promising but still inconsistent results have led to World-Wide FINGERS, a global, interdisciplinary network with a mission to share knowledge and experiences on trials for dementia prevention and risk reduction, harmonize data, and plan joint international initiatives for the prevention of cognitive impairment and dementia (<https://wwfingers.com/#about>). World-Wide FINGERS brings together, from over 40 countries, culturally specific lifestyle trials comprising dietary guidance, physical exercise, cognitive training, social activities, and management of vascular and metabolic risk factors. These trials differ by individuals targeted (asymptomatic states to early symptomatic stages of dementia); risk factors addressed; and cultural, geographic, and economic settings (31). Another ongoing multidomain lifestyle trial is the German AgeWell.de, a pragmatic, clustered, randomized controlled trial addressing cognitive decline in a primary-care population at increased risk for dementia (35).

Although multidomain interventions seem promising for selected prevention in high-risk individuals, the data are inconclusive. Questions remain with regard to the intervention "dose" needed to change behavior, the optimal intervention window during the life course, target groups, best modes of intervention delivery (face-to-face vs. virtual), and suitable implementation settings (e.g., primary care) (36). AD prevention is a dynamic research field. The potential for dementia prevention is huge and not even close to being fully understood.

DISCLOSURE

Stefan Teipel was supported by a grant from the Federal Ministry of Education and Research (BMBF), CureDem (funding code 01KX2130). Deborah Gustafson was supported by the MACS/WIHS Combined Cohort Study Brooklyn Clinical Research Site (multiple principal investigator, Deborah Gustafson), NIH/NHLBI 5U01HL146202. Stefan Teipel has served as an advisory board member for Roche, Biogen, Grifols, and Eisai. No other potential conflict of interest relevant to this article was reported.

REFERENCES

1. *The Top 10 Causes of Death*. World Health Organization; 2020.
2. *Dementia*. World Health Organization; 2021.

3. Livingston G, Huntley J, Sommerlad A, et al. Dementia prevention, intervention, and care: 2020 report of the Lancet Commission. *Lancet*. 2020;396:413–446.
4. Hardy JA, Higgins GA. Alzheimer's disease: the amyloid cascade hypothesis. *Science*. 1992;256:184–185.
5. Armstrong RA. A critical analysis of the 'amyloid cascade hypothesis.' *Folia Neuropathol*. 2014;52:211–225.
6. World Alzheimer report 2021: journey through the diagnosis of dementia. Alzheimer's Disease International website. <https://www.alzint.org/resource/world-alzheimer-report-2021/>. Published September 21, 2021. Accessed February 2, 2022.
7. Dubois B, Feldman HH, Jacova C, et al. Advancing research diagnostic criteria for Alzheimer's disease: the IWG-2 criteria. *Lancet Neurol*. 2014;13:614–629.
8. Sperling RA, Aisen PS, Beckett LA, et al. Toward defining the preclinical stages of Alzheimer's disease: recommendations from the National Institute on Aging-Alzheimer's Association workgroups on diagnostic guidelines for Alzheimer's disease. *Alzheimers Dement*. 2011;7:280–292.
9. Jack CR Jr, Bennett DA, Blennow K, et al. NIA-AA research framework: toward a biological definition of Alzheimer's disease. *Alzheimers Dement*. 2018;14:535–562.
10. Morris JC, Heyman A, Mohs RC, et al. The Consortium to Establish a Registry for Alzheimer's Disease (CERAD). Part I. Clinical and neuropsychological assessment of Alzheimer's disease. *Neurology*. 1989;39:1159–1165.
11. Weintraub S, Besser L, Dodge HH, et al. Version 3 of the Alzheimer Disease Centers' neuropsychological test battery in the Uniform Data Set (UDS). *Alzheimer Dis Assoc Disord*. 2018;32:10–17.
12. Randolph C, Tierney MC, Mohr E, Chase TN. The Repeatable Battery for the Assessment of Neuropsychological Status (RBANS): preliminary clinical validity. *J Clin Exp Neuropsychol*. 1998;20:310–319.
13. Teipel S, König A, Hoey J, et al. Use of noninvasive sensor-based information and communication technology for real-world evidence for clinical trials in dementia. *Alzheimers Dement*. 2018;14:1216–1231.
14. de Souza LC, Lamari F, Belliard S, et al. Cerebrospinal fluid biomarkers in the differential diagnosis of Alzheimer's disease from other cortical dementias. *J Neurol Neurosurg Psychiatry*. 2011;82:240–246.
15. Schindler SE, Bollinger JG, Ovod V, et al. High-precision plasma beta-amyloid 42/40 predicts current and future brain amyloidosis. *Neurology*. 2019;93:e1647–e1659.
16. Palmqvist S, Janelidze S, Stomrud E, et al. Performance of fully automated plasma assays as screening tests for Alzheimer disease-related beta-amyloid status. *JAMA Neurol*. 2019;76:1060–1069.
17. Janelidze S, Mattsson N, Palmqvist S, et al. Plasma P-tau181 in Alzheimer's disease: relationship to other biomarkers, differential diagnosis, neuropathology and longitudinal progression to Alzheimer's dementia. *Nat Med*. 2020;26:379–386.
18. Palmqvist S, Janelidze S, Quiroz YT, et al. Discriminative accuracy of plasma phospho-tau217 for Alzheimer disease vs other neurodegenerative disorders. *JAMA*. 2020;324:772–781.
19. Bergeron D, Ossenkoppelle R, Laforce RJ. Evidence-based interpretation of amyloid-beta PET results: a clinician's tool. *Alzheimer Dis Assoc Disord*. 2018;32:28–34.
20. Jansen WJ, Ossenkoppelle R, Knol DL, et al. Prevalence of cerebral amyloid pathology in persons without dementia: a meta-analysis. *JAMA*. 2015;313:1924–1938.
21. Babiloni C, Blinowska K, Bonanni L, et al. What electrophysiology tells us about Alzheimer's disease: a window into the synchronization and connectivity of brain neurons. *Neurobiol Aging*. 2020;85:58–73.
22. Wucherer D, Eichler T, Hertel J, et al. Potentially inappropriate medication in community-dwelling primary care patients who were screened positive for dementia. *J Alzheimers Dis*. 2017;55:691–701.
23. Li DD, Zhang YH, Zhang W, Zhao P. Meta-analysis of randomized controlled trials on the efficacy and safety of donepezil, galantamine, rivastigmine, and memantine for the treatment of Alzheimer's disease. *Front Neurosci*. 2019;13:472.
24. Donegan K, Fox N, Black N, Livingston G, Banerjee S, Burns A. Trends in diagnosis and treatment for people with dementia in the UK from 2005 to 2015: a longitudinal retrospective cohort study. *Lancet Public Health*. 2017;2:e149–e156.
25. Wucherer D, Eichler T, Kilimann I, et al. Antidementia drug treatment in people screened positive for dementia in primary care. *J Alzheimers Dis*. 2015;44:1015–1021.
26. Mintun MA, Lo AC, Duggan Evans C, et al. Donanemab in early Alzheimer's disease. *N Engl J Med*. 2021;384:1691–1704.
27. Swanson CJ, Zhang Y, Dhadda S, et al. A randomized, double-blind, phase 2b proof-of-concept clinical trial in early Alzheimer's disease with lecanemab, an anti-A β protofibril antibody. *Alzheimers Res Ther*. 2021;13:80.
28. He W, Wang M, Jiang L, Li M, Han X. Cognitive interventions for mild cognitive impairment and dementia: an overview of systematic reviews. *Complement Ther Med*. 2019;47:102199.
29. Huntley JD, Gould RL, Liu K, Smith M, Howard RJ. Do cognitive interventions improve general cognition in dementia? A meta-analysis and meta-regression. *BMJ Open*. 2015;5:e005247.
30. *Risk Reduction of Cognitive Decline and Dementia: WHO Guidelines*. World Health Organization; 2019.
31. Kivipelto M, Mangialasche F, Snyder HM, et al. World-Wide FINGERS network: a global approach to risk reduction and prevention of dementia. *Alzheimers Dement*. 2020;16:1078–1094.
32. Ngandu T, Lehtisalo J, Solomon A, et al. A 2 year multidomain intervention of diet, exercise, cognitive training, and vascular risk monitoring versus control to prevent cognitive decline in at-risk elderly people (FINGER): a randomised controlled trial. *Lancet*. 2015;385:2255–2263.
33. Moll van Charante EP, Richard E, Eurelings LS, et al. Effectiveness of a 6-year multidomain vascular care intervention to prevent dementia (preDIVA): a cluster-randomised controlled trial. *Lancet*. 2016;388:797–805.
34. Chhetri JK, de Souto Barreto P, Cantet C, et al. Effects of a 3-year multi-domain intervention with or without omega-3 supplementation on cognitive functions in older subjects with increased CAIDE dementia scores. *J Alzheimers Dis*. 2018;64:71–78.
35. Zülke A, Luck T, Pabst A, et al. *AgeWell.de*: study protocol of a pragmatic multi-center cluster-randomized controlled prevention trial against cognitive decline in older primary care patients. *BMC Geriatr*. 2019;19:203.
36. Hussenoeder FS, Riedel-Heller SG. Primary prevention of dementia: from modifiable risk factors to a public brain health agenda? *Soc Psychiatry Psychiatr Epidemiol*. 2018;53:1289–1301.
37. Blennow K. Cerebrospinal fluid protein biomarkers for Alzheimer's disease. *NeuroRx*. 2004;1:213–225.
38. Janelidze S, Stomrud E, Smith R, et al. Cerebrospinal fluid p-tau217 performs better than p-tau181 as a biomarker of Alzheimer's disease. *Nat Commun*. 2020;11:1683.
39. Mattsson N, Cullen NC, Andreasson U, Zetterberg H, Blennow K. Association between longitudinal plasma neurofilament light and neurodegeneration in patients with Alzheimer disease. *JAMA Neurol*. 2019;76:791–799.

Radiotracers to Address Unmet Clinical Needs in Cardiovascular Imaging, Part 2: Inflammation, Fibrosis, Thrombosis, Calcification, and Amyloidosis Imaging

John C. Stendahl*¹, Jennifer M. Kwan*¹, Darko Pucar², and Mehran M. Sadeghi^{1,3}

¹Section of Cardiovascular Medicine, Yale University School of Medicine, New Haven, Connecticut; ²Department of Radiology and Biomedical Imaging, Yale University School of Medicine, New Haven, Connecticut; and ³Veterans Affairs Connecticut Healthcare System, West Haven, Connecticut

Learning Objectives: On successful completion of this activity, participants should be able to describe (1) different classes of targets used for molecular imaging of inflammation; (2) emerging radiotracers for cardiovascular inflammation and thrombosis imaging; and (3) emerging radiotracers for cardiovascular fibrosis, calcification and amyloidosis imaging.

Financial Disclosure: This work was supported by grants from NIH (R01AG065917 and R01HL138567) and the Department of Veterans Affairs (10-BX004038). Dr. Pucar is a board member, officer, or trustee for the Society of Nuclear Medicine and Molecular Imaging, a consultant or advisor for Cohere Health, an employee of Yale University, an investigator for the National Institutes of Health, and a meeting participant or lecturer for Telix Pharmaceuticals. Dr. Kwan is a board member, officer, or trustee for the American Physician Scientists Association. Dr. Sadeghi is an inventor on Yale University MMP and fibrosis tracer patent applications, and a member of the Board of Directors of the American Society of Nuclear Cardiology. The authors of this article have indicated no other relevant relationships that could be perceived as a real or apparent conflict of interest.

CME Credit: SNMMI is accredited by the Accreditation Council for Continuing Medical Education (ACCME) to sponsor continuing education for physicians. SNMMI designates each *JNM* continuing education article for a maximum of 2.0 AMA PRA Category 1 Credits. Physicians should claim only credit commensurate with the extent of their participation in the activity. For CE credit, SAM, and other credit types, participants can access this activity through the SNMMI website (<http://www.snmmilearningcenter.org>) through July 2025.

Cardiovascular imaging is evolving in response to systemwide trends toward molecular characterization and personalized therapies. The development of new radiotracers for PET and SPECT imaging is central to addressing the numerous unmet diagnostic needs that relate to these changes. In this 2-part review, we discuss select radiotracers that may help address key unmet clinical diagnostic needs in cardiovascular medicine. Part 1 examined key technical considerations pertaining to cardiovascular radiotracer development and reviewed emerging radiotracers for perfusion and neuronal imaging. Part 2 covers radiotracers for imaging cardiovascular inflammation, thrombosis, fibrosis, calcification, and amyloidosis. These radiotracers have the potential to address several unmet needs related to the risk stratification of atheroma, detection of thrombi, and the diagnosis, characterization, and risk stratification of cardiomyopathies. In the first section, we discuss radiotracers targeting various aspects of inflammatory responses in pathologies such as myocardial infarction, myocarditis, sarcoidosis, atherosclerosis, and vasculitis. In a subsequent section, we discuss radiotracers for the detection of systemic and device-related thrombi, such as those targeting fibrin (e.g., ⁶⁴Cu-labeled fibrin-binding probe 8). We also cover emerging radiotracers for the imaging of cardiovascular fibrosis, such as those targeting fibroblast activation protein (e.g., ⁶⁸Ga-fibroblast activation protein inhibitor). Lastly, we briefly review radiotracers for imaging of cardiovascular calcification (¹⁸F-NaF) and amyloidosis (e.g., ^{99m}Tc-pyrophosphate and ¹⁸F-florbetapir).

Key Words: molecular imaging; fibrosis; inflammation; radiotracers; thrombosis

J Nucl Med 2022; 63:986–994

DOI: 10.2967/jnumed.121.263507

There is a growing trend in cardiovascular medicine toward molecular characterization and personalized therapies. The development of improved radiotracers for PET and SPECT imaging is central to addressing the clinical needs of the evolving clinical landscape. This 2-part review examines key technical considerations pertaining to cardiovascular radiotracer development and discusses emerging radiotracers in important areas of cardiovascular imaging. Technical considerations and radiotracers for cardiovascular perfusion and neuronal imaging were discussed in part 1. Part 2 covers emerging radiotracers for imaging cardiovascular inflammation, fibrosis, thrombosis, calcification, and amyloidosis (Table 1).

RADIOTRACERS FOR IMAGING CARDIOVASCULAR INFLAMMATION

Inflammation promotes atherosclerosis, mediates cardiomyopathy, and plays central roles in myocarditis and sarcoidosis (1–3). In atherosclerosis, enhanced inflammation is considered a marker of plaque vulnerability and can lead to plaque rupture and acute myocardial infarction (MI) (1). Myocardial injury promotes both focal and systemic inflammation, where different subsets of immune cells have distinct roles in tissue damage and repair. Early on, the recruitment of neutrophils and inflammatory monocytes (which differentiate into an M1-like proinflammatory phenotype) promotes tissue damage. After the initial phase of injury, tissue repair is supported by the transition to cells with an M2-like, inflammation-resolving phenotype (4). Regulatory T cells are critical to this transition (5). Accordingly, tissue

Received Nov. 14, 2021; revision accepted Feb. 22, 2022.

For correspondence or reprints, contact Mehran M. Sadeghi (mehran.sadeghi@yale.edu).

*Contributed equally to this work.

COPYRIGHT © 2022 by the Society of Nuclear Medicine and Molecular Imaging.

TABLE 1

Select Radiotracers for Imaging of Cardiovascular Inflammation, Thrombosis, Fibrosis, Calcification, and Amyloidosis

Application	Radiotracer	Mechanism/target	Status	Reference
Inflammation	¹⁸ F-FDG	Glucose analog	FDA-approved for myocardial viability imaging	(11,12)
	¹¹ C-PK11195	Mitochondrial TSPO	Initial clinical evaluations	(17,18)
	¹¹ C-PBR28	TSPO	Initial clinical evaluations	(19,21)
	¹⁸ F-PBR06	TSPO	Initial clinical evaluations	(19)
	¹⁸ F-GE180	TSPO	Initial clinical evaluations	(20)
	⁶⁸ Ga-DOTATATE	SSTR	FDA-approved for neuroendocrine tumor imaging	(23)
	⁶⁸ Ga-DOTATOC	SSTR	FDA-approved for neuroendocrine tumor imaging	(26)
	⁶⁸ Ga/ ⁶⁴ Cu-DOTA-ECL1i	CCR2	Initial clinical evaluations	(31,32)
	⁶⁴ Cu-DOTA-vMIP-II	Chemokine receptors (broad)	Preclinical	(33)
	⁶⁸ Ga-pentixafor	CXCR4	Initial clinical evaluations	(30)
	^{99m} Tc-RP805	MMPs	Preclinical	(38)
	¹¹¹ In-RP782	MMPs	Preclinical	(35,36)
	^{99m} Tc-RYM1	MMPs	Preclinical	(38)
	⁸⁹ Zr-DFO-anti-CD3	CD3+ T cells	Preclinical	(44)
	⁸⁹ Zr-DFO-CD4	CD4+ T cells	Preclinical	(45)
⁸⁹ Zr-DFO-CD8a	CD8+ T cells	Preclinical	(45)	
Thrombosis	⁶⁴ Cu-FBP8	Fibrin	Initial clinical evaluations	(49,50)
	¹⁸ F-GP1	Glycoprotein IIb/IIIa	Initial clinical evaluations	(54,55)
	¹⁸ F-ENC2015	Factor XIIIa substrate	Preclinical	(58)
Fibrosis	⁶⁸ Ga-FAPI	FAP	Initial clinical evaluations	(67,68)
	^{99m} Tc-collagelin, ⁶⁸ Ga-collagelin	Type I and III collagen	Preclinical	(70,71)
	⁶⁸ Ga-CBP7, ⁶⁸ Ga-CBP8	Type I collagen	Initial clinical evaluations	(72,73)
Calcification	¹⁸ F-NaF	Hydroxyapatite	FDA-approved for bone imaging	(74–77)
Amyloidosis	^{99m} Tc-pyrophosphate, ^{99m} Tc-HMDP, ^{99m} Tc-DPD	Transthyretin amyloid fibrils	Expanding clinical use*	(82)
	¹¹ C-Pittsburgh compound B	Amyloid fibrils (AL, ATTR)	Initial clinical evaluations	(83)
	¹⁸ F-florbetapir, ¹⁸ F-flutemetamol, ¹⁸ F-florbetaben	Amyloid fibrils (AL, ATTR)	FDA-approved for imaging brain β-amyloid plaques	(84–86)

*^{99m}Tc-pyrophosphate is FDA-approved for imaging of bone, acute MI, and blood pool.

inflammation plays a dual role after myocardial injury, and dysregulation of this process can lead to cardiomyopathy and heart failure. T lymphocytes also play major roles in autoimmune and viral myocarditis (2), as well as in sarcoidosis, where the secretion of cytokines such as interferon γ is crucial to granuloma formation (6). Chemokines and chemokine receptors, such as chemokine receptor type 2 (CCR2) and CXC chemokine receptor type 4 (CXCR4), mediate the recruitment of monocytes and other inflammatory cells (7). These inflammatory cells are sources of proteases that modulate inflammation and tissue remodeling, including cathepsins and matrix metalloproteases (MMPs) (8,9). Dysregulated protease activation can

destabilize atheroma and contribute to adverse myocardial remodeling (8,10).

Cardiovascular inflammation in pathologies such as vasculitis and sarcoidosis has traditionally been imaged with ¹⁸F-FDG PET (11,12). ¹⁸F-FDG uptake in inflammation is attributed to the high metabolic activity of immune cells, such as macrophages and neutrophils (13,14). One challenge with ¹⁸F-FDG PET for imaging of cardiovascular inflammation is its lack of specificity, which, for instance, mandates dietary interventions to suppress myocardial uptake. In addition, ¹⁸F-FDG cannot distinguish between subsets of inflammatory cells that characterize the different stages of the

inflammatory process and play distinct roles in cardiovascular disease. Addressing this limitation by targeting more specific molecular signatures may help to better define disease stages, monitor disease progression, guide the selection of therapeutic interventions, and follow responses to treatment. The availability of highly specific tracers, potentially in the setting of multitracer PET and SPECT imaging to fine-tune diagnoses, will be critical for expanded diagnostic and theranostic applications in cardiovascular inflammation. The potential of dual-tracer imaging is illustrated in a recent dual-tracer PET study of patients with ischemic stroke and ipsilateral carotid stenosis, which revealed that uptake of ^{18}F -FDG (inflammation) and ^{18}F -NaF (microcalcification) were both greater in culprit than nonculprit atheroma, although ^{18}F -NaF was concentrated at carotid bifurcations and ^{18}F -FDG was distributed more evenly throughout arteries (Fig. 1) (15). This differential uptake may reflect the distinct roles of inflammation and calcification in plaque development and vulnerability.

Several radiotracers that were initially developed for other applications also bind to target molecules on inflammatory cells and could be of value for imaging cardiovascular inflammation. Radiotracers with preexisting human studies, including those with U.S. Food and Drug Administration (FDA) approval for other indications, expedite the process for testing and potential clinical introduction. Examples of radiotracers potentially useful for imaging cardiovascular inflammation, including some initially developed for other applications, are reviewed in the following sections.

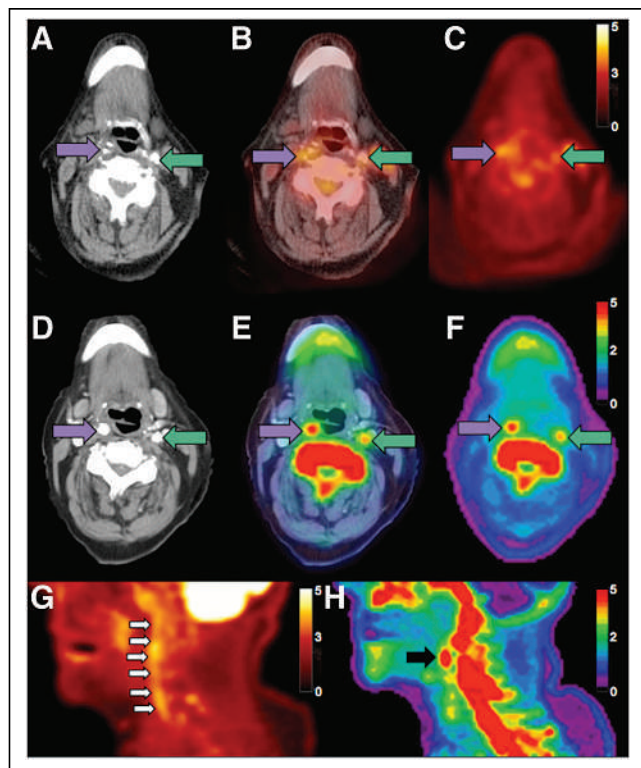


FIGURE 1. Differential distributions of inflammation and microcalcification in symptomatic carotid atheroma. Axial noncontrast CT (A), ^{18}F -FDG PET/CT (B), ^{18}F -FDG PET (C), CT angiography (D), ^{18}F -NaF PET/CT (E), and ^{18}F -NaF PET (F) show symptomatic right carotid artery (purple arrow) and asymptomatic left carotid artery (green arrow); sagittal ^{18}F -FDG PET/CT (G) shows diffuse uptake in symptomatic carotid artery (arrows); and ^{18}F -NaF PET (H) shows focal uptake in symptomatic carotid artery (arrow). (Reprinted from (15).)

Mitochondrial Translocator Protein (TSPO) Imaging

TSPO, a ubiquitous mitochondrial protein involved in a large number of cellular functions, including mitochondrial cholesterol transport and steroid hormone biosynthesis (16), is classically used as a marker of neuroinflammation. More recently, expression of TSPO in activated macrophages has motivated the evaluation of radiotracers targeting TSPO for imaging of cardiovascular inflammation in pathologies such as MI, myocarditis, sarcoidosis, atherosclerosis, and vasculitis. Examples of such radiotracers include 1-[2-chlorophenyl]-*N*-methyl-*N*-[1-methyl-propyl]-3-isoquinoline carboxamide (^{11}C -PK11195) (17,18), *N*-acetyl-*N*-(2- ^{11}C -methoxybenzyl)-2-phenoxy-5-pyridinamine (^{11}C -PBR28) (19), ^{18}F -*N*-fluoroacetyl-*N*-(2,5-dimethoxybenzyl)-2-phenoxyaniline (^{18}F -PBR06) (19), and ^{18}F -flutriciclamide (^{18}F -GE180) (20). The prototypic TSPO tracer ^{11}C -PK11195 has been evaluated for the detection of inflammation in human carotid atherosclerotic plaques, where plaques associated with recent ipsilateral stroke or transient ischemic attack were shown to have greater ^{11}C -PK11195 uptake than those without a recent event (target-to-background ratio, 1.06 ± 0.20 vs. 0.86 ± 0.11 , $P = 0.001$) (17). Plaques associated with stroke or transient ischemic attack also had lower CT attenuation, but there was no correlation between ^{11}C -PK11195 target-to-background ratio and CT plaque attenuation. Importantly, the combination of these 2 features had 100% sensitivity and a 100% positive predictive value in identifying patients with recent stroke or transient ischemic attack. Although these results are promising, it is not known whether the same approach can be used to identify the plaques at risk for future events. ^{11}C -PK11195 PET has also demonstrated increased uptake in patients with large-vessel vasculitis (Fig. 2) (18). However, in another study of patients with stroke or vasculitis, other TSPO tracers (^{11}C -PBR28 and ^{18}F -PBR06) did not produce significant *in vivo* signals (19). Of note, there is also considerable uptake of ^{11}C -PBR28 in normal myocardium (21), which may limit its utility for imaging of cardiac inflammation.

Another TSPO-targeting tracer, ^{18}F -GE180, has shown greater binding to M1-polarized macrophages than M2-polarized macrophages (20). In a murine study of MI, an early increase in ^{18}F -GE180 uptake was observed at the site of infarct, with signals returning to the reference range after 4 wk, suggesting that the TSPO signal may reflect early post-MI inflammation (20). Importantly, global ^{18}F -GE180 uptake at 1 wk predicted a future reduction in left ventricular ejection fraction. Small-scale human studies have confirmed the early increase in post-MI ^{18}F -GE180 signal (20), and additional clinical studies are being conducted to evaluate this tracer for imaging cardiac sarcoidosis (NCT03561025). Unresolved issues regarding TSPO-targeted imaging of cardiovascular inflammation include noninflammatory cell expression of TSPO, the selectivity of the

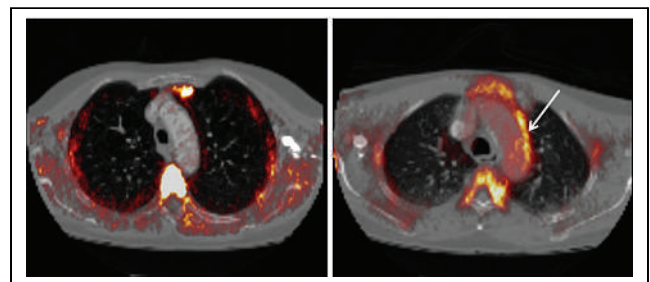


FIGURE 2. ^{11}C -PK11195 PET imaging of large-vessel vasculitis in patients with systemic inflammatory disorders. ^{11}C -PK11195 PET images fused with CT angiograms demonstrate minimal radiotracer uptake in asymptomatic patient (A) and elevated uptake in symptomatic patient (B). Arrow indicates inflamed region of aortic arch. (Reprinted from (18).)

tracers for different TSPO isoforms and multimers, and whether the magnitude of radiotracer signals is sufficient for clinical applications. In addition, interpretation of human studies is affected by a genetic polymorphism that influences tissue binding of certain TSPO radiotracers (22). Addressing these limitations will be necessary for routine use of TSPO-targeted imaging in clinical cardiovascular medicine.

Somatostatin Receptor (SSTR) Imaging

SSTR-targeted radiotracers have been classically used as neuroendocrine tumor imaging agents. There are 5 subtypes of SSTRs, with peripheral blood mononuclear cells expressing mainly SSTR subtypes 2 and 3. Macrophages mainly express SSTR subtype 2, with the highest expression detected in inflammatory M1 macrophages (23), whereas lymphocytes express mainly SSTR subtype 3 (24). There are important variations in receptor subtype affinity profiles between different SSTR-targeted tracers (25). The ^{68}Ga -labeled somatostatin analog ^{68}Ga -DOTATATE binds to SSTR2 with high affinity and selectivity relative to other SSTRs (25). In a prospective study of patients with cardiovascular disease, ^{68}Ga -DOTATATE uptake in atherosclerotic plaques was shown to be macrophage-specific and discriminate between culprit and nonculprit plaques in patients with acute coronary syndrome and cerebrovascular accidents (23). Furthermore, the ^{68}Ga -DOTATATE signal in plaques was associated with high-risk coronary CT features (e.g., spotty calcification, low attenuation, positive remodeling) and correlated with Framingham risk score ($r = 0.53$, $P < 0.0001$) and ^{18}F -FDG uptake ($r = 0.73$, $P < 0.0001$) (23). In a separate study of sarcoidosis patients, PET imaging with ^{68}Ga -DOTATOC, which has a high affinity for SSTR2 and moderate affinity for SSTR5, performed better than conventional ^{67}Ga -scintigraphy for the detection of sarcoidosis lesions (26). However, whereas basal uptake of ^{68}Ga -DOTATOC in the heart was minimal, none of the patients in the study had active cardiac sarcoidosis. As such, additional information is needed to establish the value of SSTR2-targeted radiotracers for imaging of cardiovascular inflammation. In this regard, potential impediments to clinical applications of ^{68}Ga -DOTATATE for imaging of cardiovascular inflammation include the modest level of increase in SSTR2 expression in culprit atherosclerotic plaques (23).

Chemokine Receptor Imaging

Chemokines are a family of small chemoattractant proteins that play key roles in leukocyte recruitment and activation through binding to chemokine receptors. Radiotracers that target chemokine receptors such as CXCR4 and CCR2 have recently emerged as promising agents for imaging inflammation (27,28). ^{68}Ga -pentixafor was initially developed for CXCR4 imaging in cancer (29). Recent studies on mice have shown that post-MI ^{68}Ga -pentixafor uptake is increased in parallel with leukocyte infiltration (30). In patients with acute MI, PET imaging showed variable patterns of ^{68}Ga -pentixafor uptake (30). Furthermore, whereas there was no correlation with summed rest perfusion defect score, late gadolinium enhancement, or edema score by MRI, the ^{68}Ga -pentixafor signal correlated with a combination of infarct size and time of imaging after reperfusion ($r_{\text{multiple}} = 0.73$, $P = 0.03$) (30). Examples of other radiotracers that target chemokine receptors include ^{68}Ga - and ^{64}Cu -DOTA-ECL1i (31,32), which target CCR2, and ^{64}Cu -viral macrophage inflammatory protein-II (^{64}Cu -DOTA-vMIP-II), which targets a broad range of chemokine receptors (33). CCR2 is upregulated on inflammatory cells after myocardial injury (34) and in abdominal aortic aneurysms (AAAs) (32). CCR2-targeted imaging with ^{64}Cu -DOTA-ECL1i is undergoing clinical evaluation in patients with AAAs (NCT04592991). This study follows

promising results with ECL1i-based tracers in rodent studies that established the ability to detect CCR2+ monocytes and macrophages within post-MI hearts (^{68}Ga -DOTA-ECL1i) (31) and demonstrated greater radiotracer uptake in AAAs that subsequently ruptured (^{64}Cu -DOTA-ECL1i) (32).

MMP Imaging

Inflammatory cells are a major source of proteases, and MMP activation contributes to atherosclerotic plaque vulnerability, adverse left ventricular remodeling after MI, and AAA development and rupture. MMP-targeted radiotracers that target a broad range of MMPs, including ^{111}In -RP782, $^{99\text{m}}\text{Tc}$ -RP805, and $^{99\text{m}}\text{Tc}$ -RYM1, have shown promise in preclinical studies of post-MI remodeling, atherosclerosis, calcific aortic valve disease, and aortic aneurysms (35–40). Tissue uptake of these tracers correlates well with both MMP activity and CD68 macrophage expression in murine models of atherosclerosis (35,41), calcific aortic valve disease (39), and aneurysm (40). Accordingly, MMP-targeted imaging may indirectly inform on the extent of cardiovascular inflammation. For instance, in a murine model of angiotensin-II-induced AAA, aortic $^{99\text{m}}\text{Tc}$ -RP805 signals on small-animal SPECT/CT images correlated with MMP activity quantified by zymography ($r = 0.83$, $P < 0.001$), as well as CD68 messenger RNA expression, a marker of monocytes and macrophages ($r = 0.89$, $P < 0.0001$) (40). Importantly, the MMP signal at 1 wk after angiotensin-II infusion correlated with AAA size at 4 wk ($r = 0.53$, $P < 0.01$), highlighting the potential of MMP-targeted imaging for AAA risk stratification. $^{99\text{m}}\text{Tc}$ -RYM1, which has a fast blood clearance, allows for imaging at 1 h after tracer injection and can similarly detect aortic MMP activity in murine models of aneurysm (Fig. 3) (38). Clinical studies with these MMP-targeted radiotracers are expected soon. The relative effectiveness of these broad-spectrum tracers as compared with emerging tracers that target specific members of the MMP family (e.g., MMP-12) remains to be determined (42).

T-Cell Imaging

Different lymphocyte subsets play distinct roles in inflammation. For instance, CD4+ T lymphocytes can activate and recruit other immune cells, whereas CD8+ T cells can mediate cell killing via release of intracellular granzymes (43). Several novel radiotracers that are in early stages of development for oncologic applications can potentially detect T-cell infiltration and may be valuable in cardiovascular applications such as myocarditis or sarcoidosis. Examples of these radiotracers include ^{89}Zr -desferrioxamine (DFO)-anti-CD3, which targets all types of T cells (44), ^{89}Zr -DFO-CD4 (45), and ^{89}Zr -DFO-CD8a (45). Future studies should address the value of these and related imaging agents in the diagnosis and management of inflammatory cardiovascular disease.

RADIOTRACERS FOR THROMBOSIS IMAGING

Thrombosis plays a central role in the pathogenesis of multiple disabling diseases, including MI, stroke, and pulmonary embolism. Detection and localization of the primary thrombus and any secondary emboli are often critically important for diagnosis and treatment. As such, there has been considerable interest in the development of nuclear imaging techniques that could potentially provide sensitive and specific whole-body detection of thrombi.

Fibrin Imaging

Fibrin is the end-product of the coagulation cascade and is one of the most widely pursued targets of radiotracers for thrombus

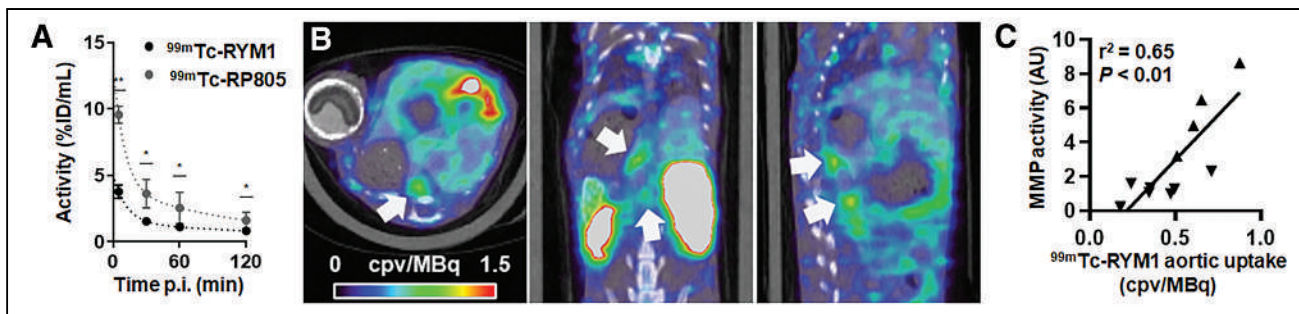


FIGURE 3. ^{99m}Tc -RYM1 imaging of AAA. (A) Comparison of blood clearance of ^{99m}Tc -RYM1 and ^{99m}Tc -RP805 in mice. (B) Examples of fused ^{99m}Tc -RYM1 SPECT/CT images of AAA in angiotensin II-infused mice at 4 wk after aneurysm induction. Arrows point to tracer uptake in AAA on axial (left), coronal (middle), and sagittal (right) views. (C) Aortic ^{99m}Tc -RYM1 signal in vivo correlates well with MMP activity quantified by ex vivo zymography. %ID = percentage injected dose; AU = arbitrary units; cpv = counts per voxel; p.i. = after injection. (Reprinted from (38).)

imaging (46). As fibrin is present in developing and mature thrombi, and absent from circulating blood, specific detection relies on target-selective binding to distinguish it from fibrinogen, its similar, widely circulating precursor (46). Early fibrin-targeted molecular diagnostic procedures were performed with radiolabeled fibrinogen and later with radiolabeled antifibrin antibodies and antibody fragments. However, the field has since moved in the direction of fibrin-binding peptides, given their generally more favorable production, binding, and pharmacokinetic characteristics. Numerous fibrin-binding peptides have been developed and labeled for MR, PET, PET/MR, and SPECT imaging in preclinical thrombosis models (46–48). One such fibrin-targeted PET radiotracer, ^{64}Cu -labeled fibrin-binding probe 8 (^{64}Cu -FBP8), demonstrated highly accurate carotid artery and femoral vein thrombus detection in rats (97.6%; 95% CI, 92–100) (49). Moreover, the ^{64}Cu -FBP8 signal provided insight into clot chronicity and composition, as ^{64}Cu -FBP8 uptake was greater in younger than older clots in both arteries and veins. This result was corroborated by quantitative histopathology, which demonstrated an age-dependent reduction in thrombus fibrin content. ^{64}Cu -FBP8 is undergoing clinical investigation to evaluate its effectiveness for left atrial appendage thrombus imaging (NCT03830320) (50). Initial results demonstrated that ^{64}Cu -FBP8 is metabolically stable and undergoes rapid bloodstream clearance. In addition, maximum SUVs in left atrial appendages were significantly greater in patients with transesophageal imaging–confirmed left atrial appendage thrombi than those with negative imaging results (median, 4.0 [interquartile range, 3.0–6.0] vs. median, 2.3 [interquartile range, 2.1–2.5]; $P < 0.001$). ^{64}Cu -FBP8 is also being evaluated clinically for the detection of deep venous thrombosis and pulmonary embolism (NCT04022915).

Activated Platelet Imaging

Similar to fibrin, activated platelets are essentially present in large numbers only in developing thrombi and healing wounds and are thus attractive targets for acute thrombus imaging. The most common target on activated platelets is glycoprotein IIb/IIIa, a heterodimeric membrane receptor that, when activated, binds to von Willebrand factor and to its primary ligand, fibrinogen, to mediate platelet adhesion and aggregation (51). ^{99m}Tc -apcitide is an early SPECT imaging agent targeting glycoprotein IIb/IIIa that was approved by the FDA for detection of acute deep venous thrombosis. However, enthusiasm was ultimately tempered by the fact that it was not particularly effective for detecting pulmonary embolism (52). ^{18}F -glycoprotein I (GP1) is an ^{18}F -labeled derivative of the small-molecule glycoprotein IIb/IIIa antagonist

elarofiban (53–55). The binding of ^{18}F -GP1 to glycoprotein IIb/IIIa is highly specific and appears to be minimally affected by aspirin or heparin treatment (55). In preliminary clinical evaluations, ^{18}F -GP1 demonstrated the ability to identify thrombotic lesions in patients with acute deep venous thrombosis or pulmonary embolism (53), acute arterial thrombi (54), bioprosthetic valve thrombi (56), left atrial appendage thrombi (56), jugular vein thrombi (56), and left ventricular assist device thrombi (Fig. 4) (56). However, ^{18}F -GP1's vessel-level detection rate of pulmonary embolism was significantly lower than that for deep venous thrombosis (60% vs. 89%, $P < 0.001$), a finding that may relate to lower levels of activated platelets in older, embolic thrombi or inhibition of platelet activation in the setting of large pulmonary embolism (53). Further evaluation of ^{18}F -GP1 in various clinical settings, including acute deep venous thrombosis (NCT04156230) and bioprosthetic valve thrombosis (NCT04073875), is in progress.

Factor XIIIa Imaging

Factor XIIIa is an activated enzyme that crosslinks fibrin during the terminal step of the coagulation pathway and is thus another molecular target for imaging of thrombosis (57). Several factor XIIIa–targeted radiotracers based on α_2 -antiplasmin, a substrate of factor XIIIa in the transglutaminase crosslinking reaction, have been evaluated in preclinical models. ^{18}F -ENC2015 is a fluorescent and positron-emitting factor XIIIa–targeting probe that has demonstrated rapid, selective binding to thrombi in initial preclinical carotid artery thrombosis models (58). Ultimately, information on the sensitivity of ENC2015 and other tracers to small foci of thrombosis, their effectiveness in the presence of antiplatelet and anticoagulant agents, and their ability to differentiate between active and chronic thrombi will be key to their acceptance as clinical tools.

RADIOTRACERS FOR CARDIOVASCULAR FIBROSIS IMAGING

Tissue fibrosis is a consequence of dysregulated repair responses to various types of injury. Excessive extracellular matrix deposition (mainly collagen) leading to interstitial or replacement fibrosis is the result of dysregulated fibroblast activation and myofibroblast transformation. Inflammation, activation of transforming growth factor β , focal secretion of other cytokines, and MMP activation drive this process (59). In the myocardium, fibrosis can lead to cardiac dysfunction and serve as a nidus for arrhythmias (60). The burden of myocardial fibrosis related to nonischemic cardiomyopathy and myocardial injuries from MI, cytotoxic chemotherapy or radiation, and inflammatory or immune-mediated conditions (e.g., myocarditis) has

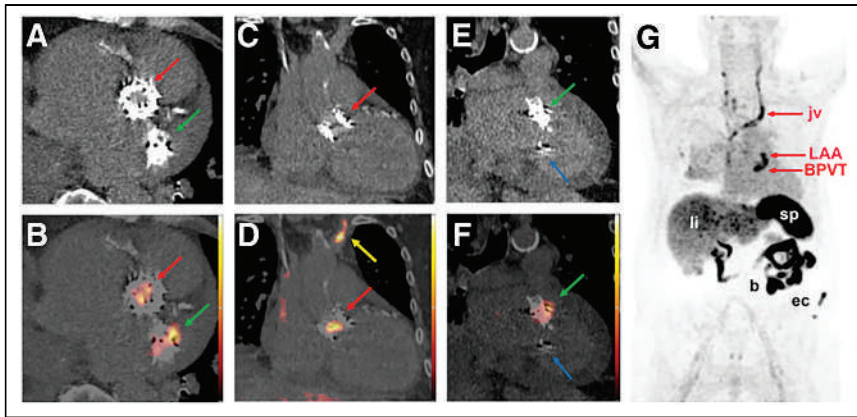


FIGURE 4. Thrombus detection via ^{18}F -GP1 PET/CT. (A–F) Axial (A and B), coronal (C and D), and parasagittal (E and F) unenhanced CT (top) and corresponding ^{18}F -GP1 PET/CT images (bottom) demonstrating bioprosthetic valve (BPVT), left atrial appendage (LAA), and left jugular vein thromboses (jv). (G) Anterior maximum-intensity-projection ^{18}F -GP1 PET image showing distribution of tracer in this patient. (Reprinted from (56).)

prognostic value for cardiovascular outcomes (61,62). Fibrosis also plays a key role in the pathogenesis of vascular diseases such as atherosclerosis (63). Given the association between fibrous cap thickness and vulnerability to plaque rupture, the evaluation of collagen content in atherosclerotic plaques may inform on plaque stability. However, the spatial resolution of current nuclear imaging modalities and the presence of fibrosis elsewhere within the vessel wall are major impediments to this approach.

Classic nuclear cardiology studies such as myocardial perfusion imaging and viability testing allow for indirect assessment of cardiac fibrosis through detection of scar tissue. Measurement of delayed gadolinium enhancement by MRI is another means of assessing myocardial fibrosis. However, these techniques are not sufficiently sensitive for detecting early stages of fibrosis and cannot distinguish between active fibrosis (fibrogenesis) and stable fibrosis or scar. In addition, they provide no information on collagen turnover, which is a target of emerging therapeutic interventions to treat fibrosis (64). Molecular imaging may provide a noninvasive means to monitor and quantify the presence of active fibrosis and determine the efficacy of therapeutics targeting fibrotic processes.

Fibroblast Activation Protein (FAP) Imaging

FAP, a type II transmembrane glycoprotein with collagenase activity, has recently emerged as a promising target for fibrogenesis imaging. This marker of fibroblast activation is not detectable in most healthy adult tissues but can be upregulated in pathologic states such as cancer, atherosclerosis, arthritis, and tissue fibrosis (65). FAP's overexpression in human tumors and documented role in promoting tumor growth in animal models have led to its evaluation as a diagnostic and therapeutic target in ongoing oncologic clinical trials (NCT04147494 and NCT04554719). In parallel, FAP-targeted tracers are emerging as potential tools for imaging fibroblast activation and fibrosis in other settings, such as cardiovascular disease. ^{68}Ga -FAP inhibitor (FAPI)–04 PET imaging in a rodent model of MI has shown significantly increased tracer uptake in injured myocardium 6 d after coronary ligation, with immunohistochemistry and autoradiography demonstrating that the PET signals corresponded to FAP-positive myofibroblasts concentrated in the infarct border zones (66). Cardiac expression of FAP has also been studied indirectly in cancer patients undergoing ^{68}Ga -FAPI PET imaging. In one study, left ventricular uptake of ^{68}Ga -FAPI

correlated strongly with reduced ejection fraction by univariate analysis ($r^2 = 0.74$, $P < 0.01$) and had weaker, but significant, correlations with age ($r^2 = 0.15$, $P = 0.04$) and the presence of coronary artery disease ($r^2 = 0.16$, $P = 0.03$) (Fig. 5) (67). Another study demonstrated that left ventricular ^{68}Ga -FAPI uptake correlated with the presence of cardiovascular risk factors such as overweight status (odds ratio, 2.6; $P = 0.023$), type 2 diabetes (odds ratio, 2.9; $P = 0.041$), and histories of platinum-based chemotherapy (odds ratio, 3.0; $P = 0.034$) and chest radiation (odds ratio, 3.5; $P = 0.024$) (68). Finally, a retrospective analysis of ^{68}Ga -FAPI PET/CT images obtained for noncardiovascular indications showed that focal arterial uptake of the tracer correlated negatively with calcification ($r = -0.27$, $P < 0.01$) (69). Several ongoing clinical

trials seek to establish the role of FAPI imaging to detect post-MI cardiac fibrosis (NCT04803864, NCT04723953).

Extracellular Matrix Imaging

Collagens, especially types I and III, constitute the bulk of fibrotic tissue and accordingly have been used as targets for imaging of fibrosis. Several SPECT and PET tracers that target different types of collagen, including $^{99\text{m}}\text{Tc}$ -collagelin (70), ^{68}Ga -collagelin (71), ^{64}Cu -collagen-binding probe (CBP) 7 (72), and ^{64}Cu -CBP8 (73), have been used in animal and human studies to evaluate fibrosis. However, there are only a few reports of using these tracers in the cardiovascular system. For instance, in a rat model of MI, $^{99\text{m}}\text{Tc}$ -collagelin tracer uptake occurred in areas of histologically confirmed fibrosis (70). Additional studies are needed to establish the utility of these radiotracers for cardiovascular fibrosis imaging. Given the role of MMPs in extracellular matrix remodeling, MMP-targeted imaging may also provide valuable information on fibrotic processes in cardiovascular disease.

^{18}F -NAF PET IMAGING OF CARDIOVASCULAR CALCIFICATION

Ectopic calcification in arteries and cardiac valves is driven by osteoblastic differentiation of vascular smooth muscle cells and valvular interstitial cells. The role of calcification in cardiovascular

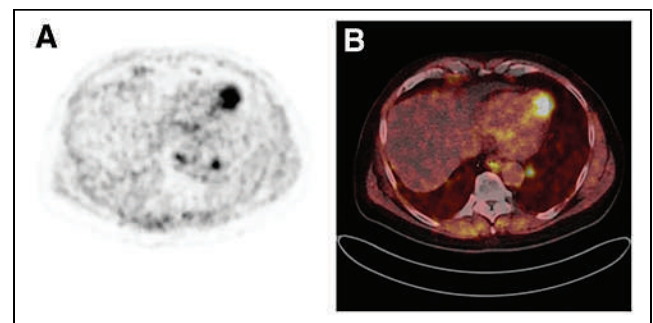


FIGURE 5. Detection of cardiac fibroblast activation via ^{68}Ga -FAPI PET/CT. Transaxial images of ^{68}Ga -FAPI PET (A) and ^{68}Ga -FAPI PET/CT (B) demonstrate left ventricular radiotracer uptake in patient with papillary thyroid cancer. (Reprinted from (67).)

pathology is complex and context-dependent. In coronary arteries, microcalcification is considered a classic feature of vulnerable plaque that is prone to rupture, whereas macrocalcification may be associated with plaque stability (74). In valvular disease, calcification directly contributes to the development of valvular dysfunction. Accordingly, there is potential value in detecting calcification as a diagnostic and possibly prognostic tool in cardiovascular disease. Although CT can detect established, macroscopic foci of calcification, ^{18}F -NaF PET has recently emerged as a promising tool to detect the process of calcification. Fluoride binds to hydroxyapatite in calcified tissue through an exchange process with hydroxyl groups. Microcalcifications have greater surface area per mass for ^{18}F -NaF binding than do macrocalcifications and thus tend to produce more intense signals (74). Recent studies have shown greater uptake of ^{18}F -NaF in culprit plaques after recent acute coronary syndrome (75), and a post hoc analysis of several observational studies showed that global estimates of coronary ^{18}F -NaF signals in patients with known coronary artery disease may predict future risks of MI (76). Ongoing studies such as the Prediction of Recurrent Events with ^{18}F -Fluoride (PREFFIR, NCT02278211) should further clarify the role of ^{18}F -NaF PET imaging in determining risk for future cardiovascular events.

^{18}F -NaF PET has also demonstrated potential clinical utility for imaging of valvular calcification. In patients with calcific aortic valve stenosis and mitral annular calcification, valvular ^{18}F -NaF PET signals have been shown to correlate with the severity of calcification detected by CT. Moreover, ^{18}F -NaF PET signals on valves have been shown to predict the development of macroscopic calcification several years before detection on CT (77–79), and greater ^{18}F -NaF PET signals have been linked to faster progression of calcification, although not independently of baseline CT-derived calcium scoring (77). Several recent comprehensive reviews provide more detailed discussions of the potential of ^{18}F -NaF PET for studying cardiovascular pathophysiology and assessing vascular (carotid and coronary artery atherosclerosis, abdominal aortic aneurism) and valvular diseases and their responses to therapy (80,81).

RADIOTRACERS FOR CARDIAC AMYLOIDOSIS IMAGING

Amyloidosis affects multiple organ systems through extracellular accumulation of amyloid fibrils. These insoluble fibrils form as the result of misfolding and aggregation of various precursor proteins, many of which are normal constituents of plasma. Cardiac involvement is common in the 2 most prevalent forms of amyloidosis, transthyretin amyloidosis (ATTR) and immunoglobulin light-chain amyloidosis (AL). Nuclear imaging has emerged to play a key role in the diagnosis of ATTR and AL cardiomyopathies. Early and accurate detection of these conditions is important given the availability of effective but time-sensitive treatments.

ATTR cardiomyopathy can be diagnosed noninvasively through semiquantitative analysis of planar or SPECT images using $^{99\text{m}}\text{Tc}$ -labeled bisphosphonate derivatives that were initially developed for bone imaging. $^{99\text{m}}\text{Tc}$ -pyrophosphate is used most in the United States, whereas $^{99\text{m}}\text{Tc}$ -hydroxymethylene diphosphonate ($^{99\text{m}}\text{Tc}$ -HMDP) and $^{99\text{m}}\text{Tc}$ -3,3-diphosphono-1,2-propanodicarboxylic acid ($^{99\text{m}}\text{Tc}$ -DPD) are more commonly used in Europe. These radiotracers are generally considered to have similar diagnostic performance, although direct comparisons are limited. In a multicenter study of patients with suspected amyloid cardiomyopathy, pooled scintigraphy data using these 3 radiotracers demonstrated that the presence of myocardial radiotracer uptake was more than 99%

sensitive and 86% specific for histologically confirmed ATTR, with false-positives related almost exclusively to low-level uptake in the setting of AL (82). Notably, the combination of grade 2 and 3 scintigraphic uptake and negative urine or serum monoclonal protein analysis had a specificity and positive predictive value for ATTR of 100%.

PET radiotracers that were initially developed for imaging of brain amyloid plaques related to Alzheimer disease have been evaluated for the detection of cardiac amyloidosis. In initial studies, ^{11}C -Pittsburgh compound B (83), ^{18}F -florbetapir (84), and ^{18}F -florbetaben (85) have demonstrated potential diagnostic utility for detecting both AL and ATTR cardiomyopathies. ^{18}F -flutemetamol, an ^{18}F -based analog of ^{11}C -Pittsburgh compound B, has also been studied for cardiac amyloid imaging, although more recent work has raised questions about its sensitivity (86). ^{18}F -florbetapir and ^{18}F -florbetaben are currently undergoing evaluation in clinical trials. In all, quantitative PET-based approaches for imaging cardiac amyloidosis may provide additional benefits beyond diagnosis, such as correlating amyloid burden with prognosis (83) or responses to novel disease-modifying treatments (85). Because of the short half-life of ^{11}C , which restricts its use to centers with on-site cyclotrons, ^{18}F -based agents have greater potential for large-scale clinical use.

CONCLUSIONS AND FUTURE PERSPECTIVES

Molecular imaging is anticipated to play an increasingly more prominent role in clinical cardiovascular medicine. Although many radiotracers with potential cardiovascular applications have been evaluated in preclinical and clinical studies, only a select few to date have advanced to mainstream clinical usage. Aside from the technical and performance-related requirements of radiotracer development, clinical implementation requires clear definition of their diagnostic roles and demonstration of added value beyond existing clinical imaging techniques. Moreover, the clinical market for emerging radiotracers must be large enough to justify their initial research and development costs, an issue that may be addressed by targeting key, common biologic processes rather than specific diseases. Although these factors seemingly pose formidable barriers, the demand for new radiotracers is increasing because of evolving trends in medicine toward molecular characterization and personalized therapies. Technical advances in areas such as radiotracer chemistry, instrumentation, and data analysis are facilitating radiotracer development to address the numerous unmet clinical needs.

REFERENCES

1. Soehnlein O, Libby P. Targeting inflammation in atherosclerosis: from experimental insights to the clinic. *Nat Rev Drug Discov*. 2021;20:589–610.
2. Tschöpe C, Ammirati E, Bozkurt B, et al. Myocarditis and inflammatory cardiomyopathy: current evidence and future directions. *Nat Rev Cardiol*. 2021;18:169–193.
3. Murphy SP, Kakkar R, McCarthy CP, Januzzi JL Jr. Inflammation in heart failure: JACC state-of-the-art review. *J Am Coll Cardiol*. 2020;75:1324–1340.
4. Nahrendorf M, Frantz S, Swirski FK, et al. Imaging systemic inflammatory networks in ischemic heart disease. *J Am Coll Cardiol*. 2015;65:1583–1591.
5. Weirather J, Hofmann UD, Beyersdorf N, et al. Foxp3+ CD4+ T cells improve healing after myocardial infarction by modulating monocyte/macrophage differentiation. *Circ Res*. 2014;115:55–67.
6. Grunewald J, Eklund A. Role of CD4+ T cells in sarcoidosis. *Proc Am Thorac Soc*. 2007;4:461–464.
7. Hughes CE, Nibbs RJB. A guide to chemokines and their receptors. *FEBS J*. 2018; 285:2944–2971.
8. Lindsey ML. Assigning matrix metalloproteinase roles in ischaemic cardiac remodelling. *Nat Rev Cardiol*. 2018;15:471–479.

9. Liu CL, Guo J, Zhang X, Sukhova GK, Libby P, Shi GP. Cysteine protease cathepsins in cardiovascular disease: from basic research to clinical trials. *Nat Rev Cardiol.* 2018;15:351–370.
10. Newby AC. Proteinases and plaque rupture: unblocking the road to translation. *Curr Opin Lipidol.* 2014;25:358–366.
11. Slart RH. FDG-PET/CT(A) imaging in large vessel vasculitis and polymyalgia rheumatica: joint procedural recommendation of the EANM, SNMMI, and the PET Interest Group (PIG), and endorsed by the ASNC. *Eur J Nucl Med Mol Imaging.* 2018;45:1250–1269.
12. Chareonthaitawee P, Beanlands RS, Chen W, et al. Joint SNMMI-ASNC expert consensus document on the role of ¹⁸F-FDG PET/CT in cardiac sarcoid detection and therapy monitoring. *J Nucl Med.* 2017;58:1341–1353.
13. Tavakoli S, Zamora D, Ullevig S, Amis R. Bioenergetic profiles diverge during macrophage polarization: implications for the interpretation of ¹⁸F-FDG PET imaging of atherosclerosis. *J Nucl Med.* 2013;54:1661–1667.
14. Chen DL, Schuster DP. Positron emission tomography with [¹⁸F]fluorodeoxyglucose to evaluate neutrophil kinetics during acute lung injury. *Am J Physiol Lung Cell Mol Physiol.* 2004;286:L834–L840.
15. Evans NR, Tarkin JM, Chowdhury MM, et al. Dual-tracer positron-emission tomography for identification of culprit carotid plaques and pathophysiology in vivo. *Circ Cardiovasc Imaging.* 2020;13:e009539.
16. Ilkan Z, Akar FG. The mitochondrial translocator protein and the emerging link between oxidative stress and arrhythmias in the diabetic heart. *Front Physiol.* 2018;9:1518.
17. Gaemperli O, Shalhoub J, Owen DR, et al. Imaging intraplaque inflammation in carotid atherosclerosis with ¹¹C-PK11195 positron emission tomography/computed tomography. *Eur Heart J.* 2012;33:1902–1910.
18. Lamare F, Hinz R, Gaemperli O, et al. Detection and quantification of large-vessel inflammation with ¹¹C-(R)-PK11195 PET/CT. *J Nucl Med.* 2011;52:33–39.
19. Schollhammer R, Lepreux S, Barthe N, et al. In vitro and pilot in vivo imaging of 18 kDa translocator protein (TSPO) in inflammatory vascular disease. *EJNMMI Res.* 2021;11:45.
20. Thackeray JT, Hupe HC, Wang Y, et al. Myocardial inflammation predicts remodeling and neuroinflammation after myocardial infarction. *J Am Coll Cardiol.* 2018;71:263–275.
21. Toczek J, Kukreja G, Zhang J, et al. TSPO-targeted PET imaging in aging heart [abstract]. *J Nucl Cardiol.* 2020:1866.
22. Yoder KK, Nho K, Risacher SL, Kim S, Shen L, Saykin AJ. Influence of TSPO genotype on ¹¹C-PBR28 standardized uptake values. *J Nucl Med.* 2013;54:1320–1322.
23. Tarkin JM, Joshi FR, Evans NR, et al. Detection of atherosclerotic inflammation by ⁶⁸Ga-DOTATATE PET compared to [¹⁸F]FDG PET imaging. *J Am Coll Cardiol.* 2017;69:1774–1791.
24. Lichtenauer-Kaligis EG, Dalm VA, Oomen SP, et al. Differential expression of somatostatin receptor subtypes in human peripheral blood mononuclear cell subsets. *Eur J Endocrinol.* 2004;150:565–577.
25. Pauwels E, Cleeren F, Bormans G, Deroose CM. Somatostatin receptor PET ligands: the next generation for clinical practice. *Am J Nucl Med Mol Imaging.* 2018;8:311–331.
26. Nobashi T, Nakamoto Y, Kubo T, et al. The utility of PET/CT with ⁶⁸Ga-DOTATOC in sarcoidosis: comparison with ⁶⁷Ga-scintigraphy. *Ann Nucl Med.* 2016;30:544–552.
27. Kircher M, Tran-Gia J, Kemmer L, et al. Imaging inflammation in atherosclerosis with CXCR4-directed ⁶⁸Ga-pentixafor PET/CT: correlation with ¹⁸F-FDG PET/CT. *J Nucl Med.* 2020;61:751–756.
28. Heo GS, Bajpai G, Li W, et al. Targeted PET imaging of chemokine receptor 2-positive monocytes and macrophages in the injured heart. *J Nucl Med.* 2021;62:111–114.
29. Herrmann K, Lapa C, Wester HJ, et al. Biodistribution and radiation dosimetry for the chemokine receptor CXCR4-targeting probe ⁶⁸Ga-pentixafor. *J Nucl Med.* 2015;56:410–416.
30. Thackeray JT, Derlin T, Haghikia A, et al. Molecular imaging of the chemokine receptor CXCR4 after acute myocardial infarction. *JACC Cardiovasc Imaging.* 2015;8:1417–1426.
31. Heo GS, Kopecky B, Sultan D, et al. Molecular imaging visualizes recruitment of inflammatory monocytes and macrophages to the injured heart. *Circ Res.* 2019;124:881–890.
32. English SJ, Sastriques SE, Detering L, et al. CCR2 positron emission tomography for the assessment of abdominal aortic aneurysm inflammation and rupture prediction. *Circ Cardiovasc Imaging.* 2020;13:e009889.
33. Liu Y, Pierce R, Luehmann HP, Sharp TL, Welch MJ. PET imaging of chemokine receptors in vascular injury–accelerated atherosclerosis. *J Nucl Med.* 2013;54:1135.
34. Dutta P, Sager Hendrik B, Stengel Kristy R, et al. Myocardial infarction activates CCR2+ hematopoietic stem and progenitor cells. *Cell Stem Cell.* 2015;16:477–487.
35. Razavian M, Tavakoli S, Zhang J, et al. Atherosclerosis plaque heterogeneity and response to therapy detected by in vivo molecular imaging of matrix metalloproteinase activation. *J Nucl Med.* 2011;52:1795–1802.
36. Su H, Spinale FG, Dobrucki LW, et al. Noninvasive targeted imaging of matrix metalloproteinase activation in a murine model of postinfarction remodeling. *Circulation.* 2005;112:3157–3167.
37. Fujimoto S, Hartung D, Ohshima S, et al. Molecular imaging of matrix metalloproteinase in atherosclerotic lesions: resolution with dietary modification and statin therapy. *J Am Coll Cardiol.* 2008;52:1847–1857.
38. Toczek J, Ye Y, Gona K, et al. Preclinical evaluation of RYMI, a matrix metalloproteinase-targeted tracer for imaging aneurysms. *J Nucl Med.* 2017;58:1318–1323.
39. Jung JJ, Razavian M, Challa AA, et al. Multimodality and molecular imaging of matrix metalloproteinase activation in calcific aortic valve disease. *J Nucl Med.* 2015;56:933–938.
40. Golestani R, Razavian M, Nie L, et al. Imaging vessel wall biology to predict outcome in abdominal aortic aneurysm. *Circ Cardiovasc Imaging.* 2014;8:e002471.
41. Razavian M, Nie L, Challa A, et al. Lipid lowering and imaging protease activation in atherosclerosis. *J Nucl Cardiol.* 2014;21:319–328.
42. Gona K, Toczek J, Ye Y, et al. Hydroxamate-based selective macrophage elastase (MMP-12) inhibitors and radiotracers for molecular imaging. *J Med Chem.* 2020;63:15037–15049.
43. Laidlaw BJ, Craft JE, Kaech SM. The multifaceted role of CD4(+) T cells in CD8(+) T cell memory. *Nat Rev Immunol.* 2016;16:102–111.
44. Beckford Vera DR, Smith CC, Bixby LM, et al. Immuno-PET imaging of tumor-infiltrating lymphocytes using zirconium-89 radiolabeled anti-CD3 antibody in immune-competent mice bearing syngeneic tumors. *PLoS One.* 2018;13:e0193832.
45. Kristensen LK, Fröhlich C, Christensen C, et al. CD4(+) and CD8a(+) PET imaging predicts response to novel PD-1 checkpoint inhibitor: studies of Sym021 in syngeneic mouse cancer models. *Theranostics.* 2019;9:8221–8238.
46. Oliveira BL, Caravan P. Peptide-based fibrin-targeting probes for thrombus imaging. *Dalton Trans.* 2017;46:14488–14508.
47. Rezaei-nipour S, Bozorgi AH, Moghimi A, et al. Synthesis and biological evaluation of cyclic [^{99m}Tc]-HYNIC-CGPRPPC as a fibrin-binding peptide for molecular imaging of thrombosis and its comparison with [^{99m}Tc]-HYNIC-GPRPP. *Mol Imaging Biol.* 2017;19:256–264.
48. Starms LW, van Duijnhoven SM, Rossin R, et al. Evaluation of ¹¹¹In-labeled EPep and FibPep as tracers for fibrin SPECT imaging. *Mol Pharm.* 2013;10:4309–4321.
49. Blasi F, Oliveira BL, Rietz TA, et al. Multisite thrombus imaging and fibrin content estimation with a single whole-body PET scan in rats. *Arterioscler Thromb Vasc Biol.* 2015;35:2114–2121.
50. Izquierdo-Garcia D, Desogere P, Philip AL, et al. Detection and characterization of thrombosis in humans using fibrin-targeted positron emission tomography and magnetic resonance. *JACC Cardiovasc Imaging.* October 7, 2021 [Epub ahead of print].
51. Jamasbi J, Ayabe K, Goto S, Nieswandt B, Peter K, Siess W. Platelet receptors as therapeutic targets: past, present and future. *Thromb Haemost.* 2017;117:1249–1257.
52. Dunzinger A, Hafner F, Schaffler G, Piswanger-Soelkner JC, Brodmann M, Lipp RW. ^{99m}Tc-apcitide scintigraphy in patients with clinically suspected deep venous thrombosis and pulmonary embolism. *Eur J Nucl Med Mol Imaging.* 2008;35:2082–2087.
53. Kim C, Lee JS, Han Y, et al. Glycoprotein IIb/IIIa receptor imaging with ¹⁸F-GP1 positron emission tomography for acute venous thromboembolism: an open-label, non-randomized, first-in-human phase 1 study. *J Nucl Med.* 2018;60:244–249.
54. Chae SY, Kwon TW, Jin S, et al. A phase 1, first-in-human study of ¹⁸F-GP1 positron emission tomography for imaging acute arterial thrombosis. *EJNMMI Res.* 2019;9:3.
55. Lohrke J, Siebeneicher H, Berger M, et al. ¹⁸F-GP1, a novel PET tracer designed for high-sensitivity, low-background detection of thrombi. *J Nucl Med.* 2017;58:1094–1099.
56. Hugenberg V, Zerna M, Berndt M, et al. GMP-compliant radiosynthesis of [¹⁸F]GP1, a novel PET tracer for the detection of thrombi. *Pharmaceuticals (Basel).* 2021;14:739.
57. Reyes Gil M. Overview of the coagulation system. In: Shaz BH, Hillyer CD, Reyes Gil M, eds. *Transfusion Medicine and Hemostasis*. 3rd ed. Elsevier; 2019:559–564.
58. Andrews JPM, Portal C, Walton T, et al. Non-invasive in vivo imaging of acute thrombosis: development of a novel factor XIIIa radiotracer. *Eur Heart J Cardiovasc Imaging.* 2020;21:673–682.
59. Henderson NC, Rieder F, Wynn TA. Fibrosis: from mechanisms to medicines. *Nature.* 2020;587:555–566.
60. Soejima K, Stevenson WG. Ventricular tachycardia associated with myocardial infarct scar. *Circulation.* 2002;106:176–179.
61. Kwon DH, Hachamovitch R, Adeniyi A, et al. Myocardial scar burden predicts survival benefit with implantable cardioverter defibrillator implantation in patients with severe ischaemic cardiomyopathy: influence of gender. *Heart.* 2014;100:206.
62. Aljaroudi WA, Flamm SD, Saliba W, Wilkoff BL, Kwon D. Role of CMR imaging in risk stratification for sudden cardiac death. *JACC Cardiovasc Imaging.* 2013;6:392–406.
63. Lan TH, Huang XQ, Tan HM. Vascular fibrosis in atherosclerosis. *Cardiovasc Pathol.* 2013;22:401–407.

64. McVicker BL, Bennett RG. Novel anti-fibrotic therapies. *Front Pharmacol*. 2017; 8:318.
65. Fitzgerald AA, Weiner LM. The role of fibroblast activation protein in health and malignancy. *Cancer Metastasis Rev*. 2020;39:783–803.
66. Varasteh Z, Mohanta S, Robu S, et al. Molecular imaging of fibroblast activity after myocardial infarction using a ⁶⁸Ga-labeled fibroblast activation protein inhibitor, FAPI-04. *J Nucl Med*. 2019;60:1743–1749.
67. Siebermair J, Köhler MI, Kupusovic J, et al. Cardiac fibroblast activation detected by Ga-68 FAPI PET imaging as a potential novel biomarker of cardiac injury/remodeling. *J Nucl Cardiol*. 2021;28:812–821.
68. Heckmann MB, Reinhardt F, Finke D, et al. Relationship between cardiac fibroblast activation protein activity by positron emission tomography and cardiovascular disease. *Circ Cardiovasc Imaging*. 2020;13:e010628.
69. Wu M, Ning J, Li J, et al. Feasibility of in vivo imaging of fibroblast activation protein in human arterial walls. *J Nucl Med*. September 16, 2021 [Epub ahead of print].
70. Muzard J, Sarda-Mantel L, Loyau S, et al. Non-invasive molecular imaging of fibrosis using a collagen-targeted peptidomimetic of the platelet collagen receptor glycoprotein VI. *PLoS One*. 2009;4:e5585.
71. Velikyan I, Rosenström U, Bulenga TN, Eriksson O, Antoni G. Feasibility of multiple examinations using ⁶⁸Ga-labelled collagelin analogues: organ distribution in rat for extrapolation to human organ and whole-body radiation dosimetry. *Pharmaceuticals (Basel)*. 2016;9:31.
72. Désogère P, Tapias LF, Rietz TA, et al. Optimization of a collagen-targeted PET probe for molecular imaging of pulmonary fibrosis. *J Nucl Med*. 2017;58:1991.
73. Montesi SB, Izquierdo-Garcia D, Désogère P, et al. Type I collagen-targeted positron emission tomography imaging in idiopathic pulmonary fibrosis: first-in-human studies. *Am J Respir Crit Care Med*. 2019;200:258–261.
74. Creager MD, Hohl T, Hutcheson JD, et al. ¹⁸F-fluoride signal amplification identifies microcalcifications associated with atherosclerotic plaque instability in positron emission tomography/computed tomography images. *Circ Cardiovasc Imaging*. 2019;12:e007835.
75. Joshi NV, Vesey AT, Williams MC, et al. ¹⁸F-fluoride positron emission tomography for identification of ruptured and high-risk coronary atherosclerotic plaques: a prospective clinical trial. *Lancet*. 2014;383:705–713.
76. Kwiecinski J, Tzolos E, Adamson PD, et al. Coronary ¹⁸F-sodium fluoride uptake predicts outcomes in patients with coronary artery disease. *J Am Coll Cardiol*. 2020;75:3061–3074.
77. Jenkins WS, Vesey AT, Shah AS, et al. Valvular ¹⁸F-fluoride and ¹⁸F-fluorodeoxyglucose uptake predict disease progression and clinical outcome in patients with aortic stenosis. *J Am Coll Cardiol*. 2015;66:1200–1201.
78. Dweck MR, Jones C, Joshi NV, et al. Assessment of valvular calcification and inflammation by positron emission tomography in patients with aortic stenosis. *Circulation*. 2012;125:76–86.
79. Massera D, Trivieri MG, Andrews JPM, et al. Disease activity in mitral annular calcification. *Circ Cardiovasc Imaging*. 2019;12:e008513.
80. Tzolos E, Kwiecinski J, Berman D, Slomka P, Newby DE, Dweck MR. Latest advances in multimodality imaging of aortic stenosis. *J Nucl Med*. 2022;63:353–358.
81. Tzolos E, Dweck MR. ¹⁸F-sodium fluoride (¹⁸F-NaF) for imaging microcalcification activity in the cardiovascular system. *Arterioscler Thromb Vasc Biol*. 2020;40:1620–1626.
82. Gillmore JD, Maurer MS, Falk RH, et al. Nonbiopsy diagnosis of cardiac transthyretin amyloidosis. *Circulation*. 2016;133:2404–2412.
83. Lee SP, Suh HY, Park S, et al. Pittsburgh B compound positron emission tomography in patients with AL cardiac amyloidosis. *J Am Coll Cardiol*. 2020;75:380–390.
84. Dorbala S, Vangala D, Semer J, et al. Imaging cardiac amyloidosis: a pilot study using ¹⁸F-florbetapir positron emission tomography. *Eur J Nucl Med Mol Imaging*. 2014;41:1652–1662.
85. Kircher M, Ihne S, Brumberg J, et al. Detection of cardiac amyloidosis with ¹⁸F-florbetaben-PET/CT in comparison to echocardiography, cardiac MRI and DPD-scintigraphy. *Eur J Nucl Med Mol Imaging*. 2019;46:1407–1416.
86. Papathanasiou M, Kessler L, Carpinteiro A, et al. ¹⁸F-flutemetamol positron emission tomography in cardiac amyloidosis. *J Nucl Cardiol*. October 6, 2020 [Epub ahead of print].

Female Authors in Nuclear Medicine Journals: A Survey from 2014 to 2020

Charline Lasnon^{1,2}, Gilles Girault³, Rachida Lebtahi⁴, Catherine Ansquer^{5,6}, Justine Lequesne⁷, and Elske Quak¹

¹Nuclear Medicine Department, Comprehensive Cancer Center F. Baclesse, Unicancer, Caen, France; ²Normandy University, UNICAEN, INSERM 1086 ANTICIPE, Caen, France; ³Medical Library, Comprehensive Cancer Center F. Baclesse, Unicancer, Caen, France; ⁴Department of Nuclear Medicine, Beaujon Hospital, Clichy, France; ⁵Department of Nuclear Medicine, University Hospital of Nantes, Nantes, France; ⁶University of Nantes and CNRS, INSERM, CRCINA, Nantes, France; and ⁷Biostatistics Department, Comprehensive Cancer Center F. Baclesse, Unicancer, Caen, France

Despite the feminization of the medical workforce, women do not have the same career perspectives as men. In nuclear medicine, little information is available on the sex gap regarding prominent author positions in scientific articles. Therefore, the purpose of this study was to evaluate recent trends in the sex distribution of first and last authorship of articles published in nuclear medicine journals. **Methods:** We conducted a bibliometric analysis of first and last author sex of articles published from 2014 to 2020 in 15 nuclear medicine journals. Manuscript title, article type, journal impact factor, date of publication, and first and last name and country of provenance of first and last authors were noted. The Gender API software was used to determine author sex. All statistics were descriptive. **Results:** Women represented 32.8% of first authors and 19.6% of last authors. Female authorship increased from 28.2% (428 of 1,518 articles) in 2014 to 35.5% (735 of 2,069 articles; relative increase, 72%) in 2020 ($P < 0.001$) for first authors and from 15.6% (237 of 1,518 articles) in 2014 to 20.5% (424 of 2,069 articles; relative increase, 79%) in 2020 ($P < 0.001$) for last authors. Parity was forecast for 2035 for first authors and 2052 for last authors. Female authorship increased in Europe for first authors ($P = 0.014$) and last authors ($P < 0.001$), in high-ranking journals for first authors ($P = 0.004$) and last authors ($P < 0.001$), and in other journal ranks for last authors ($P = 0.01$). Female first and last authorship rose for original articles ($P = 0.02$ and $P = 0.01$, respectively) and case reports ($P < 0.001$ and $P = 0.002$, respectively). Regarding collaborations, the proportion of articles produced by male first and last authors decreased from 62.2% in 2014 to 52.9% in 2020 in favor of female first and last authors (odds ratio, 1.07; $P < 0.001$), male first and female last authors (odds ratio, 1.05; $P < 0.001$), and female first and male last authors (odds ratio, 1.03; $P < 0.001$). **Conclusion:** Female first and last authorship in nuclear medicine journals increased substantially from 2014 to 2020, in particular in high-ranking journals, in Europe, and for original articles and case reports. Male-to-male collaborations decreased by 10% in favor of all other collaborations. Parity can be foreseen in a few decades.

Key Words: physicians; women; authorship; nuclear medicine

J Nucl Med 2022; 63:995–1000

DOI: 10.2967/jnumed.121.262773

Received Jun. 23, 2021; revision accepted Sep. 25, 2021.

For correspondence or reprints, contact Elske Quak (e.quak@baclesse.unicancer.fr).

Published online Oct. 21, 2021.

Immediate Open Access: Creative Commons Attribution 4.0 International License (CC BY) allows users to share and adapt with attribution, excluding materials credited to previous publications. License: <https://creativecommons.org/licenses/by/4.0/>. Details: <http://jnm.snmjournals.org/site/misc/permission.xhtml>.

COPYRIGHT © 2022 by the Society of Nuclear Medicine and Molecular Imaging.

Despite efforts to offset the tendency, sex gaps and prejudices broadly persist in modern-day society, and despite the feminization of the workforce in medicine, women do not have the same career perspectives or pay as men (1–4). In the field of medical imaging, the pipeline to the top positions has been described as leaky for female talent, and leadership positions are held predominantly by men (5–10).

Regarding nuclear medicine, the literature on the sex gap and sex-related career challenges is scarce. A recent study reported the underrepresentation of women in academic and leadership positions compared with men in North America and Canada, despite equal academic performance (11). In Europe, a 2007 membership survey of the European Association of Nuclear Medicine showed that one third of physicians were women, with an increasing percentage of female physicians over time and at a younger age (12). However, the sex distribution varied widely between countries, and the evolution of the sex gap in nuclear medicine over time and higher on the career ladder has received little attention.

As scientific publishing is a key factor for career advancement, trends in the sex distribution of prominent author positions may reflect future evolution of women toward leadership positions. Therefore, the main objective of the current study was—through a descriptive bibliometric analysis—to evaluate recent trends in the sex distribution of the most prestigious author positions, that is, first and last authorship, in articles published in anglophone nuclear medicine journals from 2014 to 2020.

MATERIALS AND METHODS

This study was exempt from local institutional review board approval.

We performed a PubMed search for 2014 to 2020 to retrieve all articles published in the 15 purely anglophone nuclear medicine journals in the “Radiology, Nuclear Medicine, and Medical Imaging” category of the Journal Citation Reports 2019: *Journal of Nuclear Medicine*, *European Journal of Nuclear Medicine and Molecular Imaging*, *Clinical Nuclear Medicine*, *Seminars in Nuclear Medicine*, *Journal of Nuclear Cardiology*, *Molecular Imaging and Biology*, *Molecular Imaging*, *EJNMMI Research*, *Annals of Nuclear Medicine*, *EJNMMI Physics*, *Nuclear Medicine and Biology*, *Contrast Media & Molecular Imaging*, *Quarterly Journal of Nuclear Medicine and Molecular Imaging*, *Nuclear Medicine Communications*, and *Hellenic Journal of Nuclear Medicine*. The bibliographic references of all articles were imported into the bibliographic data management software Endnote. An import filter was created to add the following PubMed bibliographic data to the usual bibliographic fields: publication date, first

and last name of all authors, affiliation addresses, and article type. This dataset was exported to Excel, and the following variables were recorded for each entry: manuscript title, publication year, first and last name of the first and last authors, article type, journal impact factor according to the Journal Citation Reports 2019, and country of provenance of first and last authors. The Gender API software (<https://gender-api.com/>) was used to determine the sex of the first and last authors. Performance metrics of this software can be found elsewhere (13). The date of censoring for 2020 was February 24, 2021. Preprints of 2020 were excluded. In the event of missing data, entries were excluded, as were entries with a single author. The following article types were excluded: “Published Erratum,” “Retracted Publication,” “News,” “Lecture,” “Historical Article,” “Biography,” “Portrait,” “Introductory Journal Article,” and “English Abstract.”

The main aim of the study was to analyze the evolution of the percentages of female first and last authorship over the study period. Secondary aims were to forecast the year in which parity will be attained for first and last authors; to evaluate sex distributions according to continent, journal rank, and article type; and to evaluate collaborations between the sexes. For the analysis of author sex according to provenance, countries were classified according to continent. For the analysis of author sex according to journal rank, references were classed as high-ranking (journal impact factor, 7.887–6.622) or others (journal impact factor, 3.544–0.982). For the analysis of author sex according to article type, references were categorized as original article, review, case report, and editorial/letter. References tagged solely as “Journal Article” by PubMed were categorized as original article.

Collaboration between first and last author sex was explored by classifying articles in the 4 following categories: male first and last authors, female first and male last authors, male first and female last authors, and female first and last authors.

All statistics were descriptive. Fisher exact tests were used to analyze the distribution of female authorship from 2014 to 2020. Linear regression was used to forecast the year in which parity for first and last authorship will be reached. A multinomial logistic regression model was constructed to measure the evolution of the distribution of collaborations over time, in which male first and male last authorship was considered the reference. Graphic and statistical analyses were performed on XLSTAT Software (XLSTAT 2007: Data Analysis and Statistical Solutions for Microsoft Excel; Addinsoft, 2017) and R Software (version 4.0.2). For all statistical tests, a 2-tailed *P* value of less than 0.05 was considered statistically significant.

RESULTS

Data Characteristics

In total, 15,720 references were imported, of which 12,450 (79.2%) fulfilled the article type criteria and presented complete data regarding first and last author sex and provenance. Data characteristics are presented in Table 1.

First Authors

Overall, 4,082 of 12,450 (32.8%) first authors were female (Table 1). Female first authorship increased over time from 428 of 1,518 (28.2%) in 2014 to 735 of 2,069 (35.5%) in 2020 ($P < 0.001$) (Fig. 1), representing a relative increase of 72% in 7 y (+307 articles). At this rate, parity was forecast for 2035 (Fig. 1). Conversely, male first authorship increased by 22% between 2014 and 2020 (+244 articles). Detailed absolute numbers of articles for each year between 2014 and 2020 for female and male first authors are depicted in Figure 2.

Regarding the geographic provenance of first authors, 12,054 of 12,450 (96.8%) articles came from 3 continents: Asia (3,370 of 12,450 [27.1%]), Europe (5,699 of 12,450 [45.8%]), and North

TABLE 1
Data Characteristics

Variable	Data
Number of publications	12,450
Year	
2014	1,518 (12.2)
2015	1,594 (12.8)
2016	1,783 (14.3)
2017	1,869 (15)
2018	1,660 (13.3)
2019	1,957 (15.7)
2020	2,069 (16.6)
First-author sex	
Female	4,082 (32.8)
Male	8,368 (67.2)
First-author continent	
Africa	64 (0.5)
Asia	3,370 (27.1)
Europe	5,699 (45.8)
North America	2,985 (24.0)
Oceania	211 (1.7)
South America	121 (1.0)
Last-author sex	
Female	2,445 (19.6)
Male	10,005 (80.4)
Last-author continent	
Africa	62 (0.5)
Asia	3,290 (26.4)
Europe	5,638 (45.3)
North America	3,135 (25.2)
Oceania	217 (1.7)
South America	108 (0.9)
Journal rank*	
High-ranking	6,205 (49.8)
Others	6,245 (50.2)
Article type	
Original article	8,612 (69.2)
Review	1,017 (8.2)
Case report	2,394 (19.2)
Editorials/letters	427 (3.4)

*High-ranking = impact factor of 7.887–6.622; others = impact factor of 3.544–0.982.

Data are number followed by percentage.

America (2,985 of 12,450 [24.0%]). Data from Africa, Oceania, and South America were insufficient to be included in the analysis and can be found in Supplemental Figure 1 (supplemental materials are available at <http://jnm.snmjournals.org>). In Europe, female first authorship increased from 232 of 700 articles (33.1%) in 2014 to 385 of 910 articles (42.3%) in 2020 ($P = 0.014$). In Asia

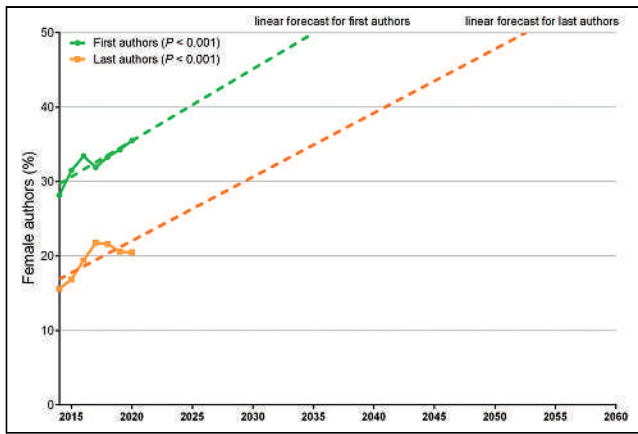


FIGURE 1. Female authorship increased from 28.2% in 2014 to 35.5% in 2020 ($P < 0.001$) for first authors and from 15.6% in 2014 to 20.5% in 2020 ($P < 0.001$) for last authors. For female last authors, peak of 21.8% was observed in 2017. Linear forecasts show that at current rate, parity is predicted in 2035 for first authors and in 2052 for last authors.

and North America, percentages of female first authorship per year did not significantly differ from 2014 to 2020 ($P = 0.06$ and $P = 0.15$, respectively) (Fig. 3A).

Regarding journal rank, percentages of female first authorship in high-ranking journals increased from 240 of 847 articles (28.3%) in 2014 to 371 of 1,015 articles (36.6%) in 2020 ($P = 0.004$). No changes were observed for the other journal ranks ($P = 0.11$) (Fig. 3C).

Regarding article type, female first authorship increased for original articles from 338 of 1,116 articles (30.3%) in 2014 to 516 of 1,428 articles (36.1%) in 2020 ($P = 0.03$) and for case reports from 64 of 288 articles (22.2%) in 2014 to 153 of 389 articles (39.3%) in 2020 ($P < 0.001$). No change was observed for reviews or editorials/letters over time ($P = 0.08$ and 0.48 , respectively). Female first authors were underrepresented in the category editorial/letters (Fig. 3E).

Last Authors

Overall, 2,445 of 12,450 (19.6%) last authors were female (Table 1). Female last authorship increased over time from 237 of

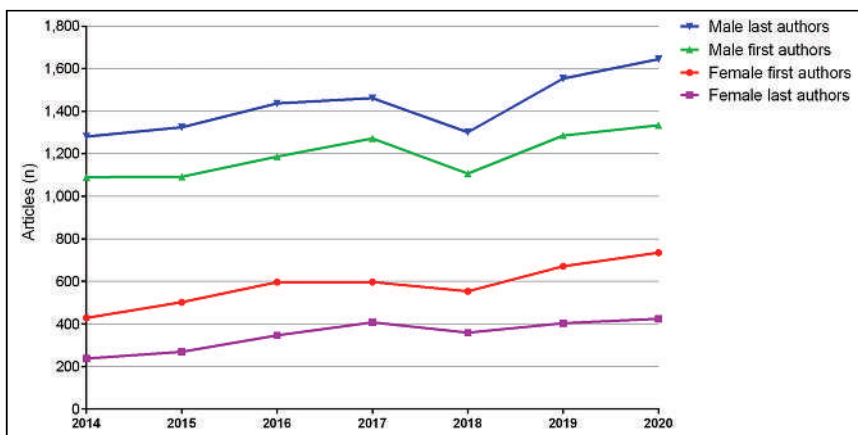


FIGURE 2. Absolute numbers of articles for female and male first and last authors from 2014 to 2020. Articles by female first authors increased from 428 of 1,518 in 2014 to 735 of 2,069 in 2020, whereas articles by male first authors increased from 1,090 of 1,518 in 2014 to 1,334 of 2,069 in 2020. Articles by female last authors increased from 237 of 1,518 in 2014 to 424 of 2,069 in 2020, whereas articles by male last authors increased from 1,281 of 1,518 in 2014 to 1,645 of 2,069 in 2020.

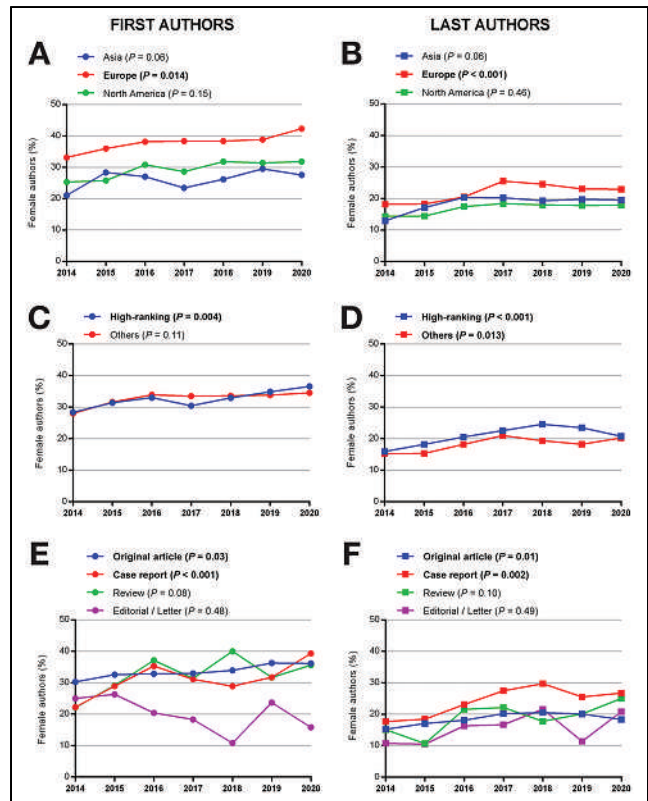


FIGURE 3. Percentage of female first authorship from 2014 to 2020 according to continent of provenance (A), journal rank (C), and article type (E), and percentage of female last authorship from 2014 to 2020 according to continent of provenance (B), journal rank (D), and article type (F). Bold values are statistically significant. Journals were ranked according to impact factor: high-ranking (impact factor, 7.887–6.622) or others (impact factor, 3.544–0.982).

1,518 (15.6%) in 2014 to 424 of 2,069 (20.5%) in 2020, representing a relative increase of 79% (+187 articles), with a peak of 21.8% in 2017 ($P < 0.001$) (Fig. 1). Parity was forecast for 2052 (Fig. 1). Conversely, male first authorship increased by 28% between 2014 and 2020 (+364 articles). Detailed absolute numbers of articles for each year between 2014 and 2020 for female and male last authors are depicted in Figure 2.

Regarding the geographic provenance of last authors, 12,063 of 12,450 (96.9%) articles again came from 3 continents: Asia (3,290 of 12,450 [26.4%]), Europe (5,638 of 12,450 [45.3%]), and North America (3,135 of 12,450 [25.2%]). Data from Africa, Oceania, and South America can be found in Supplemental Figure 1. In Europe, female last authorship increased from 126 of 693 articles (18.2%) in 2014 to 208 of 906 articles (23.0%) in 2020, with a peak of 25.5% in 2017 ($P < 0.001$). In Asia and North America, percentages of female last authorship per year did not significantly differ from 2014 to 2020 ($P = 0.06$ and $P = 0.46$, respectively) (Fig. 3B).

Regarding journal rank, female last authorship increased in high-ranking journals from 135 of 847 articles (15.9%) in 2014 to 211 of 1,015 articles (20.8%) in 2020, with a peak of 24.6% in 2018 ($P < 0.001$) and in other-ranking journals from 102 of 671 articles (15.2%) in 2014 to 213 of 1,054 (20.2%) in 2020 ($P = 0.013$) (Fig. 3D).

Regarding article type, female last authorship increased from 170 of 1,116 articles (15.2%) in 2014 to 262 of 1,428 articles (18.3%) in 2020 ($P = 0.01$) for original articles and from 51 of 288 articles (17.7%) in 2014 to 104 of 389 articles (26.7%) in 2020 for case reports, with a peak of 29.7% in 2018 ($P = 0.002$). No change was observed for reviews or editorials/letters ($P = 0.10$ and 0.49 , respectively) (Fig. 3F).

Collaborations

Assuming a linear evolution of outcomes over the study period and the year as a continuous factor, we observed a decrease in the proportion of articles produced by male first and last authors in favor of female first and last authors (odds ratio, 1.07; $P < 0.001$), male first and female last authors (odds ratio, 1.05; $P < 0.001$), and female first and male last authors (odds ratio, 1.03; $P < 0.001$). Indeed, 944 of 1,518 articles (62.2%) were produced by male first and last authors in 2014, and 1,094 of 2,069 (52.9%) in 2020. On the other hand, there was an increase in the proportion of articles produced by female first and male last authors from 337 of 1,518 articles (22.2%) in 2014 to 551 of 2,069 (26.6%) in 2020, by female first and last authors from 91 of 1,518 articles (6%) in 2014 to 184 of 2,069 (8%) in 2020, and by male first and female last authors from 146 of 1,518 articles (9.6%) in 2014 to 240 of 2,069 (11.6%) in 2020 (Fig. 4).

DISCUSSION

There was a marked sex gap in first and particularly last authorship of articles published in nuclear medicine journals from 2014 to 2020. Women's representation increased over time from 28.2% to 35.5% ($P < 0.001$) for first authors and from 15.6% to 20.5% for last authors, with a peak of 21.8% in 2017 ($P < 0.001$).

Relative increases of 72% and 79% for female first and last authorship, respectively, were observed between 2014 and 2020. Parity was predicted in 2035 for first authors and in 2052 for last authors. A significant increase in female first and last authorship was observed in Europe and for publications in high-ranking journals. Female participation increased in original articles and case reports but not in reviews or editorials/letters. The proportion of articles produced by male first and last authors decreased by 10% in favor of all other collaborations.

To our knowledge, this was the first exhaustive bibliometric analysis of author sex in a wide spectrum of anglophone nuclear medicine journals over several years. Similar sex gaps in authorship have been reported in other domains of medicine and the STEM (science, technology, engineering, mathematics) sciences (4,14,15). For example, in 2018 Bendels et al. reported 33.1% female first and 18.1% female last authorship in high-quality research in 54 journals listed in the Nature Index in the categories "Life Science," "Multidisciplinary," "Earth and Environmental," and "Chemistry" (4).

The lower percentage and rate of increase in female last authorship, a senior position, compared with female first authorship found in our study seem to confirm the presence of an invisible barrier for women to attain leadership positions: the so-called glass ceiling. Moreover, female last authorship increased from 2014 to 2017 but plateaued from 2017 to 2020. These findings could fuel the discussion recently launched by 3 European female nuclear medicine physicians about the challenges women currently face in this field dominated by men (16) and the steps that should be taken to allow female talent to achieve its full potential. Scientific societies, journal editors and publishing companies, scientific institutions, industry, funding agencies, and governments all have their role to play in the promotion of female scientific careers and the creation of a diverse and inclusive research environment. As an example, Gelardi et al. and Evangelista et al. have recently highlighted the underrepresentation of women on editorial boards of nuclear medicine journals, regardless of the rank within the board or the geographic provenance of the journal (17,18). Female participation varied from 14% to a maximum of 32%. Because our study shows that 1 in 3 first authors in nuclear medicine are female, female participation in all ranks of editorial boards should at least mirror this proportion.

Strategies could be put in place in all the aforementioned bodies to promote parity, such as providing transparency on women's representation metrics, providing training on the benefits of diversity in health care, and even proposing sex quotas just as in politics. Obviously, those propositions are not miracle solutions for equality, but they are tools with potentially strong symbolic effects. It is worth to mention here some successes. The Athena SWAN Charter and Horizon Europe within the European Research Area are examples of initiatives aiming to overcome persisting sex gaps (19,20). Also, within nuclear medicine societies, several initiatives now exist such as the EANM Women's Empowerment or the SNMMI Women in Nuclear Medicine, aiming to promote female networks and careers (21,22).

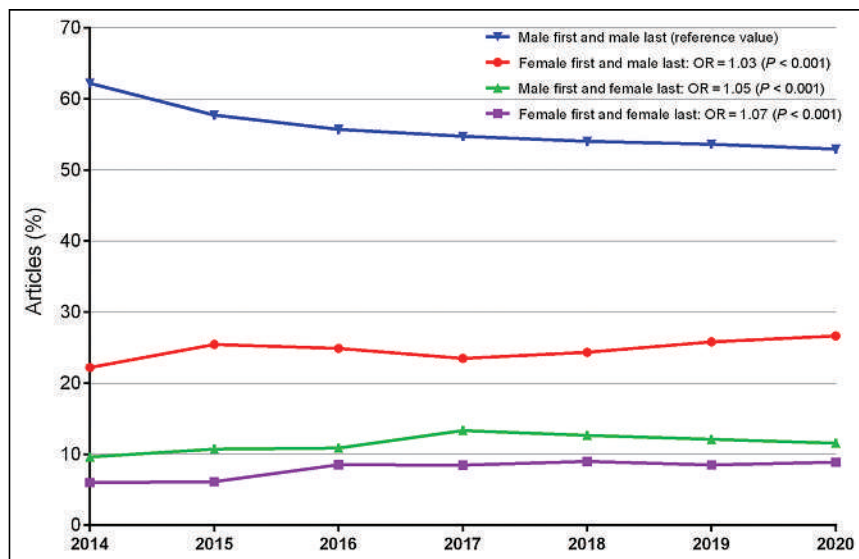


FIGURE 4. Percentage of collaboration between male and female first and last authors for articles published from 2014 to 2020. Male-to-male collaboration declined over time from 62.2% in 2014 to 52.9% in 2020 in favor of all other collaboration types. OR = odds ratio.

Female authors were equally represented among the journal ranks, and their participation increased for both high-ranking and other-ranking journals, suggesting that a possible sex bias during peer review did not result in an unbalanced representation of women across the journal ranks. However, although female participation increased for original articles and case reports, it did not change for reviews and editorials/letters. Furthermore, female first authors were underrepresented for editorials/letters. The productivity puzzle comprises many intricate pieces, and explanations for our findings are probably multifactorial. Sex differences in time management and publication patterns, thereby taking into account the cost–benefit ratio of different article types, may partly explain the unchanged female participation in reviews in favor of an increased female participation in original articles. Reviews are time-consuming to write but have less academic value than original articles in the same journal type. The potential gain in visibility by publishing a review might thus not be worth the investment when time is limited. When it comes to case reports, female participation was large and increased, although the academic value of this article type is low. Should we consider this a symptom of lower consideration by team leaders rather than a scientific achievement? Another explanation for our findings might be the invitation that can be required to write certain article types (8,19). A case-control study of sex disparities in invited commentaries showed that women had a 21% lower odds of receiving such an invitation than men despite having similar experience and that this disparity was greater for senior researchers (23).

An almost 10% decrease in the proportion of articles with a male first and last author was observed, in favor of all other collaborations. This finding might be due to the feminization of the workforce or an increased will of senior male team members to collaborate with female team members. Overall, the increasing tendency for collaboration with female first and last authors is encouraging.

This study had some principal limitations: the use of a software application to assign sex, the relatively short study period from 2014 to 2020 due to the absence of last author provenance on PubMed before 2014, insufficient data for 3 of the 6 continents, the absence of nuclear medicine publications outside the 15 journals analyzed, and the absence of professional or demographic data on the workforce worldwide, which prevented subgroup analyses or comparisons. Furthermore, there are no available data thus far on factors that impact career choices and evolutions in nuclear medicine. Nor are there any data on sex inequity in the nuclear medicine workforce, such as measures of unconscious bias, sexual/racial harassment, and the sex division of domestic labor impacting scientific productivity. National and international nuclear medicine associations could follow in the footsteps of the European Society for Medical Oncology by conducting a survey of male and female workers on sex-related challenges (24). Lastly, 2020 was marked by lockdowns due to the coronavirus disease 2019 pandemic. However, a preliminary analysis showed no alterations in the quantity of publications in medical imaging by female authors during this period (25).

CONCLUSION

Although scientific production in nuclear medicine is no exception to sex inequity, the absolute numbers and proportions of female-authored publications substantially increased from 2014 to

2020, thereby narrowing the sex gap. Parity can be foreseen in a few decades.

DISCLOSURE

Rachida Lebtahi is supported by Advanced Accelerator Applications, Ipsen, Sirtex, and Boston Scientific. Catherine Ansquer is supported by Advanced Accelerator Applications, Novartis, Ipsen, and Eisai. Elske Quak is supported by Advanced Accelerator Applications. No other potential conflict of interest relevant to this article was reported.

ACKNOWLEDGMENTS

Ray Cooke is thanked for copyediting the manuscript. Renan Le Port is thanked for drawing the cartoon for the graphical abstract.

KEY POINTS

QUESTION: What are recent trends in the sex distribution of first and last authorship for articles published in nuclear medicine journals?

PERTINENT FINDINGS: Although scientific production in nuclear medicine is no exception to sex inequity, our bibliometric study showed a substantial increase in female first and last authorship for articles published in nuclear medicine journals. We observed a wider sex gap for last than for first authorship. Although the sex gap in the authorship of original articles and case reports has narrowed over time, particularly in Europe, parity is still a few decades away.

IMPLICATIONS FOR PATIENT CARE: Diversity, equity, and inclusion can drive innovation and improve the quality of care for our diverse patient population.

REFERENCES

1. Richter KP, Clark L, Wick JA, et al. Women physicians and promotion in academic medicine. *N Engl J Med*. 2020;383:2148–2157.
2. Thibault GE. Women in academic medicine. *Acad Med*. 2016;91:1045–1046.
3. Frank E, Zhao Z, Sen S, Guille C. Gender disparities in work and parental status among early career physicians. *JAMA New Open*. 2019;2:e198340.
4. Bendels MHK, Müller R, Brueggemann D, Gronenberg DA. Gender disparities in high-quality research revealed by Nature Index journals. Lozano S, ed. *PLoS ONE*. 2018;13:e0189136.
5. Weigel KS, Kubik-Huch RA, Gebhard C. Women in radiology: why is the pipeline still leaking and how can we plug it? *Acta Radiol*. 2020;61:743–748.
6. Vernuccio F, Arzanauskaitė M, Turk S, et al. Gender discrepancy in research activities during radiology residency. *Insights Imaging*. 2019;10:125.
7. Kapoor N, Blumenthal DM, Smith SE, Ip IK, Khorasani R. Gender differences in academic rank of radiologists in U.S. medical schools. *Radiology*. 2017;283:140–147.
8. Jalilianhasanpour R, Charkhchi P, Mirbolouk M, Yousem DM. Underrepresentation of women on radiology editorial boards. *J Am Coll Radiol*. 2019;16:115–120.
9. Chapman CH, Hwang W-T, Both S, Thomas CR, Deville C. Current status of diversity by race, Hispanic ethnicity, and sex in diagnostic radiology. *Radiology*. 2014;270:232–240.
10. Huang M, Naser-Tavakolian K, Clifton M, et al. Gender differences in article citations by authors from American institutions in major radiology journals. *Cureus*. 2019;11:e5313.
11. Moghimi S, Khurshid K, Jalal S, et al. Gender differences in leadership positions among academic nuclear medicine specialists in Canada and the United States. *AJR*. 2019;212:146–150.
12. Als C, Andiel AG. Comments on profession and gender statistics of the EANM membership database 2007. *Eur J Nucl Med Mol Imaging*. 2008;35:1026–1029.
13. Santamaría L, Mihaljević H. Comparison and benchmark of name-to-gender inference services. *PeerJ Comput Sci*. 2018;4:e156.

14. Piper CL, Scheel JR, Lee CI, Forman HP. Gender trends in radiology authorship: a 35-year analysis. *AJR*. 2016;206:3–7.
15. Larivière V, Ni C, Gingras Y, Cronin B, Sugimoto CR. Bibliometrics: global gender disparities in science. *Nature*. 2013;504:211–213.
16. Ekmekcioglu O, Evangelista L, Kunikowska J. Women in nuclear medicine. *Eur J Nucl Med Mol Imaging*. 2021;48:2678–2679.
17. Gelardi F, Gozzi N. Women on board: mind the (gender) gap. *Eur J Nucl Med Mol Imaging*. 2021;48:3029–3032.
18. Evangelista L, Ekmekcioglu O, Kunikowska J. Gender balance in the editorial board of nuclear medicine journals. *Eur J Nucl Med Mol Imaging*. 2021;48:3749–3750.
19. Athena Swan Charter. Advance HE website. <https://www.advance-he.ac.uk/equality-charters/athena-swain-charter>. Accessed February 3, 2022.
20. Gender equality in research and innovation. European Commission website https://ec.europa.eu/info/research-and-innovation/strategy/strategy-2020-2024/democracy-and-rights/gender-equality-research-and-innovation_en. Accessed February 3, 2022.
21. EANM Women’s EmpoWERment. European Association of Nuclear Medicine website. https://www.eanm.org/about/organs/womens_empowerment/. Accessed February 3, 2022.
22. WINM: women in nuclear medicine. Society of Nuclear Medicine and Molecular Imaging website. <https://www.snmmi.org/WINM>. Accessed February 3, 2022.
23. Thomas EG, Jayabalasingham B, Collins T, Geertzen J, Bui C, Dominici F. Gender disparities in invited commentary authorship in 2459 medical journals. *JAMA Netw Open*. 2019;2:e1913682.
24. Banerjee S, Dafni U, Allen T, et al. Gender-related challenges facing oncologists: the results of the ESMO Women for Oncology Committee survey. *ESMO Open*. 2018;3:e000422.
25. Quak E, Girault G, Thenint MA, Weyts K, Lequesne J, Lasnon C. Author gender inequality in medical imaging journals and the COVID-19 pandemic. *Radiology*. 2021;300:E301–E307.

Errata

In the article “¹⁸F-FDG PET Imaging in Neurodegenerative Dementing Disorders: Insights into Subtype Classification, Emerging Disease Categories, and Mixed Dementia with Copathologies,” by Minoshima et al. (*J Nucl Med*. 2022; 63:2S–12S), Figures 4 and 5 were switched. *Figure 4 should be Figure 5 and Figure 5 should be Figure 4; the legends are correct.* We regret the error.

In the article “Amyloid PET in Dementia Syndromes: A Chinese Multicenter Study,” by Shi et al. (*J Nucl Med*. 2020;61:1814–1819), the author line neglected to mention that *Zhihong Shi, Li-ping Fu, Nan Zhang, and Xiaobin Zhao also contributed equally to this work.* The authors regret the error.

In the article “Production and Supply of α -Particle -Emitting Radionuclides for Targeted α -Therapy,” by Radchenko et al. (*J Nucl Med*. 2021;62: 1495–1503), affiliation 10 is incorrect. Bayer American Samoa should be *Bayer AS*. We regret the error.

In the article “¹⁷⁷Lu-Prostate-Specific Membrane Antigen Ligand After ²²³Ra Treatment in Men with Bone-Metastatic Castration-Resistant Prostate Cancer: Real-World Clinical Experience,” by Sartor et al. (*J Nucl Med*. 2022;63:410–414), affiliation 9 is incorrect. The correct affiliation should be *Nuclear Medicine and Radiometabolic Unit, IRCCS Istituto Romagnolo per lo Studio dei Tumori (IRST) “Dino Amadori”, 47014 Meldola, Italy.* The authors regret the error.

¹⁸F-FDG PET Improves Baseline Clinical Predictors of Response in Diffuse Large B-Cell Lymphoma: The HOVON-84 Study

Coreline N. Burggraaff¹, Jakoba J. Eertink¹, Pieterella J. Lugtenburg², Otto S. Hoekstra³, Anne I.J. Arens⁴, Bart de Keizer⁵, Martijn W. Heymans⁶, Bronno van der Holt⁷, Sanne E. Wiegers¹, Simone Pieplenbosch¹, Ronald Boellaard³, Henrica C.W. de Vet⁶, and Josée M. Zijlstra¹ on behalf of the HOVON Imaging Working Group and the HOVON Lymphoma Working Group

¹Department of Hematology, Amsterdam UMC, Cancer Center Amsterdam, Vrije Universiteit Amsterdam, Amsterdam, The Netherlands; ²Department of Hematology, Erasmus MC Cancer Institute, University Medical Center Rotterdam, Rotterdam, The Netherlands; ³Department of Radiology and Nuclear Medicine, Amsterdam UMC, Cancer Center Amsterdam, Vrije Universiteit Amsterdam, Amsterdam, The Netherlands; ⁴Department of Radiology, Nuclear Medicine, and Anatomy, Radboud University Medical Center, Nijmegen, The Netherlands; ⁵Department of Radiology and Nuclear Medicine, University Medical Center Utrecht, Utrecht, The Netherlands; ⁶Department of Epidemiology and Data Science, Amsterdam UMC, Amsterdam Public Health Research Institute, Vrije Universiteit Amsterdam, Amsterdam, The Netherlands; and ⁷Department of Hematology, HOVON Data Center, Erasmus MC Cancer Institute, Rotterdam, The Netherlands

We aimed to determine the added value of baseline metabolic tumor volume (MTV) and interim PET (I-PET) to the age-adjusted international prognostic index (aIPI) to predict 2-y progression-free survival (PFS) in diffuse large B-cell lymphoma. Secondary objectives were to investigate optimal I-PET response criteria (using Deauville score [DS] or quantitative change in SUV_{max} [Δ SUV_{max}] between baseline and I-PET4 [observational I-PET scans after 4 cycles of rituximab, cyclophosphamide, doxorubicin, vincristine, and prednisone administered in 2-wk intervals with intensified rituximab in the first 4 cycles [R(R)-CHOP14]). **Methods:** I-PET4 scans in the HOVON-84 (Hemato-Oncologie voor Volwassenen Nederland [Haemato Oncology Foundation for Adults in the Netherlands]) randomized clinical trial (EudraCT 2006-005174-42) were centrally reviewed using DS (cutoff, 4–5). Additionally, Δ SUV_{max} (prespecified cutoff, 70%) and baseline MTV were measured. Multivariable hazard ratio (HR), positive predictive value (PPV), and negative predictive value (NPV) were obtained for 2-y PFS. **Results:** In total, 513 I-PET4 scans were reviewed according to DS, and Δ SUV_{max} and baseline MTV were available for 367 and 296 patients. The NPV of I-PET ranged between 82% and 86% for all PET response criteria. Univariate HR and PPV were better for Δ SUV_{max} (4.8% and 53%, respectively) than for DS (3.1% and 38%, respectively). aIPI and Δ SUV_{max} independently predicted 2-y PFS (HR, 3.2 and 5.0, respectively); adding MTV brought about a slight improvement. Low or low-intermediate aIPI combined with a Δ SUV_{max} of more than 70% (37% of patients) yielded an NPV of 93%, and the combination of high-intermediate or high aIPI and a Δ SUV_{max} of 70% or less yielded a PPV of 65%. **Conclusion:** In this study on diffuse large B-cell lymphoma, I-PET after 4 cycles of R(R)-CHOP14 added predictive value to aIPI for 2-y PFS, and both were independent response biomarkers in a multivariable Cox model. We externally validated that Δ SUV_{max} outperformed DS in 2-y PFS prediction.

Key Words: DLBCL; PET; Deauville score; Δ SUV_{max}; metabolic tumor volume

J Nucl Med 2022; 63:1001–1007

DOI: 10.2967/jnumed.121.262205

Diffuse large B-cell lymphoma (DLBCL) is the most common subtype of non-Hodgkin lymphoma, characterized by an aggressive clinical course. Standard first-line treatment consists of rituximab, cyclophosphamide, doxorubicin, vincristine, and prednisone (R-CHOP) generally administered at 2-wk (R-CHOP14) or 3-wk (R-CHOP21) intervals.

No significant benefits were shown for R-CHOP14 versus R-CHOP21 in 2 large randomized clinical trials (1,2). Approximately 25%–40% of DLBCL patients experience relapse or progression in the first years after diagnosis. This problem underlines the need for early stratification between good and poor responders (3,4). An early switch to second-line treatment in poor responders might improve patient outcomes.

The international prognostic index (IPI) and age-adjusted IPI (aIPI), both consisting of baseline clinical characteristics, have retained prognostic value after the introduction of rituximab (5). However, these prognostic indices are not widely used for individual treatment adaptation except for research purposes (6), do not inform about chemosensitivity, and are unable to identify a subgroup with survival clearly below 50%. Therefore, a powerful biomarker (e.g., imaging characteristics during treatment reflecting chemosensitivity) of early response is needed. Recently, measurement of baseline metabolic tumor volume (MTV) was reported to have prognostic value in DLBCL and was suggested as an alternative to IPI (7,8). Combining MTV with early response assessment at ¹⁸F-FDG interim PET (I-PET) further improved prediction of progression-free survival (PFS) (7,8). Several operationalizations of I-PET response criteria have been proposed, such as the visual 5-point Deauville score (DS, with various possible cutoffs) (9) and quantitative changes in ¹⁸F-FDG uptake between baseline and I-PET (10,11).

Received Feb. 27, 2021; revision accepted Sep. 29, 2021.

For correspondence or reprints, contact Josée M. Zijlstra (j.zijlstra@amsterdamumc.nl).

Published online Oct. 21, 2021.

COPYRIGHT © 2022 by the Society of Nuclear Medicine and Molecular Imaging.

In the HOVON-84 study (Hemato-Oncologie voor Volwassenen Nederland [Haemato Oncology Foundation for Adults in the Netherlands]), DLBCL patients were randomized between R-CHOP14 and RR-CHOP14 (R-CHOP14 with intensified rituximab in the first 4 cycles) (12). In both arms, observational I-PET was performed after 4 cycles (I-PET4). To our knowledge, this was the first DLBCL randomized clinical trial in which I-PET4 results did not lead to treatment modification, which enables examination of its predictive value.

Our primary objective was to use prespecified cutoffs and methodologies from previous DLBCL studies to validate the potential added predictive value of baseline MTV and I-PET4 response to baseline clinical characteristics (aaIPI) for 2-y PFS in DLBCL in an independent study. A secondary objective was to determine the optimal I-PET4 response criteria.

MATERIALS AND METHODS

Study Population

Newly diagnosed DLBCL patients included in the HOVON-84 NHL study (EudraCT2006-005174-42, NTR1014) with I-PET4 were eligible. For this analysis, we combined the R-CHOP14 and RR-CHOP14 study arms, as there were no statistically significant outcome differences between the arms (12). Randomization was stratified for aaIPI score. The main eligibility criteria of the clinical study are described elsewhere (12,13). The HOVON-84 study was approved by the institutional review board of all centers, and participants signed an informed consent form.

Study Design

Patients at least 66 y old received 6 cycles of R-CHOP14 followed by 2 additional doses of rituximab; patients aged 65 y or less received 8 cycles of R-CHOP14. Baseline PET was highly recommended but not mandatory. I-PET was performed after 4 cycles of R-CHOP14 or RR-CHOP14 (without treatment modifications, I-PET4).

Qualitative and Quantitative Image Analysis

Baseline PET scans were analyzed with the semiautomatic ACCURATE tool (Fig. 1) (14) to obtain MTV using a fixed SUV of at least 4.0 (15,16). Continuous MTV values had a nonnormal distribution and were log-transformed using the natural logarithm. We used both the continuous and the dichotomized MTV with a prespecified cutoff adopted from the PETAL study to identify a high-MTV group ($>345 \text{ cm}^3$) and a low-MTV group ($\text{MTV} \leq 345 \text{ cm}^3$) (8).

I-PET4 scans were centrally reviewed by 2 independent reviewers from a pool of 10 reviewers (13) according to DS criteria (9,17). Discrepancies were resolved by adjudication. DS4–5 was categorized as no complete metabolic response (PET-positive), and DS1–3 was categorized as complete metabolic response (PET-negative) (9,17). DS4 was assigned when tumor SUV_{max} exceeded hepatic SUV_{max} by fewer than 3 times, and DS5 was assigned when there were new lymphoma lesions or when tumor SUV_{max} was 3 or more times hepatic SUV_{max} (9). The accuracy of other DS cutoffs (i.e., 1 vs. 2–5, 1–2 vs. 3–5, and 1–4 vs. 5) for I-PET4 were evaluated in sensitivity analyses.

In patients with a baseline PET scan and an I-PET4 scan with DS2–5, we measured the change in SUV_{max} between baseline and I-PET4 ($\Delta\text{SUV}_{\text{max}}$). For DS1, $\Delta\text{SUV}_{\text{max}}$ was set at 100% reduction (9). We applied a prespecified $\Delta\text{SUV}_{\text{max}}$ cutoff of 70% reduction between baseline and I-PET4 to define a positive ($\leq 70\%$) or negative ($>70\%$) I-PET result (10).

Statistical Analysis

The primary outcome measure was 2-y PFS, defined as time from randomization to disease progression, relapse, or death from any cause within 2 y (18). Survival curves were obtained with Kaplan–Meier analyses for PFS stratified by dichotomized PET response criteria and compared with log-rank tests. We used univariate and multivariable Cox proportional hazards regression models to assess the effects of baseline clinical factors (aaIPI, age, B symptoms, MTV, sex, treatment arm) and I-PET4 response criteria (DS, $\Delta\text{SUV}_{\text{max}}$) on 2-y PFS. A backward Wald elimination procedure was used to test which prognostic factors were independently associated with 2-y PFS. In addition, 2×2 contingency tables were constructed to calculate diagnostic measures (i.e., sensitivity, specificity, positive predictive value [PPV], and negative predictive value [NPV]) to predict 2-y PFS. Sensitivity, specificity, predictive values, univariate hazard ratio (HR), and receiver-operating-characteristic curve were used to define the optimal I-PET4 response criteria to predict 2-y PFS. We examined whether the addition of baseline MTV to the multivariable Cox model improved prediction. Statistical analyses were performed using SPSS Statistics (version 22; IBM) and R (version 3.6.3). A *P* value of less than 0.05 was considered statistically significant.

RESULTS

Study Population

In total, 574 eligible DLBCL patients were included in the HOVON-84 study; 534 (93%) underwent I-PET4. Twenty-one I-PET4 scans were not evaluable (Fig. 1). The distribution of baseline characteristics and 2-y PFS were similar for patients with and without baseline MTV, I-PET4, and $\Delta\text{SUV}_{\text{max}}$ evaluations (Table 1).

Prognostic Value of Baseline aaIPI and MTV

After a median follow-up of 91 mo (interquartile range, 84–101 mo), the estimated 2-y PFS was 79% (95% CI, 76%–83%). Most patients belonged to the low-intermediate or high-intermediate aaIPI groups (35% and 50%, respectively; Table 1). In the Kaplan–Meier analysis, both low and low-intermediate aaIPI survival curves and high-intermediate and high aaIPI survival curves crossed each other without statistically significant differences (Supplemental Fig. 1A; supplemental materials are available at <http://jnm.snmjournals.org>). Dichotomization into low

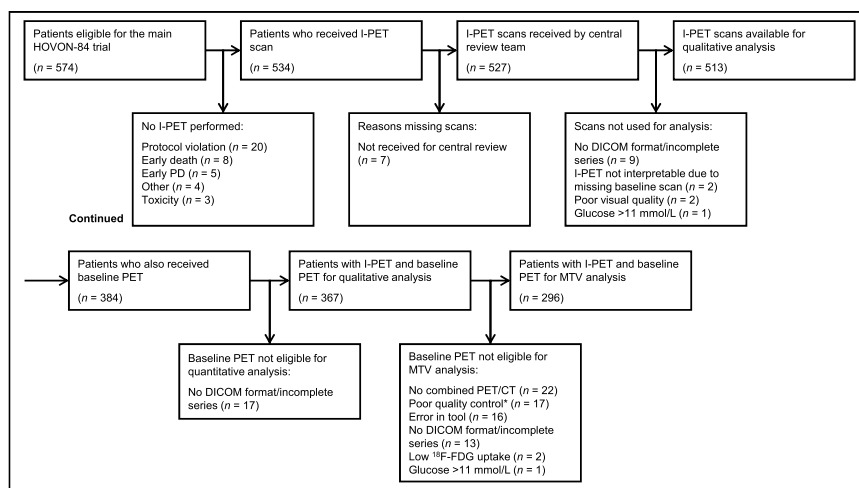


FIGURE 1. Flowchart of PET scans available for I-PET4, $\Delta\text{SUV}_{\text{max}}$, and baseline MTV analyses. *PET quality was acceptable when liver SUV_{mean} was 1.3–3.0 and total image activity was between 50%–80% of total injected dose. PD = progressive disease.

TABLE 1
Baseline Patient Characteristics

Characteristic	I-PET4	Δ SUV _{max}	MTV
Number of patients	513 (100)	367 (100)	296 (100)
Age at diagnosis (y)			
Median	65 (range, 23–80)	65 (range, 23–80)	65 (range, 23–80)
≤60	172 (33.5)	123 (33.5)	96 (32.4)
>60	341 (66.5)	244 (66.5)	200 (67.6)
Sex			
Male	267 (52.0)	192 (52.3)	150 (50.7)
Female	246 (48.0)	175 (47.7)	146 (49.3)
WHO performance status			
0	266 (51.9)	201 (54.8)	165 (55.7)
1	183 (35.7)	118 (32.2)	92 (31.1)
2	61 (11.9)	46 (12.5)	37 (12.5)
Unknown	3 (0.6)	2 (0.5)	2 (0.7)
Ann Arbor stage			
II	97 (18.9)	61 (16.6)	52 (17.6)
III	163 (31.8)	113 (30.8)	90 (30.4)
IV	253 (49.3)	193 (52.6)	154 (52.0)
LDH			
Normal	171 (33.3)	124 (33.8)	98 (33.1)
>Normal	342 (66.7)	243 (66.2)	198 (66.9)
aaIPI			
Low	36 (7.0)	23 (6.3)	21 (7.1)
Low-intermediate	177 (34.5)	127 (34.6)	97 (32.8)
High-intermediate	255 (49.7)	181 (49.3)	150 (50.7)
High	45 (8.8)	36 (9.8)	28 (9.5)
B symptoms			
No	297 (57.9)	211 (57.5)	169 (57.1)
Yes	216 (42.1)	156 (42.5)	127 (42.9)
Treatment arm			
R-CHOP14	252 (49.1)	186 (50.7)	150 (50.7)
RR-CHOP14	261 (50.9)	181 (49.3)	146 (49.3)
Diagnosis–treatment interval (d)			
Median	20 (IQR, 13–28)	20 (IQR, 13–28)	20 (IQR, 14–28)
Range	1–112	1–81	1–81
Baseline PET	384 (74.9)	367 (100)	296 (100)

IQR = interquartile range; LDH = lactate dehydrogenase; WHO = World Health Organization.
Data are number followed by percentage in parentheses, unless indicated otherwise.

or low-intermediate and high-intermediate or high yielded a 2-y PFS of 91% (95% CI, 87%–95%) and 71% (95% CI, 66%–76%), respectively, with a corresponding univariate HR of 3.6 (95% CI, 2.2–5.9; Supplemental Fig. 1B; Table 2).

Of 384 patients who underwent baseline PET, baseline MTV was measurable in 296 (52%; Fig. 1). The continuous log-transformed MTV had a univariate HR of 1.4 (95% CI, 1.2–1.8; Supplemental Table 1). Patients in the low-MTV group (MTV ≤ 345 cm³, *n* = 137; 46%) had a 2-y PFS of 86% (95% CI, 80%–92%) versus 75% (95% CI, 68%–81%) in the high-MTV group (MTV

> 345 cm³, *n* = 159; 54%), with a corresponding univariate HR of 2.0 (95% CI, 1.1–3.4; Table 2). I-PET and end-of-treatment PET scans were both available for 474 patients (Supplemental Table 2), with an overall agreement of 87% (95% CI, 84%–90%).

I-PET4 Analyses

Of 513 I-PET4 scans, 113 (22%) were rated as PET-positive (no complete metabolic response). Dichotomization of I-PET4 results into DS4–5 (positive) versus DS1–3 (negative) yielded a 2-y PFS of 61% (95% CI, 52%–70%) for I-PET4-positive patients and 84% (95% CI,

TABLE 2

Diagnostic and Prognostic Measures for aaPI, Baseline MTV, Different Cutoffs of Deauville 5-Point Scale at I-PET4, and Δ SUV_{max} for 2-Year PFS

Measure	Parameter	Patients (n)	Diagnostic information			Prognostic information			
			NPV	PPV	Sensitivity	Specificity	Univariate HR	P	Discrimination (AUC)
aaPI	L/LI vs. HI/H	213 vs. 300	91.1 (86.5–94.2)	28.7 (23.9–34.0)	81.9 (73.5–88.1)	47.6 (42.8–52.4)	3.59 (2.18–5.90)	<0.0001	0.63 (0.58–0.68)
Baseline MTV	≤345 vs. >345 cm ³	137 vs. 159	86.1 (79.4–90.9)	25.2 (19.2–32.4)	67.8 (55.1–78.3)	49.8 (43.5–56.1)	1.96 (1.13–3.38)	0.0161	0.58 (0.52–0.65)
I-PET4	DS1 vs. DS2–5	178 vs. 335	82.0 (75.7–87.0)	21.8 (17.7–26.5)	69.5 (60.2–77.5)	35.8 (31.3–40.5)	1.26 (0.83–1.91)	0.275	0.53 (0.48–0.57)
	DS1–2 vs. DS3–5	290 vs. 223	84.5 (79.9–88.2)	26.9 (21.5–33.1)	57.1 (47.6–66.2)	60.1 (55.2–64.7)	1.95 (1.32–2.87)	<0.0001	0.59 (0.54–0.64)
	DS1–3 vs. DS4–5	400 vs. 113	84.5 (80.6–87.7)	38.1 (29.6–47.3)	41.0 (32.0–50.5)	82.8 (78.9–86.2)	3.07 (2.08–4.54)	<0.0001	0.62 (0.58–0.66)
	DS1–4 vs. DS5	488 vs. 25	82.0 (78.3–85.1)	68.0 (48.4–82.8)	16.2 (10.4–22.4)	98.0 (96.2–99.0)	7.40 (4.39–12.48)	<0.0001	0.57 (0.56–0.59)
Δ SUV _{max}	>70% vs. ≤70%	329 vs. 38	82.7 (78.2–86.4)	52.6 (37.3–67.5)	26.0 (17.5–36.7)	93.8 (90.4–96.0)	4.80 (2.88–8.00)	<0.0001	0.60 (0.57–0.63)

AUC = area under receiver operating curve; L = low-risk group; LI = low- to intermediate-risk group; HI = high- to intermediate-risk group; H = high-risk group. Diagnostic information is percentage; data in parentheses are 95% CIs.

81%–88%) for I-PET4-negative patients ($P < 0.001$), with a corresponding univariate HR of 3.1 (95% CI, 2.1–4.5; Table 2; Fig. 2A). Among the patients who experienced a relapse, the median time to relapse for I-PET4-positives was 8.1 mo (interquartile range, 4.4–23.2), versus 18.1 mo (interquartile range, 8.3–46.3) for I-PET4-negatives. The corresponding PPV and NPV for 2-y PFS were 38% (95% CI, 30%–47%) and 85% (95% CI, 81%–88%), respectively.

Optimal I-PET4 Response Criterion

For various DS cutoffs, NPVs ranged between 82% and 85% for I-PET4 (Table 2). PPVs varied widely for different cutoffs (22%–68%); the highest PPV was seen for the DS5 cutoff in I-PET4 (68%). Also, the univariate HR of 7.4 was highest for the DS1–4 cutoff versus DS5, yielding the best separation between good and poor outcome (Supplemental Fig. 2). However, only 25 of 513 patients (5%) had a DS5.

Δ SUV_{max} analysis was feasible in 367 of 574 patients (64%; Fig. 1). In patients with no more than a 70% Δ SUV_{max} reduction between baseline and I-PET4 ($n = 38$, 10%), the 2-y PFS was 47% (95% CI, 31%–63%), versus 83% (95% CI, 78%–87%) for patients with more than a 70% reduction (Fig. 2B, $P < 0.001$), with a univariate HR of 4.8 (95% CI, 2.9–8.0). Corresponding PPVs and NPVs for 2-y PFS were 53% (95% CI, 37%–68%) and 83% (95% CI, 78%–86%), respectively (Table 2). Repeating these comparisons in the 296 patients with complete metrics on baseline MTV yielded similar results (Supplemental Table 3).

PPV and HRs were better for Δ SUV_{max} than for the most commonly used cutoff, DS4–5 (53% vs. 38% and 4.8 vs. 3.1, respectively). NPV was above 80% for all applied criteria. When Δ SUV_{max} was compared with the most commonly used DS cutoff, DS4–5, Δ SUV_{max} was preferred for prediction of 2-y PFS, but the highest PPV and HR were found for the DS5 cutoff.

Combined Baseline and I-PET4 Analysis

Statistically significant prognostic factors for 2-y PFS in univariate Cox regression analyses were a Δ SUV_{max} of 70% or less, a high-intermediate or high aaPI, and B symptoms. In multivariable analysis, a high-intermediate or high aaPI and no more than a 70% reduction in Δ SUV_{max} were independently associated with 2-y PFS (Supplemental Table 4). A low or low-intermediate aaPI and a Δ SUV_{max} of more than 70% (37% of patients) resulted in an NPV of 93% (95% CI, 87%–96%), whereas a high-intermediate or high aaPI and a Δ SUV_{max} of 70% or less (6% of patients) resulted in a PPV of 65% (95% CI, 45%–81%; Supplemental Fig. 3).

Dichotomized baseline MTV did not add prognostic value to Δ SUV_{max} and aaPI for prediction of 2-y PFS. When continuous log-transformed MTV was added to the multivariable Cox model, aaPI was eliminated by backward elimination, yielding log-transformed MTV, an age of more than 60 y, B symptoms, and Δ SUV_{max} as factors independently associated with 2-y PFS (Supplemental Table 1).

Overall Survival Analyses

The results of the response criteria and uni- and multivariable analyses for 2-y overall survival are presented in Supplemental Tables 5–7 and Supplemental Figure 4.

DISCUSSION

In this multicenter study, DLBCL I-PET after 4 cycles of R(R)-CHOP14 added predictive value to baseline clinical characteristics (aaPI) for 2-y PFS, with high NPVs (82%–86%) independent of all

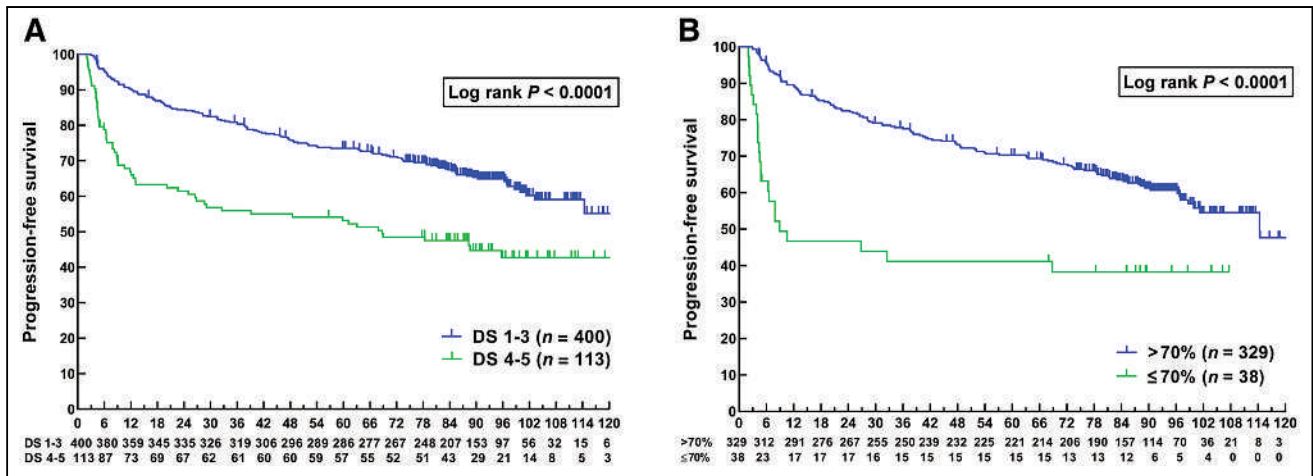


FIGURE 2. Kaplan–Meier curves with numbers at risk for PFS in months stratified by I-PET4 result according to DS (A) and according to $\Delta\text{SUV}_{\text{max}}$ result (B).

I-PET response criteria. However, the PPV was still relatively low. Combining clinical and PET data showed that aaIPI and $\Delta\text{SUV}_{\text{max}}$ were independently associated with 2-y PFS, with HRs of 3.2 and 5.0, respectively. Adding log-transformed baseline MTV only slightly improved the predictive value combined with the $\Delta\text{SUV}_{\text{max}}$ response criteria. As a secondary objective, we compared the most commonly used visual and semiquantitative criteria and externally validated that $\Delta\text{SUV}_{\text{max}}$ criteria were the optimal I-PET4 criteria to predict 2-y PFS, with a HR of 4.8 and a PPV of 53%.

On the basis of the PPV and univariate HR in I-PET, the DS5 cutoff performed best, with a PFS clearly below 50% for the DS5 group. However, the percentage of DS5-positive patients was low (5%), but this group could be of interest for future new therapy strategies. The univariate HR for 2-y PFS with a DS4–5 cutoff in I-PET4 was 3.1 (95% CI, 2.1–4.5), which is similar to the pooled HR of 3.1 (95% CI, 2.5–3.9) in a systematic review, even though in that review I-PET was performed after 1–4 cycles of treatment and less strict I-PET response criteria were applied (19). The NPV for 2-y PFS in our study was 85%, which is in line with these previous studies generally reporting NPVs above 80% (range, 64%–95%) (19).

Two recent retrospective DLBCL studies analyzed the value of I-PET after 4 cycles (20,21), and both concluded that $\Delta\text{SUV}_{\text{max}}$ had a higher accuracy and PPV than DS in predicting PFS. The retrospective study from Itti et al. ($n = 114$, I-PET after 2 cycles), who analyzed different cutoffs for DS after 2 cycles, reported PPVs for DS4–5 and $\Delta\text{SUV}_{\text{max}}$ that were remarkably identical to our study (39% vs. 38% and 52% vs. 53%, respectively) (22). A DLBCL subgroup analysis of the PETAL study also reported a more favorable PPV for $\Delta\text{SUV}_{\text{max}}$ I-PET assessment than for Deauville assessment (23).

Baseline clinical characteristics and chemoimmunotherapy sensitivity are both relevant factors in outcome prediction. This relevancy was demonstrated in our multivariable analysis, in which aaIPI and $\Delta\text{SUV}_{\text{max}}$ (reflecting chemosensitivity) were both independent predictors of 2-y PFS. Again, the subgroup with both high-intermediate or high aaIPI and a $\Delta\text{SUV}_{\text{max}}$ of 70% or less had a PFS clearly below 50% but was relatively small (6% of all patients). Selection of a poor-risk group of only 6% is justified both from a cost awareness perspective and because it is the group most likely not be cured by standard treatment. These patients can be treated within clinical trials investigating the efficacy of new drugs.

Several relatively small retrospective studies reported inconsistent results regarding associations of clinical characteristics and I-PET results (DS or $\Delta\text{SUV}_{\text{max}}$) with survival in multivariable Cox models (7,22,24). Two prospective studies concluded that only I-PET and not IPI was independently associated with event-free survival (25,26). The randomized phase III trials PETAL (I-PET after 2 cycles of R-CHOP21) and CALGB-50303 (I-PET after 2 cycles R-CHOP21 or DA-EPOCH-R [dose-adjusted etoposide, prednisone, vincristine, cyclophosphamide, doxorubicin, and rituximab]) also concluded that I-PET with $\Delta\text{SUV}_{\text{max}}$ (cutoff, 66%) and IPI were independent predictors for event-free survival and PFS (11,27), respectively.

Baseline MTV assessment was not a strong predictor of 2-y PFS in our study (Table 2; Supplemental Tables 1, 3, 5, and 7). We used a segmentation method applying a fixed SUV of at least 4.0, on the basis of a recent study showing that this method performed best and had a discriminative power similar to that of other segmentation methods (16). Addition of dichotomized baseline MTV (345-cm³ cutoff) to $\Delta\text{SUV}_{\text{max}}$ did not improve the predictive value, but log-transformed continuous MTV added some independent predictive value when combined with $\Delta\text{SUV}_{\text{max}}$. In a secondary analysis of the PETAL randomized clinical trial (DLBCL subset, I-PET after 2 cycles, same MTV software and methodology as in our study), baseline MTV and $\Delta\text{SUV}_{\text{max}}$ were the only independent outcome predictors (8,28). We could not confirm these findings; possible explanations are the different PET timing (HOVON-84: I-PET4) or patient characteristics (HOVON-84: median age 3 y higher; advanced stage, 82% vs. 58% in PETAL). We chose a higher $\Delta\text{SUV}_{\text{max}}$ because the PET timing was different (I-PET4 vs. I-PET2) and to validate a formerly presented cutoff (10,20). This choice does not explain the difference in added value of MTV, since the positivity percentages were the same (10.4% vs. 9.6% in PETAL), as was the 2-y PFS for the positive (46.9% and 46.7%) and negative (80.2% and 82.5%) groups according to the $\Delta\text{SUV}_{\text{max}}$ criteria for HOVON-84 and PETAL, respectively. Recently, Vercellino et al. showed that a combination of high baseline MTV and high performance status (≥ 2) identifies an ultra-risk DLBCL population (29). We could not confirm this extra risk in our study.

There were several strengths to our study. First, to our knowledge, there are no other large, randomized trials with a homogeneous first-line treatment regimen and observational I-PET after 4

R-CHOP14 cycles. Another strength was the central review procedure for Deauville scoring, with 2 independent reviewers and a strict DS5 definition, which allowed for an analysis to determine the optimal I-PET4 response criteria (13).

On the basis of the relatively low values for PPV, escalation of treatment for the I-PET4-positive group is not yet recommend for clinical practice, but evidence in favor of I-PET-adapted treatment is clearly growing (11,30–32). The GAINED randomized clinical trial (30) enrolled 670 DLBCL patients (aged 18–60 y, aalPI \geq 1); I-PET2-positive/I-PET4-negative patients ($n = 87$) were scheduled to receive high-dose chemotherapy with autologous stem cell transplantation and had no statistically significant difference in PFS from the I-PET2-negative/I-PET4-negative patients ($n = 401$) who continued standard treatment. However, no firm conclusions can be made, because there was no randomization within these I-PET-adapted groups.

Because the NPV is acceptable ($>80\%$ for all criteria), reduction of treatment based on I-PET4 could be of interest, especially for low-risk and elderly patients. The randomized FLYER trial showed that in a group of 592 DLBCL patients (aged 18–60 y, no aalPI risk factors, no bulky disease), 4 cycles of R-CHOP21 + 2 cycles of rituximab was not inferior to 6 cycles of R-CHOP21 (6), and in an exploratory analysis the international GOYA randomized clinical trial found no PFS benefit with 8 cycles of R-CHOP21 compared with 6 cycles of R-CHOP21 + 2 cycles of rituximab (31). The S1001 study presented 4 cycles of R-CHOP as the new standard for most patients with limited-stage disease (32).

CONCLUSION

In this large DLBCL study, I-PET after 4 cycles of R(R)-CHOP14 added predictive value to aalPI for 2-y PFS, and both were independent response biomarkers in a multivariable Cox model, yielding a high NPV of 93% for 2-y PFS. Comparing the most commonly used DS and $\Delta\text{SUV}_{\text{max}}$ cutoffs, the optimal response criterion for I-PET4 to predict 2-y PFS was $\Delta\text{SUV}_{\text{max}}$.

DISCLOSURE

This work was supported by the Alpe d'HuZes/KWF fund, provided by the Dutch Cancer Society (VU2012-5848). Pieternella Lugtenburg receives research funding from Roche, Takeda, and Servier and honoraria for advisory boards from Roche, Takeda, Servier, Genmab, Celgene, and Genentech. Josée Zijlstra receives research funding from, and is on the advisory board for, Roche. No other potential conflict of interest relevant to this article was reported.

KEY POINTS

QUESTION: What value do baseline MTV and I-PET add to aalPI in predicting 2-y PFS in DLBCL, and what are the optimal I-PET response criteria?

PERTINENT FINDINGS: aalPI and $\Delta\text{SUV}_{\text{max}}$ were independent predictors for 2-y PFS in DLBCL. Six percent of patients had a high PPV of 65% resulting in poor survival outcome. $\Delta\text{SUV}_{\text{max}}$ outperformed Deauville score in 2-y PFS prediction.

IMPLICATIONS FOR PATIENT CARE: The subgroup comprising the 6% of patients having a high or high-intermediate aalPI and a 70% or less SUV_{max} reduction at I-PET is of interest for testing new therapy strategies in DLBCL.

REFERENCES

- Cunningham D, Hawkes EA, Jack A, et al. Rituximab plus cyclophosphamide, doxorubicin, vincristine, and prednisolone in patients with newly diagnosed diffuse large B-cell non-Hodgkin lymphoma: a phase 3 comparison of dose intensification with 14-day versus 21-day cycles. *Lancet*. 2013;381:1817–1826.
- Delarue R, Tilly H, Mounier N, et al. Dose-dense rituximab-CHOP compared with standard rituximab-CHOP in elderly patients with diffuse large B-cell lymphoma (the LNH03-6B study): a randomised phase 3 trial. *Lancet Oncol*. 2013;14:525–533.
- van Imhoff GW, McMillan A, Matasar MJ, et al. Ofatumumab versus rituximab salvage chemoimmunotherapy in relapsed or refractory diffuse large B-cell lymphoma: the ORCHARRD study. *J Clin Oncol*. 2017;35:544–551.
- Gisselbrecht C, Glass B, Mounier N, et al. Salvage regimens with autologous transplantation for relapsed large B-cell lymphoma in the rituximab era. *J Clin Oncol*. 2010;28:4184–4190.
- Ziepert M, Hasenclever D, Kuhnt E, et al. Standard international prognostic index remains a valid predictor of outcome for patients with aggressive CD20+ B-cell lymphoma in the rituximab era. *J Clin Oncol*. 2010;28:2373–2380.
- Poeschel V, Held G, Ziepert M, et al. FLYER Trial Investigators; German Lymphoma Alliance. Four versus six cycles of CHOP chemotherapy in combination with six applications of rituximab in patients with aggressive B-cell lymphoma with favourable prognosis (FLYER): a randomised, phase 3, non-inferiority trial. *Lancet*. 2019;394:2271–2281.
- Mikhaeel NG, Smith D, Dunn JT, et al. Combination of baseline metabolic tumour volume and early response on PET/CT improves progression-free survival prediction in DLBCL. *Eur J Nucl Med Mol Imaging*. 2016;43:1209–1219.
- Schmitz C, Hüttmann A, Müller SP, et al. Dynamic risk assessment based on positron emission tomography scanning in diffuse large B-cell lymphoma: post-hoc analysis from the PETAL trial. *Eur J Cancer*. 2020;124:25–36.
- Barrington SF, Mikhaeel NG, Kostakoglu L, et al. Role of imaging in the staging and response assessment of lymphoma: consensus of the International Conference on Malignant Lymphomas Imaging Working Group. *J Clin Oncol*. 2014;32:3048–3058.
- Casasnovas RO, Meignan M, Berriolo-Riedinger A, et al.; Groupe d'étude des lymphomes de l'adulte (GELA). SUVmax reduction improves early prognosis value of interim positron emission tomography scans in diffuse large B-cell lymphoma. *Blood*. 2011;118:37–43.
- Dührsen U, Müller S, Hertenstein B, et al.; PETAL Trial Investigators. Positron emission tomography-guided therapy of aggressive non-Hodgkin lymphomas (PETAL): a multicenter, randomized phase III trial. *J Clin Oncol*. 2018;36:2024–2034.
- Lugtenburg PJ, de Nully Brown P, van der Holt B, et al. Rituximab-CHOP with early rituximab intensification for diffuse large B-cell lymphoma: a randomized phase 3 trial of the HOVON and the Nordic Lymphoma Group (HOVON-84). *J Clin Oncol*. 2020;38:3377–3387.
- Burggraaff CN, Cornelisse AC, Hoekstra OS, et al.; HOVON Imaging Working Group. Interobserver agreement of interim and end-of-treatment ^{18}F -FDG PET/CT in diffuse large B-cell lymphoma (DLBCL): impact on clinical practice and trials. *J Nucl Med*. 2018;59:1831–1836.
- Boellaard R. Quantitative oncology molecular analysis suite: ACCURATE [abstract]. *J Nucl Med*. 2018;59(suppl.1):1753.
- Burggraaff CN, Rahman F, Kaßner I, et al.; PETRA Consortium. Optimizing workflows for fast and reliable metabolic tumor volume measurements in diffuse large B cell lymphoma. *Mol Imaging Biol*. 2020;22:1102–1110.
- Barrington SF, Zwezerijnen BGJC, de Vet HCW, et al. Automated segmentation of baseline metabolic total tumor burden in diffuse large B-cell lymphoma: which method is most successful? A study on behalf of the PETRA consortium. *J Nucl Med*. 2021;62:332–337.
- Cheson BD, Fisher RI, Barrington SF, et al. Recommendations for initial evaluation, staging, and response assessment of Hodgkin and non-Hodgkin lymphoma: the Lugano classification. *J Clin Oncol*. 2014;32:3059–3068.
- Maurer MJ, Habermann TM, Shi Q, et al. Progression-free survival at 24 months (PFS24) and subsequent outcome for patients with diffuse large B-cell lymphoma (DLBCL) enrolled on randomized clinical trials. *Ann Oncol*. 2018;29:1822–1827.
- Burggraaff CN, de Jong A, Hoekstra OS, et al. Predictive value of interim positron emission tomography in diffuse large B-cell lymphoma: a systematic review and meta-analysis. *Eur J Nucl Med Mol Imaging*. 2019;46:65–79.
- Toledano MN, Vera P, Tilly H, Jardin F, Becker S. Comparison of therapeutic evaluation criteria in FDG-PET/CT in patients with diffuse large-cell B-cell lymphoma: prognostic impact of tumor/liver ratio. *PLoS One*. 2019;14:e0211649.
- Li X, Sun X, Li J, et al. Interim PET/CT based on visual and semiquantitative analysis predicts survival in patients with diffuse large B-cell lymphoma. *Cancer Med*. 2019;8:5012–5022.

22. Itti E, Meignan M, Berriolo-Riedinger A, et al. An international confirmatory study of the prognostic value of early PET/CT in diffuse large B-cell lymphoma: comparison between Deauville criteria and $\Delta\text{SUV}_{\text{max}}$. *Eur J Nucl Med Mol Imaging*. 2013;40:1312–1320.
23. Rekowski J, Hüttmann A, Schmitz C, et al. Interim PET evaluation in diffuse large B-cell lymphoma employing published recommendations: comparison of the Deauville 5-point scale and the $\Delta\text{SUV}_{\text{max}}$ method. *J Nucl Med*. 2021;62:37–42.
24. Nols N, Mounier N, Bouazza S, et al. Quantitative and qualitative analysis of metabolic response at interim positron emission tomography scan combined with international prognostic index is highly predictive of outcome in diffuse large B-cell lymphoma. *Leuk Lymphoma*. 2014;55:773–780.
25. Carr R, Fanti S, Paez D, et al.; IAEA Lymphoma Study Group. Prospective international cohort study demonstrates inability of interim PET to predict treatment failure in diffuse large B-cell lymphoma. *J Nucl Med*. 2014;55:1936–1944.
26. Mamot C, Klingbiel D, Hitz F, et al. Final results of a prospective evaluation of the predictive value of interim positron emission tomography in patients with diffuse large B-cell lymphoma treated with R-CHOP-14 (SAKK 38/07). *J Clin Oncol*. 2015;33:2523–2529.
27. Schöder H, Polley MY, Knopp MV, et al. Prognostic value of interim FDG-PET in diffuse large cell lymphoma: results from the CALGB 50303 clinical trial. *Blood*. 2020;135:2224–2234.
28. Schmitz C, Hüttmann A, Müller SP, et al. Supporting data for positron emission tomography-based risk modelling using a fixed-instead of a relative thresholding method for total metabolic tumor volume determination. *Data Brief*. 2019;28:104976.
29. Vercellino L, Cottreau AS, Casasnovas O, et al. High total metabolic tumor volume at baseline predicts survival independent of response to therapy. *Blood*. 2020;135:1396–1405.
30. Le Gouill S, Ghesquières H, Oberic L, et al. Obinutuzumab vs rituximab for advanced DLBCL: a PET-guided and randomized phase 3 study by LYSA. *Blood*. 2021;137:2307–2320.
31. Sehn LH, Congiu AG, Culligan DJ, et al. No added benefit of eight versus six cycles of CHOP when combined with rituximab in previously untreated diffuse large B-cell lymphoma patients: results from the international phase III GOYA study [abstract]. *Blood*. 2018;132(suppl 1):783.
32. Persky DO, Li H, Stephens DM, et al. Positron emission tomography-directed therapy for patients with limited-stage diffuse large B-cell lymphoma: results of intergroup national clinical trials network study S1001. *J Clin Oncol*. 2020;38:3003–3011.

Molecular Signature of ^{18}F -FDG PET Biomarkers in Newly Diagnosed Multiple Myeloma Patients: A Genome-Wide Transcriptome Analysis from the CASSIOPET Study

Jean-Baptiste Alberge^{1,2}, Françoise Kraeber-Bodéré¹⁻⁵, Bastien Jamet^{2,3}, Cyrille Touzeau^{1,2,5}, Hélène Caillon⁵, Soraya Wullemme⁵, Marie-Christine Béné⁵, Tobias Kampfenkel⁶, Pieter Sonneveld⁷, Mark van Duin⁷, Herve Avet-Loiseau⁸, Jill Corre⁸, Florence Magrangeas^{1,2,5}, Thomas Carlier¹⁻³, Caroline Bodet-Milin¹⁻³, Michel Chérel^{1,2,4}, Philippe Moreau^{1,2,5}, Stéphane Minvielle^{1,2,5}, and Clément Bailly¹⁻³

¹Université de Nantes, CHU Nantes, CNRS, Inserm, CRCINA, Nantes, France; ²Site de Recherche Intégrée sur le Cancer (SIRIC), Imaging and Longitudinal Investigations to Ameliorate Decision-Making (ILIAD), INCA-DGOS-Inserm 12558, Nantes, France; ³Nuclear Medicine Unit, University Hospital, Nantes, France; ⁴Nuclear Medicine Unit, ICO-Gauducheau, Nantes-Saint-Herblain, France; ⁵Haematology Department, University Hospital, Nantes, France; ⁶Janssen Research & Development, LLC, Leiden, The Netherlands; ⁷Erasmus University Medical Center Cancer Institute, Rotterdam, The Netherlands; and ⁸Unité de Génomique du Myélome, Institut Universitaire du Cancer de Toulouse, Institut National de la Santé, Oncopole, Toulouse, France

The International Myeloma Working Group recently fully incorporated ^{18}F -FDG PET into multiple myeloma (MM) diagnosis and response evaluation. Moreover, a few studies demonstrated the prognostic value of several biomarkers extracted from this imaging at baseline. Before these ^{18}F -FDG PET biomarkers could be fully endorsed as risk classifiers by the hematologist community, further characterization of underlying molecular aspects was necessary. **Methods:** Reported prognostic biomarkers (^{18}F -FDG avidity, SUV_{max} , number of focal lesions, presence of paramedullary disease [PMD] or extramedullary disease) were extracted from ^{18}F -FDG PET imaging at baseline in a group of 139 patients from CASSIOPET, a companion study of the CASSIOPEIA cohort (ClinicalTrials.gov identifier NCT02541383). Transcriptomic analyses using RNA sequencing were realized on sorted bone marrow plasma cells from the same patients. An association with a high-risk gene expression signature (IFM15), molecular classification, progression-free survival, a stringent clinical response, and minimal residual disease negativity were explored. **Results:** ^{18}F -FDG PET results were positive in 79.4% of patients; 14% and 11% of them had PMD and extramedullary disease, respectively. Negative ^{18}F -FDG PET results were associated with lower levels of expression of hexokinase 2 (*HK2*) (fold change, 2.1; adjusted $P = 0.04$) and showed enrichment for a subgroup of patients with a low level of bone disease. Positive ^{18}F -FDG PET results displayed 2 distinct signatures: either high levels of expression of proliferation genes or high levels of expression of *GLUT5* and lymphocyte antigens. PMD and IFM15 were independently associated with a lower level of progression-free survival, and the presence of both biomarkers defined a group of “double-positive” patients at very high risk of progression. PMD and IFM15 were related neither to minimal residual disease assessment nor to a stringent clinical response. **Conclusion:** Our study confirmed and extended the association between imaging biomarkers and transcriptomic programs in MM. The combined prognostic value of PMD and a high-risk IFM15 signature may help define MM patients with a very high risk of progression.

Key Words: multiple myeloma, ^{18}F -FDG PET, CASSIOPET study, genome-wide transcriptome, RNA sequencing

J Nucl Med 2022; 63:1008–1013
DOI: 10.2967/jnumed.121.262884

In the past decade, there has been increasing use of PET with ^{18}F -FDG for the staging and therapeutic evaluation of multiple myeloma (MM) patients (1). A few studies have demonstrated the prognostic value of several biomarkers extracted from ^{18}F -FDG PET at baseline—the number of focal lesions (FLs), the presence or absence of extramedullary disease (EMD) or paramedullary disease (PMD), and glucose SUV_{max} —as reviewed by Michaud-Robert et al. (2). Furthermore, ^{18}F -FDG PET results are considered to be negative in approximately 10%–20% of MM patients (2). This pattern, associated with low levels of expression of hexokinase 2 (*HK2*)—an enzyme involved in the first step of glycolysis—is usually described as a false-negative result for disease detection but seems to carry a prognostic value (3–5). Before these ^{18}F -FDG PET biomarkers could be fully endorsed as risk classifiers by the hematologist community, further characterization of underlying molecular aspects was necessary. Genome-wide transcriptomic analyses through RNA sequencing characterized, without bias, the gene expression program of tumor cells purified from bone marrow aspirates. RNA sequencing helped researchers to understand the molecular basis of MM complexity (6,7) and to identify MM patients who have with gene signatures such as GEP70, EMC-92, or IFM15 and who are at high risk of progression (8,9).

The purpose of this study was to identify gene expression patterns associated with prognostic ^{18}F -FDG PET biomarkers in newly diagnosed MM patients included in the prospective multicenter CASSIOPET study. An association with a high-risk gene expression signature, molecular classification, progression-free survival (PFS), a clinical response, and minimal residual disease (MRD) negativity at 100 d after autologous stem cell transplant (ASCT) were also explored.

Received Jul. 9, 2021; revision accepted Oct. 14, 2021.
For correspondence or reprints, contact Clément Bailly (clement.bailly@chu-nantes.fr) or Stéphane Minvielle (stephane.minvielle@univ-nantes.fr).
Published online Jan. 27, 2022.
COPYRIGHT © 2022 by the Society of Nuclear Medicine and Molecular Imaging.

MATERIALS AND METHODS

Patients

A group of 139 newly diagnosed patients from CASSIOPET (5) (Françoise Kraeber-Bodéré et al., unpublished data, 2020), a companion study of the phase 3 CASSIOPEIA trial (10), underwent gene expression profiling at baseline in addition to ^{18}F -FDG PET imaging. The aims and inclusion and exclusion criteria of the CASSIOPEIA trial (ClinicalTrials.gov identifier NCT02541383) were previously reported (10). The CASSIOPET study was locally approved by the institutional ethics committee (University Hospital, Nantes, France). Myeloma plasma cells were derived from bone marrow samples collected at the Intergroupe Francophone du Myélome and the Dutch/Belgian Haemato-Oncology Foundation for Adults in The Netherlands. Myeloma cells were purified using nanobeads and an anti-CD138 antibody (RoboSep; Stem Cell Technologies). The average MM cell purity was greater than 99% (range, 79%–100%), as assessed by May-Grunwald Giemsa staining and morphology. Finally, all samples with available material containing greater than 200 ng of RNA and an RNA integrity number of greater than 6.5 were included and sequenced.

RNA Sequencing

Libraries were prepared with NEBNext Ultra II for a directional RNA sequencing kit (reference: E7765 L, E7490 L, E6440S; New England Biolabs). Quality controls were performed with High Sensitivity D1000 (Agilent) and an NEBNext Library Quant Kit for Illumina (reference: E7630 L) on a TapeStation 2200 (Agilent). All libraries passed quality controls and were sequenced on a NovaSeqEquation 6000 (Illumina) with S2 flow cells at 2×100 cycles (reference: 20012861). Finally, the sequencing depth ranged from 74 to 163 million paired reads per library. RNA sequencing reads were aligned to the human reference genome hg38/GRCh38.p13, and genes were quantified with STAR v2.7.3 and Ensembl v99 (both products open source data/software). Standardized \log_2 values of transcripts per million units were used to compute high-risk and molecular classification scores after the removal of immunoglobulin genes (11). The threshold for high-risk classification with IFM15 ($x = 1.3$) was defined according to Decaux et al. (9). The maximum of the weighted means was used to classify patients in the 7 subgroups of the University of Arkansas for Medical Sciences (UAMS) classification (6) and determine the GEP70 signature. DESeq2 (open source R/Bioconductor package) was used to perform differential expression analysis from raw counts with plasma cell purity and site of collection (Intergroupe Francophone du Myélome or Haemato-Oncology Foundation for Adults in The Netherlands) treated as model covariates. The DESeq2 variance stabilizing transformation was used for graphical representation and statistical analysis of gene expression levels.

^{18}F -FDG PET Evaluation

^{18}F -FDG PET images were acquired at baseline according to the local protocol at each center and the recommendations of good practice for PET imaging. Briefly, all patients fasted for at least 4 h before ^{18}F -FDG injection. The blood glucose level measured before ^{18}F -FDG administration had to be ≤ 150 mg/dL. Whole-body imaging was performed between 60 and 80 min after ^{18}F -FDG injection (3–7 MBq/kg). ^{18}F -FDG PET data were centrally collected and analyzed, with masking of patient treatment and follow-up, by an independent team of nuclear medicine physicians with extensive experience in MM. As previously described (2,12) and used in the CASSIOPET protocol, ^{18}F -FDG PET negativity, number of bone FLs (defined as the presence of areas of focally increased tracer uptake in bone, with or without any underlying lytic lesion on CT, and present on at least 2 consecutive slices), and presence of EMD (defined as tracer uptake in tissue not contiguous to bone) or PMD (defined as soft-tissue invasion with contiguous bone involvement) were reported. The bone SUV_{max} was determined; it was

defined as the highest SUV_{max} on bone analysis, including FLs, PMD, and medullary uptake (measured at the lumbar vertebrae [L3–L5] and excluding focal lesions with a 3-dimensional rectangular region of interest).

MRD Assessment and Clinical Response

As reported in the CASSIOPEIA trial, MRD was evaluated by multiparametric flow cytometry of bone marrow aspirates at 100 d after ASCT. MRD negativity was defined as less than 0.001% of aberrant clonal plasma cells (10^{-5} threshold). The clinical response was assessed according to International Myeloma Working Group criteria at 100 d after ASCT (13).

Statistical Analysis

Quantitative biologic and clinical variables were described with the median and interquartile range or with the mean and SD. The significance of the average difference between groups was assessed with the Kruskal–Wallis method and the Dunn post hoc approach for multiple-group testing or the Wilcoxon test for 2 groups. Differences in distribution between groups were assessed with a χ^2 Pearson test (or a Fisher exact test, if appropriate). Absolute χ^2 residuals of greater than 2 were considered significant, as post hoc. A DESeq2 Wald test was used to assess differences in gene expression between groups. For survival analysis, PFS was calculated from randomization date to disease progression or death, whichever occurred first, or to the last follow-up date. Hazard ratios (HRs) between groups were calculated with a Cox model. Survival curves were calculated using the Kaplan–Meier method, and groups were compared using a likelihood ratio test. *P* values were corrected for multiple-group testing with the Benjamini–Hochberg method. Adjusted *P* values of less than 0.05 were considered significant. All calculations were performed with R 3.6.0. (R Foundation).

RESULTS

Demography and ^{18}F -FDG PET Results

Of the 268 patients in the CASSIOPET study, 139 patients were considered for this analysis. Because bone marrow aspiration samples for transcriptomic analyses using RNA sequencing were not mandatory in the CASSIOPET trial at diagnosis, 129 patients were enrolled in CASSIOPET before the start of this ancillary work or did not have sufficient materials available for this analysis. The included patients had demographic and clinical characteristics (age, sex, Revised International Staging System [R-ISS] staging, high-risk cytogenetics, treatment arms) similar to those of the entire CASSIOPET population (Supplemental Table 1). Our cohort included 110 patients with positive ^{18}F -FDG PET results (79%), of whom 20 (14%) and 16 (12%) had PMD and EMD, respectively, at baseline. The median baseline SUV_{max} was 3.2 (ranging from 1.5 to 12), with 35 (32%) of the 110 ^{18}F -FDG-avid MM patients having an SUV_{max} higher than 4.2. Sixty-four (46%) of our patients had 3 or more FLs, and 27 (19%) showed diffuse medullary uptake higher than the liver background. The main characteristics of our cohort with regard to ^{18}F -FDG PET imaging and gene signatures are shown in Supplemental Figure 1.

Molecular Profile of Patients with Negative Results on PET Scans

To understand which patients were most likely to have negative or normal ^{18}F -FDG PET, we explored the levels of expression of glucose transporters (GLTs) 1–5 (GLUT1–GLUT5, respectively) and of hexokinases (HKs) 1–3 (HK1–HK3, respectively). *HK2* was expressed less in patients with normal ^{18}F -FDG PET results (fold change [FC], 2.0; *P* = 0.04) (Fig. 1A) and to a lesser extent than *GLUT5* (*SLC2A5*; FC, 4.2; *P* = 7×10^{-4}), which codes for a canonical fructose receptor (14). Conversely, *GLUT3* (*SLC2A3*)

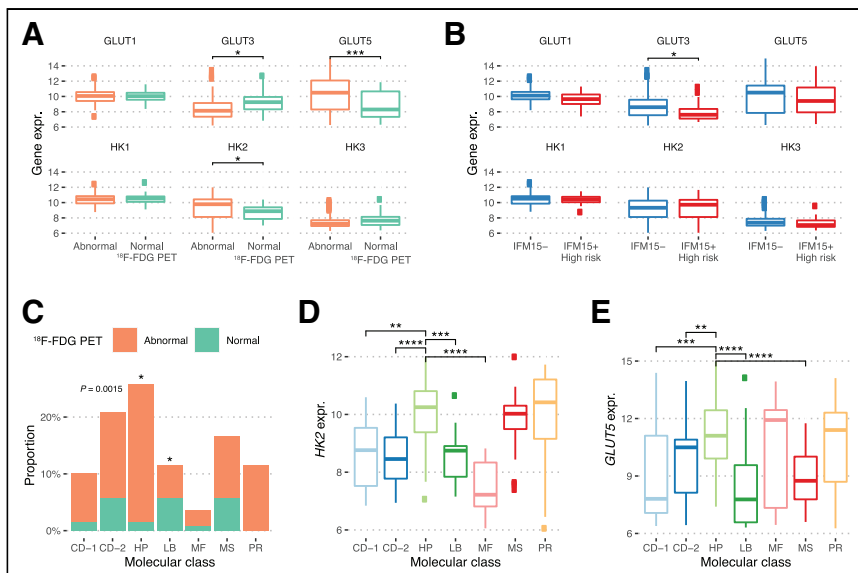


FIGURE 1. Molecular profile of ^{18}F -FDG PET negativity in CASSIOPET trial. (A) Expression (expr.) of GLUTs and HKs on ^{18}F -FDG PET scans with abnormal or positive (orange) vs. normal or negative (green) results in CASSIOPET cohort. (B) Expression of GLUTs and HKs in patients with standard-risk (blue) vs. high-risk (red) IFM15 gene expression signatures. (C) Distribution of normal ^{18}F -FDG PET results across MM molecular classes as defined by UAMS. (D and E) Expression of HK2 (D) and GLUT5 (E) in MM molecular classes. Gene expression levels are given in variance stabilizing transformation-normalized counts (see Materials and Methods). $n = 139$ patients. * $P < 0.05$. ** $P < 0.01$. *** $P < 0.001$. **** $P < 0.0001$.

was found to be overexpressed in patients with negative or normal ^{18}F -FDG PET results (FC, 2.0; $P = 0.05$) (Fig. 1A) as well as in patients assessed with the high-risk IFM15 signature (IFM15+; FC, 2.1; $P = 0.01$) (Fig. 1B). The expression of other HKs and GLUTs was comparable in both groups (IFM15+ and IFM15-) (Fig. 1B). Of note, *GLUT2* and *GLUT4* were not found to be expressed in this study (0–0.2 transcript per million, on average) and were discarded from the analysis.

The UAMS molecular classification of MM in 7 subgroups (CD-1, CD-2, HP, low level of bone disease [LB], MF, MS, proliferating [PR]) was statistically associated with normal ^{18}F -FDG PET results (Fig. 1C). In particular, an overrepresentation of negative ^{18}F -FDG PET imaging results was found in the LB group of patients compared with the reference group of HP patients. The LB group consistently showed an underexpression of *HK2* ($P = 9 \times 10^{-4}$) and *GLUT5* ($P = 1.6 \times 10^{-5}$) (Figs. 1D and 1E).

Finally, a differential analysis of gene expression performed with DESeq2 for positive or abnormal and negative or normal ^{18}F -FDG-PET results showed that 1,202 genes were deregulated. Genes that were moderately to highly expressed (≥ 500 messenger RNA [mRNA], on average) and on which the condition had an important effect (\log_2 FC, ≥ 1 , in absolute value) are shown in Figure 2. Hierarchical clustering separated 2 groups of patients with positive or normal ^{18}F -FDG PET results and distinct signatures. Ontology analysis confirmed a strong proliferation signature (*MKI-67*, *PCNA*, *TOP2A*, *STMN1*) in a proportion of patients with positive ^{18}F -FDG PET results (Fig. 2; Supplemental Table 2), whereas the other positive scans showed overexpressed lymphocyte antigens (*CD19*, *TNFSF8/CD30 L*, *TNFSF10/TRAIL*) and *SLC2A5/GLUT5*. Conversely, negative or normal ^{18}F -FDG-PET results showed a cellular machinery ontology (secretion, membrane, exocytosis) and regular expression of *SLC2A3/GLUT3*, consistent with results presented in Figure 1.

Molecular Profile Associated with ^{18}F -FDG PET Abnormalities

Among patients with positive or abnormal ^{18}F -FDG PET scan results, patients with a high-risk GEP70 signature had more frequent PMD than GEP70-negative patients ($P = 0.003$) (Supplemental Fig. 2), whereas no association was observed with the IFM15 signature (Fig. 3A). The PR subgroup of

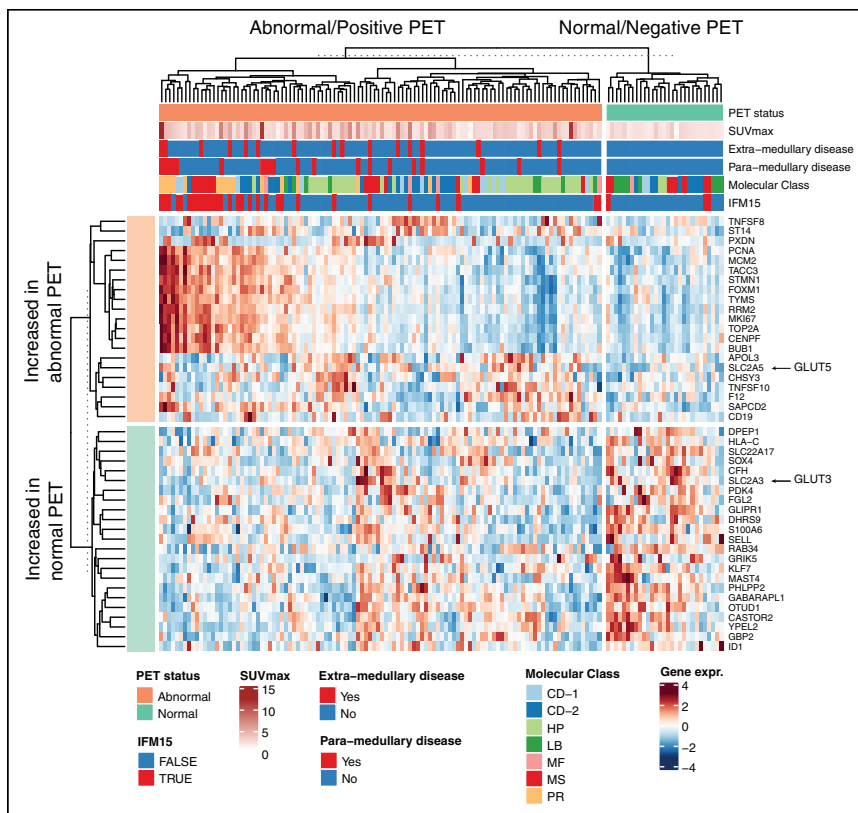


FIGURE 2. Gene expression (expr.) profiling of ^{18}F -FDG PET scans with abnormal results. Heat map representation of standardized gene expression levels of most differentially expressed genes between 2 conditions (normal and abnormal ^{18}F -FDG PET results), obtained with DESeq2. *SLC2A3* encodes GLUT3, and *SLC2A5* encodes GLUT5.

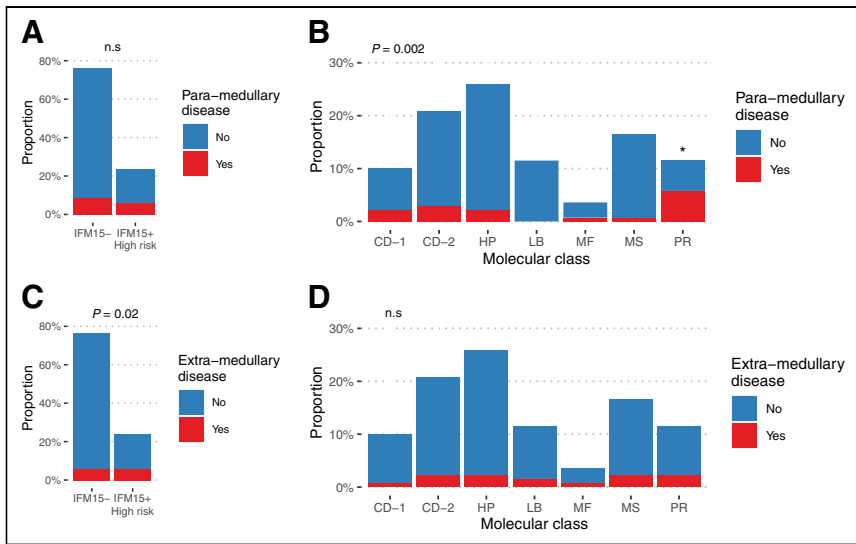


FIGURE 3. Molecular profiles of PMD and EMD on ^{18}F -FDG PET. (A and B) Distribution of patients with PMD at baseline for high-risk and standard-risk IFM15 expression signatures (A) and across myeloma molecular classes (B). (C and D) Distribution of patients with EMD at baseline for high-risk and standard-risk IFM15 expression signatures (C) and across myeloma molecular classes (D). n.s. = not significant ($P > 0.05$).

the UAMS molecular classification was associated with PMD ($P = 0.02$), whereas none of the patients in the LB cluster had PMD, despite abnormal ^{18}F -FDG PET scan results (Fig. 3B). Similar analyses for EMD showed a significantly higher proportion in the

4.3 [95% CI, 1.9–9.7] [$P < 0.001$]; HR for IFM15, 3.7 [95% CI, 1.6–8.1] [$P = 0.001$] (Fig. 4A). Of note, both variables remained significant in the model when accounting for R-ISS staging (Supplemental Table 5). Combining both PMD and IFM15 biomarkers

IFM15+ group ($P = 0.02$) (Fig. 3C) and the lack of a statistical association with GEP70 (Supplemental Fig. 2) or molecular classification (Fig. 3D).

Prognostic Impact of ^{18}F -FDG PET and High-Risk Gene Expression Signatures

The median follow-up time of our cohort was 26 mo (95% CI: 21–33 mo), during which 26 patients (19%) progressed (disease progression or death) and 9 patients (6%) died. Survival analyses were limited to PFS; overall survival was discarded because of the small number of events.

Univariate Cox analysis (Supplemental Tables 3 and 4) showed that imaging biomarkers and gene expression were prognostic for progression. In particular, PMD and IFM15 were strongly associated with relapse (HR for PMD, 5.2 [95% CI, 2.3–11]; HR for IFM15, 4.3 [95% CI, 1.9–9.4]). The combination of PMD and IFM15 in a Cox multivariate model showed the independence of these 2 variables in predicting relapse (HR for PMD, 4.3 [95% CI, 1.9–9.7] [$P < 0.001$]; HR for IFM15, 3.7 [95% CI, 1.6–8.1] [$P = 0.001$] (Fig. 4A). Of note, both variables remained significant in the model when accounting for R-ISS staging (Supplemental Table 5). Combining both PMD and IFM15 biomarkers defined a group with a very high risk of progression ($P = 4 \times 10^{-5}$) (Fig. 4B). Besides, PMD and IFM15 did not correlate with a deep clinical response, as defined by MRD negativity at 100 d after ASCT (Supplemental Fig. 3).

Similarly, patients with negative or normal ^{18}F -FDG PET results, with a good prognosis, and patients with an IFM15 signature, with a poor prognosis, seemed to complement each other in a Kaplan–Meier analysis and in a Cox multivariate model (Figs. 4C and 4D). In particular, among patients with negative ^{18}F -FDG PET results ($n = 110$), a high-risk IFM15 signature was still associated with shorter PFS (HR, 3.9 [95% CI, 1.8–8.8] [$P = 0.001$]).

DISCUSSION

The last decade witnessed significant progress in the development of risk classifiers derived from cytogenetics and gene expression profiling in newly diagnosed MM (8,9,15,16). Yet, inpatient heterogeneity, inherent to this pathology, might reduce the sensitivity of these tests—which are often based on a single localized sample that does not necessarily reflect the entire pathology (17). Thus, whole-body functional imaging such as ^{18}F -FDG PET has been proposed as

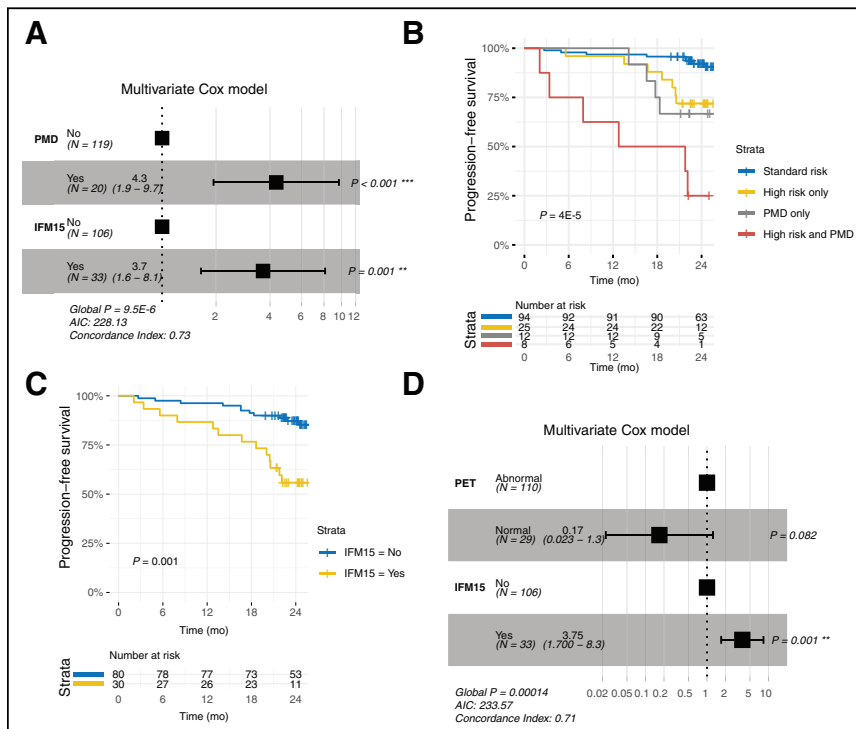


FIGURE 4. Prognostic value of imaging and gene expression profiles. (A) Multivariate Cox modeling of PFS by presence of PMD and high-risk IFM15 gene expression signature (IFM15+). (B) Kaplan–Meier curves representing PFS of MM patients separated by IFM15 and PMD status. (C) Kaplan–Meier curves depicting PFS of patients with positive ^{18}F -FDG PET results only ($n = 110/139$) and according to their IFM15 risk status. (D) Multivariate Cox modeling of PFS using PET (normal or abnormal results) and IFM15 (Yes = high risk; No = standard risk) binary variables. AIC = Akaike information criterion.

a complementary approach for prognosis at baseline. As such, both transcriptomic and imaging approaches allow the identification of patients at high risk of progression, despite the fact that they seem to be opposed in nature. The cells studied in RNA sequencing come from a single, localized bone marrow aspirate, whereas ^{18}F -FDG PET explores whole-body spatial heterogeneity. In this context, some ^{18}F -FDG PET scan results are considered negative or normal despite the clinical diagnosis established, in particular, by the presence of malignant plasma cells in the bone marrow aspirate. Yet, it seems possible that the characteristics of these 2 techniques partially overlap and that the biomarkers described in ^{18}F -FDG PET can find echoes in transcriptomic data beyond the *HK2* underexpression shown by the initial work of Rasche et al. (3).

In the present study, we reported novel associations between imaging patterns and gene expression in MM, and we extended our knowledge of the molecular profiles of negative or normal ^{18}F -FDG PET results. Our data demonstrate that normal or negative ^{18}F -FDG PET scan results are associated with the specific expression of glucose metabolism genes and with the LB molecular subgroup, whereas abnormal or positive ^{18}F -FDG PET scan results are associated with markers of cell proliferation and with a distinct transcriptomic profile including the fructose transporter *GLUT5*.

The combination of PMD and the IFM15 signature clearly identified a subset of patients with a higher risk of progression in our cohort. This result was independent of the patients' R-ISS stage and therefore extended the risk classification at diagnosis. The prognostic value of PMD or IFM15 was independent of undetectable MRD or a complete stringent clinical response. Interestingly, the only R-ISS stage 1 patient who was positive for both PMD and IFM15 progressed in 4 mo and died within 2 y. Further studies could extend these observations to overall survival and compare this new biomarker with other very high-risk groups, such as the "Double-Hit" group (18).

As for the 7 UAMS molecular subgroups, Usmani et al. previously reported that the PR, MF, and GEP70 subgroups had more EMD (19). These observations were not made in the present study, yet the PR and GEP70 subgroups were associated with PMD. To our knowledge, this finding was not reported in previous work. However, the concept of PMD, corresponding to soft-tissue invasion with contiguous bone involvement, is relatively recent. The CASSIOPET prospective study was the first to examine and report the prognostic value of this particular imaging biomarker (5). It is plausible that these 2 entities were mixed in previous work, explaining these discordant results.

Patients with negative or normal ^{18}F -FDG PET scan results at diagnosis were more likely to belong to the LB subgroup of the UAMS classification, a consistent result, since this cluster is characterized by a small number of FLs detected on MRI and both groups have a good clinical prognosis. To our knowledge, this observation was not made in previous studies.

We also confirmed the underexpression of *HK2* in this subgroup and showed that *GLUT3* and especially *GLUT5* were deregulated to a greater extent than *HK2* between patients with negative or normal ^{18}F -FDG PET scan results and patients with positive or abnormal ^{18}F -FDG PET scan results. More generally, when we extended our analysis to the genome, 2 gene expression signatures stood out for MM patients with positive ^{18}F -FDG PET results. The first involved proliferation genes (*MKI-67*, *PCNA*, *TOP2A*, *STMN1*) and proliferation groups (PR and MS). The second involved *GLUT5* and lymphocyte antigens (e.g., *CD19*, *CD30 L*, and *TRAIL*), suggesting that a particular gene expression program is associated with

glucose avidity independently of proliferation. This observation needs to be validated at the protein level and will be the subject of a prospective study with another cohort.

Similarly, 2 observations that require further investigations were made. First, strong expression of *GLUT5/SLC2A5* was associated with positive ^{18}F -FDG PET results. This finding was unexpected, since *GLUT5* does not transport glucose but transports fructose (14(p5)). High levels of expression of *GLUT5* in ^{18}F -FDG-avid tissues have been reported in the literature as a "discrepancy" in breast cancer cells expressing low levels of *GLUT1* (20). Finally, although previously described (2), the prognostic value of SUV_{max} using a threshold of 4.2 did not appear to be significant in a multivariate analysis in our work, a result for which bias due to the inherent limitations of SUV calculations in a multicenter study cannot be ruled out.

CONCLUSION

The present study enabled a better characterization of the molecular signature of ^{18}F -FDG PET biomarkers. Moreover, the combined prognostic value of PMD and a high-risk IFM15 signature may help define a group of MM patients with a very high risk of progression. This work demonstrated, once again, the added prognostic value of integrating ^{18}F -FDG PET in the management of MM.

DISCLOSURE

This work was supported by grants from the French National Agency for Research IRON Labex (ANR-11-LABX-0018-01), ArronaxPlusEquipex (ANR-11-EQPX-0004), ISITE NExT (ANR-16-IDEX-0007), SIRIC ILIAD (Imaging and Longitudinal Investigations to Ameliorate Decision-Making in Multiple Myeloma and Breast Cancer), INCA-DGOS-Inserm 12558, and Janssen Research & Development. Philippe Moreau declares being a member of advisory boards for Celgene, Janssen, Takeda, Novartis, and Amgen. Cyrille Touzeau declares fees and consultancy for Celgene, Janssen, Takeda, GlaxoSmithKline, Amgen, Abbvie, and Sanofi. No other potential conflict of interest relevant to this article was reported.

ACKNOWLEDGMENTS

We thank Elise Douillard, Magali Devic, and Nathalie Roi for excellent technical expertise and the Biogenouest sequencing platform GenoBird in Nantes, France, for the Illumina sequencing.

KEY POINTS:

QUESTION: Are baseline ^{18}F -FDG PET biomarkers in newly diagnosed MM patients associated with a specific molecular signature through RNA sequencing?

PERTINENT FINDINGS: Negative results on ^{18}F -FDG PET scans were associated with lower levels of expression of *HK2* and showed enrichment for patients with the LB subgroup, whereas positive results on ^{18}F -FDG PET scans revealed 2 distinct signatures: either high levels of expression of proliferation genes or high levels of expression of *GLUT5* and lymphocyte antigens. The combined prognostic value of PMD and a high-risk IFM15 signature defined a group of MM patients with a very high risk of progression.

IMPLICATIONS FOR PATIENT CARE: A combination of prognostic biomarkers from imaging and gene expression profiling has the potential to improve MM management and may define a novel risk stratification algorithm.

REFERENCES

1. Cavo M, Terpos E, Nanni C, et al. Role of ^{18}F -FDG PET/CT in the diagnosis and management of multiple myeloma and other plasma cell disorders: a consensus statement by the International Myeloma Working Group. *Lancet Oncol*. 2017;18:e206–e217.
2. Michaud-Robert A-V, Jamet B, Bailly C, et al. FDG-PET/CT, a promising exam for detecting high-risk myeloma patients? *Cancers (Basel)*. 2020;12:1384.
3. Rasche L, Angtuaco E, McDonald JE, et al. Low expression of hexokinase-2 is associated with false-negative FDG-positron emission tomography in multiple myeloma. *Blood*. 2017;130:30–34.
4. Abe Y, Ikeda S, Kitadate A, et al. Low hexokinase-2 expression-associated false-negative ^{18}F -FDG PET/CT as a potential prognostic predictor in patients with multiple myeloma. *Eur J Nucl Med Mol Imaging*. 2019;46:1345–1350.
5. Moreau P, Zweegman S, Perrot A, et al. Evaluation of the prognostic value of positron emission tomography-computed tomography (PET-CT) at diagnosis and follow-up in transplant-eligible newly diagnosed multiple myeloma (TE NDMM) patients treated in the phase 3 Cassiopeia study: results of the Cassiopet companion study. *Blood*. 2019;134(suppl 1):692.
6. Zhan F, Huang Y, Colla S, et al. The molecular classification of multiple myeloma. *Blood*. 2006;108:2020–2028.
7. Broyl A, Hose D, Lokhorst H, et al. Gene expression profiling for molecular classification of multiple myeloma in newly diagnosed patients. *Blood*. 2010;116:2543–2553.
8. Shaughnessy JD, Zhan F, Burington BE, et al. A validated gene expression model of high-risk multiple myeloma is defined by deregulated expression of genes mapping to chromosome 1. *Blood*. 2007;109:2276–2284.
9. Decaux O, Lodé L, Magrangeas F, et al. Prediction of survival in multiple myeloma based on gene expression profiles reveals cell cycle and chromosomal instability signatures in high-risk patients and hyperdiploid signatures in low-risk patients: a study of the Intergroupe Francophone du Myélome. *J Clin Oncol*. 2008;26:4798–4805.
10. Moreau P, Attal M, Hulin C, et al. Bortezomib, thalidomide, and dexamethasone with or without daratumumab before and after autologous stem-cell transplantation for newly diagnosed multiple myeloma (CASSIOPEIA): a randomised, open-label, phase 3 study. *Lancet*. 2019;394:29–38.
11. Barwick BG, Neri P, Bahlis NJ, et al. Multiple myeloma immunoglobulin lambda translocations portend poor prognosis. *Nat Commun*. 2019;10:1911.
12. Michaud-Robert A-V, Zamagni E, Carlier T, et al. Glucose metabolism quantified by SUVmax on baseline FDG-PET/CT predicts survival in newly diagnosed multiple myeloma patients: combined harmonized analysis of two prospective phase III trials. *Cancers (Basel)*. 2020;12:2532.
13. Kumar S, Paiva B, Anderson KC, et al. International Myeloma Working Group consensus criteria for response and minimal residual disease assessment in multiple myeloma. *Lancet Oncol*. 2016;17:e328–e346.
14. Nomura N, Verdon G, Kang HJ, et al. Structure and mechanism of the mammalian fructose transporter GLUT5. *Nature*. 2015;526:397–401.
15. Avet-Loiseau H, Li C, Magrangeas F, et al. Prognostic significance of copy-number alterations in multiple myeloma. *J Clin Oncol*. 2009;27:4585–4590.
16. Avet-Loiseau H, Attal M, Moreau P, et al. Genetic abnormalities and survival in multiple myeloma: the experience of the Intergroupe Francophone du Myélome. *Blood*. 2007;109:3489–3495.
17. Rasche L, Chavan SS, Stephens OW, et al. Spatial genomic heterogeneity in multiple myeloma revealed by multi-region sequencing. *Nat Commun*. 2017;8:268.
18. Walker BA, Mavrommatis K, Wardell CP, et al. A high-risk, Double-Hit, group of newly diagnosed myeloma identified by genomic analysis. *Leukemia*. 2019;33:159–170.
19. Usmani SZ, Heuck C, Mitchell A, et al. Extramedullary disease portends poor prognosis in multiple myeloma and is over-represented in high-risk disease even in the era of novel agents. *Haematologica*. 2012;97:1761–1767.
20. Hamann I, Krys D, Glubrecht D, et al. Expression and function of hexose transporters GLUT1, GLUT2, and GLUT5 in breast cancer: effects of hypoxia. *FASEB J*. 2018;32:5104–5118.

Prognostic Value of Whole-Body PET Volumetric Parameters Extracted from ^{68}Ga -DOTATOC PET/CT in Well-Differentiated Neuroendocrine Tumors

Philippe Thuillier^{1,2}, Virginia Liberini¹, Serena Grimaldi¹, Osvaldo Rampado³, Elena Gallio³, Bruno De Santi⁴, Emanuela Arvat⁵, Alessandro Piovesan⁵, Roberto Filippi⁶, Ronan Abgral⁷, Filippo Molinari⁴, and Désirée Deandreis¹

¹Nuclear Medicine Unit, Department of Medical Sciences, University of Turin, Turin, Italy; ²Department of Endocrinology, University Hospital of Brest, Brest, France; ³Medical Physics Unit, AOU Città della Salute e della Scienza, Turin, Italy; ⁴Biolab, Department of Electronics and Telecommunications, Politecnico di Torino, Turin, Italy; ⁵Oncological Endocrinology Unit, Department of Medical Sciences, University of Turin, Turin, Italy; ⁶Departments of Oncology and Medical Sciences, University of Turin, Turin, Italy; and ⁷Department of Nuclear Medicine, University Hospital of Brest, Brest, France

Our objective was to evaluate the prognostic value of somatostatin receptor tumor burden on ^{68}Ga -DOTATOC PET/CT in patients with well-differentiated (WD) neuroendocrine tumors (NETs). **Methods:** We retrospectively analyzed the ^{68}Ga -DOTATOC PET/CT scans of 84 patients with histologically confirmed WD NETs (51 grade 1, 30 grade 2, and 3 grade 3). For each PET/CT scan, all ^{68}Ga -DOTATOC-avid lesions were independently segmented by 2 operators using a customized threshold based on the healthy liver SUV_{max} (LIFEx, version 5.1). Somatostatin receptor-expressing tumor volume (SRETV) and total lesion somatostatin receptor expression (TLSRE = $\text{SRETV} \times \text{SUV}_{\text{mean}}$) were extracted for each lesion, and then whole-body SRETV and TLSRE (SRETVwb and TLSREwb, respectively) were defined as the sum of SRETV and TLSRE, respectively, for all segmented lesions in each patient. Time to progression (TTP) was defined as the combination of disease-free survival in patients undergoing curative surgery ($n = 10$) and progression-free survival for patients with unresectable or metastatic disease ($n = 74$). TTP and overall survival were calculated by Kaplan–Meier analysis, log-rank testing, and the Cox proportional-hazards regression model. **Results:** After a median follow-up of 15.5 mo, disease progression was confirmed in 35 patients (41.7%) and 14 patients died. A higher SRETVwb ($>39.1 \text{ cm}^3$) and TLSREwb ($>306.8 \text{ g}$) correlated significantly with a shorter median TTP (12 mo vs. not reached; $P < 0.001$). In multivariate analysis, SRETVwb ($P = 0.005$) was the only independent predictor of TTP regardless of histopathologic grade and TNM staging. **Conclusion:** According to our results, SRETVwb and TLSREwb extracted from ^{68}Ga -DOTATOC PET/CT could predict TTP or overall survival and might have important clinical utility in the management of patients with WD NETs.

Key Words: neuroendocrine tumors; ^{68}Ga -DOTATOC PET/CT; tumor burden; prognosis; somatostatin receptor expressing tumor volume; total lesion somatostatin receptor expression

J Nucl Med 2022; 63:1014–1020
DOI: 10.2967/jnumed.121.262652

Received May 28, 2021; revision accepted Oct. 4, 2021.
For correspondence or reprints, contact Philippe Thuillier (philippe.thuillier@chu-brest.fr).
Published online Nov. 5, 2021.
COPYRIGHT © 2022 by the Society of Nuclear Medicine and Molecular Imaging.

Neuroendocrine neoplasms (NENs) are a group of tumors of common embryologic origin but leading to a variety of clinical presentations and prognosis. The most frequent sites are the gastroenteropancreatic tract and the bronchopulmonary system. Although relatively rare, NENs have had a greatly increasing incidence in the last 30 years, and the incidence is currently estimated at approximately 5 cases per 100,000 population per year (1). According to the World Health Organization classification (based on Ki-67 percentage or number of mitoses per high-power field), NENs range from well-differentiated (WD) neuroendocrine tumors (NETs) to poorly differentiated carcinomas (2).

PET/CT imaging with a ^{68}Ga -DOTA-labeled somatostatin analog (SSTa) is the mainstay for in vivo evaluation of somatostatin receptor expression in NETs (3,4), and almost 90% of primary grade 1 or 2 gastroenteropancreatic NETs are PET-positive because of the high somatostatin receptor expression (5). In clinical practice, ^{68}Ga -DOTA-SSTa PET/CT has become the gold standard in the diagnosis and management of WD NETs, as it plays a major role in tumor characterization, in the assessment of disease extension, and in proper selection of patient candidates for peptide receptor radionuclide therapy (6,7). The prognostic value of ^{68}Ga -DOTA-SSTa PET/CT imaging has been widely assessed in the literature but has been focused mainly on semi-quantitative parameters such as SUV (8,9).

In several tumor models over the last few years, metabolic tumor burden on ^{18}F -FDG PET has shown major prognostic value compared with semiquantitative parameters. Calculation of metabolic tumor burden integrates the volume of metabolically active tumor, expressed by metabolic tumor volume, and total lesion glycolysis, which is the product of SUV_{mean} and metabolic tumor volume. Two studies (10,11) have interestingly demonstrated the prognostic utility of somatostatin receptor tumor burden (SRTB) in patients with WD NETs, obtained by measuring whole-body total lesion somatostatin receptor expression (TLSREwb) and whole-body somatostatin receptor-expressing tumor volume (SRETVwb) from ^{68}Ga -DOTATATE PET/CT images.

Hence, the objective of this study was to evaluate the prognostic value of SRTB extracted from ^{68}Ga -DOTATOC PET/CT in a large cohort of patients with WD NETs.

MATERIALS AND METHODS

Population

All patients ($n = 322$) consecutively referred for ^{68}Ga -DOTATOC PET/CT to the Nuclear Medicine Division of “AOU Città della Salute

e della Scienza,” from January 1, 2017, to January 4, 2020, were retrospectively evaluated and included if they had histologically proven grades 1–3 WD NETs, gastroenteropancreatic or bronchopulmonary NETs or an unknown primary site, ^{68}Ga -DOTATOC PET with at least 1 positive lesion, and follow-up at least 6 mo after PET. Exclusion criteria were an age of less than 18 y, incomplete histologic data, a neuroendocrine carcinoma, concomitant metastatic neoplasia other than NET, or negative findings on ^{68}Ga -DOTATOC PET/CT. The CONSORT diagram of the study (Consolidated Standards of Reporting Trials) is presented in Figure 1.

The study was conducted in accordance with the ethical principles set forth in the Declaration of Helsinki and was approved by the local ethical committee (approval 0004004; protocol: “NET PET Tumor Burden Study”). All enrolled patients signed an informed consent form.

Data on age, sex, TNM stage at the time of PET imaging, tumor grade according to the World Health Organization classification (12) (Ki-67 for grade 1, <3%; grade 2, 3%–20%; grade 3, >20%), functional status, and previous locoregional and systemic treatments were collected. Patients were considered treatment-naïve if they had received no previous treatment except for surgery of the primary tumor.

All patients underwent PET/CT on an analog 3-dimensional (3D) PET scanner (Philips Gemini Dual-slice EXP scanner—PET Allegro™ system with Brilliance CT scanner—Philips Medical Systems, Cleveland, OH) according to guidelines (7). The median injected tracer activity was 148 MBq (range, 92–250 MBq). After a minimal time of 45–60 min, and after a free-breathing CT acquisition for attenuation correction from the vertex to the mid thigh (5-mm slices, 40 mAs, and 120 kVp), PET data were acquired in 3-dimensional mode at 2.5 min per bed position and 6–8 bed positions per patient. The PET scans were reconstructed by ordered-subset expectation maximization (3-dimensional row-action maximum-likelihood algorithm), and the matrix size was 144×144 voxels, resulting in voxels of $4.0 \times 4.0 \times 4.0$ mm. All acquisitions were corrected for attenuation, scatter, and random coincidences.

Image Analysis and SRTB Extraction

For each PET/CT scan, all ^{68}Ga -DOTATOC-avid lesions were segmented independently by 2 nuclear medicine physicians using a semiautomatic method through freely available software (LIFEx, version 5.1; IMIV [Imagerie Moléculaire In Vivo] Lab/CEA [Le Commissariat à l’Énergie Atomique et aux Énergies Alternatives]) (13) and based on the SUV threshold method to avoid intra- and interoperator variability in manual segmentation (14,15).

The SUV_{max} threshold based on healthy-liver uptake was chosen. SUV_{max} was assessed by placing a spheric volume of interest 3 cm in diameter in the right upper lobe of the liver, as previously reported (16). For each lesion, the SRETV and TLSRE were semiautomatically extracted. TLSRE was obtained by multiplying the SRETV of each lesion by its corresponding SUV_{mean} . A visual inspection of the resulting automated volume segmentation was performed

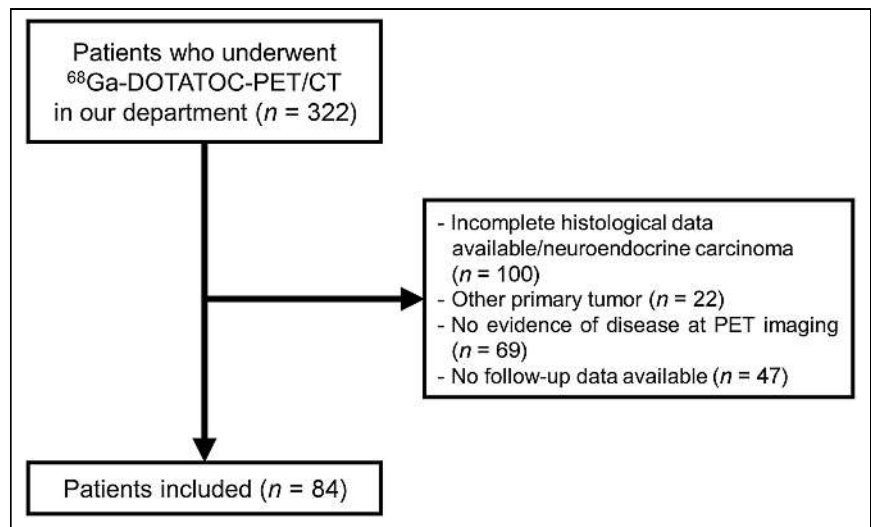


FIGURE 1. CONSORT diagram of study.

to remove background physiologic uptake (e.g., spleen, kidney, and bladder). The same analysis was performed for each patient by both operators to evaluate reproducibility.

We classified each lesion according to its site: primary tumor, lymph node, liver, bone, or other (e.g., peritoneum and lung). Then, SRETVwb and TLSREwb, defined as the sum of SRETV and TLSRE, respectively, for all lesions in each patient, were calculated (Fig. 2). When all lesions were equal to or lower than the liver SUV_{max} cutoff, SRETVwb and TLSREwb were defined as equal to 0 as previously mentioned (17). We also separated the corresponding SRETVwb (primary, lymph node, liver, bone, and other) and TLSREwb (primary, lymph node, liver, bone, and other) according to each tumor site. The details of the entire process are described in Supplemental Figure 1 (supplemental materials are available at <http://jnm.snmjournals.org>).

Statistical Analysis

Quantitative variables were expressed as median with range. The primary clinical endpoint was the time to progression (TTP), defined as the time from PET/CT imaging to the first event (progression or relapse).

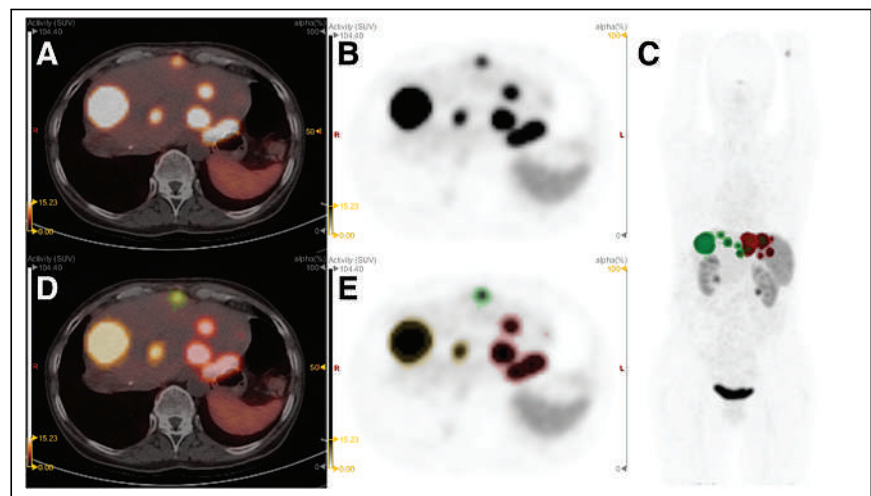


FIGURE 2. ^{68}Ga -DOTATOC PET/CT in WD pancreatic NET (PET/CT [A] and PET imaging [B]) showing high uptake in all lesions (highest SUV_{max} , 104.4). SRTB analysis (maximum-intensity projection [C], PET/CT [D], and PET imaging [E]) highlighted SRETVwb and TLSREwb values of 249 cm^3 and 4,191 g, respectively.

Because anatomopathologic confirmation of all lesions is not achievable, the TTP of the disease was based on morphologic imaging criteria or functional criteria (18). Disease progression was defined as the appearance of a new lesion or a significant increase in the size of known lesions. The secondary clinical endpoint was overall survival (OS), defined as the time from PET/CT to NET-related death. Patients were followed up until the occurrence of the primary endpoints or until October 2020.

Kaplan–Meier curves and the log-rank test were applied for survival analysis. Receiver-operating-characteristic analysis was applied to determine the best cutoff for SRETVwb and TLSREwb parameters to predict the patient’s outcome using the Youden index (19). The area under the curve, sensitivity, specificity, and accuracy were reported.

For TTP, multivariate analysis was performed by the Cox proportional-hazards regression model to estimate hazard ratios with 95% CIs, including variables that had clinical relevance or a *P* value of less than 0.05 in univariate analysis. Because of the low number of events, we did not perform multivariate analysis for OS.

We performed a subgroup analysis on patients with metastatic NETs at the time of PET/CT, using the same SRETVwb and TLSREwb thresholds as found for the whole cohort. Moreover, an exploratory analysis to assess the repartition of SRTB according to tumor site and progressive versus nonprogressive disease during follow-up was performed through the nonparametric Mann–Whitney *U* test with Bonferroni adjustment.

Interobserver agreement was evaluated for SRETVwb and TLSREwb using intraclass correlation coefficient values of between 0 and 1, with a value of more than 0.9 defining the parameter as robust (20).

All statistical tests were 2-sided, and a *P* value of less than 0.05 indicated a statistically significant difference. All analyses were performed on XLSTAT (version 2019.2.2; Addinsoft).

RESULTS

Among the 322 patients screened, 84 (38 male and 46 female; median age at PET, 60.5 y [range, 25–86 y]) were included in the study. The main characteristics of the patients are represented in Table 1. The pancreas was the most frequent site (39/84, 46.4%), and 40.5%, 55.9%, and 3.6% of the tumors were classified as grades 1, 2, and 3, respectively. Fifty-four (64.3%) patients had metastatic disease at the time of PET/CT, and 47 patients (55.9%) were defined as treatment-naïve.

SRTB

In the whole cohort, 442 lesions and subsequent volumes of interest were segmented, including primary (*n* = 36, 8.1%), lymph node (*n* = 72, 16.3%), liver (*n* = 185, 41.9%), bone (*n* = 114, 25.8%), and other sites (*n* = 35, 7.9%). The median SUV_{max}, SRETV, and TLSRE per lesion were 9.7 (range, 3.3–116.5), 4.0 cm³ (range, 0.5–1,980.3 cm³), and 24.8 g (range, 1.8–21,819.5 g), respectively. The median SRETVwb and TLSREwb were 32.4 cm³ (range, 0–3,078.7 cm³) and 338.3 g (range, 0–22,658.6 g), respectively. In 5 patients, the SRETVwb was equal to zero because the lesions were ⁶⁸Ga-DOTATOC-avid but with an SUV_{max} lower than the liver background.

Survival Analysis

Progression was detected in 35 patients (41.7%), and 14 patients died after a median follow-up of 23 mo (range, 0–41 mo). In the entire cohort, the median TTP was 22 mo (interquartile range, from 10 mo to not reached). Ten patients underwent curative surgery of the primary tumor after PET and did not show disease relapse during the follow-up.

TABLE 1
Characteristics of Patients

Characteristic	Value (total <i>n</i> = 84)
Sex	
Male	48 (57.1)
Female	36 (42.9)
Median age (y)	60.5 (range, 25–86)
Primary site	
Gastroenteropancreatic (<i>n</i> = 72)	72 (85.7)
Pancreas	39
Small intestine	21
Duodenum	3
Cecum or colon	4
Rectum	1
Stomach	4
Lung	9 (10.7)
Unknown	3 (3.6)
TNM stage	
Only primary tumor	20 (23.8)
Locoregional extension	10 (11.9)
Metastatic	54 (64.3)
Ki-67 (%)	
<3	34 (40.5)
3 to ≤20	47 (55.9)
>20	3 (3.6)
Functional	12 (14.3)
Treatment before PET	
Surgery	42 (50)
SSTa	46 (54.8)
Systemic treatment	16 (19.0)
Chemotherapy	13
Everolimus	8
Others	2
Locoregional treatment	12 (14.3)
Peptide receptor radionuclide therapy	5 (6)
Treatment after PET	
Surgery	13 (15.5)
SSTa	63 (75.0)
Systemic treatment	16 (19.0)
Chemotherapy	12
Everolimus	8
Other	0
Locoregional treatment	7 (8.3)
Peptide receptor radionuclide therapy	7 (8.3)

Data are number followed by percentage in parentheses, except for age.

Univariate Analysis for TTP/OS. For SRETVwb, the area under the receiver-operating-characteristic curve was 0.83 (best cutoff, 39.1 cm³), with a sensitivity, specificity, and accuracy of 0.86, 0.76, and 0.8, respectively. For TLSREwb, the area under the curve was 0.79 (best cutoff, 306.8 g), with a sensitivity, specificity, and accuracy of 0.86, 0.74, and 0.79, respectively. A higher SRETVwb (≥ 39.1 cm³) and TLSREwb (>306.8 g) correlated with a significantly shorter median TTP (12 mo [95% CI, 10–23 mo] vs. not reached for both; $P < 0.001$) and a shorter median OS (not reached for both; $P < 0.001$). SUV_{max} was not associated with TTP or OS ($P = 0.08$ and $P = 0.09$, respectively; Fig. 3).

The TNM stage at the time of PET, the Ki-67 percentage, and treatment history (naïve vs. previous line of treatment) were also significantly associated with a shorter TTP and OS ($P < 0.05$; Supplemental Fig. 2), whereas age, sex, and secretory syndrome were not ($P =$ not statistically significant).

Multivariate Analysis. SRETVwb and TLSREwb were strongly correlated in our study ($R = 0.916$ in Pearson correlation analysis). Thus, we performed a multivariate analysis using the Cox proportional-hazards regression model including only SRETVwb (>39.1 cm³). SRETVwb was the only independent predictor of TTP

(hazard ratio, 4.8 [95% CI, 1.6–14.5]; $P = 0.006$) regardless of TNM stage, Ki-67 percentage, and treatment history ($P = 0.58$, 0.85, and 0.39, respectively) (Table 2).

Subgroup Analysis in Metastasis-Positive Patients. The diagnostic performance of SRTB to predict TTP and OS was assessed according to lesion site in a subgroup of patients with metastatic disease ($n = 54$). Using the same threshold, Kaplan–Meier analysis revealed a significant difference, with a shorter median TTP and OS for a higher value of both SRETVwb and TLSREwb ($P = 0.002$ and $P = 0.016$, respectively; Supplemental Fig. 3). SRTB analysis according to each lesion site did not reveal any difference between patients with progressive disease and patients with nonprogressive disease (Supplemental Table 1).

Interobserver Agreement

The mean liver threshold was 5.4 ± 2.2 (range, 2.1–12.9) for operator 1 and 5.3 ± 2.0 (range, 2.1–12.2) for operator 2. The median SRETVwb and TLSREwb were 32.4 cm³ (range, 0–3,078.7 cm³) and 338.3 g (range, 0–22,658.6), respectively, for operator 1, and 32.0 cm³ (range, 0–3,100.0 cm³) and 282.0 g (range, 0–22,789.0), respectively, for operator 2. The intraclass correlation coefficients were, respectively, 0.963, 0.988, and 0.997 for liver threshold, SRETVwb, and TLSREwb.

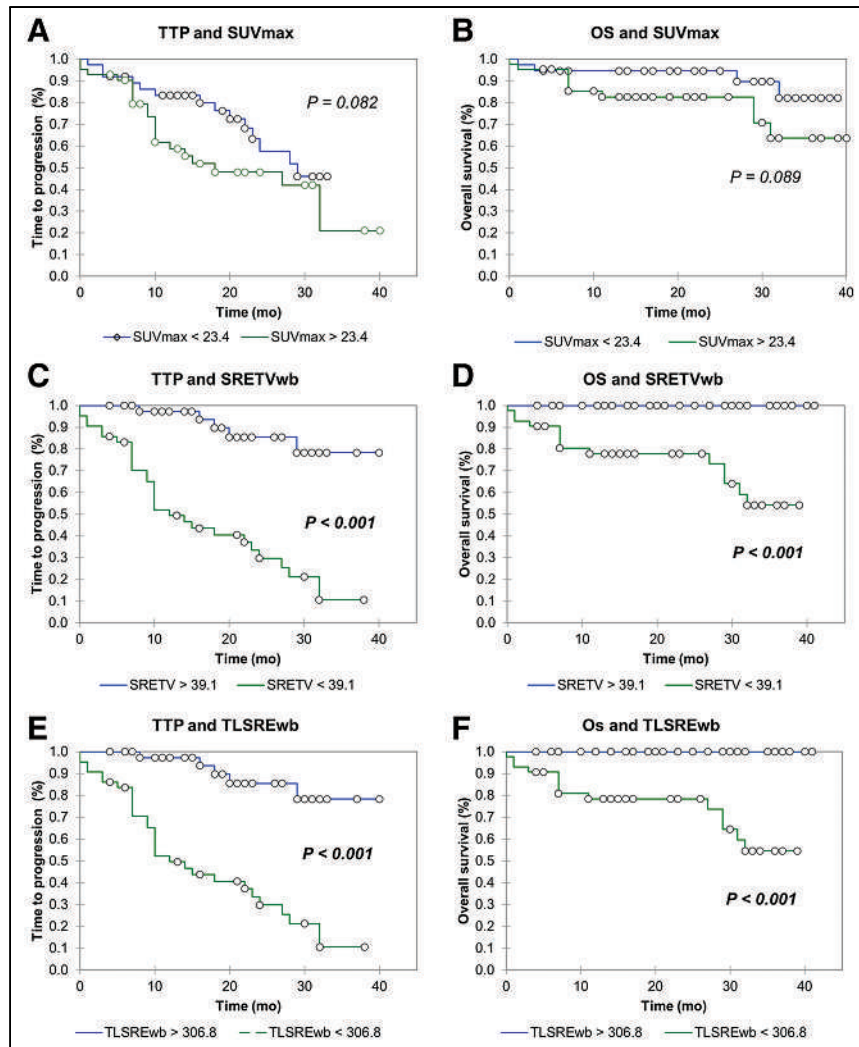


FIGURE 3. TTP (left) and OS (right) in patients according to SUV_{max} (A and B), SRETVwb (C and D), and TLSREwb (E and F).

DISCUSSION

We investigated the prognostic value of SRTB extracted from ⁶⁸Ga-DOTATOC PET/CT in patients with WD NET. SRETVwb (≥ 39.1 cm³) and TLSREwb (≥ 306.8 g) were significantly associated with TTP, but at multivariate analysis, SRETVwb was an independent prognostic parameter regardless of Ki-67 percentage, TNM stage, or treatment.

Several previous studies assessed the prognostic significance of ⁶⁸Ga-DOTATOC (17,21) and ⁶⁸Ga-DOTATATE PET/CT (10,11,22,23) volumetric parameters in patients with NETs. In a prospective study including a large population of 184 patients with grades 1–3 NETs, Tirosh et al. reported that SRETVwb of at least 7.0 cm³ and at least 35.8 cm³ obtained by ⁶⁸Ga-DOTATATE PET/CT were significantly associated with progression-free survival (PFS) and OS ($P < 0.001$ both), respectively (10). In another prospective study, including only grade 1 or 2 gastroenteropancreatic NETs, Toriihara et al. found that an SRETVwb of at least 11.1 cm³ and a TLSREwb of at least 146.48 g obtained by ⁶⁸Ga-DOTATATE PET/CT were associated with PFS but that only SRETVwb was independently associated with PFS in a survival analysis, in accordance with our study (11). Kim et al. (17), in a retrospective study including 31 patients with unresectable or metastatic WD gastroenteropancreatic NETs undergoing ⁶⁸Ga-DOTATOC PET/CT before receiving lanreotide, showed that a lower tumor-to-liver ratio, lower SUV_{max},

TABLE 2

Univariate and Multivariate Analyses Using Cox Regression for TTP According to SRETVwb, TLSREwb, and Other Characteristics of Cohort

Characteristic	Univariate analysis		Multivariate analysis	
	Hazard ratio	<i>P</i>	Hazard ratio	<i>P</i>
Sex		0.31		
Male (reference)	1			
Female	0.70 (0.35–1.39)			
Age		0.58		
≥64 y (reference)	1			
<64 y	0.83 (0.43–1.61)			
Ki-67%		0.013		0.85
<3 (reference)	1		1	
3–20	2.60 (1.16–5.81)		1.02 (0.41–2.53)	
>20	6.28 (1.64–24.00)		1.45 (0.35–6.07)	
Stage at time of PET		0.009		0.58
Local (reference)	1		1	
Locoregional	1.79 (0.11–28.75)		1.88 (0.10–34.10)	
Metastatic	12.39 (1.69–90.62)		3.22 (0.33–31.21)	
Treatment-naïve		0.001		0.39
No (reference)	1		1	
Yes	0.20 (0.00–0.515)		0.60 (0.19–1.88)	
SUV _{max}		0.09		
≥23.4 (reference)	1			
<23.4	0.56 (0.28–1.1)			
SRETV (cm ³)		<0.001		0.006
<39.1 (reference)	1		1	
≥39.1	8.48 (3.28–21.91)		4.76 (1.56–14.53)	
TLSRE (g)		<0.001		
<306.8 (reference)	1			
≥306.8	8.41 (3.25–21.74)			

Data in parentheses are 95% CIs.

and higher SRETVwb (>58.9 cm³) were significantly associated with a shorter PFS in univariate analysis, but only tumor-to-liver ratio (hazard ratio, 3.182; *P* = 0.021) remained an independent factor for PFS in multivariate analysis. In our study, SUV_{max} was not associated with TTP, as is consistent with findings by Tirosh et al. and Torihara et al. (10,11). One potential explanation is the differences in selection criteria. In fact, Kim et al. included a more homogeneous population of patients at an early stage of disease, most of whom had not undergone other types of treatment (87.1%, excluding surgery) (17). Although a high SUV on ¹⁸F-FDG PET/CT is positively associated with prognosis in almost all cancers, including NETs (24)—explaining the interest in using total lesion glycolysis—a lower SUV_{max} on ⁶⁸Ga-DOTA-SSTa PET/CT is associated with poorer prognosis in patients with WD NETs (8,9,25,26). Thus, for the same SRETVwb value, patients in whom lesions with a low SUV_{mean}—and thus a low TLSREwb value—are disclosed might tend to present a less favorable prognosis, leading to conflicting results among different studies that include different patient populations. For this reason, SRETVwb seems to be

the most prognostic parameter, but its use should be validated in further prospective future studies including populations that are more homogeneous in terms of primary site, disease course, and treatment setting.

Furthermore, the proper methodology to evaluate SRTB should be considered. In our study, a customized threshold based on liver SUV_{max} was chosen, and to our knowledge, this was the second study in which such a segmentation method was applied to ⁶⁸Ga-DOTATOC PET/CT (17). This methodology presents the advantage of being fast; hence, it could represent a useful tool in clinical practice. Interestingly, we found higher cutoffs for SRETVwb and TLSREwb than did studies assessing SRTB using ⁶⁸Ga-DOTA-TATE, whereas the SRETVwb and TLSREwb cutoffs were consistent with the study of Kim et al., performed with the same radiopharmaceutical, ⁶⁸Ga-DOTATOC (10,11,17). The literature showed that tumor uptake is higher and liver uptake lower with ⁶⁸Ga-DOTATOC than with ⁶⁸Ga-DOTATATE, leading to a higher tumor-to-liver ratio (27,28). Hence, we can assume that SRETVwb

and TLSREwb might be lower using ^{68}Ga -DOTATATE. These differences could also be explained by the difference in segmentation methodology. Torihara et al. used a 50% threshold of SUV_{max} to segment each lesion, leading to a lower SRETVwb value, especially in patients with intense radiotracer uptake (11). An example of the impact of different segmentation methods on SRTB is reported in Supplemental Figure 4.

In addition, assessing the reproducibility and robustness of SRTB calculation is important. In our study, reproducibility between the 2 operators was excellent, with an intraclass correlation coefficient of more than 0.9 for both SRETVwb and TLSREwb. To our knowledge, no study has assessed the reproducibility of SRTB parameters on ^{68}Ga -DOTA-SSTa PET/CT. Many studies showed that the segmentation method can impact the interoperator reproducibility of whole-body metabolic tumor volume on ^{18}F -FDG PET/CT imaging, especially threshold methods based on 41% of SUV_{max} (29,30). SRTB parameters in ^{68}Ga -DOTA-SSTa PET/CT might be more reproducible than whole-body metabolic tumor volume because of the higher signal-to-noise ratio. This point is a crucial one; studies are needed of the reproducibility and robustness of whole-body volumetric parameters in ^{68}Ga -DOTA-SSTa PET/CT, especially between different PET systems.

Beyond the prognostic role, evaluation of changes in SRETVwb and TLSREwb (namely change in SRETVwb and change in TLSREwb) after the initiation of systemic therapy may offer promising perspectives, especially for patients treated with peptide receptor radionuclide therapy (31), and need to be assessed. However, SSA treatment or peptide receptor radionuclide therapy can modify liver uptake, as previously reported (32), impacting the calculation of SRTB. Therefore, the systematic use of the pretherapeutic liver SUV_{max} cutoff could be a solution to following the evolution of SRTB parameters (31,33).

Our study presents some limitations. First, it was retrospective, included a heterogeneous cohort, and was conducted at a single center and on a single PET/CT scanner. Second, we included only patients with ^{68}Ga -DOTATOC-avid lesions, and using the liver SUV_{max} as the cutoff, the SRETVwb was equal to zero in 5 patients. This finding is explained by the low lesion volume in these patients, which did not impact their classification as good-prognosis patients. This point is crucial, because the same assertion should not be followed in patients with a high tumor burden without ^{68}Ga -DOTATOC uptake. In such a situation, the prognosis would be worse and ^{18}F -FDG PET/CT should be performed (5,23,24).

CONCLUSION

In our cohort, whole-body volumetric ^{68}Ga -DOTATOC PET/CT parameters (SRETVwb and TLSREwb) were associated with TTP and OS. SRTB could add value to conventional clinical prognostic parameters and other standard PET parameters (e.g., SUV_{max}) in predicting a patient's prognosis and guiding treatment decisions, thus supporting the implementation of SRTB in clinical practice. As previously mentioned, our results remain preliminary and applicable to ^{68}Ga -DOTATOC PET/CT but need to be validated in prospective studies and explored with other ^{68}Ga -peptides.

DISCLOSURE

No potential conflict of interest relevant to this article was reported.

KEY POINTS

QUESTION: Can whole-body volumetric parameters extracted from ^{68}Ga -DOTATOC PET/CT be useful in assessing the prognosis of WD NETs?

PERTINENT FINDINGS: In our cohort, whole-body volumetric ^{68}Ga -DOTATOC PET/CT parameters (SRETV and TLSRE) were associated with TTP and OS. SRETVwb was the only independent prognostic parameter, regardless of Ki-67 percentage, TNM stage at the time of PET, and treatment history (naïve vs. previous treatments) before PET scanning.

IMPLICATIONS FOR PATIENT CARE: In the future, whole-body volumetric ^{68}Ga -DOTATOC PET/CT parameters may add value to conventional prognostic parameters in predicting the prognosis of patients with WD NETs.

REFERENCES

1. Yao JC, Hassan M, Phan A, et al. One hundred years after "carcinoid": epidemiology of and prognostic factors for neuroendocrine tumors in 35,825 cases in the United States. *J Clin Oncol*. 2008;26:3063–3072.
2. Hentic O, Couvelard A, Rebours V, et al. Ki-67 index, tumor differentiation, and extent of liver involvement are independent prognostic factors in patients with liver metastases of digestive endocrine carcinomas. *Endocr Relat Cancer*. 2010;18:51–59.
3. Antunes P, Ginj M, Zhang H, et al. Are radiogallium-labelled DOTA-conjugated somatostatin analogues superior to those labelled with other radiometals? *Eur J Nucl Med Mol Imaging*. 2007;34:982–993.
4. Rufini V, Calcagni ML, Baum RP. Imaging of neuroendocrine tumors. *Semin Nucl Med*. 2006;36:228–247.
5. Carideo L, Proserpi D, Panzuto F, et al. Role of combined [^{68}Ga]Ga-DOTA-SST analogues and [^{18}F]FDG PET/CT in the management of GEP-NENs: a systematic review. *J Clin Med*. 2019;8:1032.
6. Shah MH, Goldner WS, Halfdanarson TR, et al. NCCN guidelines insights: neuroendocrine and adrenal tumors, version 2.2018. *J Natl Compr Canc Netw*. 2018;16:693–702.
7. Bozkurt MF, Virgolini I, Balogova S, et al. Guideline for PET/CT imaging of neuroendocrine neoplasms with ^{68}Ga -DOTA-conjugated somatostatin receptor targeting peptides and ^{18}F -DOPA. *Eur J Nucl Med Mol Imaging*. 2017;44:1588–1601.
8. Ambrosini V, Campana D, Bodei L, et al. ^{68}Ga -DOTANOC PET/CT clinical impact in patients with neuroendocrine tumors. *J Nucl Med*. 2010;51:669–673.
9. Sharma P, Naswa N, Kc SS, et al. Comparison of the prognostic values of ^{68}Ga -DOTANOC PET/CT and ^{18}F -FDG PET/CT in patients with well-differentiated neuroendocrine tumor. *Eur J Nucl Med Mol Imaging*. 2014;41:2194–2202.
10. Tirosh A, Papadakis GZ, Millo C, et al. Prognostic utility of total ^{68}Ga -DOTA-TATE-avid tumor volume in patients with neuroendocrine tumors. *Gastroenterology*. 2018;154:998–1008.e1.
11. Torihara A, Baratto L, Nobashi T, et al. Prognostic value of somatostatin receptor expressing tumor volume calculated from ^{68}Ga -DOTATATE PET/CT in patients with well-differentiated neuroendocrine tumors. *Eur J Nucl Med Mol Imaging*. 2019;46:2244–2251.
12. Inzani F, Petrone G, Rindi G. The new World Health Organization classification for pancreatic neuroendocrine neoplasia. *Endocrinol Metab Clin North Am*. 2018;47:463–470.
13. Nioche C, Orlhac F, Boughdad S, et al. LIFEX: a freeware for radiomic feature calculation in multimodality imaging to accelerate advances in the characterization of tumor heterogeneity. *Cancer Res*. 2018;78:4786–4789.
14. Foster B, Bagci U, Mansoor A, Xu Z, Mollura DJ. A review on segmentation of positron emission tomography images. *Comput Biol Med*. 2014;50:76–96.
15. Liberini V, De Santi B, Rampado O, et al. Impact of segmentation and discretization on radiomic features in ^{68}Ga -DOTA-TOC PET/CT images of neuroendocrine tumor. *EJNMMI Phys*. 2021;8:21.
16. Thuillier P, Maajem M, Schick U, et al. Clinical assessment of ^{177}Lu -DOTATATE quantification by comparison of SUV-based parameters measured on both post-PRRT SPECT/CT and ^{68}Ga -DOTATOC PET/CT in patients with neuroendocrine tumors: a feasibility study. *Clin Nucl Med*. 2021;46:111–118.
17. Kim Y, Yoo C, Oh SJ, et al. Tumour-to-liver ratio determined by [^{68}Ga]Ga-DOTA-TOC PET/CT as a prognostic factor of lanreotide efficacy for patients with

- well-differentiated gastroenteropancreatic-neuroendocrine tumours. *EJNMMI Res.* 2020; 15;10:63.
18. Eisenhauer EA, Therasse P, Bogaerts J, et al. New response evaluation criteria in solid tumours: revised RECIST guideline (version 1.1). *Eur J Cancer.* 2009;45:228–247.
 19. Youden WJ. Index for rating diagnostic tests. *Cancer.* 1950;3:32–35.
 20. Koo TK, Li MY. A guideline of selecting and reporting intraclass correlation coefficients for reliability research. *J Chiropr Med.* 2016;15:155–163.
 21. Ohnana J, Nataf V, Gauthier M, et al. Prognostic value of functional tumor burden on ⁶⁸Ga-DOTATOC PET/CT in patients with pancreatic neuro-endocrine tumors. *Neoplasma.* 2019;66:140–148.
 22. Ohlendorf F, Henkenberens C, Brunkhorst T, et al. Volumetric ⁶⁸Ga-DOTA-TATE PET/CT for assessment of whole-body tumor burden as a quantitative imaging biomarker in patients with metastatic gastroenteropancreatic neuroendocrine tumors. *QJ Nucl Med Mol Imaging.* April 14, 2020 [Epub ahead of print].
 23. Abdulrezak U, Kurt YK, Kula M, Tutus A. Combined imaging with ⁶⁸Ga-DOTA-TATE and ¹⁸F-FDG PET/CT on the basis of volumetric parameters in neuroendocrine tumors. *Nucl Med Commun.* 2016;37:874–881.
 24. Abgral R, Leboulleux S, Deandres D, et al. Performance of ¹⁸fluorodeoxyglucose-positron emission tomography and somatostatin receptor scintigraphy for high Ki67 (≥10%) well-differentiated endocrine carcinoma staging. *J Clin Endocrinol Metab.* 2011;96:665–671.
 25. Campana D, Ambrosini V, Pezzilli R, et al. Standardized uptake values of ⁶⁸Ga-DOTANOC PET: a promising prognostic tool in neuroendocrine tumors. *J Nucl Med.* 2010;51:353–359.
 26. Koch W, Auemhammer CJ, Geisler J, et al. Treatment with octreotide in patients with well-differentiated neuroendocrine tumors of the ileum: prognostic stratification with Ga-68-DOTA-TATE positron emission tomography. *Mol Imaging.* 2014;13:1–10.
 27. Velikyan I, Sundin A, Sorensen J, et al. Quantitative and qualitative intrapatient comparison of ⁶⁸Ga-DOTATOC and ⁶⁸Ga-DOTATATE: net uptake rate for accurate quantification. *J Nucl Med.* 2014;55:204–210.
 28. Poeppel TD, Binse I, Petersenn S, et al. ⁶⁸Ga-DOTATOC versus ⁶⁸Ga-DOTA-TATE PET/CT in functional imaging of neuroendocrine tumors. *J Nucl Med.* 2011;52:1864–1870.
 29. Eude F, Toledano MN, Vera P, Tilly H, Mihailescu S-D, Becker S. Reproducibility of baseline tumour metabolic volume measurements in diffuse large B-cell lymphoma: is there a superior method? *Metabolites.* 2021;11:72.
 30. Tutino F, Puccini G, Linguanti F, et al. Baseline metabolic tumor volume calculation using different SUV thresholding methods in Hodgkin lymphoma patients: interobserver agreement and reproducibility across software platforms. *Nucl Med Commun.* 2021;42:284–291.
 31. Liberini V, Rampado O, Gallio E, et al. ⁶⁸Ga-DOTATOC PET/CT-based radiomic analysis and PRRT outcome: a preliminary evaluation based on an exploratory radiomic analysis on two patients. *Front Med (Lausanne).* 2021;7:601853.
 32. Cherk MH, Kong G, Hicks RJ, Hofman MS. Changes in biodistribution on ⁶⁸Ga-DOTA-octreotate PET/CT after long acting somatostatin analogue therapy in neuroendocrine tumour patients may result in pseudoprogression. *Cancer Imaging.* 2018;18:3.
 33. Liberini V, Huellner MW, Grimaldi S, et al. The challenge of evaluating response to peptide receptor radionuclide therapy in gastroenteropancreatic neuroendocrine tumors: the present and the future. *Diagnostics (Basel).* 2020;10:1083.

Correlation of ^{68}Ga -FAPi-46 PET Biodistribution with FAP Expression by Immunohistochemistry in Patients with Solid Cancers: Interim Analysis of a Prospective Translational Exploratory Study

Christine E. Mona¹⁻³, Matthias R. Benz^{1,2}, Firas Hikmat¹, Tristan R. Grogan⁴, Katharina Lueckerath¹⁻³, Aria Razmaria¹, Rana Riahi⁵, Roger Slavik¹, Mark D. Girgis⁶, Giuseppe Carlucci^{1,2}, Kimberly A. Kelly⁷, Samuel W. French^{2,5}, Johannes Czernin¹⁻³, David W. Dawson^{*2,5}, and Jeremie Calais^{*1-3}

¹Ahmanson Translational Theranostics Division, Department of Molecular and Medical Pharmacology, David Geffen School of Medicine, UCLA, Los Angeles, California; ²Jonsson Comprehensive Cancer Center, UCLA, Los Angeles, California; ³Institute of Urologic Oncology, UCLA, Los Angeles, California; ⁴Department of Medicine Statistics Core, David Geffen School of Medicine, UCLA, Los Angeles, California; ⁵Department of Pathology and Laboratory Medicine, David Geffen School of Medicine, UCLA, Los Angeles, California; ⁶Division of Surgical Oncology, Department of Surgery, David Geffen School of Medicine, UCLA, Los Angeles, California; and ⁷Department of Biomedical Engineering, University of Virginia School of Engineering and Applied Sciences, and Robert M. Berne Cardiovascular Research Center, University of Virginia School of Medicine, Charlottesville, Virginia

Fibroblast activation protein (FAP)-expressing cancer-associated fibroblasts confer treatment resistance and promote metastasis and immunosuppression. Because FAP is overexpressed in many cancers, radiolabeled molecules targeting FAP are studied for their use as pancancer theranostic agents. This study aimed to establish the spectrum of FAP expression across various cancers by immunohistochemistry and to explore whether ^{68}Ga FAP inhibitor (FAPi)-46 PET biodistribution faithfully reflects FAP expression from resected cancer and non-cancer specimens. **Methods:** We conducted a FAP expression screening using immunohistochemistry on a pancancer human tissue microarray (141 patients, 14 different types of cancer) and an interim analysis of a prospective exploratory imaging trial in cancer patients. Volunteer patients underwent 1 whole-body ^{68}Ga -FAPi-46 PET/CT scan and, subsequently, surgical resection of their primary tumor or metastasis. ^{68}Ga -FAPi-46 PET SUV_{max} and SUV_{mean} was correlated with FAP immunohistochemistry score in cancer and tumor-adjacent non-cancer tissues for each patient. **Results:** FAP was expressed across all 14 cancer types on tissue microarray with variable intensity and frequency, ranging from 25% to 100% (mean, $76.6\% \pm 25.3\%$). Strong FAP expression was observed in 50%–100% of cancers of the bile duct, bladder, colon, esophagus, stomach, lung, oropharynx, ovary, and pancreas. Fifteen patients with various cancer types (colorectal [$n = 4$], head and neck [$n = 3$], pancreas [$n = 2$], breast [$n = 2$], stomach [$n = 1$], esophagus [$n = 2$], and uterus [$n = 1$]) underwent surgery after their ^{68}Ga -FAPi-46 PET/CT scan within a mean interval of 16.1 ± 14.4 d. ^{68}Ga -FAPi-46 SUVs and immunohistochemistry scores were higher in cancer than in tumor-adjacent non-cancer tissue: mean SUV_{max} 7.7 versus 1.6 ($P < 0.001$), mean SUV_{mean}

6.2 versus 1.0 ($P < 0.001$), and mean FAP immunohistochemistry score 2.8 versus 0.9 ($P < 0.001$). FAP immunohistochemistry scores strongly correlated with ^{68}Ga -FAPi 46 SUV_{max} and SUV_{mean} : $r = 0.781$ (95% CI, 0.376–0.936; $P < 0.001$) and $r = 0.783$ (95% CI, 0.379–0.936; $P < 0.001$), respectively. **Conclusion:** In this interim analysis of a prospective exploratory imaging trial, ^{68}Ga -FAPi-46 PET biodistribution across multiple cancers strongly correlated with FAP tissue expression. These findings support further exploration of FAPi PET as a pancancer imaging biomarker for FAP expression and as a stratification tool for FAP-targeted therapies.

Key Words: cancer; PET/CT; fibroblast activation protein; immunohistochemistry; ^{68}Ga -FAPi-46

J Nucl Med 2022; 63:1021–1026
DOI: 10.2967/jnumed.121.262426

Fibroblast activation protein (FAP) is strongly expressed on cancer-associated fibroblasts and is a key player in tumor progression (1). High FAP expression is restricted almost exclusively to cancer-associated fibroblasts and serves as an independent negative prognostic factor for multiple types of cancer (2). In vivo depletion of FAP-positive stromal cells inhibits tumor growth by decreasing cancer support, increasing antitumor immunity, and limiting stromal barrier effects (3–5). However, targeting the enzymatic activity of FAP with antibodies does not yield beneficial clinical effects (6,7). Recently, FAP inhibitor (FAPi)-targeting ligands labeled with radioisotopes for PET imaging (e.g., ^{68}Ga and ^{18}F for PET) and therapy (e.g., ^{177}Lu and ^{90}Y) have been introduced (8,9). The high tumor uptake that was observed with FAPi PET imaging in various cancers suggests that radiolabeled FAPi compounds have promising potential for diagnostic and therapeutic applications (10).

In this prospective translational, exploratory study, we aimed at assessing the utility of FAPi PET imaging as a pancancer imaging biomarker for FAP expression. We first surveyed tissue microarrays (TMAs) of 141 patients with 14 cancer types for the presence

Received Apr. 12, 2021; revision accepted Oct. 6, 2021.
For correspondence or reprints, contact Jeremie Calais (jcalais@mednet.ucla.edu) or Christine E. Mona (cmona@mednet.ucla.edu).

*Contributed equally to this work.

Guest Editor: Barry A. Siegel, Mallinckrodt Institute of Radiology

Published online Nov. 5, 2021.

Immediate Open Access: Creative Commons Attribution 4.0 International License (CC BY) allows users to share and adapt with attribution, excluding materials credited to previous publications. License: <https://creativecommons.org/licenses/by/4.0/>. Details: <http://jnm.snmjournals.org/site/misc/permission.xhtml>.

COPYRIGHT © 2022 by the Society of Nuclear Medicine and Molecular Imaging.

and degree of FAP expression by immunohistochemistry (11). A cohort of surgical patients representing 10 of those cancer types was then tested to determine the correlation between ^{68}Ga -FAPi-46 PET biodistribution and FAP immunohistochemistry expression in excised tumor tissue.

MATERIALS AND METHODS

TMA Screening

FAP expression in human tumor tissue was assessed using a pan-cancer TMA obtained from the University of Virginia. This TMA included 141 patients with 14 different types of cancer (bile duct, bladder, breast, colon, esophagus, stomach, liver, lung, ovary, oropharynx, pancreas, prostate, kidney, and uterus; 6–14 tumors per tissue type). Normal tissues present on the TMA were also evaluated (5–8 samples per tissue type). After deparaffinization and rehydration, heat-induced antigen retrieval (sodium citrate, 0.05% polysorbate 20, pH 6.0) was performed for 20 min using a vegetable steamer followed by quenching of endogenous peroxidase activity (3% hydrogen peroxide, 10 min). Primary antibody incubation with a 1:50 dilution of rabbit monoclonal anti-FAP α -[EPR20021] (ab207178; Abcam) was performed overnight at 4°C. Detection was performed using the ultraView Universal DAB Detection Kit (K3467; DAKO) per the manufacturer's instructions. An experienced surgical pathologist (DWD) confirmed the histologic diagnoses and performed a immunohistochemistry analysis using a semiquantitative visual scoring system (0, negative staining; 1, weak staining; 2, strong staining).

Clinical Study Design and Participants

We conducted a prospective exploratory biodistribution study of ^{68}Ga -FAPi-46 PET imaging under the Radioactive Drug Research Committee Program (title 21 of *Code of Federal Regulations*, section 361.1). The primary objective was to define the biodistribution of ^{68}Ga -FAPi-46 PET in normal and cancer tissues and further correlate with tissue expression as determined by FAP immunohistochemistry. Volunteer cancer patients scheduled to undergo surgical resection of a primary tumor or metastasis were eligible (the inclusion and exclusion criteria are in Supplemental Table 1; supplemental materials are available at <http://jnm.snmjournals.org>). The type of surgery depended on the location and disease as determined by clinical standard-of-care explorations. ^{68}Ga -FAPi-46 PET/CT imaging findings did not impact the therapy plan, and surgery was performed independently of the results of the scan findings. The study was approved by the UCLA Institutional Review Board (approval 19-000756) and registered on ClinicalTrials.gov (NCT04147494). All patients provided oral and written informed consent.

We present here the results of an interim analysis that was mandated by the UCLA Jonsson Comprehensive Cancer Center Internal Scientific Peer Review Committee and Data Safety Monitoring Board after completed enrollment of 15 patients.

FAPi PET/CT Image Acquisition

^{68}Ga -FAPi-46 was used as the FAP-targeted radioligand (8). The mean injected activity was 184 ± 3 MBq (range, 174–185 MBq). The mean uptake time was 63 ± 10 min (range, 54–96 min). Images were acquired using 64-detector PET/CT scanners (Biograph 64 mCT [$n = 7$] or Biograph 64 TruePoint [$n = 8$]; Siemens Healthcare). Unenhanced CT (120 kV, 80 mAs) was performed for attenuation correction and anatomic correlation of the PET findings. PET images were acquired from vertex to mid thigh, using an emission time of 2–4 min per bed position, depending on patient body weight. All PET images were reconstructed using correction for attenuation, dead time, random events, and scatter. PET images were reconstructed using an iterative algorithm (ordered-subset expectation maximization).

FAPi PET/CT Image Analysis

Images were analyzed in consensus by 2 readers (MRB, JCa) blinded to the histopathology and immunohistochemistry results. The readers had access to all medical records and other imaging modality results available to facilitate tumor localization. Image analysis was performed with OsiriX (Pixmeo) (12). The readers quantified the ^{68}Ga -FAPi-46 PET uptake in cancer tissue and tumor-adjacent non-cancer tissue by placing volumes of interest in the tumor lesions and the surrounding normal tissue in the same organ. The readers adapted the size of the volume of interest visually to best encompass the structure of interest and to preclude overlapping of activity between the cancer and non-cancer volumes of interest. Anatomic CT information was used to avoid activity spillover from other organs. SUV_{mean} , SUV_{max} , and lesion size by CT were recorded.

Histopathology and Immunohistochemistry Analysis

Clinical pathology reports were used to collect final pathology diagnoses and pathologic TNM staging. Representative sections of normal and tumor tissue from surgical resection specimens were obtained from the UCLA Department of Pathology through the UCLA Translational Pathology Core Laboratory. FAP immunohistochemistry staining was performed as described above.

All hematoxylin and eosin slides from each surgical pathology case were evaluated to select representative sections consisting of normal and tumor tissue for immunohistochemistry evaluation. One representative section that best reflected the overall tumor histology (i.e., histologic type and grade, relative stroma and tumor cell component), that included sampling of both the edge and the central portions of the tumor mass, and that contained surrounding adjacent normal tissue (>5 mm distance from malignant cells) was selected for each patient. Immunohistochemistry stains were independently scored by 2 pathologists (DWD, SWF) who did not know each other's scores, the clinical information, or the PET imaging results. A semiquantitative approach adapted from a prior study was used (13). Briefly, FAP expression was assessed globally across the entire cross-sectional area of tumor and adjacent nonmalignant tissue without any specific focus on invasive fronts or areas of active tumor growth. The tumor compartment was defined on the basis of morphologic assessments as the geographic area where malignant cells were present, as well as the immediately adjacent area of intratumoral and peritumoral stromal response. A score of 0 was defined as complete absence of staining or weak staining in less than 10% of the area under assessment. A score of 1 was defined as weak expression in greater than 10% of the area under assessment. A score of 2 was defined as moderate or strong expression in 10%–50% of the area under assessment. A score of 3 was defined as moderate or strong expression in more than 50% of the area under assessment.

Cross-Sectional Correlation Analysis of the FAPi PET Signal and FAP Immunohistochemistry Staining

The ^{68}Ga -FAPi-46 PET SUV and the FAP immunohistochemistry score of cancer and tumor-adjacent non-cancer tissue were evaluated for correlation on a per-patient basis: for each tumor lesion, the ^{68}Ga -FAPi-46 PET SUV of the lesion was evaluated for correlation with the immunohistochemistry score of the tumor compartment on the selected pathology slide, and the ^{68}Ga -FAPi-46 PET SUV of the normal tissue surrounding the tumor lesion was evaluated for correlation with the immunohistochemistry score of the tumor-adjacent non-cancer tissue available on the same pathology slide as that containing the tumor lesion.

Statistics

Patient characteristics and study variables were summarized using mean, SD, ranges, or frequency (%) as appropriate. To test for differences in expression levels of both immunohistochemistry and PET measures between cancer and non-cancer tissues, the 2 groups were compared using P values from a generalized-estimating-equation model (to properly account for the repeated-measures design of the

study) (14). For assessing the association between immunohistochemistry and PET findings, we computed repeated-measures correlation coefficients. Interreader agreement for the immunohistochemistry scoring was assessed using Cohen κ -statistics. *P* values of less than 0.05 were considered statistically significant. Analyses were performed using SAS (version 0.4; SAS Institute) and R (version 3.6.1, Rmcrr package; www.r-project.org). Because of the exploratory nature of this study and the Radioactive Drug Research Committee-mandated limit of 30 patients, with an interim analysis after 15 patients mandated by the UCLA Institutional Review Board, a power analysis for sample size was not performed.

RESULTS

TMA Analysis

Representative FAP immunohistochemistry scoring by cancer type performed in the TMA is shown in Figure 1. FAP expression was present in 80.9% (114/141) of tumors. Of the 114 positive tumors, FAP expression was stromal in 108, epithelial in 1, and mixed in 5 (lung cancer [*n* = 1], ovarian cancer [*n* = 1], oropharynx [*n* = 1], pancreatic [*n* = 1], and uterine cancer [*n* = 1]). No stroma was present for evaluation in 1 case of ovarian cancer (0.7%).

Although there was variability in the intensity and frequency of FAP expression, FAP was positive in more than 50% of cases from 11 of 14 cancer types. Strong FAP expression was observed in 50%–100% of cancers from the bile duct, bladder, colon,

esophagus, stomach, lung, oropharynx, ovary, and pancreas. Liver, prostate, and renal cell cancer were the 3 tumor types with the lowest FAP expression.

This TMA survey provided a rationale for the design of the subsequent clinical PET imaging study.

PET Imaging Study Cohort

Between December 2019 and May 2020, 15 patients (8 men and 7 women; mean age, 60.7 ± 10.5 y) with 7 different cancer types (colorectal [*n* = 4], head and neck [*n* = 3], pancreatic [*n* = 2], breast [*n* = 2], gastric [*n* = 1], esophageal [*n* = 2], and uterine [*n* = 1] cancer) were enrolled. Supplemental Table 2 summarizes the demographics and clinical characteristics of the study population. All 15 patients underwent ^{68}Ga -FAPi-46 PET/CT and subsequent surgery within 16.1 ± 14.4 d (range, 1–50 d) after the scan. Two patients had tumors deemed unresectable at the time of surgery (gastric linitis plastica with duodenal extension, patient 3; pancreatic cancer with venous involvement, patient 14).

^{68}Ga -FAPi-46 PET Biodistribution in Cancer Lesions, Normal Organs, and Non-Cancer Tissues

The ^{68}Ga -FAPi-46 biodistribution as determined by SUV_{mean} in normal organs is described in Supplemental Table 3 and Supplemental Figure 1. The ^{68}Ga -FAPi-46 SUVs and the size of the cancer lesions are provided in Supplemental Tables 4 (primary tumors) and 5 (metastases).

Normal Organs and Non-Cancer Tissues.

The highest normal-organ ^{68}Ga -FAPi-46 PET signals were in the urinary bladder (because of urinary excretion) and the uterus (because of normal myometrial FAP expression). Other organs with notable ^{68}Ga -FAPi-46 uptake included the submandibular glands, Waldeyer ring, pancreas, and kidneys (average $\text{SUV}_{\text{mean}} < 2.5$). ^{68}Ga -FAPi-46 uptake higher than in normal tissues was noted in 3 lesions (SUV_{max} of 4.4, 2.4, and 2.6) that subsequently revealed a benign pathology, including an elastofibroma dorsi (patient 3) and 2 areas of fibrosis or scarring in breast tissue (patient 11).

Cancer Tissues. The average ^{68}Ga -FAPi-46 SUV_{mean} and SUV_{max} was 7.2 ± 4.4 (range, 1.5–15.2) and 8.6 ± 5.2 (range, 1.7–19), respectively, in primary tumors (*n* = 15) and 4.3 ± 2.9 (range, 2.1–8.8) and 5.3 ± 3.6 (range, 2.7–10.8), respectively, in metastases (*n* = 6). The cancer types with the highest uptake were those of the pancreas, stomach, colon, and uterus. The lowest uptake was in 2 patients with a complete response to neoadjuvant therapy (patients 13 and 15) and thus low FAP expression

Immunohistochemistry Findings

Histologic sections from 13 patients who underwent tumor resection were analyzed. Normal tissue adjacent to tumors and tumor tissue from individual histologic sections were available for immunohistochemistry in 13 of 15 (87%) and 11 of 15

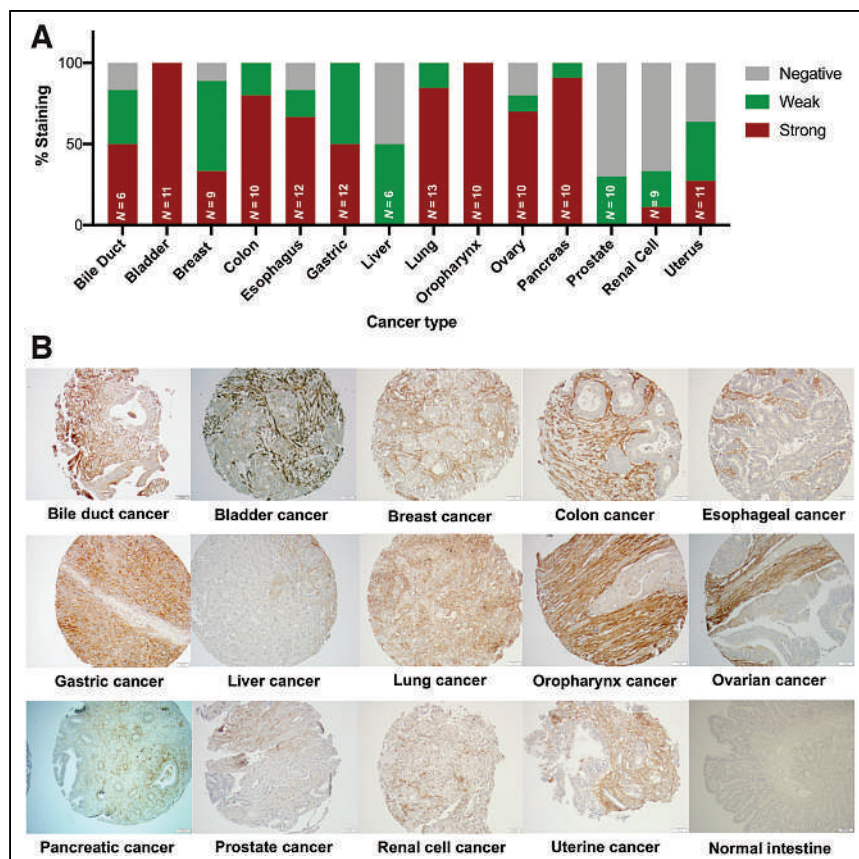


FIGURE 1. FAP expression by immunohistochemistry in 14 cancer types and normal tissues (TMA analysis). (A) Quantification of FAP expression per cancer type. FAP intensity was evaluated using semiquantitative visual scoring system that accounts for staining intensity (0, negative; 1, weak; 2, strong). (B) FAP immunohistochemistry expression on representative tissue core from indicated cancer or normal tissue type.

patients (73%), respectively. Primary tumor, metastasis, or both primary tumor and metastasis were evaluated in 7 of 11 (63%), 2 of 11 (18%), and 2 of 11 (18%) cases, respectively. The FAP scoring between the 2 pathologists was in almost perfect agreement ($\kappa = 0.89$).

Primary Tumors. The highest FAP immunohistochemistry scores were observed in pancreatic, esophageal, and breast cancer. FAP staining was confined exclusively to the tumor-associated stromal compartment in most patients (12/13; 92.3%) and ranged from weak to strong expression (1–3). The staining intensity was the greatest in stromal areas within and immediately adjacent to (peritumoral) the malignant epithelial compartment of tumors as shown in a case example in Figure 2 (patient 10).

Metastatic Lesions. All 4 evaluated metastatic lesions (3 lymph nodes and 1 liver metastasis) were positive for FAP, including stromal staining in 3 of the 4 and malignant epithelial cell staining in 1 of the 4 (uterine squamous cell carcinoma involving a left pelvic lymph node, patient 8). FAP staining was equivalent between primary and metastatic lesions in 2 patients with tissue available for comparative analysis (patients 6 and 15, Supplemental Fig. 2).

Tumor-Adjacent Non-Cancer Tissues. Staining was absent or weak in most normal tissues (71.4% negative, 25% weak, 3.6% moderate) and observed primarily in capillary and small-vessel endothelium. FAP expression was moderate in a concurrently resected benign elastofibroma dorsi (patient 3) and was moderate to strong in 2 areas of radial scarring and biopsy site changes in benign breast tissue without cancer (patient 11, Supplemental Fig. 3).

Correlation of ^{68}Ga -FAPi-46 PET Signal and FAP Immunohistochemistry Staining in Cancer and Tumor-Adjacent Non-Cancer Tissues (Per-Patient Analysis)

Supplemental Figures 4–16 depict each patient case with an available cross-sectional correlation analysis of the ^{68}Ga -FAPi-46 PET signal and FAP immunohistochemistry staining score.

^{68}Ga -FAPi-46 SUV_{max} and SUV_{mean} , and the FAP immunohistochemistry score, were higher in cancer tissue than in

tumor-adjacent non-cancer tissue: mean SUV_{max} was 7.7 (95% CI, 5.1–10.3) versus 1.6 (95% CI, 0.9–2.2; $P < 0.001$), respectively; mean SUV_{mean} was 6.2 (95% CI, 4.0–8.3) versus 1.0 (95% CI, 0.7–1.3; $P < 0.001$), respectively; and mean FAP immunohistochemistry score was 2.8 (95% CI, 2.6–3.0; $P < 0.001$) versus 0.9 (95% CI, 0.4–1.4; $P < 0.001$), respectively (Fig. 3).

The FAP immunohistochemistry score correlated positively both with ^{68}Ga -FAPi-46 SUV_{max} across cancer and tumor-adjacent non-cancer tissues ($r = 0.781$ [95% CI, 0.376–0.936], $P < 0.001$) and with SUV_{mean} ($r = 0.783$ [95% CI, 0.379–0.936], $P < 0.001$) (Fig. 4). FAP immunohistochemistry scores of 0, 1, 2, and 3 corresponded to a mean ^{68}Ga -FAPi-46 SUV_{max} of 1.2 (95% CI, 0.8–1.6), 1.9 (95% CI, 0.4–3.3), 3.9 (95% CI, 2.8–4.9), and 7.4 (95% CI, 4.5–10.3), respectively. CT size tended to correlate positively with SUV_{max} (Spearman $r = 0.57$; $P = 0.054$) and SUV_{mean} (Spearman $r = 0.54$; $P = 0.068$).

DISCUSSION

In this translational study, we aimed to establish the spectrum of FAP expression across various cancers by immunohistochemistry and to explore whether ^{68}Ga -FAPi-46 PET biodistribution faithfully reflects FAP expression in cancer patients. We report here the results of a TMA analysis from 141 patients with 14 different types of cancer and of an interim analysis of a prospective exploratory imaging trial that included 15 patients. FAP was expressed across all cancer types with variable intensity and frequency. We established a positive and significant correlation between FAP-target expression and FAPi PET SUVs.

Cancer-associated fibroblasts are key constituents of the tumor stroma that can support an immunosuppressive microenvironment and tumor cell growth, progression, and metastatic potential (1). Depleting the stroma can improve delivery of drugs or systemically applied radiation and enhance cancer immune responses (15). Thus, FAP expressed by cancer-associated fibroblasts is an attractive diagnostic and therapeutic target (16). Target specificity

and tumor-specific uptake are critical determinants of the accuracy and efficacy of PET probes for diagnosis and therapy (17). FAP frequently is strongly expressed in solid tumors, with only limited expression in normal tissues, making it an attractive theranostic target (10).

FAPi PET imaging has reported high tumor-to-background characteristics (10). However, FAPi PET human biodistribution in cancer has not been validated against tumor FAP expression as assessed by immunohistochemistry in a pancancer approach. Recently, a study showed a strong association between tumor ^{68}Ga -FAPi-46 PET uptake intensity and histopathologic FAP expression in sarcoma tumors (18). Here, we first screened TMAs from 14 cancers for FAP expression to guide patient selection for the exploratory imaging trial. Guided by our initial TMA screening, we intentionally selected multiple cancer types to validate the pancancer approach. In the interim analysis of this prospective exploratory trial, the biodistribution of ^{68}Ga -FAPi-46 PET correlated

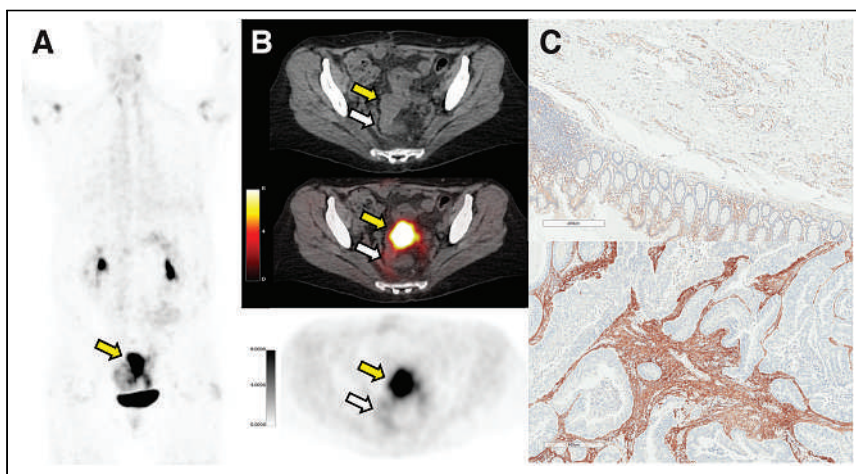


FIGURE 2. Matched ^{68}Ga -FAPi-46 PET/CT and immunohistochemistry results for patient 10, 56-y-old woman with sigmoid colon adenocarcinoma who underwent colorectal anterior resection (ypT4b N0 M0). In area corresponding to resected mass as shown by yellow arrows (PET maximum-intensity projection [A], axial CT [B, top], axial PET/CT [B, middle], and axial PET [B, bottom]), ^{68}Ga -FAPi-46 PET/CT showed intense uptake (SUV_{max} , 15.9; SUV_{mean} , 12.8). FAP immunohistochemistry on representative histologic sections demonstrated absent to weak FAP expression seen predominantly as vessel endothelial cell staining in normal tissue (C, top) and strong FAP expression in intratumoral and peritumoral stromal (C, bottom). White arrows depict normal region resected.

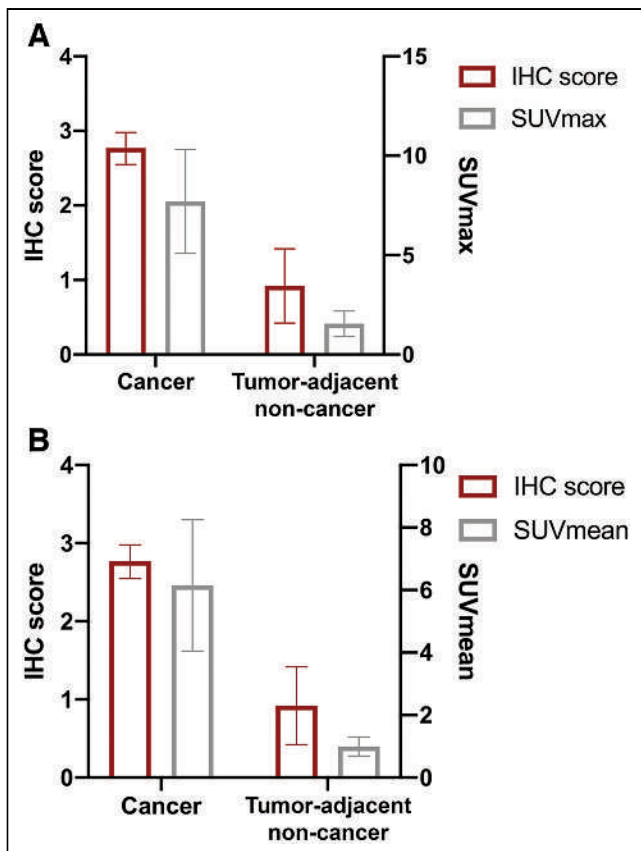


FIGURE 3. FAP immunohistochemistry (IHC) score with ^{68}Ga -FAPi-46 PET SUV_{max} (A) and SUV_{mean} (B) in cancer and tumor-adjacent non-cancer tissues. Each bar represents mean with SD.

strongly with FAP expression in cancer versus normal tissues across 7 different cancer types, supporting its potential role as a pancancer predictive biomarker for FAP-targeted therapies. In a subset of patients, the ^{68}Ga -FAPi-46 SUV_{max} of metastasis was also comparable to that of their primary tumor, suggesting that FAP expression may be consistent across primary and metastatic lesions within individual patients, which has important implications for its role as a theranostic in the setting of advanced disease (19).

These findings support further exploration of ^{68}Ga -FAPi-46 as a potential pancancer imaging biomarker for FAP expression. This use could find application as an enrichment biomarker or patient selection tool for clinical trials and as a potential predictor of treatment response in the clinic. Extensive emerging data implicate FAP-positive cells as important accomplices involved in cancer progression and metastases. Evaluating FAP-targeting small-molecule inhibitors, antibodies, bispecific T-cell engagers, and radioligand therapy requires a means for verifying whole-body target expression (20).

The main limitation of the study was the small sample size. This was an exploratory study, and local oversight committees (Internal Scientific Peer Review Committee, Data Safety Monitoring Board) mandated an interim analysis after the first 15 patients. This interim analysis revealed a strong correlation between immunohistochemistry and PET findings in 14 patients, which provided the motivation to publish the data.

Another major limitation was the intratumor heterogeneity and sampling bias inherent in the histopathology and immunochemistry analysis. Unfortunately, autoradiography was not possible in

this exploratory study because a second administration of ^{68}Ga -FAPi-46 just before surgery was not practical. We performed an evaluation of all hematoxylin and eosin slides from each surgical pathology case to select the section best representing the overall tumor histology or its surrounding tumor-adjacent non-cancer tissue.

A perfect anatomic match between tumor SUV measurements and immunohistochemistry scores was unfortunately not possible because tumors were not resected in a defined orientation (unlike in prostate cancer). Therefore, we collected the SUV_{max} and SUV_{mean} of the whole tumor lesion.

Another limitation is that visual immunohistochemistry scoring by pathologists is semiquantitative only, is subjective, and produces ordinal rather than continuous variable data. Computer-aided analysis with automatic immunohistochemistry scoring may overcome these limitations. However, even with semiquantitative ordinal data, the correlation of immunohistochemistry scoring with SUV was strong. Furthermore, the interreader scores between the 2 pathologists was in near-perfect agreement.

CONCLUSION

In this interim analysis of a prospective exploratory imaging trial, ^{68}Ga -FAPi-46 PET biodistribution correlated strongly with FAP expression in cancer and tumor-adjacent non-cancer tissues across multiple cancer types. These data support the use of ^{68}Ga -FAPi-46 PET as a pancancer predictive biomarker and stratification tool for FAP-targeted therapeutic approaches and lay the foundation for future evaluation of FAPi ligands labeled with therapeutic isotopes in clinical trials.

DISCLOSURE

This was an investigator-initiated trial with support from the Society of Nuclear Medicine and Molecular Imaging (2019 Molecular Imaging Research Grant for Junior Academic Faculty 20194491 [principal investigator, Jeremie Calais]) and the Prostate Cancer Foundation (2019 Challenge Award 19CHAL02 [principal investigator, Johannes Czernin] and 2020 Young Investigator Award 20YOUN05 [principal investigator, Jeremie Calais]). Johannes Czernin is a founder, holds equity in, and is a board member of Sofie Biosciences and Momentum Biosciences, which have licensed intellectual property of FAPi compounds from the University of Heidelberg. He is also a cofounder of Trethera Therapeutics and serves on the Medical Advisory Boards of Point Pharma and Actinium Pharmaceuticals. Jeremie Calais reports

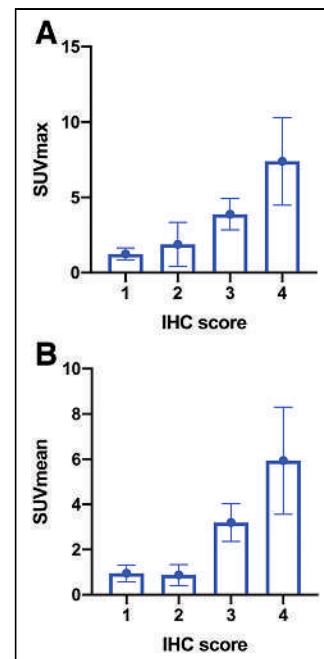


FIGURE 4. Correlation between FAP immunohistochemistry (IHC) score and ^{68}Ga -FAPi-46 PET SUV_{max} (A) and SUV_{mean} (B) across cancer and tumor-adjacent non-cancer tissues. $r = 0.781$ in A (95% CI, 0.376–0.936; $P < 0.001$) and $r = 0.783$ in B (95% CI, 0.379–0.936; $P < 0.001$).

prior consulting activities for Advanced Accelerator Applications, Blue Earth Diagnostics, Curium Pharma, GE Healthcare, Janssen Pharmaceuticals, Progenics Radiopharmaceuticals, Radiomedix, and Telix Pharmaceuticals, outside the submitted work. Christine Mona and Katharina Lueckerath report consulting activities for Sofie Biosciences/iTheragnostics outside the submitted work. No other potential conflict of interest relevant to this article was reported.

ACKNOWLEDGMENTS

We thank all the patients and their referring physicians whose willingness to participate made this study possible. We thank the whole staff of the UCLA Nuclear Medicine and Theragnostics Division, whose hard work made this study possible. We thank the UCLA Translational Pathology Core Laboratory for their excellent technical assistance.

KEY POINTS

QUESTION: Is FAPi PET imaging a reliable biomarker of FAP expression in cancer and tumor-adjacent non-cancer tissues?

PERTINENT FINDINGS: In this translational study using TMA and an interim analysis of a prospective exploratory imaging trial in 15 surgical oncology patients, the FAPi PET uptake and FAP expression per immunohistochemistry correlated strongly in cancer and tumor-adjacent non-cancer tissue.

IMPLICATIONS FOR PATIENT CARE: FAPi PET uptake correlates strongly with FAP expression in cancer patients, and FAPi PET may thus serve as a predictive biomarker for FAP-targeted therapeutic approaches.

REFERENCES

1. Gascard P, Tlsty TD. Carcinoma-associated fibroblasts: orchestrating the composition of malignancy. *Genes Dev.* 2016;30:1002–1019.
2. Fitzgerald AA, Weiner LM. The role of fibroblast activation protein in health and malignancy. *Cancer Metastasis Rev.* 2020;39:783–803.
3. Lo A, Wang LS, Scholler J, et al. Tumor-promoting desmoplasia is disrupted by depleting FAP-expressing stromal cells. *Cancer Res.* 2015;75:2800–2810.
4. Fearon DT. The carcinoma-associated fibroblast expressing fibroblast activation protein and escape from immune surveillance. *Cancer Immunol Res.* 2014;2:187–193.
5. Kraman M, Bambrough PJ, Arnold JN, et al. Suppression of antitumor immunity by stromal cells expressing fibroblast activation protein- α . *Science.* 2010;330:827–830.
6. Eager RM, Cunningham CC, Senzer N, et al. Phase II trial of talabostat and docetaxel in advanced non-small cell lung cancer. *Clin Oncol (R Coll Radiol).* 2009;21:464–472.
7. Liu R, Li H, Liu L, Yu J, Ren X. Fibroblast activation protein: a potential therapeutic target in cancer. *Cancer Biol Ther.* 2012;13:123–129.
8. Loktev A, Lindner T, Burger EM, et al. Development of fibroblast activation protein-targeted radiotracers with improved tumor retention. *J Nucl Med.* 2019;60:1421–1429.
9. Loktev A, Lindner T, Mier W, et al. A tumor-imaging method targeting cancer-associated fibroblasts. *J Nucl Med.* 2018;59:1423–1429.
10. Kratochwil C, Flechsig P, Lindner T, et al. ^{68}Ga -FAPi PET/CT: tracer uptake in 28 different kinds of cancer. *J Nucl Med.* 2019;60:801–805.
11. Kallioniemi OP, Wagner U, Kononen J, Sauter G. Tissue microarray technology for high-throughput molecular profiling of cancer. *Hum Mol Genet.* 2001;10:657–662.
12. Rosset A, Spadola L, Ratib O. OsiriX: an open-source software for navigating in multidimensional DICOM images. *J Digit Imaging.* 2004;17:205–216.
13. Henry LR, Lee HO, Lee JS, et al. Clinical implications of fibroblast activation protein in patients with colon cancer. *Clin Cancer Res.* 2007;13:1736–1741.
14. Bakdash JZ, Marusich LR. Repeated measures correlation. *Front Psychol.* 2017;8:456.
15. Barsoumian HB, Ramapriyan R, Younes AI, et al. Low-dose radiation treatment enhances systemic antitumor immune responses by overcoming the inhibitory stroma. *J Immunother Cancer.* 2020;8:e000537.
16. Narunsky L, Oren R, Bochner F, Neeman M. Imaging aspects of the tumor stroma with therapeutic implications. *Pharmacol Ther.* 2014;141:192–208.
17. Huang R, Wang M, Zhu Y, Conti PS, Chen K. Development of PET probes for cancer imaging. *Curr Top Med Chem.* 2015;15:795–819.
18. Kessler L, Ferdinandus J, Hirmas N, et al. ^{68}Ga -FAPi as a diagnostic tool in sarcoma: data from the ^{68}Ga -FAPi PET prospective observational trial. *J Nucl Med.* 2022;63:89–95.
19. Arranja AG, Pathak V, Lammers T, Shi Y. Tumor-targeted nanomedicines for cancer theragnostics. *Pharmacol Res.* 2017;115:87–95.
20. Lindner T, Loktev A, Giesel F, Kratochwil C, Altmann A, Haberkorn U. Targeting of activated fibroblasts for imaging and therapy. *EJNMMI Radiopharm Chem.* 2019;4:16.

The Quest for an Accurate Functional Tumor Volume with ^{68}Ga -DOTATATE PET/CT

Ryan P. Reddy¹, C. Ross Schmidlein¹, Romina G. Giancipoli², Audrey Mauguen³, Daniel LaFontaine¹, Heiko Schoder¹, and Lisa Bodei¹

¹Molecular Imaging and Therapy Service, Department of Radiology, Memorial Sloan Kettering Cancer Center, New York, New York;

²Department of Nuclear Medicine, La Sapienza University of Rome, Rome, Italy; and ³Department of Epidemiology and Biostatistics, Memorial Sloan Kettering Cancer Center, New York, New York

^{68}Ga -labeled somatostatin analog (SSA) PET/CT is now a standard-of-care component in the management of neuroendocrine tumors (NETs). However, treatment response for NETs is still assessed with morphologic size measurements from other modalities, which can result in inaccuracy about the disease burden. Functional tumor volume (FTV) acquired from SSA PET/CT has been suggested as a possible metric, but no validated measurement tool to measure FTV exists. We tested the precision of multiple FTV computational approaches compared with morphologic volume measurements to identify a candidate for incorporation into future FTV studies to assess tumor burden more completely and accurately. **Methods:** The clinical and imaging data of 327 NET patients were collected at Memorial Sloan Kettering Cancer Center between December 2016 and April 2018. Patients were required to have SSA PET/CT and dedicated CT scans within 6 wk and were excluded if they had any intervention between scans. When paired studies were evaluated, 150 correlating lesions demonstrated SSA. Lesions were excluded if they contained necrotic components or were lobulated. This exclusion resulted in 94 lesions in 20 patients. The FTV for each lesion was evaluated with a hand-drawn assessment and 3 automated techniques: 50% threshold from SUV_{max} , 42% threshold from SUV_{max} , and background-subtracted lesion activity. These measurements were compared with volume calculated from morphologic volume measurements. **Results:** The FTV calculation methods showed varying correlations with morphologic volume measurements. FTV using a 42% threshold had a 0.706 correlation, hand-drawn volume from PET imaging had a 0.657 correlation, FTV using a 50% threshold had a 0.645 correlation, and background-subtracted lesion activity had a 0.596 correlation. The Bland-Altman plots indicated that all FTV methods had a positive mean difference from morphologic volume, with a 50% threshold showing the smallest mean difference. **Conclusion:** FTV determined with thresholding of SUV_{max} demonstrated the strongest correlation with traditional morphologic lesion volume assessment and the least bias. This method was more accurate than FTV calculated from hand-drawn volume assessments. Threshold-based automated FTV assessment promises to better determine disease extent and prognosis in patients with NETs.

Key Words: functional tumor volume; neuroendocrine tumors; somatostatin analogs; PET/CT

J Nucl Med 2022; 63:1027–1032

DOI: 10.2967/jnumed.121.262782

Neuroendocrine tumors (NETs) encompass a group of diverse neoplasms that typically originate from the gastrointestinal tract, the pancreas, and the bronchopulmonary tract. Although they can have varying presentations, they have similar histopathologic features and may secrete biologically active compounds (1). Given a general lack of awareness of NETs and their slow-growing nature, diagnosis is missed 20%–40% of the time or is made only at a later stage because of detectable findings such as tumor mass effects or biomarker secretions. At this stage, metastatic disease is typically present, and curative options are no longer feasible (2). Common treatments include locoregional treatments and conventional chemotherapy. Recently, peptide receptor radionuclide therapy with radiolabeled somatostatin analogs (SSAs) has been approved as an additional treatment option for inoperable or metastatic gastroenteropancreatic NETs (2,3).

Imaging plays a pivotal role in diagnosis, staging, treatment selection, and follow-up of NETs (4). A combination of somatostatin receptor imaging and morphologic cross-sectional CT or MRI is now performed to acquire all clinically relevant information. Somatostatin receptor imaging targets the high density of somatostatin receptors that predominate on the cell membranes of low-grade NETs. In recent years, the use of PET/CT with ^{68}Ga -labeled SSAs, such as ^{68}Ga -DOTATATE PET/CT, has demonstrated sensitivity and resolution superior to that of conventional ^{111}In -octreotide scanning. This modality is now Food and Drug Administration–approved, has become an accepted standard-of-care imaging modality (5–7), and has substantially improved the identification and management of NETs.

Despite the introduction of SSA PET/CT, the clinical and research response of NETs to treatment is still assessed with morphologic size measurements, such as RECIST 1.1, that are obtained solely with CT and MRI. Morphologic assessment can exclude many sites of disease identifiable only on SSA PET/CT. Additionally, morphologic size measurements have limited applicability for slow-growing lesions such as NETs. This can result in underestimation of therapeutic effects and can inaccurately bias management decisions (8–10). Some lesion assessments, such as the Choi criteria, attempt to correct for these variables, but the dependence on CT or MRI still limits disease assessment for many patients with low-grade NETs (11–13).

Because the inclusion of SSA PET/CT better evaluates the full extent of NET disease, a measurement technique using these PET imaging data can provide a more complete and accurate disease assessment for NETs. Prior literature has suggested that functional

Received Jul. 1, 2021; revision accepted Oct. 25, 2021.

For correspondence or reprints, contact Ryan P. Reddy (reddyr@mskcc.org).

Published online Nov. 12, 2021.

COPYRIGHT © 2022 by the Society of Nuclear Medicine and Molecular Imaging.

tumor volume (FTV) is a possible suitable metric (14,15) and has shown promise of prognostic utility for FTV in NETs (15–19). However, no validated approach has yet been developed to calculate FTV in SSA PET/CT imaging. In prior investigations, the method to calculate FTV has varied and was often chosen arbitrarily on the basis of prior approaches and techniques with ^{18}F -FDG PET/CT. For example, Abdulrezzak et al. (16) and Toriihara et al. (17) used a 50% threshold of SUV_{max} , Ohnana et al. (18) used a 41% threshold of SUV_{max} , and Tirosh et al. (15) used a patient-customized method to subtract background uptake.

The development and validation of an algorithm or analytic process that most accurately measures FTV using SSA PET/CT imaging data would help standardize these prognostic assessments and more accurately identify the full extent of low-grade NET disease, which can be indolent on CT or MRI. This standardization could help create a more reproducible and accurate biomarker to identify patients most at risk for disease progression and to help manage treatment decisions.

We have selected some of the techniques previously used to compute tumor volume from SSA PET/CT to assess which method best approximates and correlates with morphologic size measurements, which are the current standard of practice. One of these measurement techniques is computing tumor volume using a threshold (ranging from 40% to 50%) related to the respective lesion's SUV_{max} to remove background uptake (20). We chose to test thresholds of 42% and 50%, as these have been used in prior studies evaluating tumor volume for both ^{18}F -FDG PET/CT and SSA PET/CT. Another method uses customized background-based estimation—including background-subtracted lesion activity (BSL)—that surrounds each lesion with a single volume of interest (VOI) and then analyzes the resultant histogram of that VOI to remove any background uptake for each lesion (21,22). In this study, our aim was to evaluate these different FTV measurement methods with SSA PET/CT and compare these results with lesion volumes calculated from morphologic size measurements.

MATERIALS AND METHODS

Patient and Lesion Selection

The institutional review board approved this retrospective single-center study and waived the informed consent requirement.

The Memorial Sloan Kettering Cancer Center (MSKCC) GE Healthcare PACS was retrospectively searched for patients who had undergone ^{68}Ga -DOTATATE PET/CT between December 2016 and May 2018. This search identified 327 patients with NETs cared for by our service. The clinical, histopathologic, and imaging data of these patients were obtained and organized. We then restricted our population to the 211 patients who had undergone both ^{68}Ga -DOTATATE PET/CT and contrast-enhanced CT.

Additional clinical data were used to include only patients with both a ^{68}Ga -DOTATATE PET/CT and a triphasic contrast-enhanced CT examination within 6 wk of each other. Also, to ensure that all lesions demonstrated somatostatin avidity, the study included only patients whose dictated nuclear medicine and radiology reports shows concordant findings of neoplastic disease on SSA PET/CT and CT. In addition, patients were excluded if they had any therapeutic intervention between their SSA PET/CT and CT examinations. These criteria resulted in 25 patients with paired SSA PET/CT and CT examinations and concurrent findings.

The paired ^{68}Ga -DOTATATE PET/CT and contrast-enhanced CT examinations were evaluated; 150 lesions showed SSA uptake and were clearly identifiable in all planes on CT imaging. Lesions were

then excluded if they either contained necrotic components or were lobulated, as an accurate morphologic volume would be difficult to calculate for these types of lesions from traditional morphologic size assessments. Additionally, 1 lesion was excluded because no biopsy results were obtained during that patient's care at MSKCC. This exclusion resulted in 94 clearly identifiable lesions from 20 patients. Each of these ellipsoid lesions demonstrated a precise correlation between the PET imaging and the contrast-enhanced CT imaging in all dimensions.

Diagnostic Imaging Acquisition Protocols

All patients were examined with the routine ^{68}Ga -DOTATATE PET/CT clinical protocol on a GE Healthcare Discovery 690 or 710 PET/CT scanner. Both scanners use the same PET acquisition hardware and software. Each patient received an intravenous injection of ^{68}Ga -DOTATATE with a mean injected activity of 193.51 MBq (range, 166.5–203.5 MBq) and were scanned after an average 64-min delay (range, 60–75 min). The low-dose, unenhanced CT sequence and PET sequence were obtained from the mid skull to the upper thighs. The SUVs were normalized to the patient's body weight. All PET/CT scanners used at MSKCC are cross-calibrated for the SUV measurement, allowing a valid comparison between SUV_{max} measurements made on different scanners.

All patients were also examined with separate triple-phase contrast-enhanced CT examinations performed with the routine MSKCC clinical protocol. After oral and intravenous iodinated contrast administration, multislice helical sections were obtained from the thoracic inlet to the pubic symphysis. Imaging of the abdomen included a precontrast phase, a timed arterial phase imaged 35 s after contrast injection, and a timed portal phase imaged 80 s after contrast injection.

FTV Quantification Analysis

The FTV was determined as the sum of all voxels, within the identified VOI, whose uptake matched a predetermined guideline. All FTV measurements and analyses were performed using VolumeShare software, version 7, for the Advantage Workstation (GE Healthcare). Initially, a VOI was created to encircle each identifiable lesion on the ^{68}Ga -DOTATATE PET/CT scan. Each VOI was created to select only a single lesion and to minimize the amount of physiologically elevated background uptake surrounding each lesion within the VOI.

Then, a hand-drawn volume was created to circumscribe each lesion, using each lesion's visible tumor activity as seen on the diagnostic PET images and excluding any surrounding regions of physiologically increased background activity.

The initial VOI of each lesion was then used to calculate the FTV using thresholds. The first method summed the voxels that demonstrated uptake matching or exceeding a threshold percentage of the lesion's SUV_{max} . For this method, 2 different thresholds were evaluated, 42% and 50%.

Lastly, the BSL method was performed (21,22). For each lesion, the imaging data from the initial VOI were transposed into a histogram to calculate the BSL activity. The histograms represent the voxels of the VOI as a function of SUVs. Then, the background activity surrounding the lesion was removed by subtracting a gaussian fit over the peak of the VOI's histogram. Any negative values were reset to zero. The remaining positive values in the histogram could be summed to calculate the FTV based on BSL.

To establish a reference standard for lesion volume, the contrast-enhanced CT examinations were used to measure the morphologic volume of each lesion using the GE Healthcare PACS. Each lesion was measured manually in 3 dimensions using the arterial and venous phase sequences. For each lesion, the longest diameter on segmented axial images was measured, followed by the longest perpendicular diameter. A third, craniocaudal, diameter was then measured using

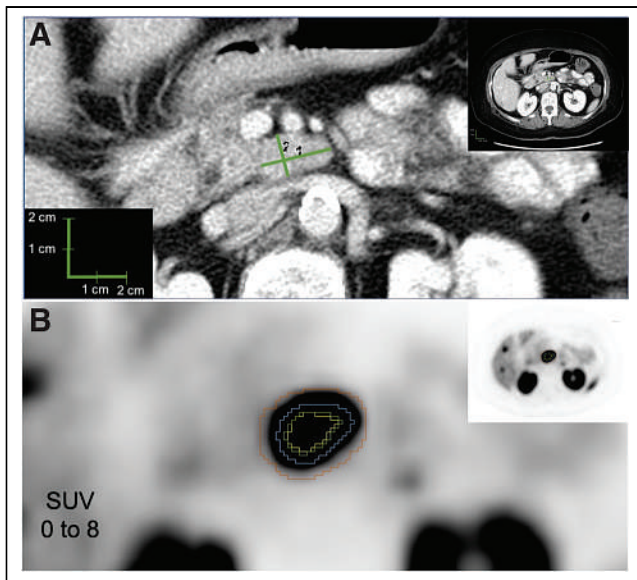


FIGURE 1. Example lesion 1. (A) CT evaluation of lymph node, with longest diameter of 2.2 cm (1) and longest perpendicular diameter of 1.3 cm (2). (B) PET evaluation of lymph node, with yellow representing 50% threshold segmentation; green, 42% threshold segmentation; blue, manual segmentation; and red, BSL segmentation.

segmented sagittal or coronal imaging sequences. Since only ellipsoidal lesions were included, the morphologic volume could be calculated as $\frac{4}{3} \pi abc$. Figures 1 and 2 demonstrate example lesions with their calculated FTVs and morphologic volumes.

Statistical Analysis

The Pearson correlation coefficient was used to evaluate the correlation of morphologic lesion volume with the 4 approaches to FTV assessment. Linear models with a random intercept were used to account for

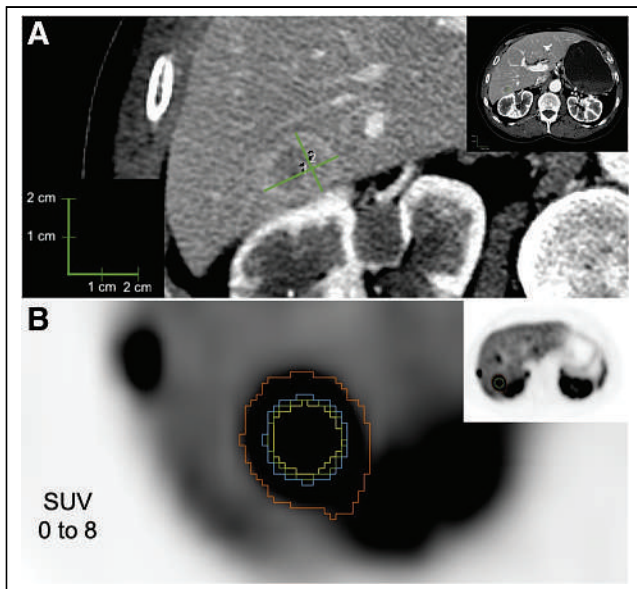


FIGURE 2. Example lesion 2. (A) CT evaluation of hepatic metastasis, with longest diameter of 2.3 cm (1) and longest perpendicular diameter of 1.8 cm (2). (B) PET evaluation of hepatic metastasis, with yellow representing 50% threshold segmentation; green, 42% threshold segmentation; blue, manual segmentation; and red, BSL segmentation.

TABLE 1
Demographic and Histopathologic Data

Characteristic	Data
Patients	20 (100%)
Sex	
Female	13 (65%)
Male	7 (35%)
Age at ⁶⁸ Ga-DOTATATE PET (y)	
Mean ± SD	56 ± 12
Range	28–78
NET primary tumor subtype (%)	
Pancreatic	11 (55%)
Small intestine	5 (25%)
Other	3 (15%)
Unknown	1 (5%)
Gastroenteropancreatic NET grade	
G1 (Ki-67 < 3%)	5 (29%)
G2 (Ki-67 = 3%–20%)	9 (53%)
G3 (Ki-67 > 20%)	3 (18%)
Local recurrence	1 (5%)
Metastases	
No	2 (10%)
Yes	18 (90%)
Metastatic sites	
Liver	18
Nodes	8
Bone	3
Adrenal	2
Mesenteric	2
Cardiac	1
Splenic	1
Clinical syndrome	
Nonfunctioning tumor	12 (60%)
Functioning tumor	8 (40%)

Data are number, except for age.

TABLE 2
Medical and Surgical Treatments Before Imaging

Treatment	<i>n</i>
Resection of primary tumor	9 (45%)
Additional treatments	
Liver-directed therapy	7 (35%)
Chemotherapy	4 (20%)
Radiotherapy	1 (5%)
Peptide radionuclide receptor therapy	0
Treatment with cold SSA at time of ⁶⁸ Ga-DOTATATE PET/CT	8 (40%)

TABLE 3
⁶⁸Ga-DOTATATE-Avid Lesion Locations and Measurements

Parameter	Data
SUV_{max}	
Mean ± SD	36.9 ± 27.0
Range	1.3–188.3
Lesions analyzed	94
Site of lesions	
Liver	69 (73.4%)
Node	10 (10.6%)
Pancreas	5 (5.3%)
Bone	5 (5.3%)
Bowel	2 (2.1%)
Perihepatic implant	2 (2.1%)
Mesenteric node	1 (1.1%)

Data are number, except for SUV_{max}.

any inpatient correlation between lesions from the same patient. Additionally, the FTVs measured by the 4 approaches were statistically compared with morphologic volume by the included Bland–Altman plots. A log transformation for the Bland–Altman plots was used to correct the skewness in the distribution of the volumes.

RESULTS

Of the 20 patients, 65% were women and 35% were men. The mean age (±SD) at the time of PET scanning was 56 ± 12 y. The primary tumor sites included pancreas for 11 patients (55%) and small intestine for 5 patients (25%). There was 1 patient with an unknown primary (5%). Additionally, there were 2 patients with a gastric primary and 1 patient with a renal primary (Table 1).

Metastases were detected in 18 patients (90%). The most common metastatic site was the liver, with 18 patients (90%). Other common sites of metastasis were nodal for 8 patients (40%) and bone for 3 patients (15%). A single patient had a local recurrence. Additionally, 2 patients had adrenal metastasis, 2 had mesenteric metastasis, 1 had cardiac metastasis, and 1 had splenic metastasis (Table 1).

According to the 2019 World Health Organization classification grading system, 5 patients (29%) with gastroenteropancreatic NETs had G1 tumors (Ki-67 < 3%), 9 (53%) had G2 tumors (Ki-67 = 3%–20%), and 3 (18%) had G3 tumors (Ki-67 > 20%). Three patients had NET carcinoid tumors without Ki-67 information (Table 1).

Only 8 patients had a clinical syndrome (diarrhea or flushing) at the time of the

diagnosis, and only 8 patients were under treatment with cold SSAs at the time of SSA PET/CT imaging. The patients had undergone a variety of prior treatments, including primary resection in 9 patients, liver-directed therapies in 7, chemotherapy in 4, and radiotherapy in 1 (Table 2).

In total, 94 lesions were analyzed for FTV. The mean SUV_{max} of the lesions was 36.9 ± 27.0. Most lesions were in the liver (69). Additional sites of lesions included the lymph nodes (10), pancreas (5), bones (5), small bowel (2), and mesentery (1), as well as a perihepatic implant (2) (Table 3).

The different FTV calculation methods demonstrated varying correlations to morphologic volume measurements for the full population of 94 lesions. Calculating FTV using the 42% threshold provided a 0.706 correlation. The hand-drawn volume from the PET imaging provided a 0.657 correlation. The method using 50% thresholding had a 0.645 correlation, and the BSL method had a 0.596 correlation (Fig. 3).

The Bland–Altman plots (Fig. 4) were well distributed across 0 for each FTV calculation method, but all 4 FTV methods had positive mean difference when compared with morphologic volume. The FTV calculated using 50% thresholding showed the smallest mean difference. This difference between FTV methods and the morphologic volume is not affected by the size of the lesion.

DISCUSSION

In our study, we evaluated different methods to calculate FTV from SSA PET/CT and compared these with morphologic volumes. An FTV calculated using thresholding methods related to SUV_{max} outperformed other techniques and may more completely

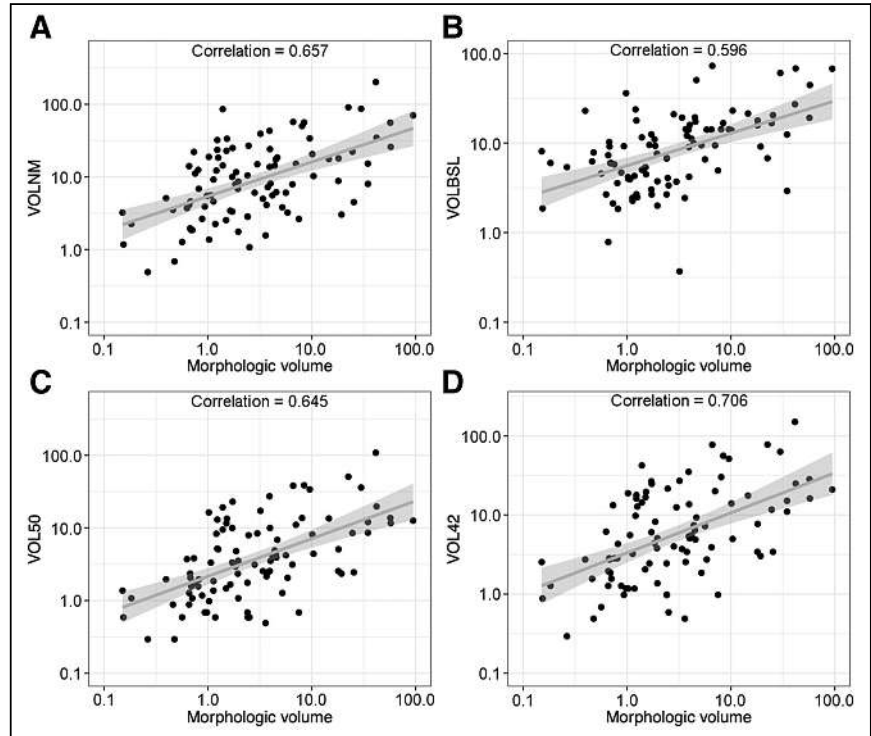


FIGURE 3. Correlation charts of FTV calculations to morphologic measurements. (A) Manual volume from PET imaging (VOLNM). (B) BSL (VOLBSL). (C) Threshold of 50% relative to SUV_{max} (VOL50). (D) Threshold of 42% relative to SUV_{max} (VOL42).

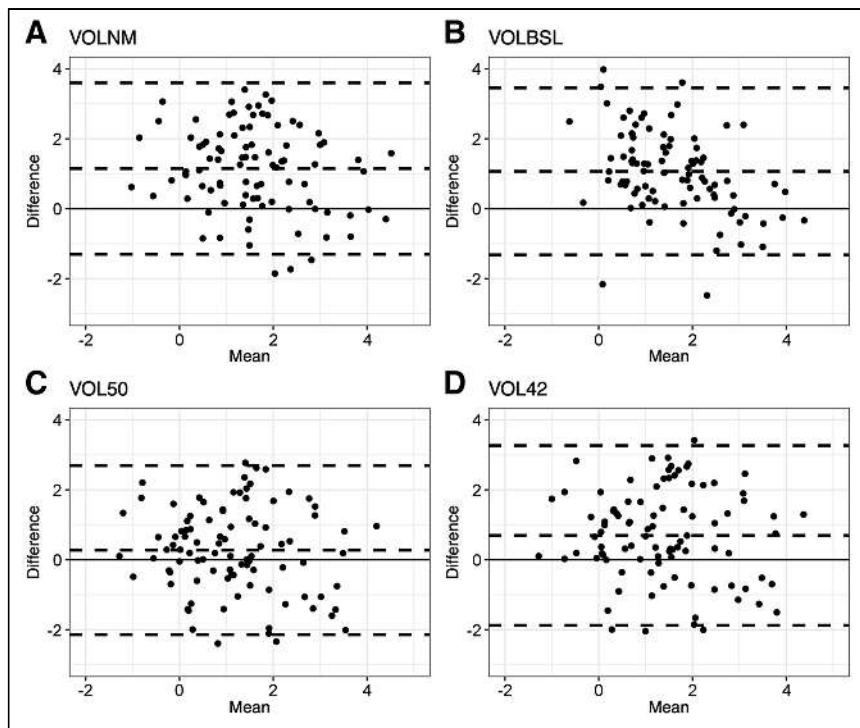


FIGURE 4. Bland-Altman scatterplots showing relative difference between FTV method as labeled and morphologic volume on y-axis and mean volume of FTV method as labeled and morphologic volume on x-axis. Dashed lines represent upper limits of agreement, lower limits of agreement, and bias (or mean difference). Log transformation was used to correct skewness in distribution of volumes. (A) Manual volume from PET imaging (VOLNM). (B) BSL (VOLBSL). (C) Threshold of 50% relative to SUV_{max} (VOL50). (D) Threshold of 42% relative to SUV_{max} (VOL42).

and accurately assess tumor burden for NETs than traditional morphologic assessments.

Since the arrival of SSA PET/CT into the clinical sphere, there have been attempts to understand how to best use it for patient management. Some have suggested that FTV may represent a better correlation with prognosis than SUV_{max} by better capturing extent of disease and response to therapy (14–19). But because there is no consensus or validated FTV method with SSA PET/CT, we appropriated some previously used FTV methods. These include SUV_{max} thresholding methods related to SUV_{max} , hand-drawn volumes, and a BSL method described in prior published studies by MSKCC.

Use of the hand-drawn volumes for calculation of FTV performed favorably, with a strong correlation to the morphologic volume. Unfortunately, this technique also consistently demonstrated the largest overestimation of lesion size compared with morphologic volume. It is unclear whether this bias is due to the companion CT images of the PET examination. An additional major limitation of this method is the time required to manually circumscribe each lesion.

Although the FTV calculation based on the BSL technique showed promise for ^{18}F -FDG PET/CT in prior studies, we demonstrated that this technique performed poorly for SSA PET/CT. This technique had the lowest correlation between calculated FTV and morphologic volume. Additionally, this technique greatly overestimated lesion size compared with morphologic volume, suggesting that the distribution of SSA uptake from the background parenchyma cannot be completely estimated by a classic gaussian distribution.

Both FTVs computed on the basis of SUV_{max} thresholds showed strong correlations with morphologic lesion volume, as well as

showing the smallest overall differences from morphologic lesion volume. The 42% threshold had the strongest correlation with morphologic volume, including the hand-drawn volume, and the second smallest mean difference. The 50% threshold demonstrated the smallest mean difference from morphologic volume, or the smallest overestimation, and the third strongest correlation with morphologic volume. This result suggests that an FTV with thresholding values may be the best candidate for an FTV measurement technique to assess tumor burden for low-grade NETs. Because use of the 42% and 50% thresholds was arbitrarily chosen given their prior use for tumor volume assessments in the literature, a threshold set to a different percentage could demonstrate a stronger correlation with morphologic tumor volume, with less bias or overestimation. As the 50% threshold with least bias demonstrated a lower correlation than the 42% threshold, it is possible that a second variable is needed to adjust FTV to best approximate morphologic volume. These results suggest that more inquiry is likely needed to answer these questions.

The main limitation of our study was our exclusion of lesions with necrotic components and with more complex 3-dimensional volumes. These were excluded because of

the difficulty of calculating an accurate morphologic volume for these lesions via CT imaging. Future studies are needed to evaluate whether an FTV method based on an SUV_{max} threshold can be used to accurately measure the SSA-positive portions of these types of NET lesions.

CONCLUSION

Because SSA PET/CT can better evaluate the full extent of NET disease than CT or MRI, a measurement technique using these PET imaging data can provide a more complete and accurate assessment of total disease. Our study demonstrated a strong correlation between FTV calculated using SUV_{max} thresholding and traditional morphologic lesion volumes. Measurements were also more accurate using this method than using morphologic lesion volumes. Additionally, this method was more accurate than FTV calculated from hand-drawn volume assessments. This FTV assessment technique is the best candidate for future evaluation and for incorporation of total-body tumor volume algorithms to more completely and accurately assess tumor burden and prognosis for NET patients.

DISCLOSURE

This research was funded in part through NIH/NCI Cancer Center Support Grant P30 CA008748. Ryan Reddy is a nonremunerated consultant for AAA-Novartis and Curium. Lisa Bodei is a nonremunerated consultant/speaker for AAA-Novartis, Ipsen, ITM, Curium, Clovis Oncology, Iba, and MTTI and received a

research grant from AAA-Novartis. No other potential conflict of interest relevant to this article was reported.

KEY POINTS

QUESTION: What is the best FTV measurement method for ^{68}Ga SSA PET/CT imaging of NETs?

PERTINENT FINDINGS: We found a strong correlation and the smallest bias between FTV and traditional morphologic lesion volume when using an SUV_{max} threshold on SSA PET/CT. Additionally, this method of computation outperformed FTV calculated from hand-drawn volume assessments with regard to accuracy.

IMPLICATIONS FOR PATIENT CARE: FTV assessment based on an SUV_{max} threshold is a promising basis for more accurate measurement of tumor volume and should be further studied to create FTV algorithms to better determine the extent of disease and the prognosis.

REFERENCES

1. Wang HY, Li ZW, Sun W, et al. Automated quantification of Ki-67 index associates with pathologic grade of pulmonary neuroendocrine tumors. *Chin Med J*. 2019;132:551–561.
2. Bodei L, Kwekkeboom DJ, Kidd M, Modlin IM, Krenning EP. Radiolabeled somatostatin analogue therapy of gastroenteropancreatic cancer. *Semin Nucl Med*. 2016;46:225–238.
3. Strosberg J, El-Haddad G, Wolin E, et al. Phase 3 trial of ^{177}Lu -Dotatate for mid-gut neuroendocrine tumors. *N Engl J Med*. 2017;376:125–135.
4. Bodei L, Sundin A, Kidd M, Prasad V, Modlin IM. The status of neuroendocrine tumor imaging: from darkness to light? *Neuroendocrinology*. 2015;101:1–17.
5. Geijer H, Breimer LH. Somatostatin receptor PET/CT in neuroendocrine tumours: update on systematic review and meta-analysis. *Eur J Nucl Med Mol Imaging*. 2013;40:1770–1780.
6. Kazmierczak PM, Rominger A, Wenter V, et al. The added value of ^{68}Ga -DOTA-TATE-PET to contrast-enhanced CT for primary site detection in CUP of neuroendocrine origin. *Eur Radiol*. 2017;27:1676–1684.
7. Hofman MS, Kong G, Neels OC, Eu P, Hong E, Hicks RJ. High management impact of Ga-68 DOTATATE (GaTate) PET/CT for imaging neuroendocrine and other somatostatin expressing tumours. *J Med Imaging Radiat Oncol*. 2012;56:40–47.
8. Yao JC, Shah MH, Ito T, et al. Everolimus for advanced pancreatic neuroendocrine tumors. *N Engl J Med*. 2011;364:514–523.
9. Pavel ME, Hainsworth JD, Baudin E, et al. Everolimus plus octreotide long-acting repeatable for the treatment of advanced neuroendocrine tumours associated with carcinoid syndrome (RADIAN-2): a randomised, placebo-controlled, phase 3 study. *Lancet*. 2011;378:2005–2012.
10. Raymond E, Dahan L, Raoul JL, et al. Sunitinib malate for the treatment of pancreatic neuroendocrine tumors. *N Engl J Med*. 2011;364:501–513.
11. de Mestier L, Dromain C, d'Assignies G, et al. Evaluating digestive neuroendocrine tumor progression and therapeutic responses in the era of targeted therapies: state of the art. *Endocr Relat Cancer*. 2014;21:R105–R120.
12. Solis-Hernandez MP, Fernandez Del Valle A, Carmona-Bayonas A, et al. Evaluating radiological response in pancreatic neuroendocrine tumours treated with sunitinib: comparison of Choi versus RECIST criteria (CRIPNET_GETNE1504 study). *Br J Cancer*. 2019;121:537–544.
13. Luo Y, Chen J, Huang K, et al. Early evaluation of sunitinib for the treatment of advanced gastroenteropancreatic neuroendocrine neoplasms via CT imaging: RECIST 1.1 or Choi criteria? *BMC Cancer*. 2017;17:154.
14. Baum RP, Kulkarni HR. THERANOSTICS: from molecular imaging using Ga-68 labeled tracers and PET/CT to personalized radionuclide therapy—the Bad Berka experience. *Theranostics*. 2012;2:437–447.
15. Tirosh A, Papadakis GZ, Millo C, et al. Prognostic utility of total ^{68}Ga -DOTA-TATE-avid tumor volume in patients with neuroendocrine tumors. *Gastroenterology*. 2018;154:998–1008.e1.
16. Abdulrezzak U, Kurt YK, Kula M, Tutus A. Combined imaging with ^{68}Ga -DOTA-TATE and ^{18}F -FDG PET/CT on the basis of volumetric parameters in neuroendocrine tumors. *Nucl Med Commun*. 2016;37:874–881.
17. Toriihara A, Baratto L, Nobashi T, et al. Prognostic value of somatostatin receptor expressing tumor volume calculated from ^{68}Ga -DOTATATE PET/CT in patients with well-differentiated neuroendocrine tumors. *Eur J Nucl Med Mol Imaging*. 2019;46:2244–2251.
18. Ohnona J, Nataf V, Gauthier M, et al. Prognostic value of functional tumor burden on ^{68}Ga -DOTATOC PET/CT in patients with pancreatic neuro-endocrine tumors. *Neoplasma*. 2019;66:140–148.
19. Ohlendorf F, Henkenberens C, Brunkhorst T, et al. Volumetric ^{68}Ga -DOTA-TATE PET/CT for assessment of whole-body tumor burden as a quantitative imaging biomarker in patients with metastatic gastroenteropancreatic neuroendocrine tumors. *Q J Nucl Med Mol Imaging*. April 14, 2020 [Epub ahead of print].
20. Foster B, Bagci U, Mansoor A, Xu Z, Mollura DJ. A review on segmentation of positron emission tomography images. *Comput Biol Med*. 2014;50:76–96.
21. Burger IA, Vargas HA, Apte A, et al. PET quantification with a histogram derived total activity metric: superior quantitative consistency compared to total lesion glycolysis with absolute or relative SUV thresholds in phantoms and lung cancer patients. *Nucl Med Biol*. 2014;41:410–418.
22. Burger IA, Casanova R, Steiger S, et al. ^{18}F -FDG PET/CT of non-small cell lung carcinoma under neoadjuvant chemotherapy: background-based adaptive-volume metrics outperform TLG and MTV in predicting histopathologic response. *J Nucl Med*. 2016;57:849–854.

Glypican-3–Targeted ^{227}Th α -Therapy Reduces Tumor Burden in an Orthotopic Xenograft Murine Model of Hepatocellular Carcinoma

Kevin P. Labadie¹, Donald K. Hamlin², Aimee Kenoyer³, Sara K. Daniel¹, Alan F. Utria¹, Andrew D. Ludwig¹, Heidi L. Kenerson¹, Lily Li⁴, Jonathan G. Sham¹, Delphine L. Chen⁵, Johnnie J. Orozco³, Raymond S. Yeung¹, Chris Orvig⁶, Yawen Li², D. Scott Wilbur², and James O. Park¹

¹Department of Surgery, University of Washington, Seattle, Washington; ²Department of Radiation Oncology, University of Washington, Seattle, Washington; ³Clinical Research Division, Fred Hutchinson Cancer Research Center, Seattle, Washington; ⁴Life Sciences Division, TRIUMF, and Medicinal Inorganic Chemistry Group, Department of Chemistry, University of British Columbia, Vancouver, British Columbia, Canada; ⁵Department of Radiology, University of Washington, Seattle, Washington; ⁶Medicinal Inorganic Chemistry Group, Department of Chemistry, University of British Columbia, Vancouver, British Columbia, Canada

Hepatocellular carcinoma (HCC) is a significant cause of morbidity and mortality worldwide, with limited therapeutic options for advanced disease. Targeted α -therapy is an emerging class of targeted cancer therapy in which α -particle-emitting radionuclides, such as ^{227}Th , are delivered specifically to cancer tissue. Glypican-3 (GPC3) is a cell surface glycoprotein highly expressed on HCC. In this study, we describe the development and in vivo efficacy of a ^{227}Th -labeled GPC3-targeting antibody conjugate (^{227}Th -octapa- α GPC3) for treatment of HCC in an orthotopic murine model. **Methods:** The chelator *p*-SCN-Bn-H₄octapa-NCS (octapa) was conjugated to a GPC3-targeting antibody (α GPC3) for subsequent ^{227}Th radiolabeling (octapa- α GPC3). Conditions were varied to optimize radiolabeling of ^{227}Th . In vitro stability was evaluated by measuring the percentage of protein-bound ^{227}Th by γ -ray spectroscopy. An orthotopic athymic Nu/J murine model using HepG2-Red-FLuc cells was developed. Biodistribution and blood clearance of ^{227}Th -octapa- α GPC3 were evaluated in tumor-bearing mice. The efficacy of ^{227}Th -octapa- α GPC3 was assessed in tumor-bearing animals with serial measurement of serum α -fetoprotein at 23 d after injection. **Results:** Octapa-conjugated α GPC3 provided up to 70% ^{227}Th labeling yield in 2 h at room temperature. In the presence of ascorbate, at least 97.8% of ^{227}Th was bound to α GPC3-octapa after 14 d in phosphate-buffered saline. In HepG2-Red-FLuc tumor-bearing mice, highly specific GPC3 targeting was observed, with significant ^{227}Th -octapa- α GPC3 accumulation in the tumor over time and minimal accumulation in normal tissue. Twenty-three days after treatment, a significant reduction in tumor burden was observed in mice receiving a 500 kBq/kg dose of ^{227}Th -octapa- α GPC3 by tail-vein injection. No acute off-target toxicity was observed, and no animals died before termination of the study. **Conclusion:** ^{227}Th -octapa- α GPC3 was observed to be stable in vitro; maintain high specificity for GPC3, with favorable biodistribution in vivo; and result in significant antitumor activity without significant acute off-target toxicity in an orthotopic murine model of HCC.

Key Words: hepatocellular carcinoma (HCC); glypican-3 (GPC3); targeted α -therapy (TAT); radioimmunotherapy

J Nucl Med 2022; 63:1033–1038
DOI: 10.2967/jnumed.121.262562

Received Jun. 3, 2021; revision accepted Oct. 8, 2021.
For correspondence or reprints, contact James O. Park (jopark@uw.edu).
Published online Nov. 12, 2021.
COPYRIGHT © 2022 by the Society of Nuclear Medicine and Molecular Imaging.

Hepatocellular carcinoma (HCC) is a significant cause of morbidity and mortality worldwide, particularly in advanced stages (1–3). Although novel combination therapies are being developed (e.g., immune checkpoint and tyrosine kinase inhibitors), these regimens are limited by modest efficacy and significant adverse effects (4–7). New therapies for advanced HCC are needed.

Targeted α -particle therapy is a promising new class of cancer therapies that create double-stranded DNA breaks via a high linear energy transfer and induce a cytotoxic T-lymphocyte-driven antitumor immune response (8–12). ^{227}Th (half-life, 18.7 d) is an α -particle-emitting radionuclide that has been attached to monoclonal antibody conjugates using bifunctional octadentate ligands, such as isothiocyanato-benzyl-DOTA and 3,2-hydroxypyridinone derivatives (13). The decay scheme of ^{227}Th is shown in Figure 1. α -emitters are appealing for the treatment of solid tumors because of the high radiation payload deposited over short distances (high linear energy transfer), which minimizes the risk of off-target toxicity. ^{227}Th -labeled antibody conjugates are currently being evaluated in the treatment of several malignancies, including acute myeloid leukemia, multiple myeloma, renal cell carcinoma, non-Hodgkin lymphoma, mesothelin-positive mesothelioma, and ovarian cancer (14–17). Glypican-3 (GPC3) is a cell surface glycoprotein highly expressed in HCC, making it a promising target for novel therapeutic and diagnostic applications (18–23). To our knowledge, no report of ^{227}Th targeted α -particle therapy directed at GPC3 for the treatment of HCC has been published to date.

The objective of this study was to develop a ^{227}Th -labeled GPC3 antibody conjugate (^{227}Th -octapa- α GPC3) and evaluate the radiolabeling properties, in vivo biodistribution, and efficacy in a GPC3-positive hepatic orthotopic xenograft murine model of HCC.

MATERIALS AND METHODS

Conjugation of α GPC3 and α BHV1 with Octapa

$^{227}\text{Th}(\text{NO}_3)_4$ was purchased from Oak Ridge National Laboratory and was purified from its decay daughters before use (24). The bifunctional chelator *p*-SCN-Bn-H₄octapa-NCS (octapa) was synthesized at the University of British Columbia (chemical structure shown in Supplemental Fig. 1; supplemental materials are available at <http://jnm.snmjournals.org>) (25,26). The anti-GPC3 antibody (α GPC3) was generated and

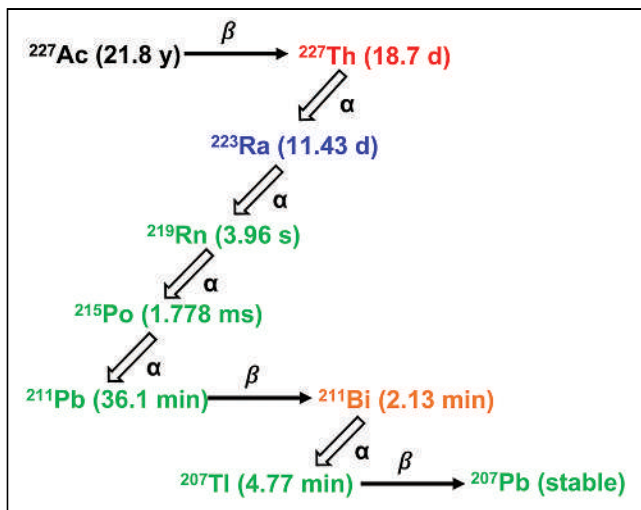


FIGURE 1. Decay scheme of ^{227}Th .

produced at the Fred Hutchinson Research Center antibody core facility as previously described (22,27). The isotope control (IgG₁) antibody against bovine herpes virus, αBHV1 , was a generous gift from the Orozco laboratory (28). The conjugation reaction was previously described (25,26). Detailed information regarding conjugation and radiolabeling is included in the supplemental methods.

^{227}Th Radiolabeling of αGPC3 -Octapa

The αGPC3 -octapa conjugate with the highest octapa-to- αGPC3 ratio and highest antigen binding was used in ^{227}Th -labeling reactions. The radiolabeling yield was optimized by varying the reaction time, pH, and temperature. Appropriate amounts of unlabeled monoclonal antibody conjugates were added to the purified product to provide 18.5 kBq (0.5 μCi) and 70 μg of antibody per dose. The remaining ^{227}Th -labeled αGPC3 -octapa was used for in vitro stability studies.

In Vitro Stability of ^{227}Th -Octapa- αGPC3

Solutions of ^{227}Th -labeled monoclonal antibodies were incubated at room temperature and pH 7.0 for 4 h, followed by refrigeration at 4°C, in the presence or absence of ascorbate acid. At 4 h, 24 h, 3 d, 7 d, and 14 d, the percentage of protein-bound ^{227}Th was determined by γ -ray spectroscopy, monitoring the 236-keV (12.9%) γ -peak of ^{227}Th . Stability in serum and in the presence of an excess of metal ions such as Ca^{2+} , Fe^{3+} , Mg^{2+} , Cu^{2+} , and Zn^{2+} will be evaluated in future studies.

Development of Orthotopic Xenograft Model

GPC3-positive HepG2-Red-FLuc cells expressing luciferase were purchased from PerkinElmer (Bioware, catalog number BW134280) and were maintained in a monolayer at 37°C in Dulbecco modified Eagle medium (Gibco) supplemented with 10% fetal bovine serum (Gibco) in a humidified chamber with 5% CO_2 .

This study was performed in accordance with the University of Washington Office of Animal Welfare guidelines for the humane use of animals, and all procedures were reviewed and approved by the Institutional Animal Care and Use Committee (protocol 4304-02). Experiments were performed in compliance with the ARRIVE guidelines (Animal Research: Reporting of In Vivo Experiments) (29). A hepatic subcapsular xenograft model was generated and described in the supplemental methods (23). To monitor orthotopic tumor growth, whole blood was obtained from the animals by a submandibular bleed and the serum concentration of α -fetoprotein (AFP) was determined (30).

Biodistribution and Blood Clearance Studies

Tumor-bearing mice were injected with ^{227}Th -octapa- αGPC3 or ^{227}Th -octapa- αBHV1 (70 μg , 500 kBq/kg). Tumors and normal organs were harvested and weighed, and ^{227}Th activity was measured by a γ -counter; the measured activity was a net sum of activity from all daughters. The percentage injected dose of radioisotope per gram (%ID/g) of blood, tumor, or organ was calculated after correcting for radioactive decay using an aliquot of the injectate, as were the tumor-to-normal-organ ratios of absorbed radioactivity.

After tumor-bearing mice were injected with ^{227}Th -octapa- αGPC3 or ^{227}Th -octapa- αBHV1 (70 μg , 500 kBq/kg), serial retroorbital blood sampling was performed at 5, 15, 30, 60, 120, and 240 min and then animals were necropsied at 24 h, 7 d, or 23 d after injection. Blood samples were measured by a γ -counter and corrected for ^{227}Th activity.

^{227}Th Radioimmunotherapy

After animals were confirmed to have tumors by IVIS imaging (PerkinElmer), they were included in the study and serum AFP was measured. Tumor-bearing animals were assigned to 1 of 4 experimental groups based on serum AFP measurements to ensure a comparable tumor burden among cohorts. In an unmasked fashion, the animals received either no treatment, αBHV1 -octapa radiolabeled with a 500 kBq/kg dose of ^{227}Th , or αGPC3 -octapa radiolabeled with a 250 or 500 kBq/kg dose of ^{227}Th via tail-vein injection without anesthesia. Twenty-three days after injection, the animals were euthanized to evaluate for early antitumor effect of ^{227}Th -octapa- αGPC3 . Serum was obtained for AFP measurement, and randomly selected livers were harvested and placed in 10% (w/v) neutral-buffered formalin.

Statistical Analysis

Statistical analysis was performed with Prism (version 8.0.0, Graph-Pad Software). The D'Agostino and Pearson normality test was performed to determine whether there was a gaussian distribution. Continuous variables were expressed as medians and means and compared by the Student *t* test or Mann-Whitney test. One-way ANOVA or a Kruskal-Wallis test with Dunn multiple comparisons was performed. In all cases, a *P* value of 0.05 or less was considered statistically significant.

RESULTS

GPC3 Conjugation with Octapa Is Highly Efficient

Octapa was conjugated to αGPC3 via reactions conducted using 5, 10, and 15 equivalents of octapa to determine the optimal conjugation ratio. The isoelectric points of the αGPC3 -octapa shifted toward the acidic isoelectric point as the number of equivalents offered increased (Fig. 2). αGPC3 -octapa 5 equivalents demonstrated a maximum shift of binding to GPC3-positive cells by flow cytometry (Supplemental Fig. 2); however, it resulted in lower chelates per antibody than did the 10 equivalents. Therefore, a 10-equivalent conjugation ratio was used for subsequent experiments. The protein recovery from the conjugation process was more than 85%, and the final concentrations were 4.6 mg/mL and 4.75 mg/mL for αGPC3 -octapa and αBHV1 -octapa, respectively. Mass spectral analysis of αGPC3 -octapa and αBHV1 -octapa conjugates produced by reaction of 10 equivalents of octapa indicated that there was an average of 3.3 octapa moieties on αGPC3 and 5 octapa moieties on αBHV1 .

^{227}Th -Labeled αGPC3 -Octapa Is Stable In Vitro

Labeling conditions were optimized using αGPC3 -octapa and small quantities of ^{227}Th in 0.1 M HNO_3 (85.1–314.5 kBq, or 2.3–8.5 μCi). The labeling yield increased from 16% to 25% to 37% as the reaction time increased from 30 min to 1 h to 2 h, respectively, but did not significantly increase after 2 h. Among the different reaction solutions

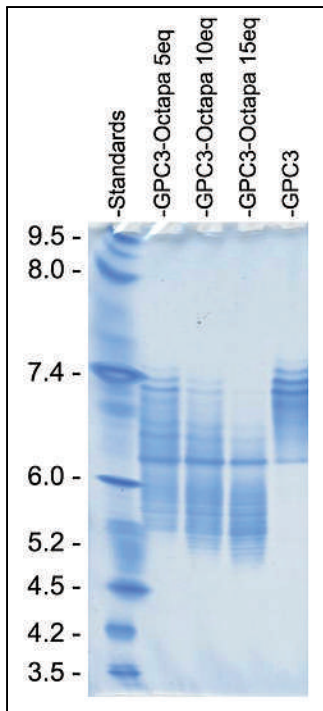


FIGURE 2. Conjugation with octapa to α GPC3: stained isoelectric focusing gel showing isoelectric point changes in unconjugated GPC3 mAb (right lane), when 5, 10, and 15 equivalents of octapa reagent are reacted with α GPC3 mAb.

antibody-bound, ^{227}Th . After 14 d, at least 97.8% of ^{227}Th was observed to be bound to α GPC3-octapa in the presence of ascorbic acid (Fig. 3).

α GPC3-Octapa Maintains Ligand Binding In Vitro and In Vivo

The affinity of α GPC3-octapa for GPC3 was assessed with flow cytometry using HepG2-Red-FLuc cells. α GPC3-octapa maintained high affinity for GPC3, with only a modest reduction in binding affinity compared with unconjugated α GPC3 (Fig. 4). In tumor-bearing mice 24 h, 7 d, and 23 d after tail-vein injection of ^{227}Th -octapa- α GPC3, elevated levels of radioactivity were detected in the tumor tissue compared with the surrounding liver and other organs (Fig. 5A; Supplemental Table 1). The %ID/g of ^{227}Th -octapa- α GPC3 remained high in tumor tissue over 23 d (Fig. 5B). The %ID/g ratio of ^{227}Th -octapa- α GPC3 in tumor tissue compared with adjacent normal liver parenchyma steadily increased over time (Fig. 5C). ^{227}Th -octapa- α BHV1, an irrelevant isotype antibody conjugate, did not significantly bind to the tumor tissue (Supplemental Fig. 3).

^{227}Th -octapa- α GPC3 did not significantly accumulate in normal tissues at 1, 7, and 23 d after injection (Fig. 5A). The %ID/g of ^{227}Th -octapa- α GPC3 was less than 5% in all tested normal tissues by day 23 after injection. The primary mode of decay for ^{227}Th is α -decay, resulting in daughter ^{223}Ra particles, a radionuclide that preferentially accumulates in bone. Measurement of radioactivity of the femur demonstrated low γ -counts after injection with ^{227}Th -octapa- α GPC3 compared with ^{227}Th -octapa- α BHV1, for which radioactivity was observed to accumulate in bone over time. This observation is presumably due to the highly specific targeting and preferential accumulation of ^{227}Th -octapa- α GPC3 in the

and pH levels tested, the highest consistent yields were obtained when 200 μL of 0.05 M sodium citrate with 1 mM ethylenediaminetetraacetic acid (pH 5.5) was combined with 5–10 μL of ^{227}Th in 0.1 M HNO_3 with the pH adjusted to 5–5.5 using 1 M sodium citrate. To this, 200 μg of α GPC3-octapa (4.0 mg/mL) were added and allowed to react for 2 h at 37°C (43%–70% radiochemical yield). Reactions conducted at the elevated temperature accounted for only about 4% higher yields; therefore, subsequent reactions were conducted at room temperature.

The in vitro stability of the ^{227}Th -labeled monoclonal antibody–octapa conjugates was evaluated with and without ascorbic acid. Because the γ -counter cannot distinguish ^{227}Th activity from its radioactive progeny, γ -spectroscopy was used to analyze radio-instant thin-layer chromatography strips from, and determine the percentage of

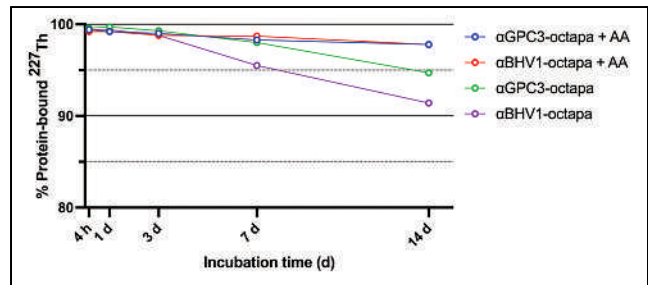


FIGURE 3. Stability of ^{227}Th -labeled mAbs in vitro: percentage bound thorium of α BHV1-octapa and α GPC3-octapa incubated in phosphate-buffered saline over 14 d with and without ascorbic acid (AA).

tumor, resulting in lower circulating radioactivity for bone deposition. High-resolution γ -ray spectroscopy was performed on select tissues demonstrating radium accumulation in bone (Supplemental Table 2), but further evaluation will be part of a future study.

Blood radioactivity cleared more rapidly after ^{227}Th -octapa- α GPC3 injection than after ^{227}Th -octapa- α BHV1, with serum half-lives of 14 and 17 h, respectively. This more rapid clearance may be secondary to increased accumulation of the radioimmunoconjugate in the tumor over time (Fig. 6).

^{227}Th -Octapa- α GPC3 Reduces Tumor Burden in Murine Model

To assess the efficacy, tumor-bearing mice received either no treatment, a 500 kBq/kg dose of ^{227}Th -octapa- α BHV1, or a 250 or 500 kBq/kg dose of ^{227}Th -octapa- α GPC3 by tail-vein injection. Serum AFP was significantly lower in mice treated with ^{227}Th -octapa- α GPC3 than in control groups 23 d after therapy administration (Fig. 7). The treatment effect was most pronounced after therapy with a 500 kBq/kg dose of ^{227}Th -octapa- α GPC3, although a modest effect was observed after therapy with 250 kBq/kg. AFP increased significantly after therapy with a 500 kBq/kg dose of ^{227}Th -octapa- α BHV1, indicating that

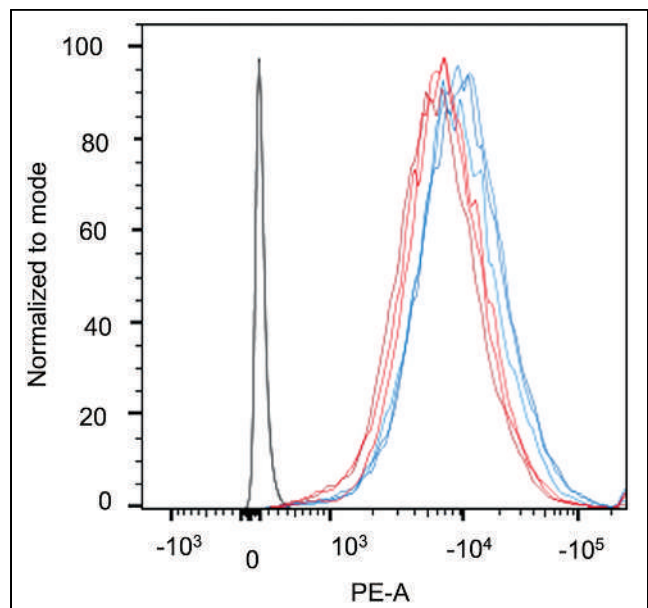


FIGURE 4. Binding affinity for GPC3 in vitro maintained by α GPC3-octapa: in vitro GPC3 binding assessed by flow cytometry on human HepG2-Red-FLuc cells with unconjugated α GPC3 (blue) and α GPC3-octapa (red), compared with unstained control (black). Three biologic replicate samples are shown.

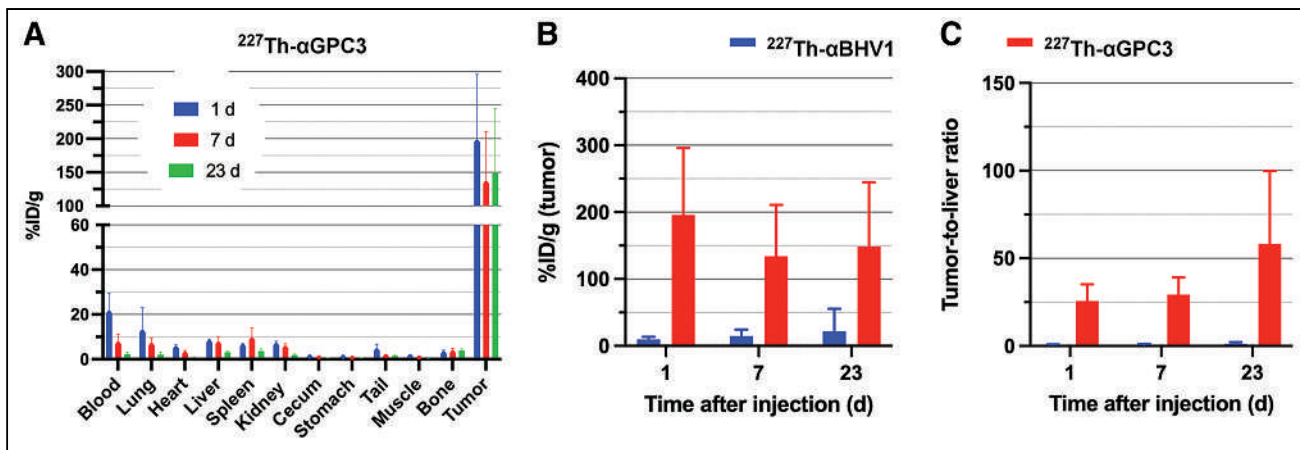


FIGURE 5. Comparative biodistribution of ^{227}Th -octapa- α GPC3 and ^{227}Th -octapa- α BHV1. (A) Tissue biodistribution of ^{227}Th -octapa- α GPC3 in tumor-bearing mice 1 d ($n = 7$), 7 d ($n = 7$), and 23 d ($n = 6$) after injection. (B) ^{227}Th accumulation in tumor tissue. (C) Tumor-to-liver ratio 1 d ($n = 7$), 7 d ($n = 5$ for α BHV1 and 3 for α GPC3), and 23 d ($n = 4$) after injection with ^{227}Th -octapa- α BHV1 or ^{227}Th -octapa- α GPC3. Bar denotes mean; error bar denotes SD.

GPC3-targeted thorium delivery induced tumor cell killing rather than the presence of systemically circulating antibody-bound ^{227}Th .

To assess for organ-specific toxicity after administration of the ^{227}Th radioimmunoconjugates, serum markers of end organ dysfunction were collected 23 d after injection, and no significant aberrations were identified in comparison to controls (Supplemental Fig. 4). No animals died before termination of the study.

DISCUSSION

In this report, we describe the development of a ^{227}Th radioimmunoconjugate targeting GPC3 and demonstrated its *in vivo* efficacy in the treatment of HCC in an orthotopic murine xenograft model. The ^{227}Th -octapa- α GPC3 radioimmunoconjugate was observed to be stable *in vitro*; maintain its specificity for GPC3, with a favorable biodistribution; and result in tumor reduction without undesired significant acute toxicity. These findings add to previous studies establishing the basis for a

GPC3-targeted theranostic platform whereby different radioimmunoconjugates can be used for diagnostic or surveillance imaging and treatment (22,23,31,32). Such a platform could improve current treatments of HCC by enabling earlier identification of disease or recurrence, increase the accuracy of staging, and allow for more targeted treatment with fewer systemic toxicities.

To radiolabel our antibody, we used a picolinic acid-containing chelate, octapa, an octadentate acyclic ligand that enables ^{227}Th radiolabeling of antibodies at room temperature, helping to maintain the 3-dimensional conformation and immunoreactivity of the conjugated targeting antibody (25,26). Optimization of the reaction conditions resulted in efficient ^{227}Th -labeling ($\leq 70\%$ radiolabeling yield) and a product with high radiochemical purity. The high *in vivo* stability of the ^{227}Th -octapa complex is demonstrated by the low bone uptake throughout the 23-d study. In its initial description, H_4octapa was used to label trastuzumab with ^{111}In and ^{177}Lu for imaging and therapy, respectively, of mice bearing ovarian cancer xenografts (25,26). Previously ^{227}Th has been radiolabeled to antibodies using an octadentate hydroxypyridinone for the treatment of CD33-positive myeloid leukemia, CD70-positive renal cell carcinoma, and mesothelin-positive malignancies (13). To our knowledge, this study is the first to describe picolinic acid ligands as a new class of ligand for ^{227}Th radiolabeling of antibody conjugates.

We have previously described conjugating GPC3 with DOTA chelate for ^{90}Y radioimmunotherapy (22,23,33). ^{90}Y produces β -ionizing radiation, with lower energy and a longer pathlength than for ^{227}Th . These differences in properties are important, as a higher energy transfer results in a lower median lethal dose, and a shorter pathlength decreases the radius of tissues affected by the radiation (10). α -therapies might be desirable over β -therapies if highly specific targeting is possible. Although research into targeted α -particle therapy for hematologic malignancies has focused on ^{211}At (half-life, 7.21 h), and a recent study for HCC described using ^{225}Ac (half-life, 9.92 d), we elected to use ^{227}Th (half-life, 18.7 d) for its longer half-life, which we hypothesize is advantageous in the treatment of solid tumors (31,34,35).

Administration of ^{227}Th -octapa- α GPC3 led to highly specific tumor uptake, rapid blood clearance, and robust antitumor activity without significant acute toxicity. Within 1 d of injection of ^{227}Th -octapa- α GPC3,

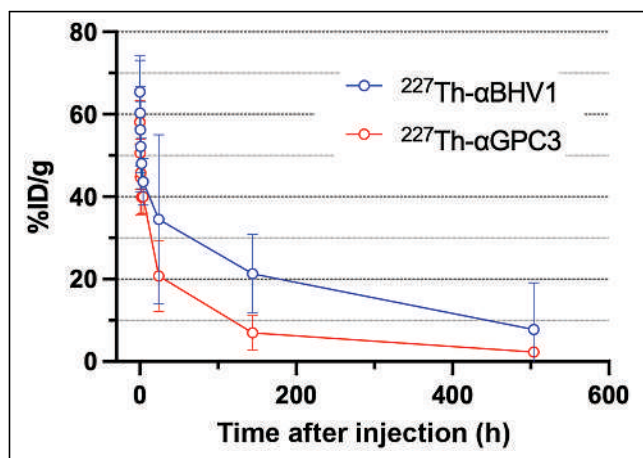


FIGURE 6. Comparative blood clearance profiles in tumor-bearing mice at 5, 15, 30, 60, 120, and 240 min; 24 h; and 7 and 23 d after injection with ^{227}Th -radiolabeled α GPC3-octapa and α BHV1-octapa ($n = 4$ /time point). Symbol denotes mean; error bar denotes SD.

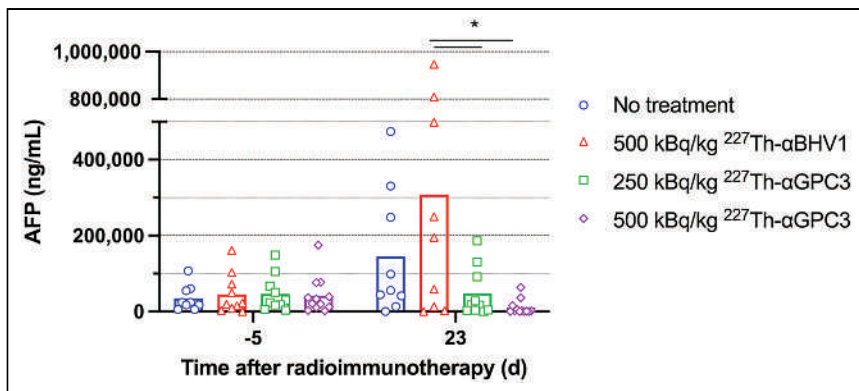


FIGURE 7. Reduction of tumor burden in murine model by ^{227}Th -octapa- α GPC3: serum AFP before (day -5) and 23 d after receiving no treatment ($n = 9$) or tail-vein injection of 500 kBq/kg dose of ^{227}Th -octapa- α BHV1 ($n = 9$) or 250 kBq/kg ($n = 10$) or 500 kBq/kg dose of ^{227}Th -octapa- α GPC3 ($n = 12$). Bar represents mean. Symbols denote individual mice. * $P < 0.05$ after unpaired 2-way ANOVA with Sidak multiple-comparison test.

significant intratumoral accumulation was observed, compared with controls. The tumor-to-liver ratio of ^{227}Th -octapa- α GPC3 steadily increased over time, and minimal off-target uptake was observed, indicating highly specific targeting and clearance. We observed modest bone uptake over time in the irrelevant isotype antibody control group, which is expected given that ^{227}Th daughter molecule ^{223}Ra delivers radiation to sites of increased osteoblastic metabolism (36).

The observed therapeutic effect of ^{227}Th -octapa- α GPC3 was dependent on antibody-targeted delivery of radiation, as evidenced by the lack of therapeutic effect observed in the nontargeting ^{227}Th -octapa- α BHV1 control group. Using an established marker of tumor burden in our model, serum AFP, we observed the therapeutic effect after treatment with a 500 kBq/kg dose of ^{227}Th - α GPC3 to be consistent, with a reduction in serum AFP in all animals except one (23). Interestingly, we observed a marked increase in tumor burden in the α BHV1 control group. The mechanism of this finding is not understood but could be related to bone marrow toxicity and suppression of alloreactive immune cells, which are present in athymic mice (37,38).

No significant acute off-target toxicity was observed in our study, with all animals surviving until study completion. There was a moderate amount of radioactivity identified in the bone, particularly in our control group. One of the challenges of using α -particle emitters for therapy is the presence of multiple radioactive daughter products that may dislocate from the target site. Although this may lead to cytopenias and marrow toxicity, data from human trials with similar radioisotopes are reassuring. In the phase 3 ALSYMPACA trial, differences in cytopenia rates were seen in patients with prior docetaxel dosing, suggesting that differences in cumulative marrow damage are more implicated than direct radioactive effects. A recently published article describing α GPC3-targeted α -particle therapy using ^{225}Ac conjugated to the humanized monoclonal antibody GC33 in a heterotopic murine xenograft model demonstrated modest antitumor activity while observing significant bone marrow suppression and toxicity (31). Although the experimental models tested were different, we postulate that the difference in toxicity between our studies is due to improved specificity of our antibody, highlighting the importance of effective targeting for delivery of the α -therapy.

There are several limitations to our study. GPC3 expression in HCC is variable and differs with the degree of differentiation (39). Human HepG2-Red-FLuc cells demonstrate high expression of GPC3 (40) and may not recapitulate low- or intermediate-grade HCC. The studies were performed on athymic mice that lack mature T cells. Although competent leukocytes are present in this model, it does not represent the complex tumor microenvironment of human HCC. We elected to omit a nonradiolabeled antibody conjugate control group because of extensive prior work by our group demonstrating that α GPC3 antibody alone does not lead to a robust antitumor response (23). Tumor size was measured indirectly in our model by serum AFP. Direct tumor size measurements via ultrasonography or bioluminescent imaging

were not performed because of the environmental health and safety constraints at our core facilities with radioactive animals. Some untreated animals showed a spontaneous reduction in AFP and tumor size without treatment, possibly secondary to an alloreactive response from native immune cells. Although these animals existed in all groups, this observation requires further investigation. More studies are warranted to evaluate the potential toxicity of ^{227}Th -octapa- α GPC3. One of the studies would be to perform a dosimetry analysis to understand the radiation dose from ^{227}Th and its α -emitting decay progenies, especially ^{223}Ra . Additionally, it is worth noting that radiation nephropathy and other toxicities were not able to be fully assessed with only 23 d of monitoring (41). A longer period of observation in addition to hematologic analysis, which was not performed because of lack of appropriate experimental equipment, is planned for future investigations.

CONCLUSION

We report the development of a GPC3-targeted ^{227}Th conjugate using octapa and demonstrate it to be stable in vitro; maintain high specificity for GPC3, with favorable biodistribution in vivo; and result in significant antitumor activity without undesirable acute toxicity. To our knowledge, this is the first description of a ^{227}Th radio-pharmaceutical targeting GPC3 and is a promising addition to the theranostic approach to treating HCC.

DISCLOSURE

This work is supported by NIH/NCI Cancer Center support grant P30 CA015704. The isotopes used in this research were supplied by the U.S. Department of Energy Isotope Program, managed by the Office of Isotope R&D and Production NSERC CREATE Iso-SiM at TRIUMF for a PhD research stipend (Lily Li) and an NSERC discovery grant (RGPIN-42394-13), as well as NSERC (CHRP 493725-16) and the Canadian Institutes of Health Research (CIHR, CPG-146482) as a Collaborative Health Research Project (Chris Orvig). TRIUMF receives federal funding via a contribution agreement with the National Research Council of Canada. No other potential conflict of interest relevant to this article was reported.

KEY POINTS

QUESTION: Does GPC3-targeted thorium radionuclide therapy localize intratumorally and reduce tumor burden in a mouse model?

PERTINENT FINDINGS: Thorium was reliably and efficiently labeled to a GPC3-targeting antibody via an octapa chelator. This radioimmunoconjugate maintained affinity for the target antigen in vitro and in vivo. Significant levels of thorium accumulated intratumorally. Orthotopic mice treated with GPC3-directed thorium had significant reductions in their tumor burden compared with control animals.

IMPLICATIONS FOR PATIENT CARE: This study identified a new approach to treating HCC using a personalized and targeted approach against a highly expressed antigen in HCC.

REFERENCES

- Bray F, Ferlay J, Soerjomataram I, Siegel RL, Torre LA, Jemal A. Global Cancer Statistics 2018: GLOBOCAN estimates of incidence and mortality worldwide for 36 cancers in 185 countries. *CA Cancer J Clin*. 2018;68:394–424.
- Kim D, Li AA, Perumpail BJ, et al. Changing trends in etiology-based and ethnicity-based annual mortality rates of cirrhosis and hepatocellular carcinoma in the United States. *Hepatology*. 2019;69:1064–1074.
- Wong MC, Jiang JY, Goggins WB, et al. International incidence and mortality trends of liver cancer: a global profile. *Sci Rep*. 2017;7:45846.
- Finn RS, Qin S, Ikeda M, et al. Atezolizumab plus bevacizumab in unresectable hepatocellular carcinoma. *N Engl J Med*. 2020;382:1894–1905.
- Finn RS, Ryoo BY, Merle P, et al. Pembrolizumab as second-line therapy in patients with advanced hepatocellular carcinoma in KEYNOTE-240: a randomized, double-blind, phase III trial. *J Clin Oncol*. 2020;38:193–202.
- Llovet JM, Kudo M, Cheng A-L, et al. Lenvatinib (len) plus pembrolizumab (pembro) for the first-line treatment of patients (pts) with advanced hepatocellular carcinoma (HCC): phase 3 LEAP-002 study [abstract]. *J Clin Oncol*. 2019;37(suppl):TPS4152.
- Yau T, Kang Y-K, Kim T-Y, et al. Nivolumab (NIVO) + ipilimumab (IPI) combination therapy in patients (pts) with advanced hepatocellular carcinoma (aHCC): results from CheckMate 040 [abstract]. *J Clin Oncol*. 2019;37(suppl):4012.
- Targeted Alpha Therapy Working Group; Parker C, Lewington V, Shore N, et al. Targeted alpha therapy, an emerging class of cancer agents: a review. *JAMA Oncol*. 2018;4:1765–1772.
- Sgouros G, Roeske JC, McDevitt MR, et al. MIRD pamphlet no. 22 (abridged): radiobiology and dosimetry of α -particle emitters for targeted radionuclide therapy. *J Nucl Med*. 2010;51:311–328.
- Kassis AI. Therapeutic radionuclides: biophysical and radiobiologic principles. *Semin Nucl Med*. 2008;38:358–366.
- Poty S, Francesconi LC, McDevitt MR, Morris MJ, Lewis JS. α -emitters for radiotherapy: from basic radiochemistry to clinical studies—part 1. *J Nucl Med*. 2018;59:878–884.
- Malamas AS, Gameiro SR, Knudson KM, Hodge JW. Sublethal exposure to alpha radiation (^{223}Ra dichloride) enhances various carcinomas' sensitivity to lysis by antigen-specific cytotoxic T lymphocytes through calreticulin-mediated immunogenic modulation. *Oncotarget*. 2016;7:86937–86947.
- Ramdahl T, Bonge-Hansen HT, Ryan OB, et al. An efficient chelator for complexation of thorium-227. *Bioorg Med Chem Lett*. 2016;26:4318–4321.
- Hagemann UB, Ellingsen C, Schuhmacher J, et al. Mesothelin-targeted thorium-227 conjugate (MSLN-TTC): preclinical evaluation of a new targeted alpha therapy for mesothelin-positive cancers. *Clin Cancer Res*. 2019;25:4723–4734.
- Hagemann UB, Mihaylova D, Uran SR, et al. Targeted alpha therapy using a novel CD70 targeted thorium-227 conjugate in in vitro and in vivo models of renal cell carcinoma. *Oncotarget*. 2017;8:56311–56326.
- Hagemann UB, Wickstroem K, Wang E, et al. In vitro and in vivo efficacy of a novel CD33-targeted thorium-227 conjugate for the treatment of acute myeloid leukemia. *Mol Cancer Ther*. 2016;15:2422–2431.
- Wickstroem K, Hagemann UB, Cruciani V, et al. Synergistic effect of a mesothelin-targeted ^{227}Th conjugate in combination with DNA damage response inhibitors in ovarian cancer xenograft models. *J Nucl Med*. 2019;60:1293–1300.
- Nakatsura T, Yoshitake Y, Senju S, et al. Glypican-3, overexpressed specifically in human hepatocellular carcinoma, is a novel tumor marker. *Biochem Biophys Res Commun*. 2003;306:16–25.
- Nishida T, Kataoka H, Fehrmann RSN, van der Vegt B, de Vries EGE, de Groot DJA. Glypican 3 overexpression across a broad spectrum of tumor types discovered with functional genomic mRNA profiling of a large cancer database. *Am J Pathol*. 2018;188:1973–1981.
- Sham JG, Kievit FM, Grierson JR, et al. Glypican-3-targeting F(ab')₂ for ^{89}Zr PET of hepatocellular carcinoma. *J Nucl Med*. 2014;55:2032–2037.
- Sham JG, Kievit FM, Grierson JR, et al. Glypican-3-targeted ^{89}Zr PET imaging of hepatocellular carcinoma. *J Nucl Med*. 2014;55:799–804.
- Ludwig AD, Labadie KP, Seo YD, et al. Yttrium-90-labeled anti-glypican 3 radioimmunotherapy halts tumor growth in an orthotopic xenograft model of hepatocellular carcinoma. *J Oncol*. 2019;2019:4564707.
- Ferrier MG, Li Y, Chyan MK, et al. Thorium chelators for targeted alpha therapy: rapid chelation of thorium-226. *J Labelled Comp Radiopharm*. 2020;63:502–516.
- Price EW, Cawthray JF, Bailey GA, et al. H₄octapa: an acyclic chelator for ^{111}In radiopharmaceuticals. *J Am Chem Soc*. 2012;134:8670–8683.
- Price EW, Zeglis BM, Cawthray JF, et al. H₄octapa-trastuzumab: versatile acyclic chelate system for ^{111}In and ^{177}Lu imaging and therapy. *J Am Chem Soc*. 2013;135:12707–12721.
- Wayner EA, Hoffstrom BG. Development of monoclonal antibodies to integrin receptors. *Methods Enzymol*. 2007;426:117–153.
- Page JM, Matthews DC, Kenoyer A, et al. Pretargeted radioimmunotherapy using anti-CD45 monoclonal antibodies to deliver radiation to murine hematolymphoid tissues and human myeloid leukemia. *Cancer Res*. 2009;69:185–192.
- Percie du Sert N, Hurst V, Ahluwalia A, et al. The ARRIVE guidelines 2.0: updated guidelines for reporting animal research. *Exp Physiol*. 2020;105:1459–1466.
- Golde WT, Gollobin P, Rodriguez LL. A rapid, simple, and humane method for submandibular bleeding of mice using a lancet. *Lab Anim (NY)*. 2005;34:39–43.
- Bell MM, Gutsche NT, King AP, et al. Glypican-3-targeted alpha particle therapy for hepatocellular carcinoma. *Molecules*. 2020;26:4.
- Kelada OJ, Gutsche NT, Bell M, et al. ImmunoPET as stoichiometric sensor for glypican-3 in models of hepatocellular carcinoma. *BioRxiv* website. <https://www.biorxiv.org/content/10.1101/2020.01.31.926972v1.full>. Published February 2, 2020. Accessed February 23, 2022.
- Labadie KP, Ludwig AD, Lehnert AL, et al. Glypican-3 targeted delivery of ^{89}Zr and ^{90}Y as a theranostic radionuclide platform for hepatocellular carcinoma. *Sci Rep*. 2021;11:3731.
- O'Steen S, Comstock ML, Orozco JJ, et al. The alpha-emitter astatine-211 targeted to CD38 can eradicate multiple myeloma in a disseminated disease model. *Blood*. 2019;134:1247–1256.
- Orozco JJ, Back T, Kenoyer A, et al. Anti-CD45 radioimmunotherapy using ^{211}At with bone marrow transplantation prolongs survival in a disseminated murine leukemia model. *Blood*. 2013;121:3759–3767.
- Suominen MI, Fagerlund KM, Rissanen JP, et al. Radium-223 inhibits osseous prostate cancer growth by dual targeting of cancer cells and bone microenvironment in mouse models. *Clin Cancer Res*. 2017;23:4335–4346.
- Festing MF, May D, Connors TA, Lovell D, Sparrow S. An athymic nude mutation in the rat. *Nature*. 1978;274:365–366.
- Benestad HB, Hersleth IB, Rolstad B. Thymus and T cells are not essential for rat leucopoiesis. *Eur J Haematol*. 1989;43:150–157.
- Suzuki M, Sugimoto K, Tanaka J, et al. Up-regulation of glypican-3 in human hepatocellular carcinoma. *Anticancer Res*. 2010;30:5055–5061.
- Gao W, Tang Z, Zhang YF, et al. Immunotoxin targeting glypican-3 regresses liver cancer via dual inhibition of Wnt signalling and protein synthesis. *Nat Commun*. 2015;6:6536.
- Kiess AP, Minn I, Vaidyanathan G, et al. (2S)-2-(3-(1-carboxy-5-(4- ^{211}At -astato-benzamido)pentyl)ureido)-pentanedioic acid for PSMA-targeted α -particle radiopharmaceutical therapy. *J Nucl Med*. 2016;57:1569–1575.

Enhancing ^{223}Ra Treatment Efficacy by Anti- $\beta 1$ Integrin Targeting

Claudia Paindelli^{1,2}, Stefano Casarin³, Feng Wang⁴, Luis Diaz-Gomez⁵, Jianhua Zhang⁴, Antonios G. Mikos⁵, Christopher J. Logothetis¹, Peter Friedl^{1,2,6}, and Eleonora Dondossola¹

¹Department of Genitourinary Medical Oncology and David H. Koch Center for Applied Research of Genitourinary Cancers, University of Texas M.D. Anderson Cancer Center, Houston, Texas; ²Department of Cell Biology, Radboud University Medical Center, Nijmegen, The Netherlands; ³Center for Computational Surgery, Department of Surgery and Houston Methodist Academic Institute, Houston Methodist Research Institute, Houston, Texas; ⁴Department of Genomic Medicine, University of Texas M.D. Anderson Cancer Center, Houston, Texas; ⁵Department of Bioengineering, Rice University, Houston, Texas; and ⁶Cancer Genomics Centre, Utrecht, The Netherlands

^{223}Ra is an α -emitter approved for the treatment of bone metastatic prostate cancer (PCa), which exerts direct cytotoxicity toward PCa cells near the bone interface, whereas cells positioned in the core respond poorly because of short α -particle penetrance. $\beta 1$ integrin ($\beta 1$) interference has been shown to increase radiosensitivity and significantly enhance external-beam radiation efficiency. We hypothesized that targeting $\beta 1$ would improve ^{223}Ra outcome. **Methods:** We tested the effect of combining ^{223}Ra and anti- $\beta 1$ antibody treatment in PC3 and C4-2B PCa cell models expressing high and low $\beta 1$ levels, respectively. In vivo tumor growth was evaluated through bioluminescence. Cellular and molecular determinants of response were analyzed by ex vivo 3-dimensional imaging of bone lesions and by proteomic analysis and were further confirmed by computational modeling and in vitro functional analysis in tissue-engineered bone mimetic systems. **Results:** Interference with $\beta 1$ combined with ^{223}Ra reduced PC3 cell growth in bone and significantly improved overall mouse survival, whereas no change was achieved in C4-2B tumors. Anti- $\beta 1$ treatment decreased the PC3 tumor cell mitosis index and spatially expanded ^{223}Ra lethal effects 2-fold, in vivo and in silico. Regression was paralleled by decreased expression of radioresistance mediators. **Conclusion:** Targeting $\beta 1$ significantly improves ^{223}Ra outcome and points toward combinatorial application in PCa tumors with high $\beta 1$ expression.

Key Words: ^{223}Ra ; prostate cancer; bone metastasis; integrin $\beta 1$

J Nucl Med 2022; 63:1039–1045

DOI: 10.2967/jnumed.121.262743

Prostate cancer (PCa) is the fifth leading cause of death from cancer worldwide and the most common malignancy in elderly men (1). Androgen receptor signaling inhibitors and chemotherapy are effective in local tumors, with a 99% survival rate at 5 y from diagnosis but responses of short duration for advanced metastatic disease (<30% survival at 5 y) (1). Bone is the most frequent site for PCa distant colonization, as identified in 84% of the patients with metastatic lesions (2). The interactions between cancer and bone-resident cells disrupt the finely balanced biology of bone,

leading to symptomatic remodeling, spinal cord compression, fractures, limited mobility, and ultimately the patient's death (3,4).

^{223}Ra , a bone-targeted radionuclide, has recently been approved for the treatment of advanced metastatic PCa patients with bone lesions (5). This α -emitter accumulates in mineralized bone tissue because of its calcium-mimetic properties and is enriched in areas with high bone turnover (6,7). The short penetration range of α -particles (<100 μm) minimizes the impact on the healthy bone marrow tissue, thus reducing side effects associated with treatment with β -emitters (6,8). ^{223}Ra low systemic toxicity coupled to improved survival and significant delay of first symptomatic skeletal events led to clinical testing in other neoplasias in bone, including multiple myeloma; renal cell carcinoma; and breast, lung, and thyroid cancer (9).

Recently, we demonstrated that ^{223}Ra kills with maximum efficiency PCa cells proximal to the bone surface (within 100 μm), whereas it leaves the distant core unperturbed (7). On the basis of this strictly zonal toxicity, ^{223}Ra therapy was more effective when applied to lesions of limited size (7). As an alternative, the combination of ^{223}Ra with other agents that radiosensitize PCa cells could enhance its efficacy.

The inhibition of integrin pathways increases the effectiveness of external-beam radiation in multiple cancer types, including head and neck, breast, and prostate, both locally and in metastatic sites (10–14). Integrins are heterodimeric transmembrane receptors composed of α - and β -subunits, which mediate interactions with extracellular matrix ligands (15) and signaling cross-talk with growth factor receptors (16). Through these combined functions, integrins support cell growth, decrease cell death by promoting anchorage-dependent survival, and enable radioresistance mechanisms on exposure to ionizing γ -radiation, including induction of adhesion and survival signaling and enhanced DNA repair (14,17,18). Anti- $\beta 1$ integrin ($\beta 1$) targeting improves irradiation treatment outcomes in breast cancer cells in 3-dimensional cultures and in vivo subcutaneous xenografts, reaching efficacy comparable to high-dose radiotherapy (11). Blocking $\beta 1$ in PC3 PCa subcutaneous tumors further inhibits their growth on irradiation (13). Consequently, targeting of $\beta 1$ in combination with γ -radiation can increase response and reduce survival of cancer cells.

MATERIALS AND METHODS

In Vivo Studies

Animal studies were approved by the Institutional Animal Care and Use Committee of the University of Texas M.D. Anderson Cancer

Received Jun. 15, 2021; revision accepted Oct. 15, 2021.
For correspondence or reprints, contact Eleonora Dondossola (edondossola@mdanderson.org).
Published online Oct. 28, 2021.
COPYRIGHT © 2022 by the Society of Nuclear Medicine and Molecular Imaging.

Center and were performed according to the institutional guidelines for animal care and handling. Luciferase-expressing PCa cells were administered in the tibia as previously reported (7). Details on in vivo studies are provided in the supplemental information.

Statistical Analysis

Statistical analysis was performed using Prism, version 8.0 (Graph-Pad Software). An unpaired 2-sided Student *t* test was applied to analyze 2 populations, whereas 1-way ANOVA, followed by the Tukey honestly-significant-difference post hoc test, was performed to compare more than 2 populations. All statistical tests were 2-sided, and statistical significance was considered for a *P* value of less than 0.05. Data are shown as mean \pm SD.

Further experimental methods are detailed in the supplemental information.

RESULTS

Expression of β 1I and Consequences of Targeting, In Vitro

To define the relevance of anti- β 1I targeting in PCa bone metastasis, we confirmed its expression by interrogating transcriptomic data from the Stand Up to Cancer/Prostate Cancer Foundation database, which contains RNA sequence data derived from a cohort of 150 bone or soft-tissue biopsies (19). The β 1I transcript showed heterogeneous expression in both sample types, with no significant differences (Fig. 1A), indicating that PCa bone metastases can retain β 1I expression at different levels. To recapitulate the role of β 1I targeting in PCa, we used PC3 and C4-2B cells as models for high or low β 1I expression (20), respectively, which was confirmed by flow cytometry and immunofluorescence analysis (Figs. 1B and 1C). For targeting, we used the antihuman β 1I 4B4 blocking monoclonal antibody (4B4-mAb), which sensitizes solid tumors to γ -irradiation (21). To explore the functional significance of β 1I interference, we monitored PCa cell growth in the presence of 4B4-mAb. PC3 cell proliferation and mitotic index were significantly reduced by 4B4-mAb treatment (Supplemental Fig. 1A; supplemental materials are available at <http://>

jnm.snmjournals.org), whereas C4-2B cell culture was not affected by anti- β 1I targeting (Supplemental Fig. 1B). These results suggest that β 1I is variably expressed in PCa patients and cell lines and that its targeting has biologically active effects in a PCa subset endowed with higher expression levels.

Effects of Combined ^{223}Ra and Anti- β 1I Treatment on PCa Cell Growth in the Tibia

To determine the effects of ^{223}Ra and anti- β 1I combinatorial treatment on PCa bone lesions, luciferase-expressing PC3 cells were injected into mouse tibiae ($n = 13\text{--}19$ tibiae/group), randomized at day 3 after implantation and treated with a single dose of ^{223}Ra (300 kBq/kg) and 4B4-mAb (100 $\mu\text{g}/\text{mouse}$), alone or in combination, and tumor growth was monitored longitudinally by macroscopic bioluminescence imaging (Fig. 2A; Supplemental Fig. 2). 4B4-mAb specifically targets human β 1I without cross-reactivity to murine integrins (22), thus allowing identification of direct effects exerted on human tumor cells without perturbing the murine bone microenvironment. PC3 tumors retained β 1I expression in vivo (Supplemental Fig. 3), and treatment with 4B4-mAb delayed their growth and significantly extended mouse survival compared with control-treated animals (Fig. 2B; Supplemental Fig. 2A). ^{223}Ra treatment alone extended survival more efficiently, and combinatorial treatment further significantly improved mouse survival, with approximately 70% of mice still alive 40 d after treatment (Fig. 2B). No signs of increased distress (including major weight loss, reduced hydration, difficulties in breathing, aberrant behavior and movements, abdominal cavity swelling) were identified in mice treated with ^{223}Ra or 4B4-mAb, alone or in combination.

When tested in C4-2B tumors implanted in bone ($n = 8\text{--}10$ tibiae/group), 4B4-mAb improved neither survival nor the efficacy of ^{223}Ra (Fig. 2C; Supplemental Figure 2B), indicating insensitivity to β 1I targeting, probably due to low β 1I expression levels in vivo (Supplemental Fig. 3). By comparison with PC3 bone lesions, C4-2B tumors showed negligible growth until day 21 after ^{223}Ra treatment. To rule out the possibility that therapeutic improvement by 4B4-mAb treatment was confounded by this strong response, a second cohort ($n = 9\text{--}12$ tibiae/group) received low-dose ^{223}Ra treatment (100 kBq/kg) combined with 4B4-mAb. Reduced dosing of ^{223}Ra resulted in accelerated tumor progression, but similar to the high-dose regimen, 4B4-mAb did not improve ^{223}Ra outcome (Fig. 2D; Supplemental Fig. 2C). These results suggest that combining β 1I targeting and ^{223}Ra treatment improves efficacy of ^{223}Ra in PCa tumors with higher β 1I expression.

^{223}Ra and 4B4-mAb Zonal Toxicity in PCa Bone Lesions

To determine the cellular effects of combined ^{223}Ra and 4B4-mAb treatment on PC3 bone lesions, we monitored cytotoxicity exerted by combinatorial therapy versus single treatments by single-cell cytometry in transversal 3-dimensional bone sections captured at the confocal microscope 4 d after treatment (Fig. 3A). PC3 lesions were segmented, and the number of mitotic and apoptotic events was quantified for subregions with a 100-, 200-, or greater than 200- μm distance from cortical bone (Fig. 3B), a corridor that fully accommodates the short distance reached by α -particles ($<100\ \mu\text{m}$) (8). PC3 tumor cells were easily distinguishable from resident bone marrow cells on the basis of the large nuclear size and pattern of heterochromatin; also, mitotic figures and cell death were clearly identifiable on the basis of their typical nuclear pattern (Supplemental Fig. 4). Control-treated lesions lacked a zonal increase

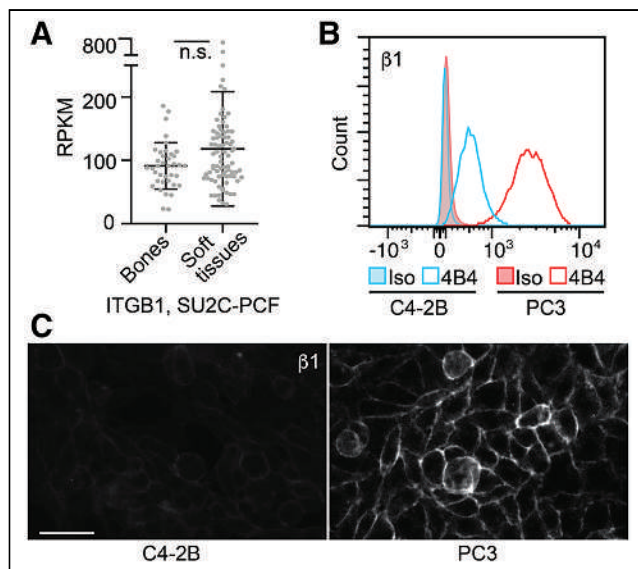


FIGURE 1. β 1I expression, in vitro. (A) RNA expression of ITGB1 in bones and soft-tissue metastasis, Stand Up to Cancer/Prostate Cancer Foundation database. (B and C) Flow cytometry and immunofluorescence analysis of β 1I expression in PC3 and C4-2B cells. Experiment was repeated twice. Bar = 50 μm ; n.s. = nonsignificant.

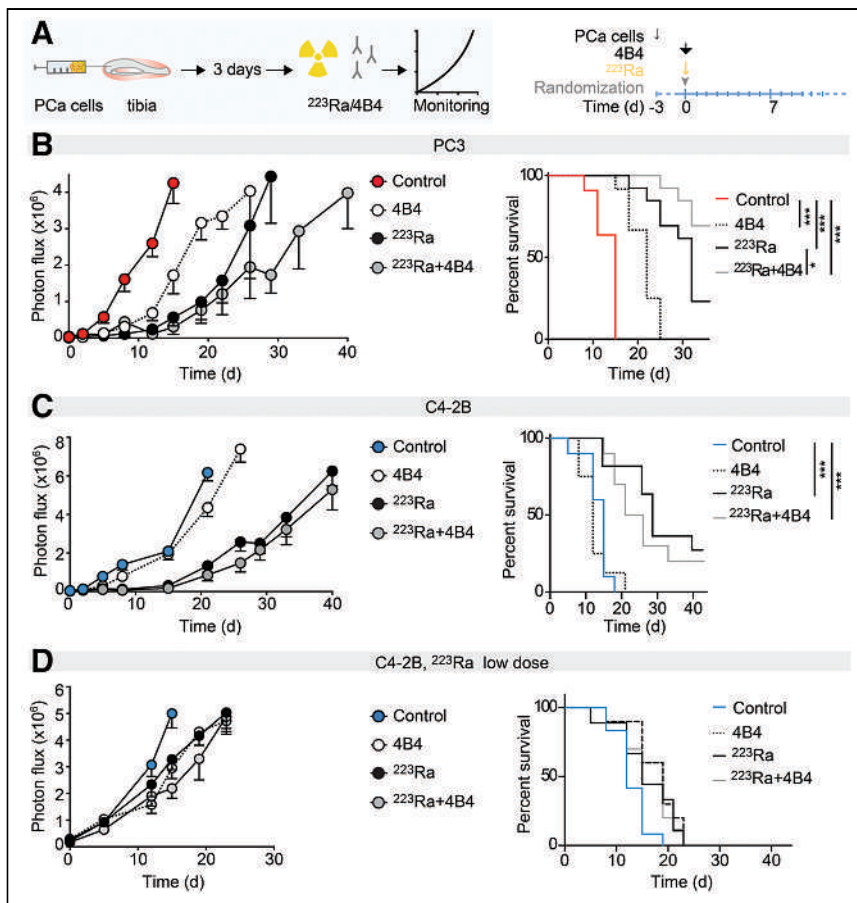


FIGURE 2. In vivo response of PCa cells in bone to anti- β 11 (4B4) and ^{223}Ra treatments. (A) Experimental design and timeline of treatment schedule. (B) PC3 tumors, growth, and survival curve over time (^{223}Ra , 300 kBq/kg; 4B4-mAb, 100 $\mu\text{g}/\text{mouse}$; $n = 13$ –19 tumors). (C and D) C4-2B tumors, growth curve, and survival curve over time (^{223}Ra , 300 kBq/kg; 4B4-mAb, 100 $\mu\text{g}/\text{mouse}$; $n = 8$ –10 tumors [C]; ^{223}Ra , 100 kBq/kg; 4B4-mAb, 100 $\mu\text{g}/\text{mouse}$; $n = 9$ –12 tumors [D]). * $P < 0.05$. *** $P < 0.001$, 1-way ANOVA, followed by Tukey honestly-significant-difference post hoc test.

in mitotic or apoptotic cells; 4B4-mAb induced a uniform decrease in mitotic index throughout the tumor (Fig. 3C), whereas ^{223}Ra induced zonal toxicity with higher rates of cell death next to the cortical bone (0–100 μm) and a decreasing effect at a greater distances (Fig. 3C), as described (7). The combination of ^{223}Ra and 4B4-mAb improved zonal efficacy by decreasing the mitosis-to-apoptosis ratio (Fig. 3C). This effect was mediated by coupling of significantly increased levels of apoptosis with a significant reduction in mitosis, compared with ^{223}Ra alone (Fig. 3D). These results suggest that both the spatial extension of ^{223}Ra cytotoxic effects and a decrease in mitosis contribute to improved outcome (Fig. 2B).

Enlargement of the tumor cell nucleus induced by genome replication without cell division follows exposure to high doses of ionizing radiation and is already visible during the first days after irradiation (23–25). No changes in size were evident in control- or 4B4-treated lesions at any distance from bone, as quantified using ImageJ and StarDist software (26,27). ^{223}Ra induced a tumor cell nuclear size enlargement within 100 μm , compared with both 100–200 μm and more than 200 μm of distance from bone, whereas the ^{223}Ra -4B4 combination showed a significantly increased size up to a 200- μm distance from bone,

confirming that a broader area was impacted by radiation effects (Supplemental Figs. 5A and 5B).

Overall, these results indicate that β 11 targeting decreases mitosis and sensitizes PC3 cells to ^{223}Ra by broadening the tumor volume fraction that responds to radiation therapy.

Sensitization of Tumor Cells to Radiation Through 4B4-mAb Treatment

To address the ability of β 11 interference to radiosensitize for ^{223}Ra , we implemented PC3 cell treatment with ultra-low ^{223}Ra doses in a 3-dimensional in vitro bone mimetic environment (BME). This system consists of a polycaprolactone scaffold functionalized by human mesenchymal stem cells differentiated to bioactive osteoblasts that produce a calcified bone matrix (Fig. 4A), which incorporates ^{223}Ra efficiently and simulates in vivo distribution (28). PCa tumoroids were seeded on BMEs and were treated with 4B4-mAb or ^{223}Ra (10 Bq/mL (28)), and the response was evaluated longitudinally by live-cell microscopy (Fig. 4A). Individually, neither ^{223}Ra nor 4B4-mAb as single modalities significantly impaired PC3 viability or growth. When combined, however, they significantly decreased tumoroid growth and increased the number of apoptotic cells (Figs. 4B and 4C; Supplemental Fig. 6). To further identify whether β - or γ -emission (which represent 3.6% and 1.1% of ^{223}Ra decay series, respectively (29)) may contribute to ^{223}Ra -mediated cytotoxicity, we preadsorbed ^{223}Ra at high doses (1,600 Bq/mL) to BMEs, washed them, and fit them in a Transwell system

(Corning) at more than a 1-mm distance from PC3 cells, ruling out α -particles (Supplemental Fig. 7A). ^{223}Ra was retained within BMEs, with negligible release in the medium (<2%; Supplemental Fig. 7B). However, PC3 cell growth was significantly reduced in this large-distance culture by ^{223}Ra alone and was further diminished by ^{223}Ra + 4B4-mAb treatment (Supplemental Fig. 7C). These data indicate that, besides a direct short-range effect of α -particles, ^{223}Ra cytotoxicity may be supported by β - or γ -emission, but considering the limited fraction emitted (29), a minor contribution can be expected at therapeutic doses.

Interestingly, functional proteomics (reverse-phase protein array) performed on PC3 bone lesions treated with 4B4-mAb showed that the top proteins mostly affected by β 11 targeting (Supplemental Table 1) were involved in tumor cell proliferation and radiosensitization, including lactate dehydrogenase-A (30), bromodomain-containing protein 4 (31), and mitogen-activated protein kinase (32). Lactate dehydrogenase-A overexpression in PCa has been linked to aggressive tumors with a higher frequency of local relapse on radiotherapy treatments, whereas its knockdown causes radiosensitization of PC3 cells (30). Bromodomain-containing protein 4 plays a central role in

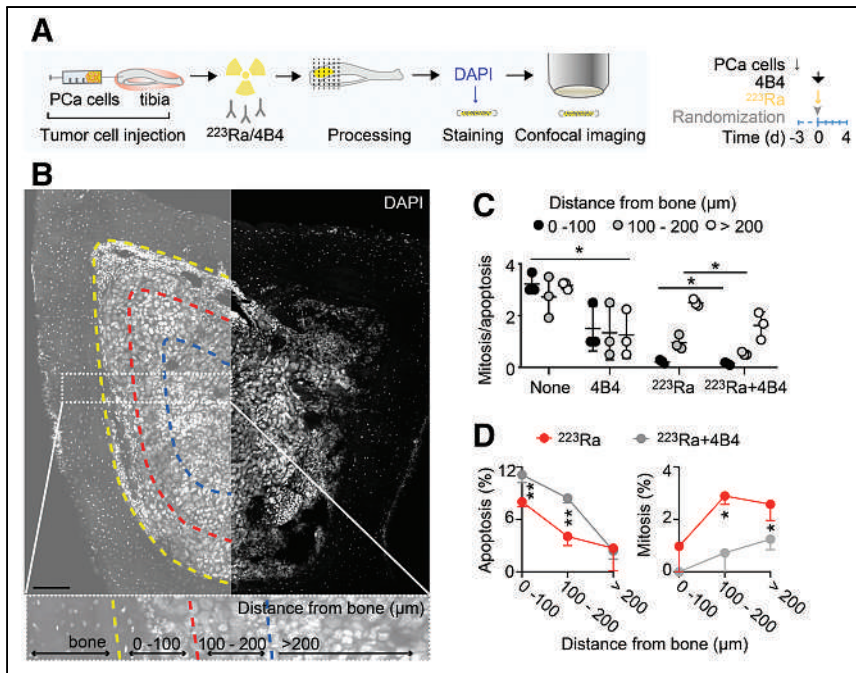


FIGURE 3. Cellular mechanisms of response to anti- β 1I and ^{223}Ra treatments. (A) Cartoon and timeline. (B) Representative overview micrograph. Insert shows zoomed subregions segmented every 100 μm from bone interface. Bar = 100 μm . (C) Quantification of mitosis/apoptosis nucleus ratio for each treatment condition. Data are mean \pm SD ($n = 3$ bones/treatment, 3–5 slices/bone). (D) Zonal comparison of apoptotic and mitotic cells for ^{223}Ra and $^{223}\text{Ra} + 4\text{B}4$ treatments. * $P < 0.05$. ** $P < 0.01$ by 1-way ANOVA and honestly-significant-difference post hoc test. DAPI = 4',6-diamidino-2-phenylindole.

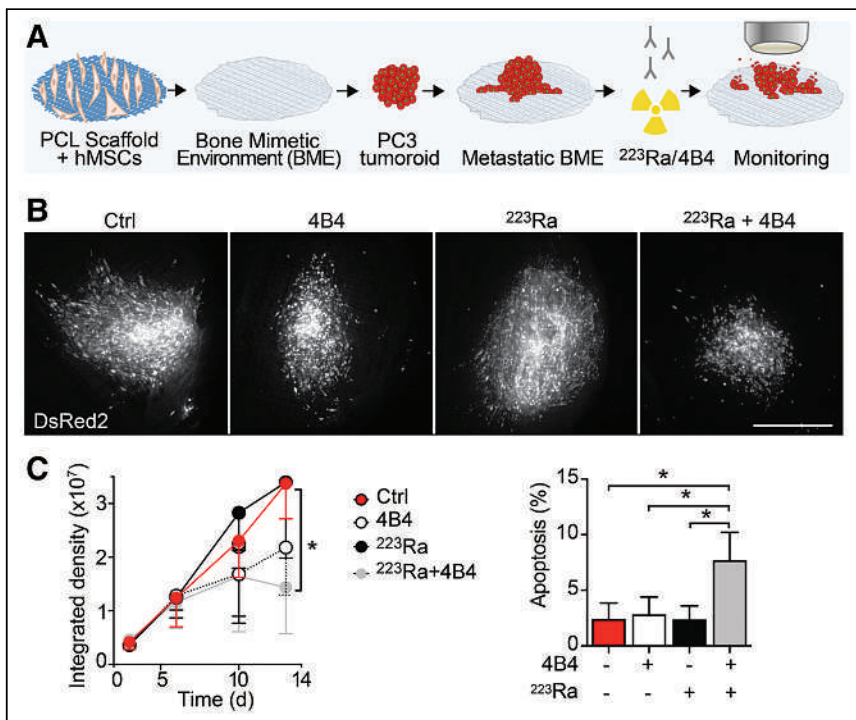


FIGURE 4. Effects of 4B4-mAb treatment on α -radiation sensitization. (A) Cartoon of experimental pipeline. (B and C) Representative pictures of PC3 tumoroids treated with 4B4-mAb (15 $\mu\text{g}/\text{mL}$) and ^{223}Ra (10 Bq/mL) alone or in combination (B); growth curve, with 3 independent experiments performed (means \pm SD, 6 scaffolds/condition; C, left panel); and percentage of apoptotic cells after treatment (means \pm SD, 6 scaffolds/treatment; C, right panel). Bar = 100 μm . * $P < 0.05$ by 1-way ANOVA and honestly-significant-difference post hoc test.

the repair of DNA double-strand breaks, and high expression is associated with poor prognosis after PCa radiation therapy (31). Mitogen-activated protein kinase regulates the activation of the mitogen-activated protein kinase/extracellular signal-regulated kinase pathway, thus affecting the survival of nonadherent cells (33), whereas its inhibition increases radiosensitivity of PCa xenografts via c-Myc downregulation (32). Transcription factor A, glutaminase, and fatty acid synthase have been also linked to radioresistance (34–36).

Overall, these results suggest that anti- β 1I treatment can sensitize tumor cells to ^{223}Ra treatment.

Mathematic Modeling of ^{223}Ra and 4B4-mAb Zonal Toxicity in PCa Bone Lesions

Our analyses suggest that β 1I interference decreases mitosis rates, and when combined with ^{223}Ra treatment, increases apoptosis along the bone interface. This dual effect may translate into tumor growth reduction and improved survival. To confirm whether decreased mitosis combined with extended zonal toxicity could mechanistically explain in vivo outcome, we performed in silico simulation based on an agent-based model that recapitulates zonal toxicity of ^{223}Ra on tumors in bone (7,37). The agent-based model was further developed to account for the response to 4B4-mAb based on probabilities of mitosis or apoptosis obtained from 4B4-treated mice (Figs. 3C and 5A). Tumor growth simulations in response to 4B4-mAb as a single agent or in combination with ^{223}Ra were performed for up to 800 h in tumors of different sizes (1–9,800 cells; Figs. 5A and 5B). The responses to combinatorial regimen and tumor size were inversely correlated, with potent tumor rejection of single or few cells and further efficacy improvement in bigger lesions that responded poorly to ^{223}Ra monotherapy (e.g., initial size of 2,400 cells; Fig. 5B; Supplemental Table 2). Control and 4B4-treated lesions did not show any spatial correlate for mitotic or apoptotic probabilities (Fig. 5C; Supplemental Fig. 8), as expected. ^{223}Ra treatment increased the apoptotic index along the bone interface, in a time-dependent manner accounting for ^{223}Ra decay. Combined ^{223}Ra and 4B4-mAb broadened the zone and duration of an elevated apoptotic index. These results confirm that 4B4-mediated extension of ^{223}Ra lethal effects combined with mitosis reduction support increased efficacy in vivo.

DISCUSSION

Metastatic cancer to bone is a persistent clinical challenge and a source of significant morbidity and mortality for patients afflicted with PCa. The inefficiency of current clinical investigations can be overcome, in part, by identifying new vulnerabilities and markers that can be used to select patients and monitor therapy response. We were motivated to perform this work to address the promising but limited efficacy that recently emerged from targeting bone metastasis by ^{223}Ra . βII interference increased ^{223}Ra therapeutic outcome in tumors expressing higher levels of βII by decreasing tumor growth and improving mouse survival via combined reduction of tumor cell mitosis and extension of ^{223}Ra -mediated zonal apoptosis. Although βII interference increases the efficacy of radiotherapy by means of external-beam radiation, we here establish integrin targeting as an efficient radiosensitizing strategy to improve the efficacy of α -particle-emitting bone-seeking radioisotopes.

Activation of βII occurs during PCa progression and has been detected in 65% and 72% of primary PCa or lymph node specimens compared with normal prostatic tissue (38). Variable expression of transcripts has been also identified in both soft-tissue and bone metastatic patient samples (19). Accordingly, βII is constitutively activated in highly metastatic PC3 cells compared with low metastatic C4-2B. Notably, βII expression levels in PCa cells do not correlate with their lytic function, as strongly osteoblastic MDA PCa 118b tumors display higher expression levels of βII than do PC3 cells (20).

βII represents a potential marker to select a subset of metastatic patients who would benefit of cotargeting by ^{223}Ra as a novel therapeutic strategy. Here, we tested only 2 cell lines endowed with βII expression levels that differ by about 1 log in vitro and 1.5–2 log in vivo. The resistance of C4-2B cells to 4B4-mAb treatment suggests that βII expression levels can correlate with targeting efficacy; however, we do not exclude that further alternative mechanisms could support resistance to this treatment. To better characterize this process and define a threshold for effective targeting of malignant cells, expression of βII in vivo should be tested in a variety of PCa patient-derived xenografts (39) followed by combined ^{223}Ra /anti- βII treatment and response monitoring. Patient-derived xenografts have the advantage of replicating the heterogeneity of human cancer biology with high fidelity, thus more accurately modeling these aspects in translational therapeutic studies. In this work, we identified the consequences of specific tumor cell targeting by 4B4-mAb, which blocks exclusively human βII and does not cross-react with the mouse stroma. Although being mechanistically informative about the direct effects on the tumor compartment, this approach does not address the role of targeting the bone environment. Besides in tumor cells, this integrin is expressed by bone stromal and immune cells (40), the targeting of which could further improve outcome, such as by interfering with the vicious cycle that supports cancer progression. On the other hand, stronger ^{223}Ra -mediated effects on bone cells might exacerbate bone remodeling or increase bone marrow toxicity, which can be mitigated by administration of bisphosphonates or granulocyte-stimulating factor, respectively. These studies would require analysis in syngeneic or genetically engineered models using an antimouse βII antibody that targets both tumor and stromal cells.

Combination of 4B4-mAb with ^{223}Ra extended cancer cell apoptosis beyond the spatial range expected to be reached by

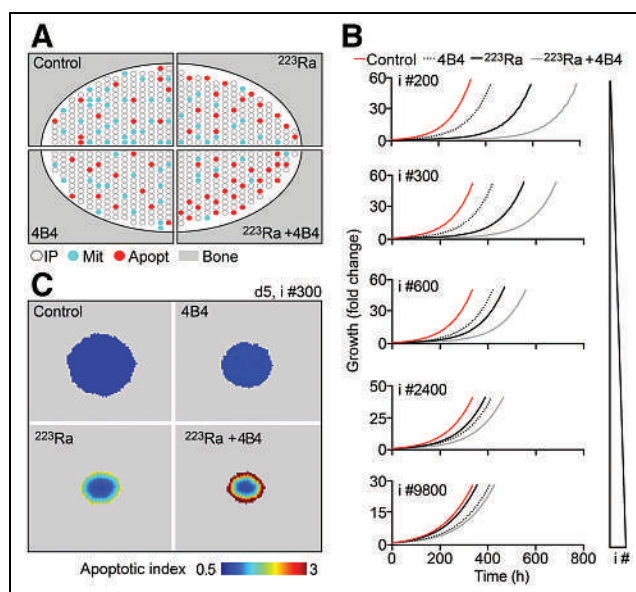


FIGURE 5. Mathematical modeling of ^{223}Ra and 4B4 response. (A) Schematic representation of in silico tumor lesions in bone. White dot = interphase (IP) cell; red dot = apoptotic cell; cyan dot = mitotic cell. (B) In silico simulations of tumor growth by lesions of different sizes in control, 4B4-mAb, ^{223}Ra , or ^{223}Ra + 4B4 treated samples (data represent means of 10 simulations). $i\#$ = initial number of tumor cells. (C) Apoptotic index (probability of apoptosis/probability of mitosis for each agent).

α -particles ($<100\ \mu\text{m}$). Reduced tumor density, caused by death induction, may allow the α -particles to travel farther than in a tighter, denser cellular matrix. In addition, we showed in a high-dose setting, in vitro, that long-range cytotoxicity can be in principle caused by ^{223}Ra , but further biophysical analyses are needed to dissect the relative contribution of α -, β -, or γ -radiation to the zonal cytotoxic effect achieved in bone at a therapeutically administered dose. Lastly, enhanced bystander effects may account for broadened zonal cytotoxicity by ^{223}Ra . Irradiation can induce a mutagenic response and cell activation, followed by juxtacrine bystander signaling toward nonirradiated neighboring cells through cell–cell interactions and release of soluble factors, including reactive oxygen species, toxic metabolites, and cytokines, which might be amplified by βII targeting (41,42). In line with these concepts, indirect effects of ^{223}Ra are supported by recent mouse and computational modeling, showing that a robust bystander effect component was required to simulate results achieved in vivo whereas a direct-effect component contributed modestly and was insufficient to explain in vivo outcome (43,44).

Interestingly, a humanized anti- βII monoclonal antibody has recently been developed for applications in patients and is currently being tested in a phase I clinical trial for glioblastoma (45). Therefore, clinical βII targeting combined with ^{223}Ra may be a realistic option in patients on identification of suitable candidates based on its expression levels.

CONCLUSION

Targeting bone metastasis by ^{223}Ra resulted in promising but limited therapeutic efficacy due to short α -particle penetrance. Our

work identified β 1-integrin interference as the first cotargeting strategy to improve ^{223}Ra outcome.

DISCLOSURE

This work was supported by the Cancer Prevention and Research Institute of Texas (RP140482); the Prostate Cancer Foundation (16YOUN24); Prostate Cancer SPOR (P50 CA140388-07); the European Research Council (ERC-CoG DEEPINSIGHT, 617430); the National Institutes of Health (U54 CA210184-01; P41 EB023833; P30 CA016672); and the Cancer Genomics Center, The Netherlands. ^{223}Ra is from Bayer. The funders had no role in the design of the study; the collection, analysis, or interpretation of the data; the writing of the manuscript; or the decision to submit the manuscript for publication. No other potential conflict of interest relevant to this article was reported.

ACKNOWLEDGMENT

We thank Dr. Kent Gifford (University of Texas M.D. Anderson Cancer Center) for the insightful discussion.

KEY POINTS

QUESTION: Can we improve the promising (but limited) efficacy that recently resulted from targeting bone metastasis by ^{223}Ra ?

PERTINENT FINDINGS: β 1I interference combined with ^{223}Ra reduced PCa cell growth in bone and significantly improved overall mouse survival. Targeting β 1I significantly decreased the tumor cell mitosis index and spatially doubled ^{223}Ra lethal effects through radiosensitization and reduction of radioresistance mediators.

IMPLICATIONS FOR PATIENT CARE: β 1I expression can represent a biomarker to select a subset of metastatic patients who would benefit from cotargeting by ^{223}Ra ; the availability of a humanized anti- β 1I monoclonal antibody will soon make combinatorial testing in patients clinically feasible.

REFERENCES

1. Steele CB, Li J, Huang B, Weir HK. Prostate cancer survival in the United States by race and stage (2001-2009): findings from the CONCORD-2 study. *Cancer*. 2017;123(suppl 24):5160-5177.
2. Gandaglia G, Abdollah F, Schifmann J, et al. Distribution of metastatic sites in patients with prostate cancer: a population-based analysis. *Prostate*. 2014;74:210-216.
3. D'Oronzo S, Coleman R, Brown J, Silvestris F. Metastatic bone disease: pathogenesis and therapeutic options: up-date on bone metastasis management. *J Bone Oncol*. 2019;15:004-4.
4. Park SH, Eber MR, Widner DB, Shiozawa Y. Role of the bone microenvironment in the development of painful complications of skeletal metastases. *Cancers (Basel)*. 2018;10:141.
5. Parker C, Nilsson S, Heinrich D, et al. Alpha emitter radium-223 and survival in metastatic prostate cancer. *N Engl J Med*. 2013;369:213-223.
6. Bruland ØS, Nilsson S, Fisher DR, Larsen RH. High-linear energy transfer irradiation targeted to skeletal metastases by the alpha-emitter ^{223}Ra : adjuvant or alternative to conventional modalities? *Clin Cancer Res*. 2006;12:6250s-6257s.
7. Dondossola E, Casarin S, Paindelli C, et al. Radium 223-mediated zonal cytotoxicity of prostate cancer in bone. *J Natl Cancer Inst*. 2019;111:1042-1050.
8. Abou DS, Ulmert D, Doucet M, Hobbs RF, Riddle RC, Thorek DL. Whole-body and microenvironmental localization of radium-223 in naive and mouse models of prostate cancer metastasis. *J Natl Cancer Inst*. 2016;108:djv380.
9. Morris MJ, Corey E, Guise TA, et al. Radium-223 mechanism of action: implications for use in treatment combinations. *Nat Rev Urol*. 2019;16:745-756.
10. Nam JM, Chung Y, Hsu HC, Park CC. β 1 integrin targeting to enhance radiation therapy. *Int J Radiat Biol*. 2009;85:923-928.
11. Park CC, Zhang HJ, Yao ES, Park CJ, Bissell MJ. β 1 integrin inhibition dramatically enhances radiotherapy efficacy in human breast cancer xenografts. *Cancer Res*. 2008;68:4398-4405.
12. Cordes N, Blaese MA, Meineke V, Van Beuningen D. Ionizing radiation induces up-regulation of functional β 1-integrin in human lung tumour cell lines in vitro. *Int J Radiat Biol*. 2002;78:347-357.
13. Goel HL, Sayeed A, Breen M, et al. Beta1 integrins mediate resistance to ionizing radiation in vivo by inhibiting c-jun amino terminal kinase 1. *J Cell Physiol*. 2013;228:1601-1609.
14. Eke I, Deuse Y, Hehlhans S, et al. B1 integrin/FAK/cortactin signaling is essential for human head and neck cancer resistance to radiotherapy. *J Clin Invest*. 2012;122:1529-1540.
15. Lu X, Lu D, Scully M, Kakkar V. The role of integrins in cancer and the development of anti-integrin therapeutic agents for cancer therapy. *Perspect Medicin Chem*. 2008;2:57-73.
16. Eliceiri BP. Integrin and growth factor receptor crosstalk. *Circ Res*. 2001;89:1104-1110.
17. Blandin AF, Renner G, Lehmann M, Lelong-Rebel I, Martin S, Döntenwill M. Beta1 integrins as therapeutic targets to disrupt hallmarks of cancer. *Front Pharmacol*. 2015;6:279.
18. Dickreuter E, Eke I, Krause M, Borgmann K, van Vugt MA, Cordes N. Targeting of β 1 integrins impairs DNA repair for radiosensitization of head and neck cancer cells. *Oncogene*. 2016;35:1353-1362.
19. Robinson D, Van Allen EM, Wu YM, et al. Integrative clinical genomics of advanced prostate cancer. *Cell*. 2015;161:1215-1228.
20. Lee YC, Lin SC, Yu G, et al. Identification of bone-derived factors conferring de novo therapeutic resistance in metastatic prostate cancer. *Cancer Res*. 2015;75:4949-4959.
21. Haeger A, Alexander S, Vullings M, et al. Collective cancer invasion forms an integrin-dependent radioresistant niche. *J Exp Med*. 2020;217:e20181184.
22. Takada Y, Puzon W. Identification of a regulatory region of integrin beta 1 subunit using activating and inhibiting antibodies. *J Biol Chem*. 1993;268:17597-17601.
23. Schwarz-Finsterle J, Scherthan H, Huna A, et al. Volume increase and spatial shifts of chromosome territories in nuclei of radiation-induced polyploidizing tumour cells. *Mutat Res*. 2013;756:56-65.
24. Gasperin P Jr, Gozy M, Pauwels O, et al. Monitoring of radiotherapy-induced morphonuclear modifications in the MXT mouse mammary carcinoma by means of digital cell image analysis. *Int J Radiat Oncol Biol Phys*. 1992;22:979-987.
25. Chen J, Niu N, Zhang J, et al. Polyploid giant cancer cells (PGCCs): the evil roots of cancer. *Curr Cancer Drug Targets*. 2019;19:360-367.
26. Schmidt U, Weigert M, Broaddus C, Myers G. Cell detection with star-convex polygons. In: Frangi A, Schnabel J, Davatzikos C, Alberola-López C, Fichtinger G, eds. *Medical Image Computing and Computer Assisted Intervention—MICCAI 2018*. 2018:265-273.
27. Schneider CA, Rasband WS, Eliceiri KW. NIH Image to ImageJ: 25 years of image analysis. *Nat Methods*. 2012;9:671-675.
28. Paindelli C, Navone N, Logothetis CJ, Friedl P, Dondossola E. Engineered bone for probing organotypic growth and therapy response of prostate cancer tumouroids in vitro. *Biomaterials*. 2019;197:296-304.
29. Eckerman K, Endo A. ICRP publication 107: nuclear decay data for dosimetric calculations. *Ann ICRP*. 2008;38:7-96.
30. Koukourakis MI, Giatromanolaki A, Panteliadou M, et al. Lactate dehydrogenase 5 isoenzyme overexpression defines resistance of prostate cancer to radiotherapy. *Br J Cancer*. 2014;110:2217-2223.
31. Li X, Baek G, Ramanand SG, et al. Brd4 promotes DNA repair and mediates the formation of tmprss2-erg gene rearrangements in prostate cancer. *Cell Rep*. 2018;22:796-808.
32. Ciccarelli C, Di Rocco A, Gravina GL, et al. Disruption of MEK/ERK/c-Myc signaling radiosensitizes prostate cancer cells in vitro and in vivo. *J Cancer Res Clin Oncol*. 2018;144:1685-1699.
33. Kyjacova L, Hubackova S, Krejčíkova K, et al. Radiotherapy-induced plasticity of prostate cancer mobilizes stem-like non-adherent, Erk signaling-dependent cells. *Cell Death Differ*. 2015;22:898-911.
34. Jiang X, Wang J. Down-regulation of TFAM increases the sensitivity of tumour cells to radiation via p53/TIGAR signalling pathway. *J Cell Mol Med*. 2019;23:4545-4558.

35. Fu S, Li Z, Xiao L, et al. Glutamine synthetase promotes radiation resistance via facilitating nucleotide metabolism and subsequent DNA damage repair. *Cell Rep.* 2019;28:1136–1143.e4.
36. Rae C, Haberkorn U, Babich JW, Mairs RJ. Inhibition of fatty acid synthase sensitizes prostate cancer cells to radiotherapy. *Radiat Res.* 2015;184:482–493.
37. Casarin S, Dondossola E. An agent-based model of prostate cancer bone metastasis progression and response to radium-223. *BMC Cancer.* 2020;20:605.
38. Lee YC, Jin JK, Cheng CJ, et al. Targeting constitutively activated beta1 integrins inhibits prostate cancer metastasis. *Mol Cancer Res.* 2013;11:405–417.
39. Palanisamy N, Yang J, Shepherd PDA, et al. The MD Anderson prostate cancer patient-derived xenograft series (MDA PCa PDX) captures the molecular landscape of prostate cancer and facilitates marker-driven therapy development. *Clin Cancer Res.* 2020;26:4933–4946.
40. Hughes DE, Salter DM, Dedhar S, Simpson R. Integrin expression in human bone. *J Bone Miner Res.* 1993;8:527–533.
41. Wang R, Coderre JA. A bystander effect in alpha-particle irradiations of human prostate tumor cells. *Radiat Res.* 2005;164:711–722.
42. Narayanan PK, Goodwin EH, Lehnert BE. Alpha particles initiate biological production of superoxide anions and hydrogen peroxide in human cells. *Cancer Res.* 1997;57:3963–3971.
43. Rajon DA, Canter BS, Leung CN, et al. Modeling bystander effects that cause growth delay of breast cancer xenografts in bone marrow of mice treated with radium-223. *Int J Radiat Biol.* 2021;97:1217–1228.
44. Leung CN, Canter BS, Rajon D, et al. Dose-dependent growth delay of breast cancer xenografts in the bone marrow of mice treated with ²²³Ra: the role of bystander effects and their potential for therapy. *J Nucl Med.* 2020;61:89–95.
45. Convection-enhanced delivery of OS2966 for patients with high-grade glioma undergoing a surgical resection. ClinicalTrials.gov website. <https://clinicaltrials.gov/ct2/show/nct04608812>. Published October 29, 2020. Updated January 26, 2022. Accessed February 24, 2022.

Affibody-Mediated PNA-Based Pretargeted Cotreatment Improves Survival of Trastuzumab-Treated Mice Bearing HER2-Expressing Xenografts

Maryam Oroujeni*¹, Hanna Tano*², Anzhelika Vorobyeva^{1,3}, Yongsheng Liu¹, Olga Vorontsova¹, Tianqi Xu¹, Kristina Westerlund², Anna Orlova^{3,4}, Vladimir Tolmachev^{1,3}, and Amelie Eriksson Karlström²

¹Department of Immunology, Genetics, and Pathology, Uppsala University, Uppsala, Sweden; ²Department of Protein Science, School of Engineering Sciences in Chemistry, Biotechnology, and Health, KTH Royal Institute of Technology, AlbaNova University Center, Stockholm, Sweden; ³Research Centrum for Oncotheranostics, Research School of Chemistry and Applied Biomedical Sciences, Tomsk Polytechnic University, Tomsk, Russia; and ⁴Department of Medicinal Chemistry, Uppsala University, Uppsala University, Uppsala, Sweden

J Nucl Med 2022; 63:1046–1051

DOI: 10.2967/jnumed.121.262123

Treatment of patients with human epidermal growth factor receptor 2 (HER2)-expressing tumors using the monoclonal antibody trastuzumab increases survival. The Affibody-based peptide nucleic acid (PNA)-mediated pretargeted radionuclide therapy has demonstrated efficacy against HER2-expressing xenografts in mice. Structural studies suggest that Affibody molecules and trastuzumab bind to different epitopes on HER2. The aim of this study was to test the hypothesis that a combination of PNA-mediated pretargeted radionuclide therapy and trastuzumab treatment of HER2-expressing xenografts can extend survival compared with monotherapies. **Methods:** Mutual interference of the primary pretargeting probe $Z_{\text{HER2:342}}\text{-SR-HP1}$ and trastuzumab in binding to HER2-expressing cell lines was investigated in vitro. Experimental therapy evaluated the survival of mice bearing HER2-expressing SKOV-3 xenografts after treatment with vehicle, trastuzumab only, pretargeting using Affibody-PNA chimera $Z_{\text{HER2:342}}\text{-SR-HP1}$ and complementary probe $^{177}\text{Lu-HP2}$, and combination of trastuzumab and pretargeting. The ethical permit limited the study to 90 d. The animals' weights were monitored during the study. After study termination, samples of liver and kidneys were evaluated by a veterinary pathologist for toxicity signs. **Results:** The presence of a large molar excess of trastuzumab had no influence on the affinity of $Z_{\text{HER2:342}}\text{-SR-HP1}$ binding to HER2-expressing cells in vitro. The affinity of trastuzumab was not affected by a large excess of $Z_{\text{HER2:342}}\text{-SR-HP1}$. The median survival of mice treated with trastuzumab (75.5 d) was significantly longer than the survival of mice treated with a vehicle (59.5 d). Median survival of mice treated with pretargeting was not reached by day 90. Six mice of 10 in this group survived, and 2 had complete remission. All mice in the combination treatment group survived, and tumors in 7 mice had disappeared at study termination. There was no significant difference between animal weights in the different treatment groups. No significant pathologic alterations were detected in livers and kidneys of treated animals. **Conclusion:** Treatment of mice bearing HER2-expressing xenografts with the combination of trastuzumab and Affibody-mediated PNA-based radionuclide pretargeting significantly increased survival compared with monotherapies. Cotreatment was not toxic for normal tissues.

Key Words: trastuzumab; PNA pretargeting; Affibody molecules; radionuclide therapy; HER2

Human epidermal growth factor receptor 2 (HER2) is a transmembrane tyrosine kinase receptor overexpressed in about 20%–30% of breast cancer (1), 18% of gastric and gastroesophageal cancer (2), and 9%–32% of ovarian carcinoma cases (3). The humanized monoclonal antibody trastuzumab binds to domain IV in the extracellular part of HER2. HER2-targeted therapy using trastuzumab together with nontargeted chemotherapy is a standard combination for treatment of patients with HER2-positive breast, gastric, and gastroesophageal cancers (4–6). However, resistance to trastuzumab treatment is often developed despite preserved HER2 expression (7).

In vitro studies have demonstrated that treatment with trastuzumab increases the sensitivity of breast cancer cell lines to radiation (8,9). Clinical data suggest that adding trastuzumab to local adjuvant radiotherapy significantly reduces the risk of breast cancer locoregional recurrence (10,11). It would also be attractive to combine radiation therapy and trastuzumab medication in a systemic treatment of disseminated HER2-expressing cancers. HER2-targeted radionuclide therapy might be a solution for such a combination treatment. However, the straightforward use of monoclonal antibodies labeled with cytotoxic radionuclides is problematic for the treatment of solid tumors (12,13). The slow clearance of bulky antibodies from the circulation results in high exposure of the radiosensitive bone marrow, which prevents sufficient delivery of radionuclides to tumors. The use of smaller targeting agents such as Affibody (Affibody AB) molecules (7 kDa) might be an alternative. Safety, tolerability, and excellent targeting of HER2-expressing breast cancer metastases using Affibody molecules have been confirmed in clinics (14). However, direct application of radiolabeled Affibody molecules for radionuclide therapy is excluded because of their high reabsorption in the kidneys (15). To avoid renal reabsorption, an Affibody-based pretargeting approach was investigated, and peptide nucleic acid (PNA)-mediated pretargeting appeared to be the most efficient of the tested strategies (16). PNAs are synthetic DNA analogs with charge-neutral and flexible peptide-like backbones (Supplemental Fig. 1A; supplemental materials are available at <http://jnm.snmjournals.org>) and are highly stable in human serum and cellular extracts (17). The pretargeting system is based on 2 complementary

Received Feb. 10, 2021; revision accepted Oct. 15, 2021.

For correspondence or reprints, contact Vladimir Tolmachev (vladimir.tolmachev@igp.uu.se).

*Contributed equally to this work.

Published online Oct. 28, 2021.

COPYRIGHT © 2022 by the Society of Nuclear Medicine and Molecular Imaging.

15-meric PNA probes: the primary *HP1* probe and the secondary *HP2* probe (18). The secondary *HP2* probe contains both a DOTA chelator and tyrosine, which enable labeling with a variety of radiometals and radioiodine (16,19). The primary *HP1* probe is site-specifically conjugated to the HER2-targeting Affibody molecule $Z_{HER2:342}$, forming the $Z_{HER2:342}$ -SR-*HP1* Affibody-PNA chimera. A DOTA chelator is also incorporated into $Z_{HER2:342}$ -SR-*HP1*, which enables labeling of this agent for preclinical development and for imaging within therapeutic applications (20). The sequences of $Z_{HER2:342}$ -SR-*HP1* and *HP2* are shown in Supplemental Figure 1B. This Affibody molecule-based PNA-mediated approach reduced renal uptake 70-fold compared with direct targeting using ^{177}Lu -labeled parental Affibody molecules (16). A schematic illustration of the PNA-mediated pretargeted therapy approach is shown in Supplemental Figure 1C. Experimental therapy using $Z_{HER2:342}$ -SR-*HP1*/ ^{177}Lu -*HP2* pretargeting significantly increased the median survival of mice bearing HER2-expressing xenografts without bone marrow and renal toxicity (21).

Importantly, structural studies (22) have shown that the epitope of the anti-HER2 Affibody binding to HER2 is distant from the epitope of trastuzumab (Fig. 1). This distance creates a precondition for independent binding of trastuzumab and the primary probe without mutual interference and should enable cotreatment using trastuzumab and Affibody-mediated pretargeting.

The goal of this study was to test the hypothesis that Affibody-mediated PNA-based pretargeting cotreatment can improve the survival of mice with HER2-expressing xenografts treated with trastuzumab. We evaluated interference between the binding of trastuzumab and $Z_{HER2:342}$ -SR-*HP1* to HER2-expressing cancer cell lines in vitro. Further, we compared the effect on tumor growth and survival of mice treated by cotargeting with the effects of treatment with trastuzumab and pretargeting alone.

MATERIALS AND METHODS

Carrier-free $^{177}\text{LuCl}_3$ was purchased from Curium. HER2-expressing ovarian cancer SKOV-3 and breast cancer BT474 cells were purchased from the American Type Culture Collection. Cells were cultured at 37°C in 5% CO_2 in RPMI medium (Flow Laboratories) supplemented with 10% fetal calf serum, 2 mM L-glutamine, 100 IU/mL penicillin, and 100 $\mu\text{g}/\text{mL}$ streptomycin.

Radiolabeling

The PNA probes (*HP1* and *HP2*) and the HER2-binding Affibody were produced, purified, and characterized (Supplemental Figs. 2–5) as described earlier (18). The primary probe $Z_{HER2:342}$ -SR-*HP1* was prepared from the *HP1* probe and the Affibody molecule using an optimized conjugation protocol (23). The secondary probe *HP2* was radiolabeled with ^{177}Lu using a previously described method (23). For in vitro experiments, the primary probe $Z_{HER2:342}$ -SR-*HP1* was labeled with ^{177}Lu and trastuzumab was labeled with ^{125}I as previously described (24,25).

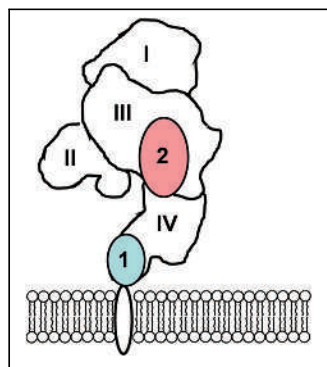


FIGURE 1. Epitopes for binding of trastuzumab (1) and Z_{HER2} Affibody molecule (2) to extracellular domain of HER2 (22).

In Vitro Studies

To check whether trastuzumab and $Z_{HER2:342}$ -SR-*HP1* interfere with each other's

binding to HER2-expressing cell lines in vitro, the following assay was performed. Cells were seeded into cell culture dishes with a density of 10^6 cells per dish. Four sets of 3 dishes were used for each conjugate. For blocking, nonlabeled $Z_{HER2:342}$ -SR-*HP1*, trastuzumab, or the control anti-VEGF antibody bevacizumab (both from F. Hoffmann-La Roche) were added to sets of 3 dishes each to obtain concentrations of 200 nM. An equal volume of medium was added to the fourth set of dishes. After incubation at room temperature for 15 min, ^{177}Lu - $Z_{HER2:342}$ -SR-*HP1* or ^{125}I -trastuzumab was added to all dishes to obtain a concentration of 1 nM. The cells were incubated for 1 h at 37°C. Thereafter, the cells were washed, the cells were detached by trypsin, and the cell-associated radioactivity was measured.

To evaluate the mutual interference of the targeting agents further, the affinity of their interaction with SKOV-3 cells in vitro was measured using a LigandTracer Yellow instrument (Ridgeview Instruments AB) as described earlier (19). Two concentrations of ^{177}Lu - $Z_{HER2:342}$ -SR-*HP1* (1 and 3 nM) were used to estimate an association rate. The measurements were performed either in the presence of trastuzumab (70 nM) or in its absence. The association rate of ^{125}I -trastuzumab was measured with concentrations of 1 and 3 nM, in the presence of $Z_{HER2:342}$ -SR-*HP1* (140 nM) or in its absence. The calculations of affinities and their visualization were performed using the InteractionMap software (Ridgeview Diagnostics AB). Experiments were performed in duplicate.

Experimental In Vivo Therapy

Animal experiments were performed in accordance with the national legislation for work with laboratory animals. Approval was granted by the Ethical Committee for Animal Research in Uppsala. According to the ethical permit, the therapy should not continue longer than 90 d.

Female BALB/c nu/nu mice (Scanbur) were subcutaneously (abdomen area) implanted with 10^7 SKOV-3 cells. The subcutaneous xenograft model was selected because it permits more exact tumor volume measurement than a disseminated tumor model. The mice were randomly divided into 4 groups of 10 animals each. Treatment started 1 wk after tumor implantation. The injected activity and number of injections were calculated using mouse dosimetry data (21) to provide the absorbed doses: approximately 100 Gy to tumor, 20 Gy to kidney, and 1 G to bone marrow. Group A (control) was subcutaneously injected with 100 μL of 0.5% bovine serum albumin in phosphate-buffered saline. Group B (trastuzumab treatment) was subcutaneously (neck area) injected with 6 injections of trastuzumab (4 mg/kg for 2 wk followed by 2 mg/kg weekly, that is, the same dosing as in clinics (26)). Group C (radionuclide pretargeting treatment) was intravenously injected with 100 μg (7.6 nmol) of $Z_{HER2:342}$ -SR-*HP1* and 16 h later with 3.5 μg (0.68 nmol/16 MBq) of ^{177}Lu -*HP2* in a 100- μL solution containing 0.5% bovine serum albumin and 4 mg of Gelofusine (Hausmann Laboratories Ltd.) once a week. In total, 6 injections were performed. Group D (cotreatment) was treated with pretargeting (same as group C) in combination with trastuzumab (the same as group B). The tumor volumes at the start of treatment were 91 ± 25 , 99 ± 42 , 91 ± 34 , and 97 ± 30 mm^3 , for mice treated with 0.5% bovine serum albumin/phosphate-buffered saline, trastuzumab, pretargeting, and combined trastuzumab and pretargeting, respectively (no significant difference in ANOVA, Supplemental Fig. 6A).

Throughout the experiment, tumor volumes and body weights were monitored twice per week. The tumor volumes were determined by caliper measurement of the largest longitudinal (length) and transverse (width) diameter and calculated by the following formula: tumor volume = $\frac{1}{2}$ [length (mm)] \times [width (mm)]².

The animals were euthanized when tumors reached a size of 1,000 mm^3 or became ulcerated, or if an animal's weight dropped by more than 10% during 1 wk or by more than 15% since the study began. Ninety days after treatment started, all animals were euthanized using xylazine/ketamine anesthesia. After euthanasia, tumor, kidneys, and liver were excised for subsequent histologic and immunohistochemistry evaluations.

The evaluations were performed at the Swedish National Veterinary Institute. The samples were formalin-fixed and paraffin-embedded. Tumor sections (4 μm) were stained with hematoxylin and eosin for histologic evaluation and using the HercepTest Kit (Agilent) to determine HER2 expression.

Imaging During Experimental Therapy

To confirm efficient tumor pretargeting, SPECT/CT imaging of 2 mice from group C and 2 mice from group D was performed 24 h after every injection of ^{177}Lu -HP2. Imaging was performed using a nano-Scan SPECT/CT device (Mediso Medical Imaging Systems) under sevoflurane anesthesia as described earlier (21).

Statistical Analysis

Data were analyzed by an unpaired, 2-tailed *t* test or 1-way ANOVA with Bonferroni adjustment for multiple comparisons. Survival data were analyzed by a log-rank test. Tumor ulceration was considered to be identical to the tumor size endpoint in the test. Prism (version 7.03 for Microsoft Windows; GraphPad Software) was used to determine significant statistical differences ($P < 0.05$).

RESULTS

Radiolabeling

The correct molecular weights of the primary and secondary probes were confirmed using mass spectrometry (Supplemental Figs. 2 and 3). The purity of the probes was over 95% (Supplemental Figs. 4 and 5). Radiolabeling of HP2 with ^{177}Lu was achieved in high yields (>95%) at a maximum molar activity of 23.5 MBq/nmol.

In Vitro Studies

The results of the mutual blocking assay of trastuzumab and $Z_{\text{HER2:342}}\text{-SR-HP1}$ to HER2-expressing cell lines are presented in Figure 2. The cell-associated radioactivity of ^{125}I -trastuzumab for both HER2-expressing cell lines was significantly ($P < 0.005$) decreased when HER2 receptors were saturated with nonlabeled trastuzumab. No significant difference in binding was observed when cells were saturated with the primary agent $Z_{\text{HER2:342}}\text{-SR-HP1}$ or bevacizumab (Fig. 2A). The cell-associated radioactivity of ^{177}Lu - $Z_{\text{HER2:342}}\text{-SR-HP1}$ to both HER2-expressing cell lines was significantly ($P < 0.0001$) decreased when HER2 receptors were saturated with $Z_{\text{HER2:342}}\text{-SR-HP1}$. The binding of ^{177}Lu - $Z_{\text{HER2:342}}\text{-SR-HP1}$ was also significantly decreased by pretreatment with trastuzumab ($P < 0.05$). However, the decrease was much smaller in this case and was at the same level after treatment with the control anti-VEGF antibody bevacizumab (Fig. 2B).

The data concerning the effect of trastuzumab presence on the binding affinity of ^{177}Lu - $Z_{\text{HER2:342}}\text{-SR-HP1}$ to HER2 receptors are presented in Table 1 and Supplemental Figure 7. The data concerning the influence of $Z_{\text{HER2:342}}\text{-SR-HP1}$ presence on the binding affinity of ^{125}I -trastuzumab to HER2 receptors are presented in Table 2 and Supplemental Figure 8. No interference of trastuzumab presence on the binding affinity of ^{177}Lu - $Z_{\text{HER2:342}}\text{-SR-HP1}$, or of $Z_{\text{HER2:342}}\text{-SR-HP1}$ presence on the binding affinity of ^{125}I -trastuzumab, to HER2 receptors was observed.

Experimental In Vivo Therapy

SPECT/CT imaging (Fig. 3) demonstrated efficient delivery of ^{177}Lu to tumors. The tumor uptake in mice treated with both pretargeting and trastuzumab was on the same level as in mice treated with pretargeting alone (Supplemental Fig. 9). Six pretargeted treatment cycles did not decrease the maximum uptake of ^{177}Lu -HP2 in tumors (Supplemental Fig. 9).

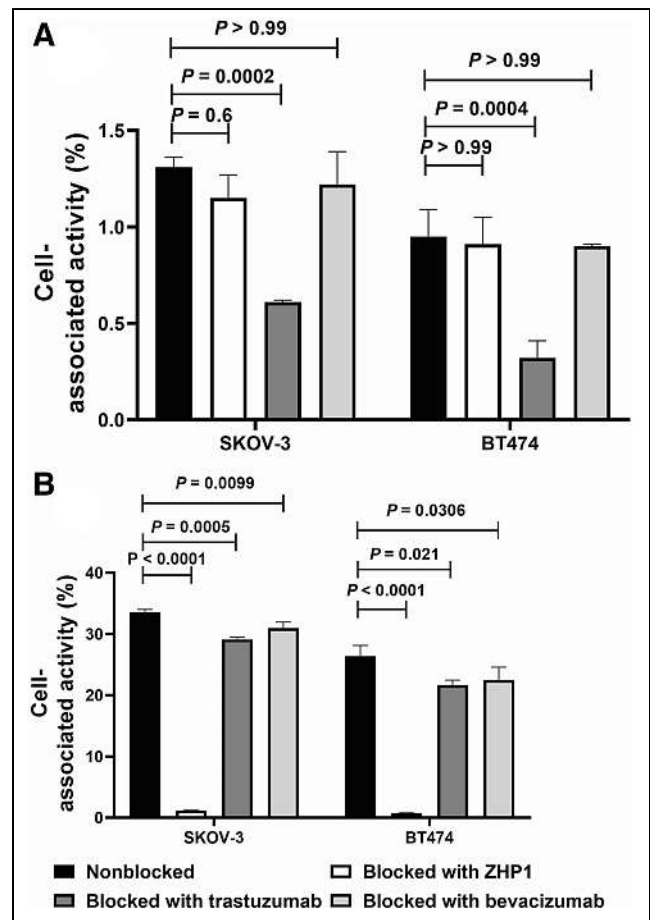


FIGURE 2. In vitro binding specificity of ^{125}I -trastuzumab (A) and ^{177}Lu - $Z_{\text{HER2:342}}\text{-SR-HP1}$ (B) on HER2-expressing SKOV-3 and BT-474 cells. For both experiments, 1 nM of labeled conjugate and 200 nM of blocking agents were used. Data are presented as average value from 3 samples \pm SD. ZHP1 = $Z_{\text{HER2:342}}\text{-SR-HP1}$.

Information concerning tumor growth, body weight, and survival in different groups of animals is presented in Figures 4 and 5. All treatment modalities slowed the tumor growth rate. Seven days after the first injection, the average tumor volume in all treatment groups was significantly smaller than the average volume in the control group (group A) (Supplemental Fig. 6B). The median survival was the shortest in the control group (59.5 d), and all animals in this group were euthanized by day 74 (Fig. 5A). The treatment with trastuzumab alone (group B) significantly increased ($P < 0.05$) the median survival to 75.5 d (Fig. 5A). Two of 4 surviving mice had very small, less than 10 mm^3 , tumors. Pretargeted monotherapy (group C) was somewhat more efficient than monotherapy with trastuzumab. The median survival in group C was not reached within the permitted experiment time, but there was no significant difference between survival in groups C and D (Figs. 4 and 5). Tumors in 2 of 6 surviving mice disappeared completely at the time of euthanasia, and 1 mouse had a tumor smaller than 10 mm^3 . The combination of pretargeting and trastuzumab treatment (group D) was the most efficient, according to the results of the log-rank test (Fig. 5A). All mice survived until study termination. Seven mice had complete remission at that moment, and 2 mice had a tumor smaller than 10 mm^3 . Still, the small tumors contained viable tumor cells undergoing mitosis (Supplemental Fig. 10).

TABLE 1

Association Rate (k_a), Dissociation Rate (k_d), and Equilibrium Dissociation (K_D) Constants for Interaction Between ^{177}Lu -Z_{HER2:342}-SR-HP1 and HER2-Expressing SKOV-3 Cells in Presence and Absence of Trastuzumab Determined Using Interaction Map Analysis of LigandTracer Sensorgrams

Parameter	k_a [(1/M × s) × 10 ⁴]	k_d [(1/s) × 10 ⁻⁶]	K_D (pM)
^{177}Lu -Z _{HER2:342} -SR-HP1 only	3.5 ± 0.4	2.6 ± 0.6	78 ± 28
^{177}Lu -Z _{HER2:342} -SR-HP1 with trastuzumab	3.5 ± 0.3	2.90 ± 0.04	85 ± 7

TABLE 2

Association Rate (k_a), Dissociation Rate (k_d), and Apparent Equilibrium Dissociation (K_D) Constants for Interaction Between ^{125}I -Trastuzumab and HER2-Expressing SKOV-3 Cells in Presence and Absence of Z_{HER2:342}-SR-HP1 Determined Using Interaction Map Analysis of LigandTracer Sensorgrams

Parameter	k_a [(1/M × s) × 10 ⁵]	k_d [(1/s) × 10 ⁻⁶]	K_D (pM)
^{125}I -trastuzumab only	5.6 ± 0.0	2 ± 0.7	3.7 ± 1.2
^{125}I -trastuzumab with ZHER2:342-SR-HP1	4.5 ± 0.2	1.9 ± 0.1	4.4 ± 0.7

Although tumors from groups A, B, and C retained HER2 expression on a 3+ level, the remaining tumors from group D had heterogeneous HER2 expression (Supplemental Fig. 11).

When the outcomes were categorized as no response (animals were euthanized before the study endpoint), response (animals with

visible tumors survived until the study endpoint), and remission (no visible tumors at the study endpoint), a Pearson χ^2 test revealed significant differences among all groups (Supplemental Fig. 12).

The therapy was well tolerated. The average weight of the animals in the treatment groups did not differ significantly (ANOVA, $P < 0.05$) from the average weight in the control group at any time point (Fig. 5B). According to the histopathology evaluation, there was no evidence of renal toxicity in the treatment groups. No structures of the renal parenchyma in the treated animals differed from these structures in the kidneys of mice in the control group (Supplemental Fig. 13). In some livers of mice from the treatment groups, scattered mitoses were found among the hepatocytes, a finding that could indicate an ongoing regenerative activity (Supplemental Fig. 14). In the livers of 2 mice from the combined-treatment group, infiltrates of mononuclear leukocytes were observed in a few portal areas. According to the pathologist, these changes were very subtle.

DISCUSSION

Targeted therapies offer the advantage of a specific antitumor effect and minimize systemic toxicity. Therefore, there is an apparent trend to increase the targeted component in the treatment, such as by combining trastuzumab and pertuzumab treatment already in the first-line therapy of advanced breast cancer (27). In addition, the combination of 2 different therapeutics with different mechanisms of action has a potential to suppress resistance development (28). The use of radionuclide targeting is an attractive addition to trastuzumab because this antibody sensitizes the tumor to irradiation. Such a combination requires an absence of mutual interference of targeting agents in the binding to HER2. Trastuzumab does not interfere with binding of the small monomeric form of the anti-HER2 Affibody in vitro or in vivo (29). However, coupling of HP1 makes the Z_{HER2:342}-SR-HP1 chimera bulkier, and interference could not be excluded. The results of the binding test (Fig. 2A) showed that there was no significant decrease in cell-associated radioactivity of ^{125}I -trastuzumab when HER2-expressing cancer cells were pretreated with a large molar excess of Z_{HER2:342}-SR-HP1. There was a small but significant reduction of cell-bound radioactivity of ^{177}Lu -Z_{HER2:342}-SR-HP1 when cells were pretreated with an excess of trastuzumab.

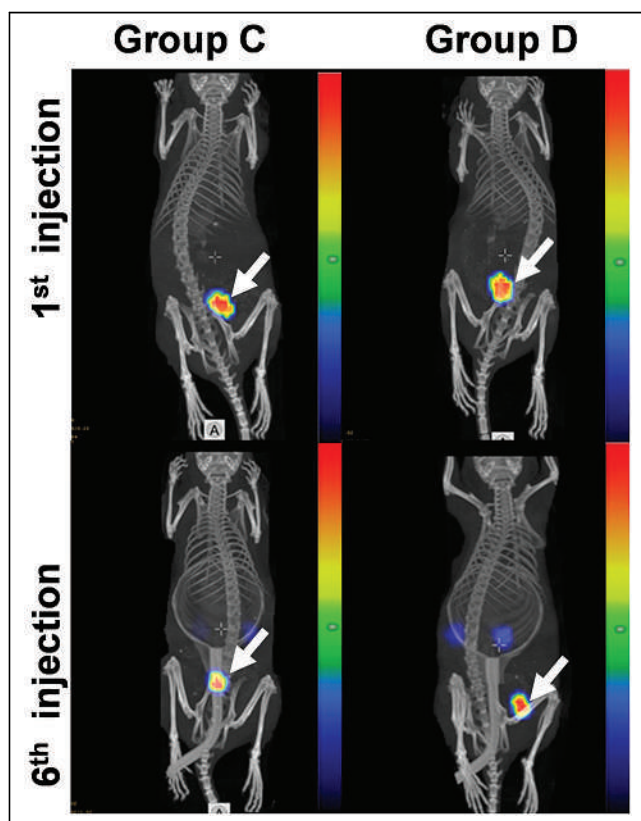


FIGURE 3. Representative SPECT/CT images (maximum-intensity projections) of mouse from treatment group C and mouse from treatment group D. Imaging was performed 24 h after first injection and sixth injection of ^{177}Lu -HP2. Arrows point at tumors. Linear relative scale (arbitrary units normalized to a maximum count rate) is applied.

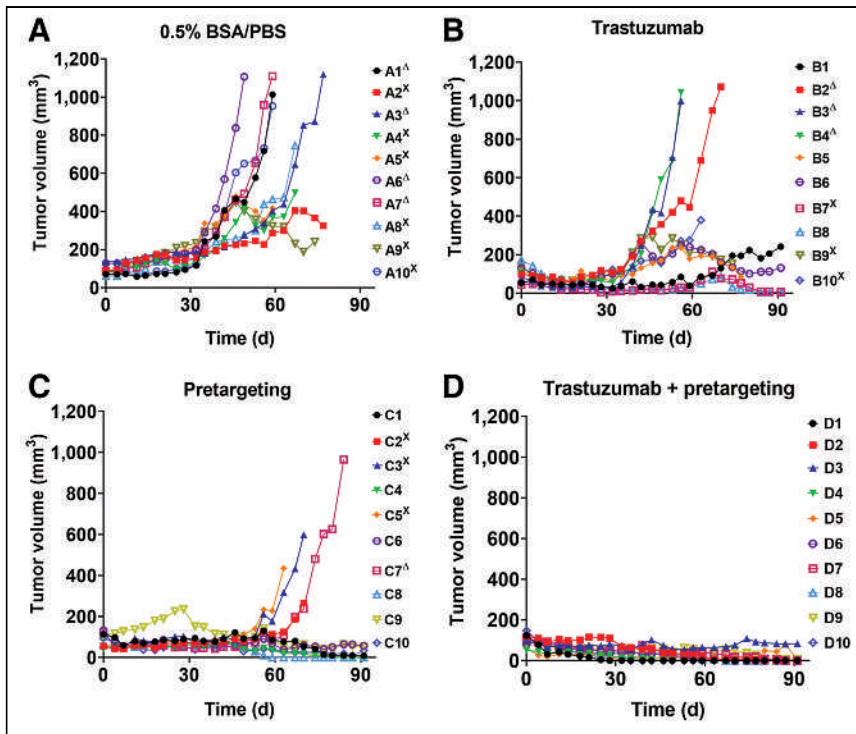


FIGURE 4. Experimental therapy with tumor volume growth curves for individual mice in each group. SKOV-3 cells were subcutaneously implanted into belly of nude BALB/c nu/nu-mice. Mice were treated with 0.5% bovine serum albumin/phosphate-buffered saline (BSA/PBS) (control) (A), trastuzumab only (B), pretargeting only (C), and combination of trastuzumab and pretargeting (D). ^ΔMice were euthanized when volume of subcutaneous xenografts exceeded 1,000 mm³. ^XMice were euthanized when bleeding ulcers on xenografts were observed.

However, treatment with the control antibody bevacizumab (which does not bind to HER2) had a similar effect. Thus, this phenomenon should not be associated with the blocking of ¹⁷⁷Lu-Z_{HER2:342}-SR-HP1 binding to the target. The measurement by LigandTracer did not show any impact of trastuzumab presence on the affinity of ¹⁷⁷Lu-Z_{HER2:342}-SR-HP1 binding to HER2-expressing cells (Table 2; Supplemental Fig. 7) or of Z_{HER2:342}-SR-HP1 presence on the affinity of ¹²⁵I-trastuzumab binding (Table 2; Supplemental Fig. 8). No influence of trastuzumab treatment on pretargeted delivery of ¹⁷⁷Lu to tumors was observed by SPECT imaging performed during therapy (Fig. 3; Supplemental Fig. 9). The level of uptake was approximately the

same with and without trastuzumab. Therefore, it is obvious from these experiments that the primary agent and trastuzumab are binding to different sites on HER2 receptors without mutual interference.

The experimental therapy data (Figs. 4 and 5) suggested that the tested hypothesis is correct. Trastuzumab as a monotherapy extended the median survival of mice from 59.5 d (vehicle-injected control) to 75.5 d. The median survival for mice treated with pretargeted radionuclide therapy was not reached within the permitted time of the therapy experiment but was apparently longer than 90 d. This treatment resulted in complete disappearance of tumors in 2 animals of 10, whereas residual tumors remained in all mice treated with trastuzumab. The combination therapy was the most efficient. It prevented tumor growth or ulceration more effectively than did pretargeting therapy alone (Fig. 4). There was complete remission in 7 animals of 10, and not a single animal had to be euthanized. A heterogeneous HER2 expression in the remaining tumors from this group indicates that down-regulation of HER2 or a selection of clones with low HER2 expression might be a mechanism of resistance (or at least a reason for incomplete remission). At the same time, no severe toxicity was detected in any of the treatment groups. Noteworthy, SKOV-3 is appreciably more radioresistant than 2 other cell lines with high HER2 expression, SK-BR-3 and BT-474 (30), and can be considered the worst-case model for radionuclide therapy.

A precondition for a successful combination treatment is an additive effect of the drugs on tumors but different toxicity profiles. This requirement was fulfilled in the proposed therapy. No toxicity of anti-HER2 Affibody molecules was detected in rodents (31). No Affibody-caused toxicity has been found in clinical studies (14), nor has PNA toxicity has been found in clinics (32). The only toxicity in the pretargeted radionuclide therapy is expected from the radionuclide, and the kidneys are expected to be the dose-limiting organ (21). The most severe side effect of trastuzumab is cardiotoxicity (33). Hence, the toxicity profiles of the proposed therapeutics are different. Pathology investigation did not reveal any serious side effects in this study. HER2-targeted therapy remains an area of intensive development (34). As far as we know, our approach is the only one that does not rely on radioresistance of mice but keeps the dose limits to both kidneys and bone marrow within limits accepted in clinics.

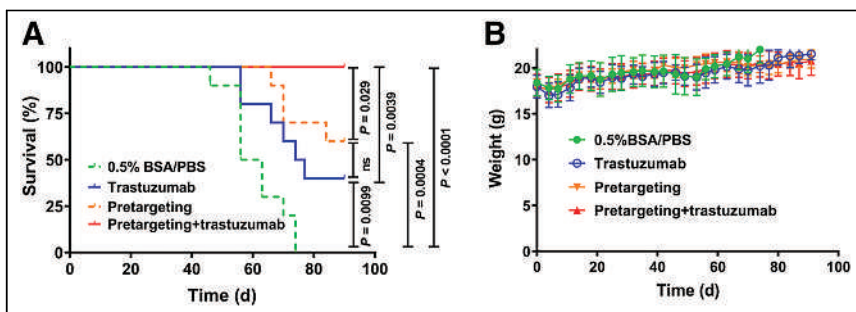


FIGURE 5. (A) Survival of BALB/C nu/nu-mice with SKOV-3 xenografts treated with pretargeting plus trastuzumab, pretargeting alone, trastuzumab alone, or 0.5% bovine serum albumin in phosphate-buffered saline (0.5% BSA/PBS). (B) Average animal weight during therapy. Data are presented as average value \pm SD. BSA = bovine serum albumin; PBS = phosphate-buffered saline.

CONCLUSION

We have shown that combined injection of the monoclonal antibody trastuzumab with Affibody-mediated PNA-based pretargeting

significantly increased the median survival in mice bearing HER2-expressing tumors compared with trastuzumab only. This makes the combination of trastuzumab and pretargeting a promising candidate for clinical translation.

DISCLOSURE

This work has been supported by grants from the Swedish Cancer Society, Swedish Research Council, and Swedish Agency for Innovation VINNOVA. Vladimir Tolmachev and Anna Orlova are members of the Technical Advisory Board of Affibody AB (Solna, Sweden) and have shares in this company. No other potential conflict of interest relevant to this article was reported.

KEY POINTS

QUESTION: Does the addition of PNA-mediated Affibody-based pretargeted therapy increase the efficacy of trastuzumab treatment of HER2-expressing xenografts?

PERTINENT FINDINGS: The combination of PNA-mediated Affibody-based radionuclide pretargeting and trastuzumab therapy has a stronger antitumor effect than either modality alone. The combination treatment is not associated with any additional toxicity.

IMPLICATIONS FOR PATIENT CARE: Data from this study support further development of combination targeting therapy, which might improve the survival of patients with HER2-expressing cancer.

REFERENCES

- Slamon DJ, Clark GM, Wong SG, et al. Human breast cancer: correlation of relapse and survival with amplification of the HER-2/neu oncogene. *Science*. 1987; 235:177–182.
- Abraham-Machado LF, Scapulatempo-Neto C. HER2 testing in gastric cancer: an update. *World J Gastroenterol*. 2016;22:4619–4625.
- Meden H, Kuhn W. Overexpression of the oncogene c-erbB-2 (HER2/neu) in ovarian cancer: a new prognostic factor. *Eur J Obstet Gynecol Reprod Biol*. 1997;71:173–179.
- Smith I, Procter M, Gelber RD, et al. 2-year follow-up of trastuzumab after adjuvant chemotherapy in HER2-positive breast cancer: a randomised controlled trial. *Lancet*. 2007;369:29–36.
- Slamon D, Eiermann W, Robert N, et al. Adjuvant trastuzumab in HER2-positive breast cancer. *N Engl J Med*. 2011;365:1273–1283.
- Giordano SH, Temin S, Chandarlapaty S, et al. Systemic therapy for patients with advanced human epidermal growth factor receptor 2-positive breast cancer: American Society of Clinical Oncology clinical practice guideline. *J Clin Oncol*. 2014; 32:2078–2099.
- Rexer BN, Arteaga CL. Intrinsic and acquired resistance to HER2-targeted therapies in HER2 gene-amplified breast cancer: mechanisms and clinical implications. *Crit Rev Oncog*. 2012;17:1–16.
- Liang K, Lu Y, Jin W, Ang KK, Milas L, Fan Z. Sensitization of breast cancer cells to radiation by trastuzumab. *Mol Cancer Ther*. 2003;2:1113–1120.
- Sato S, Kajiyama Y, Sugano M, et al. Monoclonal antibody to HER-2/neu receptor enhances radiosensitivity of esophageal cancer cell lines expressing HER-2/neu oncoprotein. *Int J Radiat Oncol Biol Phys*. 2005;61:203–211.
- Kiess AP, McArthur HL, Mahoney K, et al. Adjuvant trastuzumab reduces locoregional recurrence in women who receive breast-conservation therapy for lymph node-negative, human epidermal growth factor receptor 2-positive breast cancer. *Cancer*. 2012;118:1982–1988.
- Peterson DJ, Truong PT, Sadek BT, et al. Locoregional recurrence and survival outcomes by type of local therapy and trastuzumab use among women with node-negative, HER2-positive breast cancer. *Ann Surg Oncol*. 2014;21:3490–3496.
- Larson SM, Carrasquillo JA, Cheung NK, Press OW. Radioimmunotherapy of human tumours. *Nat Rev Cancer*. 2015;15:347–360.
- Bartholomä MD. Radioimmunotherapy of solid tumors: approaches on the verge of clinical application. *J Labelled Comp Radiopharm*. 2018;61:715–726.
- Sörensen J, Veliky I, Sandberg D, et al. Measuring HER2-receptor expression in metastatic breast cancer using [⁶⁸Ga]ABY-025 Affibody PET/CT. *Theranostics*. 2016;6:262–271.
- Fortin MA, Orlova A, Malmström PU, Tolmachev V. Labelling chemistry and characterization of [⁹⁰Y/¹⁷⁷Lu]-DOTA-ZHER2:342-3 Affibody molecule, a candidate agent for locoregional treatment of urinary bladder carcinoma. *Int J Mol Med*. 2007;19:285–291.
- Altai M, Membreno R, Cook B, Tolmachev V, Zeglis BM. Pretargeted imaging and therapy. *J Nucl Med*. 2017;58:1553–1559.
- Demidov VV, Potaman VN, Frank-Kamenetskii MD, et al. Stability of peptide nucleic acids in human serum and cellular extracts. *Biochem Pharmacol*. 1994;48: 1310–1313.
- Westerlund K, Honarvar H, Tolmachev V, Eriksson Karlström A. Design, preparation, and characterization of PNA-based hybridization probes for affibody molecule-mediated pretargeting. *Bioconjug Chem*. 2015;26:1724–1736.
- Honarvar H, Westerlund K, Altai M, et al. Feasibility of affibody molecule-based PNA-mediated radionuclide pretargeting of malignant tumors. *Theranostics*. 2016; 6:93–103.
- Vorobyeva A, Westerlund K, Mitran B, et al. Development of an optimal imaging strategy for selection of patients for affibody-based PNA-mediated radionuclide therapy. *Sci Rep*. 2018;8:9643.
- Westerlund K, Altai M, Mitran B, et al. Radionuclide therapy of HER2-expressing human xenografts using an affibody molecule-based PNA-mediated pretargeting: in vivo proof-of-principle. *J Nucl Med*. 2018;59:1092–1098.
- Eigenbrot C, Ultsch M, Dubnovitsky A, Abrahmsén L, Härd T. Structural basis for high-affinity HER2 receptor binding by an engineered protein. *Proc Natl Acad Sci USA*. 2010;107:15039–15044.
- Altai M, Westerlund K, Velletta J, et al. Evaluation of affibody molecule-based PNA-mediated radionuclide pretargeting: development of an optimized conjugation protocol and ¹⁷⁷Lu labeling. *Nucl Med Biol*. 2017;54:1–9.
- Tano H, Oroujeni M, Vorobyeva A, et al. Comparative evaluation of novel [¹⁷⁷Lu]Lu-labelled PNA conjugates for affibody mediated PNA-based pretargeting. *Cancers (Basel)*. 2021;13:500.
- Westerlund K, Vorobyeva A, Mitran B, et al. Site-specific conjugation of recognition tags to trastuzumab for peptide nucleic acid-mediated radionuclide HER2 pretargeting. *Biomaterials*. 2019;203:73–85.
- Vogel CL, Cobleigh MA, Tripathy D, et al. First-line Herceptin® monotherapy in metastatic breast cancer. *Oncology*. 2001;61(suppl 2):37–42.
- Giordano SH, Temin S, Chandarlapaty S, et al. Systemic therapy for patients with advanced human epidermal growth factor receptor 2-positive breast cancer: ASCO clinical practice guideline update. *J Clin Oncol*. 2018;36: 2736–2740.
- Saputra EC, Huang L, Chen Y, Tucker-Kellogg L. Combination therapy and the evolution of resistance: the theoretical merits of synergism and antagonism in cancer. *Cancer Res*. 2018;78:2419–2431.
- Orlova A, Tolmachev V, Pehrson R, et al. Synthetic affibody molecules: a novel class of affinity ligands for molecular imaging of HER2-expressing malignant tumors. *Cancer Res*. 2007;67:2178–2186.
- Steffen AC, Göstring L, Tolmachev V, Palm S, Stenerlöw B, Carlsson J. Differences in radiosensitivity between three HER2 overexpressing cell lines. *Eur J Nucl Med Mol Imaging*. 2008;35:1179–1191.
- Ahlgren S, Orlova A, Wällberg H, et al. Targeting of HER2-expressing tumors using ¹¹¹In-ABY-025, a second-generation affibody molecule with a fundamentally reengineered scaffold. *J Nucl Med*. 2010;51:1131–1138.
- Cohen M. The efficacy of a peptide-nucleic acid solution (Reticulose) for the treatment of hepatitis A and hepatitis B: a preliminary controlled human clinical trial. *J R Soc Health*. 1992;112:266–270.
- Chavez-MacGregor M, Zhang N, Buchholz TA, et al. Trastuzumab-related cardiotoxicity among older patients with breast cancer. *J Clin Oncol*. 2013;31:4222–4228.
- Altunay B, Morgenroth A, Beheshti M, et al. HER2-directed antibodies, affibodies and nanobodies as drug-delivery vehicles in breast cancer with a specific focus on radioimmunotherapy and radioimmunoinaging. *Eur J Nucl Med Mol Imaging*. 2021;48:1371–1389.

In Vivo ¹⁸F-Flortaucipir PET Does Not Accurately Support the Staging of Progressive Supranuclear Palsy

Maura Malpetti*¹, Sanne S. Kaalund*¹, Kamen A. Tsvetanov¹, Timothy Rittman^{1,2}, Mayen Briggs^{2,3}, Kieren S.J. Allinson^{2,3}, Luca Passamonti^{1,2,4}, Negin Holland^{1,2}, P. Simon Jones¹, Tim D. Fryer^{1,5}, Young T. Hong^{1,5}, Antonina Kouli¹, W. Richard Bevan-Jones^{2,6}, Elijah Mak⁶, George Savulich⁶, Maria Grazia Spillantini¹, Franklin I. Aigbirhio^{1,5}, Caroline H. Williams-Gray^{1,2}, John T. O'Brien^{†2,6}, and James B. Rowe^{†1,2,7}

¹Department of Clinical Neurosciences, University of Cambridge, Cambridge, United Kingdom; ²Cambridge University Hospitals NHS Foundation Trust, Cambridge, United Kingdom; ³Cambridge University Brain Bank, Cambridge, United Kingdom; ⁴Istituto di Bioimmagini e Fisiologia Molecolare (IBFM), Consiglio Nazionale delle Ricerche (CNR), Milano, Italy; ⁵Wolfson Brain Imaging Centre, University of Cambridge, Cambridge, United Kingdom; ⁶Department of Psychiatry, University of Cambridge, Cambridge, United Kingdom; and ⁷Medical Research Council Cognition and Brain Sciences Unit, University of Cambridge, Cambridge, United Kingdom

Progressive supranuclear palsy (PSP) is a neurodegenerative disorder characterized by neuroglial tau pathology. A new staging system for PSP pathology postmortem has been described and validated. We used a data-driven approach to test whether postmortem pathologic staging in PSP can be reproduced in vivo with ¹⁸F-flortaucipir PET.

Methods: Forty-two patients with probable PSP and 39 controls underwent ¹⁸F-flortaucipir PET. Conditional inference tree analyses on regional binding potential values identified absent/present pathology thresholds to define in vivo staging. Following the postmortem staging approach for PSP pathology, we evaluated the combinations of absent/present pathology (or abnormal/normal PET signal) across all regions to assign each participant to in vivo stages. ANOVA was applied to analyze differences among means of disease severity between stages. In vivo staging was compared with postmortem staging in 9 patients who also had postmortem confirmation of the diagnosis and stage. **Results:** Stage assignment was estimable in 41 patients: 10, 26, and 5 patients were classified in stage I/II, stage III/IV, and stage V/VI, respectively, whereas 1 patient was not classifiable. Exploratory substaging identified 2 patients in stage I, 8 in stage II, 9 in stage III, 17 in stage IV, and 5 in stage V. However, the nominal ¹⁸F-flortaucipir-derived stage was not associated with clinical severity and was not indicative of pathology staging postmortem. **Conclusion:** ¹⁸F-flortaucipir PET in vivo does not correspond to neuropathologic staging in PSP. This analytic approach, seeking to mirror in vivo neuropathology staging with PET-to-autopsy correlational analyses, might enable in vivo staging with next-generation tau PET tracers; however, further evidence and comparisons with postmortem data are needed.

Key Words: progressive supranuclear palsy, ¹⁸F-flortaucipir, staging, tau pathology, PET-to-autopsy studies

J Nucl Med 2022; 63:1052–1057

DOI: 10.2967/jnumed.121.262985

Progressive supranuclear palsy (PSP) is a severe neurodegenerative disorder resulting in diverse clinical phenotypes with restricted eye movements, an akinetic-rigid syndrome, falls, and cognitive and behavioral deficits (1). The neuropathology of PSP is characterized by intracellular aggregates of 4-repeat tau in neurons and glia (2–5); these aggregates are distributed in a progressive sequence starting in the substantia nigra, globus pallidus and subthalamic nucleus, then pons, striatum and the precentral gyrus in the cerebral cortex, before reaching the cerebellum and frontal cortex (6). Later, the neuroglial pathology might extend to the occipital cortex (7).

A new neuropathologic staging system for PSP tau pathology postmortem was recently introduced and independently validated (7,8). This method confirms an association between pathology stage and clinical severity before death. To stage disease severity antemortem requires a different methodology. For the tauopathy of Alzheimer disease, for example, ¹⁸F-flortaucipir PET can reproduce staging in vivo (9–16).

Here, we test whether regional binding of the radioligand ¹⁸F-flortaucipir (also known as ¹⁸F-AV-1451), quantified using nondisplaceable binding potential, can be used to replicate the staging of PSP pathology in vivo. We validated the staging in 2 ways: correlation with clinical severity at the time of ¹⁸F-flortaucipir PET and neuropathologic staging of a subset of participants postmortem.

MATERIALS AND METHODS

Participants

We recruited 42 patients with a clinical diagnosis of probable PSP using Movement Disorder Society PSP 2017 criteria (1) (19 women and 23 men; mean age, 70.3 y [SD, 7.0 y; range, 50–84 y]; 35 with PSP Richardson syndrome and 7 with other phenotypes) and included data from 39 cognitively healthy controls (16 women and 23 men; mean age, 65.8 y [SD, 8.2 y; range, 48–84 y]; mean revised Addenbrooke's Cognitive Examination score, 96.2 [SD, 2.9; range, 89–100]). Disease severity was measured using the PSP rating scale (PSPRS) (mean, 36.6 [SD, 14.2; range, 10–74]). To date, 9 of the 42 patients donated their brain to the Cambridge Brain Bank, after a mean of 2.45 (SD, 0.98) years from PET. All of these patients had postmortem pathologic confirmation of PSP pathology.

All participants underwent dynamic PET imaging for 90 min after ¹⁸F-flortaucipir injection (GE Signa PET/MRI for 22 patients; GE

Received Jul. 31, 2021; revision accepted Oct. 8, 2021.
For correspondence or reprints, contact Maura Malpetti (mm2243@medschl.cam.ac.uk).

*Contributed equally to this work.

†Contributed equally to this work.

Published online Nov. 18, 2021.

Immediate Open Access: Creative Commons Attribution 4.0 International License (CC BY) allows users to share and adapt with attribution, excluding materials credited to previous publications. License: <https://creativecommons.org/licenses/by/4.0/>. Details: <http://jnm.snmjournals.org/site/misc/permission.xhtml>.

COPYRIGHT © 2022 by the Society of Nuclear Medicine and Molecular Imaging.

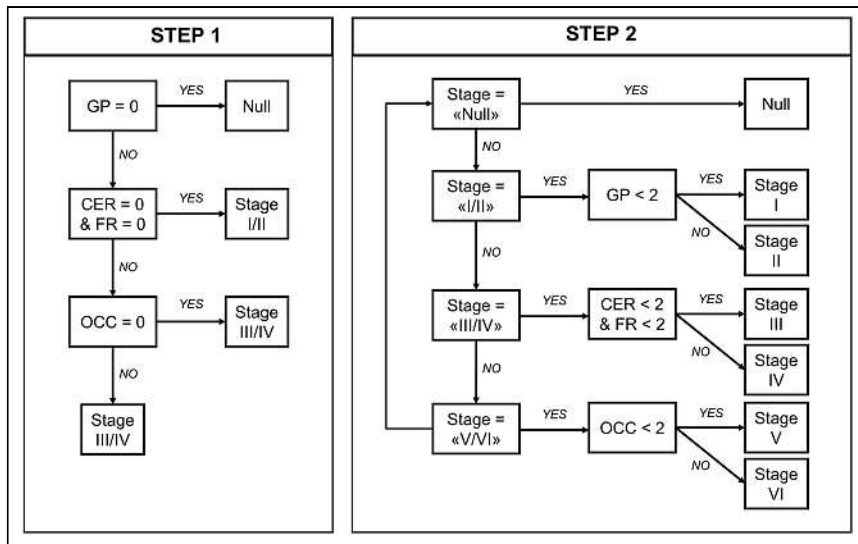


FIGURE 1. In vivo staging rules. Step 1: in vivo stages are defined with cumulative evidence of absence (region = 0) or presence (region = 1) of pathology in each of 5 regions considered, as defined by region-specific thresholds (regional *w*-score > threshold = 1; regional *w*-score ≤ threshold = 0). Step 2: in vivo substages are defined within each step 1 stage, considering 3-level pathology severity scale (0 = none; 1 = mild/moderate pathology; 2 = moderate/severe pathology). Regions: cerebellum (CER; white matter and dentate nucleus), middle frontal gyrus (FR), globus pallidus (GP), and occipital lobe (OCC; lingual gyrus and cuneus).

Discovery 690 PET/CT for 13 patients; GE Advance PET for 7 patients; GE Signa PET/MRI for 24 controls; GE Discovery 690 PET/CT for 7 controls; GE Advance PET for 8 controls (all scanners were from GE Healthcare). The sensitivity advantage of the PET/MRI scanner was used to reduce the target injection activity by 50% compared with that used in the PET and PET/CT scans, leading to a comparable signal-to-noise ratio in the acquired data across the scanners. Full details of the imaging protocols were published elsewhere (17,18). Seven of the 9 patients who donated their brains underwent ¹⁸F-flortaucipir imaging with GE Discovery 690 PET/CT; the other 2 were scanned with GE Advance PET.

Relevant approvals were granted by the Cambridge Research Ethics Committee (references: 13/EE/0104, 16/EE/0529, and 18/EE/0059), the East of England–Essex Research Ethics Committee (16/EE/0445), and the Administration of Radioactive Substances Advisory Committee. All participants provided written informed consent in accordance with the Declaration of Helsinki.

Determination of Regional ¹⁸F-Flortaucipir Binding

¹⁸F-flortaucipir nondisplaceable binding potential was calculated in regions of interest corresponding closely to those used for post-mortem staging of PSP by Kovacs et al. (7): globus pallidus, cerebellum (white matter and dentate nucleus), middle frontal gyrus, and occipital lobe (lingual gyrus and cuneus) (Supplemental Fig. 1A) (supplemental materials are available at <http://jnm.snmjournals.org>). The

striatum and subthalamic nucleus were excluded because of ¹⁸F-flortaucipir off-target binding or challenges in defining the PET signal. Regional values were quantified using a modified version of the n30r83 Hamman-Smith atlas (<http://brain-development.org/brain-atlases/adult-brain-atlases/adult-brain-maximum-probability-map-hammersmith-atlas-n30r83-in-mni-space/>), which includes parcellation of the brain stem and cerebellum, and a basis function implementation of the simplified reference tissue model (19), with cerebellar cortex gray matter as the reference region. Before kinetic modeling, regional PET data were corrected for partial-volume effects from cerebrospinal fluid by dividing the regional PET value by the mean regional gray matter plus white matter fraction determined from Statistical Parametric Mapping (SPM12, <https://www.fil.ion.ucl.ac.uk/spm/>) segmentation. Left and right regional nondisplaceable binding potential values were averaged bilaterally. Using regional mean and SD values from controls, we calculated *z*-scores (z-scores adjusted for the effect of covariates, Supplemental Fig. 1B), accounting for phenotypic and systematic differences, such as age and

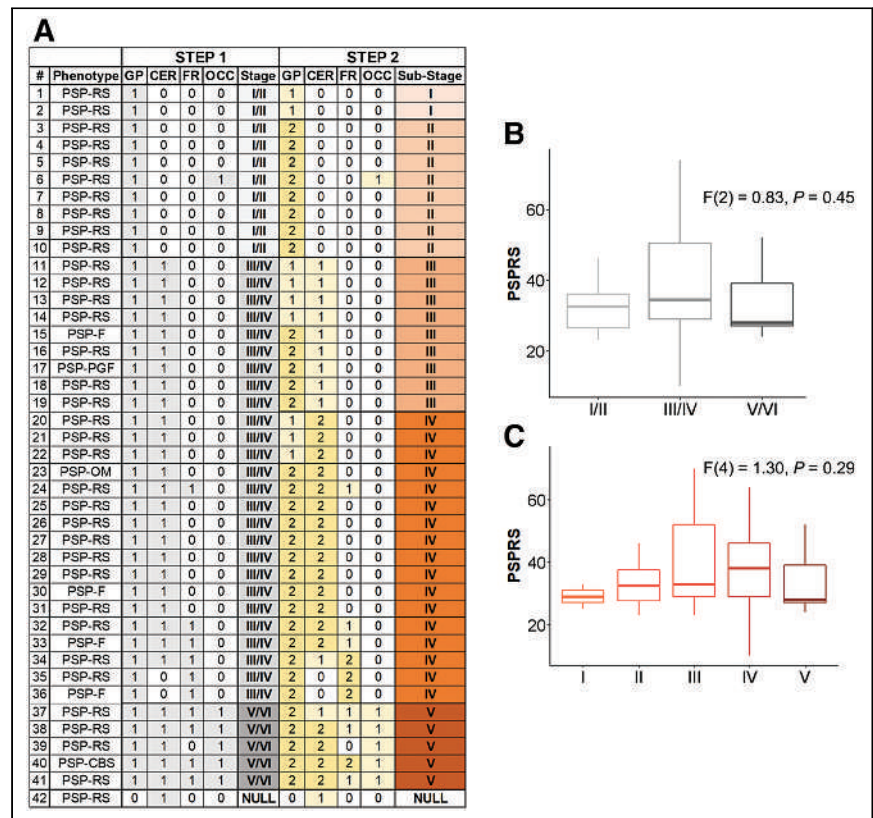


FIGURE 2. In vivo staging based on data-driven thresholds. (A) Severity scores are reported for each group of regions considered to define in vivo stages (step 1: 0 = absent; 1 = present) and sub-stages (step 2: 0 = none; 1 = mild/moderate pathology; 2 = moderate/severe pathology). (B and C) Box plots of PSPRS scores by stages defined with step 1 (B) and step 2 (C). CER = cerebellum (white matter and dentate nucleus); FR = middle frontal gyrus; GP = globus pallidus; OCC = occipital lobe (lingual gyrus and cuneus); PSP-CBS = PSP-corticobasal syndrome; PSP-F = PSP-frontal; PSP-OM = PSP-oculomotor; PSP-PGF = PSP-progressive gait freezing; PSP-RS = PSP-Richardson syndrome.

scanner type (PET/MRI vs. non-PET/MRI); see Malpetti et al. (17) for a discussion on harmonization of PET and PET/CT data.

In Vivo Staging Based on ¹⁸F-Flortaucipir Binding

Data-Driven Severity Thresholds. To quantify pathology severity in each region, we used a conditional inference tree analysis to define in a data-driven manner region-specific ¹⁸F-flortaucipir binding thresholds of w-scores, entering both patients and controls in the model. This method is similar to that used previously for imaging-based pseudo-Braak staging of Alzheimer disease (9). Specifically, region-specific thresholds were identified using nonparametric binary recursive partitioning with the function “*cree*” in R (v. 4.0.0, R Core Team - R Foundation for Statistical Computing) and running this tree analysis on w-scores for each region separately. Using these region-specific thresholds, we assigned binary severity scores to individual regional w-scores (w-score ≤ regional threshold: 0 or absent; w-score > regional threshold: 1 or present).

In Vivo Staging. First, using the staging system described by Kovacs et al. (7), which is based on cumulative and progressive pathology severity, we evaluated the combination of absent/present values across all 4 regions to assign each participant to stages I/II, III/IV, or V/VI (step 1 on Fig. 1). Second—in an explorative analysis—within each stage defined in the previous step, a 3-point pathology severity system was applied to each region (w-score ≤ regional threshold: absent, coded as 0; w-score > regional threshold: mild/moderate pathology, coded as 1; w-score > 2 times the threshold: moderate/severe pathology, coded as 2), and 1 of the 6 stages was assigned accordingly (stages I–VI; step 2 on Fig. 1). We repeated these staging analyses with a second analytic approach, using a preselected number of SD values from region-specific nondisplaceable binding potential control means to define pathology severity (Supplemental Fig. 2). ANOVA was applied to analyze differences among means of disease severity (PSPRS) between stages.

Postmortem Diagnosis and Staging Based on Immunohistochemistry

Tissue blocks of the left hemisphere were sampled according to National Institute of Neurological Disorders and Stroke standard guidance for neurodegenerative diseases from the brain stem, subcortical, and cortical areas. These were evaluated for the initial pathologic diagnosis of PSP (hyperphosphorylated tau; AT8, MN1020; Thermo Scientific, possible concomitant pathologies of amyloid β (clone 6F/3D, M0872; Dako), α-synuclein (SA3400; Enzo Life Sciences), and TDP-43 (TIP-PTD-P02; Cosmo Bio Co. Ltd.); and vascular pathology. Using the previously described staging scheme (7,8), we evaluated neuronal and oligodendroglial tau pathology in the globus pallidus, subthalamic nucleus, and cerebellar white matter and dentate nucleus and astrocytic tau pathology in the striatum, middle frontal gyrus, and occipital cortex. The regional cytopathologies were rated on a 4-level system (none, mild, moderate, and severe) using the guidelines proposed by Briggs et al. (8). In vivo staging results with both data-driven and SD approaches were compared with postmortem staging in the 9 patients who donated their brain.

RESULTS

The conditional inference tree analysis identified region-specific pathologic thresholds of ¹⁸F-flortaucipir binding for the globus pallidus (w-score, >0.795), cerebellar white matter (w-score, >0.783) and dentate nucleus (w-score, >0.845), and middle frontal gyrus (w-score, >1.416). For the occipital lobe, the analysis did not identify the threshold, so we used 1.645 as the w-score critical value ($P = 0.05$). A simple set of decision rules (Fig. 1) enabled plausible Kovacs stages to be estimated in 41 patients (Fig. 2A): 10 patients were classified in stage I/II because of

increased ¹⁸F-flortaucipir binding limited to the globus pallidus, 26 were classified in stage III/IV because of additional increased ¹⁸F-flortaucipir binding in the frontal or cerebellar regions, and 5 were classified in stage V/VI because of additional increased ¹⁸F-flortaucipir binding in the occipital lobe; 1 patient could not be classified because no increased binding was found in the globus pallidus. The explorative substaging (6 stages) identified 2 patients in stage I (mild/moderate pathology in the globus pallidus), 8 in stage II (moderate/severe pathology in the globus pallidus), 9 in stage III (mild/moderate pathology in the frontal lobe or cerebellum), 17 in stage IV (moderate/severe pathology in the frontal lobe or cerebellum), and 5 in stage V (mild/moderate pathology in the occipital lobe). When the same approach was applied to controls, 31, 5, 1, and 2 participants were classified in no stage, stage I, stage II, and stage III, respectively. Four patients (Fig. 2A, patients 6, 35, 36, and 39) showed an atypical severity pattern that was discordant with the description of Kovacs et al. (7).

Across all patients, the estimated in vivo stages did not relate to clinical severity ($P > 0.05$ in an ANOVA) (Figs. 2B and 2C). In 8 of the 9 patients who donated their brains, pathology stage as determined by in vivo ¹⁸F-flortaucipir PET was less than or equal to that determined postmortem (Fig. 3). In vivo staging and postmortem staging were not significantly correlated (Spearman r , 0.168; $P = 0.67$). Correlation analyses were also used to test the residuals of each staging

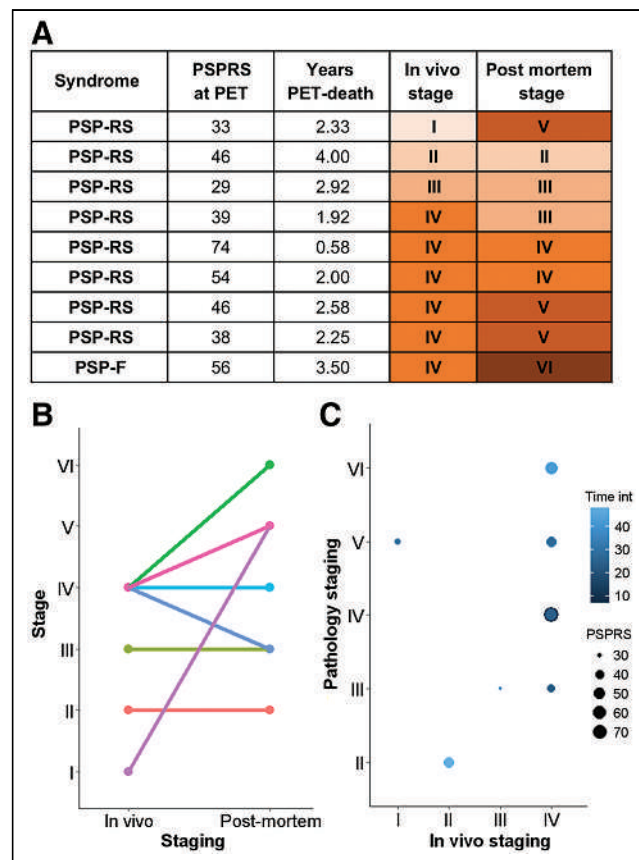


FIGURE 3. Comparison of in vivo and postmortem stages for 9 patients who underwent ¹⁸F-flortaucipir PET and pathology autopsy. (A) Clinical and staging details. (B) Single-subject (lines) comparisons of in vivo and postmortem staging. (C) Graphical representation of the effect of interval from PET to time of death (Time int) and clinical severity on association between in vivo staging and postmortem staging. PSP-F = PSP-frontal; PSP-RS = PSP-Richardson syndrome.

variable (in vivo and postmortem staging) after regressing out clinical severity (PSPRS scores) and the interval from PET to time of death. The correlation was not statistically significant (Spearman r , 0.150; $P = 0.70$). Figure 4 shows examples of ^{18}F -flortaucipir nondisplaceable binding potential maps and corresponding postmortem staining data for patients who were classified in stage II (patient 4) and stage IV (patient 26) by both in vivo staging and postmortem staging.

DISCUSSION

The principal finding of the present study was that ^{18}F -flortaucipir PET does not provide accurate in vivo staging corresponding to neuropathologic staging for PSP. The nominal stage derived from ^{18}F -flortaucipir PET did not correlate with disease severity or relate to staging postmortem.

As a result of the data-driven in vivo staging system, compared with controls, we observed higher ^{18}F -flortaucipir binding in the globus pallidus in all but 1 patient, with a few patients showing increased ^{18}F -flortaucipir binding in the occipital cortex (Fig. 2A). This regional distribution of ^{18}F -flortaucipir binding was in line with the pathologic description of PSP and with what was previously described for ^{18}F -flortaucipir in PSP (13,17,18,20). Whereas the ^{18}F -flortaucipir binding patterns allowed us to nominally apply PSP pathology staging in vivo, the in vivo staging was not systematically predictive of pathology staging postmortem. As expected because of the time interval between the PET scan and autopsy, in 8 of 9 cases with autopsy, the individual in vivo staging was less than or equal to the postmortem staging. However, 4 patients who were labeled as stage IV in vivo were then classified in 4 different stages postmortem (Fig. 3). Neither clinical severity nor the time interval between the PET scan and death was useful for predicting the individual postmortem stage from in vivo staging.

The number of patients with a positive signal for ^{18}F -flortaucipir in the cerebellum ($n = 29$) exceeded the number of patients with a positive result for frontal ^{18}F -flortaucipir binding ($n = 10$). Although this finding might reflect earlier involvement of the cerebellum in our cohort, regional differences in the density of tau aggregates and predominant cytopathologies could contribute to regional differences in tracer retention (11,13,21)—for example, neuronal and oligodendroglial tau predominates in the cerebellum, whereas astrocytic tau predominates in cortical regions.

Off-target binding for ^{18}F -flortaucipir is well characterized, but this problem alone would still leave open the possibility of quantifying tau pathology in areas without significant monoamine

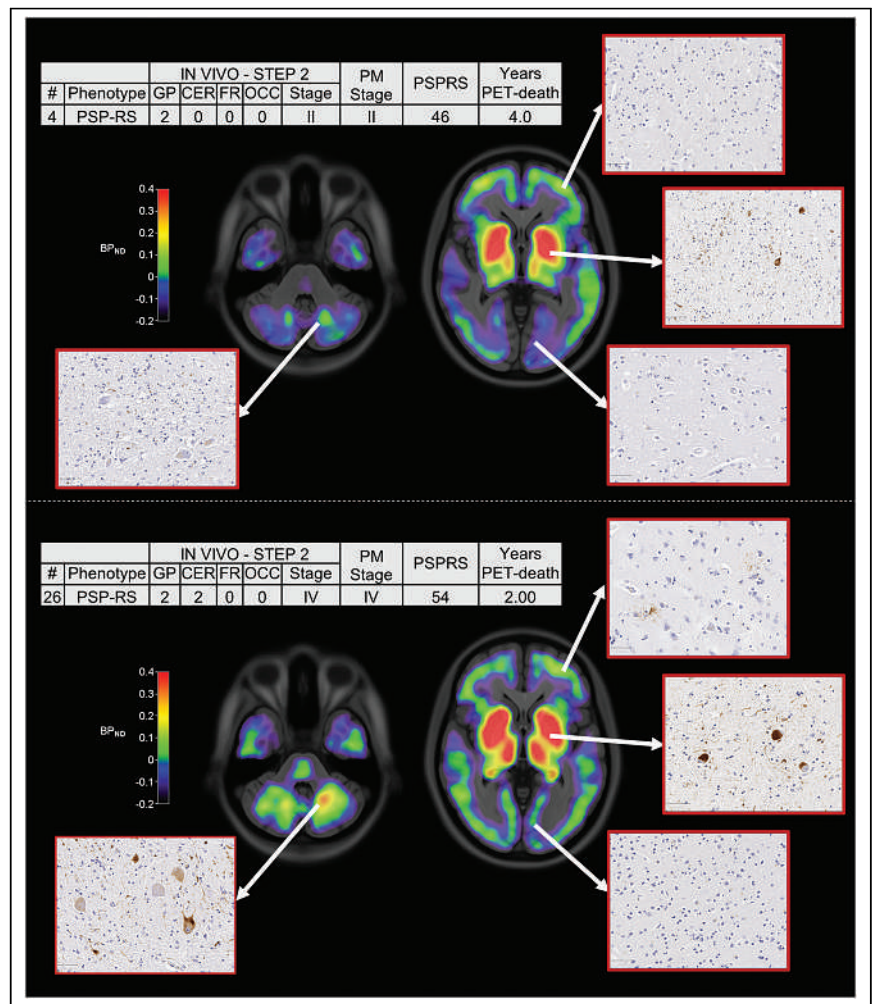


FIGURE 4. ^{18}F -flortaucipir nondisplaceable binding potential (BP_{ND}) maps, postmortem staining, and related clinical details for 2 patients classified in stage II (top) and stage IV (bottom) with both in vivo staging and postmortem staging. Spatially normalized BP_{ND} maps are shown in radiologic format overlaid on ICBM MNI152 2009a T1 MRI template (<https://www.bic.mni.mcgill.ca/ServicesAtlases/ICBM152Nlin2009>). CER = cerebellum; FR = middle frontal gyrus; GP = globus pallidus; OCC = occipital lobe; PM stage = postmortem stage; PSP-RS = PSP-Richardson syndrome.

oxidase levels or neuromelanin, such as the cerebellum and medial frontal cerebral cortex (22). However, recent PET-to-autopsy correlational studies suggested that ^{18}F -flortaucipir PET does not reliably correspond to postmortem tau pathology in non-Alzheimer tauopathies (13,23). This finding suggests that ^{18}F -flortaucipir lacks sensitivity in non-Alzheimer tau pathology. This characteristic might explain the underperformance of this tracer in defining an in vivo classification that systematically aligns with postmortem staging. Next-generation tau tracers might prove to be more useful for tracking in vivo PSP pathology progression because of a combination of good affinity for 4-repeat tau and lower off-target binding to monoamine oxidases (i.e., ^{18}F -PI-2620 (24)). However, evidence from PET-to-autopsy studies for these new ligands is needed, together with better segmentation and signal detection from small regions. These features would be particularly important for early-stage pathology detection and the classification of stage I/II of the system of Kovacs et al. (7).

CONCLUSION

We conclude that ^{18}F -flortaucipir PET is not a useful marker of the neuropathologic stage in PSP, despite increased binding and some regional concordance between tau pathology and ligand binding. This analytic approach, seeking to mirror in vivo neuropathology staging with PET-to-autopsy correlational analyses, could be applied to test next-generation tau PET tracers. However, comparisons with postmortem data are also required.

DISCLOSURE

This study was cofunded by the Cambridge University Centre for Parkinson-Plus (RG95450); the National Institute for Health Research (NIHR) Cambridge Biomedical Research Centre (BRC-1215-20014), including their financial support for the Cambridge Brain Bank; the PSP Association (MAPT-PSP Award); the Alzheimer's Research UK East-Network pump priming grant; the Wellcome Trust (grant number: 220258); the Medical Research Council (MR/P01271X/1; G1100464); the Association of British Neurologists; the Patrick Berthoud Charitable Trust (RG99368); the Alzheimer's Society (443 AS JF 18017); the Evelyn Trust (RG84654); RCUK/UKRI (via a Research Innovation Fellowship awarded by the Medical Research Council to Caroline H. Williams-Gray [MR/R007446/1]); and the Guarantors of Brain (G101149). James B. Rowe serves as an associate editor to *Brain* and is a nonremunerated trustee of the Guarantors of Brain, Darwin College, and the PSP Association (United Kingdom). He provides consultancy to Asceneuron, Astex, SVHealth and Curasen, and UCB and has received research grants from AZ-Medimmune, Janssen, and Lilly as industry partners in the Dementias Platform U.K. John T. O'Brien has received honoraria for work as Drug and Safety Monitoring Board chair or member for TauRx, Axon, Eisai, and Novo Nordisk; has acted as a consultant for Biogen and Roche; and has received research support from Alliance Medical and Merck. Maria Grazia Spillantini is in the Scientific Advisory Board of the Tau Consortium supported by the Rainwater Charitable Foundation. Caroline H. Williams-Gray has received honoraria from Lundbeck and Profile Pharma Ltd. and consultancy fees from Modus Outcomes and Evidera, Inc./GlaxoSmithKline. Unrelated to this work, Timothy Rittman has received honoraria from Biogen, Oxford Biomedica, and the National Institute for Health and Clinical Excellence (NICE). No other potential conflict of interest relevant to this article was reported.

ACKNOWLEDGMENTS

We thank our participant volunteers for their participation in this study, and we gratefully acknowledge the participation of all National Institute for Health Research (NIHR) Cambridge BioResource volunteers. We thank the National Institute for Health Research Cambridge Biomedical Research Centre and staff for their contributions. We thank NIHR and NHS Blood and Transplant. We thank the radiographers and technologists at the Wolfson Brain Imaging Centre and Addenbrooke's Hospital PET/CT Unit for their role in data acquisition. We thank the East Anglia Dementias and Neurodegenerative Diseases Research Network (DeNDRoN) for help with participant recruitment. In addition, we thank Dr. Istvan Boros, Dr. Joong-Hyun Chun, and other WBIC RPU staff for the manufacture of the radioligand. We thank Avid (Lilly) for supplying the precursor for the production of flortaucipir used in this study.

KEY POINTS

QUESTION: Can the novel postmortem pathologic staging of PSP be reproduced in vivo with ^{18}F -flortaucipir PET?

PERINENT FINDINGS: Conditional inference tree analyses were performed on regional ^{18}F -flortaucipir PET binding potential values to define in vivo staging in 42 patients with probable PSP, comparing the results in 9 participants with postmortem confirmation of the diagnosis and stage. ^{18}F -flortaucipir PET did not provide accurate in vivo staging of PSP; in particular, the nominal stage derived from ^{18}F -flortaucipir PET did not correlate with disease severity or relate to staging postmortem.

IMPLICATIONS FOR PATIENT CARE: This analytic approach, seeking to mirror in vivo neuropathology staging with PET-to-autopsy correlational analyses, might be more effective with next-generation tau PET tracers.

REFERENCES

- Höglinger GU, Respondek G, Stamelou M, et al. Clinical diagnosis of progressive supranuclear palsy: the Movement Disorder Society criteria. *Mov Disord*. 2017;32:853–864.
- Dickson DW. Sporadic tauopathies: Pick's disease, corticobasal degeneration, progressive supranuclear palsy and argyrophilic grain disease. In: Esiri MM, Lee VMY, Trojanowski JQ, eds. *The Neuropathology of Dementia*. Cambridge, United Kingdom: Cambridge University Press; 2009:227–256.
- Steele JC, Richardson JC, Olszewski J. Progressive supranuclear palsy: a heterogeneous degeneration involving the brain stem, basal ganglia and cerebellum with vertical gaze and pseudobulbar palsy, nuchal dystonia and dementia. *Arch Neurol*. 1964;10:333–359.
- Litvan I, Hauw JJ, Bartko JJ, et al. Validity and reliability of the preliminary NINDS neuropathologic criteria for progressive supranuclear palsy and related disorders. *J Neuropathol Exp Neurol*. 1996;55:97–105.
- Hauw JJ, Daniel SE, Dickson D, et al. Preliminary NINDS neuropathologic criteria for Steele-Richardson-Olszewski syndrome (progressive supranuclear palsy). *Neurology*. 1994;44:2015–2019.
- Williams DR, Holton JL, Strand C, et al. Pathological tau burden and distribution distinguishes progressive supranuclear palsy-parkinsonism from Richardson's syndrome. *Brain*. 2007;130:1566–1576.
- Kovacs GG, Lukic MJ, Irwin DJ, et al. Distribution patterns of tau pathology in progressive supranuclear palsy. *Acta Neuropathol (Berl)*. 2020;140:99–119.
- Briggs M, Allinson KSJ, Malpetti M, Spillantini MG, Rowe JB, Kaalund SS. Validation of the new pathology staging system for progressive supranuclear palsy. *Acta Neuropathol*. 2021;141:787–789.
- Schöll M, Lockhart SN, Schonhaut DR, et al. PET imaging of tau deposition in the aging human brain. *Neuron*. 2016;89:971–982.
- Schwarz AJ, Yu P, Miller BB, et al. Regional profiles of the candidate tau PET ligand ^{18}F -AV-1451 recapitulate key features of Braak histopathological stages. *Brain*. 2016;139:1539–1550.
- Lowe VJ, Lundt ES, Albertson SM, et al. Tau-positron emission tomography correlates with neuropathology findings. *Alzheimers Dement*. 2020;16:561–571.
- Fleisher AS, Pontecorvo MJ, Devous MD, et al. Positron emission tomography imaging with [^{18}F]flortaucipir and postmortem assessment of Alzheimer disease neuropathologic changes. *JAMA Neurol*. 2020;77:829–839.
- Soleimani-Meigooni DN, Iaccarino L, La Joie R, et al. ^{18}F -flortaucipir PET to autopsy comparisons in Alzheimer's disease and other neurodegenerative diseases. *Brain*. 2020;143:3477–3494.
- Marquié M, Siao Tick Chong M, Antón-Fernández A, et al. [^{18}F]-AV-1451 binding correlates with postmortem neurofibrillary tangle Braak staging. *Acta Neuropathol (Berl)*. 2017;134:619–628.
- Smith R, Wibom M, Pawlik D, Englund E, Hansson O. Correlation of in vivo [^{18}F]flortaucipir with postmortem Alzheimer disease tau pathology. *JAMA Neurol*. 2019;76:310–317.

16. Maass A, Landau S, Baker SL, et al. Comparison of multiple tau-PET measures as biomarkers in aging and Alzheimer's disease. *Neuroimage*. 2017;157:448–463.
17. Malpetti M, Passamonti L, Rittman T, et al. Neuroinflammation and tau colocalize in vivo in progressive supranuclear palsy. *Ann Neurol*. 2020;88:1194–1204.
18. Passamonti L, Vázquez Rodríguez P, Hong YT, et al. ¹⁸F-AV-1451 positron emission tomography in Alzheimer's disease and progressive supranuclear palsy. *Brain*. 2017;140:781–791.
19. Gunn RN, Lammertsma AA, Hume SP, Cunningham VJ. Parametric imaging of ligand-receptor binding in PET using a simplified reference region model. *Neuroimage*. 1997;6:279–287.
20. Schonhaut DR, McMillan CT, Spina S, et al. ¹⁸F-flortaucipir tau positron emission tomography distinguishes established progressive supranuclear palsy from controls and Parkinson disease: a multicenter study. *Ann Neurol*. 2017;82:622–634.
21. Marquié M, Normandin MD, Vanderburg CR, et al. Validating novel tau positron emission tomography tracer [F-18]-AV-1451 (T807) on postmortem brain tissue. *Ann Neurol*. 2015;78:787–800.
22. Tong J, Meyer JH, Furukawa Y, et al. Distribution of monoamine oxidase proteins in human brain: implications for brain imaging studies. *J Cereb Blood Flow Metab*. 2013;33:863–871.
23. Ghirelli A, Tosakulwong N, Weigand SD, et al. Sensitivity–specificity of tau and amyloid β positron emission tomography in frontotemporal lobar degeneration. *Ann Neurol*. 2020;88:1009–1022.
24. Brendel M, Barthel H, Van Eimeren T, et al. Assessment of ¹⁸F-PI-2620 as a biomarker in progressive supranuclear palsy. *JAMA Neurol*. 2020;77:1408–1419.

Neuropsychologic Profiles and Cerebral Glucose Metabolism in Neurocognitive Long COVID Syndrome

Andrea Dressing*^{1,2}, Tobias Bormann*^{1,2}, Ganna Blazhenets³, Nils Schroeter¹, Lea I. Walter¹, Johannes Thurow³, Dietrich August⁴, Hanna Hilger⁴, Katarina Stete⁴, Kathrin Gerstaecker⁵, Susan Arndt⁵, Alexander Rau⁶, Horst Urbach⁶, Siegbert Rieg⁴, Dirk Wagner⁴, Cornelius Weiller^{1,2}, Philipp T. Meyer*³, and Jonas A. Hosp*¹

¹Department of Neurology and Clinical Neuroscience, Medical Center – University of Freiburg, Faculty of Medicine, University of Freiburg, Freiburg, Germany; ²Freiburg Brain Imaging Center, Medical Center – University of Freiburg, Faculty of Medicine, University of Freiburg, Freiburg, Germany; ³Department of Nuclear Medicine, Medical Center – University of Freiburg, Faculty of Medicine, University of Freiburg, Freiburg, Germany; ⁴Division of Infectious Diseases, Department of Medicine II, Medical Center – University of Freiburg, Faculty of Medicine, University of Freiburg, Freiburg, Germany; ⁵Department of Otorhinolaryngology – Head and Neck Surgery, Medical Center – University of Freiburg, Faculty of Medicine, University of Freiburg; and ⁶Department of Neuroradiology, Medical Center – University of Freiburg, Faculty of Medicine, University of Freiburg, Freiburg, Germany

During the coronavirus disease 2019 (COVID-19) pandemic, Long COVID syndrome, which impairs patients through cognitive deficits, fatigue, and exhaustion, has become increasingly relevant. Its underlying pathophysiology, however, is unknown. In this study, we assessed cognitive profiles and regional cerebral glucose metabolism as a biomarker of neuronal function in outpatients with long-term neurocognitive symptoms after COVID-19. **Methods:** Outpatients seeking neurologic counseling with neurocognitive symptoms persisting for more than 3 mo after polymerase chain reaction (PCR)-confirmed COVID-19 were included prospectively between June 16, 2020, and January 29, 2021. Patients ($n = 31$; age, 53.6 ± 2.0 y) in the long-term phase after COVID-19 (202 ± 58 d after positive PCR) were assessed with a neuropsychologic test battery. Cerebral ^{18}F -FDG PET imaging was performed in 14 of 31 patients. **Results:** Patients self-reported impaired attention, memory, and multitasking abilities (31/31), word-finding difficulties (27/31), and fatigue (24/31). Twelve of 31 patients could not return to the previous level of independence/employment. For all cognitive domains, average group results of the neuropsychologic test battery showed no impairment, but deficits (z score < -1.5) were present on a single-patient level mainly in the domain of visual memory (in 7/31; other domains $\leq 2/31$). Mean Montreal Cognitive Assessment performance (27/30 points) was above the cutoff value for detection of cognitive impairment (< 26 points), although 9 of 31 patients performed slightly below this level (23–25 points). In the subgroup of patients who underwent ^{18}F -FDG PET, we found no significant changes of regional cerebral glucose metabolism. **Conclusion:** Long COVID patients self-report uniform symptoms hampering their ability to work in a relevant fraction. However, cognitive testing showed minor impairments only on a single-patient level approximately 6 mo after the infection, whereas functional imaging revealed no distinct pathologic changes. This clearly deviates from previous findings in subacute COVID-19 patients, suggesting that underlying neuronal causes are different and possibly related to the high prevalence of fatigue.

Key Words: long COVID syndrome; cognition; fatigue; ^{18}F -FDG PET; Montreal Cognitive Assessment

J Nucl Med 2022; 63:1058–1063
DOI: 10.2967/jnumed.121.262677

As the coronavirus disease 2019 (COVID-19) pandemic proceeds, the long-term consequences such as chronic neurocognitive symptoms after infection with the severe acute respiratory syndrome coronavirus 2 (SARS-CoV-2) are an increasingly recognized problem. A multitude of previously healthy patients self-report symptoms such as brain-fog, memory loss (18%–40%), attentional problems (16%–34%), and fatigue (60%–70%) months after the acute infection has long subsided (1–6). The label “long COVID syndrome” has recently been established for these symptoms in the aftermath of an acute SARS-CoV-2 infection (7); however, the underlying pathophysiology remains unclear.

We described impaired cognitive functions associated with frontoparietal hypometabolism (indicating cortical dysfunction) on ^{18}F -FDG PET (8) in COVID-19 patients approximately 1 mo after the acute infection. When voxelwise principal components analysis is used, a COVID-19-related spatial covariance pattern has emerged, the expression of which tightly correlates with performance in the Montreal Cognitive Assessment (MoCA). In a subgroup of these patients, a long-term follow-up (6–7 mo after infection) revealed a substantial but still incomplete recovery of cognitive deficits and cortical dysfunction on ^{18}F -FDG PET (9). Likewise, a predominantly frontal cortical hypometabolism, which improved during follow-up after 6 mo, was detected in patients with COVID-19-related encephalopathy (10). Deviating from these findings, regional hypometabolism of limbic and paralimbic regions extending to the brain stem and cerebellum (11) or hypometabolism of the right parahippocampal gyrus and thalamus (12) has been described in COVID-19 patients examined at 3–4 mo after symptom onset.

Postmortem neuropathologic examinations in COVID-19 patients revealed pronounced glial activation and infiltration by cytotoxic T lymphocytes in the brain stem and cerebellum (13), likely caused by a systemic inflammatory response or a cytokine release (14). Because the cortical gray matter is largely unaffected by inflammatory

Received Jun. 8, 2021; revision accepted Oct. 4, 2021.
For correspondence or reprints, contact Jonas A. Hosp (jonas.hosp@uniklinik-freiburg.de).
*Contributed equally to this work.
Published online Oct. 14, 2021.
Immediate Open Access: Creative Commons Attribution 4.0 International License (CC BY) allows users to share and adapt with attribution, excluding materials credited to previous publications. License: <https://creativecommons.org/licenses/by/4.0/>. Details: <http://jnm.snmjournals.org/site/misc/permission.xhtml>.
COPYRIGHT © 2022 by the Society of Nuclear Medicine and Molecular Imaging.

changes (8,13), reduction of cortical glucose metabolism in early subacute patients (8–10) might be caused by a functional decoupling from afferents, which is in line with recovery of cognitive deficits and cortical metabolism in long-term follow-up investigations (9,10,15).

Thus, the question arises whether alterations in cerebral glucose metabolism are also present in patients with long COVID syndrome as a potential pathophysiologic correlate of the neurocognitive symptoms. We present data from a prospective cohort of outpatients about 6 mo after SARS-CoV-2 infection who self-reported persistent subjective neurocognitive symptoms. Cognitive performance and cerebral ^{18}F -FDG PET were assessed to objectify subjective symptoms and to investigate possible similarities to previously observed changes in early subacute patients.

MATERIALS AND METHODS

Participants

We report data from a monocentric, prospective cohort of 31 patients (age, 53.6 ± 12.0 y; 11 men, 20 women) who were admitted to the outpatient clinic of the Department of Neurology and Clinical Neuroscience of the University Hospital Freiburg between June 16, 2020, and January 29, 2021 due to lasting neurocognitive symptoms in the chronic phase (>3 mo) after COVID-19. Inclusion criteria were a history of reverse transcription polymerase chain reaction (rt-PCR)-confirmed SARS-CoV-2 infection, presence of new subjective neurocognitive symptoms persisting for longer than 3 mo after positive rt-PCR, and age > 18 y. Exclusion criteria were any preexisting neurodegenerative disorders. One patient refused to participate. Detailed demographic data are provided in Supplemental Table 1 (supplemental materials are available at <http://jnm.snmjournals.org>).

Importantly, the current long COVID cohort shares no overlap with previous studies on COVID-19 from our group (8,9). In these, subacute inpatients (3–4 wk post-COVID) were screened independently from subjective complaints and included if they met inclusion criteria (most importantly, at least 2 new neurologic symptoms to qualify for PET) (8). A subset of 8 patients was furthermore eligible for a follow-up (9). In contrast, the present cohort results from self-referral because of new neurocognitive symptoms, which may not necessarily be verified by further examinations (see the section “Cognitive Functions”).

The present study was approved by the local ethics committee of the University Medical Center Freiburg (EK 211/20) and complies with the Helsinki Declaration of 1975, as revised in 2008. Written informed consent was obtained from all patients.

General Examination

General neurologic deficits were examined in a complete neurologic assessment by a board-certified neurologist (>5 y of training). The degree of actual disability was graded as follows: 0, no relevant restrictions; 1, relevant restrictions but able to work; 2, reduction of work quota necessary; 3, inability to work or restriction of daily life activities. Disease severity during the acute stage was scored according to a modified version of the German definitions (16): 1, no signs of pneumonia; 2, pneumonia, outpatient treatment; 3, pneumonia, inpatient treatment; 4, acute respiratory distress syndrome, endotracheal ventilation in intensive care unit. A subgroup of 6 patients received structural MRI (supplemental methods).

Cognitive Functions

All patients were examined with a 50-min cognitive battery administered in German (native language) in a set order by a trained neuropsychologist. The neuropsychologic test battery comprised the Hopkins Verbal Learning Test-Revised (HVLT (17)), Brief Visuospatial Memory Test-Revised (BVRT-R (18)), Digit Span forward/

reverse (19), Trail Making Test part A/B (20), Color-Word Interference Test (FWIT (21)), Symbol-Digit Modalities Test (SDMT (22)), and a semantic and letter fluency test (23). Individual raw scores were z-transformed based on the normative sample as reported in the manuals. Results were stratified by age and education where available. In the case of the FWIT, raw scores were assigned a T score, which then was transformed into a z score. z scores for each domain and a composite z score that represents overall cognitive functions of the patients were calculated by averaging the z scores based on Lazar et al. (24) with minor adjustments. The threshold for impaired performance was defined as 1.5 SDs below the normative mean (24). Additionally, the MoCA (version 7.1, www.mocatest.org (25)) was applied (maximum achievable score = 30, higher scores indicating better performance). The cutoff score for cognitive impairment was defined as performance below 26 (25). A correction for years of education (YoE) was performed (+1 point in case of ≤ 12 YoE). Fatigue was assessed using the Würzburg Fatigue Inventory in Multiple Sclerosis (WEIMuS (26)), a self-rating questionnaire for symptoms of physical and cognitive fatigue. In addition, the Geriatric Depression Scale-15 (GDS (27)) was included. Scores for the MoCA, fatigue, and the GDS were not included in the composite score.

^{18}F -FDG PET Imaging

Cerebral ^{18}F -FDG PET was recommended to all patients on the basis of clinical indication for diagnosis of persistent unexplained cognitive impairment (including the exclusion of other causes) based on previous reports on altered cerebral glucose metabolism in COVID-19 patients (8,10–12). Imaging was performed in 14 of 31 patients on average 197.9 ± 61.1 d after manifestation of COVID-19 as indicated by the first positive PCR. PET scans (10-min duration) were acquired on a fully digital Vereos PET/CT scanner (Philips Healthcare) 50 min after intravenous injection of 211 ± 9 MBq of ^{18}F -FDG under euglycemic conditions at rest (eyes open, reduced ambient noise). All individual scans were read as part of the clinical routine by 2 experienced nuclear medicine physicians (>20 and 5 y of experience in brain PET) using highly standardized displays of 30 transaxial ^{18}F -FDG PET slices (hot metal color scale; maximum and minimum thresholds set to 1.8 [100%] and 0.09 [5%], respectively, after voxelwise data normalization to mean uptake in brain parenchyma) and voxel-based statistical analyses using 3-dimensional stereotactic surface projections (3D-SSP/Neurostat (28)) and appropriate age-matched controls.

Group analyses were performed as previously described (8): after spatial normalization and smoothing (isotropic gaussian kernel, 10 mm in full width at half maximum), the pattern expression score (PES) of the previously established COVID-19-related spatial covariance pattern was derived by the topographic profile rating algorithm, reflecting the expression of the established pattern in each individual's data. For statistical comparison, we also assessed the PES of the COVID-19-related covariance pattern in control patients ($n = 45$; age, 63.0 ± 9.1 y; age range, 50–85 y; 27 men, 18 women) scanned under identical conditions (8). As confirmatory analysis, a voxelwise analysis of covariance (ANCOVA) with age and sex as covariates was calculated with statistical parametric mapping (SPM) for comparison of long COVID and control patients. For count rate normalization, we used proportional scaling of each individual's ^{18}F -FDG PET data to the mean uptake in a brain parenchyma mask (SPM tissue probability map, white and gray matter probability > 50% excluding cerebrospinal fluid with probability > 30%). A false-discovery rate (FDR)-corrected $P < 0.05$ was used as a statistical threshold. The correlation between mean z scores of the domains (attention, executive function, processing speed, verbal and visual memory), composite z score, MoCA, WEIMuS cognitive and physical fatigue scores, and voxelwise ^{18}F -FDG uptake was analyzed by SPM-based regression analyses. FDR-corrected $P < 0.05$ and uncorrected $P < 0.005$ (cluster size > 30 voxels)

were used as statistical thresholds. All processing steps were implemented with an in-house pipeline using MATLAB (The MathWorks, Inc.) and SPM (SPM12; The Wellcome Centre for Human Neuroimaging, UCL Queen Square Institute of Neurology) software.

Statistical Analysis

Statistical analyses were performed using SPSS Statistics, version 27 (IBM) and R (<https://www.R-project.org/>). Shapiro–Wilk and Kolmogorov–Smirnov tests were used to confirm normal distribution. Correlations between demographic and clinical data and neurocognitive test scores were exploratorily assessed with the Spearman rank correlation test. For group comparisons of neurocognitive test scores, 1-sample *t* or Mann–Whitney *U* tests were performed. The group difference of the PES of long COVID patients and control patients was tested with an ANCOVA including age and sex as covariates. The strength of the relationship between the PES of the COVID-19–related covariance pattern and the results from cognitive assessments was estimated with a Spearman rank partial correlation test adjusted for the patient’s age.

RESULTS

The neurologic examination (202.3 ± 57.5 d after first positive COVID-19 PCR) revealed no focal deficit related to SARS-CoV-2 infection. On the contrary, all patients complained about difficulties in attention, memory, and multitasking abilities. Moreover, 24 of 31 (77%) complained about fatigue. Three of 31 (10%) patients reduced their work quota due to these symptoms; 9 of 31 (29%) patients were unable to work or restricted their activities of daily living at the time of examination. Actual disability was significantly correlated with severity of initial disease ($R = 0.38$; $P = 0.03$). Basic clinical data are summarized in Supplemental Table 2.

Six of 31 patients underwent cerebral MRI (4 with contrast enhancement). On visual assessment, microembolic subacute cortical infarction was observed in the left occipital lobe in 1 patient (65-y-old man), and slight microangiopathic changes corresponding to Fazekas 2 were present in a 61-y-old female patient. No other structural changes, and in particular no sign of atrophy, acute encephalitis, or leptomeningeal enhancement, were found.

Cognitive Functions

The mean *z* scores of verbal and visual memory domains and composite *z* score were not significantly different from zero (all $P > 0.1$). The mean *z* scores for executive functions ($P < 0.05$), attention ($P < 0.01$), and processing speed ($P < 0.01$) were even higher than zero and, in total, almost half of the patients ($n = 15$, 49%) were completely unimpaired in the neurocognitive test battery (Supplemental Table 3). However, some patients exhibited mild to moderate impairments in single domains: the most frequently impaired domain was visual memory (7/31 [23%] patients; other domains $\leq 2/31$ [$\leq 7\%$]). Impaired individual tests on a single-subject level were most frequently observed for verbal and visual memory tests (number of impaired patients 3–7 [10%–23%] and 4–8 [13%–26%], respectively; Supplemental Table 3).

Although the mean group MoCA performance (26.6 ± 2.2 points) was above the cutoff (25), mild impairment was detected in 9 patients (29%; range, 23–25 points). The greatest variance was observed for the recall task of the MoCA (3.2 ± 1.6 points, 16/31 patients scoring below 4 points). The group of patients with an impaired MoCA test did not differ in terms of age or delay between infection and examination from the rest of the cohort (both $P > 0.5$).

On a self-rating questionnaire, 61% ($n = 19$) revealed overall symptoms of fatigue. On a subscore level, 67% ($n = 21$) were above the cutoff for cognitive fatigue and 42% ($n = 13$) were above the cutoff for physical fatigue (Supplemental Table 4). The GDS (3.9 ± 2.6) indicated no relevant level of depression in the present patient cohort; only 4 individuals slightly exceeded the cutoff value (range, 8–10 points) indicating mild depressive symptoms (Supplemental Table 4) (27).

Performance on MoCA was correlated with the composite *z* score of the neurocognitive test battery ($R = 0.53$; $P < 0.05$). In turn, self-rated fatigue (WEIMuS sum score) correlated significantly with self-rated depression (GDS, albeit in a subclinical range; $R = 0.61$; $P < 0.001$). MoCA test scores and the overall composite *z* score did not correlate with self-rated depression or any aspect of self-rated fatigue. Except for positive correlations of initial disease severity with physical fatigue ($R = 0.37$; $P < 0.05$), clinical parameters such as disease severity and degree of actual disability did not correlate with performance on cognitive and other tests.

¹⁸F-FDG PET Imaging

Patients undergoing ¹⁸F-FDG PET did not differ from those who did not in terms of epidemiologic variables (age, sex) or results of the neuropsychologic test battery (all $P > 0.05$, Supplemental Tables 1–4). Clinical routine assessments of each patient’s ¹⁸F-FDG PET scan revealed no distinct pathologic findings (Fig. 1). In particular, none of the patients exhibited a frontoparietal predominant hypometabolic pattern previously described in subacute COVID-19 inpatients (8). Likewise, PET scans suggested no alternative diagnoses (e.g., encephalitis, neurodegenerative dementia) in any case.

Group-averaged ¹⁸F-FDG PET scans in long COVID and control patients are shown in Figure 2. None of the patients expressed the previously established COVID-19–related spatial covariance pattern, with individual PES ranging from -7 to -60 . There was

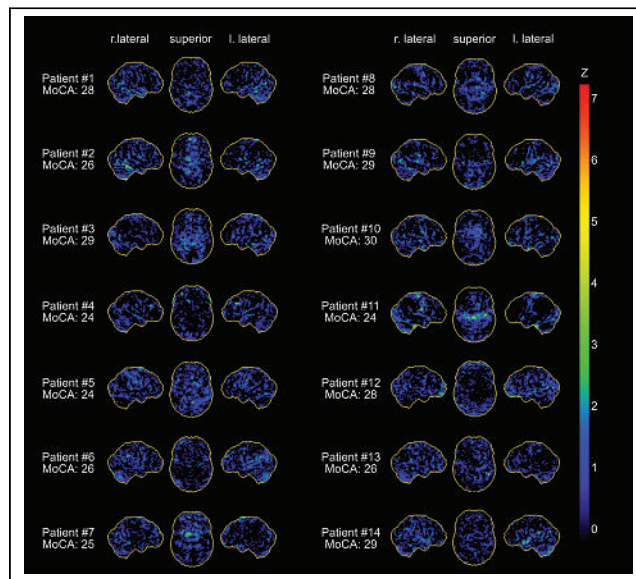


FIGURE 1. Individual results of voxelwise statistical analysis of ¹⁸F-FDG PET data with NeuroSTAT/3D-SSP (stereotactic surface projection). Shown are lateral and superior views of brain. Metabolic deficits compared with age-matched control subjects are color-coded as *z* scores. *Z* = *z* score.

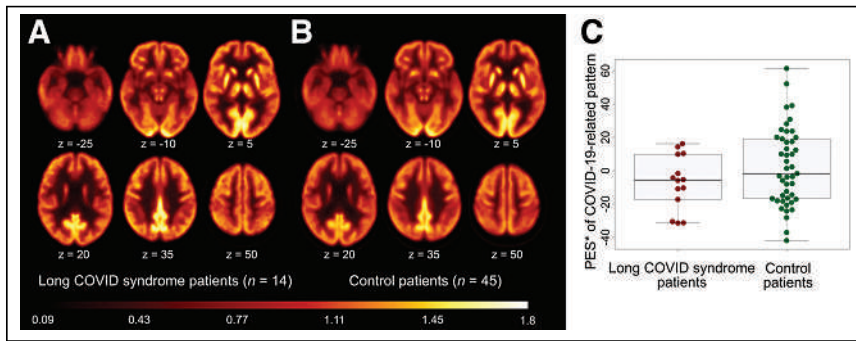


FIGURE 2. ^{18}F -FDG PET in patients with long COVID syndrome. (A and B) Transaxial sections of group averaged, spatially normalized ^{18}F -FDG PET scans in patients with long COVID syndrome (A) and control patients (B). (C) The pattern expression score (PES; *adjusted for age and sex, for illustration purposes) of previously established COVID-19-related spatial covariance pattern was not significantly different between patients with long COVID syndrome and control patients. Box plots (gray), as well as individual values for COVID-19 patients (red) and the control cohort (green), are displayed.

no significant group difference in PES between long COVID patients (-36.7 ± 17.3) and control patients (-11.3 ± 29.2) after adjustment for age and sex (ANCOVA, factor group: $P = 0.14$).

In contrast to our previous studies in COVID-19 inpatients with novel neurologic symptoms in the subacute stage (8) and at follow-up (9), no significant relationship between MoCA and PES was found ($R = -0.17$, $P > 0.5$). There was also no significant correlation of PES with fatigue, composite or domains z scores (all $P > 0.5$). Confirmatory voxelwise SPM analyses yielded no regions with significantly (FDR-corrected $P < 0.05$) different glucose metabolism (neither hyper- nor hypometabolism) in long COVID patients compared with control patients. Moreover, no association to MoCA, domain z scores, composite z score, or WEIMus fatigue scores were found by voxelwise regression analyses (FDR-corrected $P < 0.05$). No relevant findings were observed at an exploratory statistical threshold of uncorrected $P < 0.005$.

DISCUSSION

The present study reports a prospective assessment of 31 patients self-presenting to our outpatient clinic because of neurocognitive symptoms more than 6 mo after a SARS-CoV-2 infection with long COVID syndrome. Although 39% of patients report a relevant disability at work and everyday life due to these symptoms, an exhaustive assessment including a detailed cognitive battery showed only mild impairment in individual patients, and cerebral ^{18}F -FDG PET failed to reveal a distinct pathologic signature.

Cognitive profiles in our sample revealed an overall normal to higher-than-normal performance in all cognitive domains (verbal memory, visual memory, processing speed, attention, executive function) and on MoCA (average score 27/30, cutoff value for detection of any cognitive impairment $< 26/30$ (25)). However, impairments were present on a single-patient level, especially in the domain of visual memory (Supplemental Table 3). Furthermore, 9 of 31 (29%) patients performed below the MoCA cutoff value, indicating mild cognitive impairments.

These results indicate that in some patients with long COVID, discrete neurocognitive impairments may be present, which is in line with findings from other studies: deficits in verbal and visual memory, executive functions, verbal fluency, attention, and language were reported 6–9 mo after the infection, which were correlated in

their expression with the initial degree of severity (29). Another study reported mild deficits in episodic memory function (up to 6 mo after the infection) and vigilance and motivation deficits (up to 9 mo after the infection); the deficits normalized after the corresponding period of time (15). This, in combination with the longitudinal assessment of COVID-19 patients from our group (8,9), suggests that the cognitive deficits are subject to a dynamic process, which might also explain why most patients are cognitively unimpaired in the present long-term study.

It has to be noted that a rather liberal threshold for definition of impaired cognition was used ($1.5 \text{ SD} < \text{normative mean}$). This threshold corresponds to a 1-sided P value of about 0.07, which increases the risk of false-positive results and is only

slightly below the frequency of impaired observations on detailed tests (Supplemental Table 3: 45/496, 9.1%). That impaired scales accumulated in verbal and visual memory tests is not surprising, as the Hopkins verbal learning test and BVMT are especially challenging and susceptible for attentional fluctuations (24,28). Such fluctuations may also explain why more patients showed impairments in the recognition (i.e., 8/31) when compared with the delayed recall part (i.e., 4/31) of the BVMT—although the latter usually detects deficits with a higher sensitivity (30). Although the comprehensive neuropsychologic test battery indicated slight deficits at the level of individual patients, affection of MoCA performance seemed to be more severely pronounced. This could also be explained by motivational deficits, attentional fluctuations and exhaustion as the MoCA was performed at the end of the test battery.

Previous studies in subacute COVID-19 patients showed deficits in executive and attentional functions, memory, and visuospatial functions that point to a cortical dysfunction with a frontoparietal emphasis (4,29,31). As a correlate of impaired cognitive functions, we recently described a predominantly frontoparietal cortical hypometabolism on ^{18}F -FDG PET in subacute COVID-19 patients (8,9). Thus, we also performed ^{18}F -FDG PET in the present sample of patients with neurocognitive long COVID syndrome to objectify changes of regional neuronal function by an approach that is independent of the patients' test compliance and can be analyzed completely observer-independent. Individual ^{18}F -FDG PET reads did not reveal any distinct pathologic finding, including possible alternative diagnoses, in any of the patients. We also analyzed the PES of the previously established COVID-19-related metabolic covariance pattern. However, whereas this pattern tightly correlated to MoCA performance and was still elevated at trend level compared with control patients at follow-up in our studies in COVID-19 inpatients (at the subacute stage and 6 mo later) (8,9), none of the patients with long COVID syndrome exhibited this pattern. Notably, this also includes 4 of 14 patients showing impaired performance on MoCA who underwent ^{18}F -FDG PET. To exclude the possibility that the COVID-19-related metabolic covariance pattern established in subacute inpatients is simply not appropriate for patients with long COVID syndrome, we also conducted a conventional SPM group analysis, which, again, showed no pathologic finding. Even for a subgroup of patients with abnormal MoCA scores ($n = 4$), we did not find any

relevant differences in glucose metabolism compared with the remaining patients or the control cohort (voxelwise SPM group analysis, exploratory threshold of $P < 0.005$, data not shown). Although we cannot exclude the possibility that long COVID-associated changes of neuronal activity are too subtle to be captured by an ^{18}F -FDG PET group analysis, we consider this unlikely. Indeed, ^{18}F -FDG PET is a well-established marker of neuronal dysfunction for prodromal stages of neurologic diseases of similar cognitive impact. Thus, together with the in large parts unimpaired cognitive battery across the entire group of patients, it appears reasonable that factors other than the cortical hypometabolism observed in patients during the early subacute stage after an infection (8) contribute to the symptoms in neurocognitive long COVID syndrome.

Our results have to be compared with other recent studies that used cerebral ^{18}F -FDG PET for the assessment of COVID-19-associated metabolic changes. A frontal and, to a lesser extent, temporoparietal cortical hypometabolism, which improved during follow-up at 1 and 6 mo, was detected by Kas et al. (10), which is in line with our observations (8,9). Of note, different from our previous cohort (8,9) patients included in the aforementioned study (10) suffered from COVID-19-related encephalopathy including delirium, seizures, myocloni, and focal neurologic signs, whereas such severe symptoms were absent in the patients of our subacute cohort (8,9). Clearly deviating from those studies and the present study, a profile of hypometabolism in limbic and paralimbic regions extending to the brain stem and cerebellum was reported for patients with putative long COVID (including decreasing glucose metabolism of the right temporal lobe with longer time after first COVID-19 symptoms) (11). Factors such as pooling of variable time points of examination (about 1–5 mo after COVID-19, on average 96 ± 31 d) and the use of cortical regions for count rate normalization of PET data may have contributed to these discordant findings that are also counterintuitive regarding recovery from COVID-related cognitive deficits in longitudinal investigations (9,15) (a detailed discussion appears in Meyer et al. (32)). Sollini et al. (12) described a hypometabolism particularly of the right parahippocampal gyrus and thalamus in long COVID patients examined at about 3–4 mo after symptom onset. Again, technical factors may explain different findings (e.g., extraction of brain scans from whole-body examination, which may yield inferior data quality if whole-body PET acquisition parameters are not matched to brain acquisitions; retrospective use of brain images of oncologic patients as control data, which limits standardization of behavior/sensory input during ^{18}F -FDG uptake; and liberal statistical thresholds such as $P < 0.005$ on the voxel level). Finally, a thorough qualitative and quantitative assessment of cognitive profiles and correlation to changes in cerebral glucose metabolism was not pursued by other studies (10–12), which underlines the particular value of the present work.

The lack of significant findings on ^{18}F -FDG PET and only mild impairments on neuropsychologic testing is in contrast to the severe and lasting disability reported by the patients (e.g., cognitive symptoms, inability to work). Moreover, neither MoCA performance nor the composite z score of the neurocognitive test battery correlated with disability. On the other hand and in line with other reports in long COVID (33,34), fatigue was particularly prevalent in our cohort (61%, WEIMuS sumscore). Fatigue is a common sequela of systemic viral infections (35,36) and systemic inflammatory diseases (37) and has been related to immune dysregulation processes (38,39) as in the systemic inflammatory

response and cytokine release (14) in COVID-19. Fatigue has also been linked to the myalgic encephalomyelitis/chronic fatigue syndrome (5) in long COVID, which is characterized by functional impairment (e.g., disability to work) in a considerable number of patients (40). Taken together, it is tempting to speculate that the pathophysiologic background of self-reported cognitive symptoms, disability, and even mild impairments in the neuropsychologic test battery in single patients is primarily caused by fatigue.

As a limitation of the present study, only patients self-presenting with long-lasting symptoms were included in our cohort, thereby potentially presenting a small subgroup of COVID-19 patients. However, deficits reported in our cohort are corroborated by the rate of previously reported deficits (2,3), and the fraction of patients that were still unable to work 3–4 mo after infection reported previously (2) is in accordance with our cohort (i.e., 32% vs. 39%). As an inherent problem of studies like ours, no data are available concerning the premorbid cognitive and neuropsychologic status of the patients. Thus, we cannot comment on a possible particular vulnerability or preexisting deficits, which is of particular interest if the detected impairment is small and inconsistent. Furthermore, the number of subjects is relatively small, which precluded in-depth multivariate statistical analyses and limited the possibility to make reliable statements about the frequency of cognitive deficits in long COVID patients. For instance, in contrast to the general observation that male sex is a risk factor for severe disease courses in COVID-19 (41), female sex seems to be slightly overrepresented in the present study. Longitudinal studies are needed to define the prognosis of neurocognitive symptoms in patients with long COVID syndrome. In this regard, the lack of long-lasting alterations of cerebral functioning on ^{18}F -FDG PET would be compatible with a favorable outcome.

DISCLOSURE

Philipp T. Meyer received honoraria for lectures and consulting by GE and Philips. Horst Urbach received honoraria for lectures from Bracco, Bayer, Union Chimique Belge (UCB) pharma, Eisai, and Stryker. Nils Schroeter and Andrea Dressing were supported by the Berta-Ottenstein-Program for Clinician Scientists, Faculty of Medicine, University of Freiburg. No other potential conflict of interest relevant to this article was reported.

KEY POINTS

QUESTION: Long-term neurocognitive symptoms after COVID-19 are an increasingly recognized problem—is the underlying pathophysiology a residual state of cortical dysfunction detected in subacute patients?

PERTINENT FINDINGS: In patients ($n = 31$) in the long-term phase after COVID-19 (202.3 ± 57.5 d after positive PCR) with self-reported symptoms of long COVID, an exhaustive neuropsychologic test battery revealed slight impairments only in individual cases, whereas fatigue was highly prevalent. Cerebral ^{18}F -FDG PET failed to reveal a distinct pathologic signature in the subgroup of patients undergoing ^{18}F -FDG PET ($n = 14$).

IMPLICATIONS FOR PATIENT CARE: The findings deviate from previous reports in patients in the early subacute stage of COVID-19 and suggest that underlying causes of long COVID might be related to fatigue but not to persistent cortical dysfunction.

ACKNOWLEDGMENTS

The use in this work of ScAnVP software, copyright © 2020 The Feinstein Institute for Medical Research, is hereby acknowledged. The data that support the findings of this study are available on request from the corresponding author. The data are not publicly available due to their containing information that could compromise the privacy of research participants.

REFERENCES

- Honigsbaum M, Krishnan L. Taking pandemic sequelae seriously: from the Russian influenza to COVID-19 long-haulers. *Lancet*. 2020;396:1389–1391.
- Garrigues E, Janvier P, Kherabi Y, et al. Post-discharge persistent symptoms and health-related quality of life after hospitalization for COVID-19. *J Infect*. 2020;81:e4–e6.
- Halpin SJ, McIvor C, Whyatt G, et al. Postdischarge symptoms and rehabilitation needs in survivors of COVID-19 infection: a cross-sectional evaluation. *J Med Virol*. 2021;93:1013–1022.
- Woo MS, Malsy J, Pöttgen J, et al. Frequent neurocognitive deficits after recovery from mild COVID-19. *Brain Commun*. 2020;2:fcaa205.
- Wildwing T, Holt N. Similarities between the neurological symptoms of COVID-19 and functional neurological disorder: a systematic overview of systematic reviews and implications for future neurological healthcare services. *Ther Adv Chronic Dis*. January 28, 2021 [Epub ahead of print].
- Davis HE, Assaf GS, McCorkell L, et al. Characterizing long COVID in an international cohort: 7 months of symptoms and their impact. *EClinicalMedicine*. 2021;38:101019.
- NICE guideline [NG188], National Institute for Health and Care Excellence. COVID-19 rapid guideline: managing the long-term effects of COVID-19. National Institute for Health and Care Excellence (NICE) website. <https://www.nice.org.uk/guidance/ng188>. December 2020. Accessed May 23, 2022.
- Hosp JA, Dressing A, Blazhenets G, et al. Cognitive impairment and altered cerebral glucose metabolism in the subacute stage of COVID-19. *Brain*. 2021;144:1263–1276.
- Blazhenets G, Schröter N, Bormann T, et al. Slow but evident recovery from neocortical dysfunction and cognitive impairment in a series of chronic COVID-19 patients. *J Nucl Med*. 2021;62:910–915.
- Kas A, Soret M, Pyatigorskaya N, et al. The cerebral network of COVID-19-related encephalopathy: a longitudinal voxel-based ¹⁸F-FDG-PET study. *Eur J Nucl Med Mol Imaging*. 2021;48:2543–2557.
- Guedj E, Champion JY, Dudouet P, et al. ¹⁸F-FDG brain PET hypometabolism in patients with long COVID. *Eur J Nucl Med Mol Imaging*. 2021;48:2823–2833.
- Sollini M, Morbelli S, Ciccirelli M, et al. Long COVID hallmarks on [¹⁸F]FDG-PET/CT: a case-control study. *Eur J Nucl Med Mol Imaging*. 2021;48:3187–3197.
- Matschke J, Lütgehetmann M, Hagel C, et al. Neuropathology of patients with COVID-19 in Germany: a post-mortem case series. *Lancet Neurol*. 2020;19:919–929.
- Mehta P, McAuley DF, Brown M, Sanchez E, Tattersall RS, Manson JJ. COVID-19: consider cytokine storm syndromes and immunosuppression. *Lancet*. 2020;395:1033–1034.
- Zhao S, Shibata K, Hellyer PJ, et al. Rapid vigilance and episodic memory decrements in COVID-19 survivors. *Brain Commun*. 2022;4:fcab295.
- COVID-19 Guidelines Robert Koch-Institute. Notes on the identification, diagnosis and treatment of patients with COVID-19. Robert-Koch Institut website. https://www.rki.de/EN/Content/infections/epidemiology/outbreaks/COVID-19/Diagnosis-Treatment-STAKOB.pdf?__blob=publicationFile. Accessed May 23, 2022.
- Brandt J, Benedict R. *Hopkins Verbal Learning Test—Revised*. Administration Manual. Lutz, FL: Psychological Assessment Resources; 2001.
- Benedict RHB, Schretlen D, Groninger L, Dobraski M, Shpritz B. Revision of the Brief Visuospatial Memory Test: studies of normal performance, reliability, and validity. *Psychol Assess*. 1996;8:145–153.
- Lepach A, Petermann F. *Wechsler Memory Scale—Revised*. Göttingen: Hogrefe; 2012.
- Lezak MD. *Neuropsychological Assessment*. 3rd ed. New York: Oxford University Press; 1995.
- Bäumler G. Farbe-Wort-Interferenztest (FWIT) nach J.R. Stroop. Göttingen: Hogrefe; 1985.
- Langdon DW, Amato MP, Boring J, et al. Recommendations for a Brief International Cognitive Assessment for Multiple Sclerosis (BICAMS). *Mult Scler*. 2012;18:891–898.
- Aebi C, Monsch AU, Berres M, Brubacher D, Staehelin HB. Validation of the German CERAD-neuropsychological assessment battery. *Neurobiol Aging*. 2002;23:27–28.
- Lazar RM, Pavol MA, Bormann T, et al. Neurocognition and cerebral lesion burden in high-risk patients before undergoing transcatheter aortic valve replacement. *JACC Cardiovasc Interv*. 2018;11:384–392.
- Nasreddine ZS, Phillips NA, Bédirian V, et al. The Montreal Cognitive Assessment, MoCA: a brief screening tool for mild cognitive impairment. *J Am Geriatr Soc*. 2005;53:695–699.
- Flachenecker P, Müller G, König H, Meissner H, Toyka KV, Rieckmann P. “Fatigue” in multiple sclerosis: development and validation of the “Würzburger Fatigue Inventory for MS.” *Nervenarzt*. 2006;77:165–166, 168–170, 172–174.
- Sheikh JI, Yesavage JA. 9/Geriatric Depression Scale (GDS): recent evidence and development of a shorter version. *Clin Gerontol*. 1986;5:165–173.
- Minoshima S, Frey KA, Koeppe RA, Foster NL, Kuhl DE. A diagnostic approach in Alzheimer’s disease using three-dimensional stereotactic surface projections of fluorine-18-FDG PET. *J Nucl Med*. 1995;36:1238–1248.
- Voruz P, Allali G, Benzakour L, et al. Long COVID neuropsychological deficits after severe, moderate or mild infection. medRxiv website. <https://www.medrxiv.org/content/10.1101/2021.02.24.21252329v1>. Published February 26, 2021. Accessed April 11, 2022.
- Baddeley AD, Eysenck MW, Anderson MC. *Memory*. London: Routledge; 2020.
- Almeria M, Cejudo JC, Sotoca J, Deus J, Krupinski J. Cognitive profile following COVID-19 infection: Clinical predictors leading to neuropsychological impairment. *Brain Behav Immun Health*. 2020;9:100163.
- Meyer PT, Blazhenets G, Prinz M, Hosp JA. Reply: from early limbic inflammation to long COVID sequelae. *Brain*. 2021;144:e66.
- Townsend L, Dyer AH, Jones K, et al. Persistent fatigue following SARS-CoV-2 infection is common and independent of severity of initial infection. *PLoS ONE*. 2020;15:e0240784.
- Kedor C, Freitag H, Meyer-Armdt L, et al. Chronic COVID-19 syndrome and chronic fatigue syndrome (ME/CFS) following the first pandemic wave in Germany: a first analysis of a prospective observational study. medRxiv website. <https://www.medrxiv.org/content/10.1101/2021.02.06.21249256v1.full.pdf>. Published February 8, 2022. Accessed April 11, 2022.
- Moldofsky H, Patcai J. Chronic widespread musculoskeletal pain, fatigue, depression and disordered sleep in chronic post-SARS syndrome; a case-controlled study. *BMC Neurol*. 2011;11:37.
- Islam MF, Cotler J, Jason LA. Post-viral fatigue and COVID-19: lessons from past epidemics. *Fatigue*. 2020;8:61–69.
- Zielinski MR, Systrom DM, Rose NR. Fatigue, sleep, and autoimmune and related disorders. *Front Immunol*. 2019;10:1827.
- Sotzny F, Blanco J, Capelli E, et al. Myalgic encephalomyelitis/chronic fatigue syndrome: evidence for an autoimmune disease. *Autoimmun Rev*. 2018;17:601–609.
- Komaroff AL, Cho T. Role of infection and neurologic dysfunction in chronic fatigue syndrome. *Semin Neurol*. 2011;31:325–337.
- Vink M, Vink-Niese F. Work rehabilitation and medical retirement for myalgic encephalomyelitis/chronic fatigue syndrome patients: a review and appraisal of diagnostic strategies. *Diagnostics (Basel)*. 2019;9:124.
- Weiss P, Murdoch DR. Clinical course and mortality risk of severe COVID-19. *Lancet*. 2020;395:1014–1015.

Independent Prognostic Utility of ^{11}C -Pittsburgh Compound B PET in Patients with Light-Chain Cardiac Amyloidosis

You-Jung Choi¹, Youngil Koh², Hyun-Jung Lee¹, In-Chang Hwang³, Jun-Bean Park^{1,4}, Yeonyee E. Yoon^{3,4}, Hack-Lyoung Kim^{4,5}, Hyung-Kwan Kim^{1,4}, Yong-Jin Kim^{1,4}, Goo-Yeong Cho^{3,4}, Dae-Won Sohn^{1,4}, Jin-Chul Paeng⁶, and Seung-Pyo Lee^{1,4}

¹Division of Cardiology, Department of Internal Medicine, Seoul National University Hospital, Seoul, South Korea; ²Division of Hemato Oncology, Department of Internal Medicine, Seoul National University Hospital, Seoul, South Korea; ³Department of Internal Medicine and Cardiovascular Center, Seoul National University Bundang Hospital, Seongnam, Gyeonggi-do, South Korea; ⁴Department of Internal Medicine, Seoul National University College of Medicine, Seoul, South Korea; ⁵Division of Cardiology, Department of Internal Medicine, Boramae Medical Center, Seoul National University College of Medicine, Seoul, South Korea; and ⁶Department of Nuclear Medicine, Seoul National University Hospital and Seoul National University College of Medicine, Seoul, South Korea

^{11}C -Pittsburgh compound B (PiB) PET/CT visualizes the amount of myocardial amyloid deposit and can be used to prognosticate patients with amyloid light-chain (AL) cardiac amyloidosis (CA). However, whether ^{11}C -PiB PET/CT has any independent additional prognostic value beyond the commonly used biomarkers remains unknown.

Methods: This prospective study was on a cohort of 58 consecutive patients with AL CA who underwent ^{11}C -PiB PET/CT. The patients were stratified into 2 groups on the basis of a visual assessment of whether there was myocardial ^{11}C -PiB uptake on PET/CT. The primary endpoint was 1-y overall mortality. The independent prognostic utility of ^{11}C -PiB PET/CT was analyzed using net reclassification improvement and integrated discrimination improvement. **Results:** Among the 58 patients enrolled, 35 were positive for myocardial ^{11}C -PiB uptake on PET/CT. Patients with myocardial ^{11}C -PiB uptake had a worse 1-y overall survival rate than those without (81.8% vs. 45.5%, $P = 0.003$ by log-rank test). In the multivariate analysis, positivity for myocardial ^{11}C -PiB uptake on PET/CT was an independent predictor of 1-y mortality (adjusted hazard ratio, 3.382; 95% CI, 1.011–11.316; $P = 0.048$). In analysis of 3 subgroups of patients—those with a troponin I level of at least 0.1 ng/mL, those with an N-terminal pro-B-type natriuretic peptide (NT-proBNP) level of at least 1,800 pg/mL, and those with a difference of at least 180 mg/L between free light chains (the 3 commonly used biomarkers and their thresholds for staging in AL amyloidosis)—Kaplan–Meier curves showed for all 3 subgroups that patients positive for myocardial ^{11}C -PiB uptake on PET/CT had a worse prognosis than those who were negative. Additionally, when the results of ^{11}C -PiB PET/CT were added to these 3 biomarkers, the performance of 1-y mortality prediction significantly improved by net reclassification improvement (troponin I, 0.861; NT-proBNP, 0.914; difference between free light chains, 0.987) and by integrated discrimination improvement (0.200, 0.156, and 0.108, respectively). **Conclusion:** ^{11}C -PiB PET/CT is a strong independent predictor of 1-y overall mortality and provides incremental prognostic benefits beyond the 3 commonly used biomarkers of AL amyloidosis staging. Considering the recent development of numerous amyloid-targeting molecular imaging agents, further investigations are warranted on whether PET/CT should be included in risk stratification for patients with AL CA.

Key Words: ^{11}C -Pittsburgh compound B PET; cardiac amyloidosis; survival; risk stratification

J Nucl Med 2022; 63:1064–1069
DOI: 10.2967/jnumed.121.263033

Amyloidosis is a rare group of disorders caused by the accumulation of proteinaceous fibrils in certain organs that compromises their structure and function (1). Cardiac amyloidosis (CA) refers to the myocardial deposition of amyloid fibrils, of which the immunoglobulin amyloid light chain (AL) and transthyretin are the most common types (2). Cardiac involvement is the major determinant of prognosis in AL amyloidosis patients; therefore, accurate evaluation of the degree of involvement is crucial for prognostication (3).

Endomyocardial biopsy is commonly used for the evaluation of CA, for which the presence of AL proteins can be evaluated, together with its degree of deposition (4). However, endomyocardial biopsy involves invasive removal of the myocardial tissue and does not provide information on disease activity or the hemodynamic consequences. In contrast, biomarkers such as serum cardiac troponins and N-terminal pro-B-type natriuretic peptide (NT-proBNP)/BNP, which are associated with the hemodynamic burden to the heart, are used for cardiac staging, albeit not specific for CA (5–7). The absolute difference between the involved and uninvolved free light chains (dFLC), as a parameter for hematologic disease burden, is also incorporated into the staging system and improves the risk stratification of AL amyloidosis patients (8). Additionally, imaging markers such as left ventricular strain on speckle-tracking echocardiography and the gadolinium enhancement pattern on cardiovascular MRI are helpful for the prognostication of AL amyloidosis patients (9–14).

To date, advances in nuclear imaging have allowed a more specific, noninvasive approach to the diagnosis and prognostication of CA (15). We and others have shown that ^{11}C -Pittsburgh compound B (PiB) PET/CT may be used for diagnosis of AL CA by reflecting the amount of myocardial amyloid deposited and that this amount is associated with patient prognosis (16–18). However, for a new imaging test to be clinically useful, verification is needed of whether

Received Aug. 11, 2021; revision accepted Dec. 9, 2021.
For correspondence or reprints, contact Seung-Pyo Lee (sroll1@snu.ac.kr).
Published online Dec. 16, 2021.
COPYRIGHT © 2022 by the Society of Nuclear Medicine and Molecular Imaging.

it has any independent additional prognostic value beyond the commonly used conventional prognosticators. In this study, we aimed to determine whether ^{11}C -PiB PET/CT could provide independent incremental prognostic value over serum biomarkers in patients with AL CA.

MATERIALS AND METHODS

Study Population

This prospective study was on a cohort of patients with AL CA diagnosed at Seoul National University Hospital between 2012 and 2019. Cardiac involvement of AL amyloidosis was diagnosed with confirmation by monoclonal gammopathy in the peripheral blood and lineage-restricted expansion of plasma cells in the bone marrow, together with either a positive endomyocardial biopsy result or a cardiac imaging–based diagnosis with histologic confirmation of amyloid infiltration by noncardiac biopsies (average left ventricular wall thickness ≥ 12 mm on echocardiography with no identifiable cause; unexplained low voltage QRS amplitude < 0.5 mV in the limb leads of the 12-lead electrocardiogram; typical features of CA on cardiovascular MRI, including diffuse late gadolinium enhancement and myocardial extracellular volume expansion) (19–21).

The endomyocardial biopsy was performed in a standard manner (22). Deposition of amyloid in the myocardium was confirmed by positive amyloid P staining by immunohistochemistry and by apple-green birefringence by Congo-red staining (23).

The study complied with the declaration of Helsinki and was approved by the Institutional Review Boards. All subjects signed an informed-consent form.

^{11}C -PiB PET/CT Protocol and Image Interpretation

^{11}C -PiB PET/CT was performed using a dedicated PET/CT machine (Biograph 40; Siemens Medical Solutions). After low-dose CT scanning, ^{11}C -PiB (555 MBq) was injected intravenously. Thirty minutes later, a 3-dimensional PET/CT scan was obtained at 3 min per bed position, with a spatial resolution of 4.2 mm. The detailed ^{11}C -PiB PET/CT protocol has been published elsewhere (16). Images were displayed in transaxial, coronal, and sagittal planes 5 mm thick. Because the purpose of this study was not to analyze the diagnostic accuracy of ^{11}C -PiB PET/CT for AL CA but to demonstrate the clinical utility of ^{11}C -PiB PET/CT in AL CA—and taking into consideration our previous finding that static ^{11}C -PiB PET/CT reflects the myocardial amyloid load (17)—we used visual estimation of the static PET/CT images to divide the study population into groups either positive or negative for myocardial ^{11}C -PiB uptake (Fig. 1) instead of using the quantified best cutoff SUV as in our previous study (16,17). The ^{11}C -PiB PET/CT findings were considered positive when the myocardial ^{11}C -PiB uptake was visually discernible from the blood pool (i.e., left ventricular cavity) (Supplemental Fig. 1; supplemental materials are available at <http://jnm.snmjournals.org>). The individual images and interpretations of ^{11}C -PiB PET/CT for all participants are listed in Supplemental Figure 2. All images were interpreted by a single expert masked to all other findings; in ambiguous cases, another independent observer participated in the visual analysis.

Echocardiography and Biomarker Measurement

Two-dimensional echocardiography was performed within 2 wk of PET/CT according to current guidelines (24). We measured early diastolic transmitral inflow velocity (E velocity)

and early diastolic mitral annular velocity (e' velocity) at the septal annulus by Doppler echocardiography to calculate the E/ e' ratio.

We collected data on the serum biomarkers retrospectively, based on the electronic medical records. A serum free-light-chain assay was performed at the initial diagnosis of amyloidosis, and dFLC was calculated from these results. Serum NT-proBNP and troponin I were measured within 1 mo from ^{11}C -PiB PET/CT. Subgroups were analyzed in patients with serum biomarker values higher than the thresholds for each biomarker used in the revised Mayo staging system (troponin I ≥ 0.1 ng/mL, NT-proBNP $\geq 1,800$ pg/mL, and dFLC ≥ 180 mg/L) (8).

Outcome Ascertainment

The outcome of the study was all-cause death, confirmed either by medical records or by reviewing the official nationwide data on death certification provided by the National Statistical Office of Korea. Patients were censored when they underwent heart transplantation. Each patient was followed from the date of the ^{11}C -PiB PET/CT scan to either the date of death or up to 1 y.

Statistical Analysis

Continuous variables are described as mean \pm SD or as median and interquartile range (IQR), and categorical variables are described as frequencies and percentages. We compared continuous variables using the Student t test or the Mann–Whitney U test after testing for normality with the Shapiro–Wilk test. We compared categorical variables between the 2 groups using either the χ^2 test or the Fisher exact test.

We used the Kaplan–Meier estimate to describe and compare the survival curves between groups with the log-rank test. The proportional hazards assumption was checked using a statistical test based on the Schoenfeld residuals and their plots. Hazard ratios (HRs) with a 95% CI were determined using the Cox proportional hazards regression. Covariates with a P value of less than 0.05 on univariate Cox analysis were included in the multivariable model. Time zero was defined as the time of the ^{11}C -PiB PET/CT scan. To determine the incremental predictive value of ^{11}C -PiB PET/CT in addition to the 3 conventional serum biomarkers (troponin I, NT-proBNP, and dFLC), the net reclassification improvement and the integrated discrimination improvement were computed in regard to 1-y overall mortality (25).

All analyses used a 2-sided P value, and a P value of less than 0.05 was considered statistically significant. Statistical analyses were performed with SPSS statistics, version 25.0 (IBM Corp.), or R programming, version 4.0.5 (<http://www.R-project.org>).

RESULTS

Patient Characteristics

Among the 62 patients diagnosed with CA who underwent ^{11}C -PiB PET/CT, 58 were included in the final analysis, excluding

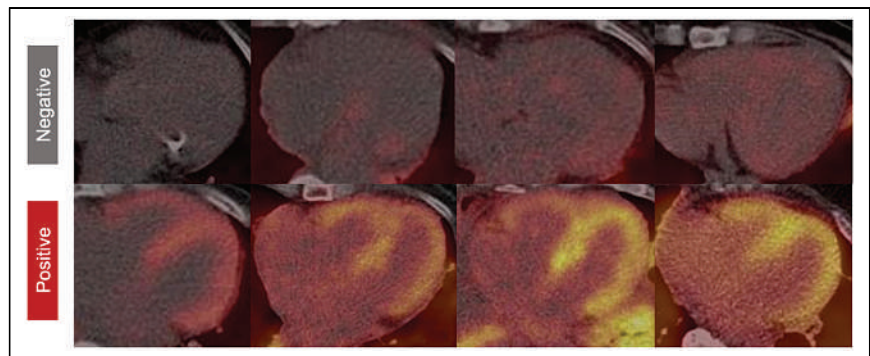


FIGURE 1. Representative positive vs. negative ^{11}C -PiB PET/CT images. ^{11}C -PiB PET/CT findings were classified into either negative (top panels) or positive (bottom panels) based on visually estimated retention of ^{11}C -PiB in myocardium.

those with non-AL CA ($n = 4$). Among the 58 patients, 53 were histologically diagnosed with CA by endomyocardial biopsy, and the diagnosis in the remaining 5 was based on findings strongly suggestive of CA on at least 2 noninvasive modalities, such as echocardiography, cardiovascular MRI, or electrocardiography. The average age was 64.0 ± 9.1 y, and 43% were male. There were 35 patients with a positive ^{11}C -PiB PET/CT result. The baseline demographic and clinical data are compared according to myocardial ^{11}C -PiB PET uptake in Table 1.

The average age was higher in patients with a positive ^{11}C -PiB PET/CT result than in those with a negative result (65.5 ± 9.8 y vs. 61.7 ± 7.6 y, $P = 0.121$). The systolic blood pressure was lower in patients with a positive ^{11}C -PiB PET/CT result (median, 104.0 mm Hg [IQR, 92.5–114.0 mm Hg] vs. 111.0 mm Hg [IQR, 104.5–122.5 mm Hg]; $P = 0.034$). During the 1-y follow-up, more patients with a negative ^{11}C -PiB PET/CT result received autologous peripheral blood stem cell transplantation (30.4% vs. 8.6%, $P = 0.040$). As for the echocardiography data, there was no significant difference between the 2 groups, except for E velocity ($P = 0.021$), e' velocity ($P = 0.043$), and E/e' ratio ($P = 0.004$).

Outcome Comparison According to the ^{11}C -PiB PET/CT Results

During the 1-y follow-up, 23 patients died. Among 35 patients with a positive ^{11}C -PiB PET/CT result, 16 (54.3%) died, whereas 4 (17.4%) of those with a negative result died. In the entire cohort, the 1-y overall survival rate was 59.3%; the survival rates at 3 mo and 6 mo were 77.2% and 59.3%, respectively (Fig. 2A). Kaplan–Meier survival curves showed that the 1-y overall survival rate was significantly worse in patients with a positive ^{11}C -PiB PET/CT result (81.8% vs. 45.5%; $P = 0.003$ by log-rank test; Fig. 2B). In the multivariate analysis, positivity for myocardial ^{11}C -PiB PET uptake was an independent predictor of 1-y overall survival (adjusted HR, 3.382; 95% CI, 1.011–11.316; $P = 0.048$) (Supplemental Table 1).

Incremental Value of ^{11}C -PiB PET/CT in Addition to Serum Biomarkers for AL CA Prognostication

Among the 58 AL CA patients, 34, 39, and 47 had values available for troponin I (median, 0.14 ng/mL; IQR, 0.07–0.39 ng/mL), NT-proBNP (median, 3,733 pg/mL; IQR, 1,117–7,232 pg/mL),

TABLE 1
Baseline Characteristics of Study Participants

Variable	Entire population ($n = 58$)	Negative ^{11}C -PiB PET/CT ($n = 23$)	Positive ^{11}C -PiB PET/CT ($n = 35$)	<i>P</i>
Demographics				
Age (y)	64.0 ± 9.1	61.7 ± 7.6	65.5 ± 9.8	0.121
Male	25 (43.1%)	9 (39.1%)	16 (45.7%)	0.787
Systolic blood pressure (mm Hg)	109.5 (100.2–119.5)	111.0 (104.5–122.5)	104.0 (92.5–114.0)	0.034
Diastolic blood pressure (mm Hg)	68.0 ± 7.5	68.5 ± 7.7	67.6 ± 7.5	0.663
Body mass index (kg/m^2)	22.6 ± 3.1	23.1 ± 3.4	22.2 ± 3.9	0.270
Comorbidities				
Hypertension	13 (22.4%)	5 (21.7%)	8 (22.9%)	0.999
Diabetes	13 (22.4%)	2 (8.7%)	11 (31.4%)	0.087
Dyslipidemia	6 (10.3%)	1 (4.3%)	5 (14.3%)	0.386
End-stage renal disease	4 (6.8%)	2 (8.7%)	2 (5.7%)	0.999
Atrial fibrillation	5 (8.6%)	4 (17.4%)	1 (3.0%)	0.075
Chemotherapy	51 (87.9%)	22 (95.7%)	29 (82.9%)	0.224
Autologous PBSCT	10 (17.2%)	7 (30.4%)	3 (8.6%)	0.040
Echocardiography data				
LV end-diastolic dimension (mm)	43.8 ± 5.2	45.1 ± 6.0	43.0 ± 4.4	0.134
LV end-systolic dimension (mm)	28.8 ± 5.2	29.2 ± 6.0	28.5 ± 4.7	0.640
LV mass index (kg/m^2)	121.2 ± 34.7	116.8 ± 36.8	124.2 ± 33.5	0.430
LV ejection fraction (%)	56.5 (52.0–62.0)	58.0 (51.5–66.5)	56.0 (52.5–60.5)	0.321
LV ejection fraction < 60%	19 (32.8%)	10 (43.5%)	9 (25.7%)	0.261
E velocity (m/s)	0.85 ± 0.28	0.76 ± 0.23	0.91 ± 0.31	0.021
e' velocity (cm/s)	4.1 ± 1.1	4.4 ± 1.0	3.8 ± 1.1	0.043
E/e' ratio	19.9 (14.9–29.5)	16.7 (13.4–21.0)	22.5 (17.0–33.3)	0.004
Estimated PASP (mm Hg)	38.0 (32.5–45.0)	37.0 (31.5–42.5)	40.5 (32.8–45.0)	0.441
Left atrial size (mm)	43.3 ± 6.7	43.1 ± 7.2	43.4 ± 6.4	0.863

PBSCT = peripheral blood stem cell transplantation; LV = left ventricular; PASP = pulmonary arterial systolic pressure.

Data for continuous variables are mean \pm SD or median followed by IQ. Data for categoric variables are frequencies followed by percentages. *P* values are for comparisons between positive and negative ^{11}C -PiB PET/CT groups.

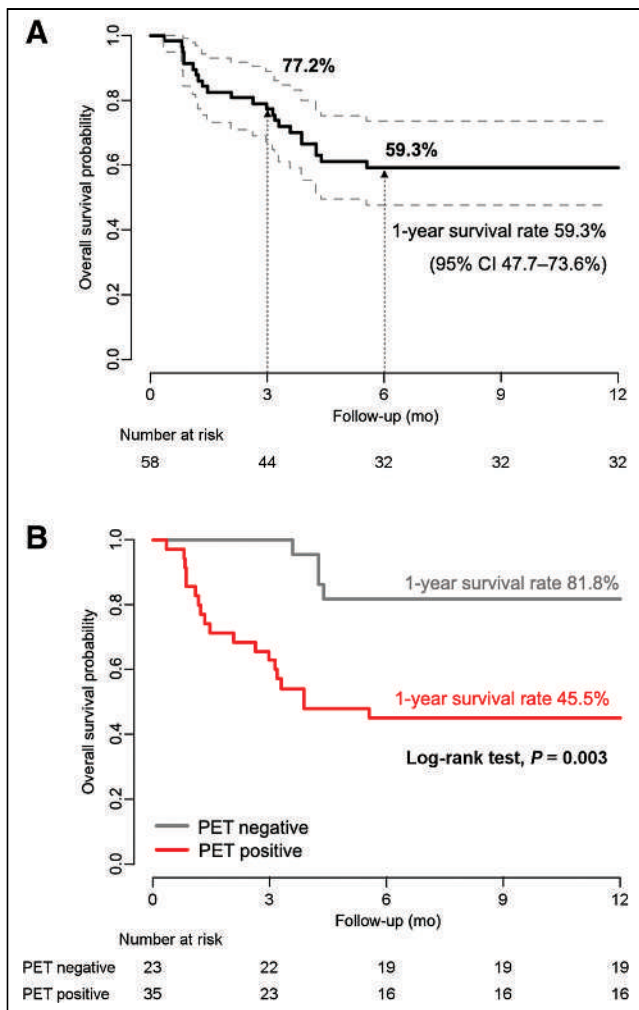


FIGURE 2. Kaplan–Meier survival curves for 1-y overall survival in entire AL CA population in current cohort (A) and according to myocardial ^{11}C -PiB PET uptake as in Figure 1 (B).

and dFLC (median, 291.7 mg/L; IQR, 155.2–744.8 mg/L). There were no statistically significant differences in the 3 serum biomarkers between patients positive and patients negative for myocardial ^{11}C -PiB PET uptake (Fig. 3).

We performed a subgroup analysis on the subset of patients with levels of troponin I, NT-proBNP, and dFLC higher than the thresholds of the revised Mayo staging system (troponin I ≥ 0.1 ng/mL, NT-proBNP $\geq 1,800$ pg/mL, and dFLC ≥ 180 mg/L) (8)—the subset of patients considered high-risk. Among the patients with a higher level of troponin I, positivity for myocardial ^{11}C -PiB PET uptake was associated with worse overall survival during the 1-y follow-up ($P = 0.013$ by log-rank test, Fig. 4A [unadjusted HR, 8.884; 95% CI, 1.121–70.410; $P = 0.039$]). This pattern was similar in the patients with a higher level of NT-proBNP ($P = 0.020$ by log-rank test, Fig. 4B [unadjusted HR, 7.892; 95% CI, 1.011–61.610; $P = 0.049$]) and in the patients with a higher level of dFLC ($P = 0.050$ by log-rank test, Fig. 4C [unadjusted HR, 5.923; 95% CI, 0.783–44.82; $P = 0.085$]). Additionally, the cardiac staging system incorporating ^{11}C -PiB PET/CT in combination with the 2004 Mayo classification system (26) also significantly predicted 1-y overall survival (Supplemental Fig. 3).

To determine the incremental predictive value of ^{11}C -PiB PET/CT in regard to outcome, the net reclassification improvement and integrated discrimination improvement were measured when the results of ^{11}C -PiB PET/CT were added to the 3 conventional biomarkers (troponin I, NT-proBNP, and dFLC). Both the net reclassification and the integrated discrimination for prediction of 1-y overall survival showed a consistent significant improvement when the results of ^{11}C -PiB PET/CT were added (net reclassification improvements of 0.861, 0.914, and 0.987, respectively [all $P < 0.01$]; integrated discrimination improvements of 0.200, 0.156, and 0.108, respectively [all $P < 0.05$]) (Supplemental Table 2).

DISCUSSION

To our knowledge, this was the first study to prove that in patients with AL CA, ^{11}C -PiB PET/CT adds incremental prognostic power to conventional serum biomarkers, including troponin I, NT-proBNP, and dFLC. The main findings of the study were that ^{11}C -PiB PET/CT predicts 1-y overall survival in patients with AL CA; that positivity for ^{11}C -PiB PET uptake in the myocardium is a robust prognosticator capable of reclassifying subjects stratified as high-risk on the basis of the conventional biomarkers; and that compared with conventional biomarkers, ^{11}C -PiB PET/CT provides additional independent prognostic information for predicting 1-y survival.

^{11}C -PiB, the prototype PET amyloid tracer, is one of the most studied and widely used amyloid β peptide imaging agents. ^{11}C -PiB PET was first used to image and quantify amyloid deposits in Alzheimer dementia (27,28) and is effective in diagnosing CA and predicting its prognosis as in our previous studies (16–18). However, the lack of evidence for an independent predictive power apart from the previously well-validated biomarkers for cardiac staging, such as troponin I, NT-pro BNP, and dFLC (8), limits the clinical application of ^{11}C -PiB PET/CT in these patients. The current study expanded on our previous research and demonstrated the clinical implications of ^{11}C -PiB PET/CT as a risk predictor for AL CA patients, independent of the commonly used biomarkers. Notably, we demonstrated that positivity for ^{11}C -PiB PET uptake in the myocardium remains one of the strongest independent predictors of 1-y overall survival.

Patients with AL CA have a dismal prognosis, with nearly half dying within 1 y of the diagnosis as in the current study. Therefore, previous cardiac staging systems have recommended using cardiac biomarkers such as troponin I and NT-proBNP for risk stratification of AL amyloidosis (7,8). However, circulating cardiac biomarkers are not generally specific to AL CA and are also elevated in heart failure of other etiologies (29). Given the strong association between myocardial ^{11}C -PiB PET uptake and worse clinical outcome in AL CA patients, we propose that for more accurate cardiac staging, ^{11}C -PiB PET/CT be considered. The prognostic power of ^{11}C -PiB PET/CT was maintained even in patients with higher levels of dFLC. Therefore, it is expected that ^{11}C -PiB PET/CT could play a greater role in risk prediction of AL CA patients who are likely to be falsely considered high-risk, possibly because of nonspecific elevations of the serum biomarkers.

Among the biopsy-confirmed AL CA patients, there was a certain proportion with very low myocardial uptake of ^{11}C -PiB when using SUVs as a measure of tracer uptake (16). In the current study, visual assessment of the ^{11}C -PiB PET/CT images demonstrated that a

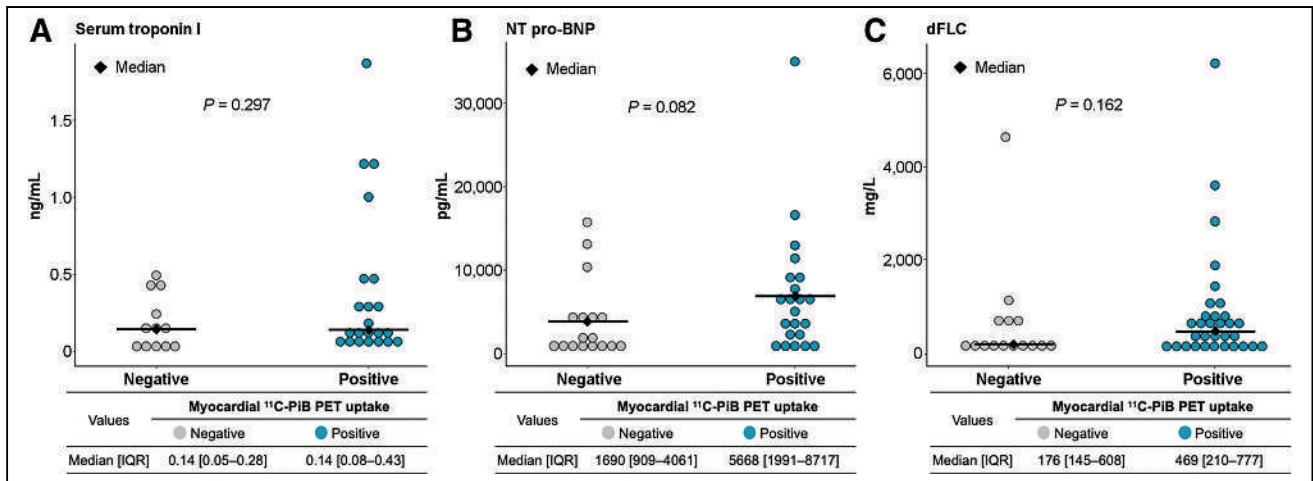


FIGURE 3. Circulating biomarkers in patients with AL CA stratified by myocardial ¹¹C-PiB PET uptake. Dot plot of each cardiac biomarker is according to myocardial ¹¹C-PiB PET uptake: troponin I (A), NT-pro-BNP (B), and dFLC (C).

significant number of patients who may be quantified as positive may actually have a negligible amount of myocardial ¹¹C-PiB PET uptake that could be considered negative in the visual assessment, as is also supported by our previous work (17). These patients with low or visually negative myocardial ¹¹C-PiB PET uptake had a significantly better prognosis than those with strong uptake, suggesting that uptake reflects the amount of amyloid deposited in the myocardium and can be used to determine the prognosis of patients with AL CA (17). Similarly, a small pilot study of 9 patients diagnosed with CA found that cardiac function and symptoms remained stable if there was no myocardial ¹¹C-PiB PET uptake but that the prognosis was poor if there was uptake (30). Taking these findings together, it is expected that myocardial ¹¹C-PiB PET uptake is strongly related to an advanced stage of disease. Further studies may be needed on standardized protocols using quantitative or semiquantitative methods to define the cutoffs that could be used to identify high-risk groups.

To date, no imaging tool has been included in the cardiac staging of patients with AL amyloidosis. However, staging is essential for prognostication, such as the identification of high-risk populations (31,32), and for optimal management. Given the need for

improved cardiac staging systems in AL amyloidosis, we provide evidence for using ¹¹C-PiB PET/CT to discriminate high-risk patients. Furthermore, our findings warrant further investigation, possibly by multicenter studies, into whether an additive imaging study is needed to accurately predict the prognosis of AL CA patients.

Our study was not without limitations. First, although the study was prospective, the sample size was small, and there is therefore a possibility of overfitting in the multivariate analysis. Second, because troponin I, NT-pro-BNP, and dFLC levels were not measured for all patients, a selection bias may exist. Third, not all patients with AL CA defined by clinically acceptable imaging-based criteria underwent an endomyocardial biopsy. However, all patients underwent noncardiac biopsies for histologic confirmation of systemic amyloidosis, and the diagnosis of AL CA followed the universally accepted diagnostic criteria. Finally, in contrast to most studies, which have used dynamic ¹¹C-PiB PET for early detection of CA, we used static ¹¹C-PiB PET/CT images because these have been shown to be a good alternative (33). Additionally, the static scan has the advantages of patient convenience, practicality for routine clinical use, and the potential to evaluate the whole body for amyloid deposits.

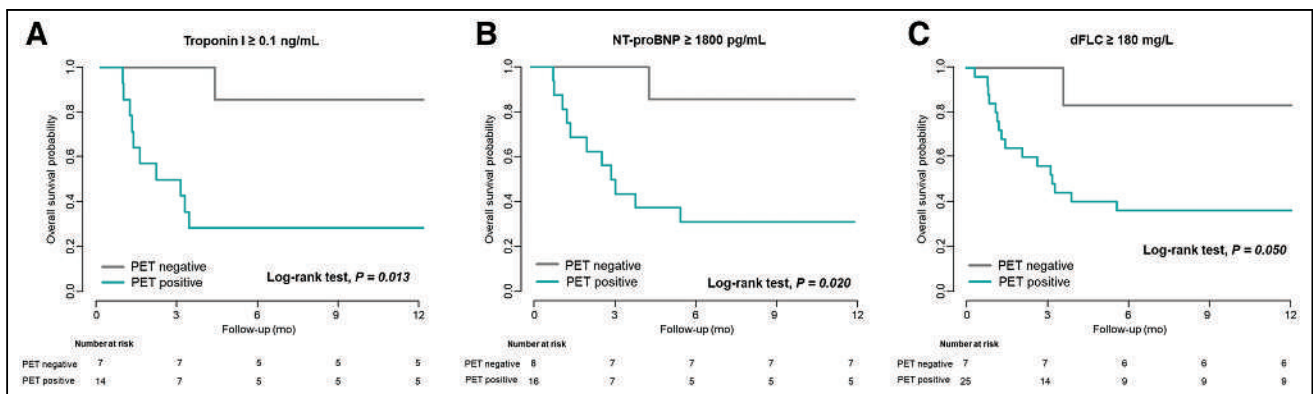


FIGURE 4. Kaplan-Meier survival curves for 1-y overall survival in patients with AL CA according to myocardial ¹¹C-PiB PET uptake in patients with troponin I \geq 0.1 ng/mL (A), NT-pro-BNP \geq 1,800 pg/mL (B), and dFLC \geq 180 mg/L (C).

CONCLUSION

¹¹C-PiB PET/CT is a strong, independent predictor of 1-y overall survival in patients with AL CA and is additive to well-validated serum biomarkers such as troponin I, NT-proBNP, and dFLC. Therefore, ¹¹C-PiB PET/CT may be useful as a novel imaging marker for cardiac staging beyond established predictors in AL CA. Considering the recent development of numerous amyloid-targeting molecular imaging agents, future prospective studies are warranted on whether PET/CT should be included in risk stratification for AL CA patients.

DISCLOSURE

No potential conflict of interest relevant to this article was reported.

ACKNOWLEDGMENT

We thank the Medical Research Collaborating Center of Seoul National University Hospital for statistical review and consultation.

KEY POINTS

QUESTION: Does ¹¹C-PiB PET/CT provide independent incremental prognostic value over conventional serum biomarkers in patients with AL CA?

PERTINENT FINDINGS: ¹¹C-PiB PET/CT was a strong independent predictor of 1-y overall survival in patients with AL CA and provided incremental prognostic benefits that were additive to well-established serum biomarkers such as troponin I, NT-proBNP, and dFLC.

IMPLICATIONS FOR PATIENT CARE: ¹¹C-PiB PET/CT may be useful as a novel imaging marker for cardiac staging beyond established predictors in AL CA patients.

REFERENCES

- Benson MD, Buxbaum JN, Eisenberg DS, et al. Amyloid nomenclature 2018: recommendations by the International Society of Amyloidosis (ISA) nomenclature committee. *Amyloid*. 2018;25:215–219.
- Maleszewski JJ. Cardiac amyloidosis: pathology, nomenclature, and typing. *Cardiovasc Pathol*. 2015;24:343–350.
- Mahmood S, Palladini G, Sancharawala V, Wechalekar A. Update on treatment of light chain amyloidosis. *Haematologica*. 2014;99:209–221.
- Crotty TB, Li CY, Edwards WD, Suman VJ. Amyloidosis and endomyocardial biopsy: correlation of extent and pattern of deposition with amyloid immunophenotype in 100 cases. *Cardiovasc Pathol*. 1995;4:39–42.
- Palladini G, Campana C, Klersy C, et al. Serum N-terminal pro-brain natriuretic peptide is a sensitive marker of myocardial dysfunction in AL amyloidosis. *Circulation*. 2003;107:2440–2445.
- Dispenzieri A, Kyle RA, Gertz MA, et al. Survival in patients with primary systemic amyloidosis and raised serum cardiac troponins. *Lancet*. 2003;361:1787–1789.
- Dispenzieri A, Gertz MA, Kyle RA, et al. Serum cardiac troponins and N-terminal pro-brain natriuretic peptide: a staging system for primary systemic amyloidosis. *J Clin Oncol*. 2004;22:3751–3757.
- Kumar S, Dispenzieri A, Lacy MQ, et al. Revised prognostic staging system for light chain amyloidosis incorporating cardiac biomarkers and serum free light chain measurements. *J Clin Oncol*. 2012;30:989–995.
- Lee MH, Lee SP, Kim YJ, Sohn DW. Incidence, diagnosis and prognosis of cardiac amyloidosis. *Korean Circ J*. 2013;43:752–760.
- Lee SP, Park JB, Kim HK, Kim YJ, Grogan M, Sohn DW. Contemporary imaging diagnosis of cardiac amyloidosis. *J Cardiovasc Imaging*. 2019;27:1–10.
- Buss SJ, Emami M, Mereles D, et al. Longitudinal left ventricular function for prediction of survival in systemic light-chain amyloidosis: incremental value compared with clinical and biochemical markers. *J Am Coll Cardiol*. 2012;60:1067–1076.
- Boynton SJ, Geske JB, Dispenzieri A, et al. LGE provides incremental prognostic information over serum biomarkers in AL cardiac amyloidosis. *JACC Cardiovasc Imaging*. 2016;9:680–686.
- Arenja N, Andre F, Riffel JH, et al. Prognostic value of novel imaging parameters derived from standard cardiovascular magnetic resonance in high risk patients with systemic light chain amyloidosis. *J Cardiovasc Magn Reson*. 2019;21:53.
- Hwang IC, Koh Y, Park JB, et al. Time trajectory of cardiac function and its relation with survival in patients with light-chain cardiac amyloidosis. *Eur Heart J Cardiovasc Imaging*. 2021;22:459–469.
- Paeng JC, Choi JY. Nuclear imaging for cardiac amyloidosis: bone scan, SPECT/CT, and amyloid-targeting PET. *Nucl Med Mol Imaging*. 2021;55:61–70.
- Lee SP, Lee ES, Choi H, et al. ¹¹C-Pittsburgh B PET imaging in cardiac amyloidosis. *JACC Cardiovasc Imaging*. 2015;8:50–59.
- Lee SP, Suh HY, Park S, et al. Pittsburgh B compound positron emission tomography in patients with AL cardiac amyloidosis. *J Am Coll Cardiol*. 2020;75:380–390.
- Antoni G, Lubberink M, Estrada S, et al. In vivo visualization of amyloid deposits in the heart with ¹¹C-PiB and PET. *J Nucl Med*. 2013;54:213–220.
- Dorbala S, Ando Y, Bokhari S, et al. ASNC/AHA/ASE/EANM/HFSA/ISA/SCMR/SNMMI expert consensus recommendations for multimodality imaging in cardiac amyloidosis: part 1 of 2—evidence base and standardized methods of imaging. *J Card Fail*. 2019;25:e1–e39.
- Garcia-Pavia P, Rapezzi C, Adler Y, et al. Diagnosis and treatment of cardiac amyloidosis: a position statement of the ESC Working Group on Myocardial and Pericardial Diseases. *Eur Heart J*. 2021;42:1554–1568.
- Brooks J, Kramer CM, Salerno M. Markedly increased volume of distribution of gadolinium in cardiac amyloidosis demonstrated by T1 mapping. *J Magn Reson Imaging*. 2013;38:1591–1595.
- Cunningham KS, Veinot JP, Butany J. An approach to endomyocardial biopsy interpretation. *J Clin Pathol*. 2006;59:121–129.
- Gertz MA, Comenzo R, Falk RH, et al. Definition of organ involvement and treatment response in immunoglobulin light chain amyloidosis (AL): a consensus opinion from the 10th International Symposium on Amyloid and Amyloidosis, Tours, France, 18–22 April 2004. *Am J Hematol*. 2005;79:319–328.
- Lang RM, Badano LP, Mor-Avi V, et al. Recommendations for cardiac chamber quantification by echocardiography in adults: an update from the American Society of Echocardiography and the European Association of Cardiovascular Imaging. *J Am Soc Echocardiogr*. 2015;28:1–39.e14.
- Pencina MJ, D’Agostino RB Sr, D’Agostino RB Jr, Vasan RS. Evaluating the added predictive ability of a new marker: from area under the ROC curve to reclassification and beyond. *Stat Med*. 2008;27:157–172.
- Dispenzieri A, Gertz MA, Kyle RA, et al. Serum cardiac troponins and N-terminal pro-brain natriuretic peptide: a staging system for primary systemic amyloidosis. *J Clin Oncol*. 2004;22:3751–3757.
- Klunk WE, Engler H, Nordberg A, et al. Imaging brain amyloid in Alzheimer’s disease with Pittsburgh compound-B. *Ann Neurol*. 2004;55:306–319.
- Engler H, Blomqvist G, Bergstrom M, et al. First human study with a benzothiazole amyloid-imaging agent in Alzheimer’s disease and control subjects [abstract]. *Neurobiol Aging*. 2002;23(suppl 1):S429.
- Luciani M, Troncone L, Monte FD. Current and future circulating biomarkers for cardiac amyloidosis. *Acta Pharmacol Sin*. 2018;39:1133–1141.
- Minamimoto R, Awaya T, Iwama K, et al. Significance of ¹¹C-PiB PET/CT in cardiac amyloidosis compared with ^{99m}Tc-aprotinin scintigraphy: a pilot study. *J Nucl Cardiol*. 2020;27:202–209.
- Sperry BW, Ikram A, Hachamovitch R, et al. Efficacy of chemotherapy for light-chain amyloidosis in patients presenting with symptomatic heart failure. *J Am Coll Cardiol*. 2016;67:2941–2948.
- Gertz MA. Immunoglobulin light chain amyloidosis: 2020 update on diagnosis, prognosis, and treatment. *Am J Hematol*. 2020;95:848–860.
- Rosengren S, Skibsted Clemmensen T, Tolbod L, et al. Diagnostic accuracy of [¹¹C]PiB positron emission tomography for detection of cardiac amyloidosis. *JACC Cardiovasc Imaging*. 2020;13:1337–1347.

Lung Scintigraphy for Pulmonary Embolism Diagnosis in COVID-19 Patients: A Multicenter Study

Pierre-Yves Le Roux¹, Pierre-Benoit Bonnefoy², Achraf Bahloul³, Benoit Denizot⁴, Bertrand Barres⁵, Caroline Moreau-Triby⁶, Astrid Girma⁷, Amandine Pallardy⁸, Quentin Ceyrat⁹, Laure Sarda-Mantel¹⁰, Micheline Razzouk-Cadet¹¹, Reka Zsigmond¹², Cachin Florent⁵, Gilles Karcher³, and Pierre-Yves Salaun¹

¹Service de Médecine Nucléaire, Université Européenne de Bretagne, Université de Brest, EA3878 (GETBO) IFR 148, CHRU de Brest, Brest, France; ²Service de Médecine Nucléaire, CHU de Saint-Etienne, Saint-Etienne, France; ³Service de Médecine Nucléaire, CHRU Nancy, Nancy, France; ⁴Service de Médecine Nucléaire, Centre Hospitalier Alpes Léman, Contamine sur Arve, France; ⁵Service de Médecine Nucléaire, Centre Jean Perrin, Clermont Ferrand, France; ⁶Service de Médecine Nucléaire, Groupe Hospitalier de l'Est, Bron, France; ⁷Service de Médecine Nucléaire, Hôpital Foch, Suresne, France; ⁸Service de Médecine Nucléaire, CHU de Nantes, Nantes, France; ⁹Centre d'Imagerie Fonctionnelle, Bordeaux, France; ¹⁰Service de Médecine Nucléaire, Hôpital Lariboisière, APHP, Paris, France; ¹¹Service de Médecine Nucléaire, CHU Nice, Nice, France; and ¹²Centre d'Imagerie Nucléaire, Annecy, France

In patients with novel coronavirus disease 2019 (COVID-19) referred for lung scintigraphy because of suspected pulmonary embolism (PE), there has been an ongoing debate within the nuclear medicine community as to whether and when the ventilation imaging should be performed. Indeed, whereas PE diagnosis typically relies on the recognition of ventilation-perfusion (V/P) mismatched defects, the ventilation procedure potentially increases the risk of contamination to health-care workers. The primary aim of this study was to assess the role of ventilation imaging when lung scintigraphy is performed because of suspected PE in COVID-19 patients. The secondary aim was to describe practices and imaging findings in this specific population. **Methods:** A national registry was created in collaboration with the French Society of Nuclear Medicine to collect lung scans performed on COVID-19 patients for suspected PE. The practices of departments were assessed regarding imaging protocols and aerosol precautions. A retrospective review of V/P SPECT/CT scans was then conducted. Two physicians masked to clinical information reviewed each case by sequentially viewing perfusion SPECT, perfusion SPECT/CT, and V/P SPECT/CT images. The scans were classified into 1 of the 4 following categories: patients for whom PE could reasonably be excluded on the basis of perfusion SPECT only, perfusion SPECT/CT, or V/P SPECT/CT and patients with mismatched defects suggestive of PE according to the European Association of Nuclear Medicine criteria. **Results:** Data from 12 French nuclear medicine departments were collected. Lung scans were performed between March 2020 and April 2021. Personal protective equipment and dedicated cleaning procedures were used in all departments. Of the 145 V/Q SPECT/CT scans included in the central review, PE could be excluded using only perfusion SPECT, perfusion SPECT/CT, or V/P SPECT/CT in 27 (19%), 55 (38%), and 45 (31%) patients, respectively. V/P SPECT/CT was positive for PE in 18 (12%) patients, including 12 (67%) with a low burden of PE ($\leq 10\%$). **Conclusion:** In this population of COVID-19 patients assessed with lung scintigraphy, PE could confidently be excluded without the ventilation imaging in only 57% of

patients. Ventilation imaging was required to confidently rule out PE in 31% of patients. Overall, the prevalence of PE was low (12%).

Key Words: pulmonary embolism; ventilation perfusion scintigraphy; SPECT; COVID-19

J Nucl Med 2022; 63:1070–1074

DOI: 10.2967/jnumed.121.262955

A frequent complication of novel coronavirus disease 2019 (COVID-19) is coagulopathy, which manifests in the form of both microthrombosis and venous thromboembolism (1). Lung ventilation-perfusion (V/P) scintigraphy is a well-established test for diagnosis of pulmonary embolism (PE) (2). Diagnostic strategies based on lung scintigraphy have been widely validated in large studies on diagnostic accuracy (3) and management outcome (4–7), in which interpretation of the lung scan was based on recognition of wedge-shaped perfusion mismatched defects, that is, perfusion defects with normal ventilation.

However, the ventilation procedure increases the potential risk of contamination by the aerosol secretion and the expired air to health-care workers and to other patients (8,9). As a result, a variety of strategies has been proposed in the nuclear medicine literature regarding performing lung scintigraphy on COVID-19 patients with suspected acute PE (10). Some have proposed omitting the ventilation scan and performing only perfusion scintigraphy or perfusion SPECT/CT (11–14), arguing that this approach allows sufficient diagnostic performance while reducing the risk of contamination. Others have recommended systematically maintaining the standard V/P procedure, with appropriate aerosol precautions for health-care workers (15–17). The rationale for this approach is that a wide proportion of patients with confirmed COVID-19 infection and symptoms suggestive of acute PE will have abnormal findings on the perfusion scan and that not performing a ventilation scan is associated with an unacceptably high risk of false-positive results. Finally, some have proposed an intermediate approach with a standalone perfusion planar or SPECT/CT scan, followed, only when necessary, by a ventilation scan (18,19). However, although various conflicting opinions and recommendations have been published on performing

Received Jul. 27, 2021; revision accepted Sep. 29, 2021.

For correspondence or reprints, contact Pierre-Yves Le Roux (pierre-yves.leroux@chu-brest.fr).

Published online Oct. 14, 2021.

Immediate Open Access: Creative Commons Attribution 4.0 International License (CC BY) allows users to share and adapt with attribution, excluding materials credited to previous publications. License: <https://creativecommons.org/licenses/by/4.0/>. Details: <http://jnm.snmjournals.org/site/misc/permission.xhtml>.

COPYRIGHT © 2022 by the Society of Nuclear Medicine and Molecular Imaging.

lung scintigraphy on COVID-19 patients, there are currently no factual data on this specific population to support recommendations to the nuclear medicine community.

The primary aim of this study was to assess the role of ventilation imaging when performing lung scintigraphy for suspected PE in COVID-19 patients. The secondary aim was to describe practices and imaging findings in this specific population.

MATERIALS AND METHODS

Collection of Data

A national registry was created at the initiative of the French Society of Nuclear Medicine working group on lung scintigraphy to collect lung scans performed on COVID-19 patients for suspected PE. In collaboration with the French Society of Nuclear Medicine, the information was circulated to its memberships via 3 sets of e-mails in April, June, and December 2020. Physicians who had notified the investigators that they had cases of COVID-19 were then contacted to participate in the study. The protocol was approved by the nuclear medicine research ethics committee (CEMEN [Comité d'Ethique pour la Médecine Nucléaire] 2021-01). Informed consent was obtained from all participants.

Evaluation of Practices

The general practices of nuclear medicine facilities were assessed using a standardized questionnaire. The questionnaire encompassed aerosol precautions for the health-care workers (type of mask, goggles, gloves, long cap, gown), cleaning procedures, organizational adaptations in the nuclear medicine facility, and imaging protocols for the performance of lung scintigraphy on patients with confirmed COVID-19 and suspected acute PE. Nuclear medicine facilities were also questioned about any possible contamination of a health-care worker after managing a patient with COVID-19 disease.

Individual data from patients with confirmed COVID-19 who underwent lung scintigraphy for suspected acute PE were then collected. These patients include those who underwent various acquisition protocols, including planar scintigraphy (with or without ventilation), perfusion SPECT/CT (without ventilation), or V/P SPECT/CT scans. Only patients still considered contagious were analyzed, that is, patients for whom the lung scan was typically performed within 14 d after initiation of symptoms. For each patient, demographic information and lung scan images were collected.

V/P SPECT/CT Central Review

To assess the role of ventilation imaging in COVID-19 patients with suspected PE, a centralized retrospective review of scans with a complete V/P SPECT/CT protocol was then conducted. Scans of patients who underwent a planar or a perfusion SPECT/CT protocol (without ventilation) were not included in this retrospective review. A consensus reading of images was performed by 2 board-certified nuclear medicine physicians masked to clinical information. Each case was reviewed by sequentially using perfusion SPECT, perfusion SPECT/CT, and V/P SPECT/CT images. First, only perfusion SPECT images were used. Scans with normal perfusion were classified as negative for PE. Second, in patients with an abnormal result on perfusion SPECT, CT images were added. Scans whose perfusion defects were matched with CT findings were classified as negative for PE. Finally, in patients with mismatched perfusion SPECT/CT defects, ventilation SPECT images were added for interpretation. V/P SPECT/CT scans were then interpreted as negative or positive for PE according to the presence of V/P mismatched defects suggestive of acute PE according to the European Association of Nuclear Medicine criteria (20,21). Accordingly, scans were classified into 1 of the 4 following categories: patients for whom PE could reasonably be excluded on the basis of

perfusion SPECT only, perfusion SPECT/CT, or V/P SPECT/CT and patients with mismatched V/P defects suggestive of PE. In patients with a positive V/Q SPECT/CT result, the number of segmental and subsegmental mismatched defects was recorded.

RESULTS

Data from 183 patients with confirmed COVID-19 disease who underwent lung scintigraphy for suspected acute PE between March 2020 and April 2021 in 12 French nuclear medicine departments were collected.

Evaluation of Practices

The practices of the 12 nuclear medicine departments are presented in Table 1. Personal protective equipment and dedicated cleaning and disinfecting procedures were used in all departments. Scans were formed in a dedicated room in 8 (67%) centers and at the end of the day in 10 (83%). Eleven (92%) centers systematically performed a ventilation scan before the perfusion acquisition. V/P SPECT/CT was the first-line imaging procedure in 8 (75%) centers. Of the 12 nuclear medicine facilities, there was no reported case of possible contamination of a health-care worker after managing a COVID-19 patient.

Of the 183 patients, 117 (64%) were female. The median age was 74 y (range, 15–102 y). Sixty-eight (37%) were older than 80 y, and 26 (14%) were older than 90 y. A ventilation scan was performed on 168 patients (92%), using Technegas (Cyclomedica Australia Pty.

TABLE 1
Practices of Nuclear Medicine Facilities

Practice	Centers (n)
Aerosol precautions	12 (100%)
Mask	12 (100%)
Filtering facepiece 1	1 (8%)
Filtering facepiece 2	11 (92%)
Goggles	12 (100%)
Long cap	12 (100%)
Gloves	12 (100%)
Gown	12 (100%)
Specific COVID-19 cleaning and disinfecting procedures	12 (100%)
Organizational adaptation in nuclear medicine facility	
Camera or room dedicated to COVID-19 patients	8 (67%)
Scans performed at end of day	10 (83%)
Dedicated circuit within nuclear medicine department	3 (25%)
Standard lung scan protocol for COVID-19 patients	
Systematic ventilation scan	11 (92%)
Technegas	8 (73%)
^{81m} Kr gas	3 (27%)
First-line imaging	
Planar	3 (25%)
SPECT	0 (0%)
SPECT/CT	9 (75%)

Ltd.) aerosol in 144 (86%) and ^{81m}Kr gas in 24 (14%). Twenty-four (13%) had only a planar scan, and 159 (87%) had a SPECT/CT scan.

V/Q SPECT/CT Interpretation

In total, 145 complete V/P SPECT/CT scans were centrally reviewed. Of them, PE could be excluded using only perfusion SPECT, perfusion SPECT/CT, or V/P SPECT/CT in 27 (19%), 55 (38%), and 45 (31%) patients, respectively (Fig. 1). Examples of negative perfusion SPECT/CT findings for which perfusion defects matched chest CT findings of COVID-19 disease are shown in Figure 2. Examples of false-positive results using the perfusion SPECT/CT approach are presented in Figure 3. V/P SPECT/CT imaging was positive for PE in 18 (12%) patients. The burden of PE was 10% or less in 12 (67%) patients, more than 10% but no more than 20% in 4 (22%) patients, and more than 20% in 2 (11%) patients. Examples of positive V/P SPECT/CT scans are shown in Figure 4.

DISCUSSION

In this population of COVID-19 patients assessed with lung scintigraphy, PE could confidently be excluded without ventilation in 57% of patients. In contrast, ventilation imaging was required in the remaining 43% to confidently rule out (31%) or confirm (12%) the PE diagnosis.

Interpretation of lung scans for PE typically relies on recognition of V/P mismatched defects (22). The sensitivity of the test—that is, the ability to detect PE—relies on recognition of defects on perfusion images. Normal findings on a perfusion scan have been shown to safely rule out a PE diagnosis (4–7). However, there are many nonthromboembolic lung diseases that may cause perfusion defects. To increase the specificity—that is, the ability of the test to detect whether a patient is free of disease—perfusion scintigraphy has to be compared with ventilation images to differentiate V/P mismatched defects highly suggestive of acute PE from V/P matched defects of other etiologies. With the advent of SPECT/CT cameras has come a proposal to coregister SPECT data with a low-dose CT scan to further increase the specificity of the test. Some groups have proposed replacing the ventilation SPECT.

In our series, only 19% of COVID-19 patients had strictly normal results on the perfusion SPECT scan. In this specific population of COVID-19 patients with suspected acute PE, there is therefore a high

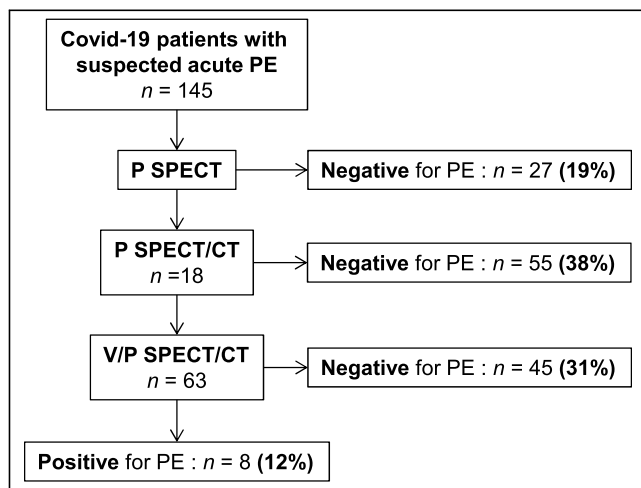


FIGURE 1. Results of central review. P = perfusion.

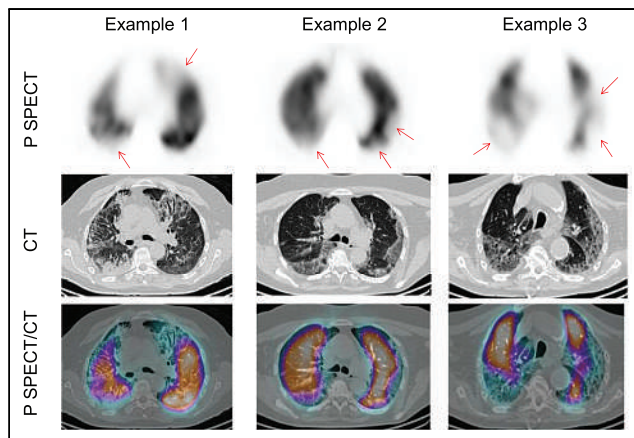


FIGURE 2. Examples of negative perfusion SPECT/CT results, with perfusion defects (arrows) matched with chest CT findings of COVID-19 disease. P = perfusion.

likelihood (nearly 4 in 5 chance) that an approach consisting of performing only a perfusion lung scan, without CT images, will be nondiagnostic. When perfusion SPECT images were coregistered with a low-dose CT scan, 38% more scans became diagnostic, as all perfusion defects could confidently be explained by non-PE morphologic findings. Overall, perfusion SPECT/CT imaging would have allowed confident exclusion of PE in 57% of COVID-19 patients, without exposing the health-care workers to an increased risk of contamination due to the ventilation procedure. Nevertheless, the benefit of omitting the ventilation procedure should be balanced against the risk of increasing the number of patient transfers through health-care facilities and increasing the amount of contact between individuals.

In the remaining 43% of patients, a ventilation scan was required to exclude (31%) or confirm (12%) the diagnosis of PE. Most patients with a positive scan result did not have a massive PE with multiple wedge-shaped perfusion defects highly suggestive of PE irrespective of the ventilation scan. On the contrary, the ventilation

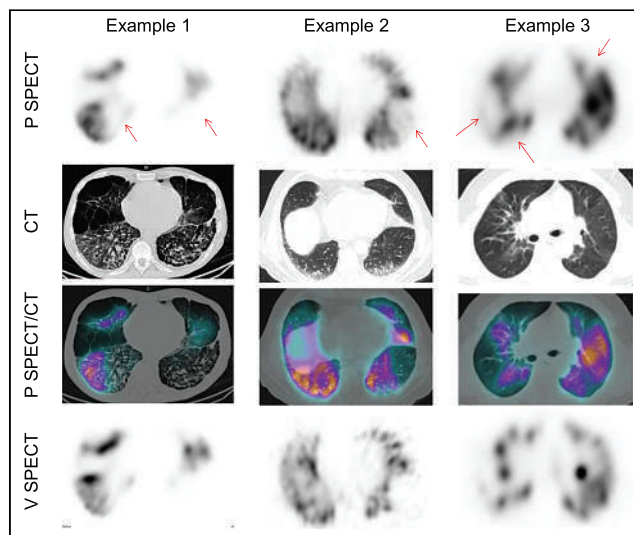


FIGURE 3. Examples of false-positive perfusion SPECT/CT results. Perfusion SPECT images showed perfusion defects (arrows), without significant abnormality on CT images. Perfusion SPECT/CT scans would therefore have been read as positive for PE. However, ventilation SPECT demonstrated matched defects. V/Q SPECT/CT scans were therefore interpreted as negative for PE. P = perfusion; V = ventilation.

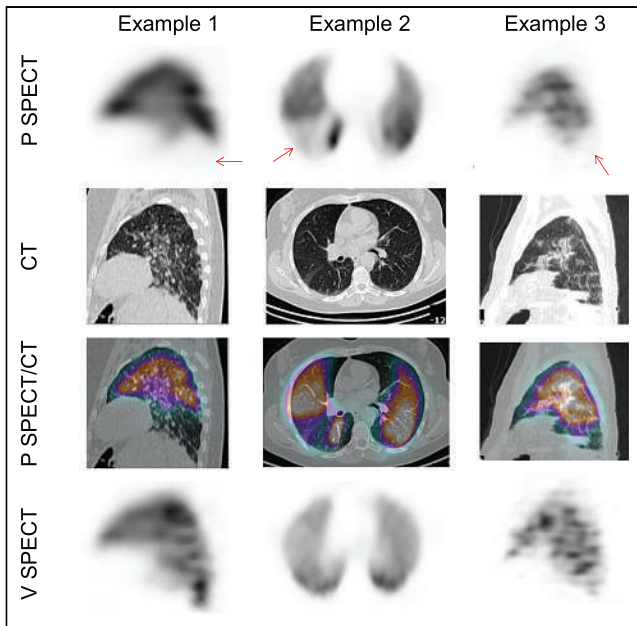


FIGURE 4. Examples of positive V/P SPECT/CT results. Perfusion SPECT images showed perfusion defects (arrows), whereas coregistered ventilation SPECT images showed normal ventilation (mismatched V/P defects). P = perfusion; V = ventilation.

study was helpful in most positive scans, which demonstrated only 1 or 2 segmental perfusion mismatched defects.

Our data confirm the high risk of a false-positive result when omitting the ventilation scan. In a retrospective series of 393 patients assessed by V/P SPECT imaging for suspected PE, 15% of patients with a negative V/P SPECT result would have been wrongly diagnosed with PE using a perfusion SPECT/CT approach (23). In another series of 81 patients, the specificity decreased from 100% with V/P SPECT/CT to 51% with perfusion SPECT/CT (24). Similarly, in a study of 93 patients, 17% of V/Q SPECT scans with negative results were falsely positive when compared with perfusion SPECT/CT (25). The risk of false-positive results was even higher in our population of COVID-19 patients, probably because most patients had COVID-19 parenchymal lung disease and thus abnormal lung perfusion. Also noteworthy is the age of the population, with a median of 74 y, and with 37% of patients older than 80 y, increasing the likelihood of abnormal perfusion from any lung disease.

A false-positive diagnostic test may have major consequences for patients with suspected acute PE. Indeed, current clinical guidelines suggest extended anticoagulation in patients with no identifiable risk factor or with a minor transient or reversible risk factor for the index PE event (2). Accordingly, a false-positive lung scintigraphy result will mean lifelong anticoagulant therapy and its risks of bleeding for many patients (15).

Surprisingly, the prevalence of positive scans was low (12%) in this population of COVID-19 patients with suspected PE assessed with V/Q SPECT/CT imaging. This prevalence is much lower than that of PE across studies on V/Q SPECT in non-COVID-19 patients—a prevalence that ranges from 17% to 54% (median, 26%) (26). This prevalence is also low as compared with studies assessing other imaging tests for PE (e.g., CT pulmonary angiography or planar V/P scanning). In a metaanalysis performed before the COVID-19 pandemic including 29,684 patients from 49 studies, the pooled prevalence of PE was 22.6% (27). As it is now

well established that COVID-19 predisposes patients to thrombotic events (28), this prevalence probably means that there is more suspected PE in COVID-19 patients than in non-COVID-19 patients, likely resulting from the combination of poorly explained respiratory symptoms in patients at risk for venous thromboembolism. Furthermore, in patients positive for PE, the burden of disease was low, with only 11% of patients having a PE burden of more than 20%. It is likely that most patients admitted to intensive care units or with signs of hemodynamic instability were referred for CT pulmonary angiography rather than for lung scintigraphy (29).

An assessment of general practices showed a major trend among the 12 French institutions. The typical examination was a V/P SPECT/CT acquisition as commonly performed on non-COVID-19 patients (30), with personal protective equipment for the health-care workers and dedicated cleaning procedures. Most institutions obtained acquisitions on a dedicated camera at the end of the day. No case of possible contamination of a health-care worker after managing a COVID-19 patient was reported, although this finding should be interpreted with caution.

Our study had some limitations. First, the results of the central review were not compared with an independent reference standard, and patient follow-up data were not collected. Accordingly, we cannot assert that all patients with a negative scan result did not have PE and that all patients with a positive scan result did have PE. Despite these limitations resulting from the retrospective design of this multicenter study based on a national registry, this was, to our knowledge, the first large series that assessed the usefulness of the ventilation scan in COVID-19 patients. Major trends have emerged with regard to the prevalence of PE and the proportion of inconclusive results with the various lung scan protocols. These results may assist nuclear physicians in the performance of lung scintigraphy on COVID-19 patients with suspected acute PE, according to their own local situation. Second, assessment of general practices probably does not reflect the reality in nuclear medicine facilities around the world. Indeed, the French Society of Nuclear Medicine working group on lung scintigraphy recommended that ventilation scans be performed on COVID-19 patients—a recommendation that is likely to have influenced practices in France. Furthermore, institutions that followed these recommendations may have been more inclined to participate in the study. However, our results show that the usual V/P SPECT/CT approach can be used in daily practice on COVID-19 patients. In our series, there was no reported case of possible contamination of a health-care worker after managing a COVID-19 patient. However, this finding was just observational, and we did not perform formal testing such as swabbing for virus. Accordingly, we cannot draw any conclusions on the risk of contamination. Third, according to the European Association of Nuclear Medicine guidelines for lung scintigraphy (20) or the French Society of Nuclear Medicine guidelines for lung scintigraphy protocols (31), the CT was performed as a low-dose scan during continuous shallow breathing. Accordingly, the CT scans do not fulfill the criteria for diagnostic quality. Optimization of acquisition and reconstruction parameters could enhance the diagnostic performance of the CT scans. Finally, we performed a consensual interpretation of scans and did not assess interobserver agreement.

CONCLUSION

In 57% of COVID-19 patients assessed with lung scintigraphy, PE could be confidently excluded without a ventilation study. This approach allows us to limit the risk of contamination to

health-care workers but should be balanced against the risk of increasing transfers of the remaining 43% of patients through health-care facilities. Indeed, our study clearly confirmed the high risk of false-positive results when omitting the ventilation study, a risk that appears unacceptable given the risk of bleeding and the trend toward an indefinite duration of anticoagulation in many patients. Strategies should be adapted to each local situation, but providing the best imaging test available should remain the priority. Ruling out PE without the use of a ventilation scan is likely safe. However, confirming PE requires a ventilation scan. Otherwise, the referring physician should be advised of the risk of a false-positive result.

DISCLOSURE

No potential conflict of interest relevant to this article was reported.

ACKNOWLEDGMENTS

We acknowledge the French Society of Nuclear Medicine for its collaboration. We also acknowledge Doxaca, and especially Sylver Imhoff, for their assistance in managing the central review.

KEY POINTS

QUESTION: In COVID-19 patients assessed with lung scintigraphy for suspected acute PE, what is the role of the ventilation scan?

PERTINENT FINDINGS: In a retrospective review of 145 V/P SPECT/CT scans of COVID-19 patients referred for suspected acute PE, PE could confidently be excluded without the ventilation study in only 57% of patients. In contrast, the ventilation study was required to confidently rule out PE in 31% of patients, confirming the high risk of false-positive results when omitting the ventilation study.

IMPLICATIONS FOR PATIENT CARE: In COVID-19 patients, confirming a diagnosis of PE with lung scintigraphy requires a ventilation scan.

REFERENCES

- Moores LK, Tritschler T, Brosnahan S, et al. Prevention, diagnosis, and treatment of VTE in patients with coronavirus disease 2019: CHEST guideline and expert panel report. *Chest*. 2020;158:1143–1163.
- Konstantinides SV, Meyer G, Becattini C, et al; ESC Scientific Document Group. 2019 ESC guidelines for the diagnosis and management of acute pulmonary embolism developed in collaboration with the European Respiratory Society (ERS). *Eur Heart J*. 2020;41:543–603.
- PIOPED Investigators. Value of the ventilation/perfusion scan in acute pulmonary embolism: results of the prospective investigation of pulmonary embolism diagnosis (PIOPED). *JAMA*. 1990;263:2753–2759.
- Perrier A, Desmarais S, Miron MJ, et al. Non-invasive diagnosis of venous thromboembolism in outpatients. *Lancet*. 1999;353:190–195.
- Wells PS, Ginsberg JS, Anderson DR, et al. Use of a clinical model for safe management of patients with suspected pulmonary embolism. *Ann Intern Med*. 1998;129:997–1005.
- Anderson DR, Kahn SR, Rodger MA, et al. Computed tomographic pulmonary angiography vs ventilation-perfusion lung scanning in patients with suspected pulmonary embolism: a randomized controlled trial. *JAMA*. 2007;298:2743–2753.
- Salaun PY, Couturaud F, Le Duc-Pennec A, et al. Noninvasive diagnosis of pulmonary embolism. *Chest*. 2011;139:1294–1298.
- Williams DA, Carlson C, McEnerney K, et al. Technetium-99m DTPA aerosol contamination in lung ventilation studies. *J Nucl Med Technol*. 1998;26:43–44.
- Brudecki K, Borkowska E, Gorzkiewicz K, et al. ^{99m}Tc activity concentrations in room air and resulting internal contamination of medical personnel during ventilation-perfusion lung scans. *Radiat Environ Biophys*. 2019;58:469–475.
- Zuckier LS. To everything there is a season: taxonomy of approaches to the performance of lung scintigraphy in the era of COVID-19. *Eur J Nucl Med Mol Imaging*. 2021;48:666–669.
- Lu Y, Macapinlac HA. Perfusion SPECT/CT to diagnose pulmonary embolism during COVID-19 pandemic. *Eur J Nucl Med Mol Imaging*. 2020;47:2064–2065.
- Tulchinsky M, Osmany S. The American College of Nuclear Medicine guidance on operating procedures for a nuclear medicine facility during COVID-19 pandemic. *Clin Nucl Med*. 2021;46:571–574.
- Burger IA, Niemann T, Patriki D, et al. Is there a role for lung perfusion [^{99m}Tc]-MAA SPECT/CT to rule out pulmonary embolism in COVID-19 patients with contraindications for iodine contrast? *Eur J Nucl Med Mol Imaging*. 2020;47:2062–2063.
- Das JP, Yeh R, Schoder H. Clinical utility of perfusion (Q)-single-photon emission computed tomography (SPECT)/CT for diagnosing pulmonary embolus (PE) in COVID-19 patients with a moderate to high pre-test probability of PE. *Eur J Nucl Med Mol Imaging*. 2021;48:794–799.
- Le Roux PY, Le Gal G, Salaun PY. Lung scintigraphy for pulmonary embolism diagnosis during the COVID-19 pandemic: does the benefit-risk ratio really justify omitting the ventilation study? *Eur J Nucl Med Mol Imaging*. 2020;47:2499–2500.
- Recommendations for Performing V/Q Scans in the Context of COVID19*. Belgian Society of Nuclear Medicine; 2020:1–2.
- Le Roux PY. Recommendations for Performing Lung Scintigraphy in the Context of an Epidemic Due to the COVID-19 Virus [in French]. French Society of Nuclear Medicine and Molecular Imaging. 2020:1–2.
- Zuckier LS, Moadel RM, Haramati LB, et al. Diagnostic evaluation of pulmonary embolism during the COVID-19 pandemic. *J Nucl Med*. 2020;61:630–631.
- Schaefer WM, Knollmann D, Meyer PT. V/Q SPECT/CT in the time of COVID-19: changing the order to improve safety without sacrificing accuracy. *J Nucl Med*. 2021;62:1022–1024.
- Bajc M, Schumichen C, Gruning T, et al. EANM guideline for ventilation/perfusion single-photon emission computed tomography (SPECT) for diagnosis of pulmonary embolism and beyond. *Eur J Nucl Med Mol Imaging*. 2019;46:2429–2451.
- Le Roux PY, Robin P, Delluc A, et al. V/Q SPECT interpretation for pulmonary embolism diagnosis: which criteria to use? *J Nucl Med*. 2013;54:1077–1081.
- Le Roux PY, Robin P, Salaun PY. New developments and future challenges of nuclear medicine and molecular imaging for pulmonary embolism. *Thromb Res*. 2018;163:236–241.
- Le Roux PY, Robin P, Delluc A, et al. Additional value of combining low-dose computed tomography to V/Q SPECT on a hybrid SPECT-CT camera for pulmonary embolism diagnosis. *Nucl Med Commun*. 2015;36:922–930.
- Gutte H, Mortensen J, Jensen CV, et al. Detection of pulmonary embolism with combined ventilation-perfusion SPECT and low-dose CT: head-to-head comparison with multidetector CT angiography. *J Nucl Med*. 2009;50:1987–1992.
- Palmowski K, Oltmanns U, Kreuter M, et al. Diagnosis of pulmonary embolism: conventional ventilation/perfusion SPECT is superior to the combination of perfusion SPECT and nonenhanced CT. *Respiration*. 2014;88:291–297.
- Le Roux PY, Robin P, Tromeur C, et al. Ventilation/perfusion SPECT for the diagnosis of pulmonary embolism: a systematic review. *J Thromb Haemost*. 2020;18:2910–2920.
- Dronkers CEA, van der Hulle T, Le Gal G, et al. Towards a tailored diagnostic standard for future diagnostic studies in pulmonary embolism: communication from the SSC of the ISTH. *J Thromb Haemost*. 2017;15:1040–1043.
- Schulman S, Hu Y, Konstantinides S. Venous THROMBOEMBOLISM in COVID-19. *Thromb Haemost*. 2020;120:1642–1653.
- Bompard F, Monnier H, Saab I, et al. Pulmonary embolism in patients with COVID-19 pneumonia. *Eur Respir J*. 2020;56:2001365.
- Le Roux PY, Pelletier-Galameau M, De Laroche R, et al. Pulmonary scintigraphy for the diagnosis of acute pulmonary embolism: a survey of current practices in Australia, Canada, and France. *J Nucl Med*. 2015;56:1212–1217.
- Le Roux PY, Blanc-Béguin F, Bonnefoy PB, et al. Guide for writing protocols for lung scintigraphy [in French]. *Médecine Nucléaire*. 2021;45:85–92.

Lung Dose Measured on Postradioembolization ^{90}Y PET/CT and Incidence of Radiation Pneumonitis

Martina Stella, Rob van Rooij, Marnix G.E.H. Lam, Hugo W.A.M. de Jong, and Arthur J.A.T. Braat

Division of Imaging and Oncology, University Medical Center Utrecht, Utrecht University, Utrecht, The Netherlands

Radiation pneumonitis is a rare but possibly fatal side effect of ^{90}Y radioembolization. It may occur 1–6 mo after therapy, if a significant part of the ^{90}Y microspheres shunts to the lungs. In current clinical practice, a predicted lung dose greater than 30 Gy is considered a criterion to exclude patients from treatment. However, contrasting findings regarding the occurrence of radiation pneumonitis and lung dose were previously reported in the literature. In this study, the relationship between the lung dose and the eventual occurrence of radiation pneumonitis after ^{90}Y radioembolization was investigated. **Methods:** We retrospectively analyzed 317 ^{90}Y liver radioembolization procedures performed during an 8-y period (February 2012 to September 2020). We calculated the predicted lung mean dose (LMD) using $^{99\text{m}}\text{Tc}$ -MAA planar scintigraphy (LMD_{MAA}) acquired during the planning phase and left LMD ($\text{LMD}_{\text{Y-90}}$) using the ^{90}Y PET/CT acquired after the treatment. For the lung dose computation, we used the left lung as the representative lung volume, to compensate for scatter from the liver moving in the craniocaudal direction because of breathing and mainly affecting the right lung. **Results:** In total, 272 patients underwent ^{90}Y procedures, of which 63% were performed with glass microspheres and 37% with resin microspheres. The median injected activity was 1,974 MBq (range, 242–9,538 MBq). The median LMD_{MAA} was 3.5 Gy (range, 0.2–89.0 Gy). For 14 procedures, LMD_{MAA} was more than 30 Gy. Median $\text{LMD}_{\text{Y-90}}$ was 1 Gy (range, 0.0–22.1 Gy). No patients had an $\text{LMD}_{\text{Y-90}}$ of more than 30 Gy. Of the 3 patients with an $\text{LMD}_{\text{Y-90}}$ of more than 12 Gy, 2 patients (one with an $\text{LMD}_{\text{Y-90}}$ of 22.1 Gy and an LMD_{MAA} of 89 Gy; the other with an $\text{LMD}_{\text{Y-90}}$ of 17.7 Gy and an LMD_{MAA} of 34.1 Gy) developed radiation pneumonitis and consequently died. The third patient, with an $\text{LMD}_{\text{Y-90}}$ of 18.4 Gy (LMD_{MAA} , 29.1 Gy), died 2 mo after treatment, before the imaging evaluation, because of progressive disease. **Conclusion:** The occurrence of radiation pneumonitis as a consequence of a lung shunt after ^{90}Y radioembolization is rare (<1%). No radiation pneumonitis developed in patients with a measured $\text{LMD}_{\text{Y-90}}$ lower than 12 Gy.

Key Words: ^{90}Y radioembolization; lung-dose; radiation pneumonitis; ^{90}Y PET dosimetry; $^{99\text{m}}\text{Tc}$ -MAA lung dose predicted

J Nucl Med 2022; 63:1075–1080

DOI: 10.2967/jnumed.121.263143

Radioembolization is a well-established treatment for primary and metastatic liver malignancies (1). It is defined as percutaneous, transarterial injection (2) of embolic particles (diameter, 20–60 μm) loaded with ^{90}Y or ^{166}Ho . Because hepatic tumors are

preferentially fed by the blood supply from the hepatic artery, radioembolization preferentially deposits radioactive microspheres in the peritumoral and intratumoral arterial vasculature through the hepatic artery, relatively sparing normal liver parenchyma (3). Three devices are commercially available: glass ^{90}Y microspheres (TheraSphere; Boston Scientific Corp.), resin ^{90}Y microspheres (SIR-spheres; SIRTech Medical Limited), and poly-L-lactic acid ^{166}Ho microspheres (QuiremSpheres; Quirem BV). If a significant number of microspheres pass through tumor-associated arteriovenous shunts and lodge in the pulmonary vasculature, a dose-dependent radiation-induced pneumonitis may ensue. Therefore, the presence of significant hepatopulmonary shunting is a relative contraindication for radioembolization. The current approach to radioembolization with respect to radiation pneumonitis is driven mainly by 2 seminal publications (4,5) that have strongly influenced the guidance on lung dose limits after radioembolization. On the basis of clinical evidence from these studies, a lung dose limit of 30 Gy was recommended for a single radioembolization treatment (6) and adopted in the instruction manuals for these devices. For this reason, assessment of the lung shunt fraction (LSF), which is a prediction of the eventual lung mean dose (LMD) after the radioembolization treatment, is paramount before administration of the radioactive particles.

For ^{90}Y , this prediction is performed using $^{99\text{m}}\text{Tc}$ -macroaggregated albumin (MAA). Despite being the current clinical practice, $^{99\text{m}}\text{Tc}$ -MAA planar scintigraphy is poor in predicting the dose to the lungs, especially when computing the LSF (LSF_{MAA}) and, consequently, the predicted lung mean dose (LMD_{MAA}). SPECT/CT imaging can improve the LSF computation (7). However, discrepancies between ^{90}Y and $^{99\text{m}}\text{Tc}$ -MAA particles reduce the predictive value (8,9).

The aim of this study was to assess the occurrence of radiation pneumonitis after ^{90}Y liver radioembolization and perform lung dosimetry on ^{90}Y PET/CT to evaluate the currently assumed lung dose restriction of less than 30 Gy. Although multiple studies on lung dose after ^{90}Y radioembolization have been reported, they all focus on the $^{99\text{m}}\text{Tc}$ -MAA-based lung dose estimate during the pretreatment phase. Conversely, this study retrospectively quantified the actual dose received by the lungs after ^{90}Y radioembolization, exploiting the potential of posttreatment PET/CT (10) and accurate ^{90}Y dosimetry (11). Knowledge of the actual dose would provide a better insight into the lung dose after ^{90}Y radioembolization and the related occurrence of radiation pneumonitis.

MATERIALS AND METHODS

This single-center, retrospective analysis of all patients treated with ^{90}Y radioembolization between February 2012 and September 2020 was approved by the ethical research committee, and the need for

Received Sep. 1, 2021; revision accepted Oct. 26, 2021.

For correspondence or reprints, contact Martina Stella (m.stella@umcutrecht.nl).

Published online Nov. 12, 2021.

COPYRIGHT © 2022 by the Society of Nuclear Medicine and Molecular Imaging.

informed consent was waived. Before radioembolization treatment, patient eligibility for treatment was assessed by a ^{99m}Tc -MAA injection in the hepatic artery, to assess the intrahepatic distribution and potential extrahepatic deposition of activity (including lung shunting). After the injection, planar γ -camera scintigraphy (to compute LSF_{MAA}) and SPECT/CT (to visually assess extrahepatic depositions) were performed. To assess the treatment outcome, posttreatment ^{90}Y PET/CT was performed on the same day as, or the day after, treatment. LMD after ^{90}Y radioembolization was assessed using the posttreatment ^{90}Y PET/CT.

^{90}Y PET/CT Protocol

Images were acquired on a Biograph mCT or Biograph Vision 600 time-of-flight PET/CT scanner (Siemens Medical Solutions), with 40- and 64-slice CT scanners, respectively. The images were reconstructed using an iterative algorithm including model-based scatter correction, which encompasses a point-spread-function model of the detector response together with time-of-flight information. To correct for attenuation, a low-dose CT scan acquired right after the PET scan was used. Both PET scanners and the reconstruction protocol were validated for ^{90}Y quantitative imaging (12).

^{99m}Tc -MAA-Based LMD Predicted

To determine each patient's eligibility, LMD_{MAA} was calculated as follows:

$$\text{LMD}_{\text{MAA}} = \frac{\text{activity}_{\text{prescribed}}(\text{GBq}) \times \text{LSF}_{\text{MAA}} \times 50(\text{Gy} \times \text{kg}/\text{GBq})}{\text{lung mass}(\text{kg})},$$

where lung mass is assumed to be 1 kg and $50[\text{Gy} \times \text{kg}/\text{GBq}]$ is the standard conversion factor for ^{90}Y . LSF_{MAA} was computed as follows:

$$\text{LSF}_{\text{MAA}} = \frac{\text{count}_{\text{lungs}}}{\text{count}_{\text{lungs}} + \text{count}_{\text{liver}}} \times 100\%.$$

The counts were computed using the geometric mean following standard clinical practice (13). Lungs and liver were delineated on the planar scintigrams by the imaging technicians.

^{90}Y PET-Based LMD

To assess the LMD after treatment, lungs masks were automatically segmented on the CT scans corresponding to the PET scans used for dosimetric purposes, applying a freely available U-net that extracts the right and left lungs separately (14). All masks were visually checked to ensure correct segmentation. Since the right lung was affected by scatter from the liver moving in the craniocaudal direction because of breathing (Fig. 1), only the left lung was considered as representative for computation of the LMD. The ^{90}Y PET-based left LMD ($\text{LMD}_{\text{Y-90}}$) was computed as follows:

$$\text{LMD}_{\text{Y-90}} = \frac{\text{mean activity concentration}_{\text{left lung}} \left(\frac{\text{Bq}}{\text{mL}} \right) \times 5 \times 10^{-8}(\text{J} \times \text{s})}{\text{lung density}(\text{kg}/\text{cm}^3)}.$$

The mean activity concentration in the left lung volume of interest (measured in Bq/mL) was computed as the mean of the voxel value (Bq/mL) within the left lung mask. Lung density was assumed to be $2.6 \times 10^{-4}(\text{kg}/\text{mm}^3)$ (15), whereas $5 \times 10^{-8}(\text{J} \times \text{s})$ represents the deposited energy due to β -decay of 1 Bq of injected ^{90}Y activity (16). The mean activity concentration was corrected for ^{90}Y decay considering the time difference between the activity administration and the scanning. Three commonly applied assumptions were adapted for this study. First, the maximal range for ^{90}Y β -particles in tissue is 1.2 cm, which is on the same order of magnitude as the resolution of ^{90}Y PET; thus, it is assumed that the total energy is deposited within the voxel

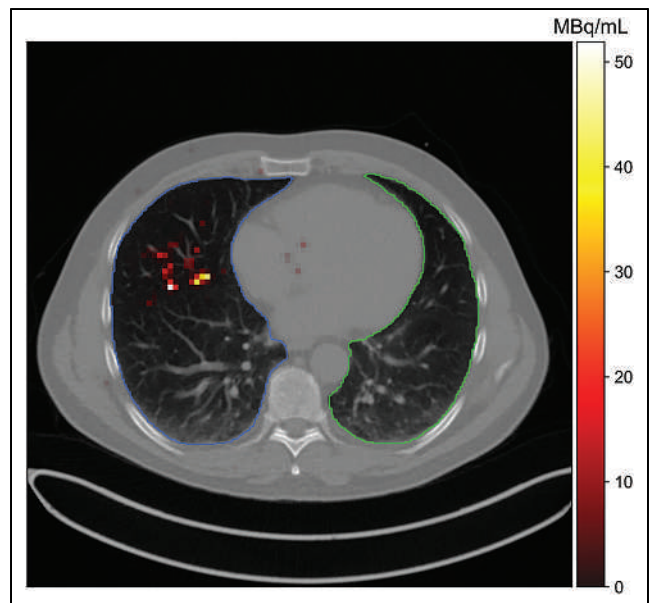


FIGURE 1. Posttreatment ^{90}Y PET/CT scan of 47-year-old man diagnosed with colorectal cancer. LMD considering both lobes was 61 Gy. ^{90}Y PET image shows activity in right lung (blue contour) due to liver motion in craniocaudal direction and rim field-of-view artifact and leading to right LMD of 100 Gy, which was main contributor to LMD. Left LMD (computed within green contour) was 3 Gy.

of origin (17). Second, ^{90}Y distributes uniformly in cases of lung shunting. Third, lung density is the same for all patients.

^{90}Y PET-Based LSF

Because LSF_{MAA} is a poor predictor for actual lung shunting, in this work LSF measured using ^{90}Y PET/CT ($\text{LSF}_{\text{Y-90}}$) was computed as a metric to evaluate differences among tumor type. $\text{LSF}_{\text{Y-90}}$ was defined as the ratio between the activity in the lungs and the total activity administered, as follows:

$$\text{LSF}_{\text{Y-90}} = \frac{\text{mean activity concentration}_{\text{lungs}} \left(\frac{\text{Bq}}{\text{mL}} \right) \times \text{lung volume}(\text{mL})}{\text{activity}_{\text{prescribed}}(\text{Bq})} \times 100\%.$$

As was done for $\text{LMD}_{\text{Y-90}}$, the mean activity concentration in the lungs was computed as the mean of the voxel value (Bq/mL) within both lung masks. Lung volume was assumed to be the same among all subjects, considering a lung mass of 1 kg and a lung density of $2.6 \times 10^{-4}(\text{kg}/\text{mL})$, previously assumed.

Statistical Analysis

The statistical variables under investigation to characterize radiation pneumonitis were LMD_{MAA} and $\text{LMD}_{\text{Y-90}}$. When assessing the eventual difference among tumor types or, in the case of hepatocellular carcinoma (HCC) patients, between the presence and absence of portal hypertension and thrombus, we considered $\text{LSF}_{\text{Y-90}}$ in order to take into account the difference in delivered activity. The normality of distribution was assessed visually and by a Q-Q plot. If variables were not normally distributed, nonparametric tests were used for further analysis.

The Mann-Whitney U test with an α -significance level of 0.05 was used for HCC patients to assess whether the occurrence of thrombus or portal hypertension caused a statistically significant difference in left LMD.

The Kruskal–Wallis H test with an α -significance level of 0.05 was used to determine whether statistical differences existed between different tumor types.

RESULTS

Patient Population

Patients and treatment characteristics are summarized in Table 1. The institutional review board approved this retrospective study and waived the need for informed consent. There were 170 men and 102 women, who underwent a total of 317 ^{90}Y radioembolization procedures (mean number of procedures per patient, 1.17; range, 1–5). Most patients were treated for liver metastases of various origins, whereas 25% had HCC. Glass microspheres were used for 200 treatments, and the remaining 117 procedures were performed with resin microspheres. The median administered activity per procedure was 2,278 MBq (range, 277–9,636 MBq) and 1,877 MBq (range, 516–3,245 MBq) for glass and resin microspheres, respectively. The median volume within the PET field of view was 1,713 mL (392–7,851 mL) and 733 mL (range, 80–3,792 mL) for both lungs and the left lung, respectively.

Data Analysis

The median LMD_{MAA} was 3.5 Gy (range, 0.2–89.0 Gy). For 14 patients, LMD_{MAA} was greater than 30 Gy, above which ^{90}Y radioembolization is contraindicated (18). Nonetheless, after clinical consideration by the treating physicians, these patients did undergo ^{90}Y radioembolization treatment.

The median posttreatment $\text{LMD}_{\text{Y-90}}$ was 1.0 Gy (range, 0.0–22.1 Gy), with 3 cases above 12 Gy. No cases of $\text{LMD}_{\text{Y-90}}$ above 30 Gy were reported.

The median $\text{LSF}_{\text{Y-90}}$ was 4.13% (range, 0.27%–39.02%). Overall, according to the Kruskal–Wallis H test, no statistically significant difference existed among tumor types ($P = 0.1$). However, pairwise comparison among tumor types returned a statistically significant difference between patients with neuroendocrine tumor and patients with colorectal cancer, HCC, or other conditions, with P values of 0.008, 0.010, and 0.022, respectively. Statistically significant P values for $\text{LSF}_{\text{Y-90}}$ from the pairwise comparison among tumor types are reported in Table 2. A box plot depicting the $\text{LSF}_{\text{Y-90}}$ per tumor type is shown in Figure 2.

$\text{LMD}_{\text{Y-90}}$ as a function of LMD_{MAA} is reported in Figure 3. The data suggest that radiation pneumonitis did not occur among subjects with an $\text{LMD}_{\text{Y-90}}$ below 12 Gy. On the basis of this empiric value and the 30-Gy limit for LMD_{MAA} , the number of true-negative, true-positive, false-negative, and false-positive cases is reported in Figure 3.

Radiation Pneumonitis

Radiation pneumonitis did not occur in any subject with an $\text{LMD}_{\text{Y-90}}$ below 12 Gy. Radiation pneumonitis occurred in 2 patients, both of whom were diagnosed with HCC and treated with glass microspheres. The first patient had the highest $\text{LMD}_{\text{Y-90}}$ (22.1 Gy) of all subjects. This patient had no thrombus or portal hypertension. During the pretreatment work-up, LMD_{MAA} was 89.0 Gy (LSF_{MAA} , 23%), and SPECT/CT showed no evidence of extrahepatic depositions in the upper abdomen. The total administered activity was 7,775 MBq. The second patient had an $\text{LMD}_{\text{Y-90}}$ of 17.7 Gy in the presence of both portal vein tumor thrombosis and portal hypertension. LMD_{MAA} was 34.1 Gy (LSF_{MAA} , 50%), and SPECT/CT showed no evidence of extrahepatic depositions in the upper abdomen. The total administered activity was

TABLE 1
Baseline and Treatment Characteristics

Characteristic	Data
Patients	272
Procedures	317
Sex	
Male	170 (62.5%)
Female	102 (37.5%)
Mean age	64.56 (17–90)
Sphere type	
Glass	200 (63%)
Resin	117 (37%)
Median administered activity (MBq)	
Glass	2,278 (277–9,636)
Resin	1,877 (516–3,245)
Mean number of ^{90}Y sessions	1.17 (1–5)
Tumor types	
Colorectal cancer	104 (38%)
HCC	68 (25%)
Neuroendocrine tumor	45 (16%)
Cholangiocellular carcinoma	21 (8%)
Others	34 (13%)
Thrombus	
Segmental right portal vein	9
Lobar left portal vein	4
Segmental right portal vein plus lobar left portal vein	1
Tumor thrombosis, main portal vein	2
Tumor thrombosis, right hepatic vein	1
Portal hypertension	33
LSF_{MAA} (%)	
Mean	5.73 (0.49–50.44)
Median	3.87 (4.60)
Number of cases > 20%	11
$\text{LSF}_{\text{Y-90}}$ (%)	
Mean	5.90 (0.27–39.02)
Median	4.13 (5.28)
Number of cases > 20%	7
$^{99\text{m}}\text{Tc}$ -based prediction of LMD (Gy)	
Mean	6.93 (0.17–89.03)
Median	3.52 (6.48)
Number of cases > 30 Gy	14
^{90}Y PET-based left lung dose (Gy)	
Mean	1.59 (0.02–22.14)
Median	0.95 (1.16)
Number of cases > 12 Gy	3
Median total lung volume (mL)	1,713 (392–7,851)
Median left lung volume (mL)	733 (80–3,792)

Qualitative data are number; continuous data are mean and range or median and interquartile range.

TABLE 2
Matrix of Statistical Significance of Differences Between Tumor Types in Terms of LSF_{Y-90}

Type	LSF _{Y-90}				
	Cholangiocellular carcinoma	Colorectal cancer	HCC	Neuroendocrine tumor	Others
Cholangiocellular carcinoma	—	0.5	0.5	0.06	0.5
Colorectal cancer		—	0.4	0.008*	0.5
HCC			—	0.01*	0.4
Neuroendocrine tumor				—	0.02*
Others					—

*Statistically significant ($P < 0.05$).

1,300 MBq. Details on this case were previously provided by Alsultan et al. (11).

Another subject, with an LMD_{Y-90} of 18.4 Gy (LMD_{MAA}, 29.1 Gy; LSF_{MAA}, 19%), died of progressive disease 2 mo after treatment, before the evaluation scan could be done.

DISCUSSION

The 30-Gy limit on maximum absorbed dose to the lungs for a single radioembolization treatment was based on clinical evidence from 2 seminal publications (4,5) that have strongly influenced the guidance on lung dose limits after radioembolization. This observational study showed that no patients with an LMD_{Y-90} below 12 Gy developed any lung-dose-related side effects. Of the 14 patients who had an LMD_{MAA} above 30 Gy, 2 developed radiation pneumonitis. However, the 12 other patients with an LMD_{MAA} above 30 Gy did not develop any lung-dose-related side effects, stressing the limitation of using ^{99m}Tc-MAA planar scintigraphy in predicting ⁹⁰Y lung shunts.

Radiation pneumonitis is a rare but potentially fatal side effect of radioembolization. As summarized by Cremonesi et al. (19), there have been various reports of the lung-dose-related side effects of ⁹⁰Y radioembolization, in an attempt to improve insight on how to define the upper dose limit to the lungs. However, although they all used the same approach to computing the lung dose, namely multiplying the LSF_{MAA} by the administered activity to estimate the LMD, different values for the lung dose above which radiation pneumonitis occurred were found (ranging between 10 and 56 Gy). In line with the 12 false-positive cases reported in this study (Fig. 3), Salem et al. (20) reported 58 patients treated with cumulative or single-treatment lung doses exceeding 30 Gy, based on LSF_{MAA}-derived calculations, who did not develop any radiation pneumonitis or lung toxicity. These findings further underline how ^{99m}Tc particles overestimate the actual lung shunt. In contrast, Leung et al. (4) reported radiation pneumonitis in 3 patients with a predicted LMD lower than 30 Gy. However,

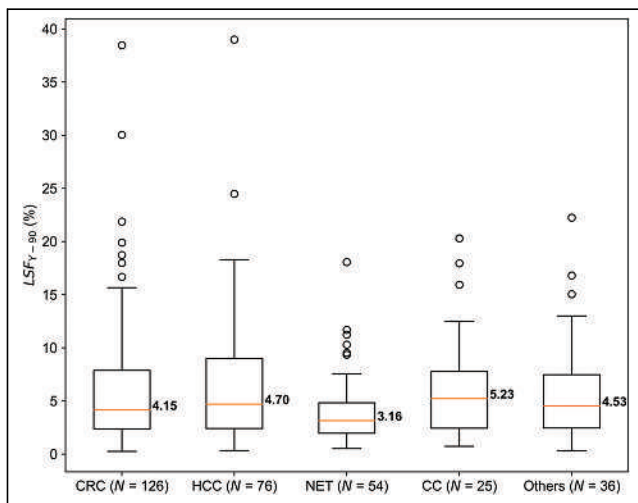


FIGURE 2. Box plots depicting LSF_{Y-90}, together with corresponding median, divided by tumor type. Statistically significant difference was reported between neuroendocrine tumor patients and colorectal cancer patients ($P = 0.008$), between neuroendocrine tumor and HCC patients ($P = 0.010$), and between neuroendocrine tumor and patients in group “others” ($P = 0.022$). CC = cholangiocellular carcinoma; CRC = colorectal cancer; NET = neuroendocrine tumor.

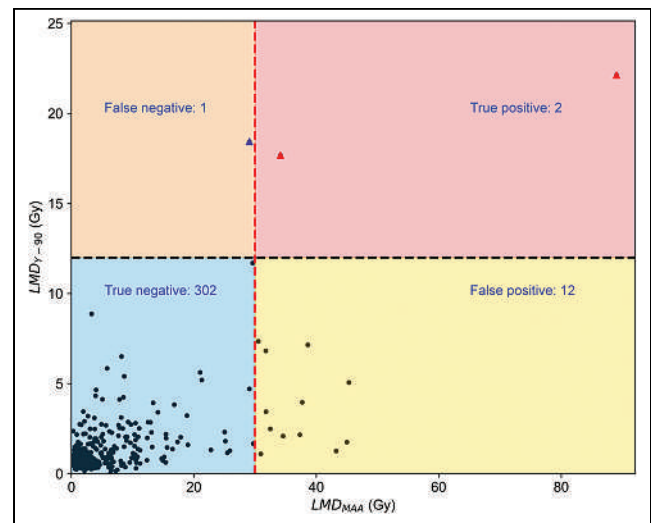


FIGURE 3. Distribution of LMD_{Y-90} as function of corresponding LMD_{MAA}. On the basis of limit of 30 Gy for estimate of absorbed radiation dose to lungs during pretreatment phase and 12 Gy for LMD_{Y-90}, below which no radiation pneumonitis cases were reported, subjects were divided into 4 quadrants: true-positive, false-positive, true-negative, and false-negative. According to chosen limits, 12 false-positives were detected. True-positive (red triangles) corresponds to 2 patients who developed radiation pneumonitis, whereas false-negative (blue triangle) corresponds to patient who died of progressive disease before follow-up.

the absorbed doses taken from the literature were derived without including attenuation correction and thus should be rescaled by an average factor of 0.6 (21). For this reason, a straight comparison with the results of the current study is difficult. In addition, in this study, LMD_{Y-90} was computed on the posttreatment ^{90}Y PET and considering only the left lung as representative of the lung volume. In this study, the same difficulties were found in determining a unique threshold for the ^{99m}Tc -MAA-based LMD estimate to avoid radiation pneumonitis, confirming an issue well documented in the literature. As an example, in a multicenter study, Braat et al. (22) reported a patient with an LSF_{MAA} of 3% who developed radiation pneumonitis, whereas the patient with the highest LSF_{MAA} , 33%, did not develop radiation pneumonitis. These contradictory findings in the literature underline the limits of ^{99m}Tc -MAA LSF, and consequently lung dose estimate, as predictive of ^{90}Y distribution (9), stressing the need for a more reliable and robust method or particle. In recent years, some alternatives to ^{99m}Tc -MAA have been suggested. Kunnen et al. (23) demonstrated in a phantom study that bremsstrahlung SPECT/CT, reconstructed with a Monte Carlo algorithm, can estimate the LSF for a ^{90}Y pretreatment procedure using a theoretically safe ^{90}Y activity of as low as 70 MBq. ^{166}Ho scout microspheres (250 MBq; QuiremScout), already used as scout particles before ^{166}Ho radioembolization, were proposed as a surrogate of ^{90}Y to determine patients' eligibility, thanks to its imaging possibility (24).

Both patients who developed radiation pneumonitis in this study had HCC. Both cirrhosis and HCC have been associated with increased arteriovenous shunting into the lungs, potentially causing increased lung doses (25). However, significant differences were observed in LSF_{Y-90} only for HCC patients when compared with NET-diagnosed subjects (Fig. 2). In the subgroup of HCC patients only, the presence of either a thrombus or portal hypertension did not play a statistically significant role in LSF_{Y-90} , suggesting that these variables might be negligible when assessing the lung-dose-related side effects of ^{90}Y . Conversely, Ward et al. (26), who reviewed 409 patients, reported a low but significant correlation between increased hepatopulmonary shunt fraction (measured using ^{99m}Tc -MAA planar scintigraphy) and HCC, hepatic vein tumor thrombosis, and portal vein tumor thrombosis.

Several limitations apply to this study, apart from its retrospective and single-center nature. Considering the ^{99m}Tc -based LMD_{MAA} computation, the main limitation is use of a surrogate model applying ^{99m}Tc -MAA particles as an approximation to ^{90}Y microsphere distribution. In addition, the lungs and liver were delineated on planar scintigraphy without an anatomic reference and assuming a fixed lung mass of 1 kg. Therefore, women, who have a smaller organ mass (27,28) than men but the same lung shunt, may have received a larger lung radiation dose for the same treatment activity. Like the ^{90}Y PET-based LMD_{Y-90} computation, a constant value for lung density was used. However, as reported by Kappadath et al. (29), use of a constant value might be a limiting factor in an accurate estimate of LMD_{Y-90} . Although this study relied on the assumption of lung homogeneity, given that the lungs were not completely within the PET field of view for some datasets, the distribution of microspheres in vivo is heterogeneous (17). The gravitational dependence of alveolar and vascular pressures within the lung causes preferential distribution of blood flow and, in parallel, microspheres to the bases of the lung (30). In addition, microsphere irradiation is microscopically nonuniform (31). However, if radiation pneumonitis occurs, the assumption of a uniform distribution in the lung was visually

confirmed by the contrast-enhanced CT scan acquired during follow-up. Regardless, these limitations reflect the current protocols and treatment of patients. Moreover, radiation pneumonitis is a rare side effect of radioembolization, with just 2 cases among the 317 procedures in this study—a number of events too limited for any realistic statistical analysis.

Despite these limitations, a better predictive particle and a new lung dose limit are essential to improve the current general method of selecting patients, avoiding unjustified patient exclusion. Given the proven value of posttreatment ^{90}Y PET/CT (20), more insight should be gained on the actual lung dose delivered than on the predicted one.

CONCLUSION

This observational study showed that radiation pneumonitis did not occur among subjects with a left LMD below 12 Gy, defined on posttreatment ^{90}Y PET/CT. A ^{99m}Tc -MAA planar scintigraphy-based estimated cutoff of 30 Gy for lung dose is capricious and, once encountered in pretreatment imaging, should be evaluated with caution to prevent unjustified treatment exclusion.

DISCLOSURE

Martina Stella is employed by the UMC Utrecht under a collaborative grant from the Dutch Research Council (NWO) between UMC Utrecht and Quirem Medical BV. Rob van Rooij and Hugo de Jong have acted as consultants for BTG/Boston Scientific. Arthur Braat has acted as a consultant for BTG/Boston Scientific and Terumo. Marnix Lam has acted as a consultant for BTG/Boston Scientific and Terumo and receives research support from BTG/Boston Scientific and Quirem Medical BV. The Department of Radiology and Nuclear Medicine of the UMC Utrecht receives royalties from Quirem Medical BV. No other potential conflict of interest relevant to this article was reported.

ACKNOWLEDGMENTS

We thank the IT staff, in particular Marloes van Ijzendoorn, for help and support in providing anonymized data. We express gratitude to Sander Ebbens, who helped with the statistical analysis.

KEY POINTS

QUESTION: What is the LMD below which radiation pneumonitis does not occur after ^{90}Y radioembolization?

PERTINENT FINDINGS: This retrospective study showed that all subjects with an LMD below 12 Gy, measured on posttreatment ^{90}Y PET/CT, did not develop radiation pneumonitis.

IMPLICATIONS FOR PATIENT CARE: Our findings suggest reconsideration of the current clinically used upper limit for LMD, 30 Gy.

REFERENCES

1. Braat AJAT, Smits MLJ, Braat MNGJA, et al. ^{90}Y hepatic radioembolization: an update on current practice and recent developments. *J Nucl Med.* 2015;56:1079–1087.
2. Salem R, Thurston KG. Radioembolization with ^{90}Y microspheres: a state-of-the-art brachytherapy treatment for primary and secondary liver malignancies—part 1: technical and methodologic considerations. *J Vasc Interv Radiol.* 2006;17:1251–1278.

3. Peterson JL, Vallow LA, Johnson DW, et al. Complications after ^{90}Y microsphere radioembolization for unresectable hepatic tumors: an evaluation of 112 patients. *Brachytherapy*. 2013;12:573–579.
4. Leung TWT, Lau WY, Ho SKW, et al. Radiation pneumonitis after selective internal radiation treatment with intraarterial ^{90}Y yttrium-microspheres for inoperable hepatic tumors. *Int J Radiat Oncol Biol Phys*. 1995;33:919–924.
5. Ho S, Lau WY, Leung TWT, Chan M, Johnson PJ, Li AKC. Clinical evaluation of the partition model for estimating radiation doses from yttrium-90 microspheres in the treatment of hepatic cancer. *Eur J Nucl Med*. 1997;24:293–298.
6. Kappadath SC, Lopez BP, Salem R, Lam MGEH. Reassessment of the lung dose limits for radioembolization. *Nucl Med Commun*. 2021;42:1064–1075.
7. Lopez B, Mahvash A, Lam MGEH, Kappadath SC. Calculation of lung mean dose and quantification of error for ^{90}Y -microsphere radioembolization using $^{99\text{m}}\text{Tc}$ -MAA SPECT/CT and diagnostic chest CT. *Med Phys*. 2019;46:3929–3940.
8. Elschot M, Nijssen JFW, Lam MGEH, et al. $^{99\text{m}}\text{Tc}$ -MAA overestimates the absorbed dose to the lungs in radioembolization: a quantitative evaluation in patients treated with ^{166}Ho -microspheres. *Eur J Nucl Med Mol Imaging*. 2014;41:1965–1975.
9. Wondergem M, Smits MLJ, Elschot M, et al. $^{99\text{m}}\text{Tc}$ -macroaggregated albumin poorly predicts the intrahepatic distribution of ^{90}Y resin microspheres in hepatic radioembolization. *J Nucl Med*. 2013;54:1294–1301.
10. Alsultan AA, Smits MLJ, Barentsz MW, Braat AJAT, Lam MGEH. The value of yttrium-90 PET/CT after hepatic radioembolization: a pictorial essay. *Clin Transl Imaging*. 2019;7:303–312.
11. D'Arienzo M, Pimpinella M, Capogni M, et al. Phantom validation of quantitative Y-90 PET/CT-based dosimetry in liver radioembolization. *EJNMMI Res*. 2017;7:94.
12. Kunnen B, Beijst C, Lam MGEH, Viergever MA, de Jong HWAM. Comparison of the Biograph Vision and Biograph mCT for quantitative ^{90}Y PET/CT imaging for radioembolisation. *EJNMMI Phys*. 2020;7:14.
13. Dittmann H, Kopp D, Kupferschlaeger J, et al. A prospective study of quantitative SPECT/CT for evaluation of lung shunt fraction before SIRT of liver tumors. *J Nucl Med*. 2018;59:1366–1372.
14. Hofmanninger J, Prayer F, Pan J, Röhrich S, Prosch H, Langs G. Automatic lung segmentation in routine imaging is primarily a data diversity problem, not a methodology problem. *Eur Radiol Exp*. 2020;4:50.
15. Rhodes CG, Wollmer P, Fazio F, Jones T. Quantitative measurement of regional extravascular lung density using positron emission and transmission tomography. *J Comput Assist Tomogr*. 1981;5:783–791.
16. Pasciak AS, Bourgeois AC, Bradley YC. A comparison of techniques for ^{90}Y PET/CT image-based dosimetry following radioembolization with resin microspheres. *Front Oncol*. 2014;4:121.
17. Bastiaannet R, Kappadath SC, Kunnen B, Braat AJAT, Lam MGEH, de Jong HWAM. The physics of radioembolization. *EJNMMI Phys*. 2018;5:22.
18. Levillain H, Bagni O, Deroose CM, et al. International recommendations for personalised selective internal radiation therapy of primary and metastatic liver diseases with yttrium-90 resin microspheres. *Eur J Nucl Med Mol Imaging*. 2021;48:1570–1584.
19. Cremonesi M, Chiesa C, Strigari L, et al. Radioembolization of hepatic lesions from a radiobiology and dosimetric perspective. *Front Oncol*. 2014;4:210.
20. Salem R, Parikh P, Atassi B, et al. Incidence of radiation pneumonitis after hepatic intra-arterial radiotherapy with yttrium-90 microspheres assuming uniform lung distribution. *Am J Clin Oncol*. 2008;31:431–438.
21. Chiesa C, Maccauro M, Romito R, et al. Need, feasibility and convenience of dosimetric treatment planning in liver selective internal radiation therapy with ^{90}Y microspheres: the experience of the National Tumor Institute of Milan. *Q J Nucl Med Mol Imaging*. 2011;55:168–197.
22. Braat AJAT, Kappadath SC, Ahmadzadehfard H, et al. Radioembolization with ^{90}Y resin microspheres of neuroendocrine liver metastases: international multicenter study on efficacy and toxicity. *Cardiovasc Intervent Radiol*. 2019;42:413–425.
23. Kunnen B, van der Velden S, Bastiaannet R, Lam MGEH, Viergever MA, de Jong HWAM. Radioembolization lung shunt estimation based on a ^{90}Y pretreatment procedure: a phantom study. *Med Phys*. 2018;45:4744–4753.
24. Prince JF, van Rooij R, Bol GH, de Jong HWAM, van den Bosch MAAJ, Lam MGEH. Safety of a scout dose preceding hepatic radioembolization with ^{166}Ho microspheres. *J Nucl Med*. 2015;56:817–823.
25. Kallini JR, Gabr A, Salem R, Lewandowski RJ. Transarterial radioembolization with yttrium-90 for the treatment of hepatocellular carcinoma. *Adv Ther*. 2016;33:699–714.
26. Ward TJ, Tamrazi A, Lam MGEH, et al. Management of high hepatopulmonary shunting in patients undergoing hepatic radioembolization. *J Vasc Interv Radiol*. 2015;26:1751–1760.
27. Molina DK, DiMaio VJM. Normal organ weights in women: part II—the brain, lungs, liver, spleen, and kidneys. *Am J Forensic Med Pathol*. 2015;36:182–187.
28. Molina DK, DiMaio VJM. Normal organ weights in men: part II—the brain, lungs, liver, spleen, and kidneys. *Am J Forensic Med Pathol*. 2012;33:368–372.
29. Kappadath SC, Lopez BP, Salem R, Lam MG. Lung shunt and lung dose calculation methods for radioembolization treatment planning. *Q J Nucl Med Mol Imaging*. 2021;65:32–42.
30. Armstrong J, Raben A, Zelefsky M, et al. Promising survival with three-dimensional conformal radiation therapy for non-small cell lung cancer. *Radiother Oncol*. 1997;44:17–22.
31. Giammarile F, Bodei L, Chiesa C, et al. EANM procedure guideline for the treatment of liver cancer and liver metastases with intra-arterial radioactive compounds. *Eur J Nucl Med Mol Imaging*. 2011;38:1393–1406.

Diagnostic Performance of Cervical Ultrasound, ^{99m}Tc-Sestamibi Scintigraphy, and Contrast-Enhanced ¹⁸F-Fluorocholine PET in Primary Hyperparathyroidism

Vincent Boudousq¹, Nicolas Guignard², Olivier Gilly³, Benjamin Chambert⁴, Adel Mamou⁵, Olivier Moranne⁶, Mathilde Zemmour⁷, Haitham Sharara⁸, and Benjamin Lallemand⁷

¹Department of Nuclear Medicine, Institut de Recherche en Cancérologie de Montpellier, INSERM U1194, CHU Nîmes, Université Montpellier, Montpellier, France; ²Department of Otolaryngology, Saint Jean Clinical, Saint Jean de Vedas, France; ³Department of Metabolic and Endocrine Disease, CHU Nîmes, Université Montpellier, Nîmes, France; ⁴Department of Nuclear Medicine, CHU Nîmes, Université Montpellier, Nîmes, France; ⁵R&D, NeuralX, Montpellier, France; ⁶Department of Nephrology, Dialysis, and Apheresis, CHU Nîmes, Université Montpellier, Nîmes, France; ⁷Department of Otolaryngology, CHU Nîmes, Université Montpellier, Nîmes, France; and ⁸Department of Radiology, CHU Nîmes, Université Montpellier, Nîmes, France

Preoperative localization of pathologic parathyroids is crucial for minimally invasive treatment of primary hyperparathyroidism (PHPT). This study compared contrast-enhanced ¹⁸F-fluorocholine PET/CT, cervical ultrasonography (CU), and conventional scintigraphic imaging modalities (MIBI scintigraphy, consisting of ^{99m}Tc-sestamibi/¹²³I-sodium iodide SPECT/CT, ^{99m}Tc-sestamibi/¹²³I-sodium iodide planar subtraction imaging, and ^{99m}Tc-sestamibi planar dual-phase imaging), combined and individually, for preoperative localization of hyperfunctional parathyroids in PHPT. The gold standard was histologic examination.

Methods: Data from consecutive patients with clinically suspected PHPT were retrospectively collected. All 3 imaging modalities were systematically performed. The ability of ¹⁸F-fluorocholine PET/CT, CU, and MIBI scintigraphy to identify a hyperfunctional parathyroid and specify the side or identify an ectopic location was noted. Patients underwent surgical exploration if at least 1 examination was positive. The findings of CU + MIBI scintigraphy combined were considered positive if CU and MIBI scintigraphy separately showed a hyperfunctional parathyroid gland on the same side or in the same ectopic location; any findings other than these were considered negative. The composite judgment criterion for pathologic parathyroid was a combination of histologic analysis and normalization of parathyroid hormone and calcium levels. **Results:** In total, 149 pathologic parathyroids were found in 143 of the 144 included patients. ¹⁸F-fluorocholine PET/CT diagnosed 148 of 149 pathologic parathyroids. Only 4 false-positives and 1 false-negative were found. The ¹⁸F-fluorocholine PET/CT sensitivity of 99.3% was superior to that of CU, at 75.2% ($P < 0.0001$); MIBI scintigraphy, at 65.1% ($P < 0.0001$); and CU + MIBI scintigraphy, at 89.9%, ($P = 0.0009$). Five of the 5 ectopic locations were diagnosed by ¹⁸F-fluorocholine PET/CT, 2 of the 5 by MIBI scintigraphy, and none by CU. Accuracy was better for ¹⁸F-fluorocholine PET/CT, at 98%, than for CU, at 84% ($P < 0.0001$); MIBI scintigraphy, at 81% ($P < 0.0001$); or CU + MIBI scintigraphy, at 91% ($P < 0.0001$). Among the 72 (50%) patients who had a negative CU + MIBI scintigraphy result, ¹⁸F-fluorocholine PET/CT correctly identified hyperfunctional thyroids in 70 (97.2%). Average uptake in the ¹⁸F-fluorocholine PET/CT hyperfunctional parathyroid was higher than that in the adjacent thyroid (SUV_{max} adjusted for lean body mass, 6.45 vs. 2.15) ($P < 0.0001$). **Conclusion:** The accuracy of ¹⁸F-fluorocholine PET/CT is higher than that of CU and

MIBI scintigraphy for localization of hyperfunctional parathyroids, justifying the systematic use of ¹⁸F-fluorocholine PET/CT as the first-line method for PHPT diagnosis.

Key Words: ¹⁸F-fluorocholine; primary hyperparathyroidism; parathyroid adenoma; ^{99m}Tc-sestamibi scintigraphy; cervical ultrasound

J Nucl Med 2022; 63:1081–1086
DOI: 10.2967/jnumed.121.261900

P rimary hyperparathyroidism (PHPT) is a pathology characterized by the presence of long-lasting hypercalcemia associated with inappropriate hyperparathyroidism. Idiopathic parathyroid adenomas are the most common cause of this pathology. PHPT treatment is mainly surgical, consisting of resection of pathologic parathyroids (1). Previously, parathyroids were located via an exploration of the 4 parathyroid sites. However, the currently favored technique is to identify and precisely locate the pathologic parathyroids by imaging in order to propose a faster, safer targeted intervention.

For many years, the gold standard for preoperative localization assessment has been cervical ultrasonography (CU) combined with ^{99m}Tc-sestamibi (MIBI) scintigraphy (CU + MIBI scintigraphy) to provide supplementary anatomic and functional information. However, the results of these examinations are negative or questionable in 10%–25% of cases (2,3), leading to further surgical explorations, the results of which are often equivocal, or to regular monitoring with repeated examinations. Defining the best diagnostic tool to minimize negative or equivocal identification is an important challenge in the surgical treatment of PHPT.

¹⁸F-fluorocholine is a marker of membrane proliferation, initially used to detect cancerous tissue of prostate origin. This radiopharmaceutical can also be sensitively and intensely absorbed by hyperfunctional parathyroid tissue. The preliminary data in the literature suggest that ¹⁸F-fluorocholine PET/CT would be beneficial when CU + MIBI scintigraphy of a parathyroid adenoma gives equivocal results (4). In practice, it has quickly become obvious that ¹⁸F-fluorocholine PET/CT may have diagnostic value superior to that of CU + MIBI scintigraphy and may soon become the gold standard first-line method for PHPT.

Received Jan. 22, 2021; revision accepted Nov. 8, 2021.
For correspondence or reprints, contact Nicolas Guignard (nicolas.guignard87@gmail.com).
Published online Dec. 2, 2021.
COPYRIGHT © 2022 by the Society of Nuclear Medicine and Molecular Imaging.

To test this hypothesis, we aimed to compare the diagnostic performance of CU, MIBI scintigraphy, ¹⁸F-fluorocholine PET/CT, and CU + MIBI scintigraphy for preoperative identification of hyperfunctional parathyroids in PHPT.

MATERIALS AND METHODS

This was a single-center, retrospective study on patients included from July 2016 to January 2020 at the ear, nose, and throat; endocrinology; and nuclear medicine departments of a French university hospital. The institutional review board approved this retrospective study, and the requirement to obtain informed consent was waived.

Patients

The study included adults who had been referred for surgical consultation regarding PHPT and had at least 1 image indicating a hyperfunctional parathyroid gland on at least 1 of the imaging modalities (CU, MIBI scintigraphy, or ¹⁸F-fluorocholine PET/CT) between July 2016 and January 2020. The participants formed a consecutive series. PHPT was defined by hypercalcemia (>2.55 mmol/L) associated with high serum parathyroid hormone (PTH) levels or inappropriate levels in the absence of vitamin D deficiency. Patients who had an associated nodular dystrophy of the thyroid were included, but any who had previously undergone surgery of the thyroid compartment were excluded, as were any who had another pathologic condition that could modify phosphocalcic metabolism, such as chronic renal failure, hyper- or hypovitaminosis D, sarcoidosis, multiple endocrine neoplasia, or progressive neoplasia.

Over the 43-mo recruiting period, 157 patients with PHPT underwent all imaging studies; 144 fulfilled the inclusion criteria by having a positive target on at least 1 of the imaging modalities and underwent surgery. The patient characteristics are described in Table 1. Briefly, we included 26 men and 118 women, with a mean age of 63 y (25–92 y) and a mean preoperative PTH level of 143 pg/mL (39–849 pg/mL).

TABLE 1
Characteristics of PHPT Patients Who Underwent Surgery (*n* = 144)

Characteristic	Data
Age (y)	63 (25–92)
Sex	
Male	26 (18.1%)
Female	118 (81.9%)
Preoperative PTH (pg/mL)	143 (39–849)
Postoperative PTH (pg/mL)	42 (6–126)
Patients with multiple resected hyperfunctional thyroids	6
Ectopic adenomas	5
Size of resected parathyroids (mm)	17 (7–35)
Weight of resected parathyroids (g)	1.12 (0.1–7.5)
Mean SUL _{max} of hyperfunctional parathyroids	6.46 (1.56–22.9)

Qualitative data are number; continuous data are mean and range.

Preoperative Examinations

All patients underwent CU, MIBI scintigraphy, and ¹⁸F-fluorocholine PET/CT in no set order. For each examination, the presence or absence of images suggestive of a hyperfunctional parathyroid gland was noted, along with their position in the left and right thyroid beds and ectopically. We did not differentiate the upper and lower positions. Questionable images were considered negative in the treatment decision and in analysis of the results. The radiologists who evaluated the images knew the results of the other examinations. Patients without surgical targets on the 3 imaging modalities did not undergo surgery and were not included in the study.

High-Resolution CU. CU was performed by an experienced radiologist on an iU22 high-resolution ultrasound scanner (Philips) (first used in 2012). The patient was examined supine, with the neck in extension. CU was performed using high-frequency linear transducers (7–12 MHz) for cervical examination over a field extending from the angles of the mandible to the sternal notch. The upper mediastinum was studied using an endocavitary probe for retrosternal exploration (4.5–7.2 MHz probe). Transversal and longitudinal views were obtained; images of regions of interest were recorded as video images. The parathyroid glands were sought on the posterior side of the thyroid lobes and on all cervical and upper mediastinal ectopic sites. A parathyroid was defined as pathologic (adenoma or hyperplasia) if the gland was elongated or flattened, hypoechoic, and separated from the thyroid parenchyma by a wall, which was mobile on swallowing and well vascularized. The thyroid parenchyma was also analyzed, and any possible dystrophy was described in detail.

Conventional Scintigraphic Imaging. Conventional (i.e., non-PET/CT) scintigraphic imaging (MIBI scintigraphy) consisted of ^{99m}Tc-sestamibi/¹²³I sodium iodide SPECT/CT, ^{99m}Tc-sestamibi/¹²³I-sodium iodide subtraction imaging, and ^{99m}Tc-sestamibi dual-phase imaging. A combined-imaging protocol was used, enabling same-day acquisition of all 3 modalities. Scintigraphy was performed on a Discovery 670 imager (GE Healthcare). The γ -camera was equipped, first, with a pinhole collimator allowing a cervical planar acquisition and, second, with low-energy, high-resolution collimators allowing a cervicothoracic planar and tomography acquisition. A matrix of 256 × 256 was used with, for dual-isotope acquisition, a 10% energy window centered on 159 keV (recommended for ¹²³I), and a 15%–20% window centered on 140 keV (recommended for ^{99m}Tc). A 16-MBq dose of ¹²³I was injected, followed 2 h later by a 10 MBq/kg dose of ^{99m}Tc-sestamibi. Five minutes after the last injection, a double-isotope planar pinhole cervical acquisition was performed for 10 min. After the collimator had been changed, a cervicothoracic early planar double-isotope acquisition and a SPECT double-isotope acquisition combined with cervicothoracic CT were performed for 15 min. Ninety minutes later, another cervical planar acquisition was done (delayed planar image of dual-phase protocol). The following images were obtained: an early and delayed large field-of-view planar image of the neck and mediastinum (from the skull base to the heart base), a pinhole double-isotope view of the thyroid bed region, and a cervicothoracic SPECT/CT double-isotope acquisition. Unless there was a contraindication, iodinated contrast medium was injected 80 s before the CT acquisition to improve visualization of the CT and fused images.

For dual-phase imaging analysis, early and delayed ^{99m}Tc-sestamibi planar images were compared; regional uptake of ^{99m}Tc-sestamibi with slower washout than from thyroid tissue was considered to represent hyperfunctioning parathyroid tissue.

For dual-tracer protocols, images were inspected visually and normalized to thyroid counts, and ¹²³I images were subtracted from the ^{99m}Tc images in the thyroid gland and surrounding soft tissue. Persistence of a focal accumulation of radiopharmaceutical adjacent to the thyroid after subtraction was considered suggestive of a hyperfunctioning parathyroid gland.

For SPECT/CT imaging, regional ^{99m}Tc -sestamibi uptake not associated with thyroid tissue visualized on ^{123}I or CT images was considered to represent hyperfunctioning parathyroid tissue. Physiologic hyperuptake (salivary glands, inflammatory lymph nodes) was not retained.

This study performed a combined assessment of the 3 conventional scintigraphic imaging methods, with any positive finding—according to the interpretation criteria described above—being considered to represent hyperfunctioning parathyroid tissue.

^{18}F -Fluorocholine PET. ^{18}F -fluorocholine PET/CT was performed 1 h after intravenous injection of a dose ranging from 150 to 185 MBq of ^{18}F -fluorocholine, using a Discovery PET/CT 710 Elite imager (GE Healthcare). The strategy was to obtain first a CT topogram, then a low-dose attenuation-correction CT scan, then a PET acquisition, and finally an additional intravenous contrast-enhanced diagnostic CT scan. When contrast medium was contraindicated, a diagnostic CT scan was performed instead of the attenuation-correction CT scan. The acquisition protocol included a thickness of 2.5 mm, an interval of 1.25 mm, a display field of view of 70, tension of 120 kV, and automatic mA regulation. The acquisition was centered on the cervicothoracic region. Iterative reconstruction of PET images was performed with the Q-Clear algorithm (GE Healthcare) to improve the signal-to-noise ratio using a β of 600. Because contrast-enhanced CT allowed more precise anatomic localization, iodinated contrast medium—unless contraindicated—was injected 80 s before the CT acquisition to optimize the CT and fused-image analysis. Neck or mediastinal hyperuptake matching a scanner image compatible with an adenoma or hyperplasia was considered a hyperfunctional parathyroid. Physiologic hyperuptake (salivary glands, inflammatory lymph nodes) was not retained. The SUV_{max} adjusted for lean body mass (SUL_{max}) was calculated to quantify the intensity of uptake.

Surgery

All patients with at least 1 image indicating a hyperfunctional parathyroid gland on at least 1 imaging modality underwent surgery. The same 2-cm lateral incision was used, allowing access to both upper and lower locations. If bilateral exploration was necessary, a midline incision was made. The hyperfunctional parathyroid tissue was located and removed with a retrothyroid approach under general or local anesthesia. If there was any doubt about the nature of the resected tissue, an extemporaneous anatomopathologic analysis was used to confirm the presence of parathyroid tissue. Surgery could be combined with a thyroid lobectomy when there were suggestive or questionable thyroid nodules on the preoperative evaluation. When the surgeon found no pathologic parathyroid tissue during the surgical exploration, complete emptying of the laterotracheal fatty cell tissue (level VIb) was performed to limit the risk of operator-related failure to identify a pathologic parathyroid.

Statistical Analysis

The diagnostic values were defined using a judgment criterion combining histologic analysis (pathologic tissue: adenoma/hyperplasia or normal) and the biologic workup (postoperative normalization of PTH and calcium (5)). Images evoking a hyperfunctional parathyroid were considered true-positive if confirmed as a pathologic parathyroid on histologic examination or false-positive if not. In the absence of an evocative image, if surgical exploration was performed (i.e., in the event of conflicting results between the different types of images), the result was considered true-negative if no hyperfunctional parathyroid was found or false-negative if a pathologic parathyroid was found. For parathyroid sites not surgically explored because of negative imaging by all methods, the result was considered true-negative if a hyperfunctional parathyroid was found on contralateral surgical exploration and the biologic test results normalized, or a result was considered

impossible to conclude if no hyperfunctional parathyroid was found after contralateral surgical exploration and the biologic test results had not returned to normal. For each examination method, sensitivity, specificity, positive predictive, and negative predictive values and their 95% CIs were calculated.

The accuracy, sensitivity, and specificity of ^{18}F -fluorocholine PET/CT were compared with the performance of CU, MIBI scintigraphy, and CU + MIBI scintigraphy.

The results of CU + MIBI scintigraphy were considered positive if CU and MIBI scintigraphy separately showed a hyperfunctional parathyroid gland on the same side. The results were considered negative if there was a discrepancy between CU and MIBI scintigraphy or if both were negative. A McNemar test for paired data was used for the comparison. A P value of less than 0.02, adjusted for multiple comparisons with a Bonferroni adjustment, was considered statistically significant.

The statistical analyses were done using the RStudio software, version 1.2.5001.

The scientific committee of the Nimes University Hospital Center approved the experiments.

RESULTS

For each patient, the pre- and postoperative PTH levels, the result of each preoperative examination to locate the parathyroids, and the histologic results (including size and weight) of the parathyroids were recorded (Supplemental Table 1; supplemental materials are available at <http://jnm.snmjournals.org>).

Surgical Results and Anatomopathologic Data

At least 1 hyperfunctional parathyroid was found in 143 of the 144 patients who underwent surgery. In total, 149 pathologic parathyroids were removed: 134 patients had a single parathyroid adenoma, 3 patients had isolated parathyroid hyperplasia, and 6 patients had a hyperfunctional parathyroid at 2 sites. In 1 patient, no pathologic parathyroid was found.

These pathologic glands were in the right thyroid compartment in 45.4% of cases (65/143), the left compartment in 46.9% of cases (67/143), the right and left thyroid compartments in 4.2% of cases (6/143), and an ectopic location in 3.5% of cases (5/143): 2 superior mediastinal, 1 midanterior mediastinal, 1 left retroesophageal, and 1 behind the left sternoclavicular joint. No adverse events were noted during the various imaging examinations.

Diagnostic Values for CU, MIBI Scintigraphy, and ^{18}F -Fluorocholine PET/CT

The diagnostic values for CU, MIBI scintigraphy, CU + MIBI scintigraphy, and ^{18}F -fluorocholine PET/CT are given in Table 2. According to histologic confirmation, hyperfunctional parathyroids were correctly identified (true-positive) in 112 (75%) of the 149 cases by CU, in 97 (65%) by MIBI scintigraphy, in 148 (99%) by ^{18}F -fluorocholine PET/CT, and in 134 (90%) by CU + MIBI scintigraphy (reference standard).

CU wrongly diagnosed a hyperfunctional parathyroid (false-positive) in 8 cases, compared with 3 for MIBI scintigraphy and 4 for ^{18}F -fluorocholine PET/CT.

The ^{18}F -fluorocholine PET/CT sensitivity was higher than that of CU ($P < 0.0001$) or MIBI scintigraphy ($P < 0.0001$), alone or combined ($P = 0.0009$). Finally, accuracy was better for ^{18}F -fluorocholine PET/CT, at 98%, than for CU, at 84% ($P < 0.0001$), MIBI scintigraphy, at 81% ($P < 0.0001$), or CU + MIBI scintigraphy, at 91% ($P < 0.0001$).

In 72 patients (50%), the results of CU versus MIBI scintigraphy were conflicting or found no adenomas. In these negative or

TABLE 2
Diagnostic Values for CU, MIBI Scintigraphy, CU + MIBI Scintigraphy, and ¹⁸F-Fluorocholine PET/CT (*n* = 288)

Imaging method	TP	FP	TN	FN	Accuracy	Sensitivity	Specificity	PPV	NPV
¹⁸ F-fluorocholine PET/CT	148	4	130	1	98% (96%–99%)	99.3% (97%–100%)	97.0% (95%–99%)	97.4% (94%–99%)	99.2% (96%–100%)
CU	112	8	126	37	84% (78%–89%)	75.2% (68%–82%)	94.0% (90%–98%)	93.3% (89%–98%)	77.3% (71%–84%)
<i>P</i>					<0.0001	<0.0001	0.25		
MIBI scintigraphy	97	3	131	52	81% (75%–85%)	65.1% (57%–72%)	97.8% (95%–100%)	97.0% (94%–100%)	71.6% (65%–78%)
<i>P</i>					<0.0001	<0.0001	0.47		
CU + MIBI scintigraphy	134	10	124	15	91% (86%–95%)	89.9% (85%–94%)	92.5% (88%–97%)	93.1% (89%–97%)	89.2% (84%–94%)
<i>P</i>					<0.0001	0.0009	0.09		

TP = true-positive; FP = false-positive; TN = true-negative; FN = false-negative; PPV = positive predictive value; NPV = negative predictive value.

Data in parentheses are 95% CIs.

equivocal situations, ¹⁸F-fluorocholine PET/CT correctly identified hyperfunctional thyroids in 70 (97.2%) patients.

Analysis of Incorrect ¹⁸F-Fluorocholine PET/CT Results

¹⁸F-fluorocholine PET/CT generated 4 false-positive images (patients 4, 64, 82, and 124), which might have been due to localization to a thyroid nodule or lymph node. ¹⁸F-fluorocholine PET/CT generated 1 false-negative image (patient 87).

Ectopic Locations

Five patients had a hyperfunctional parathyroid in an ectopic location (2 superior anterior mediastinal, 1 midanterior mediastinal, 1 left retroesophageal, and 1 behind the left sternoclavicular joint). CU did not locate pathologic parathyroids in these ectopic situations (0/5 cases), and MIBI scintigraphy found only 1 case. In contrast, ¹⁸F-fluorocholine PET/CT located all of them.

Analysis of SUL_{max} of Hyperfunctional Thyroids and Comparison with Physiologic SUL_{max} of Thyroid

We compared the SUL_{max} of the parathyroids against that of the adjacent thyroid parenchyma with physiologic ¹⁸F-fluorocholine uptake. The average SUL_{max} was 6.45 (SD, 3.15) for hyperfunctional parathyroids, compared with 2.15 (SD, 0.79) for the thyroid. Thus, the SUL_{max} of hyperfunctional parathyroids averaged 200% higher than that of the thyroid parenchyma (*P* < 0.0001). The difference in ¹⁸F-fluorocholine uptake between the parathyroid and thyroid, combined with the spatial analysis of the distant parathyroid, facilitates interpretation of the examination. Only patient 31 had a parathyroid SUL_{max} lower than the thyroid SUL_{max} (4.00 vs. 4.82, –17%). This patient had a previous history of Hashimoto thyroiditis with a relatively high thyroid uptake, which might explain the current high thyroid uptake. However, there were no difficulties in diagnosing the hyperfunctional parathyroid in this patient, as the parathyroid tissue was anatomically distinct from the thyroid.

DISCUSSION

This study was conceived because of the increasing number of centers using ¹⁸F-fluorocholine PET/CT to localize hyperfunctional

parathyroid glands during PHPT, despite lack of sufficient data in the literature to justify use of this examination instead of the gold standard, CU + MIBI scintigraphy. The aim of this work was to compare the diagnostic value of ¹⁸F-fluorocholine PET/CT versus that of CU + MIBI scintigraphy. In this study, ¹⁸F-fluorocholine PET/CT had a sensitivity and negative predictive value of 99.0% (95% CI, 97%–100%), a specificity of 97.0% (95% CI, 95%–99%), and a positive predictive value of 97.4% (95% CI, 94%–99%). These diagnostic values are superior to those of CU (*P* < 0.0001) and MIBI scintigraphy (*P* < 0.0001), alone or combined (*P* = 0.0009). These results confirm and reinforce previously published preliminary data (6–16) on a larger series of patients.

Previous publications have suggested reserving ¹⁸F-fluorocholine PET/CT for situations in which CU + MIBI scintigraphy has failed to detect hyperfunctional thyroids. Our study demonstrated the clear diagnostic superiority of ¹⁸F-fluorocholine PET/CT and justifies its indication as a first-line technique in suspected PHPT.

Michaud et al. compared the 3 examinations for preoperative evaluation of primary and secondary hyperparathyroidism in 17 patients (6). Only 1 case of adenoma was poorly recognized by the 3 imaging methods. In this limited series, the sensitivities of CU, MIBI scintigraphy, and ¹⁸F-fluorocholine PET/CT were 42%, 83%, and 96%, respectively.

Another study evaluated the benefit of MIBI scintigraphy and ¹⁸F-fluorocholine PET/CT in 24 patients with PHPT (7). Sensitivity was significantly better with ¹⁸F-fluorocholine PET/CT (92%) than with MIBI scintigraphy (44%–64%, depending on the acquisition technique). A prospective study on 54 patients with PHPT compared CU, MIBI scintigraphy, and ¹⁸F-fluorocholine PET/CT (8). In this study, the sensitivity of the 3 imaging techniques was 69.3%, 80.7%, and 100%, respectively, and the positive predictive values were 87.1%, 97.7%, and 96.3%, respectively.

In a prospective series of 18 suspected parathyroid adenoma sites, 17 adenomas were correctly located by ¹⁸F-fluorocholine PET/CT, with 1 false-positive, producing a sensitivity of 89% (9), comparable to the sensitivity of 90% and a positive predictive value of 100% found in another prospective series of 10 patients (10). A retrospective series of 151 patients who underwent surgery for PHPT and for whom ¹⁸F-fluorocholine PET/CT was performed

at the preoperative evaluation (11) found a positive predictive value of 96.8%. Unfortunately, CU and MIBI scintigraphy were not systematically performed, preventing direct comparison.

Finally, in a recent metaanalysis on 20 studies including a total of 796 patients, Whitman et al. reported that ^{18}F -fluorocholine PET/CT had a superior sensitivity of 96% (95% CI, 94%–98%), compared with 54% (95% CI, 29%–79%) for MIBI scintigraphy ($P < 0.001$). In these studies, like ours, limited to patients with PHPT, ^{18}F -fluorocholine PET/CT had a superior sensitivity of 97% (95% CI, 94%–100%), compared with 55% (95% CI, 32%–78%) for MIBI scintigraphy (12). In our study, MIBI scintigraphy had a sensitivity of 65.1% (95% CI, 57%–72%); this can be compared with the 10 studies (301 patients) included for comparison with MIBI scintigraphy in the metaanalysis. Six (including 41% of the analyzed patients) used dual-phase, dual-tracer sestamibi imaging with SPECT/CT. Three used SPECT, 2 of which used sestamibi alone. One did not describe the sestamibi imaging. The heterogeneity of techniques used for MIBI scintigraphy can lead to inconsistencies between the studies used for the comparison analysis. The same conventional scintigraphic imaging methods ($^{99\text{m}}\text{Tc}$ -sestamibi SPECT/CT, $^{99\text{m}}\text{Tc}$ -sestamibi/perchnetate subtraction imaging, and $^{99\text{m}}\text{Tc}$ -sestamibi dual-phase imaging) were used by Cuderman et al. on 103 PHPT patients imaged preoperatively, with a sensitivity of 65%. This sensitivity was similar to that found in our study (13).

^{18}F -fluorocholine PET/CT has numerous advantages that justify its systematic use for the initial evaluation of hyperfunctional parathyroids in patients with clinically suspected PHPT. First, its diagnostic values are statistically better than those of CU + MIBI scintigraphy, making the preoperative evaluation more reliable for locating hyperparathyroids. Second, ^{18}F -fluorocholine PET/CT is more efficient and generated a lower radiation dose than MIBI scintigraphy. Indeed, ^{18}F -fluorocholine PET/CT requires shorter acquisition times—1 h after injecting the tracer for ^{18}F -fluorocholine PET/CT compared with over 2 h for MIBI scintigraphy—and the patient spends less time under the camera and thus experiences less discomfort. ^{18}F -fluorocholine PET/CT produces better image quality due to a higher spatial resolution (13–16), around 4 mm on the latest-generation PET scanner, and a better-quality mobile scanner, allowing diagnosis of smaller lesions and increased sensitivity. Whole-body ^{18}F -fluorocholine PET/CT emits less radiation than MIBI scintigraphy, with an effective dose of 2.8 mSv versus 6.8 mSv (17).

Third, ^{18}F -fluorocholine PET/CT is the best examination for identifying ectopic adenomas. In a previous study on 54 patients, of whom 6 had hyperfunctional thyroids in ectopic locations (2 mediastinal, 2 in the tracheoesophageal corner, 1 paravertebral, and 1 in the mammary tissue), only ^{18}F -fluorocholine PET/CT correctly identified all parathyroid adenomas (8). Similarly, in another study, 1 ectopic parathyroid adenoma in 10 patients was correctly identified by ^{18}F -fluorocholine PET/CT and MIBI scintigraphy but was missed by CU (10). In another study, consisting of 63 patients, 5 patients underwent ^{18}F -fluorocholine PET/CT because of discordant CU and MIBI scintigraphy, and 1 case of mediastinal adenoma was diagnosed, having been missed by the 2 other imaging techniques (18). For Taywade et al., of 7 parathyroid adenomas diagnosed, 3 were ectopic parathyroids with strong ^{18}F -fluorocholine uptake (19). In our study, all 5 ectopic parathyroids from 144 patients were correctly identified with ^{18}F -fluorocholine PET/CT.

Finally, ^{18}F -fluorocholine PET/CT is a less operator-dependent examination and therefore more reliable than ultrasound scanning. Thyroid nodular dystrophy can easily lead to confusion between a thyroid nodule and the parathyroid on ultrasound scans, even with

a skilled operator. In our experience, this confusion is much less common with an ^{18}F -fluorocholine PET/CT examination. Indeed, physiologic ^{18}F -fluorocholine uptake is low in the thyroid and is almost always lower than that of the parathyroid tissue. In the rare cases of hot thyroid nodules, CT analysis can easily distinguish between intraparenchymal uptake and uptake at a distance from the thyroid parenchyma. To the best of our knowledge, in the literature no association has been described between thyroiditis and strong ^{18}F -fluorocholine uptake of the thyroid. In our study, the only patient with a parathyroid SUL_{max} lower than that of the thyroid had Hashimoto thyroiditis. Therefore, we suggest particular attention when one is interpreting a ^{18}F -fluorocholine PET/CT scan that shows positivity for antithyroid antibodies and a parathyroid adenoma contiguous with the thyroid, as the risk of a false-negative could be greater in such a case. This situation may also lead to problems in rare cases of intrathyroid parathyroid adenomas.

The fact that all CUs in our study were performed by a highly experienced operator (~100 ultrasound parathyroid scans and 1,200 thyroid ultrasound scans per year) probably explains why the diagnostic values of the ultrasound scan were above those generally described in the literature. The MIBI scintigraphy was performed with injected iodine in our study, thus increasing its diagnostic values compared with other centers. The nuclear medicine physicians were experienced in analyzing ^{18}F -fluorocholine PET/CT cervical images but not for this indication. Nevertheless, the diagnostic values of ^{18}F -fluorocholine PET/CT were higher than those of CU, demonstrating the less operator-dependent nature of this examination than of ultrasound scanning.

The main disadvantages of ^{18}F -fluorocholine PET/CT are the inaccessibility and high cost. Certain authors suggest reserving ^{18}F -fluorocholine PET/CT for when there is a disagreement or negative results with CU and MIBI scintigraphy (6,9,10,20–22). In our study, the results of CU and MIBI scintigraphy were discordant or negative for 50% of cases, and in 97.2% of these situations ^{18}F -fluorocholine PET/CT gave the correct location of hyperfunctional parathyroids. These results reinforce the idea of using ^{18}F -fluorocholine PET/CT alone as a first-line option, as suggested by Bossert et al. (23).

This work had limitations. It was a single-center, retrospective analysis, with the biases that this design entails, especially regarding a center effect. The study included only patients with at least 1 positive image, probably leading to selection of patients with higher biochemical profiles and larger adenomas or hyperplastic glands and excluding patients with milder disease. This effect would inflate the diagnostic accuracy measures. The median weight of resected parathyroids was 1.12 g (range, 0.1–7.5 g), compared with 0.4 g (range, 0.1–10.9 g) in the 103 patients tested in a previous study (15). Nevertheless, the mean preoperative PTH level was 143 pg/mL (range, 39–849 pg/mL), similar to the 145 pg/mL (range, 40–1,076 pg/mL) in that previous study. Moreover, we did not consider in this study patients affected by hyperparathyroidism with normal levels of calcium, even though patients with normal levels of calcium but with symptoms may be scheduled for surgery. The result could be a bias in the accuracy evaluation. For some authors, ^{18}F -fluorocholine PET/CT could be considered a first-line imaging technique for the identification of pathologic parathyroid glands in patients with normocalcemic and hypercalcemic hyperparathyroidism, even when the parathyroid volume is small (22). Furthermore, the order of the examinations was not standardized, and comparisons were not performed with masking of the results of the other imaging techniques. We also did not differentiate the

upper and lower localizations on the imaging results. This distinction is highly subjective and interpreter-dependent, and there is little value to distinguishing between upper and lower because the same surgical approach is used. Making this distinction would have no impact on the different diagnostic values. The ^{18}F -fluorocholine PET/CT acquisition was performed using a 60-min delay after injection, rather than 15 min as chosen by some teams; thus, adenomas with fast tracer washout might have been missed (24). This is relevant in only a small number of cases (potentially 1 in our series). It is essential to pursue this work by performing a complete medicoeconomic study on the 3 techniques.

CONCLUSION

The diagnostic values of ^{18}F -fluorocholine PET/CT found in this study were clearly superior to those of CU and MIBI scintigraphy for preoperative localization of pathologic hyperfunctional parathyroid glands in PHPT. To the best of our knowledge, with 144 patients having undergone surgery, this is the largest comparative cohort in the literature. This superiority seems related to a strong contrast between the uptake of hyperfunctional parathyroids and the neighboring tissue and to a high spatial resolution allowing detection of small or ectopic parathyroids, which may be missed by other imaging techniques. We suggest using ^{18}F -fluorocholine PET/CT as a first-line examination in preference to CU and MIBI scintigraphy.

DISCLOSURE

No potential conflict of interest relevant to this article was reported.

ACKNOWLEDGMENT

We thank Sarah Kabani, medical writer, for editing the manuscript.

KEY POINTS

QUESTION: How does ^{18}F -fluorocholine PET/CT compare with CU, MIBI scintigraphy, or CU + MIBI scintigraphy for diagnostic localization of hyperfunctional parathyroid glands during PHPT?

PERTINENT FINDINGS: In this single-center, retrospective study of 144 patients, ^{18}F -fluorocholine PET/CT had a sensitivity and negative predictive value of over 99.0%, a specificity of 97.0%, and a positive predictive value of 97.3%. These diagnostic values are superior to those of CU and MIBI scintigraphy, alone or combined, and confirm and reinforce—in a larger series of patients—previously published preliminary data.

IMPLICATIONS FOR PATIENT CARE: Previous publications have suggested reserving ^{18}F -fluorocholine PET/CT for situations in which CU + MIBI scintigraphy has failed to detect hyperfunctional thyroids, but our study demonstrated the clear diagnostic superiority of ^{18}F -fluorocholine PET/CT and justifies its use as a first-line technique in suspected PHPT.

REFERENCES

- Fraser WD, William D. Hyperparathyroidism. *Lancet*. 2009;374:145–158.
- Udelsman R, Janice LP, Sturgeon C, Young JEM, Clark OH. Surgery for asymptomatic primary hyperparathyroidism: proceedings of the third international workshop. *J Clin Endocrinol Metab*. 2009;94:366–372.
- Civelek AC, Ozalp E, Donovan P, Udelsman R. Prospective evaluation of delayed technetium-99m sestamibi SPECT scintigraphy for preoperative localization of primary hyperparathyroidism. *Surgery*. 2002;131:149–157.
- Rep S, Lezaic L, Kocjan T, et al. Optimal scan time for evaluation of parathyroid adenoma with [^{18}F]-fluorocholine PET/CT. *Radiol Oncol*. 2015;49:327–333.
- Calzada-Nocaudie M, Chanson P, Conte-Devolx B, et al. Management of asymptomatic primary hyperparathyroidism: French Society of Endocrinology expert consensus. *Ann Endocrinol (Paris)*. 2006;67:7–12.
- Michaud L, Balogova S, Burgess A, et al. A pilot comparison of ^{18}F -fluorocholine PET/CT, ultrasonography and $^{123}\text{I}/^{99\text{mTc}}$ -sestamibi dual-phase dual-isotope scintigraphy in the preoperative localization of hyperfunctioning parathyroid glands in primary or secondary hyperparathyroidism: influence of thyroid anomalies. *Medicine (Baltimore)*. 2015;94:e1701.
- Lezaic L, Rep S, Sever MJ, Kocjan T, Hocevar M, Feticch J. ^{18}F -fluorocholine PET/CT for localization of hyperfunctioning parathyroid tissue in primary hyperparathyroidism: a pilot study. *Eur J Nucl Med Mol Imaging*. 2014;41:2083–2089.
- Thanseer N, Bhadada SK, Sood A, et al. Comparative effectiveness of ultrasonography, $^{99\text{mTc}}$ -sestamibi, and ^{18}F -fluorocholine PET/CT in detecting parathyroid adenomas in patients with primary hyperparathyroidism. *Clin Nucl Med*. 2017;42:e491–e497.
- Michaud L, Burgess A, Huchet V, et al. Is ^{18}F -fluorocholine-positron emission tomography/computerized tomography a new imaging tool for detecting hyperfunctioning parathyroid glands in primary or secondary hyperparathyroidism? *J Clin Endocrinol Metab*. 2014;99:4531–4536.
- Kluijfhout WP, Pasternak JD, Gosnell JE, et al. ^{18}F fluorocholine PET/MR imaging in patients with primary hyperparathyroidism and inconclusive conventional imaging: a prospective pilot study. *Radiology*. 2017;284:460–467.
- Hocevar M, Lezaic L, Rep S, et al. Focused parathyroidectomy without intraoperative parathormone testing is safe after pre-operative localization with ^{18}F -fluorocholine PET/CT. *Eur J Surg Oncol*. 2017;43:133–137.
- Whitman J, Allen I, Bergsland E, et al. Assessment and comparison of ^{18}F -fluorocholine PET and $^{99\text{mTc}}$ -sestamibi scans in identifying parathyroid adenomas: a meta-analysis. *J Nucl Med*. 2021;62:1285–1291.
- Cuderman A, Senica K, Rep S, et al. ^{18}F -fluorocholine PET/CT in primary hyperparathyroidism: superior diagnostic performance to conventional scintigraphic imaging for localization of hyperfunctioning parathyroid glands. *J Nucl Med*. 2020;61:577–583.
- Beheshti M, Hehenwarter L, Paymani Z, et al. ^{18}F -fluorocholine PET/CT in the assessment of primary hyperparathyroidism compared with $^{99\text{mTc}}$ -MIBI or $^{99\text{mTc}}$ -tetrofosmin SPECT/CT: a prospective dual-centre study in 100 patients. *Eur J Nucl Med Mol Imaging*. 2018;45:1762–1771.
- Araz M, Soydal C, Özkan E, et al. The efficacy of fluorine-18-choline PET/CT in comparison with $^{99\text{mTc}}$ -MIBI SPECT/CT in the localization of a hyperfunctioning parathyroid gland in primary hyperparathyroidism. *Nucl Med Commun*. 2018;39:989–994.
- Prabhu M, Kumari G, Damle N, et al. Assessment of the role of early dynamic PET/CT with ^{18}F -fluorocholine in detection of parathyroid lesions in patients with primary hyperparathyroidism. *Nucl Med Commun*. 2018;39:1190–1196.
- Rep S, Hocevar M, Vaupotic J, et al. ^{18}F -choline PET/CT for parathyroid scintigraphy: significantly lower radiation exposure of patients in comparison to conventional nuclear medicine imaging approaches. *J Radiol Prot*. 2018;38:343–356.
- Kluijfhout WP, Vorselaars W, Vriens M, et al. Enabling minimal invasive parathyroidectomy for patients with primary hyperparathyroidism using Tc-99m-sestamibi SPECT-CT, ultrasound and first results of ^{18}F -fluorocholine PET-CT. *Eur J Radiol*. 2015;84:1745–1751.
- Taywade SK, Damle N, Behera A, et al. Comparison of ^{18}F -fluorocholine positron emission tomography/computed tomography and four-dimensional computed tomography in the preoperative localization of parathyroid adenomas: initial results. *Indian J Endocrinol Metab*. 2017;21:399–403.
- Huber GF, Hüßler M, Schmid C, et al. Benefit of ^{18}F -fluorocholine PET imaging in parathyroid surgery. *Eur Radiol*. 2018;28:2700–2707.
- Quak E, Blanchard D, Houdu B, et al. F18-choline PET/CT guided surgery in primary hyperparathyroidism when ultrasound and MIBI SPECT/CT are negative or inconclusive: the APACHI study. *Eur J Nucl Med Mol Imaging*. 2018;45:658–666.
- Grimaldi S, Young J, Kamenicky P, et al. Challenging pre-surgical localization of hyperfunctioning parathyroid glands in primary hyperparathyroidism: the added value of ^{18}F -fluorocholine PET/CT. *Eur J Nucl Med Mol Imaging*. 2018;45:1772–1780.
- Bossert I, Chytiris S, Hodolic M, et al. PET/CT with ^{18}F -choline localizes hyperfunctioning parathyroid adenomas equally well in normocalcemic hyperparathyroidism as in overt hyperparathyroidism. *J Endocrinol Invest*. 2019;42:419–426.
- Petranović Ovcariček P, Giovannella L, Carrió Gasset I, et al. The EANM practice guidelines for parathyroid imaging. *Eur J Nucl Med Mol Imaging*. 2021;48:2801–2822.

Improved Prognosis of Treatment Failure in Cervical Cancer with Nontumor PET/CT Radiomics

Tahir I. Yusufaly¹, Jingjing Zou², Tyler J. Nelson³, Casey W. Williamson⁴, Aaron Simon⁴, Meenakshi Singhal³, Hannah Liu³, Hank Wong³, Cheryl C. Saenz⁵, Jyoti Mayadev^{3,4}, Michael T. McHale⁵, Catheryn M. Yashar⁴, Ramez Eskander⁵, Andrew Sharabi^{3,4}, Carl K. Hoh⁶, Sebastian Obrzut⁶, and Loren K. Mell^{3,4}

¹Russell H. Morgan Department of Radiology and Radiological Sciences, Johns Hopkins University, School of Medicine, Baltimore, Maryland; ²Department of Family Medicine and Public Health and Department of Mathematics, University of California San Diego, La Jolla, California; ³Center for Precision Radiation Medicine, La Jolla, California; ⁴Department of Radiation Medicine and Applied Sciences, University of California San Diego, La Jolla, California; ⁵Department of Obstetrics, Gynecology and Reproductive Sciences, Division of Gynecologic Oncology, University of California San Diego, La Jolla, California; and ⁶Department of Radiology, Division of Nuclear Medicine, University of California San Diego, La Jolla, California

Radiomics has been applied to predict recurrence in several disease sites, but current approaches are typically restricted to analyzing tumor features, neglecting nontumor information in the rest of the body. The purpose of this work was to develop and validate a model incorporating nontumor radiomics, including whole-body features, to predict treatment outcomes in patients with previously untreated locoregionally advanced cervical cancer. **Methods:** We analyzed 127 cervical cancer patients treated definitively with chemoradiotherapy and intracavitary brachytherapy. All patients underwent pretreatment whole-body ¹⁸F-FDG PET/CT. To quantify effects due to the tumor itself, the gross tumor volume (GTV) was directly contoured on the PET/CT image. Meanwhile, to quantify effects arising from the rest of the body, the planning target volume (PTV) was deformably registered from each planning CT to the PET/CT scan, and a semiautomated approach combining seed-growing and manual contour review generated whole-body muscle, bone, and fat segmentations on each PET/CT image. A total of 965 radiomic features were extracted for GTV, PTV, muscle, bone, and fat. Ninety-five patients were used to train a Cox model of disease recurrence including both radiomic and clinical features (age, stage, tumor grade, histology, and baseline complete blood cell counts), using bagging and split-sample-validation for feature reduction and model selection. To further avoid overfitting, the resulting models were tested for generalization on the remaining 32 patients, by calculating a risk score based on Cox regression and evaluating the c-index (c-index > 0.5 indicates predictive power). **Results:** Optimal performance was seen in a Cox model including 1 clinical biomarker (whether or not a tumor was stage III-IVA), 2 GTV radiomic biomarkers (PET gray-level size-zone matrix small area low gray level emphasis and zone entropy), 1 PTV radiomic biomarker (major axis length), and 1 whole-body radiomic biomarker (CT bone root mean square). In particular, stratification into high- and low-risk groups, based on the linear risk score from this Cox model, resulted in a hazard ratio of 0.019 (95% CI, 0.004, 0.082), an improvement over stratification based on clinical stage alone, which had a hazard ratio of 0.36 (95% CI, 0.16, 0.83). **Conclusion:** Incorporating nontumor radiomic biomarkers can improve the performance of prognostic models compared with using only clinical and tumor radiomic biomarkers. Future work should look to further test these models in larger, multi-institutional cohorts.

Key Words: oncology; GYN; PET/CT; statistical; analysis; cervical cancer; outcomes; radiomics; whole-body

J Nucl Med 2022; 63:1087–1093
DOI: 10.2967/jnumed.121.262618

Radiomics is the application of machine learning methods to extract clinically useful information from medical imaging datasets, with an emphasis on systematic, high-throughput mining of “big data” (1–4). Radiomics classifiers have been previously found to enhance prognostic modeling for lung (5,6) and head and neck (7,8) cancers. Recently, this approach has also been applied to cervical cancer, where it has been observed that various radiomic features of the tumor periphery and vascular invasion from PET/MRI are prognostic for locoregional recurrence (9–17). However, PET/MRI machines are not always accessible, particularly in underresourced settings, compared with more established PET/CT techniques (18).

In addition, radiomic analyses in oncology have investigated the predictive information encoded in tumor features, whereas nontumor features, particularly those related to whole-body structures such as bone, bone marrow, fat, muscle, and other organs, have been less studied, although it is worth mentioning a notable recent exception (19), where PET bone marrow features predicted treatment outcome in locally advanced cervical cancer. More generally, such whole-body features may be associated with immune system function, thereby influencing cancer outcomes (20,21). For example, sarcopenia is associated with the release of inflammatory cytokines, such as tumor necrosis factor and interleukin-6 (22), and is a putative marker of disease severity and predictor of outcomes in women with cancer (23,24). Along the same lines, obesity and inflamed adipose tissue are known to impact systemic inflammatory markers and alter the tumor microenvironment (25). Such observations indicate the potential of whole-body imaging, and more generally nontumor features, to provide additional prognostic information beyond that available from tumor features alone. Whole-body PET/CT, with its relatively low cost and widespread availability, is an example of an imaging modality that could provide such information in a cost-effective manner.

Presently, risk-stratification in cervical cancer predominantly depends on clinical examination and standard imaging evaluations.

Received May 21, 2021; revision accepted Oct. 20, 2021.
For correspondence or reprints, contact Tahir I. Yusufaly (tyusufa2@jhmi.edu).

Published online Oct. 28, 2021.

COPYRIGHT © 2022 by the Society of Nuclear Medicine and Molecular Imaging.

Treatment failures are common, particularly in patients with locoregionally advanced disease, where rates of disease progression may be 30% or more (26). Improved methods to risk-stratify patients with cervical cancer are needed, to appropriately select patients for intensive treatment approaches and identify patients who may selectively benefit from novel therapeutic strategies, such as immunotherapy (27). We therefore sought to determine whether nontumor radiomic features associated with treatment outcomes could be identified in cervical cancer patients undergoing treatment with chemoradiotherapy and imaged using whole-body PET/CT.

MATERIALS AND METHODS

Study Design, Population, and Sampling Methods

The University of California San Diego institutional review board approved this retrospective cohort study and the requirement to obtain informed consent was waived. We initially identified 245 patients with newly diagnosed, previously untreated, biopsy-proven locoregionally advanced (stage IB–IVA) carcinoma of the cervix treated with chemoradiotherapy at our institution between April 2006 and September 2019. We included patients who underwent pretreatment ^{18}F -FDG PET/CT (PET/CT) and treatment with intensity-modulated radiation therapy (IMRT) followed by intracavitary brachytherapy, resulting in a final cohort of 127 patients (Fig. 1).

The 127-patient cohort was divided into a training set of 95 patients (75%) and a test set of 32 patients (25%), with 23 and 7 events, respectively. The choice of a 75–25 split was made on the basis of a desire to maintain a sufficient number of events in the training set to be able to adequately train radiomics-based predictors while still keeping enough events in the test set to validate the models. It is important to note that this choice is somewhat arbitrary and, therefore, any conclusions made from model training and validation must be carefully assessed for robustness using extensive bootstrap resampling methods.

Model training and validation consisted of 4 steps region-of-interest (ROI) definition and feature extraction in the entire cohort, identification

of robust features in the training set, forward stepwise feature selection from the subset of robust features, and model validation based on comparison of *c*-indices in the training set and test set. The primary outcome was time from diagnosis to first instance of locoregional or distant cancer recurrence, or censoring, whichever occurred first.

PET/CT Imaging Methods

The pretreatment PET/CT images were acquired on analog Discovery (GE Healthcare) machines, with CT images constructed using filtered backprojection reconstruction for $512 \times 512 \times 1$ voxels and PET images constructed with 1 of 2 settings: ordered-subset expectation maximization (OSEM) reconstruction, with 20 subsets and 2 iterations, using a 4.0-mm gaussian filter cutoff, a 128×128 matrix, and a lutetium-yttrium oxyorthosilicate (LYSO) crystal; or OSEM reconstruction with time-of-flight measurements and point-spread function modeling (VUE Point FX; GE Healthcare), with 24 subsets and 2 iterations, using a 5.0-mm gaussian filter cutoff, a 192×192 matrix, a 9×6 LYSO crystal, and Sharp iterative reconstruction quantitation.

ROI Definitions

We generated ROI segmentations using the workflow illustrated in Figure 1. Three clinical experts manually contoured the gross tumor volume (GTV) for each patient based on the presence of focal hypermetabolic activity within the cervix as well as CT-based anatomic evidence of the primary mass lesion. Grossly involved lymph nodes were not included in the GTV for this study. Additionally, a planning target volume (PTV) consisting of the gross tumor, cervix, uterus, parametria, and pelvic lymph nodes, with a 5- to 15-mm planning margin, were defined on the simulation CT scan by the treating radiation oncologist (5 different radiation oncologists in total), then registered to the whole-body PET/CT using deformable image registration implemented in MIM Maestro (MIM Software Inc.) (28).

For whole-body ROI segmentations, we used a semiautomated approach combining seed-growing (29) and manual editing for muscle contours (Fig. 2). Seed-growing settings were defined as follows: bone – lower bound: 100 Hounsfield units (HU), upper bound: 1,129 HU, tendril diameter: 1 cm, filling level: none; fat – lower bound: –157 HU, upper bound: –123 HU, tendril diameter: 3 cm, filling level: medium; muscle – lower bound: –23 HU, upper bound: 142 HU, tendril diameter: 3 cm, filling level: medium. Additionally, to differentiate skeletal muscle from other smooth or cardiac muscle, further manual editing of the muscle contour was performed. To do this, an exclusion region was generated consisting of internal organs interior to the rib cage and body wall, extending craniocaudally from the trachea to the vagina, and laterally to encompass the breasts (and implants, if present), lungs, and mediastinal contents at the thoracic level, the abdominal organs at the abdominal level, and the reproductive organs at the pelvic level. The psoas muscles were included in the muscle volume rather than in the exclusion region.

Feature Extraction

Radiomics features were extracted using the PyRadiomics (30) software package (version 3.0). For each of the 5 structures (GTV, PTV, bones, muscle, and fat), we calculated all non-redundant features available in PyRadiomics. PyRadiomics can calculate up to 111 features for a given contour and image (17 shape,

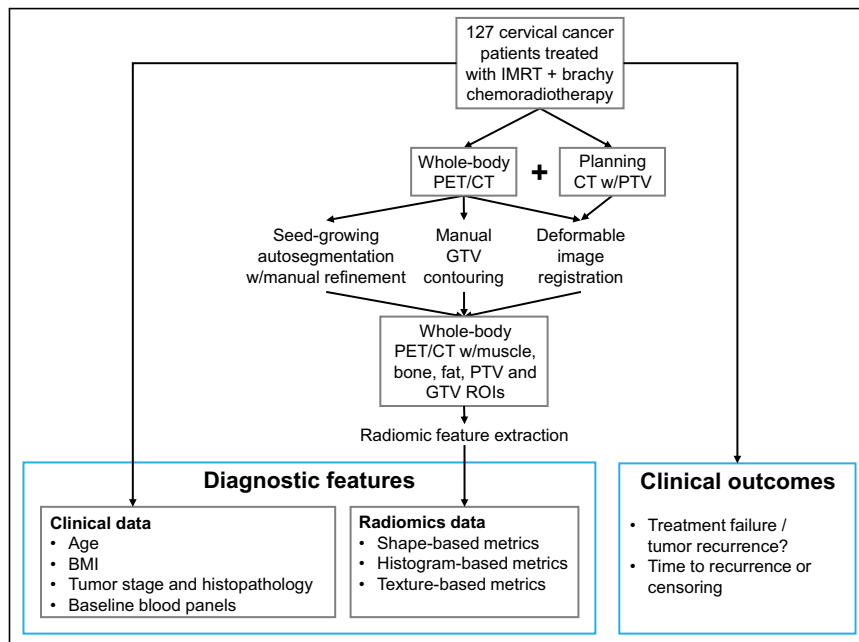


FIGURE 1. Workflow for patient sampling, segmentation, and extraction of high-throughput radiomic features for downstream analysis. BMI = body mass index; Brachy = Brachytherapy; IMRT = intensity-modulated radiation therapy; PET/CT = ^{18}F -FDG PET/CT; ROI = region of interest.

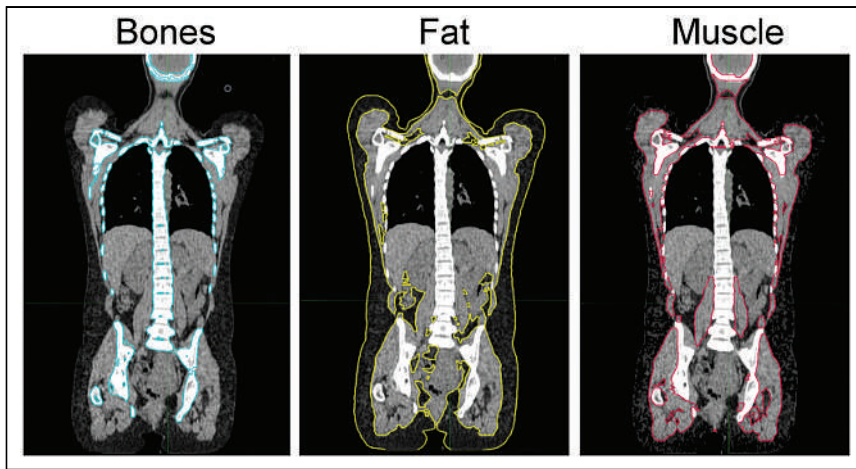


FIGURE 2. Sample output from autosegmentation of whole-body bone, fat, and muscle contours (with manual muscle contour refinement).

19 first-order, 24 gray level correlation matrix [GLCM], 16 gray level run-length matrix [GLRLM], 16 gray level size-zone matrix [GLSZM], 14 gray level difference matrix [GLDM], 5 neighboring gray tone difference matrix [NGTDM]). Of these, 4 shape features can be excluded for redundancy reasons: voxel volume, which is just an approximation of mesh volume, and compactness 1, compactness 2 and spheric disproportion, all of which are completely determined by sphericity. Two first-order features can similarly be ignored: total energy, which is completely determined by the energy and the mesh volume, and the SD, which is just the square root of the variance. Finally, 2 GLCM features, dissimilarity and homogeneity 2, are likewise deprecated as they are equal to the difference average and inverse difference moment, respectively.

These redundancy restrictions result in 193 total features per structure, including 13 shape features and 90 each of CT-based and PET-based intensity features (17 first-order, 22 GLCM, 16 GLRLM, 16 GLSZM, 14 GLDM, 5 NGTDM), resulting in 965 radiomic features. All CT images were resampled, using B-spline interpolation (the default for PyRadiomics), to a $0.98 \times 0.98 \times 2.5$ mm resolution, and all PET images were resampled to a $5.47 \times 5.47 \times 3.27$ mm resolution, based on the lowest resolutions of PET and CT images in the dataset. Radiomic features were extracted using a 25 HU fixed bin width for CT and a 0.5 SUV fixed bin width for PET, based on recommendations from previous radiomic studies (31–34). Notably, choosing the highest resolution PET and CT dimensions results in anisotropic voxels, which previous studies have shown can influence some features, particularly those related to texture matrices (35). Future work systematically assessing how results change with voxel geometry, as well as with use of alternative spline interpolation schemes, is merited. Nevertheless, to the extent that using a consistent choice of settings identifies robust predictors, any findings from this study remain valuable and accessible to the broader community, as long as users make sure to exactly reproduce the extraction settings that are used here.

We also extracted 9 baseline clinical features: age at diagnosis (y), body mass index (kg/m^2), tumor histopathology (adenocarcinoma vs. squamous cell carcinoma), stage (I-II vs. III-IVA), and baseline complete blood counts (white blood cells [$\text{k}/\mu\text{L}$], neutrophils [$\text{k}/\mu\text{L}$], hemoglobin [g/dL], and platelets [$\text{k}/\mu\text{L}$]), resulting in 974 candidate features for prediction.

Feature Reduction

To prevent model overfitting and numeric instability due to noise, we first sought to confine our initial set of 974 features to a subset of

features that were significantly associated with recurrence. Feature reduction was accomplished through a “bagging” procedure (36). Each bag consisted of a random subset of 57 patients from the training set, with the “out-of-bag” sample consisting of the remaining 38 patients from the training set. For each of the 974 features, we used the bagged subset to train a univariate Cox proportional hazards model, with a single regression coefficient. This process was repeated for 1,000 different bagging subsets, resulting in a $974 \times 1,000$ matrix of feature coefficients. From this matrix, 99% CIs for each of the 974 coefficients were computed. A feature was defined as robust if the 99% CI excluded zero, indicating a statistically significant association with outcome, for a P value cutoff of 0.01. This process resulted in a final set of robust features (hereafter, candidate biomarkers) from the initial feature set. A table

of univariate hazard ratios and CIs resulting from this procedure is shown in the Supplemental Table 1 (supplemental materials are available at <http://jnm.snmjournals.org>), for all the clinical features as well as for all robust radiomic biomarkers.

TABLE 1
Sample Characteristics for Training and Test Sets

Characteristic	Training set	Test set
<i>n</i> (no. of events)	95 (23)	32 (7)
Stage (<i>n</i>)		
IA	2 (2%)	0
IB	23 (24%)	10 (31%)
IIA	7 (7%)	3 (9%)
IIB	32 (33%)	9 (28%)
IIIA	3 (3%)	0
IIIB	16 (17%)	5 (16%)
IIIC	6 (6%)	2 (6%)
IVA	6 (6%)	1 (4%)
IVB	0	2 (6%)
Histology (<i>n</i>)		
Adenocarcinoma	23 (24%)	12 (38%)
Squamous carcinoma	72 (76%)	20 (62%)
Clinical features*		
Age (y)	50.6 (13.7)	49.0 (12.9)
BMI (kg/m^2)	29.0 (6.5)	28.3 (6.8)
Baseline WBC ($\text{k}/\mu\text{L}$)	8.23 (3.26)	7.98 (3.46)
Baseline ANC ($\text{k}/\mu\text{L}$)	5.39 (2.75)	5.45 (3.17)
Baseline hemoglobin (g/dL)	11.6 (1.8)	11.3 (1.5)
Baseline platelet count ($\text{k}/\mu\text{L}$)	288 (79)	279 (109)

*Data for clinical features are mean, with SD in parentheses.

BMI = body mass index; WBC = white blood cell count; ANC = absolute neutrophil count.

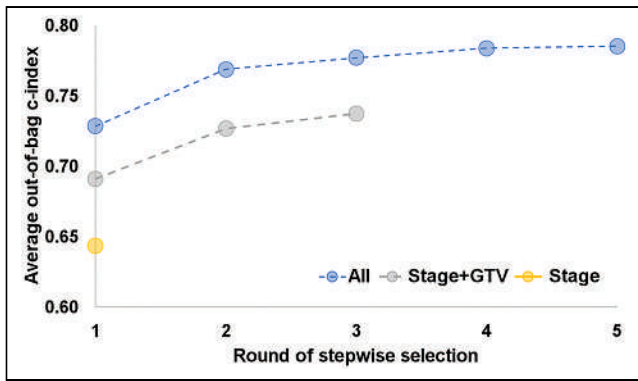


FIGURE 3. Bootstrap averaged out-of-bag (OOB) c-indices during model training, as a function of the number of biomarkers successively added in the forward stepwise selection. Data are shown for selection on only nonradiomic biomarkers (there is only 1, stage, so the stepwise selection trivially stops after 1 round), selection on stage and GTV radiomic biomarkers, and selection on all biomarkers. As the pool of biomarkers available for selection increases, the average OOB c-index at each round likewise increases, and the stepwise selection takes more rounds to reach an optimum. These results suggest that tumor radiomic information, as encoded in the GTV features, adds predictive power beyond that available with just TNM staging, and that off-tumor radiomic information, as encoded in all the other non-GTV features, further adds predictive power beyond that.

Forward Stepwise Feature Selection and Final Model Selection and Validation

We next sought to identify an optimal subset of candidate biomarkers to include as variables in a final Cox model. Potential model variables were selected from the candidate biomarkers using forward stepwise selection. We ran 100 split-sample validations for a model that included a candidate biomarker that we were considering adding to our model. We generated the corresponding 95% CI for each of the model coefficients, as well as the corresponding average out-of-bag c-indices. Additional biomarkers were included in the final model, if they increased the out-of-bag c-index while also maintaining model stability (i.e., the 95% CI for the coefficient estimates for all the model covariates excluded 0). This process was iteratively repeated until either the c-index peaked or there were no more biomarkers that could be stably added. To isolate the effects of tumor radiomic features, and thereby assess the added value of nontumor radiomic information, we repeated the stepwise selection considering only clinical and GTV radiomic biomarkers.

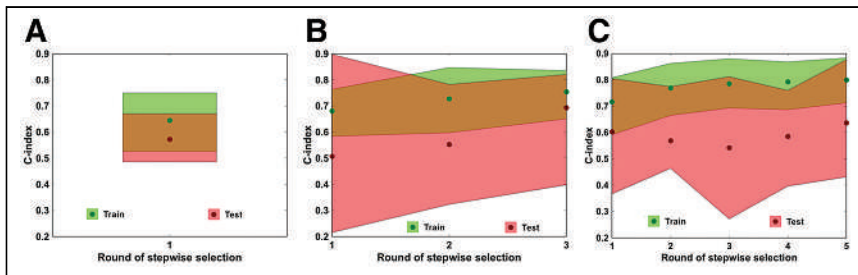


FIGURE 4. 95% CIs for c-index estimates, on both training and test set data, as a function of the number of features successively added in the forward stepwise selection. Results are shown for stepwise selection with stage only (A), stage and GTV biomarkers (B), and all biomarkers (C). The c-index distributions, from which the 95% CI can be determined, are calculated by bootstrap resampling of both the train and the test data. Circular points indicate median values, and color coded bounds indicate upper and lower CI limits, with green corresponding to results for the training set and red corresponding to results for the test set.

Lastly, a Cox model was trained on the entire ($n = 95$) training set using the subset of optimal biomarkers selected on each round of forward stepwise selection and evaluated on the unseen test set ($n = 32$) to test for generalization and overfitting, based on the c-index. To estimate the uncertainty of the c-index, we generated 100 bootstrap resamples each on both the training and the test sets. The likelihood ratio for goodness-of-fit while accounting for Bonferroni multiple-hypothesis-testing corrections as well as the proportional hazards assumption were both tested using the package “survival” (version 3.2-3) in R (R Core Team and R Project for Statistical Computing; www.r-project.org) (37). All P values were 2-sided unless otherwise indicated.

RESULTS

Sample characteristics are given in Table 1. The median follow-up time was 2.12 y in the training set and 2.42 y in the test set.

Following our feature reduction process, the final feature set included 42 candidate biomarkers: 1 clinical biomarker (stage III-IVA vs. I-II), 9 PTV radiomic biomarkers (6 shape, 1 CT-based, 2 PET-based), 13 GTV radiomic biomarkers (1 shape, 1 CT-based, 11 PET-based), 5 muscle radiomic biomarkers (3 shape, 2 CT-based), 10 bone radiomic biomarkers (8 CT-based, 2 PET-based), and 4 fat radiomic biomarkers (1 shape, 3 CT-based). Supplemental Figure 1 shows a hierarchical clustering dendrogram and labeled heat map of these biomarkers, based on the cosine similarity distance, indicating a high degree of collinearity and redundancy.

The forward stepwise selection process resulted in an out-of-bag c-index that peaked after 5 rounds of feature addition, as shown in Figure 3. Furthermore, comparison with the corresponding stepwise selection using only the stage and GTV radiomic biomarkers demonstrated that the prognostic value from nontumor radiomics was additive to tumor radiomics, as this reduced stepwise selection peaked after only 3 rounds and at each round had an out-of-bag c-index consistently lower than the corresponding c-index that could be obtained when including all biomarkers.

As shown in Figure 4, bootstrap resampling to estimate the c-index distributions indicated that the 95% CIs for both the training- and the test-set c-indices overlapped at all rounds of stepwise selection. However, it is imperative to note that the CIs, particularly for the test set, are quite substantial due to the small number of events.

The resulting 5 biomarkers in the model are a categorical biomarker that is 0 if the disease is stage I-II and 1 if it is stage III-IVA (mean: 0.32, SD: 0.47); PTV Major Axis Length (mean: 206 mm, SD: 46 mm); CT bone root mean square (mean: 1,394.5 HU, SD: 97.5 HU); PET GTV GLSZM Small Area Low gray Level Emphasis, hereafter SALGLE (mean: 0.045, SD: 0.046); and PET GTV GLSZM Zone Entropy (mean: 5.16, SD: 1.09). Reassuringly, when the stepwise selection is repeated considering only the subset of stage and GTV biomarkers, the resulting 3 biomarkers that emerge are the same categorical stage biomarker and 2 PET GTV GLSZM biomarkers that are found in the full stepwise selection. Model estimates are displayed in Table 2. The likelihood ratio for the Cox model using all 5 biomarkers is $1.0E-05$, whereas for the Cox model using only stage and the 2 GTV biomarkers it is $3.8E-04$, both indicating statistically

TABLE 2
Cox Model Hazard Ratio Estimates

Biomarker	Hazard ratio (95% CI)	<i>P</i> (coefficients)	<i>P</i> (PH assumption)
Optimal 5-biomarker model*			
Stage III–IV (vs. I–II)	1.65 (1.04, 3.23)	<0.01	0.85
CT PTV major axis length	1.97 (1.29, 3.33)	<0.01	0.02
CT bone root mean square	3.39 (1.57, 12.55)	<0.01	0.31
PET GTV GLSZM SALGLE	0.15 (0.01, 0.56)	<0.01	0.07
PET GTV GLSZM zone entropy	0.38 (0.10, 0.91)	<0.01	0.06
3-biomarker model†			
Stage III–IV (vs. I–II)	2.01 (1.37, 3.28)	<0.01	0.87
PET GTV GLSZM SALGLE	0.18 (0.04, 0.48)	<0.01	0.11
PET GTV GLSZM zone entropy	0.54 (0.24, 0.99)	<0.01	0.12

*Cox model hazard ratio estimates from the training set, for the optimal 5-biomarker model, for the endpoint of disease recurrence, along with *P* values of the coefficients (all less than 0.01), as well as *P* values testing the proportional hazards assumption (all greater than 0.01). All model inputs were normalized to the training set SD.

†Corresponding estimates for the 3-biomarker model that results when only considering stage and GTV biomarkers during stepwise selection.

PH = proportional hazards.

significant goodness-of-fit even when accounting for Bonferroni multiple-hypothesis-testing corrections. All variables satisfied the proportional hazards assumption ($P > 0.01$), and a 1-way ANOVA test (Supplemental Table 2) indicated that none of the selected biomarkers have a statistically significant dependence on acquisition mode or interrater PTV and GTV segmentation variability ($P > 0.05$).

The radiomics-based Cox model demonstrates great potential for prognosis and risk stratification, as demonstrated by the results

shown in Figures 5 and 6. The predicted receiver-operating-characteristic curve for 2-y cancer recurrence, for Cox models both with and without nontumor radiomic biomarkers, lies above the diagonal, and the Kaplan–Meier curves stratifying patients into high- and low-risk groups yields improved hazard ratio estimates compared with stratification based on early- and late-stage groups.

DISCUSSION

Our results suggest that a radiomics model incorporating nontumor radiomic biomarkers leads to improved prognostic modeling of cancer recurrence, compared with using clinical and tumor radiomic biomarkers alone. A novel aspect of our study is the inclusion of semiautomatable whole-body radiomic features as candidate biomarkers for outcome prediction. In addition, whereas much work has been done in identifying CT radiomic biomarkers, the incorporation of PET radiomics remains relatively challenging (38–40), due in part to issues related to feature reproducibility (41) and optimal feature selection in the presence of highly redundant features (42). The approach we developed here has identified 2 PET-based biomarkers of the GTV that seem to be robustly correlated to outcome.

Limitations of this study include the single-institution data source and the size of our cohort, with relatively few total recurrence events. Despite our extensive efforts to maintain quality control (Supplemental Table 3 shows the calculated radiomics quality score (2) for this study) and to cull spurious radiomic features, given the persistent possibility of model overfitting, future work to assess the prognostic power of our results on a larger multiinstitutional cohort is needed to validate the particular predictive model developed in this study. Second, to confine the initial candidate feature set, we focused on particular whole-body features related to bone, fat, and muscle, reasoning that these metrics could reflect variation in patients' global inflammatory state. Further analysis to study radiomic features of other organs, including other reticuloendothelial organs (liver, spleen) would be of interest. Further

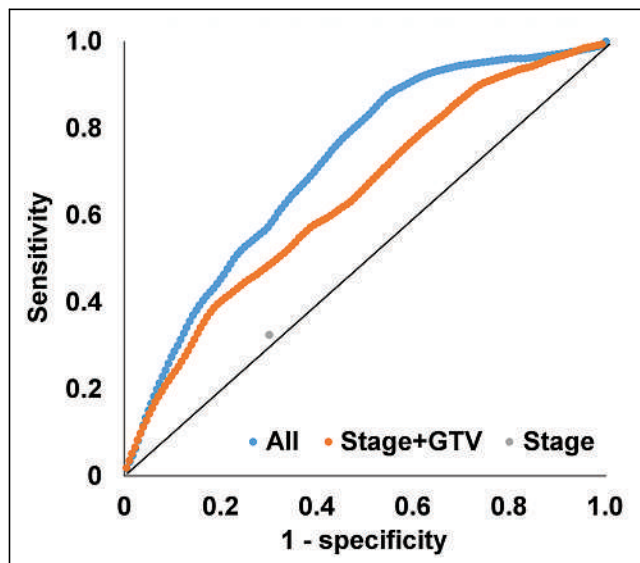


FIGURE 5. Two-year receiver-operating-characteristic curve for model based on stage only, stage + GTV radiomic biomarkers, and all biomarkers, evaluated on the entire 127-patient cohort. Solid black line corresponds to an area under the curve of 0.5, indicating no predictive performance.

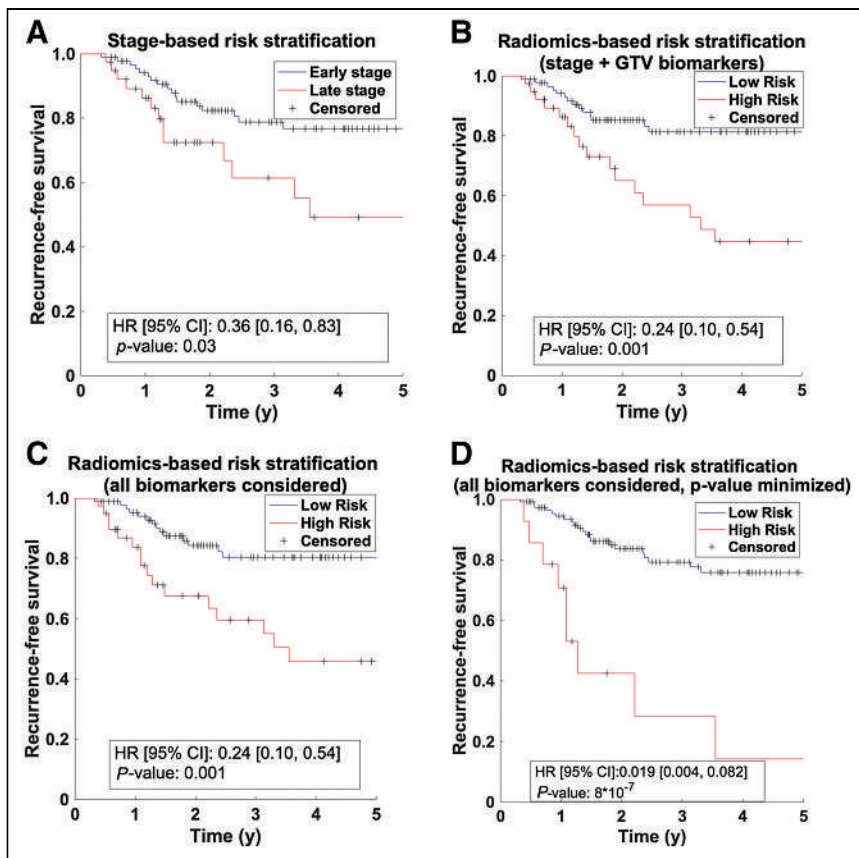


FIGURE 6. (A) Kaplan–Meier curve based on stratification into early- and late-stage groups. We also list a hazard ratio (HR), with 95% CI and logrank *P* value. (B) Corresponding Kaplan–Meier curve showing stratification into high- and low-risk groups, based on a stage + GTV radiomic risk score cutoff. The cutoff that minimizes the *P* value, by coincidence, happens to be at a value such that the number of data points in the high- and low-risk groups equals the corresponding number of late- and early-stage cases. (C) Corresponding Kaplan–Meier curve based on the risk score that fully incorporates stage, GTV radiomic, and non-GTV radiomic biomarkers. The cutoff is chosen so that the number of data points in the high- and low-risk groups equals the corresponding number of late- and early-stage cases. (D) Kaplan–Meier stratification with the model in C but with the cutoff chosen to minimize the *P* value.

extensions to this study could include augmenting radiomic information with additional molecular-level details, as in radiogenomics (43,44), or more detailed examination of the 3D spatial dose distribution (45).

The radiomic predictors we have identified in this work all demonstrate relationships to clinically interpretable physiologic information as identified in previous studies. The PTV Major Axis Length is probably the easiest to understand, being approximately a higher resolution version of tumor stage. A 1-way ANOVA test found that early- and late-stage patients had different mean values of this metric with a *P* value < 1E–05.

We found 2 PET-based metrics, namely the GTV GLSZM SALGLE, which measures the abundance of small-volume, low-activity “patches,” and the GTV GLSZM zone entropy (46), a measure of textural heterogeneity known to be predictive of outcome. Interestingly, these 2 metrics have a significant, but not perfect, negative correlation ($\rho = -0.76$). This strong association suggests that the SALGLE combined with the zone entropy capture certain specific aspects of metabolic heterogeneity in and around the tumor microenvironment that are most directly predictive of outcome. Encouragingly, these textural metrics are also

similar to a class of PET/MRI radiomic biomarkers that were recently identified (15) and externally validated (16) by Lucia et al. More broadly, this finding is consistent with the established result, both in radiomics and in the oncology community more generally, that metabolic heterogeneity is predictive of cancer recurrence (10,47–49).

The final predictor, the CT Bone Root Mean Square, is probably the most novel one. We found that although age and skeletal muscle volume, as candidate prognostic factors, did not withstand our feature selection algorithm, both were strongly associated with the key bone radiomic metric that did come through (CT Bone Root Mean Square). This suggests that the Root Mean Square CT Bone Number is associated with age-related degeneration of skeletal muscle, as occurs in sarcopenia, a known correlate with inflammation (50,51), which in turn has been shown to be predictive of outcome in locally advanced cervical cancer when combined with PET metrics (19). In fact, multiple studies have found that bone and muscle undergo endocrine crosstalk (52–54), leading some to even suggest that sarcopenia in skeletal muscle and osteoporosis in bones might just be 2 sides of the same underlying condition (55).

CONCLUSION

In summary, we found that incorporating radiomic features, including both tumor and nontumor metrics, improved prognostic modeling of disease recurrence in cervical cancer patients compared with using clinical information alone.

KEY POINTS

QUESTION: Can radiomic models that incorporate pretreatment nontumor PET/CT features improve the prognosis of treatment failure in locoregionally advanced cervical cancer patients, compared with models that use only clinical variables or tumor radiomic features?

PERTINENT FINDINGS: In a retrospective analysis of a single-institutional cohort of 127 patients, optimal performance was seen in a Cox model including 1 clinical staging biomarker, 1 shape feature of the PTV, 2 PET-based features of the GTV, and 1 CT-based feature of whole-body bone segmentation. Stratification into high- and low-risk groups, based on the linear risk score from this Cox model, resulted in a statistically significant improvement in the hazard ratio relative to stratification based on clinical stage alone.

IMPLICATIONS FOR PATIENT CARE: These findings indicate that incorporating nontumor PET/CT radiomic information can improve prognosis of cervical cancer patients undergoing standard-of-care treatment and also identify patients who may benefit from alternative or more intensive treatment regimens.

REFERENCES

- Gillies RJ, Kinahan PE, Hricak H. Radiomics: images are more than pictures, they are data. *Radiology*. 2016;278:563–577.
- Lambin P, Leijenaar RTH, Deist TM, et al. Radiomics: the bridge between medical imaging and personalized medicine. *Nat Rev Clin Oncol*. 2017;14:749–762.
- Sanduleanu S, Woodruff HC, de Jong EEC, et al. Tracking tumor biology with radiomics: a systematic review utilizing a radiomics quality score. *Radiother Oncol*. 2018;127:349–360.
- Aerts HJWL. The potential of radiomic-based phenotyping in precision medicine: a review. *JAMA Oncol*. 2016;2:1636.
- Wu W, Parmar C, Grossmann P, et al. Exploratory study to identify radiomics classifiers for lung cancer histology. *Front Oncol*. 2016;6:71.
- Grossmann P, Stringfield O, El-Hachem N, et al. Defining the biological basis of radiomic phenotypes in lung cancer. *eLife*. 2017;6:e23421.
- Parmar C, Grossmann P, Rietveld D, Rietbergen MM, Lambin P, Aerts HJWL. Radiomic machine-learning classifiers for prognostic biomarkers of head and neck cancer. *Front Oncol*. 2015;5:272.
- Elhalawani H, Lin TA, Volpe S, et al. Machine learning applications in head and neck radiation oncology: lessons from open-source radiomics challenges. *Front Oncol*. 2018;8:294.
- Rao YJ, Grigsby PW. The role of PET imaging in gynecologic radiation oncology. *PET Clin*. 2018;13:225–237.
- Hao H, Zhou Z, Li S, et al. Shell feature: a new radiomics descriptor for predicting distant failure after radiotherapy in non-small cell lung cancer and cervix cancer. *Phys Med Biol*. 2018;63:095007.
- Fang M, Kan Y, Dong D, et al. Multi-habitat based radiomics for the prediction of treatment response to concurrent chemotherapy and radiation therapy in locally advanced cervical cancer. *Front Oncol*. 2020;10:563.
- Li Z, Li H, Wang S, et al. MR-based radiomics nomogram of cervical cancer in prediction of the lymph-vascular space invasion preoperatively: preoperative prediction of LVSI. *J Magn Reson Imaging*. 2019;49:1420–1426.
- Han K, Welch M, Weiss J, Pintilie M, Fyles TW, Milosevic M. An MRI-based radiomic signature for disease-free survival in locally advanced cervical cancer. *Int J Radiat Oncol Biol Phys*. 2018;102:S84.
- Reuzé S, Orhac F, Chargari C, et al. Prediction of cervical cancer recurrence using textural features extracted from ¹⁸F-FDG PET images acquired with different scanners. *Oncotarget*. 2017;8:43169–43179.
- Lucia F, Visvikis D, Desseroit M-C, et al. Prediction of outcome using pretreatment ¹⁸F-FDG PET/CT and MRI radiomics in locally advanced cervical cancer treated with chemoradiotherapy. *Eur J Nucl Med Mol Imaging*. 2018;45:768–786.
- Lucia F, Visvikis D, Vallières M, et al. External validation of a combined PET and MRI radiomics model for prediction of recurrence in cervical cancer patients treated with chemoradiotherapy. *Eur J Nucl Med Mol Imaging*. 2019;46:864–877.
- Ferreira M, Lovinfosse P, Hermesse J, et al. [¹⁸F]FDG PET radiomics to predict disease-free survival in cervical cancer: a multi-scanner/center study with external validation. *Eur J Nucl Med Mol Imaging*. 2021;48:3432–3443.
- Ehman EC, Johnson GB, Villanueva-Meyer JE, et al. PET/MRI: where might it replace PET/CT? *J Magn Reson Imaging*. 2017;46:1247–1262.
- Schernberg A, Reuze S, Orhac F, et al. A score combining baseline neutrophilia and primary tumor SUVpeak measured from FDG PET is associated with outcome in locally advanced cervical cancer. *Eur J Nucl Med Mol Imaging*. 2018;45:187–195.
- Aggarwal BB, Gehlot P. Inflammation and cancer: how friendly is the relationship for cancer patients? *Curr Opin Pharmacol*. 2009;9:351–369.
- Brenner DR, Scherer D, Muir K, et al. A review of the application of inflammatory biomarkers in epidemiologic cancer research. *Cancer Epidemiol Biomarkers Prev*. 2014;23:1729–1751.
- Bian A-L, Hu H-Y, Rong Y-D, Wang J, Wang J-X, Zhou X-Z. A study on relationship between elderly sarcopenia and inflammatory factors IL-6 and TNF- α . *Eur J Med Res*. 2017;22:25.
- Lee J, Chang C-L, Lin J-B, et al. Skeletal muscle loss is an imaging biomarker of outcome after definitive chemoradiotherapy for locally advanced cervical cancer. *Clin Cancer Res*. 2018;24:5028–5036.
- Caan BJ, Cespedes Feliciano EM, Prado CM, et al. Association of muscle and adiposity measured by computed tomography with survival in patients with nonmetastatic breast cancer. *JAMA Oncol*. 2018;4:798.
- Iyengar NM, Gucalp A, Dannenberg AJ, Hudis CA. Obesity and cancer mechanisms: tumor microenvironment and inflammation. *J Clin Oncol*. 2016;34:4270–4276.
- Bandyopadhyay A, Mukherjee U, Ghosh S, Ghosh S, Sarkar SK. Pattern of failure with locally advanced cervical cancer: a retrospective audit and analysis of contributory factors. *Asian Pac J Cancer Prev*. 2018;19:73–79.
- Chen R, Gong Y, Zou D, Wang L, Yuan L, Zhou Q. Correlation between subsets of tumor-infiltrating immune cells and risk stratification in patients with cervical cancer. *PeerJ*. 2019;7:e7804.
- Kirby N, Chuang C, Ueda U, Pouliot J. The need for application-based adaptation of deformable image registration: Need for application-based adaptation of deformable registration. *Med Phys*. 2013;40:011702.
- Adams R, Bischof L. Seeded region growing. *IEEE Trans Pattern Anal Mach Intell*. 1994;16:641–647.
- van Griethuysen JJM, Fedorov A, Parmar C, et al. Computational radiomics system to decode the radiographic phenotype. *Cancer Res*. 2017;77:e104–e107.
- Kadoya N, Tanaka S, Kajikawa T, et al. Homology-based radiomic features for prediction of the prognosis of lung cancer based on CT-based radiomics. *Med Phys*. 2020;47:2197–2205.
- Welch ML, McIntosh C, Haibe-Kains B, et al. Vulnerabilities of radiomic signature development: the need for safeguards. *Radiother Oncol*. 2019;130:2–9.
- Foley KG, Hills RK, Berthon B, et al. Development and validation of a prognostic model incorporating texture analysis derived from standardised segmentation of PET in patients with oesophageal cancer. *Eur Radiol*. 2018;28:428–436.
- Leijenaar RTH, Nalbantov G, Carvalho S, et al. The effect of SUV discretization in quantitative FDG-PET Radiomics: the need for standardized methodology in tumor texture analysis. *Sci Rep*. 2015;5:11075.
- Lee S-H, Cho H, Lee HY, Park H. Clinical impact of variability on CT radiomics and suggestions for suitable feature selection: a focus on lung cancer. *Cancer Imaging*. 2019;19:54.
- Breiman L. Bagging predictors. *Mach Learn*. 1996;24:123–140.
- Grambsch PM, Therau TM. Proportional hazards tests and diagnostics based on weighted residuals. *Biometrika*. 1994;81:515–526.
- Cook GJR, Azad G, Owczarczyk K, Siddique M, Goh V. Challenges and promises of PET radiomics. *Int J Radiat Oncol Biol Phys*. 2018;102:1083–1089.
- Lv W, Yuan Q, Wang Q, et al. Radiomics analysis of PET and CT components of PET/CT imaging integrated with clinical parameters: application to prognosis for nasopharyngeal carcinoma. *Mol Imaging Biol*. 2019;21:954–964.
- Lv W, Ashrafinia S, Ma J, Lu L, Rahmim A. Multi-level multi-modality fusion radiomics: application to PET and CT imaging for prognostication of head and neck cancer. *IEEE J Biomed Health Inform*. 2020;24:2268–2277.
- Papp L, Rausch I, Grahovac M, Hacker M, Beyer T. Optimized feature extraction for radiomics analysis of ¹⁸F-FDG PET imaging. *J Nucl Med*. 2019;60:864–872.
- Wu J, Lian C, Ruan S, et al. Treatment outcome prediction for cancer patients based on radiomics and belief function theory. *IEEE Trans Radiat Plasma Med Sci*. 2019;3:216–224.
- Bodalal Z, Trebeschi S, Nguyen-Kim TDL, Schats W, Beets-Tan R. Radiogenomics: bridging imaging and genomics. *Abdom Radiol (NY)*. 2019;44:1960–1984.
- Lo Gullo R, Daimiel I, Morris EA, Pinker K. Combining molecular and imaging metrics in cancer: radiogenomics. *Insights Imaging*. 2020;11:1.
- Liang B, Yan H, Tian Y, et al. Dosimetrics: extracting 3D spatial features from dose distribution to predict incidence of radiation pneumonitis. *Front Oncol*. 2019;9:269.
- Paulov J. The zone-size-dependent entropy formula and spatial interaction modeling: a note on some implications. *Environ Plann A*. 1991;23:557–570.
- Ceriani L, Milan L, Martelli M, et al. Metabolic heterogeneity on baseline ¹⁸F-FDG-PET/CT scan is a predictor of outcome in primary mediastinal B-cell lymphoma. *Blood*. 2018;132:179–186.
- Chung HH, Kang SY, Ha S, et al. Prognostic value of preoperative intratumoral FDG uptake heterogeneity in early stage uterine cervical cancer. *J Gynecol Oncol*. 2016;27:e15.
- Hanaoka K, Hosono M, Tatsumi Y, et al. Heterogeneity of intratumoral ¹¹¹In-ibritumomab tiuxetan and ¹⁸F-FDG distribution in association with therapeutic response in radioimmunotherapy for B-cell non-Hodgkin's lymphoma. *EJNMMI Res*. 2015;5:10.
- Feliciano EM, Kroenke CH, Meyerhardt JA, et al. Association of systemic inflammation and sarcopenia with survival in nonmetastatic colorectal cancer: results from the C SCANS study. *JAMA Oncol*. 2017;3:e172319.
- Borges TC, Gomes TLN, Pichard C, Laviano A, Pimentel GD. High neutrophil to lymphocytes ratio is associated with sarcopenia risk in hospitalized cancer patients. *Clin Nutr*. 2021;40:202–206.
- Brotto M, Johnson ML. Endocrine crosstalk between muscle and bone. *Curr Osteoporos Rep*. 2014;12:135–141.
- He C, He W, Hou J, et al. Bone and muscle crosstalk in aging. *Front Cell Dev Biol*. 2020;8:585644.
- Argilés JM, Stemmler B, López-Soriano FJ, Busquets S. Inter-tissue communication in cancer cachexia. *Nat Rev Endocrinol*. 2018;15:9–20.
- Reginster J-Y, Beaudart C, Buckinx F, Bruyère O. Osteoporosis and sarcopenia: two diseases or one? *Curr Opin Clin Nutr Metab Care*. 2016;19:31–36.

Biodistribution and Radiation Dosimetry of Intraperitoneally Administered ^{124}I -Omburtamab in Patients with Desmoplastic Small Round Cell Tumors

Milan Grkovski¹, Shakeel Modak², Pat B. Zanzonico¹, Jorge A. Carrasquillo^{3,4}, Steven M. Larson^{3,4}, John L. Humm¹, and Neeta Pandit-Taskar^{3,4}

¹Department of Medical Physics, Memorial Sloan Kettering Cancer Center, New York, New York; ²Department of Pediatrics, Memorial Sloan Kettering Cancer Center, New York, New York; ³Molecular Imaging and Therapy Service, Department of Radiology, Memorial Sloan Kettering Cancer Center, New York, New York; and ⁴Department of Radiology, Weill Cornell Medical College, New York, New York

The aim of this study was to assess the pharmacokinetics, biodistribution, and radiation dosimetry of ^{124}I -omburtamab administered intraperitoneally in patients with desmoplastic small round cell tumor.

Methods: Eligible patients diagnosed with desmoplastic small round cell tumor with peritoneal involvement were enrolled in a phase I trial of intraperitoneal radioimmunotherapy with ^{131}I -omburtamab. After thyroid blockade and before radioimmunotherapy, patients received approximately 74 MBq of ^{124}I -omburtamab intraperitoneally. Five serial PET/CT scans were obtained up to 144 h after injection. Multiple blood samples were obtained up to 120 h after injection. Organ-absorbed doses were calculated with OLINDA/EXM. **Results:** Thirty-one patients were studied. Blood pharmacokinetics exhibited a biphasic pattern consisting of an initial rising phase with a median half-time (\pm SD) of 23 ± 15 h and a subsequent falling phase with a median half-time of 56 ± 34 h. Peritoneal distribution was heterogeneous and diffuse in most patients. Self-dose to the peritoneal cavity was 0.58 ± 0.19 mGy/MBq. Systemic distribution and activity in major organs were low. The median absorbed doses were 0.72 ± 0.23 mGy/MBq for liver, 0.48 ± 0.17 mGy/MBq for spleen, and 0.57 ± 0.12 mGy/MBq for kidneys. The mean effective dose was 0.31 ± 0.10 mSv/MBq. Whole-body and peritoneal cavity biologic half-times were 45 ± 9 and 24 ± 5 h, respectively. **Conclusion:** PET/CT imaging with intraperitoneally administered ^{124}I -omburtamab enables assessment of intraperitoneal distribution and estimation of absorbed dose to peritoneal space and normal organs before therapy.

Key Words: DSRCT; omburtamab; dosimetry; intraperitoneal; radioimmunotherapy

J Nucl Med 2022; 63:1094–1100

DOI: 10.2967/jnumed.121.262793

Desmoplastic small round cell tumor (DSRCT) is an aggressive soft-tissue sarcoma seen in adolescents and young adults (1). DSRCT is composed of nests of small round cells with polyphenotypic differentiation, typically a mixture of epithelial, mesenchymal, and neural features surrounded by a prominent desmoplastic

stroma (1). This rare malignancy is associated with a t(11;22)(p13;q12) chromosomal translocation that creates the aberrant transcription factor EWS-WT1 (2,3). The disease primarily involves the abdomen and pelvic cavity, typically with widespread peritoneal disease. Treatment involves a multimodal approach including chemotherapy, surgery, and whole abdominopelvic radiotherapy (4). However, the median overall survival is low, ranging between 14 and 38 mo, with a long-term progression-free survival of $< 20\%$ (5), highlighting the need for novel therapeutic options to improve outcomes.

The murine monoclonal IgG1 antibody omburtamab (previously called 8H9) was developed at our institution. Omburtamab binds to the cell surface of the glycoprotein B7-H3 (CD276), which is expressed in most pediatric solid tumors, including 96% of DSRCT, whereas expression is restricted in normal tissues (6). Radiolabeled omburtamab using either ^{131}I or ^{124}I was developed for theranostics (7) and has been evaluated for the radioimmunotherapy (RIT) of leptomeningeal metastases of solid tumors including neuroblastoma by intraventricular administration (NCT00089245) (8) or intratumoral administration for diffuse intrinsic pontine glioma (NCT01502917) (9). Preclinical experiments have demonstrated that the injection of a radiolabeled agent via the intraperitoneal compartment achieved high peritoneal activities long term, high peritoneal time-integrated activity coefficients, and only limited transfer of therapeutic agents into the systemic circulation (10). Compartmentalized therapy with radioimmunotargeted agents facilitates delivery of higher radiation dose to the tumor target sites because of higher tumor-to-normal-tissue ratios and lower systemic activity, thereby causing lower systemic radioisotope-related toxicity (11,12). We have previously reported on the use of intraventricularly administered ^{124}I -omburtamab imaging for dosimetry and biodistribution assessment before therapeutic administration of ^{131}I -omburtamab (11).

Extending the concept of compartmental therapy with radiolabeled antibodies, we conducted a phase I study with ^{131}I -omburtamab administered intraperitoneally for therapy of patients with DSRCT and other B7-H3-expressing tumors. We demonstrated that intraperitoneal ^{131}I -omburtamab therapy is safe and can be administered in the outpatient setting. In the phase I study, treatment ^{131}I -omburtamab activities ranging from 1.11 to 3.33 GBq/m² were administered without significant normal-organ toxicity, and recommended phase II activity was established at 2.96 GBq/m² (13). In this report, we present in detail the biodistribution, organ uptake, and dosimetry of ^{124}I -omburtamab PET/CT imaging after intraperitoneal administration in patients with DSRCT.

Received Jun. 24, 2021; revision accepted Oct. 8, 2021.

For correspondence or reprints, contact Neeta Pandit-Taskar (pandit-n@mskcc.org).

Published online Dec. 2, 2021.

COPYRIGHT © 2022 by the Society of Nuclear Medicine and Molecular Imaging.

MATERIALS AND METHODS

Patients

Patients older than 1 y with a proven diagnosis of DSRCT with peritoneal involvement or other refractory or relapsed B7-H3-expressing tumors involving the peritoneum were enrolled and treated in an institutional review board–approved phase I trial (NCT01099644). All patients or their legal guardians provided written informed consent. Salient exclusion criteria were active serious infection or \geq grade 2 toxicities with the exception of myelosuppression. Patients underwent prior debulking surgery followed by insertion of an indwelling intraperitoneal catheter. Patency of the intraperitoneal catheter was maintained by twice-daily saline flushes. Intraperitoneal administration of ^{124}I -omburtamab was performed 7–14 d after catheter placement. All patients received thyroid protective medication with oral saturated solution of potassium iodide (SSKI) and liothyronine (25–75 mcg orally daily) starting 5–7 d before ^{124}I -omburtamab and continued for a total of 42 d.

^{124}I -omburtamab was radiolabeled with ^{124}I at our institutional Radiochemistry and Molecular Imaging Probes core facility and was injected within 6 h of production. After a check for good flow and patency of the intraperitoneal catheter, 74 MBq of ^{124}I -omburtamab (volume, 5.0–10.8 mL) were injected intraperitoneally over 10–15 min using a Graseby pump (Sims Graseby Ltd.) followed immediately by a 130-mL normal saline flush. This was followed 1 h later by intraperitoneal infusion of 1,200 mL/m² normal saline to ensure dispersion of the radioimmunoconjugate. After completion of infusion, patients were instructed to move and shift positions actively for up to 2 h to promote uniform distribution within the intraperitoneal cavity.

Pharmacokinetics and Radiation Dosimetry Assessment

Pharmacokinetic analysis for ^{124}I -omburtamab was performed using 2 modalities: blood clearance by radioassays of measured aliquots of serial blood draws and whole-body and organ activity measured by serial PET/CT scans. Blood samples for radioassay were drawn at multiple time points including 1 baseline sample before injection of the radiolabeled antibody (time 0) and at 1.1 \pm 0.2 h (range, 0.9–2.0 h), 2.2 \pm 0.4 h (range, 1.8–4.0 h), 4.7 \pm 1.4 h (range, 2.8–8.5 h), 20.4 h, 23.9 h, and 47.8 h (range, 29.9–69.9 h) after ^{124}I -omburtamab injection. Aliquots of blood were assayed in duplicate in a scintillation well counter (LKB Wallac, Inc.) calibrated for ^{124}I and the net count rates converted to activity concentrations in percentage of the injected activity per gram. The resulting time–activity concentration data decay-corrected to the time of administration were fit to a biexponential function. The fitted biologic clearance constants were converted to effective clearance constants by incorporation of ^{124}I physical decay constant and time-integrated activity concentration calculated by analytic integration of the resulting function. The mean blood-absorbed dose was calculated by multiplying the blood time-integrated activity concentration ($\mu\text{Ci}\cdot\text{hr}/\text{g}$) by the ^{124}I energy per decay (formerly the equilibrium dose constant) for nonpenetrating radiations ($\Delta_{\text{np}} = 0.418 \text{ cGy}\cdot\text{g}/\mu\text{Ci}\cdot\text{hr}$).

^{124}I -Omburtamab PET/CT Imaging. Five serial PET/CT scans were completed after the injection of ^{124}I -omburtamab up to 144 h after injection. Due to practical reasons, patients were not required to avoid voiding before first scan. All scans were obtained on a Discovery STE or 710 PET/CT scanner (GE Healthcare) using the ^{124}I decay parameters (positron yield, 0.23; half-life, 4.18 d).

The field of imaging included vertex to the mid-thigh. The acquisition time was 5 min per field of view. PET emission data were corrected for attenuation, scatter, and random events using the vendor-supplied corrections. The CT scan of the PET/CT was mainly for attenuation correction and was obtained using a combination of ultralow (10 mA) and low mA (40–80 mA based on body weight) with 140 keV for the multiple

scanning times. The CT dose ranged from 9.2 to 18.4 mSv in patients. Images were reconstructed using standard clinical reconstruction parameters: ordered-subset expectation maximization using 2 iterations with 16 subsets and a gaussian postprocessing filter with a full width half maximum of 6.0 mm.

Organ Dosimetry Calculation

Absorbed doses to total body and individual organs were calculated on the basis of the time–activity data derived from each patient’s set of PET/CT images. Volumes of interest were drawn manually over normal organs (heart, liver, spleen, kidneys, stomach contents, thyroid, gastrointestinal tract, and peritoneal cavity) and whole body in Hybrid Viewer (HERMES Medical Solution, Inc.). Volumes of interest were placed on PET images using corresponding CT and fused PET/CT image guidance. The decay-corrected mean activity concentrations $[A(t)]$ (in kBq/cc) in all investigated organs were each fit to a mathematic function of the following form:

$$[A(t)] = [A_{\text{plateau}}] (1 - \exp(-0.693/T_{\text{uptake}} \times t)) \exp(-0.693/T_{\text{clearance1}} \times t).$$

The decay-corrected total-body activity concentrations were each fit to a mathematic function of the following form:

$$[A(t)] = [A_0] \exp(-0.693/T_{\text{clearance2}} \times t),$$

where t is the time after administration; $[A_{\text{plateau}}]$ is the plateau activity concentration in the investigated organs; T_{uptake} and $T_{\text{clearance1}}$ are the uptake and clearance half-times, respectively, in the investigated organs; $[A_0]$ is the zero-time–activity concentration in total-body; and $T_{\text{clearance2}}$ is the clearance half-time in the total body. The foregoing fitted time–activity functions were integrated analytically from $t = 0$ (i.e., the time of injection) to time $t = \infty$ (i.e., the time of complete radioactive decay), incorporating the physical half-life of ^{124}I (4.18 d = 100.3 h) into the respective decay-corrected uptake T_{uptake} and clearance half-times, $T_{\text{clearance1}}$ and $T_{\text{clearance2}}$. The resulting time-integrated activity concentrations were converted to total-organ time-integrated activities by multiplying by the corresponding organ masses in the Reference Man anatomic model (14) closest in total-body mass to that of the patient and then to time-integrated activity coefficients by dividing by the administered activity. These time-integrated activity coefficients were entered into the OLINDA/EXM 1.1 radiation dosimetry program (14), with ^{124}I as the radionuclide and the Reference Man anatomic model closest in age to that of the patient selected. For adult patients, both female and male models were used. A peritoneal cavity model (15,16) as implemented in OLINDA/EXM was applied.

RESULTS

Patients

Thirty-one patients (26 men and 5 women; age, 21 \pm 8 y; age range, 8–38 y) received ^{124}I -omburtamab and underwent 4 (all patients) or 5 (20 patients) PET/CT scans. The mean injected activity was 73 \pm 3 MBq (range, 65–77 MBq). The mean times for PET/CT scan acquisitions were 3.6 \pm 0.8 (range, 2.4–5.4), 22.3 \pm 2.5 (range, 17.6–27.0), 46.4 \pm 2.6 (range, 42.5–52.3), 69.0 \pm 1.4 (range, 66.1–71.7), and 125.1 \pm 14.9 (range, 114.1–171.2) h after injection of ^{124}I -omburtamab.

Biodistribution

Imaging showed localization of tracer in the peritoneal cavity dispersed within 4 quadrants of the abdomen and pelvis and cleared over time as noted on serial imaging (Fig. 1). The distribution was heterogeneous, with prominent activity noted in most patients in the bilateral paracolic gutters, lower abdomen, and pelvis.

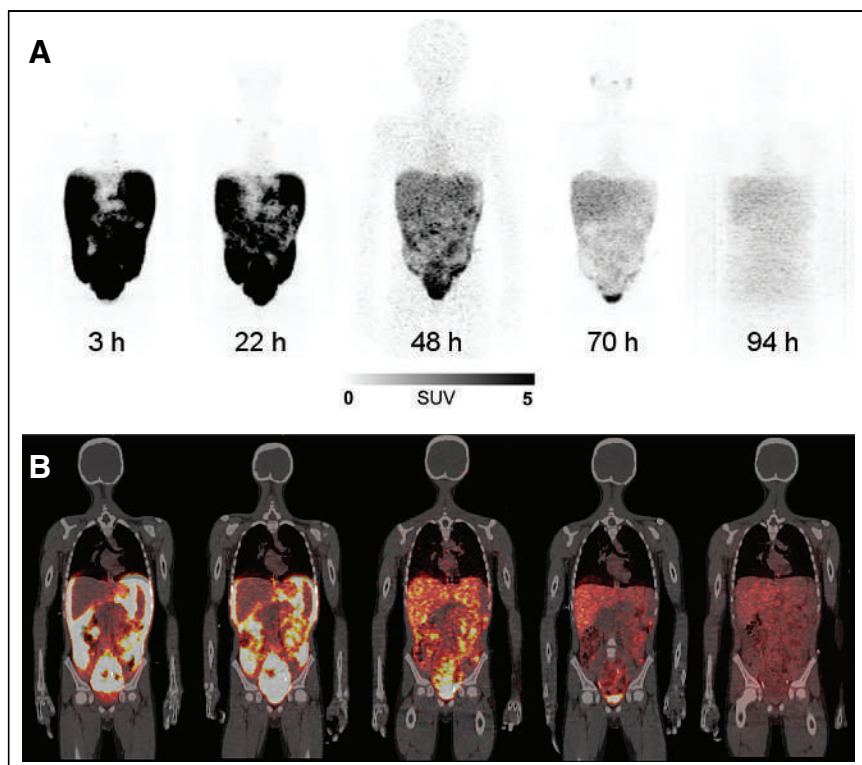


FIGURE 1. ^{124}I -omburtamab imaging. Maximum-intensity-projection (A) and coronal (B) images after ^{124}I -omburtamab injection. Cardiac blood-pool activity is low at all time points. Peritoneal distribution is most intense initially and decreasing with time. Mild activity in salivary glands is noted in later images.

In 4 patients, the distribution was noted in all quadrants but with asymmetric increased activity in either the right or the left abdomen. In 3 patients, the activity showed a more localized pattern in the lower abdomen and pelvis, although distribution was noted in all quadrants. Overall, radiotracer activity in the peritoneum decreased with time, with an average biologic half-time of 24 ± 5 (range, 18–45) h. Perihepatic uptake in the peritoneum was variable, with moderate to intense uptake seen in 10 patients whereas others showed mild or minimal activity (Fig. 2). Moderate to prominent uptake was noted in the peritoneum superiorly around the spleen in all patients (Fig. 2). Minimal (barely discernible) to mild uptake was observed in the cardiac blood pool that initially increased within 24–72 h and later decreased as noted in delayed imaging (Figs. 1 and 2). Minimal activity was noted within the liver or spleen parenchyma in the initial 48 h. Mild activity was noted in the salivary glands for all patients. Thyroid activity was minimal to mild in all patients (Fig. 1), except in 2 patients. These 2 patients had prominent activity in the thyroid and known prior hypothyroidism; in 1 patient, this was related to underlying chronic thyroiditis (Fig. 2). The uptake in the thyroid generally increased with time up to 72 h, after which the activity decreased. Bladder contents activity was noted as early as the first PET/CT scan in many patients.

^{124}I -omburtamab activity in the lymph nodes was observed in 24 patients in early imaging at 22 h after injection and in 17 patients at 125 h after injection. The nodal visualization included internal mammary (76% of cases), supraclavicular (57% of cases), and mediastinal nodes (52% of cases). Also observed were paratracheal,

subcarinal, preaortic, cervical, subaortic, pretracheal, substernal, intrathoracic, parasophageal, periportal, and retroclavicular lymph nodes. An example patient with nodal uptake is shown in Figure 2. Activity in the lung in the pleural–diaphragmatic region and posteriorly in the lung periphery and pleural region was noted in some patients, primarily in those who showed ipsilateral nodal activity.

Time–activity curves for normal organs revealed a gradual increase in radioactivity (quantified as ^{124}I -omburtamab SUV_{mean} normalized by body weight) in heart blood pool, liver, and kidneys, reaching a plateau between 24 and 48 h after injection and subsequently decreasing (Fig. 3; detailed information is provided in Supplemental Table 1 [supplemental materials are available at <http://jnm.snmjournals.org>]). Although splenic parenchyma activity was generally very low, uptake was highest in the first PET/CT scan and decreased thereafter. The uptake in stomach contents increased initially, being most prominent at 24 h, and decreased thereafter. Bladder contents activity was noted as early as the first scan and was variably seen in subsequent scans in all patients, suggesting renal excretion. ^{124}I -omburtamab cleared from intraperitoneal space exponentially, with an SUV_{mean} of 10 ± 1 at 4 h after injection (range, 7–19)

and falling to 0.5 ± 0.1 at 125 h after injection (range, 0.2–0.9). The SUV_{max} in the peritoneal space also exhibited a similar pattern, decreasing from 53 ± 14 (range, 14–114) at 4 h after injection to 2.2 ± 0.5 (range, 0.2–4.6) at 125 h after injection.

Kinetic Analysis

Blood pharmacokinetics in 28 patients showed a biphasic pattern consisting of an initial rising phase with a median half-time of 23 ± 15 h and a subsequent falling phase with a median half-time of 56 ± 34 h. Blood activity reached a plateau after 24 h, approaching a maximum of 1.8 percentage of injected activity per liter (Fig. 4B).

The whole-body clearance conformed to a monoexponential function (Fig. 4A). Mean whole-body biologic half-time was 45 ± 9 h, and time-integrated activity coefficients for whole body and peritoneal cavity were 44 ± 6 and 20 ± 7 h, respectively (Table 1). ^{124}I -omburtamab organ dosimetry is summarized in Table 2. Median absorbed dose to the peritoneum was 0.58 mGy/MBq. The mean absorbed doses were 0.72 ± 0.23 mGy/MBq for liver, 0.48 ± 0.17 mGy/MBq for spleen, 0.57 ± 0.12 mGy/MBq for kidneys, 0.84 ± 0.29 mGy/MBq for urinary bladder wall, and 0.19 ± 0.05 mGy/MBq for lungs. The radiation dose to the thyroid was 0.25 ± 0.19 mGy/MBq (mean \pm SD) for all patients except the 2 with prior hypothyroidism whose thyroid-stimulating hormone could not be suppressed. Time-integrated activity coefficients and normal-organ dosimetry for 3 subgroups based on patient age are summarized in Supplemental Tables 2 and 3.

The estimated mean effective dose was 0.31 ± 0.10 mSv/MBq. The total dose to blood from the 73 MBq of ^{124}I -omburtamab

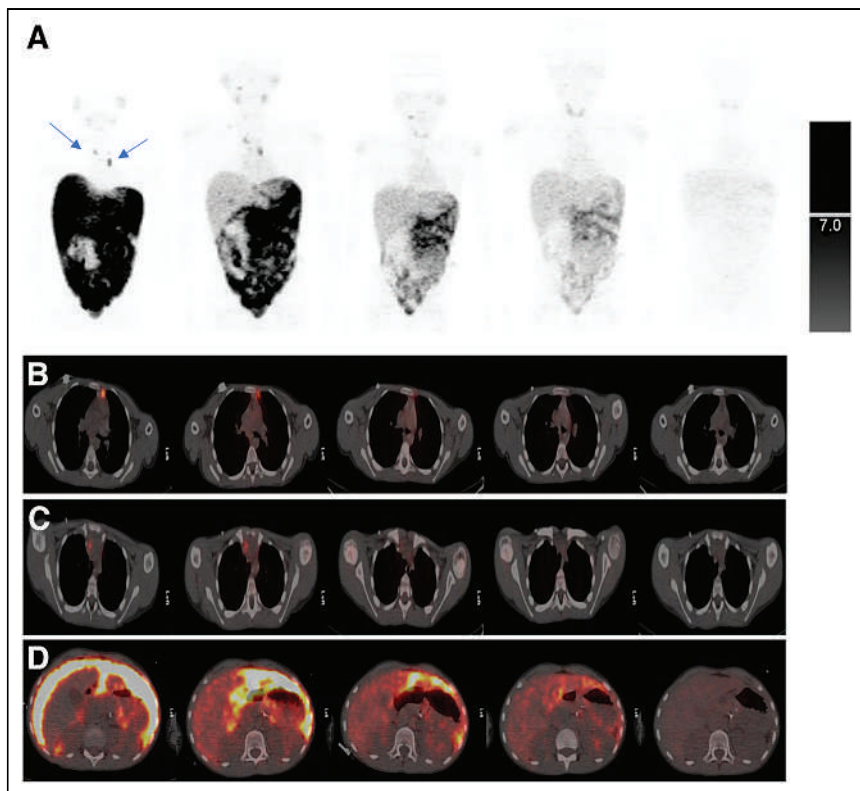


FIGURE 2. Serial images after ^{124}I -omburtamab injection. Maximum-intensity-projection (A) and fused transaxial images PET/CT images (B–D). Peritoneal activity is intense (A and D). Distribution is noted along all quadrants with slightly more in bilateral paracolic gutters. Peritoneal distribution decreases with time along with increasing blood-pool activity and thyroid uptake in later images that decreases in last image. Right supraclavicular and mediastinal lymph nodes are visualized in early images (arrows), demonstrating decreased visualization with time.

injection, as calculated from blood sample data, was 1.1 ± 0.6 cGy (range, 0.2–3.1) or 0.15 ± 0.08 mGy/MBq (range, 0.02–0.42).

DISCUSSION

We have used ^{131}I - or ^{124}I -labeled 8H9/omburtamab antibody theranostically for localized compartmental therapies with intraventricular/intrathecal administration for metastatic leptomeningeal disease in neuroblastoma or other B7-H3-expressing tumors (8,12). Both ^{131}I -omburtamab and ^{124}I -omburtamab have an advantage as theranostic agents, as imaging allows for assessment of individual patient activity distribution and dosimetric estimation for radiation absorbed doses for both normal tissues and tumors before therapy (11). An additional advantage of ^{124}I -omburtamab is imaging with PET/CT scanners that have higher resolution allows for quantitation that is easier and more accurate than γ -camera imaging. Omburtamab is a highly specific antibody that targets B7-H3, an antigen expressed in several tumors including most DSRCTs, making it an attractive target for radioimmunotherapy (6), as noted in early preclinical studies (7,10). We have developed radiolabeled omburtamab and treated patients with $^{124}/^{131}\text{I}$ -omburtamab in 3 phase I/II trials using compartmental delivery systems, namely, peritoneal cavity (intraperitoneal infusions), cerebrospinal fluid space (intraventricular/intrathecal injections), or localized intratumoral delivery using a convection-enhanced delivery method in patients with diffuse intrinsic pontine glioma (7–9). We have

shown the feasibility and use of ^{124}I -omburtamab imaging for biodistribution and dosimetry assessment and as a therapeutic (9). Intraperitoneal RIT has the potential to deliver higher radiation doses to the tumor while limiting systemic organ and blood doses to low radiation doses (16).

For DSRCT, which primarily involves the peritoneum, we used intraperitoneal administration of RIT and showed the safety of intraperitoneal ^{131}I -omburtamab RIT (13). Patients receiving doses of ^{131}I -omburtamab up to 3.33 GBq/m² (90 mCi/m²) did not exhibit major toxicities, and all toxicities were reversible without intervention. Intraperitoneal RIT appeared to be associated with a decreased risk of abdominopelvic DSRCT relapse compared with historical data, with 9 of 23 patients receiving the recommended phase II activity dose of 2.96 GBq/m² being alive disease-free at a median follow up of 42 mo after RIT. Here we present details of the ^{124}I -omburtamab PET/CT imaging used for assessment of biodistribution and radiation dosimetry of normal organs and examine its potential for treatment planning.

In this phase I study, ^{124}I -omburtamab imaging before ^{131}I -omburtamab intraperitoneal radioimmunotherapy showed favorable biodistribution with dispersion within all quadrants of the peritoneal cavity and low systemic activity in other organs.

The peritoneal distribution was heterogeneous but localized in all 4 quadrants of the abdomen in all patients. There was no clear pattern of variation of distribution noted in patients. The overall retention time in the peritoneum was long (mean biologic half-time of 24.5 ± 5.2 h). The dosimetry estimates showed low normal-organ doses. The assessment of organ uptake enabled assessment of projected dosimetry with ^{131}I -omburtamab (13). Because most patients had surgical debulking and were required to have no measurable disease, any specific tumor dosimetry estimation could not be performed.

Uptake of ^{124}I -omburtamab in major organs such as the liver and spleen was low (maximum uptake of ~ 0.003 percentage of the injected activity per gram for both), reflecting slow systemic distribution of the tracer, as also noted by low cardiac blood-pool activity over all imaging time points and low cross-reactivity with normal tissues. The uptake pattern of the organs showed an initial increase, suggesting slow systemic absorption from intraperitoneal activity, followed by clearance that paralleled the blood activity, which also showed an initial increase before clearance. The low systemic absorption resulted in low blood and bone marrow exposures. The elimination pathway appears to be primarily renal, as suggested by urine activity within the bladder, low liver activity, and lack of gallbladder or gastrointestinal tract activity, suggesting that hepatobiliary clearance was not prominent. Thyroid doses were overall low. Two patients with underlying hypothyroidism had higher doses likely

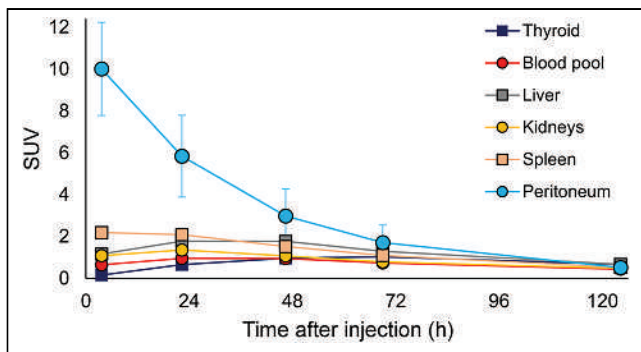


FIGURE 3. Mean SUV_{bw} for normal organs and peritoneum ($n = 31$ patients).

due to inherent high thyroid-stimulating hormone stimulation. Clinical follow-up with measured thyroid-stimulating hormone did not reveal hypothyroidism resulting from ^{131}I -omburtamab therapy in any patients (13).

Lymph node uptake was variable; the nodes visualized were not metastatic as assessed by concurrent or follow-up diagnostic CT scans. The significance of the nodal uptake is unclear, however. In many patients who showed nodal uptake, activity was noted along the pleuroperitoneal surface, as was diffuse uptake along inferior posterior aspects of the pleura on the ipsilateral side of the nodal uptake, suggesting a likely mechanism related to transit of ^{124}I -omburtamab along the lymphatics and thoracic duct to mediastinal nodes (17). Overall, the normal-organ and whole-body radiation dosimetry profile of imaging with ^{124}I -omburtamab patients was favorable, with low uptake and radiation absorbed

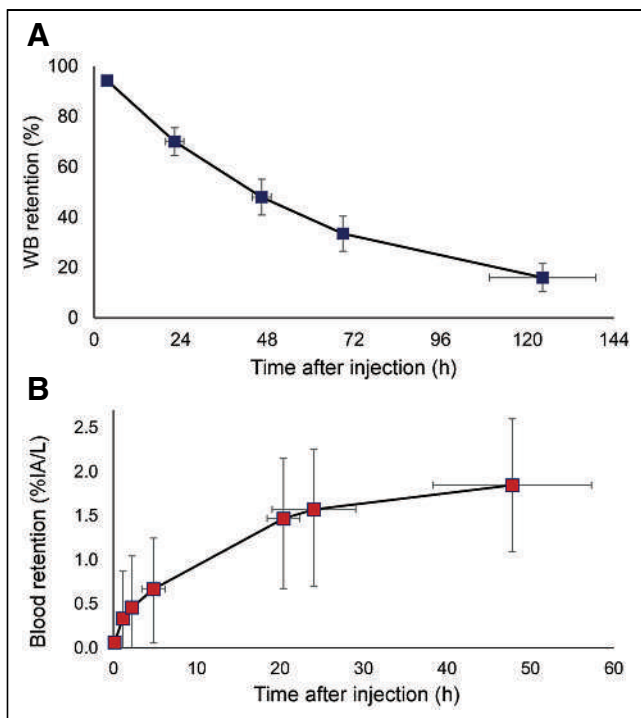


FIGURE 4. Whole-body (WB) (A) and blood (B) clearance of ^{124}I -omburtamab displayed in aggregate decay-corrected mean values. %IA = percentage injected activity. Mean \pm SD.

TABLE 1
Time-Integrated Activity Coefficients (h) for Selected Organs for Intraperitoneal Administration of ^{124}I -Omburtamab

Organ	Mean	SD	Median	Minimum	Maximum
Liver	3.5	1.6	3.1	1.5	7.3
Kidneys	0.4	0.1	0.4	0.3	0.7
Spleen	0.3	0.2	0.3	0.1	0.7
Stomach*	0.9	0.5	0.7	0.3	2.1
Urinary bladder*	1.1	0.5	1.0	0.3	2.9
Thyroid	0.07	0.21	0.01	0.00	1.22
Peritoneal cavity [†]	20.4	6.9	19.2	9.0	32.6
Rest of body	17.3	7.7	17.8	3.8	34.6
Whole-body	44.3	6.0	44.1	34.2	57.4

*Dose for cavity/content.

[†]Dose to peritoneal cavity wall per disintegration in peritoneal cavity.

doses noted. The total body effective dose was 0.3 mSv/MBq for intraperitoneal administration, which is similar or slightly lower than the approximately 0.5 mSv/MBq noted after intraventricular administration of ^{124}I -omburtamab in 42 patients with metastatic leptomeningeal tumors (11) and with convection-enhanced intratumoral delivery in patients with diffuse intrinsic pontine glioma (NCT01502917). Peritoneal-to-liver and peritoneal-to-blood-pool SUV ratios were very high (12 ± 9 and 21 ± 10 , respectively, on the first PET/CT).

^{124}I -omburtamab imaging allows assessment of biodistribution and dosimetry before intraperitoneal delivery of ^{131}I -omburtamab antibody for therapy. In this phase I study, ^{124}I -omburtamab imaging was used to predict organ and peritoneal doses from therapeutic administration of ^{131}I -omburtamab (13). Our study used PET/CT imaging to derive dose estimates for intraperitoneal RIT, unlike prior studies that used radioimmunoconjugates targeting surface antigens and assessed biodistribution and dosimetry either by γ -camera imaging or external radiation probes as applied, for example, to single-photon emitters such as β -emitting ^{90}Y or α -emitting ^{211}At and ^{212}Pb for therapy (18–21). In our study, pediatric and adolescent patients with DSRCT scheduled to undergo treatment with ^{131}I -omburtamab were imaged with companion theranostic positron-emitting radioimmunoconjugate ^{124}I -omburtamab. This allowed for more comprehensive quantitative imaging at multiple time points with higher spatial resolution than γ -camera imaging performed in other studies of intraperitoneal RIT. The predicted doses of ^{131}I -omburtamab for intraperitoneal radioimmunotherapy were within acceptable normal-organ limits, and therapy was well tolerated by all DSRCT patients with no dose-limiting toxicities noted (13). The systemic activity and blood and organ radiation doses were low from both ^{124}I -omburtamab and ^{131}I -omburtamab, favoring use of this theranostic pair for compartmental intraperitoneal radioimmunotherapy. On the basis of these encouraging data, we have initiated a phase II study of ^{131}I -omburtamab-based intraperitoneal RIT in

TABLE 2

Normal-Organ Absorbed Dose and Effective Dose Estimates for Intraperitoneal Administration of ^{124}I -Omburtamab

Mean absorbed doses (mGy/MBq)	Mean	SD	Median	Minimum	Maximum
Adrenals	0.45	0.07	0.44	0.27	0.59
Brain	0.09	0.06	0.08	0.02	0.21
Breasts	0.12	0.04	0.11	0.07	0.21
Gallbladder wall	0.21	0.07	0.20	0.10	0.36
Lower large intestine wall	0.23	0.06	0.21	0.15	0.35
Small intestine	0.50	0.09	0.48	0.30	0.68
Stomach wall	0.66	0.16	0.65	0.44	1.10
Upper large intestine wall	0.46	0.08	0.46	0.28	0.62
Heart wall	0.39	0.07	0.38	0.26	0.53
Kidneys	0.57	0.12	0.55	0.38	0.80
Liver	0.73	0.22	0.68	0.41	1.26
Lungs	0.19	0.05	0.17	0.13	0.30
Muscle	0.20	0.05	0.18	0.14	0.30
Ovaries	0.40	0.02	0.40	0.36	0.41
Pancreas	1.07	0.26	1.03	0.59	1.54
Red marrow	0.22	0.04	0.21	0.15	0.30
Osteogenic cells	0.25	0.07	0.23	0.16	0.38
Skin	0.11	0.04	0.10	0.06	0.19
Spleen	0.48	0.17	0.50	0.22	1.00
Testes	0.13	0.06	0.11	0.06	0.25
Thymus	0.15	0.05	0.13	0.08	0.25
Thyroid	0.27	0.24	0.19	0.07	1.03
Urinary bladder wall	0.85	0.29	0.78	0.36	1.52
Uterus	1.21	0.21	1.14	1.00	1.50
Total body	0.22	0.05	0.21	0.15	0.32
Peritoneum self-dose	0.57	0.19	0.57	0.22	1.07
Effective dose (mSv/MBq)	0.31	0.10	0.30	0.20	0.71

Units are mGy/MBq unless otherwise noted.

combination with external-beam radiotherapy for DSRCT and other B7-H3-expressing tumors involving the peritoneum (NCT04022213).

CONCLUSION

PET/CT imaging with intraperitoneally administered ^{124}I -omburtamab enables the assessment of both intraperitoneal and systemic distribution, allowing for estimation of absorbed dose to the peritoneum and normal organs before therapy.

DISCLOSURE

This work was supported by funding from Taybandz, Steven Vanover Foundation, Sarcoma SPORE, and the NIH/NCI Cancer Center Support Grant P30 CA008748. Milan Grkovski reports personal fees from Y-mAbs Therapeutics, Inc. unrelated to the submitted work. Neeta Pandit-Taskar is or has served as a consultant

and advisory board member and has received honoraria from Actinium Pharma, Progenics, Medimmune/AstraZeneca, Illumina, Imaginab, and Y-mAbs and conducts research institutionally supported by Y-mAbs, Imaginab, Bristol Myers Squibb, Bayer, Clarity Pharma, Janssen, and Regeneron. Shakeel Modak has a consulting or advisory role for Y-mAbs Therapeutics and Illumina RP and has 2 patents pending with no financial benefit. Pat B. Zanzonico, Jorge A. Carrasquillo, Steven M. Larson, and John L. Humm have a consulting or advisory role with Y-mAbs Therapeutics. No other potential conflict of interest relevant to this article was reported.

ACKNOWLEDGMENTS

We thank our institutional nuclear medicine research nurses, radiopharmacy, technologists, radiation safety, surgical team, and inpatient nurse practitioners for their work in patient care.

KEY POINTS

QUESTION: What is the feasibility, safety, and clinical utility of ^{124}I -omburtamab PET/CT imaging for patients with DSRCT?

PERTINENT FINDINGS: In this phase I study, 31 patients were imaged with ^{124}I -omburtamab administered intraperitoneally before treatment with ^{131}I -omburtamab. Dosimetry and biodistribution were favorable, with minimal uptake in organs and long retention in the peritoneal cavity.

IMPLICATIONS FOR PATIENT CARE: ^{124}I -omburtamab PET/CT enables theranostic imaging assessment in patients and has a potential role in planning therapy. A phase II study is under way.

REFERENCES

1. Mora J, Modak S, Cheung NK, et al. Desmoplastic small round cell tumor 20 years after its discovery. *Future Oncol*. 2015;11:1071–1081.
2. Sawyer JR, Tryka AF, Lewis JM. A novel reciprocal chromosome translocation t(11;22)(p13;q12) in an intraabdominal desmoplastic small round-cell tumor. *Am J Surg Pathol*. 1992;16:411–416.
3. Ladanyi M, Gerald W. Fusion of the EWS and WT1 genes in the desmoplastic small round cell tumor. *Cancer Res*. 1994;54:2837–2840.
4. Quaglia MP, Brennan MF. The clinical approach to desmoplastic small round cell tumor. *Surg Oncol*. 2000;9:77–81.
5. Lal DR, Su WT, Wolden SL, Loh KC, Modak S, La Quaglia MP. Results of multimodal treatment for desmoplastic small round cell tumors. *J Pediatr Surg*. 2005;40:251–255.
6. Modak S, Kramer K, Gultekin SH, Guo HF, Cheung NK. Monoclonal antibody 8H9 targets a novel cell surface antigen expressed by a wide spectrum of human solid tumors. *Cancer Res*. 2001;61:4048–4054.
7. Modak S, Guo HF, Humm JL, Smith-Jones PM, Larson SM, Cheung NK. Radioimmunotargeting of human rhabdomyosarcoma using monoclonal antibody 8H9. *Cancer Biother Radiopharm*. 2005;20:534–546.
8. Kramer K, Kushner BH, Modak S, et al. Compartmental intrathecal radioimmunotherapy: results for treatment for metastatic CNS neuroblastoma. *J Neurooncol*. 2010;97:409–418.
9. Souweidane MM, Kramer K, Pandit-Taskar N, et al. Convection-enhanced delivery for diffuse intrinsic pontine glioma: a single-centre, dose-escalation, phase I trial. *Lancet Oncol*. 2018;19:1040–1050.
10. Modak S, Gerald W, Cheung NK. Disialoganglioside GD2 and a novel tumor antigen: potential targets for immunotherapy of desmoplastic small round cell tumor. *Med Pediatr Oncol*. 2002;39:547–551.
11. Pandit-Taskar N, Zanzonico PB, Kramer K, et al. Biodistribution and dosimetry of intraventricularly administered ^{124}I -omburtamab in patients with metastatic leptomeningeal tumors. *J Nucl Med*. 2019;60:1794–1801.
12. Kramer K, Pandit-Taskar N, Zanzonico P, et al. Low incidence of radionecrosis in children treated with conventional radiation therapy and intrathecal radioimmunotherapy. *J Neurooncol*. 2015;123:245–249.
13. Modak S, Zanzonico P, Grkovski M, et al. B7H3-directed intraperitoneal radioimmunotherapy with radioiodinated omburtamab for desmoplastic small round cell tumor and other peritoneal tumors: results of a phase I study. *J Clin Oncol*. 2020;JCO.20.01974.
14. Stabin MG, Sparks RB, Crowe E. OLINDA/EXM: the second-generation personal computer software for internal dose assessment in nuclear medicine. *J Nucl Med*. 2005;46:1023–1027.
15. Watson EE, Stabin MG, Davis JL, Eckerman KF. A model of the peritoneal cavity for use in internal dosimetry. *J Nucl Med*. 1989;30:2002–2011.
16. Larson SM, Carrasquillo JA, Colcher DC, et al. Estimates of radiation absorbed dose for intraperitoneally administered iodine-131 radiolabeled B72.3 monoclonal antibody in patients with peritoneal carcinomatosis. *J Nucl Med*. 1991;32:1661–1667.
17. Parungo CP, Soybel DI, Colson YL, et al. Lymphatic drainage of the peritoneal space: a pattern dependent on bowel lymphatics. *Ann Surg Oncol*. 2007;14:286–298.
18. Alvarez RD, Huh WK, Khazaeli MB, et al. A phase I study of combined modality ^{90}Y trium-CC49 intraperitoneal radioimmunotherapy for ovarian cancer. *Clin Cancer Res*. 2002;8:2806–2811.
19. Oei AL, Verheijen RH, Seiden MV, et al. Decreased intraperitoneal disease recurrence in epithelial ovarian cancer patients receiving intraperitoneal consolidation treatment with yttrium-90-labeled murine HMFG1 without improvement in overall survival. *Int J Cancer*. 2007;120:2710–2714.
20. Cederkrantz E, Andersson H, Bernhardt P, et al. Absorbed doses and risk estimates of ^{211}At -MX35 F(ab')₂ in intraperitoneal therapy of ovarian cancer patients. *Int J Radiat Oncol Biol Phys*. 2015;93:569–576.
21. Hallqvist A, Bergmark K, Bäck T, et al. Intraperitoneal α -emitting radioimmunotherapy with ^{211}At in relapsed ovarian cancer: long-term follow-up with individual absorbed dose estimations. *J Nucl Med*. 2019;60:1073–1079.

Radioembolization Dosimetry with Total-Body ^{90}Y PET

Gustavo Costa¹, Benjamin Spencer¹, Negar Omidvari¹, Cameron Foster², Michael Rusnak², Heather Hunt², Denise T. Caudle², Rex T. Pillai², Catherine Tram Vu², and Emilie Roncali^{1,2}

¹Department of Biomedical Engineering, University of California–Davis, Davis, California; and ²Department of Radiology, University of California–Davis, Davis, California

Transarterial radioembolization (TARE) is a locoregional radiopharmaceutical therapy based on the delivery of radioactive ^{90}Y microspheres to liver tumors. The importance of personalized dosimetry to make TARE safer and more effective has been demonstrated in recent clinical studies, stressing the need for quantification of the dose–response relationship to ultimately optimize the administered activity before treatment and image it after treatment. ^{90}Y dosimetric studies are challenging because of the lack of accurate and precise methods but are best realized with PET combined with Monte Carlo simulations and other image modalities to calculate a segmental dose distribution. The aim of this study was to assess the suitability of imaging ^{90}Y PET patients with the total-body PET/CT uEXPLORER and to investigate possible improvements in TARE ^{90}Y PET-based dosimetry. The uEXPLORER is the first commercially available ultra-high-resolution (171 cps/kBq) total-body digital PET/CT device with a 194-cm axial PET field of view that enables the whole body to be scanned at a single bed position. **Methods:** Two PET/CT scanners were evaluated in this study: the Biograph mCT and the total-body uEXPLORER. Images of a National Electrical Manufacturers Association (NEMA) image-quality phantom and 2 patients were reconstructed using our standard clinical oncology protocol. A late portal phase contrast-enhanced CT scan was used to contour the liver segments and create corresponding volumes of interest. To calculate the absorbed dose, Monte Carlo simulations were performed using Geant4 Application for Tomographic Emission (GATE). The absorbed dose and dose–volume histograms were calculated for all 6 spheres (diameters ranging from 10 to 37 mm) of the NEMA phantom, the liver segments, and the entire liver. Differences between the phantom doses and an analytic ground truth were quantified through the root mean squared error. **Results:** The uEXPLORER showed a higher signal-to-noise ratio at 10- and 13-mm diameters, consistent with its high spatial resolution and system sensitivity. The total liver-absorbed dose showed excellent agreement between the uEXPLORER and the mCT for both patients, with differences lower than 0.2%. Larger differences of up to 60% were observed when comparing the liver segment doses. All dose–volume histograms were in good agreement, with narrower tails for the uEXPLORER in all segments, indicating lower image noise. **Conclusion:** This patient study is compelling for the use of total-body ^{90}Y PET for liver dosimetry. The uEXPLORER scanner showed a better signal-to-noise ratio than mCT, especially in lower-count regions of interest, which is expected to improve dose quantification and tumor dosimetry.

Key Words: Monte Carlo simulation; radioembolization; ^{90}Y ; microspheres; radionuclide therapy; personalized medicine

J Nucl Med 2022; 63:1101–1107

DOI: 10.2967/jnumed.121.263145

Transarterial radioembolization (TARE) is a locoregional radionuclide therapy based on the delivery of radioactive ^{90}Y microspheres to liver tumors (1,2). TARE is increasingly integrated in multitherapy approaches for both primary and metastatic liver cancer and has shown good potential to improve quality of life or downstage tumors for transplantation (3–6). It has also demonstrated a reduction in time to progression (6), with low toxicity (7,8), and has been adopted as the primary treatment for hepatocellular carcinoma at some institutions (3). The 2 commercially available ^{90}Y microspheres—resin (SIR-Spheres; Sirtex) and glass (TheraSphere; Boston Scientific)—are directly injected into the hepatic arteries through a catheter. The glass and resin microspheres have an average diameter of 20–60 μm and 20–30 μm , respectively, and unit activity of 2,500 Bq and 50 Bq, respectively, the latter requiring a larger amount of resin microspheres to achieve the same administered activity (9). The microspheres are transported mainly by the blood flow and tend to form clusters, thus presenting a very heterogeneous distribution in the liver. This distribution can cause the absorbed dose to locally achieve values of close to 400 Gy, much greater than the total liver target of 120 Gy and threatening sensitive hepatic structures (10–14). One major challenge in making TARE safer and more effective is the lack of accurate methods to assess this heterogeneous dose distribution in the tumor and the rest of the liver after treatment. Because there is mounting evidence that TARE patient outcome correlates with the absorbed dose (15–19), it becomes critical to develop dosimetry methods that allow for quantitative evaluation of this relationship (e.g., progression-free survival vs. absorbed dose in Gy). Quantification of the dose–response relationship is required to optimize and understand the effects of administered activity and the potential need for retreatment or treatment of adverse effects; 3-dimensional (3D) image-based dosimetry is a promising approach to achieve these goals (20).

Significant effort has been put into posttreatment monitoring, which is challenging because of the difficulty of imaging ^{90}Y , a β -emitter (99.98%) with a maximum energy of 2.28 MeV. Although ^{90}Y Bremsstrahlung x-ray photons are routinely imaged with a γ -camera or SPECT, they form images with a very low signal-to-noise ratio and poor spatial resolution. This is due to the low photon emission yield per β -decay and the broad energy spectrum of these x-ray photons, preventing data correction and energy windowing (21). An alternative imaging modality for dosimetry is quantitative PET, possible through the limited ^{90}Y positron emission (0.0032% of decays). The spatial resolution of ^{90}Y PET is

Received Sep. 1, 2021; revision accepted Nov. 8, 2021.
For correspondence or reprints, contact Gustavo Costa (gcosta@ucdavis.edu).

Published online Nov. 18, 2021.

COPYRIGHT © 2022 by the Society of Nuclear Medicine and Molecular Imaging.

much better than ^{90}Y SPECT (21), but ^{90}Y PET dosimetry suffers from high bias and variability in small or low-activity regions (22,23), preventing it from fully capturing the high heterogeneity of the liver dose distribution. The energy deposition at a voxel level (~ 3 mm) can nevertheless be easily computed with high accuracy through Monte Carlo simulations, such as the Geant4 Application for Tomographic Emission (GATE) toolkit. GATE is capable of modeling particle transport through matter and storing the energy deposited in a 3D map to compute voxel-based absorbed doses.

Recently, the advent of PET scanners with a long axial field of view and total-body capability has provided a substantial improvement in PET sensitivity over conventional PET scanners (24–26). The uEXPLORER scanner (Fig. 1A) has an axial field of view of 194 cm, allowing the whole body to be scanned at a single bed position, and a large acceptance angle—capabilities that, combined, allow for a relatively flat sensitivity profile across 1 m (Fig. 1B), providing a 16- to 64-fold gain in sensitivity for total-body imaging. For single-organ imaging in the abdominal region positioned within the central meter, the sensitivity gain is expected to be 4- to 10-fold. This may be especially beneficial for PET imaging of ^{90}Y , for which positron yield is 30,000 times lower than that for standard clinical oncology imaging with ^{18}F -FDG.

This work evaluated the suitability of imaging ^{90}Y PET patients with the total-body PET/CT uEXPLORER scanner (United Imaging Healthcare) installed at the University of California, Davis. We present the very first use (to our knowledge) of total-body PET for TARE dosimetry and an investigation of the possible improvement in dose accuracy expected from the uEXPLORER sensitivity, 18 times higher than that of the conventional PET scanner used in this study according to the National Electrical Manufacturers Association (NEMA) NU 2 standard, the Biograph mCT (Siemens Healthineers) (24,27). The images were used as input for Monte Carlo simulations to perform ^{90}Y liver radioembolization dosimetry and compare conventional and total-body clinical ^{90}Y PET/CT for the first time, to our knowledge.

MATERIALS AND METHODS

System Parameters

The Biograph mCT is a PET/CT scanner with a field of view of 21.8 cm. The scanner has a sensitivity of 9.6 kcps/MBq, a spatial resolution of 4.5 mm at the center (21), and a time-of-flight resolution of 550 ps (27).

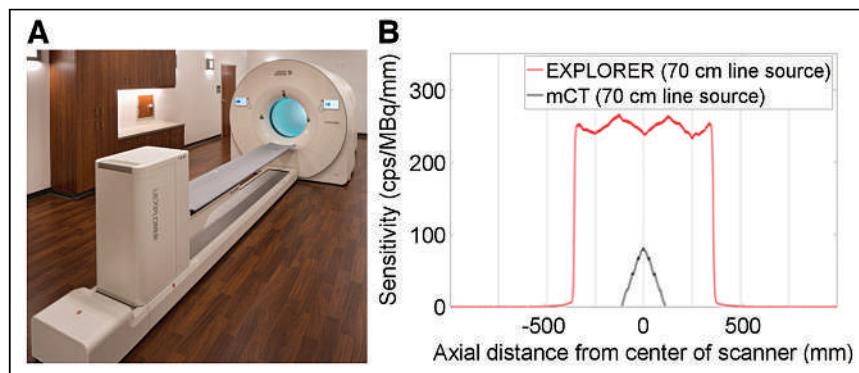


FIGURE 1. (A) Photograph of uEXPLORER total-body PET/CT scanner installed at EXPLORER Molecular Imaging Center in Sacramento, CA. (B) Comparison of sensitivity profiles between mCT and uEXPLORER.

The uEXPLORER total-body PET/CT scanner (Fig. 1) has an axial field of view of 194 cm, with a 57° axial acceptance angle. This leads to the highest sensitivity of any clinical PET scanner, 176 kcps/MBq, as measured with the NEMA NU 2 protocol. The spatial resolution is 3.0 mm (28). The time-of-flight resolution was measured to be 505 ps following NEMA NU 2 2018.

Phantom Scan

A NEMA image-quality phantom was used to evaluate the image quality of both PET/CT scanners when imaging a therapeutic dose level of ^{90}Y (1–5 GBq), with the goal of calculating the absorbed dose. A Capintec CRC-55TR dose calibrator was used for ^{90}Y dose measurements after it was calibrated with a National Institute of Standards and Technology–traceable ^{90}Y source (Eckert and Ziegler GmbH) with an accuracy of $\pm 3\%$. The phantom was filled with 2.51 GBq of ^{90}Y solution with a sphere-to-background ratio of 7.78:1 in the 6 fillable spheres (diameters, 10–37 mm). The phantom was positioned with all spheres at the center of the axial field of view and imaged on day 0 for 30 min using a single bed position, first on the mCT and then on the uEXPLORER, to allow a direct comparison between the two.

Patient Scans

A single-site prospective study was approved by the Institutional Review Board to collect PET/CT images after ^{90}Y liver radioembolization. Two patients were imaged with PET/CT after radioembolization at the University of California–Davis Health.

The first patient (P1) received a total activity of 3.363 GBq of ^{90}Y glass microspheres in 3 consecutive injections, targeting multiple neuroendocrine liver metastases. The patient was scanned 5 h after injection on the uEXPLORER total-body PET scanner (30-min duration) and then on the mCT 1 h later (30 min, 2 bed positions, 43% overlap). The second patient (P2) received a total activity of 0.985 GBq of ^{90}Y resin microspheres to treat metastatic pancreatic cancer. PET/CT images were acquired for 30 min at a single bed position covering the whole liver at 21.8 and 22.6 h after injection on the uEXPLORER and the mCT, respectively.

Image Reconstruction

Both phantom and patient data were reconstructed on the uEXPLORER using parameters adapted from the University of California–Davis clinical oncology protocol (but with an increased isotropic voxel size of 4 mm as opposed to 2.344 mm): ordered-subset expectation maximization, 20 subsets, 4 iterations, time of flight, point-spread function modeling, and no smoothing. This protocol follows the University of California–Davis low-dose image reconstruction parameters designed to reduce noise in low-count imaging such as for ^{90}Y imaging (29,30).

Image reconstruction on the mCT used ordered-subset expectation maximization, time of flight, 21 subsets, 3 iterations, point-spread function modeling, a voxel size of $4.078 \times 4.078 \times 3.75$ mm, and 5-mm gaussian smoothing following a previously published protocol (31) and closely matched the clinical oncology protocol of this scanner except for a 5.0-mm gaussian filter used to reduce noise for low-count ^{90}Y imaging.

The voxel size of the uEXPLORER reconstructions provides the closest possible match to the mCT reconstruction voxel size to reduce bias in the comparison. Given that the uEXPLORER has very high sensitivity and

high spatial resolution, uEXPLORER images without smoothing are still less noisy than mCT images (Figs. 2A and 2B), and additional smoothing would likely over-smooth the images, reducing diagnostic imaging performance.

Contrast-Enhanced CT (CECT)

Routine 4-phase abdominal CECT images acquired before treatment were used for liver contouring and segmentation. The late portal-phase image was used to identify the whole liver contour and the vasculature and to define the 8 Couinaud segments, S1–S8 (including segments 4a and 4b) (32,33). Thirteen volumes of interest (VOIs) were created (Figs. 2C and 2D), including the inferior vena cava and the left and right portal veins. The absorbed dose depends largely on the liver masses of P1 and P2 (1,504.8 g and 919.8 g, respectively), and the volumes and masses of all VOIs can be seen in Table 1. The segmentation was verified by a board-certified radiologist with 9 y of experience.

⁹⁰Y Image-Based Dosimetry Using Monte Carlo Simulation

To calculate the absorbed dose from the activity distribution in the VOI, Monte Carlo simulations were performed using GATE 9.0 (34). An attenuation map was generated for each patient or phantom using CECT and CT images, respectively, and material composition in GATE. The PET images were converted into activity distributions and then normalized to provide a probability density map of positron emission. The source and attenuation maps allowed GATE to generate and transport the primary and secondary particles (mostly electrons) and store the deposited energy in a 3D image matrix. The energy deposition

matrix was weighted by its density to produce the final 3D absorbed dose distribution in Gy. The ⁹⁰Y physics were modeled through the standardem_opt4 package with a standard energy cut of 1 mm, consistent with the liver tissue modeled in this work and as recommended for medical applications (35). The ⁹⁰Y radioactive decay energy distribution was defined by an energy spectrum generated from the Fermi theory for β -decays (36). ⁹⁰Y decays to ⁹⁰Zr through β -emission (99.998%) with a maximum energy of 2.28 MeV and mean energy of 930 keV, corresponding to a maximum electron range of 11 mm and a mean range of 2.5 mm in water (21). A low-frequency decay (0.017%) to the first excited state of ⁹⁰Zr allows transition of the internal pair production to ground state, yielding on average 31.86 positron emissions per million ⁹⁰Y decays that can be imaged with PET (37).

Phantom Absorbed Dose Calculation

The absorbed dose was estimated for each sphere insert of the NEMA image-quality phantom. To prevent any voxel outside the VOIs from containing a primary event in the Monte Carlo simulation and thus maximize the computation efficiency, a binary mask restricted the PET-based source distribution to voxels corresponding to each VOI. This method allowed the simulations to be performed with a fixed number of primary events followed by scaling to the cumulative activity instead of using the true total number of events, typically very large with therapeutic activities of 1–5 GBq. A total of 10^7 primaries was chosen to provide a statistical uncertainty of approximately 1% for the 37-mm sphere with a reasonable simulation time of 2 h in an 8-core computer at 3.2 GHz and 64 GB of random-access memory. The resolu-

tion of the volumetric dose map generated by GATE was 4-mm isotropic and $4.07 \times 4.07 \times 3.75$ mm for the uEXPLORER and the mCT, respectively. A separate Monte Carlo simulation was performed to produce the ground truth dose map through a mathematic model of the image-quality phantom. The ground truth was calculated with Monte Carlo simulation exactly as for the image-based calculations, but using geometric spheres, a homogeneous radiation source, and $0.25 \times 0.25 \times 0.25$ mm voxels to allow accurate tracking of β -particles with ranges of up to 11 mm. To compensate for the small voxel size, 10^8 primaries per sphere were used to achieve a statistical uncertainty of approximately 5% for the 37-mm sphere.

Patient Absorbed Dose Calculation

The noise in ⁹⁰Y-PET images is inherently higher than in ¹⁸F images because of the low positron yield combined with a lack of specific reconstruction methods to address the low count statistics (37). This limitation poses a unique challenge in defining the liver volume directly on the PET image, especially when respiratory motion shifts the liver position (38). Segmenting different images separately (e.g., mCT and uEXPLORER) also adds bias to the absorbed dose distributions, which was mitigated using a single VOI generated from the contoured CECT. The PET images were coregistered to the CECT and then projected onto the CECT image grid. Since PET images are used as radiation sources, every count in the image is a probable location of a primary event. To ensure that all

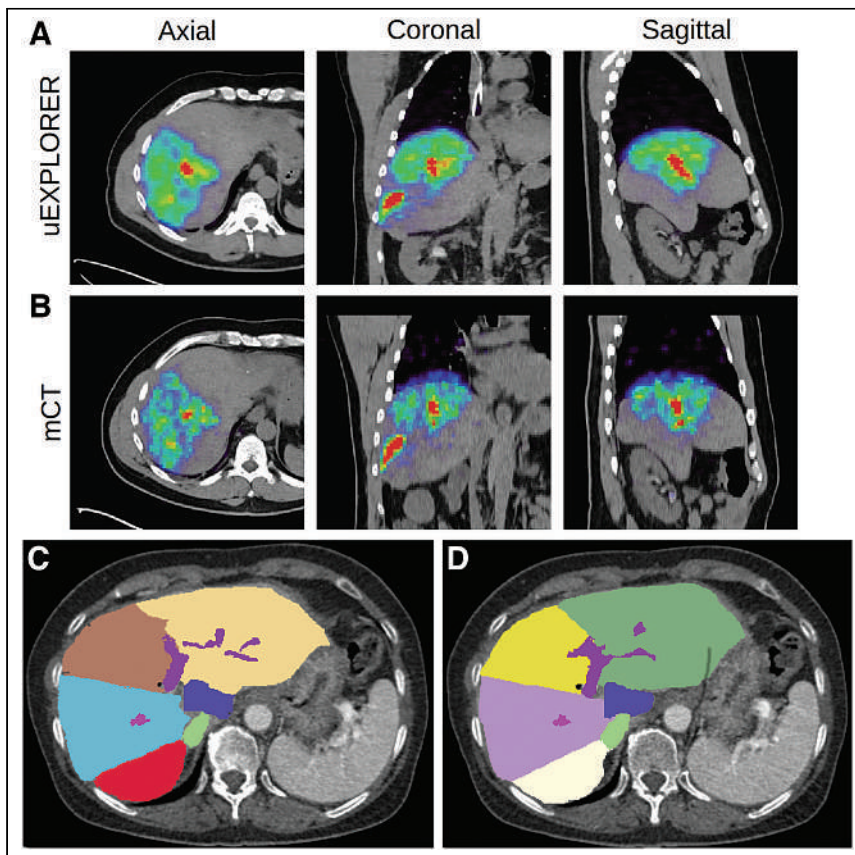


FIGURE 2. (A and B) Patient images of PET/CT at axial, coronal, and sagittal views from uEXPLORER (A) and mCT (B). uEXPLORER images without smoothing are less noisy than mCT and additional smoothing to uEXPLORER. (C and D) CECT at axial view with Couinaud segments at upper liver containing segments 2, 4a, 7, and 8 (C) and lower liver containing segments 3, 4b, 5, and 6 (D). Inferior vena cava and left and right portal veins can be visualized in both upper and lower liver.

TABLE 1
Liver and Liver Segment Volumes and Masses in P1 and P2

Patient	Parameter	Liver	IVP	LPV	RPV	Liver segment								
						1	2	3	4a	4b	5	6	7	8
P1	Volume (mL)	1,417.5	22.23	2.56	24.39	24.52	129.9	45.94	199.73	36.9	186.48	49.19	212.57	483.09
	Mass (g)	1,504.8	23.6	2.72	25.89	26.03	137.9	48.77	212.03	39.17	197.97	52.22	225.66	512.85
P2	Volume (mL)	866.5	33.96	6.61	9.6	14.04	91.46	155.39	124.9	87.93	169.27	34.0	22.66	116.67
	Mass (g)	919.8	36.05	7.02	10.19	14.9	97.09	164.96	132.59	93.35	179.7	36.09	24.06	123.86

IVC = inferior vena cava; LPV = left portal vein; RPV = right portal vein.

primary events were generated only in the liver, the same technique as used for the phantom was applied, in which the liver VOI was used as a binary image mask to restrict primary-event generation to regions within the liver (Fig. 3).

Monte Carlo simulations were performed within a voxelized phantom created from the CECT image that provided the anatomic information, mass, and density of tissue in which the β -particles propagate and interact. The activity distribution measured from PET images registered to the CECT volume was used to define the ^{90}Y source with 10^8 primary events, with a voxel size matching the spatial resolution of the CECT images ($0.74 \times 0.74 \times 1.25$ mm and $0.67 \times 0.67 \times 1.00$ mm for P1 and P2, respectively). All voxel-based absorbed doses were calculated from the dose map by averaging the voxel values in the VOI since all voxels share the same mass and density. No ground truth was computed, as no in vivo quantification of the ^{90}Y microspheres distribution can be performed to confirm the ^{90}Y activity distribution measured with PET.

Dose Characterization

The absorbed dose and dose–volume histograms (DVHs) were calculated for each phantom sphere, each liver segment, and the entire liver from the 3D absorbed dose distributions. DVHs for individual segments and the whole liver were used to assess the difference in the dose distributions computed from each PET/CT scanner. A particular range of dose bins was also evaluated, with consideration of only the voxels between 20% and 80% of the maximum absorbed dose (Gy) to build the cumulative DVH ($\text{DVH}_{20\%-80\%}$). This approach makes the data trends clearer by avoiding errors near extremes where the noise might be increased (37).

With the NEMA spheres, for which ground truth was available, the difference between the true value and the values obtained with

the scans was also quantified through the root mean squared error (RMSE) (39):

$$\text{RMSE} = \sqrt{\frac{\sum_0^{100} (\text{DVH}_{\text{PET},\phi} - \text{DVH}_{\text{True},\phi})^2}{100}}$$

where $\text{DVH}_{\text{PET},\phi}$ is the image-based absorbed dose and $\text{DVH}_{\text{True},\phi}$ is the true absorbed dose from the ground truth. The RMSE was calculated for the whole volume as well as for the 20%–80% range.

RESULTS

Phantom Analysis

Figure 4A shows the dose differences between the ground truth, the mCT, and the uEXPLORER for all 6 spheres. The mCT scanner at 10- and 13-mm diameters showed negative biases of 14.4 and 14.5 Gy, respectively. The uEXPLORER showed differences of 7.9 and 1.4 Gy, respectively, for these volumes. The lower biases were consistent with the higher sensitivity and spatial resolution of the uEXPLORER, expected to improve the dosimetry accuracy primarily in low-count ^{90}Y -PET regions resulting from small or low-activity regions.

Figure 4B shows the $\text{DVH}_{20\%-80\%}$ of the 37-mm sphere for both the uEXPLORER and the mCT, as well as for the ground truth. The ^{90}Y β -particles may deposit their energy in a neighbor voxel or even outside the sphere, leading to a heterogeneous energy deposition; therefore, $\text{DVH}_{20\%-80\%}$ exhibits a slow decrease rather than being a step function. The 37-mm sphere accounts for a larger number of voxels and thus resulted in a good RMSE agreement with the ground truth for both PET scanners, with no significant difference (0.3%) between the scanners' RMSEs. Although the RMSE was lower for the uEXPLORER in 4 of 6 spheres, including the 2 smallest spheres, of 10- and 13-mm diameter, it varied widely, with no clear trend between the 2 scanners. The 20%–80% RMSE range did not further improve the analysis, with a 36%–140% variation from the ground truth.

Patient Dosimetry

The total liver-absorbed dose calculated from the PET distribution showed excellent agreement between the uEXPLORER and the mCT, with 108 Gy (difference of 0.2 Gy, or 0.19%) for P1 and 40 Gy (difference of 0.1 Gy, or 0.16%) for P2. Much larger differences were observed when comparing the dose in liver segments, ranging from 6 to 204 Gy (differences from 0.01% to 60.8%) for

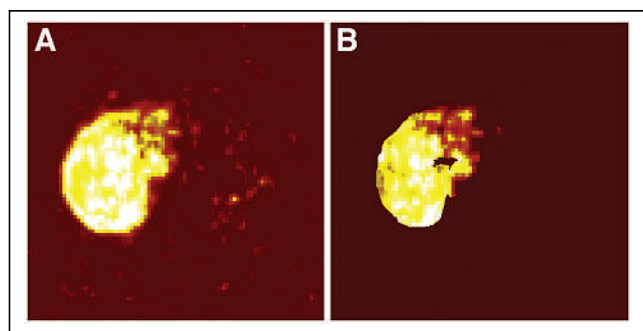


FIGURE 3. P2 activity distribution with 957 MBq in entire mCT PET image (A) and after applying mask corresponding to VOI to limit generation of events to VOI (B).

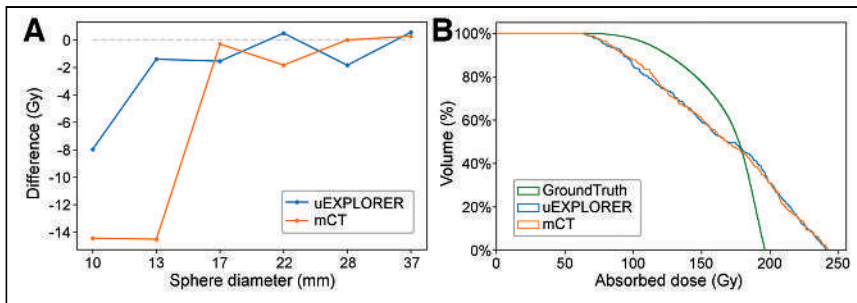


FIGURE 4. Absolute differences between uEXPLORER and mCT vs. true absorbed doses from ground truth for 6 NEMA spheres (A) and DVH of 37-mm sphere with 20%–80% range of maximum absorbed dose (Gy) (B).

P1 (Fig. 5A) and 10 to 92 Gy (differences from 0.39% to 35.8%) for P2 (Fig. 5B).

Figure 6 shows the DVH_{20%–80%} for segments 6–8 in both P1 and P2. These segments had the highest activities and absorbed doses and, thus, also better count statistics and lower noise, providing the most robust comparison between the 2 scanners. All values of DVH_{20%–80%} were in good agreement, with narrower tails for the uEXPLORER in all segments. As reported previously (39), a narrower tail might be an indicator of lower image noise. This was clearer in P2, who received a lower injected activity and was imaged at a later time point than P1 (5 h and 22 h after injection, respectively) and therefore should have a lower signal-to-noise ratio. Accordingly, the lower image noise of the uEXPLORER agreed with the improved average contrast recovery reported previously (28).

DISCUSSION

The absorbed doses calculated for the NEMA phantom spheres imaged with the uEXPLORER and mCT scanners agreed well for most of the 4 largest spheres, with an expected fluctuation due to the inherent noise present in ⁹⁰Y-PET images. In contrast, a larger discrepancy between the calculated doses and the ground truth, 1.0% and 10.2%, was observed with the uEXPLORER and the mCT, respectively, for the 13-mm-diameter sphere. This is a clear indication of the higher spatial resolution and signal-to-noise ratio of the uEXPLORER, which is especially beneficial for dose quantification in small and low-activity regions. This trend was also

observed in patient images, in which the narrower tail of the uEXPLORER DVH_{20%–80%} indicates a lower noise level, more apparent for P2, who received a lower injected activity and was scanned at a later time point, resulting in a 2-fold reduction in counts.

The DVH_{20%–80%} for both the phantom and the patients showed a very similar slope in both scanners, and the behavior of the slope indicates the heterogeneity of the dose or, in this case, the activity source. In a homogeneous source, all voxels have the same value, and therefore, the DVH_{20%–80%} would be a step function. In a heterogeneous source, the voxels have different values,

resulting in slopes such as those shown in Figures 4B and 6. Hence, the similarities in the DVH slope for both scanners suggest a similar distribution of activity. Similar distributions and heterogeneities obtained from the 2 subsequent PET scans suggest that ⁹⁰Y PET can be considered a reliable method for posttreatment dosimetry and follow-up.

P1 received 3 selective injections through the right hepatic artery targeting 3 main arterial branches supplying multiple tumors in the right hepatic lobe, resulting in high doses in target segments S5 to S8. Segments S1–S4 and the vessels should contain no or very little activity because of the injection location, meaning that the observed dose is likely due to inaccuracies in PET corrections during reconstruction (e.g., scatter and dead-time correction and lutetium yttrium orthosilicate background subtraction). P2 received a single lobar injection in the right hepatic artery before lobectomy, resulting in a more uniform absorbed dose distribution in segments S5–S8 than in P1 due to a more widespread microspheres distribution. Most of the resin microspheres were directed to the right lobe, but a substantial amount of activity reached the left lobe, possibly because the large number of microspheres led to a reflux into unintended artery branches (9), explaining the high doses in segments 4a and 4b and stressing the need for posttreatment dosimetry. Although P2 was injected with a much lower activity than P1 (25%), the absorbed dose for the entire liver volume was 35% of P1's liver dose because of the much smaller liver mass (919.8 g and 1,504.8 g, respectively). Low VOI masses (2–26 g, derived from organ volumes), such as those of the vessels, can cause even

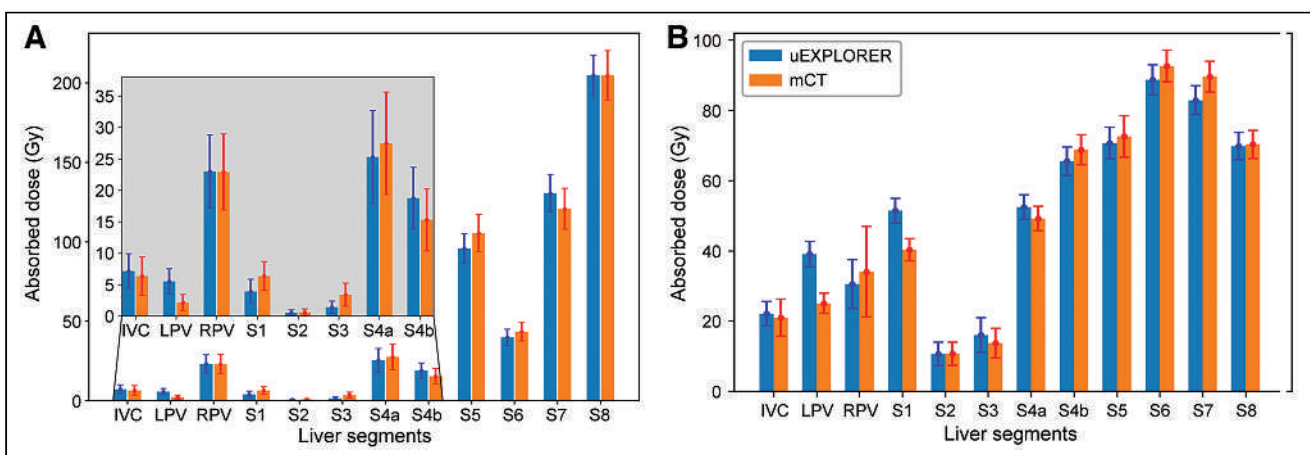


FIGURE 5. Absorbed doses for P1 (A) and P2 (B). Error bars indicate statistical uncertainty from GATE simulations. IVC = inferior vena cava; LPV = left portal vein; RPV = right portal vein.

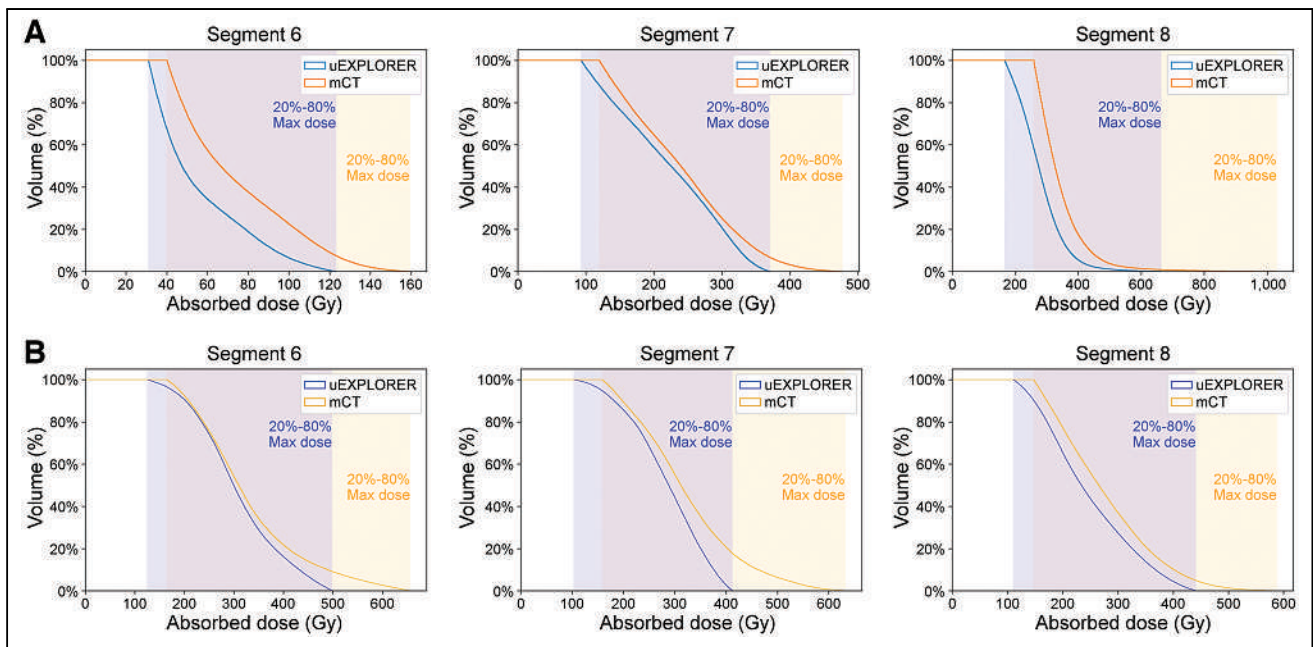


FIGURE 6. DVH with 20%–80% range of maximum absorbed dose (Gy) for segments 6–8 of P1 (A) and P2 (B).

a very low ^{90}Y activity to generate a high absorbed dose with a high degree of uncertainty. This also explains why the absorbed dose in S5 and S7 was greater for P2 than for P1 despite the lower injected activity. The intraliver discrepancies and the changes in absolute dose values indicate the importance of conducting a segmental dose assessment for ^{90}Y radioembolization instead of evaluating the whole liver dose, which includes the total mass even if not irradiated and decreases the mean absorbed dose. Furthermore, recent studies showed lobules trapping 1–453 microspheres, resulting in a highly nonuniform distribution (14) and creating high doses locally. It is therefore critical to measure dose heterogeneity and move toward high-resolution dosimetry.

CONCLUSION

Personalized dosimetry is of great interest in TARE. A detailed evaluation of the absorbed dose in the liver through the Couinaud liver segments allows a better understanding of the microsphere distribution and an evaluation of the treatment. The whole liver absorbed doses calculated from 2 different PET scans were in high agreement with each other, indicating that both conventional and total-body PET provide good ^{90}Y dosimetry. This agreement builds confidence about using ^{90}Y PET over bremsstrahlung SPECT, with the possibility of assessing microsphere placement and dosimetry after treatment. Performing segmental liver dosimetry not only can indicate the dose–response relationship of the treatment but also can help improve patient care. Understanding the activity may either confirm the planning or elucidate an unexpected distribution and might support an increase of the injected activity when low toxicity is confirmed. The uEXPLORER provides a more detailed activity and absorbed dose distribution, translating into a more accurate visualization and quantification of microsphere clusters. This ability is particularly important when analyzing liver segments or small volumes and tumors. Although uEXPLORER images are visibly clearer, only the relative difference from conventional PET can be computed, since there is no

in vivo ground truth to confirm the microsphere distributions. The better accuracy observed in the small spheres of the NEMA phantom and the greater spatial resolution of uEXPLORER made coregistration between the PET and CT images faster and more accurate, indicating the potential of total-body PET for intraliver dosimetry. This potential will be investigated in further patient studies.

DISCLOSURE

Funding for this work was provided by NIH grant R01 CA206187, which is supported by NCI, NIBIB, and the Office of the Director, and by R01 CA249422. No other potential conflict of interest relevant to this article was reported.

KEY POINTS

QUESTION: What is the impact of evaluating the TARE dose distribution at the liver-segment scale, and what is the advantage of using high-sensitivity total-body PET?

PERTINENT FINDINGS: Segmental calculation of the absorbed dose resulted in large discrepancies between the total-body and conventional PET scanners, whereas evaluation of the entire liver exhibited good agreement and the uEXPLORER showed a better signal-to-noise ratio in both phantom and patient evaluations.

IMPLICATIONS FOR PATIENT CARE: The use of PET images opens the possibility of posttreatment follow-up and dosimetry with the calculation of the dose absorbed by Couinaud liver segments, which helps in treatment evaluation through detailed separation of irradiated and nonirradiated volumes.

REFERENCES

1. About SIR-Spheres microspheres. Sirtex website. <http://www.sirtex.com/us/clinicians/about-sir-spheres-microspheres/>. Accessed April 12, 2022.

2. Pilot study of selective internal radiation therapy (SIRT) with yttrium-90 resin microspheres (SIR-Spheres microspheres) in patients with renal cell carcinoma (STX0110). Cancer Australia website. <https://www.australianclinicaltrials.gov.au/search-clinical-trials/search-results/clinical-trials-details.aspx?TrialID=335845&ds=1>. Accessed April 12, 2022.
3. Salem R, Gabr A, Riaz A, et al. Institutional decision to adopt Y90 as primary treatment for hepatocellular carcinoma informed by a 1,000-patient 15-year experience. *Hepatology*. 2018;68:1429–1440.
4. Garin E, Rolland Y, Edeline J. ⁹⁰Y-loaded microsphere SIRT of HCC patients with portal vein thrombosis: high clinical impact of ^{99m}Tc-MAA SPECT/CT-based dosimetry. *Semin Nucl Med*. 2019;49:218–226.
5. Salem R, Johnson GE, Kim E, et al. Yttrium-90 radioembolization for the treatment of solitary, unresectable HCC: the legacy study. *Hepatology*. 2021;74:2342–2352.
6. Salem R, Gordon AC, Mouli S, et al. Y90 radioembolization significantly prolongs time to progression compared with chemoembolization in patients with hepatocellular carcinoma. *Gastroenterology*. 2016;151:1155–1163.e1.
7. Padia SA, Johnson GE, Horton KJ, et al. Segmental yttrium-90 radioembolization versus segmental chemoembolization for localized hepatocellular carcinoma: results of a single-center, retrospective, propensity score-matched study. *J Vasc Interv Radiol*. 2017;28:777–785.e1.
8. Chow PKH, Gandhi M, Tan SB, et al.; Asia-Pacific hepatocellular carcinoma trials group. SIRveNIB: selective internal radiation therapy versus sorafenib in Asia-Pacific patients with hepatocellular carcinoma. *J Clin Oncol*. 2018;36:1913–1921.
9. Kallini JR, Gabr A, Thordlund K, et al. Comparison of the adverse event profile of TheraSphere® with SIR-Spheres® for the treatment of unresectable hepatocellular carcinoma: a systematic review. *Cardiovasc Intervent Radiol*. 2017;40:1033–1043.
10. Cheneler D, Ward M. Power output and efficiency of beta-emitting microspheres. *Radiat Phys Chem*. 2015;106:204–212.
11. Dewaraja YK, Schipper MJ, Shen J, et al. Tumor-absorbed dose predicts progression-free survival following ¹³¹I-tositumomab radioimmunotherapy. *J Nucl Med*. 2014;55:1047–1053.
12. Elschot M, Lam MGEH, van den Bosch MAAJ, Viergever MA, de Jong HWAM. Quantitative Monte Carlo-based ⁹⁰Y SPECT reconstruction. *J Nucl Med*. 2013;54:1557–1563.
13. Elschot M, Vermolen BJ, Lam MG, de Keizer B, van den Bosch MA, de Jong HW. Quantitative comparison of PET and bremsstrahlung SPECT for imaging the in vivo yttrium-90 microsphere distribution after liver radioembolization. *PLoS One*. 2013;8:e55742.
14. Walrand S. Microsphere deposition, dosimetry, radiobiology at the cell-scale, and predicted hepatic toxicity. In: *Handbook of Radioembolization*. Taylor and Francis; 2016:199–217.
15. Garin E, Lenoir L, Rolland Y, et al. Dosimetry based on ^{99m}Tc-macroaggregated albumin SPECT/CT accurately predicts tumor response and survival in hepatocellular carcinoma patients treated with ⁹⁰Y-loaded glass microspheres: preliminary results. *J Nucl Med*. 2012;53:255–263.
16. Fabbri C, Sarti G, Cremonesi M, et al. Quantitative analysis of ⁹⁰Y bremsstrahlung SPECT-CT images for application to 3D patient-specific dosimetry. *Cancer Biother Radiopharm*. 2009;24:145–154.
17. Fong Y, Kemeny N, Paty P, Blumgart LH, Cohen AM. Treatment of colorectal cancer: hepatic metastasis. *Semin Surg Oncol*. 1996;12:219–252.
18. Fowler KJ, Maughan NM, Laforest R, et al. PET/MRI of hepatic ⁹⁰Y microsphere deposition determines individual tumor response. *Cardiovasc Intervent Radiol*. 2016;39:855–864.
19. Garin E, Palard X, Rolland Y. Personalised dosimetry in radioembolisation for HCC: impact on clinical outcome and on trial design. *Cancers (Basel)*. 2020;12:1557.
20. Ljungberg M, Gleisner KS. 3-D image-based dosimetry in radionuclide therapy. *IEEE Trans Rad Pla Med Sci*. 2018;2:527–540.
21. O'Doherty J. A review of 3D image-based dosimetry, technical considerations and emerging perspectives in ⁹⁰Y microsphere therapy. *J Diagn Imaging Ther*. 2015;2:1–34.
22. Tang S, Liu Y, Wang J, Zhao Y, Fan X, Dong Y. Dead time correction method for long axial field-of-view, whole-body PET scanner [abstract]. *J Nucl Med*. 2019;60(suppl 1):458.
23. Tang S, Zhao Y, Wang J, Liu Y, Dong Y. Geometric correction in normalization for long axial field-of-view, whole-body PET scanner. Poster presented at: 2019 IEEE Nuclear Science Symposium and Medical Imaging Conference. October 31, 2019; Manchester, U.K. Poster 305.
24. Spencer BA, Berg E, Schmall JP, et al. Performance evaluation of the uEXPLORER total-body PET/CT scanner based on NEMA NU 2-2018 with additional tests to characterize PET scanners with a long axial field of view. *J Nucl Med*. 2021;62:861–870.
25. Karp JS, Viswanath V, Geagan MJ, et al. PennPET Explorer: design and preliminary performance of a whole-body imager. *J Nucl Med*. 2020;61:136–143.
26. Prenosil GA, Sari H, Fürstner M, et al. Performance characteristics of the Biograph Vision Quadra PET/CT system with a long axial field of view using the NEMA NU 2-2018 standard. *J Nucl Med*. 2022;63:476–484.
27. Jakoby BW, Bercier Y, Conti M, Casey ME, Bendriem B, Townsend DW. Physical and clinical performance of the mCT time-of-flight PET/CT scanner. *Phys Med Biol*. 2011;56:2375–2389.
28. Spencer BA, Omidvari N, Costa GCA, et al. Comparison between EXPLORER total-body PET and conventional PET imaging of Y-90 radioembolization: a phantom and clinical study. Presented at: 2020 IEEE Nuclear Science Symposium and Medical Imaging Conference. November 6, 2020; Boston, Massachusetts. Abstract M-17-03.
29. Badawi RD, Shi H, Hu P, et al. First human imaging studies with the EXPLORER total-body PET scanner. *J Nucl Med*. 2019;60:299–303.
30. Leung EK, Berg E, Omidvari N, et al. Quantitative accuracy in total-body imaging using the uEXPLORER PET/CT scanner. *Phys Med Biol*. 2021;66:205008.
31. Willowson KP, Hayes AR, Chan DLH, et al. Clinical and imaging-based prognostic factors in radioembolisation of liver metastases from colorectal cancer: a retrospective exploratory analysis. *EJNMMI Res*. 2017;7:46.
32. Majno P, Mentha G, Toso C, Morel P, Peitgen HO, Fasel JH. Anatomy of the liver: an outline with three levels of complexity—a further step towards tailored territorial liver resections. *J Hepatol*. 2014;60:654–662.
33. Bismuth H, Houssin D, Castaing D. Major and minor segmentectomies “régérées” in liver surgery. *World J Surg*. 1982;6:10–24.
34. Sarrut D, Bardiès M, Bousson N, et al. A review of the use and potential of the GATE Monte Carlo simulation code for radiation therapy and dosimetry applications. *Med Phys*. 2014;41:064301.
35. Beaudoux V, Blin G, Barbel B, Kantor G, Zacharatou C. Geant4 physics list comparison for the simulation of phase-contrast mammography (XPulse project). *Phys Med*. 2019;60:66–75.
36. Roncali E, Taebi A, Foster C, Vu CT. Personalized dosimetry for liver cancer Y-90 radioembolization using computational fluid dynamics and Monte Carlo simulation. *Ann Biomed Eng*. 2020;48:1499–1510.
37. Strydhorst J, Carlier T, Dieudonné A, Conti M, Buvat I. A GATE evaluation of the sources of error in quantitative ⁹⁰Y PET. *Med Phys*. 2016;43:5320.
38. Tsai YL, Wu CJ, Shaw S, Yu PC, Nien HH, Lui LT. Quantitative analysis of respiration-induced motion of each liver segment with helical computed tomography and 4-dimensional computed tomography. *Radiat Oncol*. 2018;13:59.
39. Siman W, Mikell JK, Mawlawi OR, Mourtada F, Kappadath SC. Dose volume histogram-based optimization of image reconstruction parameters for quantitative ⁹⁰Y-PET imaging. *Med Phys*. 2019;46:229–237.

Toward a Patient-Specific Traceable Quantification of SPECT/CT-Based Radiopharmaceutical Distributions

Anna-Lena Theisen, Michael Lassmann, and Johannes Tran-Gia

Department of Nuclear Medicine, University of Würzburg, Würzburg, Germany

Quantitative SPECT/CT imaging is currently the state of the art for peritherapeutic monitoring of radiopharmaceutical distributions. Because of poor resolution, however, the verification of SPECT/CT-based activity distributions is of particular importance. Because of the lack of a ground truth in patient measurements, phantoms are commonly used as a substitute for clinical validation of quantitative SPECT/CT. Because of the time-consuming and erroneous preparation of multicompartment phantoms, such as for the kidney, the usually very complex internal activity distributions are typically replaced by 1- or 2-compartment models. To provide a simplified solution for generating inhomogeneous activity distributions, this work presents a methodology for designing single-compartment phantoms that mimic inhomogeneous spatial activity distributions by using internal filling structures of different volume fractions.

Methods: A series of phantoms with different filling structures was designed, 3-dimensionally printed, and measured. After assessing the feasibility of the presented approach in a simple geometry, a set of three patient-specific kidney phantoms was designed on the basis of the contrast-enhanced CT scan of a patient with metastatic castration-resistant prostate cancer. Internal gyroid structures of different wall thicknesses were used in the renal medulla and cortex to reproduce the inhomogeneous activity distribution observed in a peritherapeutic SPECT/CT acquisition 24 h after injection of ^{177}Lu -labeled prostate-specific membrane antigen (apparent activity concentration ratios of 1:1, 1:3.5, and 1:7.5). After 3-dimensional printing, SPECT/CT experiments were performed and the results were compared with the patient data for different reconstruction settings (iterations, subsets, and postfiltering). **Results:** Good agreement was found between phantom designs and fabricated phantoms (based on high-resolution CT). No internal filling structures were visible in any of the SPECT images, indicating a sufficiently small feature size. Although good visual and quantitative agreement was achieved for certain combinations of filling structure and reconstruction, a histogram analysis indicated an even more complex activity distribution in the patient than represented by the two compartments assumed in our model. **Conclusion:** The proposed methodology provides patient-specific phantoms mimicking inhomogeneous activity distributions while using a single stock solution, thus simplifying the filling process and reducing uncertainties in the activity determination. This method enables an unprecedented possibility for patient-specific evaluation of radiopharmaceutical uptake, reducing uncertainties in internal dosimetry and individualized treatments.

Key Words: methods; SPECT/CT; 3D printing; activity distribution; kidney phantom; quantitative SPECT/CT

J Nucl Med 2022; 63:1108–1116

DOI: 10.2967/jnumed.121.262925

Received Jul. 19, 2021; revision accepted Nov. 1, 2021.

For correspondence or reprints, contact Johannes Tran-Gia (Tran_J@ukw.de).

Published online Nov. 18, 2021.

COPYRIGHT © 2022 by the Society of Nuclear Medicine and Molecular Imaging.

A fundamental problem in the clinical validation of new imaging technology such as quantitative imaging of radiopharmaceutical distributions is the lack of a ground truth in patient measurements. Since nuclear medicine imaging procedures are typically noninvasive, direct validation of the measured radiopharmaceutical distribution on the basis of tissue samples is possible in only the rarest of cases. As an example, de Jong et al. revealed the radioactivity distribution in the normal human kidney after intravenous injection of ^{111}In -diethylenetriaminepentaacetic acid octreotide using SPECT scanning before and ex vivo autoradiography of the kidney after nephrectomy in three men with single primary renal tumors (*1*). In most cases for which such information is not available, however, imaging methodologies can be validated only on a non-patient-specific basis using anthropomorphic phantom measurements.

Industrially produced phantoms, which are widely used for commissioning and quality control in nuclear medicine imaging, typically consist of one or more fillable compartments of simple geometries (e.g., spheres or cylinders). Inhomogeneous activity distributions are typically achieved by assembling a set of single-compartment phantom inserts separately filled with radioactive stock solutions of different activity concentrations. This method, however, increases the complexity and thus the error susceptibility of the phantom preparation, as each separately filled compartment adds to the total uncertainty of the measurement (e.g., because of errors in the activity and filling volume of each stock solution). On the way toward more patient-specific phantoms, increasingly complex 3-dimensionally (3D) printed phantoms have recently been proposed for quality assessment of SPECT/CT quantification (*2–5*). The combination of low costs yet very flexible design options makes the technology an ideal supplement for, or even an alternative to, industrially produced phantoms. Although in the first implementations of 3D printing technology for nuclear medicine phantom production, simple geometries with a single fillable compartment were implemented (*3*), these designs were quickly replaced by more complex structures consisting of multiple (mostly two) separately fillable compartments (*4,5*). Despite many advancements in the field of 3D printing for nuclear medicine phantom production, inhomogeneous activity distributions within a single compartment have not yet been achieved, leaving unresolved the issue of patient-specific assessment of SPECT/CT imaging.

In this work, we present a way of achieving spatially inhomogeneous activity distributions in a single fillable compartment by using internal filling structures of different volume fractions. This method, while keeping phantom filling as simple as possible, leads to apparently inhomogeneous activity distributions in SPECT/CT imaging if the structure size is smaller than the SPECT resolution. The methodology was first developed and tested in a simple cuboid geometry for validation and was then applied to create a patient-specific multicompartment

kidney of a patient with metastatic castration-resistant prostate cancer who had previously undergone ^{177}Lu -labeled prostate-specific membrane antigen (PSMA) therapy at our institution.

MATERIALS AND METHODS

SPECT/CT Imaging

All SPECT/CT data in this work (phantom as well as patient data) were acquired with a Siemens Inveo Bold SPECT/CT system with a 9.5-mm crystal thickness, a medium-energy low-penetration collimator, a 180° configuration, automatic contouring, continuous mode, 60 views, 10 s per view, a 256×256 matrix, and 3 energy windows (20% around the main photopeak of 208 keV and 2 adjacent 10% windows). Subsequent to the SPECT acquisition, low-dose CT imaging was performed for attenuation correction (130 kVp, 512×512 pixels, $1.0 \times 1.0 \times 3.0$ mm resolution). Reconstructions were performed using xSPECT Quant (Siemens), automatically converting counts to activity concentration based on a National Institute of Standards and Technology–traceable cross-calibration (the calibration of this quantitative reconstruction is performed regularly as recommended by the manufacturer) using 1 subset with different combinations of iterations (12, 24, and 48) and postfilters (0, 10, and 20 mm). All activities were decay-corrected to the starting time of the SPECT/CT acquisition.

The patient whose data were used for this study signed an informed consent form, and the local ethics committee expressed no objections to the retrospective evaluation and publication of the data in accordance with data protection regulations (reference number 20200915 01).

Gyroid Structure

The basic idea is to achieve an apparently inhomogeneous signal distribution in SPECT phantoms using a phantom filled with a radioactive solution of homogeneous activity concentration in combination with a filling structure of spatially varying volume fraction (fraction of volume occupied by the structure). As the structure fills space and thereby displaces radioactive solution to varying extents in different areas of the phantom, the apparent activity distribution (e.g., for SPECT voxels, which are typically in the range of 2–5 mm in edge length) can be varied by changing the volume fraction of the filling structure. The mass density of the hardened photopolymer resin is 1.22 ± 0.01 g/cm³, obtained by dividing the caliper-based volume of a 3D printed solid resin cube with a side length of 20.00 ± 0.05 mm (measurement of all 4 edges of a single 3D printed cube) by the weight measured with an ED224S analytic balance (Sartorius AG; average of 3 measurements). This value lies in the range of water and soft tissue, ensuring only minor differences in attenuation between the resin and water.

The filling structure needs to be periodic to ensure that any excess resin can leave the phantom during the printing process and that radioactive solution can permeate the structure during phantom preparation and emptying. In addition, the range of possible volume fractions should be as large as possible to represent even highly heterogeneous activity distributions. After testing different combinations of cylinders and spheres of different sizes, the gyroid structure (6) was selected, as it combines all required properties.

A gyroid (Fig. 1) is an infinitely connected triply periodic minimal surface structure without self-intersections. The surface is described

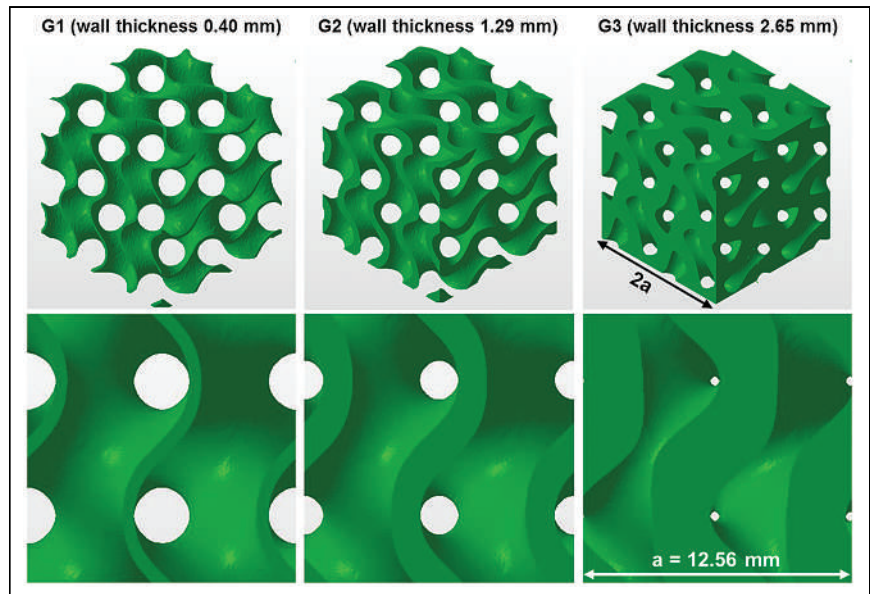


FIGURE 1. Gyroid structures used in this work. (Top) Gyroid cubes (edge length, $2a$) for a period of $a = 12.56$ mm and different wall thicknesses (G1, 0.40 mm; G2, 1.29 mm; G3, 2.65 mm). (Bottom) Corresponding cross-sections (only a single period is depicted) to illustrate the gyroid features (period, wall thickness) and the spatial volume filled by gyroid.

by the following equation, where a equals the period and t affects the thickness of the structure:

$$t(x, y, z) = \sin \frac{2\pi x}{a} \cos \frac{2\pi y}{a} + \sin \frac{2\pi y}{a} \cos \frac{2\pi z}{a} + \sin \frac{2\pi z}{a} \cos \frac{2\pi x}{a} \quad (\text{Eq. 1})$$

Three gyroid representations form the basis for all phantom designs in this work (a fixed period of $a = 4\pi$ -mm was used): Gyroid 1 (G1) had a wall thickness of 0.40 mm, which represents the minimum wall thickness supported by our 3D printer (Form 2, Formlabs). In addition, gyroids with a wall thickness of 1.29 mm (G2) and 2.65 mm (G3) were used to achieve volume fraction ratios of about 1:3.5 and 1:7.5, respectively, with regard to G1. These volume fractions were chosen because they cover the range of realistic volume fraction ratios (between 1:1 and 1:8 depending on patient, time after injection, and subregion of cortex or medulla), which we had previously determined in a retrospective evaluation (7) of autoradiography data published by de Jong et al. (7).

Cuboid Phantom

To validate our assumptions, a phantom was designed by concatenating 3 cubic structures with dimensions of $4 \times 4 \times 4$ cm³, each consisting of 1 of the 3 gyroids (G1, G2, and G3) (Fig. 2A). After creation in MATLAB R2021a (MathWorks), each of these gyroids was transferred to Netfabb Premium 2021 (Autodesk). In Netfabb, each structure was smoothed (triangle reduction with a maximum average deformation of 0.05 mm) to enable high-quality 3D printing. On the basis of these models, the volume fraction ratios between G1, G2, and G3 were determined as follows (intermediate values of the calculation can be found in Table 1): first, the volume fraction filled with resin (resin fraction) was calculated as the quotient of the gyroid structure's volume inside a cube (obtained by Netfabb) and the analytic cube volume. In addition, the fraction of each gyroid volume that was fillable with radioactive stock solution (fillable fraction) was calculated as a complement of the resin fraction. Lastly, the ratio of these resin fractions with respect to G1 was calculated (resin fraction G2 or G3 divided by resin fraction G1), which will be referred to as the resin fraction ratio. These values are crucial when

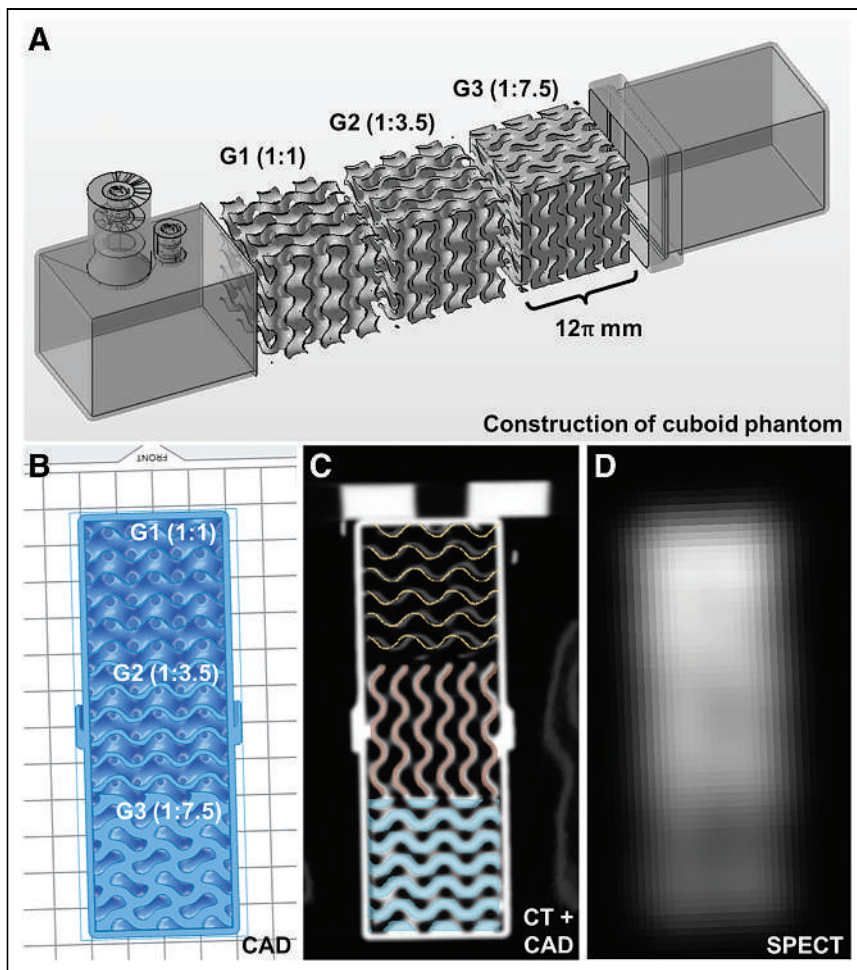


FIGURE 2. Cuboid phantom. (A) Model components (3 gyroid cubes of different volume fraction ratios and shell consisting of 2 parts). (B) Cross-section through CAD model. (C) Cross-section through CT (gray scale) superimposed by CAD model (different colors). (D) Cross-section of SPECT reconstruction (48 iterations, 1 subset, and 10-mm postprocessing filter).

designing multicompartment phantoms from 2 different gyroid representations (e.g., a kidney consisting of cortex and medulla).

To combine the 3 cubic gyroid structures in a single phantom, a cuboid shell $4 \times 4 \times 12 \text{ cm}^3$ in inner dimensions and with a 2-mm wall thickness was designed to enclose the 3 wall-less gyroid cubes (a top and a bottom part to be agglutinated after placing the gyroids inside; Fig. 2A). This shell included a funnel-shaped filling port. Finally, all parts were combined, and the model was exported in the stereolithography format.

All preparations for the 3D printing procedure (positioning, slicing, and addition of support structures) were performed in PreForm 3.8.0 (Formlabs), and printing was performed using a Form 2 printer with a layer thickness of 100 μm and the Clear V4 resin (both Formlabs).

Patient-Specific Kidney Phantom

To validate the methodology and demonstrate its potential to assess SPECT-based activity distributions obtained from patients undergoing ^{177}Lu -based radionuclide therapies, we designed a set of patient-specific kidney phantoms, performed ^{177}Lu SPECT/CT acquisitions with these phantoms, and compared the results with a clinical ^{177}Lu SPECT/CT dataset of the same patient (acquired with the same setup and system). The kidney was chosen because it represents one of the most common organs at risk in radionuclide therapies (8–10).

The clinical validation was based on a peritherapeutic SPECT/CT dataset of a patient with metastatic castration-resistant prostate cancer who had undergone ^{177}Lu -PSMA therapy at our institution (acquisition time, 24 h after injection). For design of a 2-compartment model with different activity concentrations in the cortex and medulla, high-resolution and high-contrast morphologic data were additionally needed. As the low-dose CT acquired along SPECT/CT scanning is not sufficient to reliably distinguish cortex and medulla, a temporally close contrast-enhanced CT acquisition (Siemens Biograph mCT 64; CT parameters, $0.78 \times 0.78 \times 1.00 \text{ mm}^3$ resolution, 150 mAs, 100 kVp, pitch factor of 0.8, $512 \times 512 \times 866$ slices) of the same patient was used. After anonymization (syngo.via; Siemens), the DICOM images were loaded into 3D Slicer 4.10.1 (11) for segmentation. First, the contrast-enhanced CT, which provided the anatomic information on the cortex and medulla, was registered to the low-dose CT scan of the peritherapeutic SPECT/CT acquisition using an affine registration. Then, slice-by-slice segmentations of the cortex and medulla of the left kidney were performed on the registered contrast-enhanced CT scan. These segmentations were exported in the stereolithography format for further processing (left column of Fig. 3A).

To cover a range of different internal activity distributions, a set of 3 kidney phantoms with different combinations of internal gyroid structures was designed. Because the highest uptake is typically expected in the renal cortex, the cortex of all phantoms was filled with G1, that is, with the highest fillable fraction available. In contrast, the medulla was filled with a different gyroid representation (G1, G2, and G3) for each phantom, resulting in different resin fraction ratios (1:1, 1:3.55, and 1:7.44, respectively).

All gyroid compartments were constructed in Netfabb by Boolean operations between the segmentations and the gyroid structures (Fig. 3A).

TABLE 1

Calculation of Resin Fraction and Fillable Fraction for 3 Cuboid Structures, and Resin Fraction Ratio of G2 and G3 with Respect to G1

Gyroid	Wall thickness (mm)	Resin fraction	Fillable fraction	Resin fraction ratio
G1	0.40	0.078	0.922	1:1
G2	1.29	0.277	0.723	1:3.55
G3	2.65	0.580	0.420	1:7.44

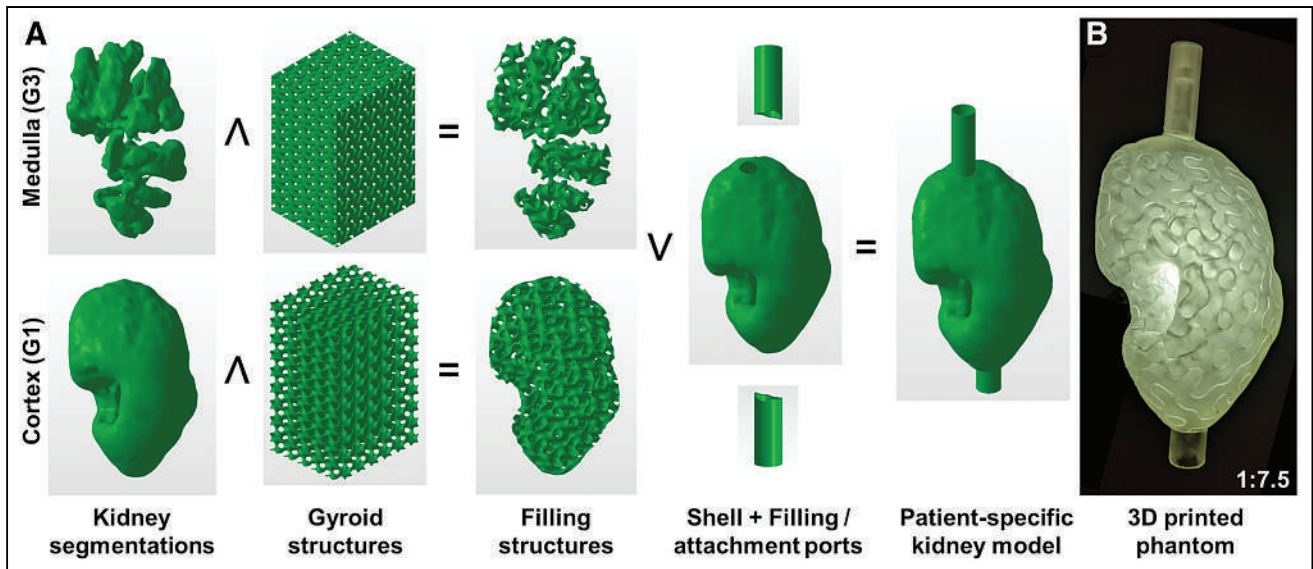


FIGURE 3. Design of patient-specific 2-compartment kidney phantom. (A) Boolean operations necessary to generate kidney CAD model out of patient-specific kidney VOIs, different gyroid and filling structures (example: G1 and G3 for cortex and medulla, respectively), attachment and filling ports, and patient-specific kidney shell. (B) 3D printed 1:7.5 kidney phantom. \wedge = Boolean “and”; \vee = Boolean “or.”

Subsequently, the 2 gyroid-filled compartments were combined with a kidney shell (wall thickness, 1 mm), as well as filling and attachment ports (Fig. 3A, center). Finally, the model was exported in the stereolithography format and 3D printed in one piece as described in the previous section (Fig. 3B).

Refinement of 3D Printed Phantoms and Quality Assurance

After printing, all phantoms were refined as follows: to remove excess resin, the phantoms were washed in 99.9% concentrated 2-propanol (IPA) for 180 min, followed by 60 min of ultraviolet curing at 60°C to reach the highest possible strength. Afterward, the support structures were manually removed. Finally, a polyamide M6 plastic thread and a filling funnel (to avoid air bubbles during filling) were glued on with a medium-viscosity 2-component epoxy adhesive.

For quality assurance, the finished phantoms underwent several quality tests. To check the agreement between the computer-aided design (CAD) model and the printed phantom, a high-resolution CT scan of the phantom was performed using the CT system integrated in our SPECT/CT system (Siemens Intevo Bold; CT parameters, $0.29 \times 0.29 \times 0.70 \text{ mm}^3$ resolution, 150 mAs, 130 kVp, pitch factor of 0.5, $512 \times 512 \times 241$ slices) and the CT images were compared with the CAD models.

As waterproofness is one of the most important prerequisites for nuclear medicine phantoms, the finished phantoms finally underwent leakage testing. In the same process, the filling volume of each phantom was determined by weighing the phantom before and after filling with a PCB 3500-2 precision mass scale (Kern and Sohn GmbH).

Activity Quantification of the Patient’s Kidney

To establish similar measurement conditions between the phantom measurements and the patient measurement, the total activities of the kidney phantom measurements were chosen to be as similar as possible to the patient kidney. For this purpose, the SPECT/CT-based activity in the left patient kidney 24 h after injection was determined by a volume-of-interest (VOI) analysis in the xSPECT Quant reconstructions (i.e., the mean of the activity concentration in a CT-based kidney VOI [Bq/mL], which had been enlarged by 6 mm to account for spill-out, multiplied by the VOI volume [mL] (12)). Activity concentrations for the stock solutions to be used in the 3 kidney phantoms were then calculated by dividing this total activity by the filling volume of each of the kidney phantoms (target activities and activity concentrations, along with the actually measured values, can be found in Table 2).

TABLE 2
Activities and Activity Concentrations Measured with Regard to Patient-Specific Kidney Phantom Measurements

Ratio	V (mL)	Target, c (MBq/mL)	HPGe-based				SPECT-based		
			c (MBq/mL)	A (MBq)	C_{Medulla} (MBq/mL)	C_{Cortex} (MBq/mL)	$A_{0 \text{ mm}}$ (MBq)	$A_{10 \text{ mm}}$ (MBq)	$A_{20 \text{ mm}}$ (MBq)
1:1	149.8	0.63	0.65	97.4	0.60	0.60	103.8	103.7	103.6
1:3.5	140.2	0.67	0.63	88.3	0.46	0.58	93.6	93.5	93.5
1:7.5	131.5	0.72	0.68	89.4	0.29	0.63	87.8	87.7	87.7

Shown are filling volume (V) as well as target, HPGe-based, and SPECT-based activity concentrations (c) and total kidney activities (A). Medulla and cortex concentrations were calculated on basis of the fillable fractions (Table 1). The SPECT-based target total activity for the patient kidney was 94.9 MBq.

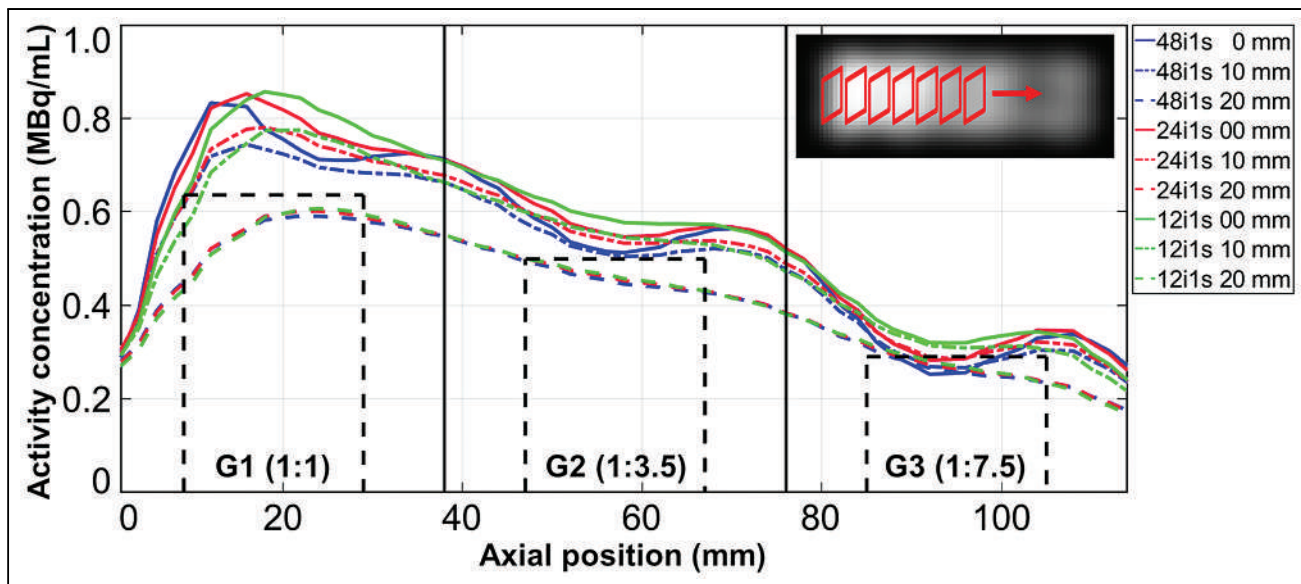


FIGURE 4. Quantitative analysis of cuboid. Depicted is the mean activity concentration in square regions of interest plotted in axial direction for different reconstruction parameters (number of iterations and postfilters). Positioning of axial regions of interest is illustrated at the top right by red boxes in the SPECT reconstruction. Solid black vertical lines represent borders between different gyroid cubes. Dashed black rectangles indicate axial position of $2 \times 2 \times 2$ cm³ cubes used for the quantitative analysis (height of each box = HPGe-based activity concentration).

Quantitative SPECT/CT Imaging of the Phantoms

To ensure homogeneous solutions and prevent sticking (or plating) of activity to the walls of vessels being used, all stock solutions consisted of ¹⁷⁷Lu-chloride dissolved in 0.1 M HCl with 100 ppm of stable lutetium (13). A VDC-405 radionuclide calibrator with a VIK-202 ionization chamber (Comerco SpA) was used for estimating the activity concentration during the phantom filling process. Subsequently, accurate activity concentrations were obtained by measuring 1-mL aliquots of all stock solutions (3 per stock solution) in a high-purity germanium (HPGe) detector (model GR4020 [Canberra] with GENIE 2000 spectroscopy software) whose energy-dependent efficiency had

previously been calibrated with several National Institute of Standards and Technology–traceable and National Physical Laboratory–traceable standards over the energy range considered. The activity concentrations of the stock solutions were determined by weighing (full minus empty stock solution container) with a PCB 3500-2 precision balance (Kern and Sohn GmbH; readability, 0.01 g; repeatability, 0.02 g). In contrast, the aliquot volumes were weighed in an ED224S analytic balance (Sartorius AG) with a readability of 0.1 mg.

Subsequently, each phantom (cuboid and 3 kidneys) was filled with a different stock solution (target and measured activity concentrations are presented in Table 2). Again, the actual filling volume was determined by

TABLE 3
Quantitative Evaluation of Different Gyroid Structures Inside Cuboid Phantom

Iterations	No postprocessing filter	10-mm gaussian	20-mm gaussian
Activity concentration G1 (1:1) gyroid (HPGe-based): 0.64			
12	0.81	0.74	0.58
24	0.79	0.74	0.58
48	0.76	0.71	0.57
Activity concentration G2 (1:3.5) gyroid (HPGe-based): 0.50			
12	0.59	0.55	0.46
24	0.57	0.55	0.46
48	0.54	0.52	0.45
Activity concentration G3 (1:7.5) gyroid (HPGe-based): 0.29			
12	0.33	0.31	0.26
24	0.32	0.31	0.26
48	0.29	0.29	0.25

Vertically are shown different numbers of iterations; horizontally are shown postfilters of different full widths at half maximum. All activity concentrations are given in MBq/mL.

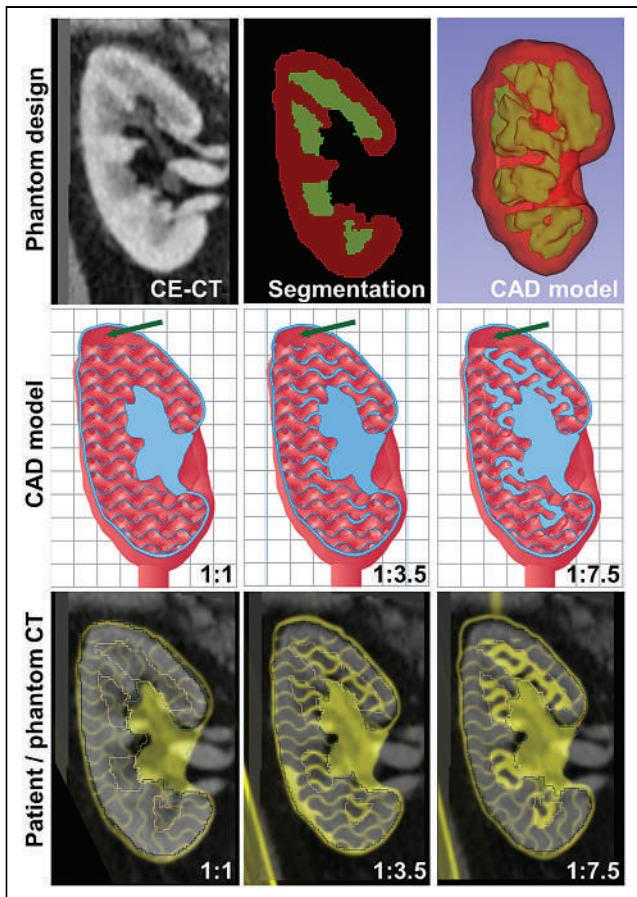


FIGURE 5. Design and validation of patient-specific kidney phantoms. (Top, left to right) Coronal contrast-enhanced CT slice of patient kidney; segmented cortex (red) and medulla (green); and 3D model of segmentation. (Center) Cross-sections through CAD models (green arrows: top sections without internal structure) for all 3 phantom designs (grid dimension, 1 cm). (Bottom) Contrast-enhanced patient CT (grayscale) overlaid with CT of phantom kidney (yellow) for all 3 phantom designs. CE = contrast-enhanced.

weighing (filled minus empty kidney phantom). Last, the phantoms were separately mounted in a water-filled Jaszczak cylinder (Data Spectrum; inside diameter and height of 216 mm and 186 mm, respectively) and SPECT/CT measurements were performed. To make the phantom data as comparable as possible to the patient data, the phantom acquisition was performed with the same acquisition parameters as used in the patient acquisition. In contrast, different reconstructions (different gaussian postfilters) were applied for phantom and patient data to assess the correspondence between the resulting activity distributions (“SPECT/CT imaging” section).

Activity Concentration–Voxel Histograms

To semiquantitatively compare the patient scan with the 3 patient-specific phantom scans, activity concentration–voxel histograms (the number of voxels containing a measured activity concentration plotted against the respective activity concentration) were calculated in MATLAB. After sorting the SPECT voxels according to their activity concentration, their subdivision into ranges of 0.01 MBq/mL resulted in the number of voxels within each of these activity concentration bins. Ideally, these histograms should consist of 2 distributions around the 2 activity concentrations of the stock solution.

RESULTS

Cuboid Phantom

Figure 2 shows the design, fabrication, and validation of the cuboid phantom. The superimposition of the CAD model and the CT image in Figure 2C especially emphasize the good visual match between model and printed phantom. The SPECT reconstruction in Figure 2D shows apparently different yet homogeneous activity distributions in each of the 3 compartments, demonstrating that the dimension of the filling structures is in an adequate range for SPECT/CT imaging with a medium-energy collimator.

Figure 4 illustrates the SPECT-based activity distribution inside the gyroid. To avoid resolution effects along the phantom edges, the averages within 2×2 cm² square regions of interest were calculated for the axial slices and plotted along the axis of the $4 \times 4 \times 12$ cm³ cuboid phantom. In general, the edges are clearly underestimated because of partial-volume effects (e.g., between axial positions 0 and 8 mm). In contrast, the activity is overestimated in the central area when no or 10-mm postfiltering is applied (solid lines). For the wider 20-mm postprocessing filter, however, the activity is increasingly spilled out of the actual object dimensions (dashed lines), leading to an underestimation of the total activity.

In a quantitative analysis of the cuboid reconstructions ($2 \times 2 \times 2$ cm³ VOIs as indicated in Fig. 4), the best match between HPGe- and SPECT-based activity was found for reconstructions with a 10-mm gaussian postprocessing filter (Table 3). Here, the nominal activity concentration in each of the gyroids was calculated by multiplying the HPGe-based activity concentration of the stock solution (0.69 ± 0.01 MBq/mL) by the fillable fraction of the corresponding gyroid (Table 1).

Patient-Specific Kidney Phantom

Figure 5 shows design and validation of the 3 patient-specific 2-compartment kidneys. At the bottom of Figure 5, the phantom and the patient CT images were superimposed to emphasize the good match between the outer contours and the internal compartments for all 3 phantoms. No filling structures were used in the top sections of each phantom to simplify the filling process (green arrows). In addition, the renal pelvis was printed as a solid structure to ensure good printing quality (light blue regions in the CAD models in the center row of Fig. 5). The linear attenuation coefficient of our ¹⁷⁷Lu SPECT/CT setup was determined as 0.148 ± 0.001 cm⁻¹ in a VOI analysis of this solid structure in the associated μ -map.

Figure 6 shows fused SPECT/CT images of the patient (top) and the 3 phantom acquisitions (bottom). Although the 1:1 phantom visually overestimates the activity concentration in the medulla (green arrows), good visual agreement is obtained for the 1:3.5 phantom. The wide 20-mm filter strongly blurs the image, such that the difference between cortex signal and medulla signal becomes difficult to assess visually. The 1:3.5 phantom with moderate filtering (10-mm gaussian) leads to the best visual match.

Table 2 shows all activities and the activity concentrations measured with regard to the patient-specific kidney phantom measurements. The table shows the filling volume (i.e., the volume filled with radioactive stock solution), the target activity concentration (based on the SPECT-based activity in the patient kidney), and the HPGe-based activity concentration and total kidney activity (the activity concentration multiplied by the filling volume), as well as the medulla and cortex activity concentrations (the stock solution activity concentration multiplied by the fillable fraction of the respective kidney phantom

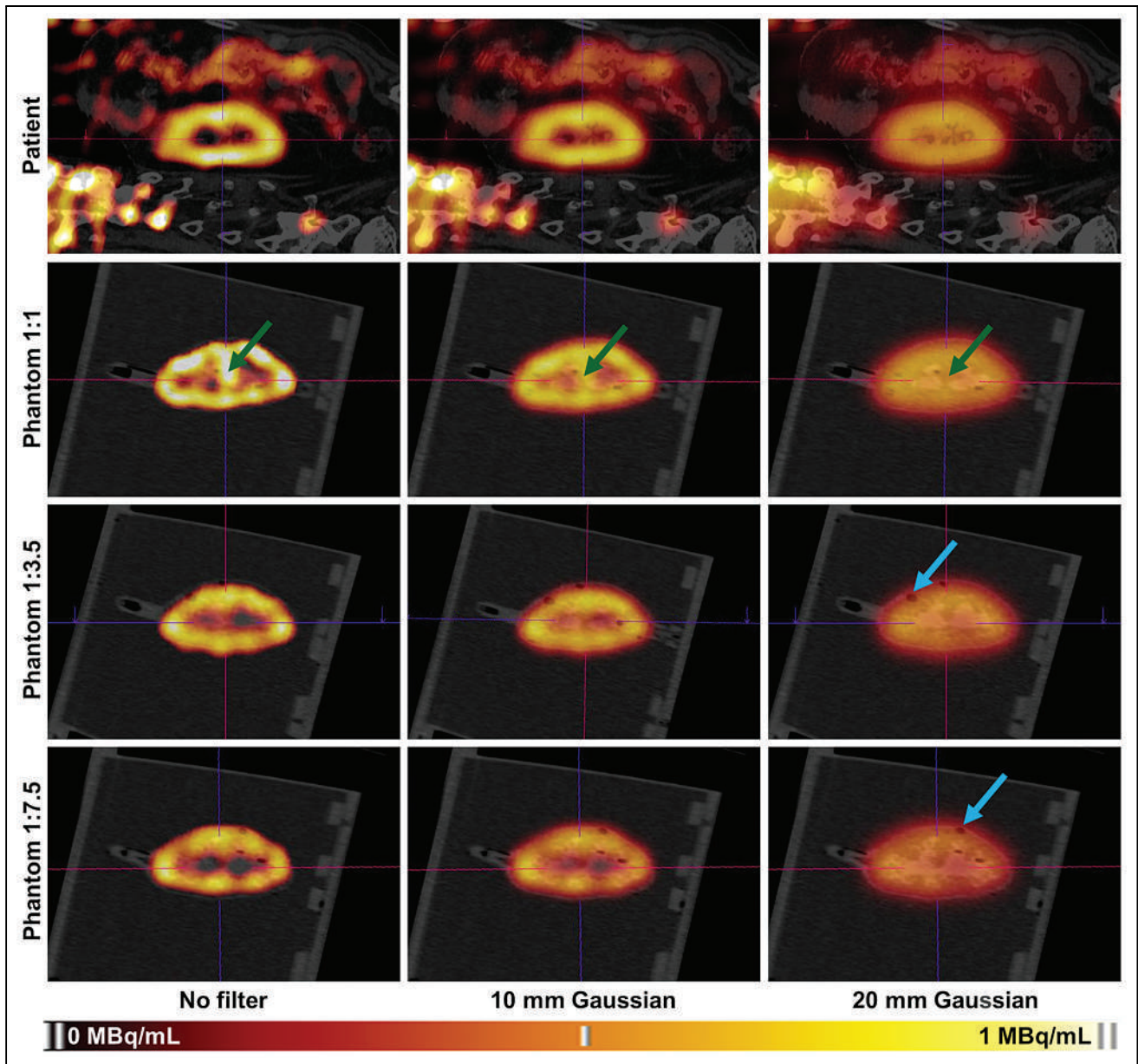


FIGURE 6. SPECT/CT fusions of patient acquisition and 3 phantoms (resin fraction ratios of 1:1, 1:3.5, and 1:7.5) for different postfilters (left to right: 0, 10, and 20 mm). Green arrows indicate overestimation of activity concentration in medulla for resin fraction ratio 1:1. Blue arrows indicate surface tension-related air bubbles.

given in Table 1) and the SPECT-based total activities (VOI analysis based on the phantom filling volume). All total kidney activities lie within 10% of the SPECT-based total kidney activity of 94.9 MBq and thus are close enough to provide equivalent measurement conditions. As the resolution lies in the range of the medulla size, considerable spill-out and spill-in is to be expected between the cortex and the medulla. In consequence, a separate evaluation of both compartments based on the SPECT scan is extremely prone to errors and was not performed.

SPECT-based activity concentration-voxel histograms (“Activity Concentration-Voxel Histograms” section) are given in Figure 7. The patient data are plotted in black, and each phantom is indicated by a different color (red, 1:7.5; blue, 1:3.5; green, 1:1). The curves

depict the number of voxels (vertical axis) containing a certain activity concentration (horizontal axis, bin width of 0.01 MBq/mL), and vertical dashed lines indicate the theoretic (HPGe-based) activity concentrations in the medulla and cortex (the values are given in Table 2). Ideally, the histogram should consist of activity distributions around these dashed lines. For the 1:1 phantom, there is only a single vertical green line, as both compartments have the same filling structure and, therefore, activity concentration. As expected, the postfilters smooth higher-activity concentration peaks, resulting in a shift toward lower activity concentrations in the filtered histograms (e.g., Fig. 7C). For the 1:7.5 resin fraction ratio (red), the peaks of the unfiltered and 10-mm gaussian curves lie in the range defined by the two theoretic activity concentrations, whereas the 20-mm gaussian

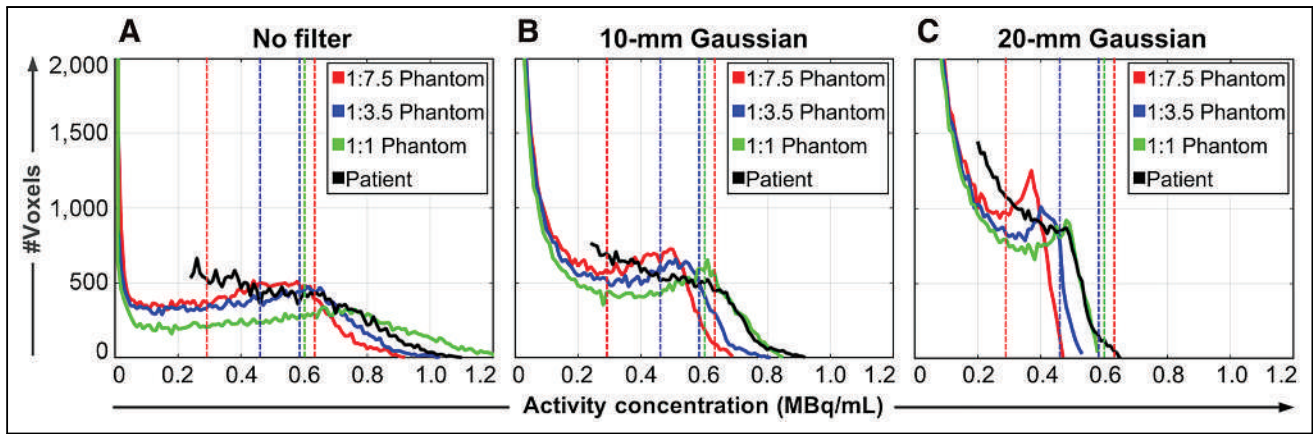


FIGURE 7. Activity concentration–voxel histograms for patient (black) and 3 phantoms (red, 1:7.5; blue, 1:3.5; green, 1:1) for 48 iterations, 1 subset, and gaussian postfilters of 0 mm (A), 10 mm (B), and 20 mm (C) in full width at half maximum. While solid curves depict number of voxels containing certain activity concentration, vertical dashed lines indicate HPGe-based activity concentrations in medulla and cortex (values are presented in Table 2).

filter leads to an underestimation. For the 1:3.5 resin fraction ratio (blue), the 10-mm gaussian filter leads to an activity concentration peak between the two theoretic values. In contrast, no filtering or a 20-mm gaussian filter results in an over- or underestimation, respectively, of the theoretic activity concentrations. For the 1:1 resin fraction ratio (green), good quantitative agreement is found for the 10-mm postprocessing filter, with the SPECT-based activity concentration peak centered exactly on the HPGe-based activity concentration. Although the 20-mm gaussian filter leads to the previously described underestimation, not applying any filter leads to a wide spectrum of activity concentrations (e.g., a maximum activity concentration up to 2 times higher than the theoretic value). In contrast to the colored phantom curves, all of which exhibit a maximum, all patient curves (black) are monotonically decreasing.

DISCUSSION

One of the main problems in the clinical validation of quantitative SPECT/CT is the lack of a ground truth in patient measurements. Depending on the image reconstruction applied, a wide variety of different spatial activity distributions can be generated without knowledge of the ground truth (7), as can be seen in Figure 7 (black lines). This observation demonstrates that an assessment of the activity distribution on a voxel level, based purely on SPECT/CT imaging, is problematic (7) and that, for validation, additional methods such as the measurement of realistic, ideally patient-specific, phantoms should ideally complement the image quantification process. Up to now, the complexity of phantom measurements has been restricted by the availability of phantoms. Multicompartment phantoms usually consisted of separate compartments filled with radioactive stock solutions of different activity concentrations, thus considerably increasing the sources of uncertainty. As a major advance, the approach proposed in this work achieves to mimic inhomogeneous activity distributions in SPECT/CT with only one single fillable compartment by making use of internal gyroid structures of different volume fractions, considerably simplifying phantom preparation and reducing uncertainties.

In addition, the new method represents another important advance: while it was previously impossible to achieve continuous transitions of activity concentrations, this is changed by the introduction of filling structures of different volume fractions. If further developed, multiple thin gyroid layers of different wall thicknesses

could be placed adjacent to each other to achieve continuously varying apparent activity concentrations while still requiring only a single stock solution. This development could take the individualization of phantoms to an unprecedented new level.

In comparison to standard, single-compartment phantoms, the gyroid structure features a large surface area with many very small congruent channels. These lead to an increased occurrence of surface tension–related air bubbles in these regions, resulting in small black regions in the CT scan (blue arrows in Fig. 6). This problem can, however, be considerably improved by reducing the surface tension of the stock solution, such as by adding soapy water. Through the addition of soap in our stock solutions, only a few air bubbles remained in the phantoms imaged in this work (e.g., Fig. 6).

Another subject to be discussed is the printing process. To keep the wall as thin as possible (e.g., a 0.4-mm thickness for the renal cortex gyroid structure), we applied a stereolithography-based 3D printing technique based on a photopolymer resin hardened layer by layer using an ultraviolet laser beam. The relatively large maximum unsupported overhang length of 3 mm allowed the entire kidney phantom to be printed as one part, in contrast to the previously used fused deposition modeling technique, by which the phantoms had to be printed in several individual parts (3,5,7). However, the techniques require that excess, uncured resin escapes the gyroid structure—a requirement that, because of the low viscosity of the resin, can be problematic for thick-walled gyroids. For our Form 2 printer, our standard period of 4π -mm with a wall thickness of 0.40–2.65 mm resulted in a realistic range of activity concentration ratios between the renal medulla and the cortex (1:1–1:8 (1,7)). Provided that careful modeling and positioning of the CAD models were done before 3D printing, reliable printing was possible even for the thickest walls of 2.65 mm thickness.

For validation, the model was tested using a patient-specific 2-compartment kidney model. A direct quantitative comparison between phantom and patient images by conventional means (e.g., using measures such as the structural similarity index) is almost impossible because of the isolated nature of the phantom in comparison to the patient kidney, which is surrounded by anatomic structures. To perform at least a semiquantitative evaluation, a histogram analysis (Fig. 7) was applied to illustrate the differences. Because an in-depth analysis of the difference between activity distributions and absorbed dose distributions for ^{177}Lu

demonstrated virtually no differences in their spatial distributions in a previous study (7), we considered only the activity concentration in this work.

Because of the unevenly shaped interface between the cortex and the medulla in combination with the SPECT resolution, which is unable to resolve the gyroid channels, the two theoretic peaks (vertical dashed lines) merge into a single peak in the SPECT/CT-based distribution of activity concentrations (Fig. 7). In contrast, all patient curves (black lines) are monotonically decreasing, indicating that the underlying activity distribution in the patient kidney is more heterogeneous than the distribution modeled by the two compartments in this study.

Given the numerous potential differences between any patient and phantom measurement (e.g., different scatter environments, different contouring of the camera, potential background radiation in the patient, and patient motion) affecting SPECT/CT-based quantification, some discrepancy between patient and associated phantom measurements is always to be expected. Considering this, the degree of similarity between patient and phantom (Fig. 6, center column) can be considered to be close to the maximum achievable. For this reason, we provide an analysis of only three example postfilters instead of trying to find the best combination of iterations, subsets, and postprocessing filter.

The routine application of dosimetry to optimize the efficacy of radionuclide therapies, and thus the need for a routine patient-specific validation of quantitative SPECT/CT imaging, currently still seems to be some way ahead. If internal individualized dosimetry becomes established, however, the methodology presented here could form the basis for a patient-specific optimization of quantitative SPECT/CT imaging (e.g., regarding imaging and reconstruction parameters). Provided that there is a certain quality level of SPECT/CT-based dose-voxel histograms, such quantitative measures could form a cornerstone for planning and monitoring of individualized radionuclide therapies, as it is already standard in external-beam radiotherapy.

CONCLUSION

We have shown that the use of internal support structures allows phantom measurements of inhomogeneous activity distributions using only a single stock solution of a single activity concentration. By keeping the dimensions of the filling structures well below the resolution of the imaging system, we were able to mimic the internal activity distribution in the kidney of a patient treated with ^{177}Lu -PSMA (24 h after injection for SPECT/CT). In a quantitative analysis, however, it was shown that a representation of the kidney by only two compartments (renal cortex and medulla) of different apparent activity concentrations still represents an oversimplification. For an even better representation, more different compartments would be required.

DISCLOSURE

This study was funded by a grant from the German Research Foundation (Deutsche Forschungsgemeinschaft TR 1380/1-1). Michael Lassmann has received research grants by IPSEN Pharma

and Nordic Nanovector. No other potential conflict of interest relevant to this article was reported.

KEY POINTS

QUESTION: Is it possible to design patient-specific kidney phantoms with only a single fillable compartment yet an inhomogeneous activity distribution for assessment of SPECT/CT-based peritherapeutic monitoring of radiopharmaceutical distributions?

PERTINENT FINDINGS: Using the presented methodology, we achieved production of a patient-specific kidney phantom for a patient with metastatic castration-resistant prostate cancer, visually and quantitatively mimicking a peritherapeutic SPECT/CT acquisition 24 h after injection of ^{177}Lu -PSMA. Despite the restriction to only a single compartment for ease of phantom preparation, an inhomogeneous activity distribution in the patient SPECT/CT scan could be reproduced.

IMPLICATIONS FOR PATIENT CARE: The presented methodology enables a patient-specific assessment of activity distributions, and thus absorbed dose depositions, in organs at risk in radionuclide therapy.

REFERENCES

1. De Jong M, Valkema R, Van Gameren A, et al. Inhomogeneous localization of radioactivity in the human kidney after injection of [^{111}In -DTPA]octreotide. *J Nucl Med.* 2004;45:1168–1171.
2. Gear JJ, Long C, Rushforth D, Chittenden SJ, Cummings C, Flux GD. Development of patient-specific molecular imaging phantoms using a 3D printer. *Med Phys.* 2014;41:082502.
3. Tran-Gia J, Schlögl S, Lassmann M. Design and fabrication of kidney phantoms for internal radiation dosimetry using 3D printing technology. *J Nucl Med.* 2016; 57:1998–2005.
4. Robinson AP, Tipping J, Cullen DM, et al. Organ-specific SPECT activity calibration using 3D printed phantoms for molecular radiotherapy dosimetry. *EJNMMI Phys.* 2016;3:12.
5. Tran-Gia J, Lassmann M. Optimizing image quantification for ^{177}Lu SPECT/CT based on a 3D printed 2-compartment kidney phantom. *J Nucl Med.* 2018;59:616–624.
6. Schoen AH. *Infinite Periodic Minimal Surfaces Without Self-Intersections.* National Aeronautics and Space Administration; 1970. NASA technical note, NASA TN D-5541.
7. Tran-Gia J, Salas-Ramirez M, Lassmann M. What you see is not what you get: on the accuracy of voxel-based dosimetry in molecular radiotherapy. *J Nucl Med.* 2020;61:1178–1186.
8. Kwekkeboom DJ, de Herder WW, Kam BL, et al. Treatment with the radiolabeled somatostatin analog [^{177}Lu -DOTA 0 ,Tyr 3]octreotate: toxicity, efficacy, and survival. *J Clin Oncol.* 2008;26:2124–2130.
9. Bodei L, Cremonesi M, Ferrari M, et al. Long-term evaluation of renal toxicity after peptide receptor radionuclide therapy with ^{90}Y -DOTATOC and ^{177}Lu -DOTATATE: the role of associated risk factors. *Eur J Nucl Med Mol Imaging.* 2008;35:1847–1856.
10. Vegt E, De Jong M, Wetzels JF, et al. Renal toxicity of radiolabeled peptides and antibody fragments: mechanisms, impact on radionuclide therapy, and strategies for prevention. *J Nucl Med.* 2010;51:1049–1058.
11. Fedorov A, Beichel R, Kalpathy-Cramer J, et al. 3D Slicer as an image computing platform for the quantitative imaging network. *Magn Reson Imaging.* 2012;30:1323–1341.
12. Tran-Gia J, Lassmann M. Characterization of noise and resolution for quantitative ^{177}Lu SPECT/CT with xSPECT Quant. *J Nucl Med.* 2019;60:50–59.
13. Tran-Gia J, Denis-Bacelar AM, Ferreira KM, et al. A multi-centre and multi-national evaluation of the accuracy of quantitative Lu-177 SPECT/CT imaging performed within the MRTDdosimetry Project. *EJNMMI Phys.* 2021;8:55.

Proceedings: PET Drugs—A Workshop on Inspections Management and Regulatory Considerations

Sue Bunning¹, Christopher Ignace², Steve Mattmuller³, Sally W. Schwarz⁴, Peter J.H. Scott⁵, Henry F. VanBrocklin⁶, and Steven S. Zigler⁷ on behalf of the Coalition of Drug Manufacturers

¹Medical Imaging and Technology Alliance, Arlington, Virginia; ²Cardinal Health, Dublin, Ohio; ³Kettering Medical Center, Kettering, Ohio; ⁴Department of Radiology, Washington University School of Medicine, St. Louis, Missouri; ⁵Department of Radiology, University of Michigan, Ann Arbor, Michigan; ⁶University of California San Francisco, San Francisco, California; and ⁷Siemens PETNET Solutions, Knoxville, Tennessee

Recent advances in the development of new molecular imaging agents for PET have led to the approval of several new molecular entities for PET imaging by the U.S. Food and Drug Administration (FDA) within the last 10 y. However, the continued use of PET drugs for diagnostic imaging procedures is reliant on a sustainable network of PET manufacturing facilities operating in accordance with the regulations for current good manufacturing practices for PET drugs (title 21, *Code of Federal Regulations*, part 212). With this goal in mind, a public workshop entitled “PET Drugs: A Workshop on Inspections Management and Regulatory Considerations” was held on the FDA campus in Silver Spring, MD, on February 21, 2020. The workshop was cosponsored by the FDA’s Center for Drug Evaluation and Research, the Society of Nuclear Medicine and Molecular Imaging, the Medical Imaging Technology Alliance, and the World Molecular Imaging Society, in collaboration with the Coalition of PET Drug Manufacturers. The organizing committee for the workshop consisted of representatives from academic and commercial PET manufacturers as well as FDA staff members. The coauthors on this paper are all members of the workshop-organizing committee.

Key Words: quality assurance; radiochemistry; radiopharmaceuticals; 21 CFR §212; PET drug manufacture; regulatory oversight

J Nucl Med 2022; 63:1117–1123

DOI: 10.2967/jnumed.121.263443

Over the last 2 decades, significant advances have been made in the development of new molecular imaging agents for PET. These developments have led to the recent approval of several new molecular entities for PET by the U.S. Food and Drug Administration (FDA). As of July 2021, the number of FDA-approved PET drugs stood at 17 (1). Most of these approvals occurred within the last decade. Notwithstanding this success, the continued use of PET drugs for diagnostic imaging applications must be ensured by a sustainable supply chain of PET manufacturing facilities operating in accordance with FDA regulations on current good manufacturing practices (cGMPs) for PET drugs (title 21, *Code of Federal Regulations* [CFR], part 212). With this goal in mind, a public workshop was held on the FDA campus in Silver Spring, MD, on February 21,

2020. Entitled “PET Drugs: A Workshop on Inspections Management and Regulatory Considerations,” the workshop was jointly sponsored by the FDA’s Center for Drug Evaluation and Research (CDER), the Society of Nuclear Medicine and Molecular Imaging, the Medical Imaging Technology Alliance, and the World Molecular Imaging Society in collaboration with the Coalition of PET Drug Manufacturers. The organizing committee for the workshop consisted of representatives from academic and commercial PET manufacturers as well as FDA staff members.

The workshop was attended by radiopharmaceutical scientists, nuclear pharmacists, regulatory affairs professionals, and compliance specialists with expertise in PET drug manufacturing. Attendees represented academic institutions, commercial suppliers, contract manufacturers, and innovators involved in the development of PET drugs. Many representatives from the FDA also attended. Approximately 150 attendees participated in person, and numerous participants joined in a live video broadcast of the event. The presentations and a recording of the workshop are available on the FDA’s website (2). The organizers defined 4 sessions for the workshop agenda: “Considerations and Trends in Inspections and Compliance,” “Life Cycle Management of PET Drug Applications,” “Chemistry and Product Quality Assurance,” and “Changing Landscape of PET Drugs, Labeling Requirements, and Electronic Filing Requirements.”

This paper describes the workshop highlights. The full agenda, as well as a complete account of each presentation and the panel discussions, appears in the supplemental materials (available at <http://jnm.snmjournals.org>) (3–33).

OPENING REMARKS

Louis Marzella, the FDA’s division director for medical imaging and radiation medicine, opened the workshop, noting that “the first principle is that the risk–benefit approach is applicable to the development of standards for quality of products . . . to ensure that safe and effective products are consistently administered to patients.” Reflecting the fact that specific good-manufacturing-practice (GMP) regulations (34) apply to the manufacturing of PET drugs, Marzella also noted, “we agree that specific considerations apply to different products, including PET drugs.” Although there was recognition that standards evolve, Marzella stressed “the importance . . . of ensuring there is a consistency of approach regarding product quality expectations during the application review process and during the inspectional process. To this end, I think that the collaboration and cross talk between the review staff and the inspectional staff is an important topic.”

Received Oct. 28, 2021; revision accepted Jan. 4, 2022.

For correspondence or reprints, contact Peter J.H. Scott (pjhscott@umich.edu).

Published online Jan. 20, 2022.

COPYRIGHT © 2022 by the Society of Nuclear Medicine and Molecular Imaging.

Sally Schwarz, a cochair of the Coalition of PET Drug Manufacturers, provided the Society of Nuclear Medicine and Molecular Imaging perspective on the workshop. The short shelf life and very low injected mass of the active radiopharmaceutical ingredient are the primary characteristics that define the risk profile of PET drugs. Secondary characteristics include the use of microbiologically hostile and often lethal synthesis steps, presterilized components, aseptic component assemblies and manipulations, and the use of closed containers during the automated synthesis process for a typical PET drug. These secondary characteristics result in an extremely low—typically zero—bioburden process stream before sterile membrane filtration in the final production step. Together, the primary and secondary characteristics greatly reduce the probability of microbiologic contamination in PET drugs. Consistent with this outcome, PET manufacturers experience low rates of sterility test failures in the routine supply of approximately 100,000 PET drug batches annually required to meet nationwide demand (~50% of the market for PET drugs is represented in these data) (3). The practical ramifications of these characteristics have resulted in negligible rates of patient adverse events after the administration of PET drugs (4–8). The clinical and commercial history of this product class have demonstrated that PET drugs are safe and low-risk. The PET GMP regulations have been effective in maintaining a safe supply of PET drugs.

Sue Bunning, the industry director for PET, provided the Medical Imaging Technology Alliance perspective. At the time of the workshop, there were approximately 50 holders of new-drug applications (NDAs) and abbreviated new-drug applications (ANDAs) supporting a dozen PET drugs. The most widely used PET drug, ¹⁸F-FDG, accounted for more than 35 NDAs or ANDAs. According to market research data, slightly more than 2 million PET scans were performed in the United States in 2018 (9). Thus, the size of the U.S. market for PET drugs is quite small compared with the pharmaceutical industry. Considering these factors, the public health risk of PET drugs is miniscule compared with that of traditionally manufactured pharmaceutical products.

Henry VanBrocklin, a cochair of the Coalition of PET Drug Manufacturers provided the World Molecular Imaging Society perspective on the future of PET imaging. New PET scanner technologies hold the promise of greater sensitivity and earlier detection of disease states. However, the expected benefits from the underlying investments in new scanner technologies will be unrealized without the continued supply of PET drugs. New PET drug approvals in the last decade have exceeded the number of approvals in the previous 30 y, but the future of PET imaging may be jeopardized if the regulatory burden on routine manufacturing undermines a sustainable supply of PET drugs.

The goals for the workshop were to discuss regulatory compliance for the development and manufacturing of PET drugs; identify pathways for PET drug application approvals, application maintenance, and inspections based on the PET GMP regulations; share perspectives from industry, academia, investigators, and regulators on inspectional findings and trends; and provide information on the management of PET GMP inspections and maintenance of PET NDAs and ANDAs.

SESSION I: CONSIDERATIONS AND TRENDS IN INSPECTIONS AND COMPLIANCE

Steve Zigler, the chief technical officer for PETNET Solutions, introduced the first session by encouraging attendees to think beyond the half-life and to consider the practical ramifications that

define the time-critical supply chain and the distributed manufacturing model for PET drugs. Decades after the first FDA approval of a PET drug, half-life constraints and their ramifications continue to define and redefine regulatory expectations in unforeseen ways. The core principle of the workshop was to provide a forum to discuss these unforeseen ramifications.

Manufacturing Process Assessment and Preapproval Inspections (PAIs)

Krishna Ghosh, a senior policy advisor in CDER's Office of Pharmaceutical Quality (OPQ), provided the FDA perspective on this topic. As part of its fulfillment of the requirements in the 1997 FDA Modernization Act (35), the FDA conducted inspections at all PET manufacturing facilities and approved all ANDAs by December 2015. The inspections consisted of a mixture of preapproval and surveillance inspections. Also in 2015, the FDA underwent a reorganization to create the OPQ, which led to a separation of the offices that manage preapproval and surveillance inspections. Consequently, since the reorganization, preapproval inspections (PAIs) have been managed by the Office of Pharmaceutical Manufacturing Assessment and the Office of Regulatory Affairs (ORA), whereas surveillance inspections have been managed by ORA in conjunction with the Office of Surveillance and the Office of Compliance. The FDA's review of inspection history since 2015 indicates a need to mature some of its original guidance documentation, a process that should be supported by a common level of understanding across stakeholders.

The FDA conducts 4 different types of inspections: PAIs, postapproval inspections, routine surveillance inspections, and for-cause inspections. PAIs are conducted for both NDAs and ANDAs. The purpose of a PAI is to make sure the facility is capable of manufacturing the product according to the conditions described in the application and according to the PET GMP regulations. These inspections are managed by the Office of Pharmaceutical Manufacturing Assessment and the ORA. Postapproval inspections are relatively new. These inspections are performed to audit for changes in production and control practices after product approval. These inspections are also managed by the Office of Pharmaceutical Manufacturing Assessment and the ORA. Routine surveillance inspections are routine periodic inspections of manufacturing facilities. These inspections are managed by the ORA, Office of Surveillance, and Office of Compliance. For-cause inspections result from a potential indication or evidence of noncompliance by the manufacturer. These inspections are managed by the Office of Compliance and the ORA.

The FDA considers at least 3 specific risk factors during the PAI process, including facility risks, process risks, and product risks. In the evaluation of facility risks, the FDA considers the compliance history of the facility, including whether the facility has been previously inspected for the unit operation described in the drug application under review. A unit operation is "from start to finish," but specific examples of the criteria that define unit operations were not included in this presentation.

Recent Experience with cGMP Surveillance Inspections of Commercial PET Manufacturers

Rick Friedman, the deputy director of the Office of Manufacturing Quality, CDER Office of Compliance, gave a presentation on recent experience with cGMP surveillance inspections of commercial PET manufacturers. The presentation began with an overview of the inspection process as conducted by the ORA. On completion of a surveillance inspection, the ORA classifies the inspection

outcome into 1 of 3 categories: no action indicated, voluntary action indicated, and official action indicated. Inspections with minor findings are classified as no action indicated or voluntary action indicated, whereas inspections with the most problematic findings may be classified as official action indicated.

Between June 2018 and January 2020, the ORA finalized the classification of 45 PET facility inspections. The breakdown of the classifications was 17 cases of no action indicated (38%), 24 of voluntary action indicated (53%), and 4 of official action indicated (9%). A total of 6 PET inspections were classified as official action indicated from January 2018 to January 2020. Three official-action-indicated inspections resulted in the issuance of a warning letter, and 3 resulted in regulatory meetings. All 3 warning letters were issued to nonacademic, nonhospital manufacturers. Two of the regulatory meetings were held with academic or hospital-based manufacturers, and the third was held with an undisclosed type of manufacturer. Friedman did not discuss the FDA's criteria for the issuance of warning letters versus regulatory meetings. All 6 official-action-indicated classifications resulted from failure to maintain a suitable environment for aseptic processing operations according to 21 CFR §212.30(a).

Since inspections are a snapshot in time, the FDA uses field alert reports to augment its assessment of quality trends over a longer time horizon. From 2016 to 2019, the FDA analyzed field alert reports from PET manufacturers and found that 27% of commercial manufacturers submitted a field alert report during this 4-y period ($n = 141$). Friedman did not comment on the submittal of field alert reports from academic manufacturers. On the basis of a review of inspection reports, the FDA found that not all sterility test failures were reported in a field alert report, even though the FDA requires PET manufacturers to immediately file a field alert report in the event of a positive sterility test result. This requirement holds even if the positive test result is later determined to be due to a laboratory error (11).

Current Trends and Observations on Inspections: The PET Community Perspective

Sally Schwarz, a professor of radiology at Washington University School of Medicine, provided the academic perspective on FDA inspections of PET manufacturers. The presentation included experiences from numerous PET manufacturing facilities and addressed questions that had been collected from the PET community before the workshop. On the basis of this feedback, several examples were provided to illustrate the inconsistent enforcement that sometimes occurs between FDA inspections and FDA regulations (34), guidance documents (13), and policy guides (14).

Peter Webner, the chief executive officer of Zionexa USA, provided the commercial perspective on FDA inspections of PET manufacturers, noting that inconsistent enforcement actions during FDA inspections also challenge commercial PET manufacturers. This is especially problematic for small innovator companies that have one or more investigational products under development. As evidenced by the numerous recent approvals of new PET drugs, the existence of the PET GMP regulations has spurred significant innovation in this domain. The PET GMP regulations provide a platform on which investors and small companies can rely over the time horizon required for investment in the development of new products. Inconsistent enforcement of the PET GMP regulations creates uncertainty in development costs and timelines and thus hinders innovation in the development of new PET drugs. Changes to FDA policies that come to light only during a PAI

threaten the viability of a new product, making it go through additional regulatory obstacles just as it almost reaches the finish line.

ORA PET Surveillance Inspections

Ileana Barreto-Pettit, a national drug expert from the FDA OPQ Operations in the ORA, provided an update on FDA surveillance inspections. The current organization chart for the ORA shows that the FDA manages surveillance inspections through a tiered system of offices that include 4 geographic divisions where inspections are conducted at the local level. The geographic divisions were formerly known as districts.

The FDA uses a risk-based site selection model to identify manufacturing facilities for surveillance inspections (16). Ranking of drug manufacturing facilities for surveillance inspections by the FDA is based on risks to drug quality. Risk-based inspectional frequency considers the compliance history of the facility, the history and nature of recalls linked to the facility, the inherent risk of the drug product, and other criteria deemed necessary and appropriate by the FDA for purposes of allocating inspection resources. From these considerations, the FDA generates a numeric risk score for the facility. Barreto-Pettit did not discuss the FDA's criteria for assigning a risk score for type of facility, patient exposure, or the inherent product risk.

FDA investigators have undergone training on the PET GMP regulations. The FDA acknowledged some gaps in training for PET GMPs. In addition, some investigators misunderstand the applicability of the PET GMPs to PET manufacturers. The FDA is working to close these deficiencies.

FDA Pilot Program for Tablet-Based Inspections for PET Drugs

Binh Nguyen, an educator for pharmaceutical programs in the ORA, described the new inspection protocol project and the eNSpect electronic management tool for the inspection of PET manufacturers.

Historically, the execution of PET inspections and the associated reporting is a time-consuming process for the FDA. A typical abbreviated PET inspection that covers 2 of the 6 quality systems requires 3–5 d for the actual inspection and an additional 5–7 d to write the establishment investigation report. A comprehensive PET inspection that covers 4 or more quality systems typically requires 3–7 d for the actual inspection and an additional 5–10 d to write the report. The new inspection protocol and the associated electronic tool (eNSpect) are designed to expedite the inspection process and preparation of the reports. The protocol will also deliver more consistent results across numerous PET manufacturing facilities. The eNSpect tool has been piloted for surveillance inspections of PET manufacturers but has not been adapted for PET PAIs.

SESSION II: LIFE CYCLE MANAGEMENT OF PET DRUG APPLICATIONS

Life Cycle Management of PET Drugs: The FDA Perspective

Ramesh Raghavachari, a branch chief in CDER's OPQ, provided an overview of the life cycle of FDA-approved drug products. The typical life cycle of a drug begins with the discovery and development phases and continues with clinical development (investigational new drug) and ultimately with FDA marketing approval (NDA) and, finally, generic drug approval (ANDA).

Changes to approved applications and the life cycle of a drug can be achieved by a variety of mechanisms based on the risk of the change. The FDA has 4 defined risk categories: prior approval changes (preapproval supplement; high risk), changes being effected

in 30 d (moderate risk), changes being effected in 0 d (low risk), and annual reportable changes (low risk). Specific details about the risk levels for changes to approved applications were not provided.

Management of PET Drug Applications: The PET Community Perspective

Peter Scott, an associate professor of radiology at the University of Michigan, described the workload for a busy academic PET manufacturing facility with more than 30 different PET drugs available for clinical use. Experience at the University of Michigan during 15 y of operation with approximately 8,000–10,000 PET scans each year indicates that no adverse events occurred during this time. This is consistent with the experience of the overall PET community, which was discussed earlier in the opening comments for the workshop, wherein a recent survey found that 4 sterility test failures (including false-positives) occurred in more than 58,000 batches produced in 2019 (3). In addition, the incidence of adverse events for radiopharmaceuticals was reported as 1.6 in 100,000 diagnostic studies (8).

SESSION III: CHEMISTRY AND PRODUCT QUALITY ASSURANCE

Product Quality Assurance: Microbiologic Regulatory Perspective

Laura Wasil, a review microbiologist in CDER's OPQ, provided the FDA's microbiologic perspective on product quality assurance for PET drugs.

Since PET drugs are administered to patients before the results of sterility testing are known, aseptic operations and procedures are critical to ensure the sterility of PET drug products. The following are critical operations that must be aseptically executed: assembly of the components used in the final product vial assembly, transfer of the assembled product vial to the hot cell or otherwise shielded area, all manufacturing steps that occur downstream of the membrane-sterilizing filter (e.g., transfer of the filtered solution into the product vial, optional product dilution, and withdrawal of quality control samples), sterility testing, gowning and gloving procedures for personnel working in aseptic areas, environmental monitoring, and cleaning and disinfection of aseptic and critical areas.

The components used in the final product vial assembly consist of needles, syringes, membrane filters, and the container. All items are commercially available as presterilized components and are aseptically assembled in the ISO 5 air environment. The components and assembly process should be described in the NDA or ANDA, as well as the storage conditions and expiration date of assembled product vials. Figure 1 illustrates a final product vial assembly commonly used in PET drug manufacturing.

Microbiologic tests for PET drugs include filter integrity, bacterial endotoxins, and sterility. For all PET drugs, the filter integrity must be evaluated after completion of membrane filtration but before release for administration. The test for bacterial endotoxins should be performed in accordance with U.S. Pharmacopeia general chapter <85>. The test should be initiated promptly after production and before release. Sterility testing cannot be completed before the release and administration of PET drugs.

Microbiologic Considerations for PET Drugs: The PET Community Perspective

David Hussong, the chief technology officer of Eagle Analytic Services and a former FDA review microbiologist, provided a

perspective on the historical regulation of PET drugs and the microbiologic risk factors associated with them. Sterility is notoriously difficult to prove and cannot be measured, even for non-PET drugs, because of statistical and microbiologic limitations in test methods (20–22). Sampling for sterility testing of pharmaceuticals can detect contaminated units only when 10% or more of the batch is contaminated (23). Therefore, a passing sterility test does not indicate sterility of the product. Instead, a passing sterility test indicates only the absence of evidence for contamination of the batch. Thus, “sterility” is a condition that cannot be proven for any pharmaceutical product. Consequently, process controls are a better indicator of product sterility than the results of the sterility test.

Henry VanBrocklin, a professor of radiology and biomedical imaging at the University of California San Francisco, summarized this presentation by noting that these controls have effectively minimized the risk of microbial contamination in PET drugs. According to a survey of 13 academic and 5 commercial PET manufacturers conducted in February 2020, more than 370,000 batches of PET drugs were manufactured from 2013 to 2019. No adverse events were reported for these batches. The frequency of out-of-specification sterility test results was 18 batches, or 0.013% (3).

Christopher Ignace, the head of scientific and regulatory affairs for nuclear and precision health solutions at Cardinal Health, discussed product quality assurance from the perspective of a commercial network of PET drug manufacturing facilities.

FDA inspections typically include daily debriefing sessions for discussion of potential issues with the sponsor. Experience has shown that some investigators will communicate only with local manufacturing staff or are unwilling to describe findings and the rationale for potential noncompliance before issuing an FDA form 483. This form's purpose is to notify the site's management of objectionable conditions found during the inspection. Investigators should always first discuss potential objectionable findings with the site's staff and if at a site of a large producer, include their corporate quality assurance staff before completing a 483.

Recent experience has shown that some FDA investigators accept staff training on microbiology topics only if the training was delivered by a degreed microbiologist. Training performed by a non-degreed microbiologist was unacceptable. By this logic, other areas of training in PET manufacturing would require degreed chemists, pharmacists, and physicists.

The scope of preapproval and surveillance inspections should be well defined. The PAI is typically the time when science-

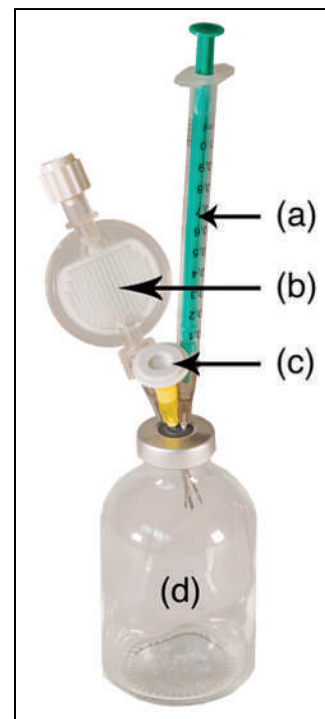


FIGURE 1. Assembled final product vial commonly used in PET manufacturing: quality control syringe (a), membrane-sterilizing filter (b), filter vent (c), and product vial (d).

related issues in the drug application are discussed and reviewed. On the other hand, a surveillance inspection is typically limited to a review of the facility's quality system and compliance with the PET GMP regulations. However, during PET surveillance inspections, FDA investigators often delve into topics typically covered in a PAI. This effectively results in a renegotiation of the original approval commitments and the appearance that an investigator is enforcing his or her personal area of expertise.

SESSION IV: CHANGING LANDSCAPE OF PET DRUGS, LABELING REQUIREMENTS, AND ELECTRONIC FILING REQUIREMENTS

Ravi Kasliwal, a review chemist in CDER's OPQ, provided the FDA's perspective on the evolution of PET drugs. Since 2009, the list of approved PET drugs has grown significantly and now includes generator-produced PET radionuclides in association with a sterile nonradioactive kit for the preparation of the injectable PET drug. There are critical differences between these 2 classes of products. In the first case, exemplified by ^{18}F -FDG injection, the marketed product is manufactured as a multiple-dose vial in a ready-to-use solution. The product is 100% tested and dispensed into unit doses under the practice of pharmacy. The second case is exemplified by ^{68}Ga -DOTATATE injection, which uses $^{68}\text{GaCl}_3$ eluted from a $^{68}\text{Ge}/^{68}\text{Ga}$ generator and a kit (the marketed product) consisting of two vials, one with the dotatate chelate and another with a buffered water solution for the injection. The radiolabeling of the kit with the generator eluate is performed under the practice of pharmacy according to instructions provided in the package insert.

CLOSING REMARKS

Closing remarks for the workshop were presented by Louis Marzella and Steve Zigler as personal observations on behalf of the organizing committee. It is clear that nonuniform inspections create confusion in the PET community concerning which regulations to follow or what guidance is applicable. This in turn jeopardizes the uniformity of the PET drug supply in the United States. A comprehensive risk profile based on the inherent characteristics of positron-emitting radionuclides and PET drug manufacturing processes does not currently exist. The little that is known in this area is not uniformly understood across the PET community and within the FDA.

A comprehensive training program for PET drug manufacturing and associated regulatory sciences does not currently exist in any pharmacy or university curriculum.

In closing the workshop, the PET community and the FDA had several aims: to enhance the effectiveness of inspections (ensuring the uniformity of PET drugs in the United States), to reach a consensus on a science-based risk profile for PET drugs, to create and implement training to enhance the consistency of FDA inspections, to periodically hold a workshop to continue the dialog between the FDA and PET stakeholders, and to hold interim informational meetings between the FDA and PET stakeholders to discuss ongoing issues with inspection of PET manufacturing facilities.

DISCUSSION: WORKSHOP SUMMARY AND RECOMMENDATIONS FROM PET MANUFACTURING STAKEHOLDERS

Four predominant themes emerged throughout the workshop: the uniformity of FDA inspections of PET manufacturing facilities, a science-based risk profile for PET drugs, improvements to

training for FDA investigators and the regulated community, and continued dialog between the FDA and the PET community.

Prior to the workshop, the organizing committee collectively defined the workshop as "a forum for the exchange of information and perspectives on the regulatory and compliance framework for PET drug manufacturing ... thereby [improving] global understanding of issues and challenges facing PET manufacturers." In that spirit, the remainder of this paper discusses each of these 4 themes, along with recommendations for consideration by the FDA.

The Uniformity of FDA Inspections at PET Manufacturing Facilities

A core principle of the PET GMP regulations is uniformity of the radiopharmaceutical supply. Under GMP, it should not matter where a drug is made, or who made it, or when it was made. A drug should always have the quality characteristics described in the application and applicable monograph.

Consequently, it seems self-evident that FDA inspections of PET drug manufacturing facilities should be uniform. As described numerous times by speakers at the workshop, experience among various PET manufacturing facilities has shown this not to be the case. For example, some FDA investigators have used traditional pharmaceutical GMP regulations (21 CFR §211) in the inspection of PET facilities. In other cases, PET facilities have been held to different inspectional standards for operator qualification, sterility testing, environment microbial monitoring, and other aspects of manufacturing. Moreover, speakers at the workshop noted that the incidence of nonuniform inspections seems to have increased recently.

The nonuniformity in FDA inspections potentially results from various factors, including inadequate organizational controls within the FDA, inadequate training of FDA investigators, inconsistent adherence to applicable FDA policies and procedures, ad hoc considerations of conditions for approval, and efforts by individual FDA investigators through "regulation by inspection." Various speakers noted that manufacturing processes evolve, science evolves, and PET manufacturers find new efficiencies. In turn, regulatory standards must evolve commensurately to maintain product quality standards. Along these lines, the regulation-by-inspection approach is often used by individual FDA investigators to spur continuous improvement in a regulated community, and this approach can lead to specific improvements at a specific manufacturing facility. On the other hand, PET manufacturers know that piecemeal implementation is not an effective strategy in a distributed manufacturing environment such as PET. Changes and improvements must be systematically implemented across all 150 PET drug facilities. In fact, a poor change implementation process can do more harm than the intended benefit of the change in the first place. Such is the case with ad hoc changes that inevitably result from nonuniform FDA inspections. Therefore, efforts to spur continuous improvement in PET drug manufacturing facilities should avoid regulation-by-inspection strategies and instead focus on revisions to regulations, guidance documents, and inspection manuals. The PET community has worked diligently to achieve a uniform supply of PET drugs through the adoption of the PET GMP regulations and the implementation of best practices (32). To continue to realize this goal, it is critical that the FDA inspection process be uniformly implemented across all PET manufacturers.

Therefore, the FDA must improve the uniformity of FDA inspections at PET manufacturing facilities. One FDA speaker at the workshop conceded that "the variability of FDA inspections is inevitable." However, the FDA can minimize, if not eliminate, variability in PET inspections by implementing the following 4 recommendations.

First, the FDA should organize a designated team of investigators to inspect PET manufacturing facilities. The team may be organized at the national level or according to regional divisions. The investigators must be trained through a comprehensive program that includes topics such as the intrinsic properties of PET drugs and the characteristics of the PET manufacturing supply chain.

Second, FDA investigators should use a prescribed checklist during inspections of PET manufacturers. This is imperative since deviations in inspectional approaches inevitably lead to nonuniform inspections. To this end, FDA speakers at the workshop described a tablet-based approach to managing inspectional checklists during PET inspections. The FDA should accelerate its efforts on this project and seek guidance on the program from the PET community. Although the FDA stated that sponsors will not be allowed to view screenshots of the tablet screen, the inspectional checklist should be publicly available to the PET community outside the inspection process. This transparency will significantly inform the PET community's efforts toward compliance and ensure a level playing field in the regulated community.

Third, during the development of the PET GMP regulations, the FDA found that product quality depends on the scope and complexity of PET manufacturing facilities. Historically, this finding has provided the FDA with the latitude to adapt inspectional strategies and regulatory actions based on whether a facility is an academic self-producer or a commercial distributor. According to today's understanding of PET manufacturing facilities, "the scope and complexity of operations" do not vary systematically from one facility to another. Some facilities produce larger quantities of a few PET drugs, and other facilities produce a greater variety in smaller quantities. Further, there are no objective metrics to differentiate the complexity of PET manufacturing facilities. In the absence of such metrics, it is reasonable to conclude that all PET facilities are similar in the day-to-day complexity of operations regardless of whether they are associated with an academic medical center or a commercial distributor. Therefore, the FDA should discontinue the practice of defining inspectional strategies and regulatory actions on the basis of whether a facility is academic or commercial.

Fourth, in the event of a disagreement between an FDA investigator and the personnel at a PET facility during an inspection, there are few options available to the PET facility for mediation of the disagreement. At the workshop, a panel discussion on this topic concluded that often the only practical option in this situation is the issuance of a 483 observation. To provide relief in the event of such disagreements, the FDA should implement a formal process for the elevation and mediation of disputes during an inspection. A possible solution would be the implementation of a mediator and resolution process/policy to evaluate disputes during inspections. The mediator should be organizationally outside the chain of command of the ORA, which manages inspections. In this way, the mediator would provide the equivalent of quality assurance oversight for inspections, much like the second-person operational checks that ensure quality and prevent the inherent bias that occurs when operators perform quality control on their own work. This solution would minimally identify variations in regulatory interpretation and provide material support to the guidance-upgrade process.

A Science-Based Risk Profile for PET Drugs

As with all medical procedures, inherent risk factors are associated with PET drugs. Several FDA speakers during the workshop described the importance of risk-based approaches for both the

review of applications for PET drugs and the inspection of PET manufacturers. This approach is consistent with the pharmaceutical quality initiative described earlier in this paper. However, the PET community is not aware of a science-based risk profile that is based on the intrinsic properties of PET drugs and the manufacturing processes used in their preparation. Further, the little information that exists in this area is not uniformly understood within the FDA or across the PET community. Thus, the application of the risk-based approach to PET drugs can be characterized only as a subjective exercise in perceived risk by individual reviewers and investigators.

To correct this deficiency, the FDA should work with PET manufacturers to develop a science-based risk profile for PET drugs. The evaluation of risk factors, rates of occurrence, and mitigating strategies should be based on the characteristics of PET drugs. The risk analysis should consider the intrinsic safety factors of PET drug products, such as the mass of the active radiopharmaceutical ingredient, the likelihood of a pharmacologic response, radioactivity levels, and potential for repeat uses. These factors are already considered in regulatory assessments such as the exploratory investigational new-drug pathway (33). The risk analysis should also include mitigation strategies used in PET manufacturing as described throughout this workshop, including the use of closed systems, presterilized components, aseptic environments, microbiologically lethal processing steps, and other manufacturing steps. The analysis should be published in the peer-reviewed literature and openly available to the regulated community. The results of this exercise, done together with PET manufacturers, will provide transparency to the regulated community and will better inform FDA review practices and inspectional policies according to the PET GMP regulations and guidance.

During the workshop, FDA speakers said that the FDA is revising the PET GMP regulations and associated guidance documents. However, speakers from the PET community described the continued track record of safety associated with PET drugs, thus putting into question the immediate need for revision of the PET GMP regulations, which have been in use for only 10 y since being finalized. If the FDA continues to pursue these revisions, the rule-making efforts should be tethered to the development of a risk profile for PET drugs (as described in the previous paragraph) and therefore may be delayed until this has been completed. This delay will allow for revisions that more accurately reflect actual risk versus perceived risk.

Improvements to Training for FDA Investigators and the Regulated Community

Over time, FDA personnel change and new people become involved in the review of PET drug applications and in the inspection of PET drug manufacturing facilities. Consequently, there is a continual need for educational resources for new entrants in this field.

Continued Dialog Between the FDA and the PET Manufacturing Community

The workshop provided an invaluable forum for the FDA and PET drug stakeholders to exchange ideas, issues, and challenges associated with the regulation of PET drugs. The workshop was only a start: the PET GMP regulations are less than 10 y old, and experiences with the FDA and the PET community will continue to evolve. Long-term, sustainable implementation of new regulations requires time and a routine dialog. It is critical for the FDA and the PET community to share information outside the formal channels of an application review or an inspection.

CONCLUSION

PET drugs have opened the door to molecular imaging and the realization of personalized medicine in the clinical environment. A regulatory framework that maintains the existing PET supply chain, guards against shortages, and ensures continued investment in the expanding pipeline of PET drugs is critical for the long-term health of this important imaging modality. To that end, adoption of the recommendations described in this publication will provide a sustainable supply of safe and effective PET drugs in the clinical environment, thus ensuring widespread patient access to lifesaving diagnoses available only through PET imaging.

DISCLOSURE

Christopher Ignace is an employee of Cardinal Health. Sally Schwarz is employed by Travarex Biomedical part-time. Peter Scott has active research grants from Bristol Myers Squibb, GE Healthcare, AbbVie, Gossamer Bio Inc., and IMRA America Inc.; has clinical trials support from Bristol Myers Squibb; is an owner of SynFAST Consulting LLC; receives editorial royalties from John Wiley and Sons; is an ad hoc consultant for GE Healthcare and the International Atomic Energy Agency; and holds leadership roles in the Society of Nuclear Medicine and Molecular Imaging and the Society of Radiopharmaceutical Sciences. Steven Zigler is an employee of Siemens PETNET Solutions. No other potential conflict of interest relevant to this article was reported.

ACKNOWLEDGMENTS

We thank the Society of Nuclear Medicine and Molecular Imaging, the World Molecular Imaging Society, the Medical Imaging Technology Alliance, and the FDA for sponsoring the workshop.

REFERENCES

1. Orange book: approved drug products with therapeutic equivalence evaluations. FDA website. <https://www.accessdata.fda.gov/scripts/cder/ob/index.cfm>. Accessed May 16, 2022.
2. PET drugs: a workshop on inspections management and regulatory considerations. FDA website. <https://www.fda.gov/drugs/pet-drugs-workshop-inspections-management-and-regulatory-considerations-02212020-02212020>. Published February 21, 2020. Accessed May 16, 2022.
3. SNMMI/MITA Survey of PET Drug Manufacturers, February 4–10, 2020, as described in Introduction to PET drugs. FDA website. <https://www.fda.gov/media/136480/download>. Published February 21, 2020. Accessed May 16, 2022.
4. Silberstein EB. Prevalence of adverse events to radiopharmaceuticals from 2007 to 2011. *J Nucl Med*. 2014;55:1308–1310.
5. Silberstein EB; Pharmacopeia Committee of the Society of Nuclear Medicine. Prevalence of adverse reactions to positron emitting radiopharmaceuticals in nuclear medicine. *J Nucl Med*. 1998;39:2190–2192.
6. Laroche ML, Quelven I, Mazère J, Merle L. Adverse reactions to radiopharmaceuticals in France: analysis of the national pharmacovigilance database. *Ann Pharmacother*. 2015;49:39–47.
7. Kennedy-Dixon T-G, Gossell-Williams M, Cooper M, Trabelsi M, Vinjamuri S. Evaluation of radiopharmaceutical adverse reaction reports to the British Nuclear Medicine Society from 2007 to 2016. *J Nucl Med*. 2017;58:2010–2012.
8. Schreuder N, Koopman D, Jager PL, Kosterink JGW, van Puijenbroek E. Adverse events of diagnostic radiopharmaceuticals: a systematic review. *Semin Nucl Med*. 2019;49:382–410.
9. *Global Imaging Market Outlook Report*. IMV Medical Information Division; 2019.
10. FDA pharmaceutical quality oversight: one quality voice. FDA website. <https://www.fda.gov/media/91721/download>. Accessed May 16, 2022.
11. Other postmarketing reports. FDA website. <https://www.accessdata.fda.gov/scripts/cdrh/cfdocs/cfcfr/cfrsearch.cfm?f=314.81>. Updated March 29, 2022. Accessed May 16, 2022.
12. Current good manufacturing practice for positron emission tomography drugs. FDA website. <https://www.accessdata.fda.gov/scripts/cdrh/cfdocs/cfcfr/CFRSearch.cfm?CFRPart=212>. Accessed May 16, 2022.
13. Guidance: PET drugs—current good manufacturing practice (CGMP). FDA website. <https://www.fda.gov/media/71013/download>. Published December 2009. Accessed May 16, 2022.
14. Positron emission tomography (PET) cGMP drug process and pre-approval inspections/investigations. FDA website. <https://www.fda.gov/media/82370/download>. Published September 11, 2015. Accessed May 16, 2022.
15. Current Good Manufacturing Practice for Finished Pharmaceuticals. FDA website. <https://www.accessdata.fda.gov/scripts/cdrh/cfdocs/cfcfr/CFRSearch.cfm?CFRPart=211>. Updated March 29, 2022. Accessed May 16, 2022.
16. Understanding CDER's risk-based site selection model. FDA website. <https://www.fda.gov/media/116004/download>. Published September 26, 2018. Accessed May 16, 2022.
17. Comparability protocols for human drugs and biologics: chemistry, manufacturing, and controls information. FDA website. <https://www.fda.gov/media/97148/download>. Published April 2016. Accessed May 16, 2022.
18. Electronic records; electronic signatures. FDA website. <https://www.accessdata.fda.gov/scripts/cdrh/cfdocs/cfcfr/CFRSearch.cfm?CFRPart=11>. Updated March 29, 2022. Accessed May 16, 2022.
19. Guidance: media fills for validation of aseptic preparations for positron emission tomography (PET) drugs. FDA website. <https://www.fda.gov/media/81974/download>. Published April 2012. Accessed May 16, 2022.
20. Halvorson HO, Ziegler NR. Application of statistics to problems in bacteriology. *J Bacteriol*. 1933;26:559–567.
21. Bowman FW. The sterility testing of pharmaceuticals. *J Pharm Sci*. 1969;58:1301–1308.
22. Bryce DM. Tests for the sterility of pharmaceutical preparations; the design and interpretation of sterility tests. *J Pharm Pharmacol*. 1956;8:561–572.
23. Sutton S. The sterility tests. In: Moldenhauer J, ed. *Rapid Sterility Testing*. Parenteral Drug Association; 2011:9–13.
24. *ISO Technical Standard 14698-1, Cleanrooms and Associated Controlled Environments—Biocontamination Control, Part 1: General Principles and Methods*. International Organization for Standardization; 2003:32.
25. Pharmaceutical CGMPs for the 21st century: a risk-based approach—final report. FDA website. <https://www.fda.gov/media/77391/download>. Published September 2004. Accessed May 16, 2022.
26. Guidance for industry: Q10 pharmaceutical quality system. FDA website. <https://www.fda.gov/media/71553/download>. Published April 2009. Accessed May 16, 2022.
27. General labeling provisions. FDA website. <https://www.accessdata.fda.gov/scripts/cdrh/cfdocs/cfcfr/CFRSearch.cfm?CFRPart=201&showFR=1>. Updated March 29, 2022. Accessed May 16, 2022.
28. Providing regulatory submissions in electronic format: certain human pharmaceutical product applications and related submissions using the eCTD specifications. FDA website. <https://www.fda.gov/media/135373/download>. Published February 2020. Accessed May 16, 2022.
29. M4 organization of the common technical document for the registration of pharmaceuticals for human use. FDA website. <https://www.fda.gov/media/71551/download>. Published October 2017. Accessed May 16, 2022.
30. Guidance for industry: integrated summaries of effectiveness and safety—location within the common technical document. FDA website. <https://www.fda.gov/media/75783/download>. Published April 2009. Accessed May 16, 2022.
31. CDER Office of Pharmaceutical Quality: report on the state of pharmaceutical quality—fiscal year 2019. FDA website. https://www.fda.gov/media/135046/download?utm_campaign=SBLA%3A%20OPQ%20Issues%20Annual%20Report%20for%202019&utm_medium=email&utm_source=Eloqua. Published June 2020. Accessed May 16, 2022.
32. Coalition for PET Drugs sponsors three sessions at SNMMI annual meeting. Coalition for PET Drug Manufacturers website. <https://coalitionforpetdrugs.org/2017/07/11/coalition-for-pet-drugs-sponsors-three-sessions-at-snmimi-annual-meeting/>. Published July 11, 2017. Accessed May 16, 2022.
33. Guidance for industry, investigators, and reviewers: exploratory IND studies. FDA website. <https://www.fda.gov/media/72325/download>. Published January 2006. Accessed May 16, 2022.
34. Current good manufacturing practice for positron emission tomography drugs. *Fed Regist*. 2009;74:65409–65436.
35. Food and Drug Administration Modernization Act of 1997. govinfo website. <https://www.govinfo.gov/content/pkg/PLAW-105publ115/pdf/PLAW-105publ115.pdf>. Published November 21, 1997. Accessed May 16, 2022.

Tumor Sink Effect: Myth or Reality?

TO THE EDITOR: We thank Prive et al. for their correspondence. As acknowledged in our publication (1), the main limitation of the study is the use of a single-time-point SUV measurement as a surrogate for radiation dose. Differential prostate-specific membrane antigen (PSMA) uptake patterns and tumor-to-background ratios are observed when PSMA PET image acquisition is performed at late time points in comparison to images acquired at 1 h after injection (2–5). Thus, it is clear that images acquired 1 h after injection cannot reflect the biologic effects of ^{177}Lu -PSMA that occur over more than 3 wk (biologic half-life). However, even if not perfectly accurate, PSMA PET imaging performed at 1 h still provides a fair estimate of the patient target expression and of the biodistribution of a PSMA-targeted radiopharmaceutical, and prior studies have reported that pretherapeutic PSMA PET measurements may be correlated with radiation dose to tumor and normal organs from ^{177}Lu -PSMA therapy (6–8).

Regarding the definition of low- and high-volume disease, it is important to note that CHARTED and LATTITUDE criteria were based on conventional imaging (9). Applying these criteria for an analysis of PSMA PET can lead to major discordance in patient stratification, as described previously (10). Therefore, we recommend explicit use of the term *PSMA-VOL* in reference to the whole-body PSMA PET volumetric assessment and not just *low-volume* or *high-volume* metastatic, as follows: very low PSMA-VOL (<25 cm³), low PSMA-VOL (25–188 cm³), moderate PSMA-VOL (189–531 cm³), high PSMA-VOL (532–1,354 cm³), and very high PSMA-VOL ($\geq 1,355$ cm³).

As the authors mention, we agree that patients with low-volume metastatic disease or oligometastases can safely benefit from PSMA-based radionuclide therapy without decreasing the commonly applied dose-activity level of 7.4 GBq per cycle currently in use in the ongoing trial NCT04443062 and as supported by preliminary data (11). On the other hand, our results suggest that the dose-activity level of ^{177}Lu -PSMA could be increased safely in patients with very high PSMA-VOL ($\geq 1,355$ cm³). Nevertheless, these findings warrant further validation by dosimetry studies and safety assessments in prospective clinical trials.

REFERENCES

- Gafita A, Wang H, Robertson A, et al. Tumor sink effect in ^{68}Ga -PSMA-11 PET: myth or reality? *J Nucl Med*. 2022;63:226–232.
- Rosar F, Bartholomä M, Maus S, et al. ^{89}Zr -PSMA-617 PET/CT may reveal local recurrence of prostate cancer unidentified by ^{68}Ga -PSMA-11 PET/CT. *Clin Nucl Med*. 2022;47:435–436.
- Beheshti M, Manafi-Farid R, Geinitz H, et al. Multiphasic ^{68}Ga -PSMA PET/CT in the detection of early recurrence in prostate cancer patients with a PSA level of less than 1 ng/mL: a prospective study of 135 patients. *J Nucl Med*. 2020;61:1484–1490.
- Hohberg M, Kobe C, Täger P, et al. Combined early and late [^{68}Ga]PSMA-HBED-CC PET scans improve lesion detectability in biochemical recurrence of prostate cancer with low PSA levels. *Mol Imaging Biol*. 2019;21:558–566.
- Alberts I, Prenosil G, Mingels C, et al. Feasibility of late acquisition [^{68}Ga]Ga-PSMA-11 PET/CT using a long axial field-of-view PET/CT scanner for the diagnosis of recurrent prostate cancer: first clinical experiences. *Eur J Nucl Med Mol Imaging*. 2021;48:4456–4462.

- Wang J, Zang J, Wang H, et al. Pretherapeutic ^{68}Ga -PSMA-617 PET may indicate the dosimetry of ^{177}Lu -PSMA-617 and ^{177}Lu -EB-PSMA-617 in main organs and tumor lesions. *Clin Nucl Med*. 2019;44:431–438.
- Violet J, Jackson P, Ferdinandus J, et al. Dosimetry of ^{177}Lu -PSMA-617 in metastatic castration-resistant prostate cancer: correlations between pretherapeutic imaging and whole-body tumor dosimetry with treatment outcomes. *J Nucl Med*. 2019;60:517–523.
- Peters SMB, Hofferber R, Privé BM, et al. [^{68}Ga]Ga-PSMA-11 PET imaging as a predictor for absorbed doses in organs at risk and small lesions in [^{177}Lu]Lu-PSMA-617 treatment. *Eur J Nucl Med Mol Imaging*. 2022;49:1101–1112.
- Cornford P, van den Bergh RCN, Briers E, et al. EAU-EANM-ESTRO-ESUR-SIOG guidelines on prostate cancer. Part II—2020 update: treatment of relapsing and metastatic prostate cancer. *Eur Urol*. 2021;79:263–282.
- Barbato F, Fendler WP, Rauscher I, et al. PSMA-PET for the assessment of metastatic hormone-sensitive prostate cancer volume of disease. *J Nucl Med*. 2021;62:1747–1750.
- Privé BM, Peters SMB, Muselaers CHJ, et al. Lutetium-177-PSMA-617 in low-volume hormone-sensitive metastatic prostate cancer: a prospective pilot study. *Clin Cancer Res*. 2021;27:3595–3601.

Andrei Gafita*

Jeremie Calais

Wolfgang P. Fendler

Matthias Eiber

*UCLA

Los Angeles, California

E-mail: agafita@mednet.ucla.edu

Published online Apr. 28, 2022.
DOI: 10.2967/jnumed.122.264119

Thoughts on “Tumor Sink Effect in ^{68}Ga -PSMA-11 PET: Myth or Reality?”

TO THE EDITOR: We read with great interest the recent article by Gafita et al. published in *The Journal of Nuclear Medicine* (1). They observed that patients with a very high tumor load showed a significantly lower SUV in healthy organs on a ^{68}Ga -prostate-specific membrane antigen (PSMA) PET scan, suggesting a tumor sink effect. A comparable observation was also described by Gaertner et al. (2). These authors postulated that a similar effect might occur with PSMA-targeted radioligand therapy. However, dissimilar results regarding the tumor sink effect have also been reported (3).

Although the results of Gafita et al. may support higher treatment activities of ^{177}Lu -PSMA for those with a very high volume of disease ($\geq 1,355$ mL), there were actually no significant differences in the SUV_{mean} of healthy organs between a very low volume of disease (<25 mL) and a high volume (<1,355 mL). These results are in line with what we recently observed in a therapeutic ^{177}Lu -PSMA study on patients with low-volume metastatic hormone-sensitive prostate cancer (4,5). We saw that the dosimetry results based on posttherapeutic SPECT imaging in patients with a maximum of 10 prostate cancer metastases—or a very low volume of metastasis following the definition of Gafita et al.—were comparable to previously reported results on patients with high-volume metastatic prostate cancer (6–8). This result suggests that the sink effect in the setting of low-volume metastatic disease may be of less concern than is commonly anticipated.

COPYRIGHT © 2022 by the Society of Nuclear Medicine and Molecular Imaging.

There are also important limitations to Gafita's study that need to be considered and also apply to the previous work investigating the sink effect. The authors did not take into account tracer pharmacokinetics or perform dosimetry but based their results on a single-time-point SUV as a surrogate for radiation dose. This choice limits the accuracy with which the radiation dose for ^{177}Lu -PSMA can be estimated, particularly as uptake in healthy organs and tumor occurs over a prolonged time (5,9). The observed effect could thus relate to an early differential distribution of tracer to tumors in a very high-volume setting ($\geq 1,355$ mL), which does not exist at later time points. Moreover, the precursor used for PSMA imaging (e.g., PSMA-11) and PSMA therapy (e.g., PSMA-617) generally differ and may thus confound the outcomes. The study was also prone to bias due to its retrospective multicenter design with varying local scan protocols. Therefore, the differences between a very low and a very high volume of disease may have differed using a different study strategy.

All in all, we do believe there is a relevant sink effect but want to emphasize that the present data suggest that patients with a very low volume of metastatic disease or oligometastases can safely benefit from PSMA radioligand therapy and should not be excluded after this recent report. A prospective study with a low oligometastatic volume and a high volume of disease in a homogeneous cohort of patients that includes dosimetry is awaited. Moreover, a post hoc analyses of the VISION data that compares the adverse events (e.g., xerostomia) in patients with low-volume and high-volume metastasis may lead to a better understanding. As a final note, the definition of high volume and low volume used in the studies also differs from what urooncologists think of as high and low volumes, as they generally follow the CHARTED or LATTITUDE criteria (10). We therefore urge future studies to base their reports on criteria that are more commonly used.

REFERENCES

- Gafita A, Wang H, Robertson A, et al. Tumor sink effect in ^{68}Ga -PSMA-11 PET: myth or reality? *J Nucl Med.* 2022;63:226–232.
- Gaertner FC, Halabi K, Ahmadzadehfard H, et al. Uptake of PSMA-ligands in normal tissues is dependent on tumor load in patients with prostate cancer. *Oncotarget.* 2017;8:55094–55103.
- Werner RA, Bundschuh RA, Bundschuh L, et al. Semiquantitative parameters in PSMA-targeted PET imaging with [^{18}F]JDCFPyL: impact of tumor burden on normal organ uptake. *Mol Imaging Biol.* 2020;22:190–197.
- Privé BM, Peters SMB, Muselaers CHJ, et al. Lutetium-177-PSMA-617 in low-volume hormone sensitive metastatic prostate cancer: a prospective pilot study. *Clinical Cancer Research.* 2021;27:3595–3601.
- Peters SMB, Privé BM, de Bakker M, et al. Intra-therapeutic dosimetry of [^{177}Lu]Lu-PSMA-617 in low-volume hormone-sensitive metastatic prostate cancer patients and correlation with treatment outcome. *Eur J Nucl Med Mol Imaging.* 2022;49:460–469.
- Violet J, Jackson P, Ferdinandus J, et al. Dosimetry of ^{177}Lu -PSMA-617 in metastatic castration-resistant prostate cancer: correlations between pretherapeutic imaging and whole-body tumor dosimetry with treatment outcomes. *J Nucl Med.* 2019; 60:517–523.
- Özkan A, Uçar B, Seymen H, Yildiz Y, Falay FO, Demirkol MO. Posttherapeutic critical organ dosimetry of extensive ^{177}Lu -PSMA inhibitor therapy with metastatic castration-resistant prostate cancer: one center results. *Clin Nucl Med.* 2020; 45:288–291.
- Delker A, Fendler WP, Kratochwil C, et al. Dosimetry for ^{177}Lu -DKFZ-PSMA-617: a new radiopharmaceutical for the treatment of metastatic prostate cancer. *Eur J Nucl Med Mol Imaging.* 2016;43:42–51.
- Jackson PA, Hofman MS, Hicks RJ, Scalzo M, Violet J. Radiation dosimetry in ^{177}Lu -PSMA-617 therapy using a single posttreatment SPECT/CT scan: a novel methodology to generate time- and tissue-specific dose factors. *J Nucl Med.* 2020; 61:1030–1036.
- Cornford P, van den Bergh RCN, Briers E, et al. EAU-EANM-ESTRO-ESUR-SIOG guidelines on prostate cancer. Part II—2020 update: treatment of relapsing and metastatic prostate cancer. *Eur Urol.* 2021;79:263–282.

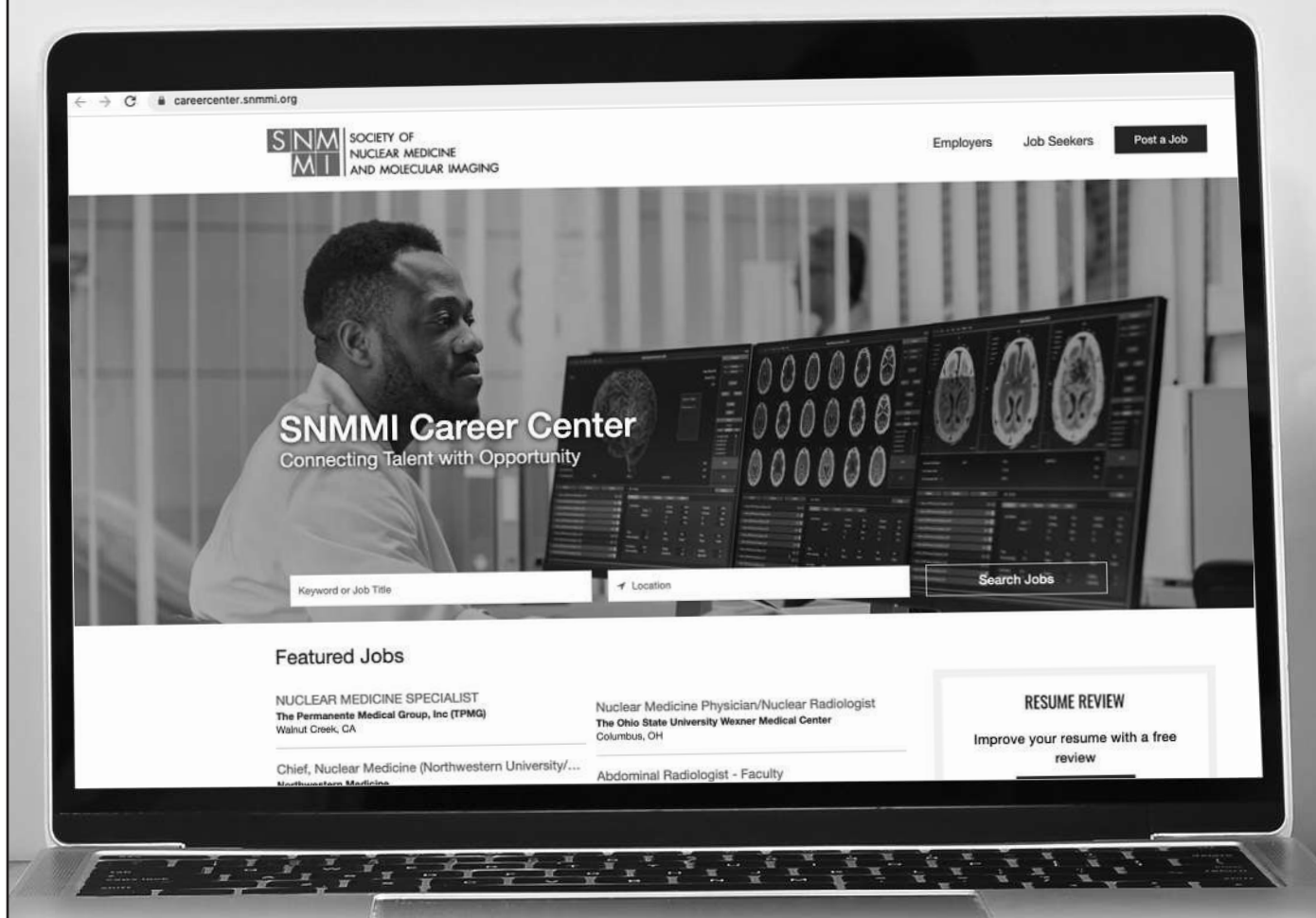
Bastiaan M. Privé*
Steffie M.B. Peters
Maïke J.M. Uijen
Marcel J.R. Janssen
Willemijn A.M. van Gemert
Michael C. Kreißl
Samer Ezzidin
Mark W. Konijnenberg
James Nagarajah

*Radboud University Medical Center
 Nijmegen, The Netherlands
 E-mail: bastiaan.prive@radboudumc.nl

Published online Jan. 13, 2022.
 DOI: 10.2967/jnumed.122.263802

Explore SNMMI's Online Career Center!

Explore the benefits of the SNMMI Career Center by logging in or creating a new account today.



careercenter.snmmi.org

**Note: Single sign-on has been enabled for this platform and you can use your member login credentials to access the Career Center. If you are unsure of your password, to go to the SNMMI password reset link to create a new password.*

RADIATION SAFETY+ Review and Essentials

Let the SNMMI-TS Help You Prepare for the NMTCB's Radiation Safety Exam

Get the tools you need to successfully prepare for the exam with the **Radiation Safety + Review and Essentials** program. This 5 module/7.75 VOICE credit course provides a comprehensive review of all aspects of radiation safety including:

- Radiation physics and instrumentation
- Dosimetry
- Mathematics
- Security and control
- Shipping and receiving
- Disposal
- Emergency procedures
- Regulations
- Radiation protection and ALARA
- Radionuclide therapy best practices

You'll review content on CT, X-ray, fluoroscopy, and MRI, as well as optimizing radiation exposure, including appropriateness criteria, Image Wisely/Image Gently, and special populations. Plus, test what you've learned with a 150 question "Mock Exam," to ensure you're fully prepared for the exam.

Member: \$99 | Non-Member: \$249

Get started today!

www.snmmi.org/RadiationPlus

2022 NMTCB
Radiation
Safety
Exam Dates
Announced!

Begin Your
Preparation!

Order this
popular
program
today!



SPECTRUM
DYNAMICS MEDICAL

VERITON-CT[®]

DIGITAL SPECT/CT



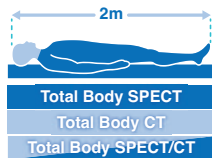
Optimization of Every Step

Spectrum Dynamics has integrated its ground-breaking BroadView Technology design into the VERITON-CT system, providing a digital platform enabling routine 3D imaging in Nuclear Medicine. The result is optimization of every step, from image acquisition to interpretation.

VERITON-CT digital SPECT/CT combines the best-in-class CZT detectors, novel system design, high resolution CT, and advanced software technology to elevate the performance of 360° digital SPECT/CT.



BroadView Technology
Proprietary swiveling detector design provides increased sensitivity for faster scans



Total Body 3D Imaging
200cm continuous coverage vertex to feet
SPECT | CT | SPECT/CT



80cm NM and CT bore
Wide Bore SPECT/CT
80cm NM and CT bore



Choice of 16/64 slice
Choice of high-resolution CT for diagnostic applications and low dose total body CTAC



TruView Console
One platform, one location for clinical care decision-making:
1. Acquisition
2. Advanced quantitative reconstruction
3. Both 3D and 4D data analysis and review

VERITON-CT Feature Application: 3D Dynamic Imaging

TruFlow for VERITON-CT offers real-time 3D in-vivo fast dynamic imaging to capture the radiopharmaceutical distribution, uptake, or clearance over time in 3D SPECT/CT parametric imaging.

TruFlow



The Journal of Nuclear Medicine

July 2022

Vol. 63

Pages 969-1125